POLITECNICO DI TORINO

Dottorato in Energetica – XXVIII ciclo

Design, development and testing of SOEC-based Power-to-Gas systems for conversion and storage of RES into synthetic methane

by

Domenico Ferrero

Thesis submitted for the
degree of Doctor of
Philosophy

Thesis supervisor: Prof. Massimo Santarelli

May 2016

Abstract

International and national initiatives are promoting the worldwide transition of energy systems towards power production mixes increasingly based on Renewable Energy Sources (RES). The integration of large shares of RES into the actual electricity infrastructure is representing a challenge for the power grids due to the fluctuating characteristics of RES. The adoption of long-term, large-scale Electric Energy Storage (EES) is envisaged as the key-option for promoting the integration of RES in the electricity sector by overcoming the issue of temporal and spatial decoupling of electricity supply and demand. Among the several EES options, one of the most promising is the conversion of energy from the electrical into the chemical form through the synthesis of H_2 and synthetic natural gas (SNG) in Power-to-Gas (P2G) systems based on the electrolysis of water (and also CO_2) in Solid Oxide Cells (SOCs). The application of SOC technology in P2G solutions shows attractiveness for the high efficiency of high-temperature electrolysis and the flexibility of SOCs that can operate reversibly as electrolyzers or fuel cells (rSOC) and can directly perform the electrochemical conversion of CO_2 and H_2O to syngas by co-electrolysis. The capability of reversible operation also allows the application of SOC-based systems to Power-to-Power (P2P) concepts designed for deferred electricity production.

This dissertation is focused on the investigation of electricity storage using Power-to-Gas/Power systems based on SOCs. The aim of this Thesis has been the investigation of the thermo-electrochemical behavior of SOCs integrated P2G/P2P systems, with the purpose to identify the system configuration and the operating conditions that ensure the most efficient electricity-to-SNG (P2G) or electricity-to-electricity (P2P) conversion within the thermal limits imposed by state-of-the art SOC materials. To this purpose, a detailed thermo-electrochemical model of an SOC has been developed at cell level, validated on experimental data, extended at stack level and coupled with models of the main P2G/P2P components for the system analysis. Model validation was performed through the characterization of planar commercial SOCs in the reversible operation as electrolyzers (SOEC) and fuel cells (SOFC) with H_2/H_2O and CO/CO_2 fuel mixtures at different reactant fractions and temperatures. The physical consistency of electrode kinetic parameters evaluated from the model was verified with the support of literature studies.

The investigation of SOC-based P2P and P2G solutions was performed using the models developed. Three different configurations were analyzed and simulated: 1) hydrogen-based P2P with rSOC, 2) SOEC-based electricity storage into hydrogen with subsequent SNG production

by methanation with CO_2 and 3) electricity storage by co-electrolysis of water and carbon dioxide with SOEC for syngas production and subsequent upgrading to SNG by methanation.

The performance of the P2P system was thoroughly assessed by analyzing the effects of rSOC stack operating parameters (inlet gas temperature, oxidant-to-fuel ratio, oxidant recirculation rate, cell current) and system configurations (pressurized/ambient rSOC operation, air/oxygen as oxidant/sweep fluid) on stack and system efficiency. The analysis allowed to identify the most efficient configuration of the P2P system, and to select the feasible operating currents (i.e., the currents included within the limits given by the physical thermal constraints of SOC materials) for which the highest roundtrip efficiency is achieved. Pressurized rSOC operation (10 bar) with pure oxygen as oxidant/sweep gas and full recirculation of the oxidant flow ensured the highest charging and discharging effectiveness, with a system roundtrip efficiency of 72% when the stack is operating at the maximum efficiency currents (-1.3 A/cm^2 in SOEC and 0.3 A/cm^2 in SOFC). A dynamic analysis was performed on the rSOC to determine the characteristic times of the thermal response of an SRU coupled with variable loads. The analysis showed that the SOEC is intrinsically more suitable to work with variable loads thanks to the balance between reaction endothermicity and losses exothermicity that reduces the magnitude and the rate of temperature fluctuations originated by current variations. A case study was presented to show the application of P2P with fluctuating RES. In the case study, the sizing of an rSOC-based P2P system designed for the minimization of the imbalance (i.e., the difference between effective and forecasted electricity production) of a 1 MW grid-connected wind farm was performed. An optimal number of cells was found, for which the imbalance is reduced by 77 %. The estimated roundtrip efficiency of the optimal-size P2P system coupled with the wind farm was 54 %.

The P2G systems analyzed are composed by three main sections: a hydrogen/syngas production and storage section based on an SOEC stack; a methanation section based on chemical reactors; and an SNG conditioning section for the upgrading of the produced SNG to grid-injection quality. The design and operating conditions of the SOEC section were selected following the results of the analysis performed on the P2P system, and the SNG production section was designed on the basis of a commercial methanation process based on catalytic reactors. The plant efficiency evaluated by simulations was 65.4% for the H_2-based P2G and 65.5% for the co-electrolysis based P2G without considering cogeneration or thermal integration between plant sections. Even if the efficiencies were similar for the two P2G configurations, the storage capacity of the H_2-based P2G plant was higher, because of the higher operating current achieved by the SOEC stack. The results suggested that even if the co-electrolysis based P2G

system presents a slightly higher efficiency, the choice of a H_2-based P2G option can ensure a better exploitation of the installed capacity, and also eliminates the risks of carbon-deposition in the stack related to the use of carbon containing mixtures and of stack poisoning related to contaminants potentially present in CO_2 streams (e.g., hydrogen sulphide). A case study assessing the effect of H_2S poisoning of the SOEC stack on the P2G system performance was also presented.

The results presented in this Thesis demonstrated that hydrogen-based P2P with rSOCs is the most efficient solution for local RES storage among the different SOC-based EES options investigated. The high values of roundtrip efficiency achieved demonstrated the competitiveness of rSOC-based P2P also with other large-scale EES options (PHS, CAES). The hydrogen-based P2P is however constrained to on-site applications due to the lack of a hydrogen transport infrastructure, while P2G solutions offer the possibility of transferring the electricity stored in the SNG form through the existing natural gas infrastructure, and also allow the direct use of SNG in already existing technologies (i.e., for mobility, heating, etc.), providing the technological bridge for transferring RES power to other markets different from the electrical one.

Sommario

Le politiche ambientali internazionali e nazionali stanno promuovendo un progressivo incremento della componente rinnovabile nel mix di risorse energetiche dedicate alla produzione elettrica. L'immissione di elevate quote di elettricità prodotta da fonti rinnovabili (RES) nelle attuali infrastrutture energetiche rappresenta una sfida per la stabilità delle reti di trasporto, a causa delle fluttuazioni indotte dalle RES nel sistema elettrico. Al fine di promuovere l'integrazione delle risorse rinnovabili nel settore elettrico, è necessario dotare il sistema di produzione e trasporto dell'elettricità di adeguate soluzioni tecnologiche per lo stoccaggio a lungo termine di elevate potenze per fronteggiare gli sbilanciamenti indotti dalle RES attraverso il disaccoppiamento (spaziale e temporale) di produzione e consumo elettrico. Tra le possibili alternative per lo stoccaggio elettrico, una delle più promettenti è quella basata sulla conversione dell'energia elettrica in forma chimica attraverso la sintesi di idrogeno o metano (denominato synthetic natural gas, o SNG) tramite sistemi basati sull'elettrolisi di H_2O (ed eventualmente anche CO_2) in celle a combustibile a ossidi solidi (SOCs). Tali sistemi sono anche conosciuti come sistemi di stoccaggio di tipo Power-to-Gas (P2G). L'impiego della tecnologia SOC in sistemi P2G è particolarmente attraente sia per l'elevata efficienza che l'elettrolisi ad alta temperatura è in grado di garantire, sia per la notevole flessibilità delle SOCs, che possono operare reversibilmente sia come elettrolizzatori che come celle a combustibile e sono in grado di convertire elettrochimicamente miscele di CO_2 e H_2O in syngas tramite il processo di co-elettrolisi. La capacità di operare reversibilmente permette l'impiego delle SOCs sia nello stoccaggio chimico dell'energia elettrica che nella riconversione a elettricità dell'energia chimica accumulata, utilizzando un unico dispositivo. Sistemi che operano in questo modo vengono definiti sistemi Power-to-Power (P2P) e sono impiegati per il disaccoppiamento temporale di produzione e consumo elettrico.

Il lavoro di Tesi ha riguardato lo studio dello stoccaggio elettrico tramite sistemi Power-to-Gas/Power basati su tecnologia SOC. L'obiettivo della Tesi è stato l'indagine del comportamento termo-elettrochimico delle celle ad ossidi solidi operanti in sistemi P2G/P2P, allo scopo di identificare la configurazione di sistema e le condizioni operative che assicurano la maggiore efficienza di conversione dell'elettricità e producono sollecitazioni termiche accettabili per i materiali attualmente impiegati nelle applicazioni SOC. Per raggiungere questo obiettivo è stato sviluppato un modello termo-elettrochimico dettagliato di una SOC a livello di singola cella, validandolo su dati sperimentali, successivamente estendendolo a livello di stack e

accoppiandolo con i modelli dei principali componenti degli impianti P2G/P2P per effettuare l'analisi dell'intero sistema. Per validare il modello sono state testate celle commerciali planari ad ossidi solidi sia in elettrolisi (SOEC) che come celle a combustibile (SOFC) con miscele di H_2/H_2O e CO/CO_2 a diverse composizioni e temperature. I parametri cinetici di elettrodo valutati tramite il modello sono stati verificati con il supporto di studi cinetici riportati in letteratura.

L'analisi dei sistemi P2P e P2G basati su SOC è stata effettuata utilizzando i modelli sviluppati. Tre diverse configurazioni sono state analizzate e simulate: 1) stoccaggio elettrico in idrogeno tramite P2P basato su SOCs reversibili (rSOCs), 2) stoccaggio in idrogeno tramite elettrolisi di H_2O in SOEC e successiva conversione dell'H_2 prodotto in SNG tramite metanazione, e 3) stoccaggio elettrico tramite co-elettrolisi di acqua e anidride carbonica finalizzata alla produzione di syngas tramite SOEC e alla sua successiva conversione in SNG tramite processi di metanazione.

Lo studio effettuato ha indagato in dettaglio il sistema P2P analizzando gli effetti dei parametri operativi dello stack (temperatura di ingresso dei gas, rapporto tra flussi anodici e catodici, frazione di ricircolo del flusso di gas ossidante, corrente elettrica di cella) e della configurazione del sistema (pressurizzato o a pressione ambiente, uso di aria o ossigeno puro come fluido ossidante) sull'efficienza di stack e di sistema. L'analisi ha permesso di identificare la configurazione di sistema più efficiente e di selezionare le correnti operative accettabili (sulla base dei vincoli termici imposti dai materiali delle SOCs) per le quali il sistema P2P opera alla massima efficienza di riconversione (valutata come elettricità rilasciata per unità di elettricità assorbita, anche detta efficienza di roundtrip). Le condizioni operative ottimali individuate prevedono di lavorare con uno stack rSOC pressurizzato (10 bar) con ossigeno puro come fluido ossidante (completamente ricircolato) per ottenere la massima efficienza di carica/scarica, e permettono di raggiungere un'efficienza di riconversione pari al 72 % quando lo stack opera alle correnti ottimali (-1.3 A/cm^2 in SOEC e 0.3 A/cm^2 in SOFC). Lo studio ha anche affrontato l'analisi dinamica della rSOC per determinare i tempi caratteristici della risposta termica di una unità di stack (SRU) accoppiata a carichi elettrici variabili. L'analisi ha mostrato che le celle operanti in modalità SOEC sono intrinsecamente più adatte a lavorare a carico variabile grazie al bilanciamento tra l'endotermicità della reazione elettrochimica e l'esotermicità delle perdite che riduce l'ampiezza e la velocità delle oscillazioni termiche causate dalla variazione della corrente operativa. È stato presentato un caso studio per mostrate l'applicazione di un sistema P2P per lo stoccaggio elettrico da RES. Nel caso studio è stato effettuato il dimensionamento di un sistema P2P basato su rSOC, progettato per la minimizzazione dello sbilanciamento (differenza tra

produzione elettrica effettiva e prevista) di un parco eolico da 1 MW connesso alla rete elettrica. Il dimensionamento ha individuato il numero ottimale di celle dello stack rSOC per il quale lo sbilanciamento viene ridotto al minimo (riduzione del 77 % rispetto al valore iniziale). L'efficienza di riconversione del sistema P2P di taglia ottimale è del 54 %.

I sistemi di tipo P2G analizzati nella Tesi sono composti da tre parti principali: una sezione dedicata alla produzione e stoccaggio di H_2/syngas basata su uno stack SOEC, una sezione di metanazione basata su reattori catalitici, e una sezione per il trattamento del metano sintetico prodotto per renderlo idoneo all'immissione nella rete del gas naturale sulla base dei requisiti richiesti dal gestore della rete. La configurazione e le condizioni operative della sezione SOEC sono state selezionate sulla base dei risultati ottenuti dall'analisi del sistema P2P, e la sezione di produzione del SNG è stata progettata basandosi su un processo commerciale di metanazione. L'efficienza di stoccaggio valutata tramite le simulazioni si attesta al 65.4% per il sistema P2G basato sulla conversione in idrogeno e al 65.5% per il sistema basato sullo stoccaggio in syngas, senza considerare cogenerazione o integrazione termica tra le sezioni dell'impianto. Anche se le efficienze ottenute per le due configurazioni P2G sono molto prossime tra di loro, la capacità di stoccaggio in idrogeno è maggiore, grazie alle più elevate correnti operative dello stack SOEC. I risultati ottenuti mostrano quindi che un sistema P2G basato sulla conversione elettrica in idrogeno oltre a garantire un'efficienza molto prossima a quella di un sistema di co-elettrolisi consente di sfruttare meglio la capacità installata (diminuendo quindi i costi di stoccaggio) e inoltre elimina il rischio di formazione di depositi di carbonio nello stack (legati all'uso di gas contenenti molecole di carbonio) e il rischio di avvelenamento dei catalizzatori catodici connesso all'eventuale presenza di contaminanti (ad esempio acido solfidrico) potenzialmente presenti nell'anidride carbonica utilizzata nel processo co-elettrolisi. In Appendice alla Tesi viene presentato un caso studio in cui si analizza l'effetto dell'avvelenamento dello stack SOEC causato dalla presenza di H_2S sulle prestazioni di un sistema P2G operante in co-elettrolisi.

I risultati presentati nella Tesi dimostrano che lo stoccaggio elettrico tramite idrogeno in sistemi P2P basati su rSOC è soluzione più efficiente tra le varie opzioni analizzate. Le elevate efficienze raggiunte hanno dimostrato la competitività dello stoccaggio elettrico tramite sistemi P2P basati su celle ad ossidi solidi anche nei confronti di altre tecnologie per l'accumulo elettrico di elevata taglia (PHS, CAES). I sistemi P2P basati sullo stoccaggio in idrogeno sono tuttavia vincolati al reimpiego locale dell'elettricità accumulata sotto forma di H_2 a causa della mancanza di un infrastruttura per il trasporto dell'idrogeno. Tali sistemi possono quindi essere impiegati efficacemente solo per il disaccoppiamento temporale tra produzione elettrica e consumo, ma

non per quello spaziale. I sistemi P2G offrono invece la possibilità di trasferire l'elettricità accumulata in forma di SNG attraverso l'esistente rete di trasporto del gas naturale e consentono l'uso diretto del metano prodotto tramite tecnologie mature già disponibili sul mercato (ad esempio nei trasporti o per riscaldamento), fornendo quindi il collegamento tecnologico che consente il trasferimento dell'elettricità prodotta da RES anche su mercati diversi da quello elettrico.

Contents

Chapter 1

Introduction

In recent years, the increasing awareness of the environmental impact of fossil fuels utilization at local and global scale as well as the consciousness of the progressive depletion of fossil resources have been the drivers of a progressive shift towards a resource-efficient, low-carbon economy based on Renewable Energy Sources (RES) to achieve sustainable growth. International and national initiatives are promoting this transition, in particular in the European Union (European Commission 2010). The move towards a renewable-based energy system is progressively increasing the share of intermittent electricity generation and the decentralization of the power system. Temporal and spatial fluctuations of power generation by RES are representing a strong challenge for the structure of the actual power grids. Grid issues arise on the one hand from the lack of an adequate electricity storage capacity that could allocate large excess of intermittent power introduced in the grid (i.e., imbalance issues) and on the other hand from the congestion of power lines that can arise if RES power production is located in areas with limited transmission capacity. The adoption of long-term, large-scale Electric Energy Storage (EES) is envisaged as the key-option for promoting the integration of RES in the electricity sector by overcoming the issue of the temporal and spatial decoupling of electricity supply and demand (IEA 2014, IEC 2011).

In the White Paper on the Electrical Energy Storage from the International Electrotechnical Commission (IEC), the chemical storage of electricity by producing hydrogen and/or synthetic natural gas (SNG) is identified as one of the most promising EES options for large-scale (GW scale), long-term (weekly and seasonal storage, equivalent to TWh scale) electricity storage (IEC 2011, Inage 2009).

Among the several EES options, the conversion of energy from the electrical into the chemical form through the synthesis of H_2 and SNG is the one that also allows the higher flexibility by storing electricity in multi-purpose energy carriers (Lehner et al. 2014). In fact, hydrogen and SNG can be either stored (e.g. in pressurized tanks or in subsurface facilities respectively for short-term or seasonal storage) for deferred electricity production with traditional thermal power generators or highly efficient fuel cells, or used as fuels for

transportation, but also injected in the existing natural gas network – not only for power production, but also for heating and other end-use applications of natural gas – or also used as industrial feedstocks for chemical processes. The development of EES technologies that allow the conversion of electricity to other energy carriers will extend the connection of electric grid to other existing energy infrastructures (i.e., natural gas grid) by providing a flexible multi-product storage solution.

In its most general sense, the concept of the chemical storage of electricity into hydrogen or SNG is called "Power-to-Gas" (P2G). In the specific case of the application of the P2G concept to the time shifting of electricity production by storing and reconverting chemical energy in the same system, the EES solution is identified with the name of "Power-to-Power" (P2P). The P2G concept can be realized with different technologies and architectures, depending on the size and the purpose of the system, and many alternative P2G routes are envisaged as possible applications of the concept, as will be explained in this introductory chapter. In general, P2G systems store electrical energy via electrolysis of water to produce hydrogen, while the synthesis of methane is an additional subsequent step, thus the P2G has its core element in the water electrolysis process.

Several EU projects on P2G/P2P were recently funded, regarding the improvement of RES integration in energy systems through hydrogen production (e.g. DonQuichote, INGRID, ELYGRID, ELYintegration, HYBALANCE) and the development of water electrolysis technologies (e.g ELECTROHYPEM, NEXPEL) (www.fch.europa.eu). All these projects aim at demonstrating kW to MW scale of P2G/P2P concepts based on low-temperature (LT) electrolysis technologies (alkaline and PEM), which have already reached the stage of commercial applications and represent the most applied technologies in the current P2G installations (Gahleitner 2013).

Beside the low-temperature technologies, great interest has been shown also toward the application of high-temperature (HT) electrolysis based on Solid Oxide Cells (SOCs) in P2G systems (Giglio et al. 2015a, Giglio et al. 2015b, Götz et al. 2016). The greatest advantage of HT-electrolysis lies in the favorable thermodynamics that allows lower electricity consumption in the process and higher efficiency with respect to LT technologies. The competitiveness of SOC-based electrolysis toward LT-electrolysis has been experimentally demonstrated (Ferrero et al. 2013) and EU projects on HT-electrolysis development (ADEL, GrInHy) and integration in P2G systems for SNG production (HELMETH) have been recently funded (www.fch.europa.eu).

The application of SOC technology in P2G solutions shows attractiveness not only for the high efficiency of HT electrolysis, but also in terms of fuel and operation flexibility. In fact, Solid Oxide Cells can perform the conversion of electricity to chemical energy and the reconversion of the stored chemical energy to electricity in the same unit with different fuels. Reversible SOCs (rSOC) can operate efficiently with a wide variety fuels: as electrolyzer (SOEC) can electrochemically reduce water and carbon dioxide or mixtures of both to produce hydrogen or syngas (gas mixture rich in H_2, CO and also CH_4 in particular conditions) and as fuel cell (SOFC) can oxidize H_2, CO and CH_4 – or even higher hydrocarbons with proper fuel conditioning – to produce electrical power. This unique flexibility nominates the rSOC applied in the concept of P2G to be an effective competitor to other EES technological solutions.

In recent years, rSOCs have been successfully tested in different configurations: single cells (planar (Ebbesen et al. 2012, Ferrero et al. 2015) or tubular (Laguna-Bercero et al. 2010)), stacks (Nguyen et al. 2013), from ambient pressure up to 10 bar (Jensen et al. 2010). State-of-the-art rSOCs materials are those typically developed for SOFC applications, as the technology benefits mainly from the development for fuel cell applications. However, novel materials are under development for the specific rSOC application (Laguna-Bercero et al. 2011, Choi et al. 2013, Fan et al. 2014). A round-trip efficiency (i.e., ratio between electricity produced from the stored chemical energy and the electricity originally converted in chemical form) higher than 60% has been estimated for hydrogen P2P with rSOC (Graves et al. 2015) and greater than 70% for pressurized large-scale P2P rSOC operation with CO_2 and H_2O aimed at storing electricity in CH_4 (Jensen et al. 2015). A recent study (Graves et al. 2015) demonstrated that the reversible cyclic operation of SOCs made with state-of-the art materials ensures the long-term cell stability required for commercial technological applications, preventing the degradation of materials reported for constant electrolysis operation (Moçoteguy and Brisse 2013).

Given this framework, this dissertation is focused on the design and analysis of P2G systems based on SOC. The work will assess three different P2G configurations: hydrogen-based P2P with rSOC, SOEC-based electricity storage into hydrogen with subsequent SNG production and the electricity storage by co-electrolysis of water and carbon dioxide with SOEC for SNG production. The research will investigate relevant operating conditions through cell, stack and system modeling. A complete thermo-electrochemical and chemical model of an SOC will be developed and validated at cell level and extended at stack level. Energy analysis of the P2G configurations will be performed by considering thermal integration of plant components and chemical SNG generation by methanation.

This introductory chapter briefly explains the motivation of the research and states the research objectives after reviewing the state-of-the-art of EES, P2G and rSOC applications and describing the operating principles of the technologies.

1.1 Motivations and Thesis objectives

This dissertation is focused on the investigation of SOEC-based Power-to-Gas systems. As it will be shown in this introductory chapter, the chemical storage of electricity into hydrogen or SNG is one of the most promising routes to promote the integration of intermittent RES in the electricity sector in the framework of the Power-to-Gas concept. P2G solutions have wide market opportunities, also due to the capability of producing multi-purpose energy carriers. The competitiveness of P2G routes against other EES options strongly depends on the technology involved in the conversion of energy from the electrical to the chemical form. Among the several technological options, great interest has been shown toward the application of high-temperature (HT) electrolysis based on Solid Oxide Cells (SOCs) in P2G systems. The research work has been focused on SOCs due to the several advantages associated to this technology, the main ones summarized as follows:

- Favorable thermodynamics and kinetics of High-Temperature electrolysis (lower electricity demand)
- Possibility of direct recycling CO_2 in co-electrolysis reactions
- Reversible operation as electrolyzer or fuel cell (rSOC)

Even if SOC characteristics make it an ideal candidate for P2G applications, the integration of SOCs in RES-based P2G systems presents several issues due to the peculiarity of the application. In particular, the thermal management of SOC systems is not straightforward as the technology is constrained by the operating temperatures and thermal gradients allowed by materials, while the coupling with P2G systems is characterized by unsteady operation which can eventually lead SOCs stacks to operate inefficiently or in unsafe conditions if a proper thermal control is not applied. The thermal behavior of SOCs is related to the intertwined phenomena that occur in an SOC system in which electrochemical and chemical heat sources contribute to generate complex temperature profiles whose prediction is fundamental to ensure safe and efficient operation. The main factors that determine temperature profiles in an SOC are: 1) electrochemical reactions, which are exothermic (oxidation of H_2 and CO in fuel cell operation) or endothermic (reduction of CO_2 and H_2O in electrolysis), 2) chemical reactions, mainly water-gas shift and CO methanation, which are endothermic or exothermic depending on the equilibrium of the reaction, 3) irreversible heating due to reactions activation and electrical charge flow, 4) gas flows entering/exiting the SOC and 5) thermal insulation of SOC toward the ambient. All these factors

mutually influence each other and the control actions implemented on the SOC to modify one of them have concatenated effects also on the others. The control strategies also affect the Balance of Plant, and as a consequence the energetic (and exergetic) efficiency of the entire system.

The aim of this research is to investigate in detail the SOCs behavior in relevant operating conditions for P2G (also including P2P) applications with the aim of identifying the most efficient system configurations and operating conditions.

To this purpose, a detailed thermo-electrochemical model at cell level has been developed and validated on experimental data collected on planar solid oxide cells. The model has been extended at stack level and coupled with models of the main P2G components for the system analysis. The leading motivation of this research is the lack in the present literature of detailed studies which have addressed the problem of SOC thermal regulation integrated in P2G systems and investigated the effect of SOC operating parameters on the system efficiency. The approach followed is based on developing a SOC model calibrated on state-of-the-art commercial cells and to focus the analysis on the prediction of their behavior in relevant P2G conditions at stack level. Materials on which are based the cells considered in this dissertation are Ni/YSZ for the fuel electrode, YSZ for the electrolyte and lanthanum-based perovskites for the oxygen electrode.

The following objectives will be addressed in this dissertation:

- Establish a thermo-electrochemical model for the prediction of SOC behavior at cell level in both electrolysis and fuel cell operation and validate the model over experimental data.
- Extend the model at the level of Stack Repeating Unit (SRU) and study the stack response to the variation of operating parameters in order to identify the optimal operating conditions and thermal limitations.
- Evaluate system efficiency and effects of operating parameters for three different P2G configurations: hydrogen-based P2P with rSOC, SOEC-based electricity storage into hydrogen with subsequent SNG production, and SOEC-based electricity storage by co-electrolysis of water and carbon dioxide with subsequent SNG production.

1.2 Electrical Energy Storage: technological overview and market opportunities

Electricity grids are characterized by two main features: 1) power generation facilities are usually located far from users' sites and are connected to them by transmission lines with limited capacity and 2) electricity is produced and provided to users with certain quality characteristics (voltage, frequency) that easily deteriorate if an imbalance between supply and demand arise, thus electricity must be consumed at the same time of the production to maintain stability and quality of power supply. These characteristics are the source of several issues in the electricity sector that generate a market need for EES. The integration of fluctuating RES (i.e., solar and wind) in the electricity grids further increases the complexity of the management of electricity distribution and extends the market opportunities for EES. Actual applications of EES are mainly related to short-term (i.e., hourly and daily) electricity storage; however the forecasted expansion of RES penetration will open new market opportunities also for long-term EES (i.e., weekly and seasonal).

This chapter will outline the roles of EES in compensating the issues affecting the electricity systems, with a particular focus on the problem of fluctuating RES integration. Roles and markets for EES will be assessed by taking into account the characteristics of different technologies to highlight the present and future opportunities for P2G systems in the context of EES applications.

1.2.1 The role of Electrical Energy Storage

The management of electricity production and transmission must face several issues related to electricity grid characteristics. The main issues and the compensating role of EES identified by IEC (IEC 2011) can be summarized as follows:

- Long distance between generation and consumption: power generation is usually located where there is availability of primary energy sources – both renewable and fossil – or where there is an easy connection to their importation networks in the case of fossil resources. Consumers are often very far from generation facilities and electricity network connections between supply and demand areas can reach considerable length (hundred kilometers). The longest the connection, the higher are the transmission losses and the risk of failures due to natural disasters (e.g. hurricanes, lightning and ice storms) or operational failures (e.g., accidents and overloads). Low-size EES located at consumer sites can ensure continuity of

power supply in case of network failures (e.g., UPS batteries). Moreover, larger EES installations located in strategic positions of the electricity network near users' areas can temporary supply electricity to multiple customers in case of interruption of the connection with generation facilities.

- Congestion in power grids: when the amount of power required to the grid exceeds the capacity of transmission lines overloads arise that can lead to the interruption of the service. Possible solutions are to build new power lines and/or shift the production nearer to the users. However, in a future electricity sector based on high share RES (mainly solar and wind), the power production plants will be located where RES are geographically available and thus only strong reinforcements of power networks would avoid congestion problems. The installation of EES at the end of congested lines can mitigate this issue by storing electricity near demand areas when connections with generation facilities are available and releasing the electricity in periods of peak demand. This approach can avoid or delay the construction of long and costly network infrastructures.
- Imbalance between supply and demand: electricity must be provided at the time the user needs it. If an amount of power lower of higher than required is introduced in the grid, an imbalance arises and the power quality deteriorates leading eventually to a service interruption. The actual grid regulation relies on accurate forecasts of demand variations and on the fine control of the output power of generating facilities that allows following the demand fluctuations second-by-second. This kind of regulation is possible only if the power generators can provide a positive and negative output margin, that is the possibility to increase or decrease rapidly the produced power on demand. Electricity generation based on fluctuating RES cannot provide positive margins when resources are not available, thus this role is played by other generators that can increase the released power when requested. This means to have sufficient installed capacity ready to go on-stream when there is lower RES availability. In future energy systems with high share of RES, if this role will be assigned to thermal generators, the electricity generation sector will have a high thermal power capacity operated inefficiently with very low utilization factors and thus not economically acceptable. The solution will be the use EES to provide regulation capability. The combination of RES with large-scale EES will allow to store sufficient amounts of electricity for regulation purposes. This EES application is already in use in the present electricity system with pumped hydro installation used to provide demand peaks.

- Need for cable connections: wireless transport of electricity is impossible. Therefore, the connection of mobile electrical devices (e.g., cars) or extremely remote areas – where is even not viable the local electricity generation – is not possible without the use of EES.
- Variability of generation costs: the price of electricity changes during the time of the day accordingly with the demand. During demand peaks price is higher and electricity is provided by flexible power generators (i.e., oil and gas fired plants) costlier than base-load plants. In off-peak periods, costly generation is not convenient and also surplus production from RES has a very low or even negative value on the market. This can eventually lead to the curtailment of RES generation when the cost of production is higher than the value of the produced electricity on the market. In the context of the economic value of electricity, EES allows the time-shifting of electricity production, enabling the base-load generation utilities to increase the produced power and store the excess electricity produced to provide it to the grid during peak periods when electricity reaches the higher prices. RES utilities can also benefit from EES by storing surplus electricity production and thus reducing generation costs by reselling it to the grid in peak demand periods. Finally, also consumers can perform demand time-shifting by buying electricity at low price in off-peak periods, storing it into batteries and use or re-sell it during peak hours.

From the previous discussion it can be highlighted that the integration of fluctuating RES generation affects almost all the issues identified and increases the complexity in the management of electricity distribution. In particular, the electricity produced by these sources is strongly intermittent on both short-term and long-term scales. This characteristic opens two different application opportunities for EES: short- and long-term storage. The first application represents the actual market for EES. In the analysis from KEMA (Grond et al. 2013), the service applications that short-term EES technologies should provide for the integration of intermittent RES in the electricity sector are identified in seven main categories:

- Frequency support: availability of ready-to-use reserve for mitigating supply/demand imbalance (e.g. in case of sudden decrease of wind power generation) with instantaneous discharge of power and short duration.
- Uninterruptable Power Supply (UPS): provide emergency power to a user when power supply is interrupted. Variable EES size from 1 kW to 1 MW depending on the application. Quick response and duration of power supply from minutes to few hours.

- Community Energy Storage (CES): EES is required for district-level energy storage. Power capacity required is in the size of MW and the supply duration is few hours.
- Home Energy Storage (HES): similar to CES, but with a dimension suitable for households (kW size).
- Forecast Hedging: stored energy is used to adjust the difference between real RES production and forecasted production to avoid penalties to RES utilities on the electricity market if their production is lower than the forecast. EES required size is up to hundreds MW and the discharge duration is few hours.
- Time shifting: storage of energy generated in low-demand periods and discharge in high-demand periods to optimize the utilization of renewable electricity by avoiding its curtailment.
- Transmission & Distribution (T&D) capacity management: use of electricity storage to mitigate the congestion in power grid in order to avoid the size upgrade of power networks.

Beside the aforementioned roles in the short-term storage, long-term EES is expected to play a fundamental role in future energy systems with high share of RES by ensuring the energy capacity required to address seasonal storage needs, as explained in *Section 1.2.3*. However EES should not be seen as the only possible measure to cope with high shares of volatile electricity production, as load management – both in supply and demand sector – and improvement of grid capacity are alternative realistic options. Another option is the overinstallation of RES capacity in different areas of high capacity power grids to ensure sufficient electricity generation also in periods with weakly RES production. Depending on the future extension of RES introduction in the electricity sector, it is likely that a combination of all these measures have to be implemented to provide technically and economically feasible solutions to RES integration.

1.2.2 Technological review of EES

EES technologies are usually classified according to the form of energy in which the electricity is stored. *Figure 1.1* shows the classification given by Fraunhofer ISE (Weber 2013) that identifies five energy forms for electricity storage: mechanical, electrochemical, chemical, electrical and thermal.

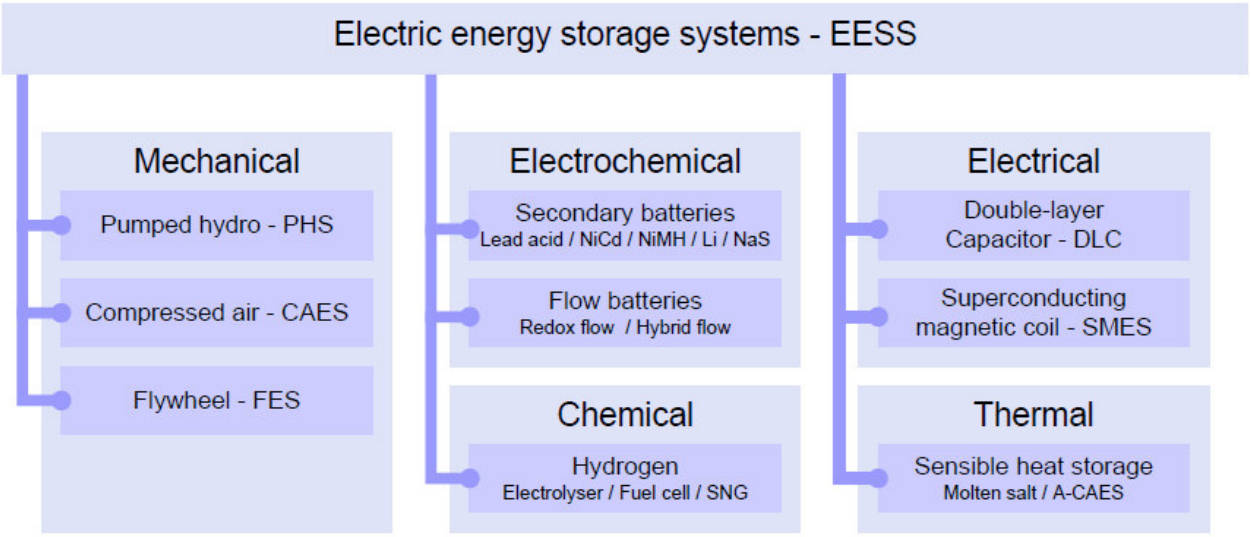

Figure 1.1 – Classification of energy storage systems. (Weber 2013)

Storage systems with their peculiar characteristics can be summarized as follows:

- Mechanical storage
  - Pumped hydro storage (PHS): according to Electric Power Research Institute (EPRI), PHS plants represent the more than 99% of the current world-wide EES capacity with 140 GW installed (IEA 2014). PHS installations use two water basins at different elevations to pump water from lower to upper basin to store electricity in potential energy to be mechanically recovered by using water turbines. Generally used for storing electricity for periods ranging from several hours to several days with a round-trip efficiency of around 80%, PHS systems supply electrical power for daily peak load coverage. PHS can provide large-scale and relatively long-term EES, but the expansion potential of these plants is strictly limited by geographical and environmental reasons (land use).
  - Compressed air storage (CAES): uses electricity to compress air and store it in pressurized vessels or underground reservoirs. Electricity recovery is performed by mixing the compressed air with natural gas, burning it and expanding the gases in a gas turbine. CAES systems with no heat recovery during air compression have round-trip efficiencies of around 50%. CAES can provide large-scale EES, but has a limited efficiency and suffers from geographical limitations (i.e., availability of underground caverns).

- Flywheel energy storage (FES): electricity is used to accelerate a rotating mass and energy is maintained by keeping constant the rotational speed of the flywheel. Electricity is obtained by decelerating the mass. FES can achieve high round-trip efficiency (80-90%) with a very fast response time and it is suitable for short-duration operation.

- Electrochemical storage
  - Secondary batteries: energy is stored in the active masses of the electrodes. Many typologies of batteries exist already mature for the market. The main ones are: lead acid (LA), NiMH, Li-ion, metal air, sodium sulphur (NaS) and sodium nickel chlorides (NaNiCl or ZEBRA). All secondary batteries are characterized by fast-response and high efficiency (60-90%). NaS and ZEBRA batteries require high operating temperature and have energy-to-power ratios that allow their use for daily storage. Li-ion batteries are the most flexible batteries that can potentially operate with discharge time of weeks for long-term storage; however the high cost actually limits the applicability to short-term storage (i.e., hours).
  - Flow batteries: electricity is charged in an electroactive species dissolved in liquid electrolytes that are stored in external vessels. The charge and discharge of the batteries is realized by flowing the electrolytes through the devices. Redox (RFB) and Hybrid (HFB) are typical flow batteries. The roundtrip efficiency is between 60% and 75%, with a size that can reach several MW and a storage duration from hours to days.

- Chemical storage: in general, chemical storage identifies all the possible conversions from electricity to other chemical energy carriers. In fact, beside the production of hydrogen and SNG on which this dissertation is focused, the synthesis of methanol, formic acid, dimethyl ether (DME) or other liquid fuels (i.e., diesel, kerosene) has been considered for the chemical storage of electricity (Budzianowski 2012, Centi and Perathoner 2014, de Vries et al. 2015, Schaub et al. 2013). In particular, two other concepts alternative to P2G have been proposed on the market by industries: “Power-to-Liquids” and “Power-to-Chemistry” (Hebling et al. 2016). The first one is focused on the catalytic conversion of hydrogen obtained by water electrolysis to liquid fuels through the reaction with CO_2 in the Fischer-Tropsch synthesis (Graves et al. 2011a, Holtappels 2013). The second one proposes the use of renewable electricity in an arc furnace to convert methane to acetylene and hydrogen. Other chemical storage options investigate

the production of ammonia from electrical-driven synthesis processes with or without the use of hydrogen; in the first case, NH_3 is produced from H_2 obtained by water electrolysis (Lan et al. 2012). In general, almost all the chemical storage routes (with very few exceptions) achieve the energy conversion from electricity to chemical bonds in the dissociation of water and/or carbon dioxide through electrolysis. The product is hydrogen (water electrolysis) or syngas (co-electrolysis of water and carbon dioxide), the first being either the final chemical output of the process or a precursor for further chemical processing and the second being always an intermediate product of a longer process chain. Therefore, the several chemical storage processes mainly rely on the production of a gaseous product or precursor. This research work will investigate in detail P2G options; a comprehensive review on P2G is given in *Chapter 1.3*. However, few details on hydrogen and SNG storage options are listed below to highlight the main technological differences of the two solutions:

- Hydrogen storage: electricity is supplied to an electrochemical cell to split water molecules and produce hydrogen and oxygen in separate chambers. Three main water electrolysis technologies, namely alkaline electrolysis (AEL), polymer electrolyte membrane electrolysis (PEMEL) and solid oxide electrolyte electrolysis (SOEC), are actually employed. The first is based on a low-temperature (70–100 °C) liquid electrolyte, PEM on a low-temperature (40–80 °C) solid electrolyte, while SOEC is based on a high-temperature (650-1000 °C) solid ceramic electrolyte. AEL and PEMEL are commercially available and currently represent the most applied technologies in P2G systems (Gahleitner 2013). The efficiency of electricity-to-hydrogen conversion depends on applied technology, system architecture and storage conditions (i.e., pressure level) with values in the range of 50-70%; when hydrogen is not compressed the system efficiency is higher (Sterner at al. 2011a). The reconversion of hydrogen to electricity can be performed in fuel cells (the same device of the electrolyzer in case of rSOC, given that electrical storage and electricity production are inevitably decoupled in time) or in conventional natural gas feed power plants, if hydrogen is injected in the NG grid. The round-trip efficiency depends on the reconversion process, Graves et al. (2015) indicate a value of 63% for rSOC without considering water vaporization and system inefficiencies. Lehner et al. (2014) report round-trip values of 34-44% considering the compression to 80 bar

and 60% of hydrogen-to-electricity efficiency. In comparison to other chemical storage paths based on electrolytic hydrogen as a fuel precursor, the hydrogen-based P2G is the fastest and most efficient way to store electricity. In fact, H_2 production is a one-step process that enables to reduce the complexity, cost and inefficiencies of conversion system based on longer process chain. Moreover, H_2 synthesis does not require a CO_2 source. Nevertheless, the conversion of H_2 to other energy carriers is attractive mainly because a hydrogen infrastructure (i.e., transport grid and end-use technologies) is currently missing and the maximum content of H_2 allowable in the NG grid is limited (see *Chapter 1.3*).

- Synthetic natural gas storage: the SNG electricity storage is a P2G process composed by two main steps: hydrogen or syngas production via electrolysis and methane synthesis by catalytic and biological reactions (Götz et al. 2016). The first step can be realized by electrolysis of water or co-electrolysis of water and carbon dioxide; in the first case AEL, PEM and SOEC technologies can be applied, while the co-electrolysis is possible only by using SOECs. In the second step, the exothermic hydrogenation of CO/CO_2 to CH_4 takes place. From the thermodynamics point of view, low temperature and high pressure are favorable conditions for methane synthesis. The efficiency of methanation process in reported to be 70-85% for the catalytic synthesis and higher than 95% for the biological production, with a total electricity-to-methane conversion efficiency of 50-65%, (Lehner et al. 2014). The produced SNG usually contains significant amounts of steam, and must be upgraded to meet the gas quality requirements for the injection in NG grids. Once SNG is produced, the reconversion to electricity can be performed in conventional natural gas feed power plants connected to NG grid or also in SOFCs that can reach higher conversion efficiencies. In this case, the operation with pure NG is not feasible and the use of steam-NG mixtures for external/internal reforming of methane is needed. The roundtrip efficiency is inevitably lower than that of hydrogen-based electricity storage. Lehner et al. (2014) report round-trip values of 30-38%. The efficiency disadvantage is balanced by the availability of an already existing NG infrastructure in which SNG-P2G systems can be integrated.

- Thermal storage: in the EES context, this is an “indirect” type of storage in which heat used in electricity generation processes is stored and re-used in a different time for the

power generation. An example of application is the heat storage in the electricity production by concentrating solar plants. Energy is stored in a molten salt heated by solar radiation and stored in a tank. The hot salt is used to produce steam which is fed to a steam turbine to generate electricity. In this case the hot storage can be seen as a form of EES because it allows the decoupling of solar energy acquisition and electricity production. Another form of thermal storage from electricity is the recovery of compression heat from CAES and its use for pre-heating the air when electricity is recovered. In general, all the types of heat recovery and storage for later use in electricity generation belong to this category.

- Electrical storage
  - Double-layer capacitors (DLC): electricity is stored in supercapacitors with high specific power density and up to MW size. This technology allows very fast charge/discharge cycles with high efficiency (90%), but is not suitable for long-term energy storage due to high self-discharge rates.
  - Superconducting magnetic energy storage (SMES): energy is stored in the magnetic field generated by the current flowing in a superconductor kept at very low temperature. Instantaneous response time and high efficiency are the main advantages of SMES; however, the need for an expensive refrigeration system and the high cost makes this application suitable only for niche applications (i.e., physics experiments and power quality control in microchip fabrication).

Figure 1.2 (IEA 2014) shows the EES grid-connected capacity currently installed worldwide.

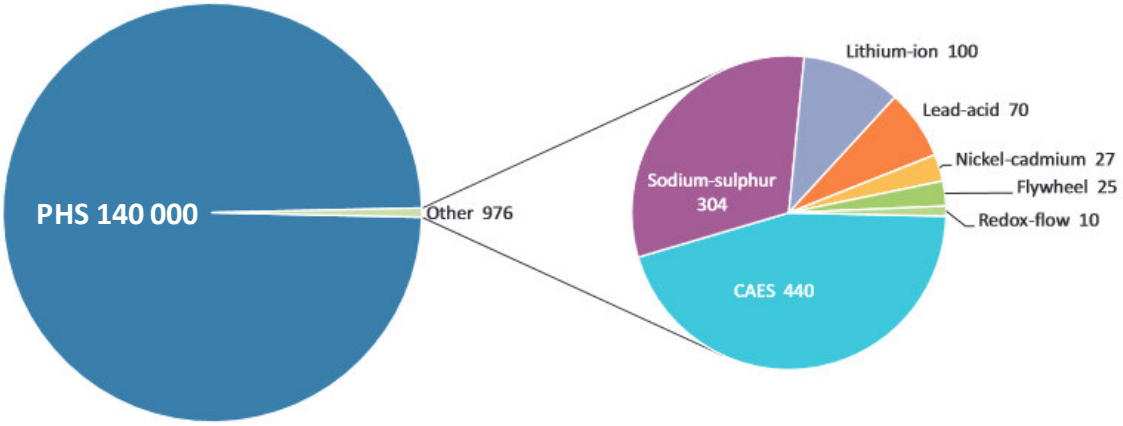

Figure 1.2 – Grid-connected electricity storage capacity (MW). (IEA 2014)

A comparative overview of the different technologies is given in *Figure 1.3*, where the EES options are organized with respect to rated power and energy capacity. Also the discharge time is indicated on the plot. Most of the technologies are modular and can be implemented to a larger scale; however, size restrictions mainly arise from economic reasons and topographical availability of suitable sites (i.e., water basins for PHS, underground storage for CAES and large-size P2G options not fully integrated with NG grids). PHS, CAES, H_2 and SNG are the only technologies available for high power ranges, with the chemical storage being the only with enough energy capacity to ensure up to TWh storage. Moreover, if we consider the energy density of these EES options, CAES and PHS have values in the range of 0.2-6 Wh/l, while P2G is three orders of magnitude higher with 600-1800 Wh/l (data from IEC 2011). Another important parameter is the response time of the technologies that determines their applicability to the short-time storage applications introduced in *Chapter 1.2.1*.

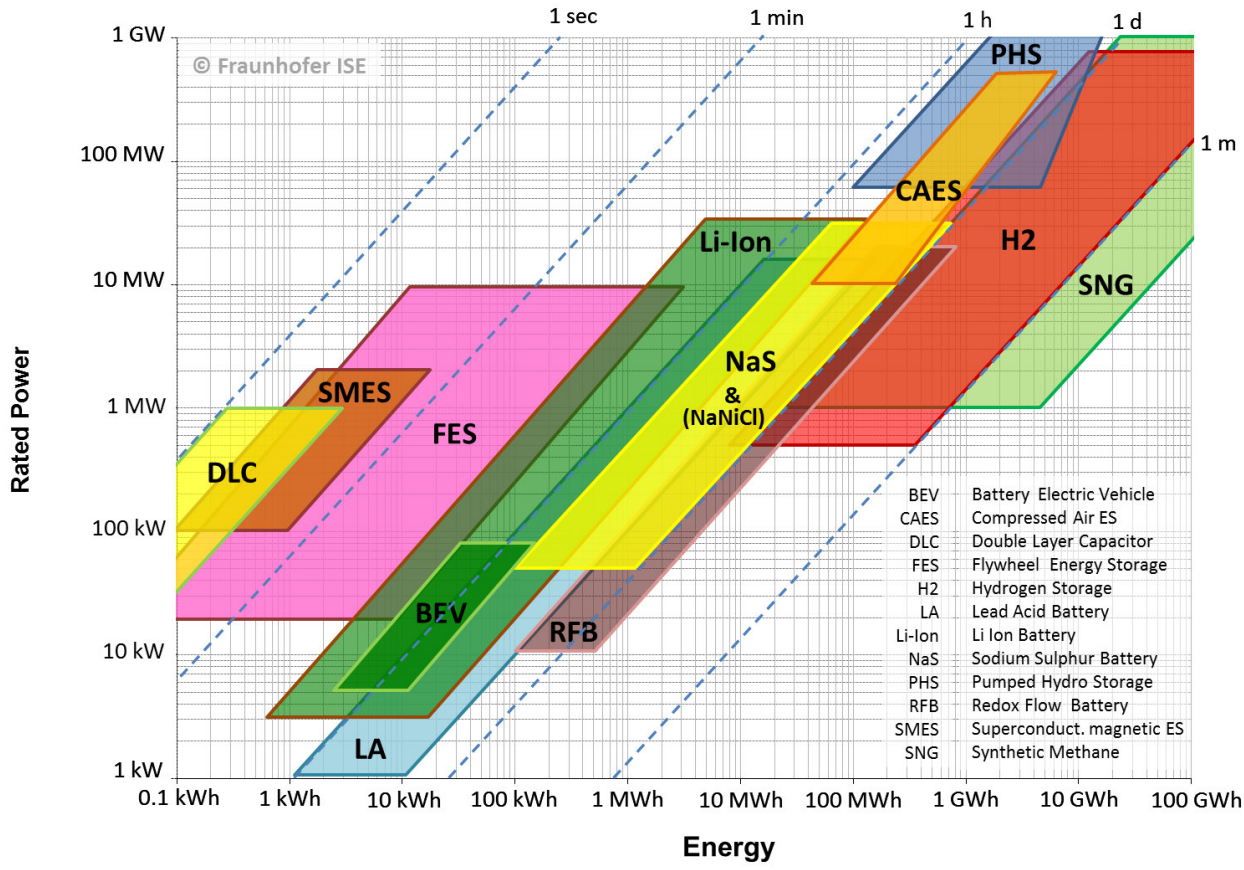

Figure 1.3 – Comparative assessment of Electric Energy Storage technologies. (Weber 2013)

Electrochemical, chemical storage and FES have a response time in the order of the second or even less, while CAES, PHS and SNG have response times of minutes. Hydrogen-based P2G

can have a response time of few seconds in the case of hot-start, while the cold-start with PEM and AEL can take few minutes, and that with SOEC can last also several hours.

Figure 1.3 shows that many EES systems can cover the demand for short and medium discharge times with a wide range of rated power. Several of these technologies, in particular FES, DLC and battery systems are mature and already available on the market. In the large-scale size, only CAES and PHS are currently available to ensure medium discharge times. For long discharge times (GWh – TWh storage) no commercial EES options are actually available and only P2G technologies show the potential to cover this sector. The P2G technology is still under development and several pilot and demonstrating plants have been realized or are under design (*Chapter 1.3*). Thanks to learning curve effects and economies of scale, the cost of this new technology is expected to decrease. In the benchmark assessment of Walker et al. (2015) is shown that the Power-to-Gas has the potential to achieve very low cost per kWh with respect to other EES technologies.

Finally, from the comparison of the different EES options, it is concluded that a technology that can cover all the energy and power ranges and thus satisfy all the different EES requirements does not exist, only a combination of different EES options can provide the solution for the actual and future issues of the electricity system.

1.2.3 Market opportunities

In this section, the present and future market opportunities for EES – and in particular for P2G – are briefly highlighted. As stated before, the present EES applications offered on the market are for the short-term storage.

The actual EES systems implemented by electric utilities are for time-shifting, power quality (i.e., maintaining voltage and frequency), postponing investment by mitigating network congestion through peak shift, providing stable power for off-grid systems and providing emergency power supply. From the consumer's side, the main uses of EES are in the time-shifting (i.e. load leveling for saving cost by buying off-peak electricity and storing it in EES) and for backup purposes to secure reliable and higher-quality power supply, the last use especially for factories and commercial facilities.

Several studies on the future market potentials for EES are presented in the IEC White Paper on the Electrical Energy Storage (IEC 2011) that identifies five new trend for EES applications: renewable energy integration, smart grids, smart microgrids, smart houses and electric vehicles. In particular, the integration of high shares of RES in the electricity sector will increase the

short-term storage market and will also generate a long-term EES demand for ensuring the energy capacity required to address seasonal storage needs. In a study by Fraunhofer ISE (Sterner et al. 2011b) the future market trend for EES in Germany – the leading country in RES introduction, with 80% planned for 2050 – is assessed. The study gives an overview on the evolution of different typologies of EES power demand by time range (i.e., hourly, daily, weekly and monthly). Results are shown in *Figure 1.4*.

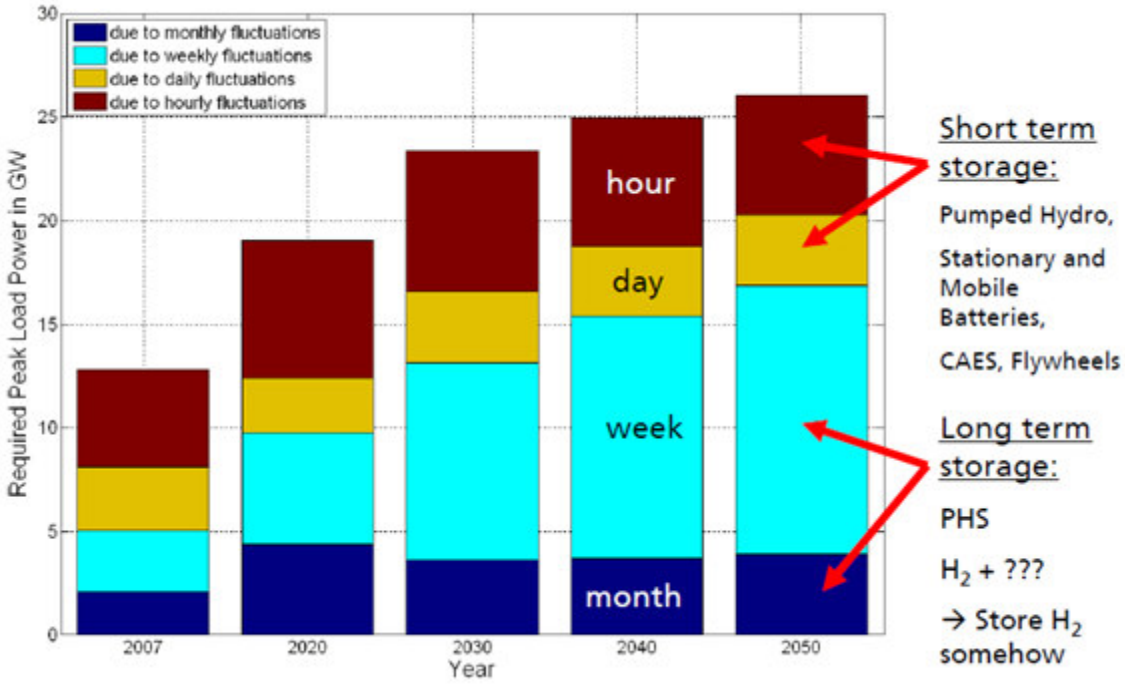

Figure 1.4 – Evolution of the distribution of required peak power by time range in Germany. (adapted from Sterner et al. 2011b)

The planned RES introduction is expected to increase the demand for weekly and monthly storage, reaching a total of 8.2 TWh needed in 2030 against 0.2 TWh required for short-term storage. Comparing with the actual storage situation, in 2013 the German Feed-in-Management resulted in 550 GWh of unused electricity that EES could recover (Bundesnetzagentur Monitorinbericht 2014). In the study, it is expected that chemical storage in H_2 and SNG will cover the long-term storage demand. In particular, the injection of H_2 and SNG in the German natural gas grid, which has 200 TWh of storage capacity, is envisaged as the key-option that allows to store large amounts of energy easily accessible for power production at any point of the NG grid. Limitations are identified for the hydrogen-based storage, whose amount in the NG grid cannot exceed 7 TWh due to technical limitations (see *Chapter 1.3*), but that can still cover a large fraction of the 8.2 TWh needed in 2030.

A study of the International Energy Agency (IEA) (Inage 2009) addresses the worldwide EES market potential to cope with RES penetration in the electricity sector. The study estimates an EES demand for 189 GW to 305 GW in 2050 to face the generation variations due to RES fluctuations.

1.3 Power-to-Gas: technological overview

The review of technologies and future markets for EES has shown how the massive introduction of RES will enhance the demand for large-scale, long-term electricity storage. Chemical storage by production of hydrogen and/or SNG is identified as one of the most promising EES options to cope with this demand. The concept of chemically store electricity into hydrogen or synthetic natural gas is called "Power-to-Gas" (P2G). P2G is the EES option that also allows the higher flexibility by converting electricity in multi-purpose energy carriers that can be either stored for deferred electricity production, or used as fuels for transportation, but also injected in the existing natural gas network – not only for power production, but also for heating and other end-use applications of natural gas – or also used as industrial feedstocks for chemical processes. The connection of electric grid to other existing infrastructures for energy transport and storage and the high volumetric energy density of the chemical medium are the main advantages of the P2G storage solution with respect to the other EES options.

This chapter will provide a technological overview on P2G by illustrating operating principles and analyzing the potential applications.

1.3.1 Introduction to Power-to-Gas: operating principles

The Power-to-Gas concept identifies all the possible routes for the conversion of electricity into a gaseous chemical medium. The energy conversion from electricity to chemical bonds is achieved by the dissociation of water and/or carbon dioxide through electrolysis. The product is hydrogen (water electrolysis) or syngas (co-electrolysis of water and carbon dioxide), the first being either the final chemical output of the process or a precursor for further chemical processing and the second being usually an intermediate product of a longer process chain. Therefore, the several P2G routes rely on the production of a gaseous final product or precursor by electrolysis.

When the purpose of P2G installation is to store electricity to chemical energy and reconvert the chemical energy to electricity in the same plant, the solution is identified with the name of "Power-to-Power" (P2P).

Figure 1.5 shows the general principle of Power-to-Gas concept based on water-electrolysis. Water-electrolysis P2G is the chemical storage route technologically closer to commercial application thanks to the use of already developed technologies for electrolysis and chemical

processing for the production of SNG or other chemicals (Schiebahn et al. 2013, Lehner et al. 2014, Schiebahn et al. 2015).

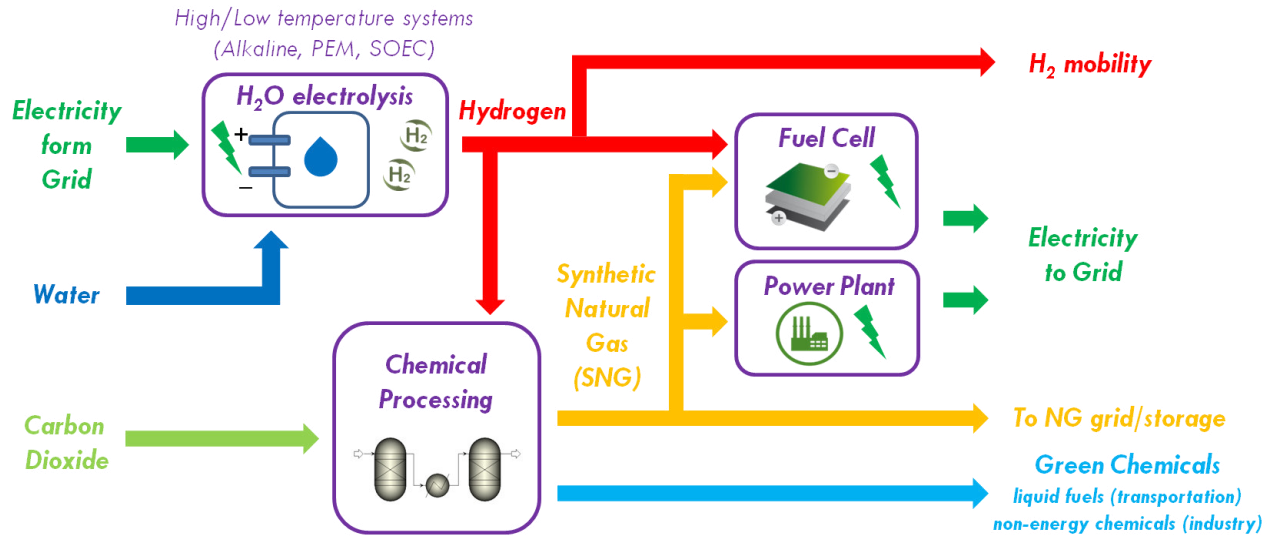

Figure 1.5 – Schematic of the Power-to-Gas concept based on water electrolysis.

Alkaline, PEM or SOEC electrolysis can be applied for the water splitting process. The former two are low-temperature technologies commercially available and currently are the most applied in P2G systems (Gahleitner 2013), the latter is the least mature technology that is experiencing great development in recent years thanks its attractiveness due to the higher efficiency and great flexibility in terms of fuel and operation. More details on the electrolysis technologies are given in the next Section (see *Section 1.3.1.1*).

In the case of P2P, produced hydrogen can be stored on-site in pressurized vessels (100~300 bar) in small amounts (0.1-10 MWh) or liquefied in cryogenic storages (0.1-100 GWh) (IEA 2015). Another solution is the high-density storage in solid metal hydrides. Large amounts of hydrogen can be stored in underground salt caverns of size up to 500,000 m^3 with operating pressure between 60 and 180 bar, corresponding to a storage capacity of 124 GWh (Bünger et al. 2016). The efficiency of electricity-to-hydrogen conversion and storage depends on applied technology, system architecture and storage conditions (i.e., pressure level) with values in the range of 50-70% or even higher when hydrogen is not compressed (Sterner at al. 2011a).

The reconversion of hydrogen to electricity can be performed in fuel cells or in conventional natural gas power plants (i.e., combustion turbines or gas engines) if hydrogen is injected in the NG grid. In this case hydrogen is mixed with natural gas, with a variable concentration in the NG

mixture between 0-12% depending on the country standards and regulations (Götz et al. 2016). The conditions required for the injection in the NG grid depend on the grid architecture, for example the German grid is divided into three supply levels operated at different pressure levels (i.e., national at 80 bar, regional at 4-6 bar, local supply lower than 4 bar) (Schiebahn et al. 2013), thus depending if the hydrogen is injected at national or regional level the pressure required can be different.

Fuel cells are currently the only option for direct on-site electricity production from stored hydrogen, as gas turbines capable of burning pure hydrogen currently do not exist at commercial level, while gas turbines adapted to burn gases with high hydrogen content (up to 45%) are commercially available (IEA 2015). On-site hydrogen reconversion is thus performed by fuel cells (alkaline, PEM or SOFC) (Gahleitner 2013) that can efficiently produce electricity from a pure hydrogen stream. The use of a reversible technology that can produce hydrogen from electricity and also reconvert the hydrogen to electricity in the same device (given that productions e re-use are necessarily taking place at different times) is envisaged as the option that shows economical advantages with respect to separate production and use through different technologies. In fact, the reversible use allows to increase the operating hours and capacity utilization and to reduce the investment cost by unifying production and use in a single device. The EU project GrInHy is investigating the option of using reversible Solid Oxide Cells for this purpose due to the superior electricity efficiency of SOC technology. The rSOC technological route for P2P will be assessed in this dissertation by cell, stack and system modeling, details and results are given in the next Chapters. Oxygen is needed for the electrochemical oxidation of H_2 and fuel cells usually utilize ambient air to provide the oxidant; however, if the oxygen produced during water electrolysis is stored, fuel cell can re-use it and work with a pure oxygen stream, achieving a higher performance. The effectiveness of this solution will be assessed in this dissertation (see *Chapter 5*). The efficiency of electricity production in fuel cells depends on the technology; values between 50-70% can be expected (IEA 2015).

The round-trip efficiency of H_2-based P2P depends not only on the electrolysis and reconversion processes, but also on the BoP. Graves et al. (2015) indicate a value of 63% for an rSOC P2P solution at atmospheric pressure without considering water vaporization and system inefficiencies. The global round-trip efficiency for Power-to-Power hydrogen-based systems reported by Lehner et al. (2014) stands at values of 34-44% considering H_2 compression to 80 bar and 60% of hydrogen-to-electricity efficiency. This research will assess the global round-trip efficiency of a H_2-based P2P solution with rSOC. Results of the analysis are shown in *Chapter 5*.

Alternative routes to P2P are the direct utilization of H_2 for transportation or industry, or its upgrading to SNG or other chemicals.

Hydrogen as transportation fuel is envisaged as a possible solution for the reduction of the emissions in the transportation, in particular in the road transport, which accounted for 75% of all transport emissions in 2012 (IEA 2015). Different pathways to use hydrogen as a fuel in transport are feasible, e.g. conversion to SNG for compressed natural gas vehicles or to methanol and direct use in Fuel Cell Electric Vehilces (FCEV). However, only FCEVs allow the direct use of hydrogen in transportation for a fully carbon-free mobility. The projections presented in the 2DS high H_2 scenario of the IEA "Technology roadmap for Hydrogen and Fuel Cells" indicate a share of FCEVs in total passenger car sales around 30% by 2050 (see *Figure 1.6*). Therefore, the demand from mobility is potentially expected to be a considerable market for P2G-produced hydrogen. In addition to the P2G-related efficiency and costs, the evaluation of the P2G-hydrogen option for transport purposes should take into account also hydrogen transport to the refueling stations (in case of centralized production) and of the gas compression into vehicle tank. In fact hydrogen for mobility applications requires high storage pressure on board, usually 350 or 700 bar in pressurized vessels, while actual commercial electrolyzers provide hydrogen at lower pressures (30 bar is the commercial standard).

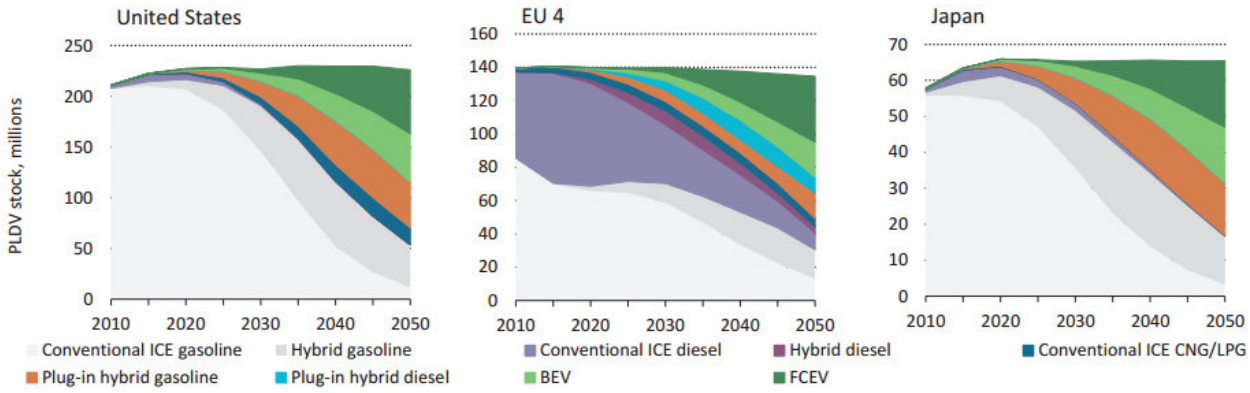

Figure 1.6 – PLDV (Passenger Light-Duty Vehicles) stock by technology in USA, EU 4 (France, Germany, Italy and the United Kingdom) and Japan (IEA 2015).

Hydrogen is currently widely applied in the industry, from chemical and refining to metallurgical, glass and electronics (Ramachandran and Menon 1998). Industrial hydrogen is commonly produced by steam-reforming of methane; the adoption of a different H_2 source strongly depends on the final cost of the produced hydrogen. Thus, the industrial sector would

represent a major end-use option for P2G-produced hydrogen, when it will reach economic competitiveness on the market.

An alternative path to electrification or direct utilization in industry and transportation is the conversion of hydrogen obtained by water electrolysis to SNG or other fuels. The second path has been investigated in particular for the production of liquid fuels (e.g., DME) through the reaction of H_2 with CO_2 in the Fischer-Tropsch synthesis. The production of SNG requires the availability of carbon-sources (e.g. from fossil power plants, biomass, industrial processes and air) and different technologies – mainly divided in chemical and biological – are currently available for SNG synthesis. More details on carbon sources and SNG synthesis technologies are given in the next section. Produced SNG can be injected in natural gas grid without particular limitations (given that it reaches the quality requirements of the NG grid) and reconverted in all the electricity generation facilities that accept NG as a fuel (included fuel cells). The efficiency of methanation process in reported to be 70-85% for the catalytic synthesis and higher than 95% for the biological production, with a total electricity-to-methane conversion efficiency of 50-65%, (Schiebahn et al. 2013). The global round-trip efficiency of the process including the reconversion to electricity stands at values of 30-38% (Schiebahn et al. 2013, Lehner et al. 2014).

For P2P applications, the hydrogen-based route is the fastest and most efficient. In fact, H_2 production is a one-step process that enables to reduce the complexity, cost and inefficiencies of conversion system based on longer process chain with SNG or other chemical carriers. Moreover, H_2 synthesis does not require a CO_2 source. Nevertheless, the conversion of H_2 to SNG is attractive mainly because a hydrogen infrastructure (i.e., transport grid and end-use technologies) is currently missing and the maximum content of H_2 allowable in the NG grid is limited. A different Power-to-Gas concept based on the co-electrolysis of water and carbon dioxide is illustrated in *Figure 1.7*.

The co-electrolysis consists in the contemporaneous dissociation of H_2O and CO_2 in an electrochemical cell. This application is only possible in SOEC electrolyzers which allow the direct utilization of CO_2. The high operating temperature of SOEC cells is sufficient to promote both homogeneous and heterogeneous reactions between fuel components (H_2O, CO_2, H_2, CO and CH_4); thus, chemical reactions occur in parallel to CO and H_2 production by electrolysis. However, reactions within the gas phase are very slow when compared to the heterogeneous ones, thus the homogeneous chemistry can be safely neglected within fuel mixtures (Zhu et al. 2005). The porous structure of the fuel electrode – a Ni/YSZ cermet in state-of-the-art cells –

acts as a catalyst for the heterogeneous reactions and typically promotes water gas shift (direct and reverse), steam reforming and methanation reactions.

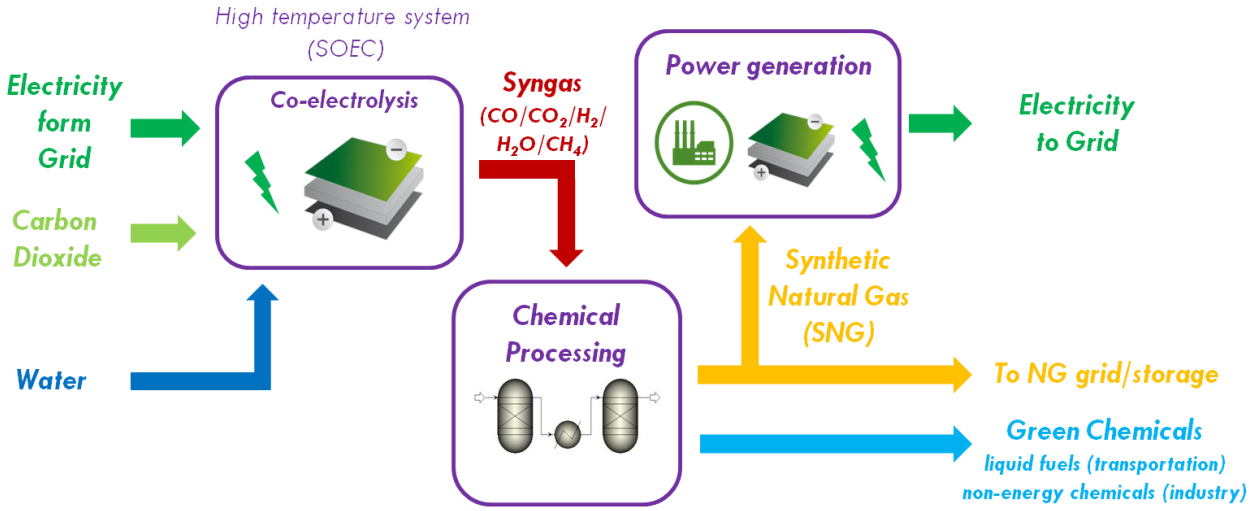

Figure 1.7 – Schematic of the Power-to-Gas concept based on co-electrolysis.

Other reactions that can occur are dry reforming, Boudouard and methane cracking, depending on operating conditions (i.e., temperature and pressure), materials and partial pressures of chemical species. The co-electrolysis option has been proposed by many authors and experimentally demonstrated at cell and stack scale (Ebbesen et al. 2009, Ebbesen et al. 2012, Fu et al. 2010, Graves et al. 2011a, Zhan et al. 2009). The concept of the proposed applications is to produce a syngas that can be upgraded to SNG or liquid fuels. A Power-to-Power configuration based on co-electrolysis has been proposed by Wendel at al. (2015a) and Jensen et al. (Jensen et al. 2015). In their work, the application of an intermediate-temperature rSOC stack operating at high pressure (20 bar) has been proposed to integrate methanation and electrolysis in the electrolysis unit. Operating conditions and materials favors the methanation reaction and a methane-rich syngas is produced. The syngas is stored in underground caverns and re-electrified in the SOC stack. The round-trip efficiency of the modeled system is higher than 70%, thanks to the thermal synergies between endothermic electrolysis reactions and exothermic methanation.

The option of SNG production in a co-electrolysis based P2G system has been investigated in this dissertation; results are given in *Chapter 6*.

1.3.1.1 Electrolysis technologies

Electrolysis technologies use electricity to split water (or carbon dioxide) molecules into hydrogen and oxygen (or carbon monoxide and oxygen). This section will provide a brief review

on electrolysis technologies, focusing mainly on water electrolysis and in particular on high-temperature electrolysis based on SOEC. The thermodynamics of the process will be discussed in *Chapter 2*.

The basic equipment common to all the electrolysis technologies is the electrochemical cell, constituted by two electrodes and an electrolyte. The electrochemical reactions that take place at the fuel-feed (i.e., feed with H_2O or CO_2) electrode generate ions (positive or negative depending on the technology) from the molecule dissociation, which are transferred through the electrolyte layer (solid or aqueous), while the electrodes are electrically connected to a power load that impose a potential difference between them to force the charge motion. Electrochemical reactions, type of ions conducted by the electrolyte, materials and operating conditions depend on the specific electrolysis technology; however, the overall reaction (1.1) of water electrolysis is the same for all them:

$$H_2O_{(l/g)} + electricity \rightarrow H_{2(g)} + \frac{1}{2}O_{2(g)} \tag{1.1}$$

In the case of CO_2 electrolysis, the basic reaction is similar:

$$CO_{2(g)} + electricity \rightarrow CO_{2(g)} + \frac{1}{2}O_{2(g)} \tag{1.2}$$

Electrolysis of water is the earliest hydrogen generation method that has been developed and commercialized (Zoulias et al. 2004) and nowadays, the electrolytic hydrogen accounts for the 4% of the worldwide hydrogen production (Mergel et al. 2013). A variety electrolysis processes which involve the dissociation of carbon dioxide – mostly in combination with water – to CO or other chemicals (e.g., methanol, ethylene, etc.) have been studied; a review is provided by Graves et al. (Graves et al. 2011a). None of these processes has been currently commercialized. Due to the focus of this dissertation on SOC-based P2G options, only the SOEC co-electrolysis of CO_2 and H_2O has been considered.

Three main types of water electrolysis technologies are actually available: alkaline electrolysis (AEL), polymer electrolyte membrane electrolysis (PEMEL) and solid oxide electrolyte electrolysis (SOEC). The respective operating principles and characteristics will be described in the following subsections.

Alkaline water electrolysis

Alkaline electrolysis (AEL) is the current standard technology for industrial water electrolysis. The operating principle of AEL is depicted in *Figure 1.8*.

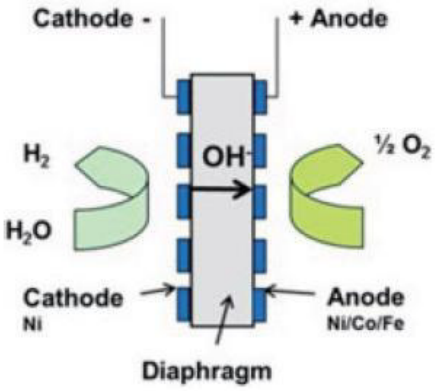

Figure 1.8 – Schematic of alkaline electrolysis cell. (Mergel et al. 2013)

The AEL cell is composed of two electrodes (mainly based on Nichel alloys), immersed in an aqueous solution of potassium hydroxide (KOH) or sodium hydroxide (NaOH) electrolyte. The reactions taking place at the electrodes involve hydroxide ions:

$$\text{Cathode} \qquad 2H_2O_{(l)} + 2e^- \rightarrow H_{2(g)} + 2OH^-_{(aq)} \tag{1.3}$$

$$\text{Anode} \qquad 2H_2O_{(l)} + 2e^- \rightarrow H_{2(g)} + 2OH^-_{(aq)} \tag{1.4}$$

A microporous diaphragm (usually based on sulfonated polymers) separates the anodic and cathodic chambers ensuring the motion of the negative ions between the chambers and avoiding the mixing of produced H_2 and O_2. The product gases are mixed with the electrolyte, thus a recirculation loop for their separation from the mixture is needed. Once hydrogen and oxygen are separated, the electrolyte is pumped back into the cell. During cell operation only water is consumed and has to be supplied to the electrolyte solution to maintain the hydroxide concentration at the desired level (20-40%). Conventional AEL systems reach the MW scale and operate at 70-90 °C and high pressures (up to 30 bar) with current densities in the range of 0.2-0.5 A/cm^2 (see *Figure 1.11*). AEL electrolyzers reach efficiencies of 60-80% and can operate at 20-100% of rated power without suffering of performance and gas quality deteriorations. In the context of P2G applications, the low current densities and the limited dynamic capability are the major limitations of the AEL technology.

Proton Exchange Membrane electrolysis

Proton Exchange Membrane (PEM) electrolyzers are less developed than AEL systems and are available on the market for smaller applications. The operating principle of PEM is depicted in *Figure 1.9*.

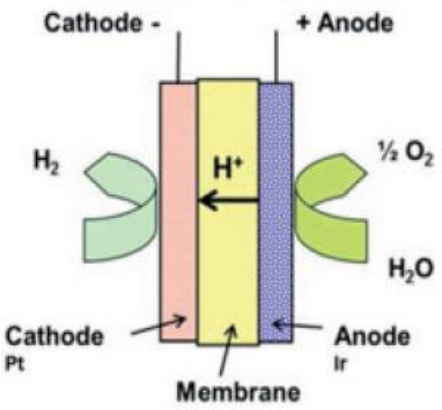

Figure 1.9 – Schematic of Proton Exchange Membrane electrolysis cell. (Mergel et al. 2013)

The electrolyte is a thin proton conductive membrane (usually based on a perfluorosulfonic acid, i.e., Nafion) which is in contact with the electrodes where the following electrochemical reactions take place:

$$\text{Anode} \qquad H_2O_{(l)} \rightarrow \frac{1}{2}O_{2(g)} + 2H^+_{(aq)} + 2e^- \qquad (1.5)$$

$$\text{Cathode} \qquad 2H^+_{(aq)} + 2e^- \rightarrow H_{2(g)} \qquad (1.6)$$

Cathodes are made by carbon-based materials with Pt and Pt-Pd catalysts, while anodes are made by TiO_2, TaC or SiC structures that supports Ru-Ir catalysts. Anode is fed with liquid water that dissociates following the oxidation reaction (1.5) producing hydrogen ions that are delivered through the membrane to the cathodic side, where hydrogen gas is released. Typical operating temperatures are lower than 80 °C due to the need for liquid water in state-of-the-art electrolyte membranes (i.e. Nafion) to ensure proton conductivity. PEM systems can work at elevated pressures (30-60 bar for most of the commercial PEM) and current densities (1-2 A/cm^2). This technology has a very high dynamic capability that allows PEM systems to operate in the whole range of rated power following highly variable loads. System efficiencies are in the range of 60%-70% and the higher size PEM stacks are in the scale of hundreds kWs. PEM

systems are well-suited to highly flexible operation and appear to be the most important competitor to alkaline systems for P2G applications in the short term.

Solid Oxide Electrolysis Cells

High-temperature electrolysis in Solid Oxide Cells has attracted great interest in recent years due to the opportunity of reducing the electricity demand of the electrolysis process. A brief introduction to SOECs is given in this subsection; the state-of-the art and a complete description of the technology are given in the next section, while the thermodynamics are described in *Chapter 2*.

A solid oxide electrolyzer cell (SOEC) is based on a thin, dense solid ceramic electrolyte that is conductive for ions (usually oxygen) at high temperature. Electrodes are porous solid structures attached to the electrolyte. The general schematic of a SOEC cell is shown in *Figure 1.10*.

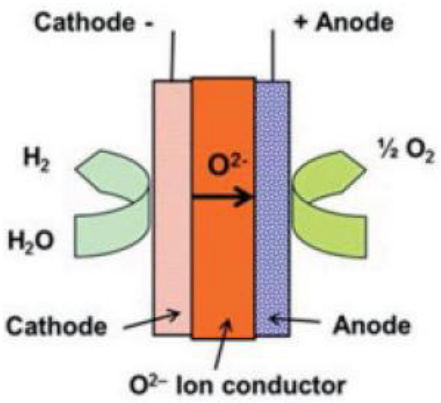

Figure 1.10 – Schematic of Solid Oxide Electrolysis Cell. (Mergel et al. 2013)

Water is fed at the cathode, where it reduces to form hydrogen gas and oxygen ions (1.7). The oxygen ions migrate through the membrane and react at the anode where oxygen gas evolves according to reaction (1.8).

$$\text{Cathode} \qquad H_2O_{(g)} + 2e^- \rightarrow H_{2(g)} + O^{2-} \tag{1.7}$$

$$\text{Anode} \qquad O^{2-} \rightarrow \frac{1}{2}O_{2(g)} + 2e^- \tag{1.8}$$

The focus of this dissertation is on conventional SOC based on oxygen-ion conductive electrolytes, for which the above described reactions are valid. However, also proton conductive

solid oxide cells have been developed, a complete review on this typology of cells is given in the work of Bi et al. (2014).

SOECs have been developed in different geometries (i.e., planar and tubular) and configurations (i.e., cathode, electrolyte or metal supported). More details on these technological aspects are given later in the next section. In general, the lower power density achieved by tubular cells due to the longer current paths has limited their development and application with respect to the planar ones (Hussain et al. 2009).

High temperatures (650–1000°C) are required for the solid oxide membranes to operate properly. Due to the high operating temperature, water is fed at the cathode as steam, which is generated outside the electrolyzer either using external heat sources and/or recovering the heat from the streams exiting the cell or, in the case of P2G applications, also from the exothermic processes (i.e., methanation) of the complete system. The heat recovery is a fundamental aspect of the BoP of SOEC systems, especially because the cooling of hydrogen and oxygen streams exiting the cell is necessary when the flows are compressed for storage purposes.

Cell components are made of ceramic materials. Compatibility and stability of cell materials at high temperatures are of particular importance. State-of-the art materials are Yttria-stabilized Zirconia (YSZ) for the electrolyte, Ni-based cermets for the cathode and perowskite oxides for the anode. Ceramic interlayers are often introduced between electrolyte and electrodes to enhance the compatibility of the materials and avoid undesired reactions between the components of the layers. More details on SOEC materials are given in the next section.

SOEC systems have been widely tested at ambient pressure; however high-pressure operation up to 15 bar has been demonstrated at lab-scale on a 10-cell stack (O'Brien et al. 2012) The higher reported operating current density for SOECs at thermoneutral voltage (1.3 V, see *Chapter 2* for the explanation of thermoneutral) is 3 A/cm^2 at 950 °C (Jensen et al. 2007); however, a practical range is between 0.5-1 A/cm^2 to avoid fast cell degradation, which is reported to be related to the current density level (Mougin et al. 2012). A brief review on SOEC degradation is given in the next section. To date, the larger size SOEC system ever operated is a 15 kW stack, tested in INL laboratories for 1000 h (Stoots, et al. 2010); however the scale-up of SOEC systems to larger size seems to be near, as Sunfire announces that 200 kW stacks will be available on the market already in 2016 (http://www.sunfire.de). The efficiency evaluation for SOECs strongly depends on the heat management of the system. In fact, the energy required by the electrolysis reaction is provided partly by electricity and partly by heat. In particular, when the SOEC is operating under the thermoneutral voltage (see *Chapter 2* for further explanations)

heat must be provided from an external source, while at thermoneutral the SOEC is able to thermally self-sustain the electrolysis and finally over this voltage heat must be removed from the SOEC. The maximum theoretical efficiency can be considered 100% at thermoneutral voltage if the system is perfectly insulated from the ambient, as all the electrical energy provided to the SOEC is available in the produced hydrogen. However, this value of efficiency is not considering the heat consumed for the production of steam, or it is assuming the availability of free-steam or free heat sources for heat vaporization. In other words the 100% efficiency is calculated at the higher heating value (HHV) of hydrogen, while a lower value results if the lower heating value (LHV) is considered (Mathiesen, et al. 2013). When the SOEC system is operating over the thermoneutral, the electrolysis produces excess heat besides hydrogen. If the heat is fully recovered, the maximum theoretical efficiency can be considered 100% on HHV basis also over the thermoneutral, while if this heat is considered lost, the efficiency is lower (Minh and Mogensen 2013). Mougin reports an SOEC system efficiency of 89% on HHV taking into account also losses in electrical converters and thermal auxiliaries and compares this value to the system efficiency of PEM (63%) and alkaline (58%) electrolysis (Mougin 2015). Solid Oxide Cells can provide very fast power regulation (0-100% within few seconds) only at their operating temperature; hence SOEC systems require to be maintained at high-temperature to provide the operation flexibility and fast-startup required by P2G applications. The cold startup requires long times (hours) and the thermal cycling can cause degradation due to the thermo-mechanical stresses suffered by the stack assembly made by materials (metallic interconnects, ceramic cells, glass-ceramic sealants) with different thermal expansion behaviors. Therefore, since frequent startup and shutdown must be avoided, the integration in P2G systems is feasible if SOC is maintained at high-temperature also when RES electricity is not available, either through the idling in hot stand-by or by operating as fuel cell.

A conclusive comparison with the other electrolysis technologies is not possible, as SOEC systems have not yet reached the maturity of alkaline and PEM electrolyzers. However, it is worth to briefly investigate the main advantages and disadvantages with respect to low-temperature technologies.

The main advantage of SOEC is the high-temperature operation that is beneficial from the thermodynamic (lower electricity requirements) and kinetic (high reaction rates and low overvoltages without using precious metal catalysts) point of views. Lower electricity required and lower overvoltages result in a favorable current-voltage SOEC characteristic, which is

compared with that of alkaline and PEM technologies in *Figure 1.11*, a plot widely used in literature and here reported in the IEA version.

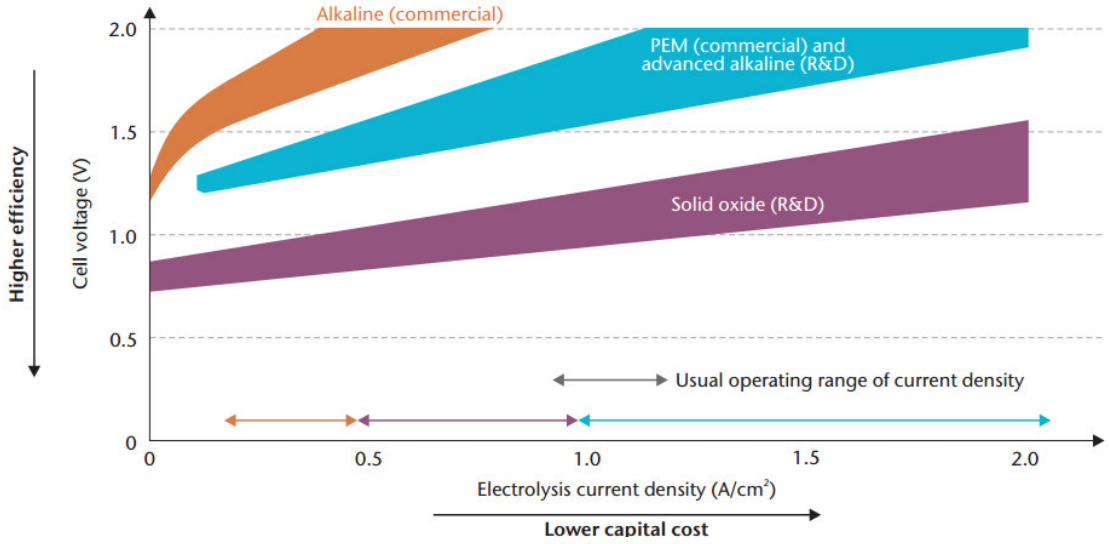

Figure 1.11 – Comparison of Alkaline, PEM and SOEC electrolysis technologies. (IEA 2015).

A lower voltage enables higher efficiency – as for SOECs – and a higher current density is related to higher hydrogen production, given a fixed electrolyzer area. Previous experimental work (Ferrero et al. 2013) has shown that an electrolyzer based on state-of-the-art SOEC cells can widely compete with a PEM system in terms of efficiency also considering system components. Economical considerations are strictly related to the current-voltage characteristics of the electrolyzers. In particular, higher efficiency means lower operational costs and higher hydrogen production rate means lower capital cost. The cost of the produced hydrogen is the indicator that encloses both these aspects. A technology comparison based on the levelised cost of hydrogen is given by Mougin (Mougin 2015). The study indicates a selling price for SOEC-produced hydrogen of 11.2 €/Nm^3/h against 11 €/Nm^3/h of PEM and 6.5 €/Nm^3/h for alkaline production. The expected technological progresses of SOEC in durability, performance and stack design as well as mass production are expected to lower the selling price to 5 €/Nm^3/h. The price of hydrogen is obviously dependent on the electricity price, if electricity not produced on-site but is bought from the grid. The effect of electricity price on the hydrogen cost is shown in *Figure 1.12*.

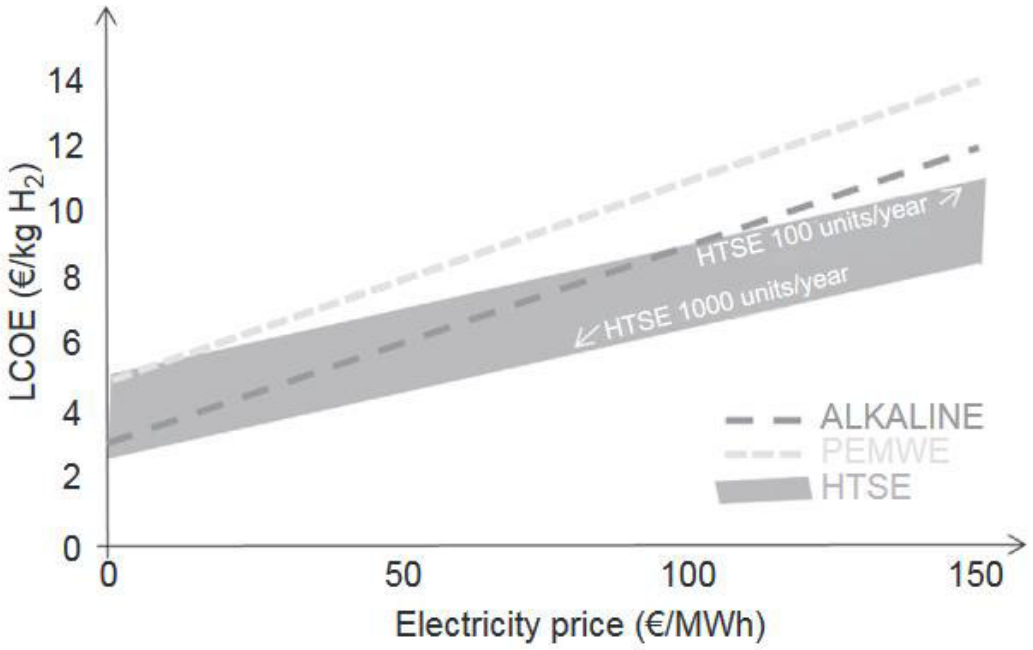

Figure 1.12 – Levelized cost for hydrogen production from alkaline, PEM and SOEC electrolysis. (Mougin 2015)

The trend of LCOE price shown is due to the lower electricity consumption of SOEC related to the high efficiency of the system that allows higher hydrogen production per unit of electricity bought. The effect of the efficiency become prevailing over the higher investment cost of SOEC with the increasing cost of electricity. An electricity price of 100 €/MWh is the break-even cost identified for reaching competitiveness with alkaline electrolysis.

The downside of high-temperature operation of SOECs is the degradation of cell and stack components, which limits the lifetime of the system. Degradation issues have been reported to arise both during steady state and cyclic operation, as explained in the next section, leading to performance losses of 2-5% or even more over 1000 h of operation, while a degradation rate of 0.2%/1000 h can be considered as a target value for the technology (Giglio et al. 2015b). However, a recent study demonstrated that the reversible operation of SOCs made with state-of-the art materials ensures the long-term cell stability required for commercial technological applications, with 4000 h of cyclic operation reached without degradation (Graves et al. 2015).

Co-electrolysis of Water and Carbon Dioxide in SOECs

The high-temperature electrolysis of water and carbon dioxide with an SOEC was first proposed and demonstrated in NASA projects during the 1960's for the production of oxygen in aerospace applications (Weissbart and Smart 1967). The co-electrolysis consists in the

contemporaneous dissociation of H_2O and CO_2 in an SOEC. The electrochemical reduction of CO_2 takes place at the cathode of the cell, similarly to water reduction:

$$\text{Cathode} \qquad CO_{2(g)} + 2e^- \rightarrow CO_{(g)} + O^{2-} \tag{1.9}$$

Reaction thermodynamics are similar to those of water electrolysis and a thermoneutral voltage can be defined also for this reaction; more details are given in *Chapter 2*. The main difference with water reduction is that both reactants and products of reaction (1.9) are gaseous from ambient to SOEC operating conditions, thus evaporation/condensation stages are avoided and the theoretical electricity to fuel efficiency is 100% in thermoneutral conditions. Even if the reduction of CO_2 in state-of-the-art cathodes (Ni/YSZ) presents slower kinetics than H_2O reduction (Ebbesen et al. 2012), the CO_2 dissociation is not negligible and significantly contributes to the charge balance of the cell during co-electrolysis.

Besides the electrochemical reduction of H_2O and CO_2, the high operating temperature of SOECs and the state-of-the-art materials of cathodes promote heterogeneous reactions between fuel components when both H_2O/H_2 and CO_2/CO mixtures are present in the cathodic stream. In particular, the porous structure of the fuel electrode – a Ni/YSZ cermet in state-of-the-art cells – is a good catalyst for water gas shift (direct and reverse) (1.11) and methanation reactions (1.10) and (1.12).

The water gas shift (WGS) promotes the conversion of H_2O-rich mixtures to CO_2-rich mixtures or vice versa if the equilibrium is favorable for the reverse reaction (RWGS). In both cases the reaction converts the "electrochemical fuel" of one of the two electrochemical reactions (1.1) and (1.2) to that of the other reaction, leaving unchanged the global availability of fuel for the co-electrolysis. The WGS/RWGS is kinetically very fast and quickly reach equilibrium within a Ni/YSZ electrode, thus the gas mixture in the active layer of the electrode (i.e., near the electrolyte) is always at equilibrium conditions. Further considerations on the effect of WGS/RWGS on cell operation will be given *Chapter 2*.

Methanation reaction occurs in the presence of high concentrations of CO and H_2 and it is favored by low temperature and high pressure. This reaction is highly exothermic and its occurrence in an SOEC can be beneficial from the thermal point of view, as the heat released balances the endothermicity of electrolysis. This thermal management strategy has been proposed by Wendel et al. (2015a) and Jensen et al. (2015) in a Power-to-Power configuration based on co-electrolysis. In their work, the application of an intermediate-temperature rSOC stack (650 °C) operating at high pressure (20 bar) has been proposed to integrate methanation

and electrolysis in the SOC stack. The round-trip efficiency of the modeled system is higher than 70%, thanks to the thermal synergies between endothermic electrolysis and exothermic methanation. At ambient-pressure and higher temperatures – the state-of-the-art conditions of actual SOEC systems – the methanation reaction only minimally occurs and cannot be considered as potential route for the thermal management of SOECs, as it will be shown later in the dissertation. More information on methanation reactions are given in the next section.

Other reactions that can occur are dry reforming of CO_2 ($CO_2 + CH_4 \leftrightarrow 2H_2 + 2CO$), Boudouard (1.13) and methane cracking ($CH_4 \leftrightarrow C + 2H_2$), depending on operating conditions (i.e., temperature and pressure), cathode materials and partial pressures of chemical species. In general, the reaction involving CH_4 are not likely to occur in co-electrolysis operation at ambient pressure if methane is not already present in the inlet cathodic stream, as its production by methanation is not relevant. A recent publication has experimentally investigated the carbon formation limits during co-electrolysis of H_2O and CO_2 in Ni-YSZ supported SOECs (Tao et al. 2014a). Although the tested conditions were not thermodynamically favorable for carbon deposition, diffusion limitations locally induced the formation of carbon deposits due to the electrochemical reduction of CO adsorbed on YSZ surface (Tao et al. 2014b). The determination of the local conditions of temperature and partial pressures of the reactants is fundamental for the investigation of the chemical reactions that can occur during co-electrolysis. In fact, local hot/cold spots and the local ratios of reactants/products can lead to reaction rates very different to those predicted for the mean cell conditions. The approach followed in this research work is to investigate the local conditions of SOECs during co-electrolysis through the numerical modeling at cell and SRU level to assess the combined effects of electrochemical and chemical reactions. To this purpose, water-gas-shift, methanation and carbon depositions reactions have been included in the electrochemical model developed.

Beside the initial development for aerospace applications, the co-electrolysis has attracted interest in recent years for the production of syngas mixtures that can be further upgraded to SNG or liquid fuels. Many authors investigated the co-electrolysis in SOECs and experimentally demonstrated the feasibility of the process at cell and stack scale (Ebbesen et al. 2009, Ebbesen et al. 2012, Fu et al. 2010, Graves et al. 2011a, Zhan et al. 2009). The use of co-electrolysis for the upgrading of syngas produced from biomass has been also proposed in Biomass-to-Liquid processes (Pozzo et al. 2015). Although the co-electrolysis is a demonstrated process, the long-term durability of SOECs operating in co-electrolysis mode has still to be proven.

The co-electrolysis option has been investigated in this dissertation for the production of syngas from CO_2 and H_2 for further upgrading to SNG. In the study of Giglio et al. (2015b) the economic effectiveness of this option has been assessed. A break-even electricity price (i.e., the price that yield an SNG cost comparable to that of fossil natural gas) of 8 $/MWh was calculated for the application of the concept with state-of-the-art technologies, while a cost of 67 $/MWh was evaluated considering improvements of SOEC technologies that lead to a reduction of degradation rates and investment costs. The energy analysis has shown that the overall efficiency (calculated on the LHV of SNG) of a co-electrolysis based P2G plant operating at 30 bar can be higher than 80%, a value even higher than the efficiency of a hydrogen based P2G plant, which is evaluated to be 76% (Giglio et al. 2015a).

In this dissertation the co-electrolysis based P2G option has been assessed in *Chapter 6*, also investigating the effect of CO_2 pollutants (i.e., H_2S for CO_2 from biogas) on cell performance and system efficiency in a case study developed.

1.3.1.2 Methanation

Hydrogen conversion to SNG requires the production of methane through the reaction with a carbon-containing molecule – typically carbon dioxide or monoxide – in a methanation process. Methane synthesis is well-known since the beginning of the XX century and widely applied in chemical and petrochemical industry. Although methanation processes are technologically mature and commercially available, several issues arise for their integration in P2G systems due to the peculiarity of this application characterized by unsteady operation.

Methanation processes can be divided in two main categories: catalytic methanation and biological methanation. The first category includes all the processes in which methanation is enhanced by inorganic catalysts, while the second includes the processes driven by bio-catalysts (enzymes). The following paragraphs describe these two pathways and the technological requirements for the integration of methanation processes with P2G systems and the injection of the produced SNG in NG grids.

Catalytic methanation

Several reactions contribute to the methanation in chemical reactors, the CO (1.10) and CO_2 (1.12) hydrogenation are the main ones, which are accompanied by other reactions as water-gas-shift (1.11) and Boudouard (1.13).

CO methanation, also called Sabatier reaction, involves the direct reaction of CO and H_2:

$$CO_{(g)} + 3H_{2(g)} \leftrightarrow CH_{4(g)} + H_2O_{(g)} \quad \Delta H^0 = -206.2 \text{ kJ/mol} \tag{1.10}$$

The reaction is strongly exothermic and always takes place in combination with reverse water-gas-shift (RWGS):

$$CO_{2(g)} + H_{2(g)} \leftrightarrow CO_{(g)} + H_2O_{(g)} \quad \Delta H^0 = +41.2 \text{ kJ/mol} \tag{1.11}$$

When H_2 and CO_2 are feed into reactors, RWGS occurs producing carbon monoxide, which is consumed by the Sabatier reaction. The complete process is the CO_2 hydrogenation, which can be seen as the combination of RWGS and Sabatier reactions:

$$CO_{2(g)} + 4H_{2(g)} \leftrightarrow CH_{4(g)} + 2H_2O_{(g)} \quad \Delta H^0 = -165.0 \text{ kJ/mol} \tag{1.12}$$

The complete reaction is still strongly exothermic, thus lower temperature shifts the equilibrium towards the products. Due the volume reduction of the reaction, high pressure enhances the conversion to the products for the le Chatelier's principle. Therefore, equilibrium thermodynamics show that low temperature and high pressure are the required conditions to achieve the higher conversion rates. However, the low temperatures dampen the reaction kinetics, hence suitable catalysts are needed to increase the reaction rates and achieve reasonable conversion rates also at moderate temperatures. Depending on the operating conditions, also the Boudouard reaction can occur:

$$CO_{2(g)} + C_{(s)} \leftrightarrow 2CO_{(g)} \quad \Delta H^0 = 172.45 \text{ kJ/mol} \tag{1.13}$$

Low temperature and high CO partial pressure are favorable conditions for the coke formation and must be carefully avoided to prevent the catalyst deactivation.

Catalytic methanation has been investigated over decades for the production of methane from syngas (e.g. obtained from coal gasification or oil refining) or for the CO_2 upgrading to SNG in large stationary plants. Recently the research has been focused on the use of biomass as feedstock for syngas production and smaller size methanation solutions suitable for this application have been investigated. Several catalytic materials and reactor concepts have been developed for the methanation. Most of the catalytic substances used for the hydrogenation of CO and CO_2 are metals such as Ni, Ru, Rh and Co. Nickel-based catalysts are the most applied in current methanation reactors, mainly due to the low cost and good performance (high activity

and good CH_4 selectivity). The main drawback of catalysts based on this material is the high sensitivity to poisons, such as halogenous and sulphurous compounds, which implies the requirement of high purity gases and consequently of a gas cleaning system for the educts. Catalytic supports are usually silica-based, zeolites or also metal carriers. To date, the methanation reactors developed can be classified in four categories:

- Fixed-bed reactors

These reactors are based on a static bed of catalyst pellets. The operating temperature are between 250°C and 700°C and the pressure between 20 and 80 bars. Methanation reactions are strongly exothermic, thus the temperature control is the major issue of the reactors. A careful control is needed in order to avoid hot spots in the bed that can irreversibly deactivate the catalyst. Most of the technologies rely on a series of adiabatic reactors (from 2 to 5) with gas cooling, gas recycling and heat recovery between each step. Some example of this concept are the Lurgi, TREMP and Linde processes. An alternative option is the cooled fixed-bed reactor, which typically control the temperature with cooling tube bundles. This solution can reduce the number of reactors needed by achieving higher conversion due to the lower temperature reached in the reactor; however, the complexity and cost of the reactor is higher with respect to the adiabatic configuration. Beside the temperature control, mass transport limitations between gases and solid catalyst are the other disadvantage of this configuration.

- Fluidized-bed reactors

Solid catalyst particles are in suspension in the gaseous reacting flow. Fluidized-bed reactors are characterized by an almost isothermal temperature profile due to the effective heat removal through the turbulent flow that ensures a good contact between gas and solid and a better control of the reaction. These advantages allow the use of a single reactor avoiding the reactor cascades needed for the fixed-bed solution. Fluidized bed reactors can operate only in the limited range of flows that allows the fluidization of the solid catalyst, hence unsteady flow rates can be a serious issue for an effective operation. Another disadvantage is the abrasion of catalyst and reactor walls that occurs due to the turbulent movement of the particles.

- Three-phase reactors

The methanation process occurs in a three-phase system composed by reacting gases, solid catalyst and a liquid heat carrier. The liquid phase allows an effective temperature control that ensures the isothermal operation of the reactor. This configuration reduces catalyst abrasion with respect to fluidized-bed reactors. However, the presence of a liquid phase increases the mass transfer resistance between the gases and solid catalyst and requires a complex hydraulic control of the reactor.

- Structured reactors

These reactors are made by monolith structures made by ceramics or metals on which the catalyst is deposited. Metal monolith reactors ensure high heat transfer and small pressure drops. The metallic structure enhance the heat transfer by orders of magnitude compared to other reactor's configurations. The main drawback is the sophisticated deposition of the catalyst on the structure and the need for re-coating the monolith when catalyst is deactivated.

Biological methanation

In biological methanation, the metal-based catalysts are substituted by enzymes which act as bio-catalyst of the process. Enzymes are produced inside the biological reactors by bacteria, which require specific conditions (temperature, pH) and nutrients (e.g. salts) to be active and realize high conversion rates. Methanogenic bacteria (Archea) produce the necessary enzymes for the CH_4 synthesis. Two reaction paths lead to the production of methane in biological reactors, one is the acetoclastic methanogenesis:

$$CH_3COOH_{(g)} \leftrightarrow CH_{4(g)} + CO_{2(g)} \tag{1.14}$$

and the other is hydrogenotrophic methanogenesis, which is equivalent to reaction (1.14) and directly converts hydrogen and carbon dioxide to methane. The reaction path based on acids (1.14) is predominant in the decomposition of biomass. Bacteria obtain the energy for their growth from the metabolic reactions, thus energy is not released in the form of heat in biological reactors.

Biological methanation proceeds at moderate temperatures (20–70 °C) under anaerobic conditions usually at ambient pressure. Goetz et al. (2016) identify two main process concepts: the in situ methanation and the methanation in separate reactor. In the first concept, hydrogen is directly fed to a biogas digester, where the CO_2 produced by acetoclastic methanogenesis is converted to CH_4 by hydrobenotrophic methanogenesis. The second concept, the gaseous products of the biologic digestion (i.e., CO_2 and CH_4) are fed to methanation reactor where H_2 and CO_2 are added to increase the methane fraction of the mixture.

The advantages compared with the chemical methanation are the low-temperature, low-pressure operation and the higher tolerance against pollutant substance in the gases, which allow to strongly simplify the architecture of the methanation system. High hydrogen conversion rates are reached, comparable with that of chemical methanation and even greater (95% reported by Grond et al. (2013)). Disadvantages are the mass-transfer limitations and the stable operating conditions required for the bacteria that give to biological systems a poor flexibility of operation. Moreover, very slow reaction rates are reached in biological reactors with respect to chemical methanation and consequently orders of magnitude larger reactor volumes are required to convert a certain hydrogen flow rate. Therefore, the biological pathway appears suitable only for small-scale applications. Finally, long-term stability of biological methanation has still to be demonstrated.

Methanation and P2G: technological requirements of integrated processes

When methanation is integrated in Power-to-Gas systems, several technological requirements arise and suitable operating strategies must be developed to ensure an effective operation of the coupled systems.

The major issue in coupling P2G and methanation is the unsteady hydrogen production from RES-driven electrolysis. The fluctuating hydrogen output is not optimal for operating methanation reactors. Therefore, hydrogen storage is needed for the temporal decoupling of H_2 production and CH_4 synthesis. The size of the storage system both depends on the fluctuations in electrolysis and the load flexibility of methanation. Also the CO_2 availability must be constant in time to allow the steady-state operation of methanation reactors; hence if the carbon source does not ensure a constant flow, also the CO_2 storage is needed.

An alternative and/or complementary option to the educts storage is the dynamic operation of methanation reactor. Currently developed technologies for chemical methanation require stable pressure and temperature, and neither frequent load changes nor start-up and shut-down are

acceptable operating conditions. Therefore, dynamic operation significantly modifies the technological requirements for catalysts and reactors. In particular, dynamic reactors must have stand-by capability with low energy requirements and catalyst must not deteriorate when exposed to stand-by mixtures. A study of Mutz et al. (2015) has shown a fast degradation of methanation catalysts under a CO_2 atmosphere, thus it is preferable that stand-by operation is managed with hydrogen to avoid catalysts oxidation. The thermal management is the major issue under dynamic operation, as strong temperature variations due to the changing conditions can lead to catalyst cracking or sintering. The development of specific catalysts that can withstand large temperature variations and the modification of actual methanation technologies for dynamic temperature control are the required steps to allow the applicability of dynamic methanation. Fast start-up and shut-down of the reactors are also required. Isothermal reactors seem the most suitable for the dynamic operation. In particular, three-phase methanation has shown a low sensibility towards the fluctuations of feed streams at lab-scale level (Lefebvre et al. 2015). Also staged reactors based on monolithic catalyst carriers are a promising reactor concept which enables a modular design (i.e,, suitable for scale-up), with low pressure losses and uniform temperature profile.

Another issue of P2G integration is the pressure level of hydrogen and carbon dioxide. When considering the methanation in chemical reactors, which is currently the only feasible option for large-size P2G applications, the educts have to reach the operational pressure of methanation reactors (i.e., usually 30 bar or more). Hydrogen can be produced at elevated pressure by low-temperature electrolysis and also SOEC-based systems have shown the capability of high-pressure operation (up to 15 bars), while carbon dioxide sources are almost always available at atmospheric pressure, thus CO_2 compression is a necessary stage in a P2G plant.

To summarize, the general requirements for methanation processes integrated in P2G systems are the modularity, easily up-scalable design, load flexibility and capability of stand-by operations. The effectiveness of the integration can be increased by utilizing the released methanation heat within the P2G system or outside as a secondary product; several examples of thermal integration can be found in literature (Giglio et al. 2015a, Steinmüller et al. 2014).

Further requirements arise when the SNG production is intended for the injection in the NG grid, as in the majority of P2G applications. In this case, the quality of the product gas must comply with the specifications for the NG grid. The prescription considered in this dissertation when assessing the SNG production for NG grid injection are those established in Italy by

"Snam Rete Gas" for pumping natural gas into pipelines (SNAM 2016). The main constraints pertain three parameters:

- Gas Gravity
- Wobbe Index
- Higher Heating Value (HHV) of SNG

Gas Gravity is the ratio between densities of produced SNG and air, while Wobbe Index is the ratio between the HHV of SNG and the square root of the Gas Gravity. Acceptability boundaries for these parameters are reported in *Table 1.1*.

Table 1.1 – SNG requirements for grid injection in Italy

HHV (MJ/Sm^3)	34.95 – 45.28
Wobbe Index (MJ/Sm^3)	47.31 – 52.33
Gas Gravity	0.5548 – 0.800

Other prescriptions affect the SNG composition, in particular the concentration of components as Oxygen, Carbon Dioxide, Water, Sulphuric molecules, particulate and liquid hydrocarbons. In the case of ideal methanation with stoichiometric hydrogen to carbon ratio of 4:1 with complete conversion, the product is a mixture of CH_4 and H_2O, which is suitable for NG grid injection after water condensation, that is necessary to cope with the grid requirements. However, in real systems the conversion is not complete and different gases can be present in the feed streams besides H_2 and CO_2, depending on its sources. Given that electrolysis produces almost pure H_2, undesired gases may come from the CO_2 stream, depending on the origin of the carbon source. Therefore, other SNG upgrade processes may be needed to reach the gas quality requirements. Examples are upgrading systems based on membranes or pressure swing adsorption. At the end of the upgrading process SNG can be injected in the grid; however, a further compression stage may be needed to reach the pressure level of the grid.

The carbon source represents another boundary of the P2G system that must be considered when assessing the issues of system integration. Conventional methanation catalyst convert both CO and CO_2 to methane, thus both gases can be considered as carbon sources. As a consequence, not only pure CO_2 streams are eligible as carbon feedstocks. Possible sources are:

- Industrial processes (including power generation)

- Biomass
- Air

A review on the state of the art technologies and future perspectives of carbon dioxide capture in various types of industrial sectors is given by Kuramochi (2011). The study includes iron and steel industry, cement industry, refineries and Natural Gas Combined Cycle power plants. Absorption, adsorption, membrane processes and carbonate looping are the carbon capture technologies adopted. In particular, amine-based absorption is the more mature technology.

Biomass processes (fermentation, gasification and combustion) can provide a wide variety of carbon-containing streams which can be exploited as CO/CO_2 sources for SNG production. In particular biogas, which is produced from the digestion of various biomass substrates, is an attractive CO_2 source. Biogas is mostly composed by CH_4 (50-70%) and CO_2 (30-50%), while trace components are H_2S, mercaptans and siloxanes. Biogas can be directly feed to methanation reactors, in this case only H_2 from electrolysis is added. Another possible application is the use of CO_2 obtained from biogas upgrading to biomethane as a carbon source. European countries and in particular Germany have a huge biogas potential already exploited for biomethane production, with up to 1.3 billion m^3 of biomethane produced in 2013, according to EBTP (EBTP "Biogas/Biomethane for use as a transport fuel" 2016). The CO_2 separated from the upgraded biogas can be converted to SNG in P2G plants offering a potential chemical storage of 12 TWh per year (Götz et al. 2016). The Audi e-gas P2G plant is based on this concept, with around 2800 tons of CO_2 per year recycled from biogas upgrading. Also biomass gasification is a very attractive carbon source for Power-to-Gas or Power-to-Liquid processes (Pozzo et al. 2015). In particular, with the integration of the processes, the oxygen stream produced in the electrolysis can be used for the gasification. According to Götz (2016), the combination of gasification with power-to-gas can double the carbon exploitation and increases the process efficiency.

A third possible route is the CO_2 capture from air. This option offers the possibility of obtaining a carbon source without being constrained by the availability of industrial sites or biomass feedstocks. Although attractive from the topographical and environmental point of view, the air capture has a cost far more higher than the other carbon separation routes.

A rough estimation of costs (Kuramochi 2011, Lackner 2009, Socolow et al. 2011) for carbon-capture from air indicates a cost from 100 to 600 \$/t CO_2, while for the capture from other sources a cost range between 20 and 60 €/t CO_2 is estimable. As a general conclusion, the

supply of CO_2 is technically feasible, but the costs associated to carbon separation and storage have a strong impact on the total cost of methanation. This cost can grow further if the CO/CO_2 stream contains pollutants and undesired compounds that must be removed to avoid catalyst deactivation of methanation reactors and also of the electrolyzer in the case CO_2 is directly provided to an SOEC for co-electrolysis processing.

This overview shows that the integration of methanation in P2G plants requires to develop specific designs depending on the electrolysis and methanation technologies applied and on the CO_2 sources involved in the process. This dissertation has addressed P2G options based on the methanation of CO_2/H_2 and syngas mixtures in state-of-the-art catalytic fixed-bed reactors. The analysis developed has been focused mostly on the integration of SOEC in P2G plants and on the effects of SOEC behavior on the system efficiency, while the methanation stage has been considered as the outlet boundary of SOEC without investigating the process in details.

1.3.2 Technology Status and Potential Applications in Europe

In recent years, P2G potential has been assessed in several studies. Technical and economic analyses (Götz et al. 2016, Jentsch et al. 2014, Tsupari et al. 2016, Kötter et al. 2016, Varone and Ferrari 2015, Schill 2014, Winkler-Goldstein and Rastetter 2013, Trost et al. 2012, Schiebahn et al. 2015, Qadrdan et al. 2015) investigated different P2G solutions for RES integration; most of them developed scenarios for the European context and in particular for Germany, where major efforts have been spent to develop this technology. Pilot and demonstration plants have been realized or are being planned worldwide, a complete overview is available in literature (Gahleitner 2013), updated to 2012. The trend is toward the installation of an increasing P2G capacity (up to MW), as shown in *Figure 1.13*, increasingly based on PEM electrolysis.

To date, more than 100 international projects have been focused on the application of the P2G concept; an exhaustive list is given in (Steinmüller et al. 2014). The technological know-how collected in these projects represents a fundamental experience for the further development of P2G. A brief summary on the current trends in Europe is given in the following paragraphs.

Germany is the undisputed leader in P2G initiatives (Schiebahn, et al. 2013) with the higher number of operative demonstration plants and projects. To be mentioned the WESpe project, with 6.7 MW alkaline electrolysis power planned and the Audi e-gas plant in Wertle (6.3 MW) for SNG production from biogas-derived CO_2, which is the biggest currently operating Power-to-Gas plant worldwide. The strong interest toward P2G in Germany is strictly related to the high electricity production from RES (around 26% of the total generation in 2014 (BDEW 2014). A

study presented in (Stolten et al. 2013) shows that a considerable expansion of wind power in the German electricity sector (up to 90% of electricity demand covered by renewable sources) will lead to an excess of generation, with 34% of the total electricity production available for valorization in P2G applications to avoid its curtailment.

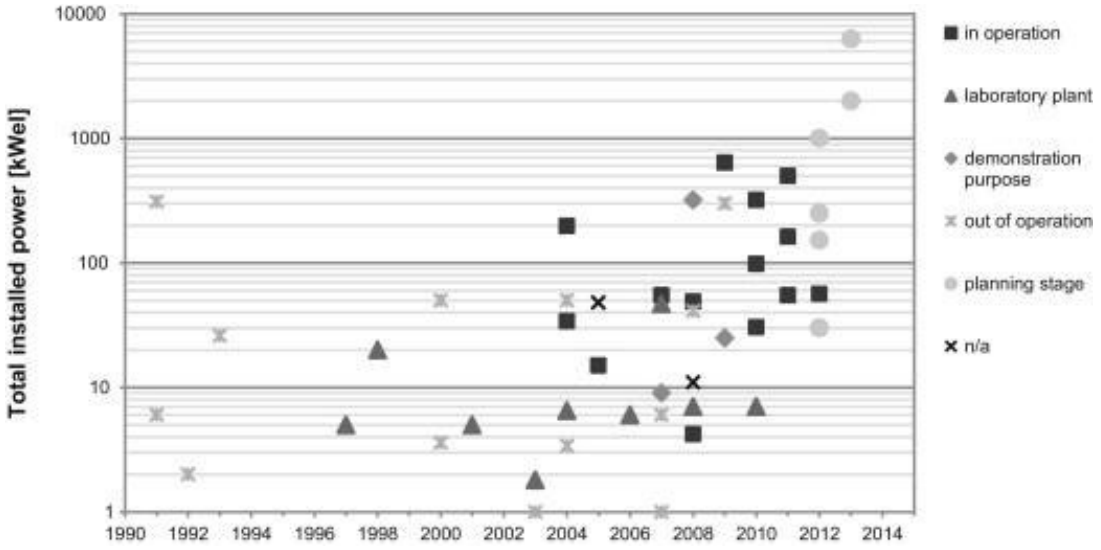

Figure 1.13 – Installed P2G capacity (Gahleitner 2013)

The role of Power-to-Gas in the Dutch energy system has been analyzed in several studies (de Joode et al. 2014, Grond et al. 2013). Results show that P2G can contribute to renewable energy targets or emission reduction targets in other sectors by facilitating the integration of RES in the electricity sector. In particular, P2G is recognized as one of the essential technologies to deliver seasonal energy storage services when aiming for a 100% renewable energy system or carbon neutral energy supply.

The Danish energy system is strongly based on wind energy, which accounts for the 34% of the total electricity supply (WWEA 2014). The issues related to the high share of wind energy are mostly mitigated by the availability of large connections with the electricity systems of the neighboring states, i.e. Germany and Scandinavian states, which offers balancing opportunities and makes almost unnecessary the installation of large storage systems. Nevertheless, the high availability of RES is seen as an opportunity to develop P2G for reducing system operation costs (Heinisch 2015) and produce hydrogen for mobility (Sørensen et al. 2004) or SNG for transportation and heating applications (BioCat Project http://biocat-project.com/power-to-gas/p2g-in-denmark/).

Also the United Kingdom is looking with interest toward P2G for mobility and gas injection in the NG grid (GRIDGAS Project http://www.gridgas.co.uk/ , Qadrdan et al. 2015). The potential for P2G valorization of electricity surpluses in France has been assessed in (EE consultant et al. 2014). The study estimates that about 25 TWh/year of hydrogen from P2G are available for injection in the NG grid, reaching 75 TWh/year in 2050. The estimated P2G capacity is 24 GW in 2050, with 5-10% dedicated to direct H_2 injection and the remaining to methanation.

1.4 Solid Oxide Cells: an overview

In this Chapter, the operating principles of Solid Oxide Cells (SOC) are introduced and the literature review of state-of-the-art materials and degradation issues is given. This research is focused on the application of SOCs either as electrolyzers (SOEC) or as reversible devices operating cyclically in electrolysis and fuel cell modality. In the second case, the cells are called reversible Solid Oxide Cells (rSOC). In particular, the SOEC operation has been investigated with H_2/H_2O and co-electrolysis mixtures, while the rSOC operation only with H_2/H_2O mixtures. The SOC operation as pure fuel cell (SOFC) has not been assessed in this dissertation. For this reason, the present Chapter focuses on the introduction and review of SOECs and rSOCs.

1.4.1 Introduction to SOCs: operating principles

A Solid Oxide Cell is a solid-state electrochemical device consisting of an ion-conducting electrolyte with porous electrically conducting electrodes on either side of the electrolyte. The cell is based on a thin (i.e., 5–200 μm), dense solid ceramic electrolyte that is conductive for ions at high or intermediate temperature, depending on materials. Electrodes are made of mixed ceramic and metallic materials and their structure is designed to ensure the contact of ions, electrons and reacting chemical species that is necessary for the electrochemical reactions to occur. The thin boundary of the electrode where ions, electrons and reacting gases come in contact is called three-phase-boundary (TPB), which has a limited extension from the electrolyte surface. A variety of materials and configurations have been developed for solid oxide cells, an overview is given the next section. This research work is focused on conventional planar SOCs based on oxygen-ion conductive electrolytes and in the following of the dissertation the terms SOC/SOEC/rSOC will indicate this type of cells unless otherwise specified.

An SOC basically “pumps” oxygen ions from an electrode to the other following the difference of ionic potential within the electrolyte established by the electrochemical reactions occurring at the electrodes. Depending on the cell polarity, an SOC can operate either as fuel cell (SOFC) for the electrochemical oxidation of fuel molecules (i.e., H_2 and CO), or as electrolyzer to reduce reactant molecules (i.e., H_2O and CO_2) within the fuel electrode (anode in SOFC mode, cathode in SOEC). On the other electrode (cathode in SOFC mode and anode in SOEC), oxygen molecules are reduced (SOFC) or oxidized (SOEC). An SOC is not a purely electrochemical device, as also chemical reactions take place within the fuel electrode. In fact, both reduction-oxidation reactions and heterogeneous reactions occur if hydrogen- and carbon-containing gases

are simultaneously fed to the SOC. A schematic of an SOC working in both modes of operation is depicted in *Figure 1.14*.

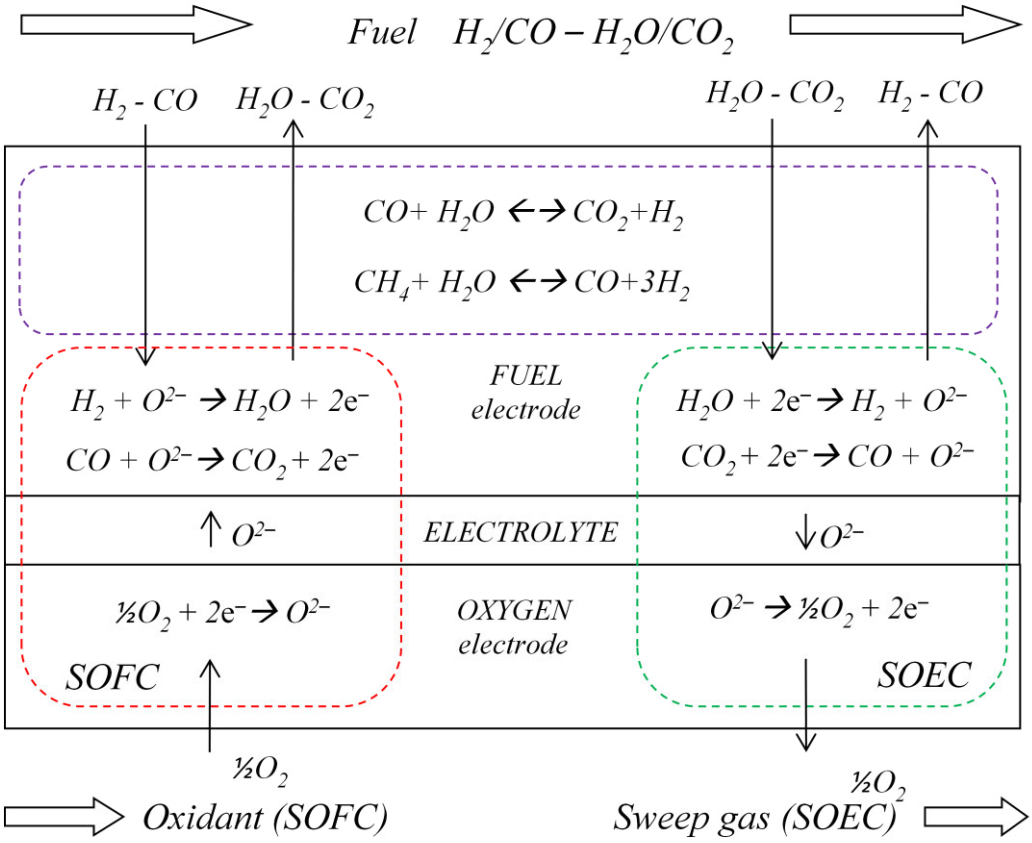

Figure 1.14 – Schematic of an SOC operating in fuel cell and electrolysis mode.

A single cell typically operates between 0.5 V (SOFC) and 1.5 V (SOEC) and cell stacking is needed to achieve an higher voltage. Therefore, in practical applications the individual cells are stacked together, and if we consider the single unit of a stack of cells, which is called SRU (i.e. Stack Repeating Unit), other components as interconnects, seals and gas channels must be taken into account. Interconnects are metallic plates which ensure the electric continuity between adjacent cells by connecting the anode of a cell to the cathode of the other and separate the gas flows of the electrically connected electrodes. During operation, reactant species are feed to the electrodes through distribution channels patterning the surface of interconnect plates. Gas tightness between adjacent SRUs is ensured by sealing frames. A schematic representation of an SRU is depicted in *Figure 1.15*.

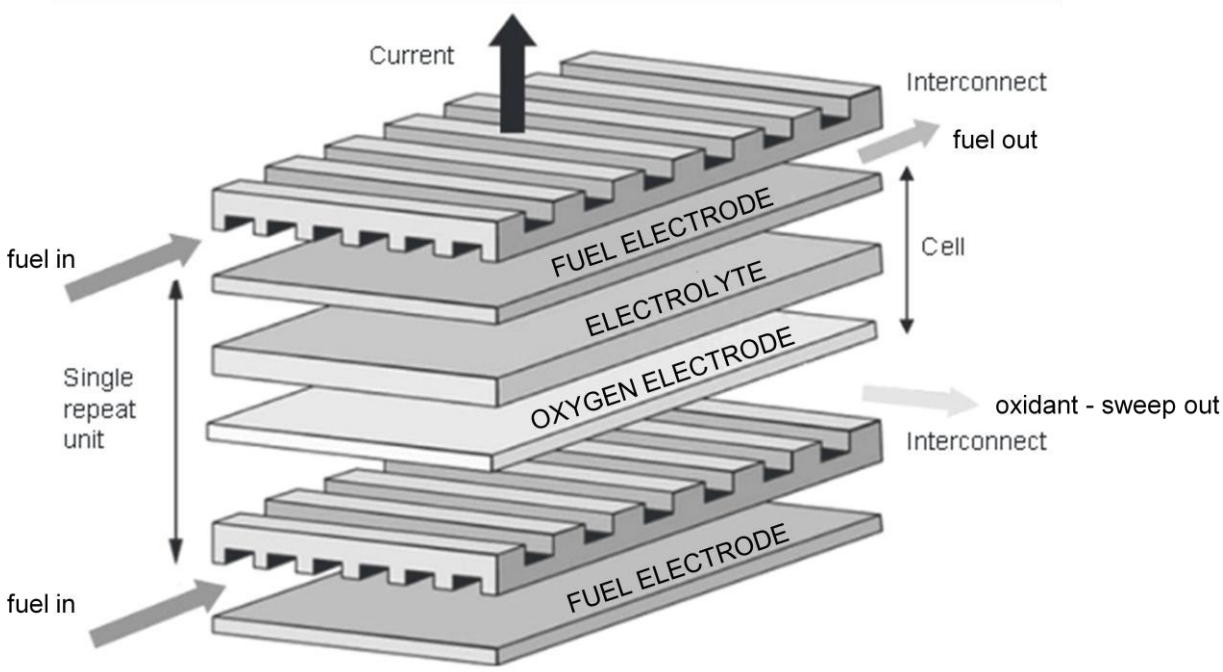

Figure 1.15 – Schematic of a Stack Repeating Unit (SRU). (adapted from: Mougin 2015)

During operation, the fuel electrode is feed with mixtures of electrochemically reacting gases (H_2/H_2O/CO/CO_2) which may contain also hydrocarbons and other chemical species, including pollutants (e.g. H_2S or siloxanes) that typically are present in traces in untreated CO_2 streams, depending on the source. The oxygen electrode requires the presence of O_2 in the feeding stream only when the cell is operating in SOFC mode. The SOEC operation does not require an oxidant, thus the gas mixture sent to anode may also not contain oxygen; in this case, the gas stream acts mainly as a carrier to entrain the produced oxygen helping its evacuation from the electrode. For this reason, the anodic mixture can be also called sweep gas in SOEC mode. The electrochemical reactants – H_2O and/or CO_2 in electrolysis operation, H_2 and/or CO in fuel cell mode – are involved in the reduction – (1.15) and (1.16) – and oxidation reactions – (1.17) and (1.18) – that take place within the fuel electrode.

$$H_2O + 2e^- \rightarrow H_2 + O^{2-} \tag{1.15}$$

$$CO_2 + 2e^- \rightarrow CO + O^{2-} \tag{1.16}$$

$$H_2 + O^{2-} \rightarrow H_2O + 2e^- \tag{1.17}$$

$$CO + O^{2-} \rightarrow CO_2 + 2e^- \tag{1.18}$$

Oxygen ions are delivered through the solid oxide membrane to the oxygen electrode where either the electro-oxidation (SOEC (1.19)) or the electro-reduction of oxygen takes place (SOFC (1.20)).

$$O^{2-} \rightarrow \frac{1}{2}O_2 + 2e^- \tag{1.19}$$

$$\frac{1}{2}O_2 + 2e^- \rightarrow O^{2-} \tag{1.20}$$

Besides the electrochemical reactions, chemical reactions can occur within the fuel stream. In principles, both homogeneous and heterogeneous reactions between the fuel components can take place depending on operating conditions (temperature and pressure) and fuel electrode materials. If we consider the typical operating conditions and gas mixtures of SOCs, the reactions that occur within the within the gas phase are very slow when compared to the heterogeneous ones, thus the homogeneous chemistry can be safely neglected (Zhu et al. 2005). With the fuel mixtures (H_2, H_2O, CO, CO_2 and CH_4) and materials of the fuel electrode (Ni/YSZ cermet) considered in this study, the heterogeneous reactions promoted by the presence of the nickel – which acts as a catalyst for the reactions – are mainly the water gas shift (direct and reverse) (1.21) and methanation/methane-reforming (1.22) reactions.

$$CO + H_2O \leftrightharpoons CO_2 + H_2 \tag{1.21}$$

$$CH_4 + H_2O \leftrightharpoons CO + 3H_2 \tag{1.22}$$

Reactions (1.21) and (1.22) can occur in both SOEC and SOFC operation depending on the local conditions of temperature, pressure and mixture compositions, thus they are not associated to a particular operating mode. Reaction (1.22) has been considered in the study – even if the methane is not directly feed to the SOC in the cases analyzed in this dissertation – because it can be produced within the fuel electrode by the reaction of CO and H_2, and the produced methane

can be consumed in the reverse reaction depending on the local conditions of the SOC. Also Boudouard and methane cracking reactions have been considered in this study:

$$CO_{2(g)} + C_{(s)} \leftrightarrow 2CO_{(g)} \tag{1.23}$$

$$CH_{4(g)} \leftrightarrow 2H_{2(g)} + C_{(s)} \tag{1.24}$$

If these reactions occur, solid carbon is deposited within the porous structure of the electrode, reducing the void fraction available for gas diffusion and the TPB surface, leading to a change of the electrode microstructure that can eventually break the cell. The issues related to carbon deposition and the approach followed for its modeling are assessed in the next chapter.

Concerning the thermal behavior of SOCs, different heat sources/sinks contribute to the temperature profile of the cell. The heat sources can be classified as: 1) electrochemical reactions, 2) chemical reactions, 3) irreversible heating due to reactions activation and electrical charge flow. The electrochemical reactions occurring in fuel cell mode – (1.15) and (1.16) – are exothermic, while the SOEC reactions – (1.17) and (1.18) – are endothermic. The chemical heat sources related to (1.21) and (1.22) can be endothermic or exothermic depending on the equilibrium of the reactions, while the irreversible heating is always exothermic. Globally, in SOFC mode the cell provides an exothermic contribution to the thermal balance, and only the chemical reactions can act as thermal sink (e.g., methane steam reforming). In SOEC mode, the thermal contribution of the cell can be positive or negative depending on the balance between reaction heat sink and irreversible heating. It is possible to identify a particular value of SOEC voltage at which the heat generation due to reactions activation and charge flow is equal to the heat absorbed by electrolysis, this voltage is called thermo-neutral. During SOEC operation in co-electrolysis, also chemical reactions can contribute to the global thermal balance; in particular, if SOEC is operating at high-pressure and in the lower level of temperatures allowed by materials, the exothermic methanation of CO can provide a non-negligible contribution to the total thermal balance of the SOC by lowering the thermoneutral voltage of the cell. The mathematical derivation of thermoneutral voltage is given in *Chapter 2*. Besides the heat sources/sinks, other two factors contribute to determine the thermal balance of the cell: gas flows entering/exiting the SOC and thermal insulation of SOC toward the ambient. The use of the oxidant gas flow (i.e., air) as thermal sink is the common practice in SOFC: excess air is sent to

the cell to remove the heat produced and maintain the SOC at a desired temperature. In SOEC mode, gas flows can be regulated to add/remove heat to the cell depending if the system is operating in endothermic or exothermic conditions. The problem of thermal regulation of SOEC and rSOC will be addressed in *Chapter 5*.

1.4.2 Literature review of SOEC and rSOC

This section provides an overview on materials, cell configurations and research experiences about SOEC and rSOC. A brief summary on the major issues affecting the durability of SOC tested in electrolysis and reversible operation is also given.

1.4.2.1 Materials and cell configurations

SOECs have been developed in different geometries (i.e., planar and tubular) and configurations (i.e., cathode, electrolyte or metal supported). In both planar and tubular cell design, the electrolyte is placed between the electrodes. Even if the tubular design insures a better sealing between air and fuel due to the closed geometry, the lower power density has limited their development and application with respect to the planar ones (Hussain et al. 2009).

Focusing on planar SOCs, several cell designs have been developed, in particular, electrolyte supported cells (ESC) and fuel-electrode supported cells. The second type of cells will be named cathode supported (CSC) in the following discussion by considering the SOEC polarity convention. In the ESCs, the electrolyte (thickness 100-200 μm) has the role of mechanically supporting the cell and electrodes (thickness 50 μm or less) are deposited on it. In cathode supported cells, the electrolyte is a very thin layer (thickness 5-20 μm) and the mechanical support is provided by the cathode (thickness 0.2-1.5 mm). Electrode supported cells requires higher operating temperature (higher than 800°C) to ensure a sufficient ionic conductivity of the thick electrolyte, while lower temperatures (from 700°C to 850°C) are allowed in CSC cells. A third type of SOC is the metal supported cell, based on an electrochemically inactive metallic support on which the ceramic components of the cell are deposited as thin layers. To date, only few tests were reported for metal-supported SOECs (Schiller et al. 2009).

Independently of cell configuration, the required properties of the electrolyte are: good ionic conductivity at the cell operating temperature, gas tightness, thermal expansion coefficient close to that of the electrodes, mechanical and chemical stability in both oxidizing and reducing environments and no reactivity with electrode materials. The most common electrolyte material are zirconia (ZrO_2) based. Zirconia is doped with various oxides (Y_2O_3, CaO, MgO and Sc_2O_3)

to obtain the properties required for the electrolyte. Among the electrolyte materials, yttria(Y_2O_3)-stabilized zirconia (YSZ) is the most commonly used due to chemical stability and economic reasons. This material shows a conductivity ranging between 0.1 S/cm at 1000 °C and between 0.02 S/cm at 800 °C (Kharton, et al. 2004). Scandia (Sc_2O_3)-stabilized zirconia (ScSZ) shows a higher ionic conductivity than YSZ and has been applied as electrolyte material for ESCs which have been tested in long-term SOEC operation (Schefold and Brisse 2014). Other potential electrolyte materials are based on ceria, usually doped with Gd_2O_3 (GDC) or Sm_2O_3 (SDC) and lanthanum gallate doped with Sr and Mg (LSGM). Results of the reversible operation of an LSGM-based cell at intermediate temperature (650°C) have been shown by Wendel et al. (2015b).

The fuel electrode must exhibit high electrocatalytic activity for the reactions (1.15)-(1.16) and sufficient ionic conductivity to allow the reaction surface to extend in the electrode volume. Moreover, the electrode structure must be porous and highly conductive for the electrons to ensure the transport of reacting species and electrons to the TPB. The most common fuel electrode material is a porous cermet composed of nickel and yttira-stabilized zirconia (Ni/YSZ). The nickel is a good electrocatalyst at high temperature which exhibits high electronic conductivity and stable expansion coefficients compatible with that of the ceramic electrolyte. Besides the excellent characteristics, the low cost of nickel compared to precious metal catalysts contributed to its success. The ionic conductivity of the cermet is provided by the YSZ, which also acts as an inhibitor for the coarsening of nickel particles during high-temperature operation. Reducing conditions must be maintained on the fuel electrode during operation to avoid nickel oxidation. This is typically accomplished by including 10% or higher mole fraction hydrogen in the inlet fuel flow. Other nickel-based cermets such as nickel/gadolinia-doped ceria (Ni/GDC) and nickel/samaria-doped ceria (Ni/SDC) have been proposed for the operation at intermediate temperatures. Innovative electrodes with mixed ionic/electronic conductivity have also been investigated for SOEC applications, in particular lanthanum-substituted strontium titanate/ceria composites (LST) and perovskite materials (LSCM) (Yue 2013).

Several materials have been studied for the oxygen electrode, which must operate in a highly oxidizing environment. Materials of the perovskite class (ABO_3 structure) have been usually considered for this electrode. In the perovskite structure, A and B are two cations of very different sizes (A much larger than B), and O is the anion that bonds with both. These perovskites exhibit p-type electrical conductivity that is enhanced by the introduction of lower-valence dopant cations (e.g. Sr^{2+}, Ca^{2+} and Ba^{2+}) to replace trivalent lanthanide ions (e.g. La^{3+},

Sm^{3+}, Gd^{3+}). Strontium doped lanthanum manganite (LSM) is the oldest and most common oxygen electrode material developed. This material provides good electronic conductivity, has a thermal expansion coefficient close to that of the electrolyte, low chemical reactivity with YSZ and exhibits tolerance to the oxidizing environment. However, the material has poor ionic conductivity and LSM composites have been developed to extend the TPB of the electrode (e.g. LSM/YSZ). Mixed ion-electron conducting electrodes have also been developed to enhance this characteristic, such as strontium, copper and cobalt-doped lanthanum ferrites (LSF, LSCuF and LSCoF). These materials are more catalytically active than LSM and therefore, yield generally better performance, especially at temperatures below 800°C. For intermediate temperature operation (i.e., lower than 700 °C), cobalt-doped lanthanum electrodes (LSC) have been developed. Intermediate layers between LSCF or LSC oxygen electrodes and electrolytes are frequently inserted to minimize the reactivity between electrolyte and electrode materials and to mitigate the mismatch between the expansion coefficients of the two layers. Gadolinia- or yttria-doped ceria are usually employed as intermediate layers.

In this dissertation, planar commercial CSCs were characterized in rSOC operation to calibrate and validate the electrochemical cell model developed (see *Chapter 4*). The fuel electrodes of tested cells consisted of Ni/YSZ cermets and the electrolytes of YSZ. Two types of oxygen electrodes were tested: one was an LSM/YSZ composite and the other was made by LSCF. These materials can be considered the state-of-the art of the current commercial cells.

Interconnects must have good electrical conductivity, high resistance to oxidizing environments and good compatibility with the cell materials both from the chemical (i.e., no reactivity) and the mechanical (i.e., similar thermal expansion coefficients) point of view. Moreover, interconnect materials must be easily workable to maintain a reasonable cost. Common interconnects materials are ferritic stainless steels, alloys that exhibit oxidation resistance at high temperature due to the formation of protective chromium oxide layers. The main issues of these alloys are the low electrical conductivity of chromium layers and the volatility of chromium compounds that can contaminate the electrodes by condensing on the active sites of the structure leading to the progressive deactivation of the cell. Special alloys with optimized compositions, such as Crofer 22 APU and 22H (ThyssenKrupp VDM) have been developed specifically for SOC applications. These alloys contain manganese that combines with chromium to form mixed manganese-chromium oxide layers which exhibit higher conductivity and lower volatility. The addition of other elements (i.e., lanthanum and titanium) improves the conductivity and limits the growth of the oxide layers. In order to improve the performance

ensure the durability of the interconnects, protective coatings have been developed (Szymczewska et al. 2016, Ajitdoss et al. 2013, Smeacetto et al. 2015).

The sealing of the cells is usually realized with glass and glass-ceramic sealants, mostly derived from SOFC applications. However, specific sealants for SOEC application have also been developed (Khedim et al. 2012).

1.4.2.2 State-of-the art of the research: long-term durability and degradation issues

Literature review of SOEC and rSOC

The high-temperature electrolysis of H_2O and CO_2 with SOEC was first proposed in NASA projects in 1960s (Weissbart and Smart 1967). In Europe, the concept of high-temperature electrolysis of steam was developed in Germany by Dornier and Lurgi (HOT ELLY project) between 1970s and 1980s, leading to a 3.5 kW demonstration unit realized based on tubular SOECs (Dönitz 1975, Donitz and Erdle 1985, Donitz and Streicher 1980, Isenberg 1981, Donitz et al. 1988, Erdle et al. 1992). The project also demonstrated the reversible operation with H_2/H_2O and CO/CO_2 mixtures. In the USA, Siemens-Westinghouse demonstrated the operation of a tubular high-temperature electrolysis cell (HTE) at the beginning of the 1980s (Isenberg 1981). The development of planar SOECs and rSOCs has been carried out in recent years in the USA by the Idaho National Engineering and Environmental Laboratory (INL) in collaboration with Ceramatec and in Europe by Risø DTU (Denmark) in collaboration with Topsoe Fuel Cell (TOFC). INL conducted the investigation on electrolyte supported cells (based on YSZ and ScSZ) from button cells to multi-cell stacks and multi-stack systems (up to 15 kW) (Stoots et al. 2010). Risø DTU (now Department of Energy Conversion and Storage, DTU) developed cathode-supported cells mainly based on state-of-the-art materials for SOCs: Ni/YSZ for the fuel electrode, YSZ electrolyte and oxygen electrodes made by LSM, LSC or LSCF (Hagen 2014). The research efforts of Risø DTU involved SOC tests in electrolysis, co-electrolysis and reversible modes from cell to stack level and from ambient pressure up to 10 bar (Jensen et al. 2007, Ebbesen et al. 2009, Graves et al. 2011b, Hauch et al. 2006, Knibbe et al. 2010, Ebbesen et al. 2010, Graves et al. 2015, Jensen et al. 2010).

The studies conducted by research centers addressed two main fields: SOC performance and long-term durability. High performance was demonstrated for planar SOCs, with a measured current density up to 3.6 A/cm^2 at 950 °C at 1.5 V (Jensen et al. 2007). The major issue evidenced by the studies was the long-term degradation of cells in stationary, cyclic and

reversible operation, especially at high current density (i.e., high power density). Finding a compromise between power density and long-term stability has been the target of the EU projects RelHy and ADEL. RelHy project developed testing protocols to investigate degradation mechanisms of solid oxide cells (CSC and ESC) and short-stacks under long term tests. At single-cell level a significantly higher power density has been observed amongst CSC cells. Tests using five-layer stacks nevertheless show that differences in power density are low (Lefebvre et al. 2010). and that ESC technology is therefore not necessarily characterized by weaker performance. Test protocols have been adapted to transient operation in the ADEL project following the need of operating the electrolysers with renewable electricity sources. In the project, demonstration of SOEC transient operation at cell (Petipas et al. 2013) and short-stack level (Fu et al. 2014) was performed.

In general, wide variety of durability tests is found in the literature. Measurements from few hundred to several thousand hours on different scales – from single cell to stack – and with different operating conditions (i.e. current density, temperature, reactant conversion) are reported. An overview is given in the following paragraphs and the major degradation issues identified are discussed.

Durability tests of SOCs can be divided in three main categories: stationary tests (fixed operating parameters for the duration of the test), cyclic tests (cycling conditions in SOEC mode) and reversible cycling tests (SOC periodically cycled from electrolysis to fuel cell mode during the test).

Stationary tests are the majority and generally are aimed at investigating the degradation rate of the cell/stack. Degradation rates are measured from the evolution of one parameter (voltage, current or ASR) versus time with respect to the value at the beginning of the test; the rates are usually expresses in %/h or in %/1000 h. A summary of the stationary durability tests reported in literature is given by Mougin (2015), who indicates degradation rates from 0.4 to 3.8 %/1000 h for different types of cells and operating conditions. The longest stationary durability test reported was performed at EIFER on an ESC developed by Kerafol (Ni/GDC cathode, SCSZ electrolyte, LSCF anode) (Schefold and Brisse 2014). The measured degradation rate was 0.6%/1000 h at 0.9 A/cm^2 and voltage near to the thermoneutral. This cell test is still running and has achieved now more than 17000 h of continuous load operation. Tests at stack level were also performed (Schimanke and Walter 2014). The degradation rate was slightly higher than in single cell tests, related to the cell contacting type. Tests up to 3000 h at 0.6 A/cm² and 40 % steam conversion showed voltage decrease rates from 10 to 15 mV/ 1000h. The lowest cell voltage

degradation of 10mV / 1000h corresponds to 0.7%/1000h, a low value but still too high for industrial applications.

Cyclic tests were performed in the ADEL project at cell and stack level. A cathode-supported cell from SOFCPower (Ni/YSZ cathode, YSZ electrolyte and LSCF/GDC anode) (Petipas et al. 2013) was subjected to 1800 cycles from 0 to 0.44 A/cm^2 during 140 h of test and showed a constant degradation rate of 5%/1000 h. A 5-cell SOEC stack by Topsoe Fuel Cell (TOFC) based on CSCs (Ni/YSZ cathode, YSZ electrolyte and CGO/LSC anode) was operated in transient operation with 756 on/off cycles from 0 to 0.6 A/cm^2 for an accumulate duration of 24 h after 2000 h of stationary operation (Fu et al. 2014). The stack showed no noticeable degradation during the short-term transient operation. Load cycling stability of SOEC was tested at SUNFIRE using a 30 cell stack (Ni/GDC cathode, SCSZ electrolyte, LSCF anode). The stack was brought to 0-80% load with constant steam supply by switching on and off the current and no degradation was reported for 20 on/off cycles (Posdziech 2015).

Reversible SOEC/SOFC cycling tests were performed by Versa Power Systems on cells and stacks (Tang et al. 2012). At cell level, a daily SOFC/SOEC cyclic test of over 600 days with a degradation rate of 1.5% per 1000 hours was reported and an accelerated 20-minute cycling was performed (over 6000 SOFC/SOEC cycles) with degradation less than 3% per 1000 cycles. At stack level (kW-class stack) a daily cyclic test of 100 cycles was conducted showing a performance loss of less 0.64 mV/cycle. The performance loss was concentrated in a cell located in the core of the stack and was attributed to a loss in electrical contact between the SOC anode and the metal interconnect. The loss of contact was linked to the thermal cycling due to SOEC/SOFC endo/exothermicity, which led to contraction of the stack core which lessened the contact pressure between components causing the loss in performance on an individual cell layer. A scale-up kW-class stack showed a cyclic decay 10 times higher than for the kW-class stack. It was concluded that the thermo-mechanical issues associated with SOFC/SOEC cyclic operation were magnified in the scale up configuration. TOFC studied the operational robustness of a 10-cell stack in rSOC operation (Wonsyld et al., 2014). No degradation was observed in 113 rSOC cycles between 0.23 (SOFC) and -0.66 (SOEC) A/cm^2 and limited temperature variations were measured in the stack. Cycles between ±0.3 A/cm^2 were also performed at low (750 °C) and high (800 °C) initial stack temperature showing no degradation during the high temperature cycling and a moderate degradation at low temperature (1.44 mΩ/cm^2/cycle in SOEC and 0.1 mΩ/cm^2/cycle in SOFC). The asymmetric load test and the high temperature symmetric load test indicated a temperature window between 760 °C and 790 °C with a very low degradation rate.

SUNFIRE performed reversible cyclic tests with 5 cell and 30 cell stacks, with up to 50 full cycles (12 h SOFC / 12 h SOEC) tested. (Posdziech 2015). The results show a slightly higher degradation rate than under steady-state conditions. An average voltage degradation of 0.06%/cycle was calculated. In the work of Njodzefon et al. (2012), a CSC (Ni/YSZ cathode, YSZ electrolyte and LSM/YSZ anode) was tested in stationary SOEC mode and cyclic reversible operation with high current densities (± 1.5 A/cm^2). The cell showed very high degradation in constant SOEC operation, which lead to cell failure after 530h of operation, while the reversible operated cell was still operational after 1060 h of test, even if high performance degradation was reported. Studies on reversible cycles were performed in the USA by NASA (Cable et al. 2011) and by General Electric (Guan et al. 2006). The first study showed very high degradation rates on symmetrical cells, the second an enhanced degradation in rSOC operation. The study of Graves et al. (2015) investigated the stationary SOEC and cyclic rSOC operation with the purpose to give an interpretation of the measured cell degradation. The study achieved 4000 h of reversible operation on a CSC cell (Ni/YSZ cathode, YSZ electrolyte and LSM/YSZ anode) and demonstrated that operating an SOC in a reversible cycling leads to negligible long-term degradation compared with constant electrolysis operation. The superior stability is attributed to the elimination of the microstructural degradation mechanism that occurs near the oxygen-electrode/electrolyte interface (more details on this and other degradation issues are given in the next paragraph). To summarize, studies on the reversible cycling demonstrated that switching an SOC from electrolysis to fuel cell mode do not lead to specific degradation related to polarity inversion. Reversing the current even demonstrated to be beneficial with respect to constant SOEC operation by eliminating degradation at the anode/electrolyte interface. However, investigations on single cells do not encompass the issues that arise at stack level due to thermal cycling that can lead to performance degradation due to thermo-mechanical effects (materials expansion/contraction).

Degradation issues in SOEC and rSOC

The Idaho National Laboratory reports in (Yan and Hino 2011) that very low degradation will be required for viable large-scale hydrogen production from SOECs; a degradation rate of 0.2%/1000 h can be considered as a target value for the technology (Giglio et al. 2015a). The review presented show that single cells are not very far from that target even if the degradation rates measured for SOECs are still higher than for SOFCs. The investigation of degradation phenomena is necessary to understand and overcome their causes.

The degradation rates are dependent on cell materials and cell operating conditions; the main parameters affecting the SOC durability during operation reported in literature are: operating temperature, current density, cell polarization, gas supplied (purity and type) and steam-to-hydrogen conversion rate. The main degradation issues are briefly discussed in the following paragraphs, a complete review can be found in the work Moçoteguy et al. (2013), on which this summary is mainly based.

Degradation of the oxygen electrode of the cell is the major cause of the accelerated degradation of SOECs. Two main phenomena determine the degradation of the SOEC anode: the delamination at the electrode/electrolyte interface and the formation of secondary phases within the electrode.

The first mechanism has been extensively reported and studied. Virkar (2010) elaborated a model for solid oxide electrolyzer cells which showed that under certain conditions, high oxygen partial pressure can develop in the electrolyte very near the oxygen electrode/electrolyte interface, leading to oxygen electrode delamination. The model explains that oxygen partial pressure in the electrolyte (at the electrolyte/air electrode interface) higher than those of the oxygen at the electrodes develops only in electrolysis mode, while the oxygen partial pressure in fuel cell mode is mathematically bounded between its values at the electrodes, so that degradation due to high oxygen pressure in the electrolyte cannot occur in fuel cell mode. This model also found that the higher is the electronic conductivity of the electrolyte, the lower is the tendency for high internal pressures to arise and showed that small changes in electronic conduction cause changes of orders of magnitude in oxygen partial pressure, and thus, a small amount of electronic conduction through the electrolyte is beneficial for the material stability. The model of Jacobsen and Mogensen also predicted the high oxygen partial pressure buildup at the anode/electrolyte interface (Jacobsen and Mogensen 2008). The extension of the reaction region beyond the electrode/electrolyte interface into the anode is envisaged as a solution to this issue. Composite YSZ/LSM or LSCF anodes allow larger electroactive volumes and the addition of GDC nanoparticles or oxygen diffusion promoters (i.e. Pd nanoparticles) to the anode can reduce the oxygen partial pressure buildup at the TPB (Moçoteguy et al. 2013). Also the cyclical reversible operation of SOCs demonstrated to be a solution to eliminate this degradation mechanism (Graves et al. 2015).

The formation of secondary phases is a mechanism originated by the dissociation of Cr containing species on the anode's surface. Volatile chrome oxides originated from stack

interconnects may deposit at the electrode–electrolyte interface and this deposition can result in deactivation of electrochemical reaction sites and/or delamination of the oxygen electrode.

Electrolyte degradation is also reported in SOEC operation. Knibbe et al. (2010) performed studies at high electrolysis current densities (> -1 A/cm^2); they observed an intergranular fracture degradation near the oxygen electrode/electrolyte interface and across the YSZ grain boundary they found pores that were attributed to the nucleation and growth of oxygen clusters in the YSZ grains. This mechanism is related to the gradient of oxygen partial pressure within the electrolyte that arise in SOEC operation. Studies on the Scandia and Ceria-doped Zirconia degradation under extreme SOEC conditions (Laguna-Bercero and Orera 2011) report that electrolyte reduction occurs near the cathode and then progresses along the thickness of the electrolyte and in some cases it is also associated with a phase change of the electrolyte. It was observed that this degradation occurs when the cells are operated at high voltage (above 1.8 V).

Cathode degradation is reported for electrolysis operation of SOCs with Ni-based electrodes under high steam content. Matsui et al. (2010) studied the influence of the fuel humidification on the performance and stability of the Ni–YSZ electrode at 1000 °C, and for high steam concentrations they found that the formation of hydroxide layers at the cermet led to performance degradation; microstructural studies confirmed a significant change in the Ni–YSZ microstructure. Hauch et al. (2008) reported degradation of SOEC performance during tests at 850°C, 50 vol.% steam and 0.5 A/cm^2; the authors observed by impedance spectroscopy that the degradation was mainly attributed to the Ni/YSZ electrode and by SEM they found the growth of Ni particles (i.e., nickel coarsening). Hauch (2007) reported the formation of impurities at the TPBs as a degradation mechanism. In particular, the phenomenon of cell passivation on the short-term shown in SOEC operation is attributed to the segregation of silica (SiO_2) originated from glass sealants or already present in the YSZ or Ni structures. The silica segregation on the TPB hinders the accessibility of electrochemically active sites causing performance degradation. This form of degradation is not totally irreversible. In fact, if the cell is operated in fuel cell mode, the opposite direction of ions migration in YSZ enhance the removal of segregated impurities from the TPB interface to the bulk of the cathode structure and partially re-activate the cell (Hauch et al. 2006). Also in this case, the reversible SOC operation is demonstrated to be beneficial for mitigating cell degradation.

1.5 Thesis outline

The Thesis is organized in the following Chapters:

- **Chapter 1: Introduction.** The context and background of this Thesis are described. An introduction to Electric Energy Storage technologies and to the Power-to-Gas concept is provided. The operating principles of SOCs are introduced and the state-of-the art of SOECs and rSOCs is reviewed.

- **Chapter 2: SOC and system modeling approach.** The physical-based SOC modeling is introduced and a detailed mathematical description of the physical phenomena included in the SOC models developed in this Thesis is given. The approaches followed in the modeling of P2G plant components are also explained.

- **Chapter 3: Numerical SOC modeling – cell and SRU models.** The implementation of the models developed at single cell and SRU levels is described. Three models are applied in this Thesis: a combined 1D/2D single-cell model for the study and validation of electrode kinetics in rSOC applications, a stationary 2D SRU model for the simulation of a stack unit in rSOC operation and a transient 3D model for the study of SRU dynamics.

- **Chapter 4: Experimental and single-cell model validation.** The experimental characterization of reversible SOCs with H_2/H_2O and CO/CO_2 gas mixtures is presented. The experimental results are discussed, and the results are used for the calibration and validation of the single-cell rSOC model presented in *Chapter 3*. The activation parameters of the electrodes evaluated from the model calibration are discussed and their physical consistency is verified.

- **Chapter 5: Analysis of SOC-based P2P applications.** The investigation of SOC-based P2P solutions is performed, different system configurations are simulated and compared. The system configuration and the operating parameters that ensure the highest charging/discharging and roundtrip efficiency are selected. A dynamic analysis of an rSOC operating in P2P conditions is performed using the 3D model described in *Chapter 3*, and the characteristic times of the thermal response of an SRU coupled with variable loads are

discussed. The size optimization of a hydrogen-based P2P plant based on rSOCs employed for the mitigation of RES fluctuations in a wind farm is presented.

- **Chapter 6: Analysis of SOEC-based P2G applications.** Two different P2G systems based on SOECs are investigated: the first is a hydrogen-based P2G system, which produces SNG from the methanation of CO_2 using the H_2 produced by water electrolysis in an SOEC stack, the second is a P2G system based on the direct co-electrolysis of H_2O and CO_2 in the SOEC stack for the production of syngas, which is then upgraded to SNG. The efficiencies of the two P2G configurations obtained from the simulations are discussed.

- **Chapter 7: Summary and conclusions.** The main conclusions of the Thesis are drawn.

Chapter 2

SOC and system modeling approach

The aim of this Thesis is the investigation of SOC-based P2G systems with state-of-the art technologies. Different configurations will be analyzed: hydrogen-based P2P with rSOC, SOEC-based electricity storage into hydrogen with subsequent SNG production and electricity storage by co-electrolysis of water and carbon dioxide with SOEC for SNG production. The analysis requires to develop models for simulation of the core-technologies of the P2G system – SOCs and methanation – and for the plant components.

In order to develop a reliable SOC model, it is necessary to establish a mathematical description of the intertwined phenomena occurring in the operation of an SOC in both electrolysis and fuel cell mode, which is discussed in this Chapter. Starting from the mathematical description, a numerical thermo-electrochemical and chemical model for the simulation of an rSOC has been developed at single cell level and validated (see *Chapter 3* and *Chapter* 4). The model has been extended at stack level for the simulation of an SOC stack repeating unit (SRU) and applied for the study of the relevant operating conditions and control strategies of SOECs and rSOCs integrated in P2G/P2P plants (see *Chapter 5* and *6*).

The introduction of this Thesis (see *Chapter 1*) has shown several technologies available for methanation. The target of this work is the investigation of SOC-based P2G with state-of-the art technologies; hence a mature methanation solution has been chosen. The fixed-bed methanation by TREMP^{TM} process was selected, as it proved to be effective for SNG production from H_2 and syngas (Giglio et al. 2015a and 2015b). This process has been developed for stationary operation; hence gas buffers have been introduced in the P2G system for decoupling the hydrogen/syngas production and methane synthesis. The modeling of methanation and P2G plant components has been addressed at system level. The approach followed is described at the end of this Chapter.

This Chapter provides a detailed description of the physics involved in SOC operation and of the approaches that can be followed for its modeling. The first part (*Section 2.1*) introduces SOC

thermodynamics before focusing on the mathematical modeling of SOCs (*Section 2.2*). System modeling is addressed in *Section 2.3* of the Chapter.

2.1 Thermodynamics of SOC systems

2.1.1 Energy balance of SOC systems

The thermodynamic analysis is performed by developing a steady-state energy balance on the SOC system shown in *Figure 2.1*. The SOC is approximated with a steady-state isothermal system at temperature T_{cell} and at pressure p_{cell}.

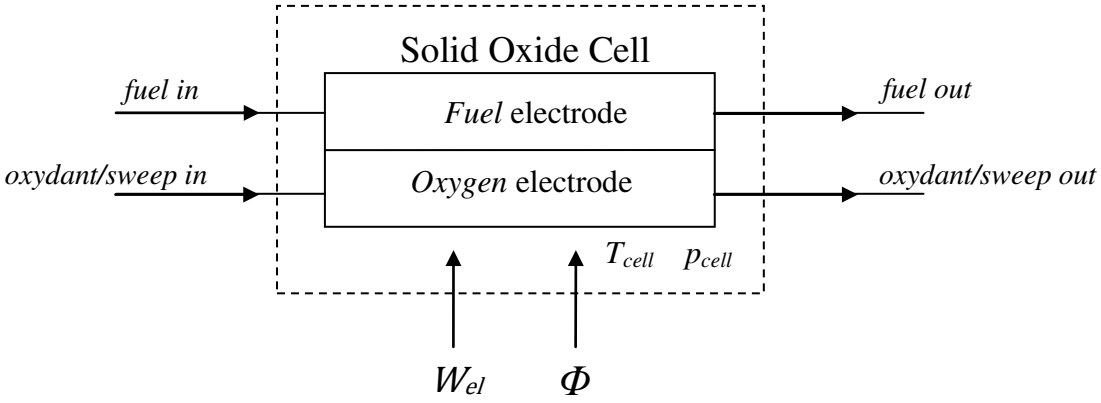

Figure 2.1 – SOC control volume, mass and energy streams of an SOC operating at temperature T_{cell} and total pressure p_{cell}.

Cell pressure is the total pressure of the gas mixture at the electrode, and it is assumed that both anode and cathode work at the same pressure p_{cell}, neglecting pressure drops in the analysis. It is worth noting that the total pressure at each electrode is the sum of the partial pressures of the gases that compose the stream fed to the electrode; although partial pressures of gases vary in the electrode during the operation of the cell (because reacting species are consumed and produced and diffuse in the electrode), the total pressure of the electrode remains unchanged. SOCs are usually operated at ambient pressure, as the cells tested in this work for the model validation (see *Chapter 4*); however pressurized SOCs systems also exist, and the operation up to 15 bar has been demonstrated (O'Brien et al. 2012). The control volume boundary is crossed by mass flows (reactants and products of the chemical and electrochemical reactions) and energy fluxes, the latter are the thermal (Φ) and electric power (W_{el}) exchanged by the cell. The heat flux Φ is positive when provided to the cell from the environment, while the electric power is described by the opposite sign convention; thus W_{el} is positive when generated by the cell. The kinetic and potential energy variations of inlet and outlet streams have been neglected in the calculation of energy balances.

As the thermodynamic analysis is focused only on the SOC, it is assumed that all the mass flows enter the system at the cell temperature and pressure; hence neither the heat needed for preheating the reactants, nor the heat recovery from the exiting streams have been considered. The gas flows accounted in the energy balance are only those that directly participate at the reactions, because the unreacted flows pass through the cell without adding or subtracting any energy flow, as a direct consequence the isothermal system assumption. Although they are not directly accounted in the global energy balance, the unreacted chemical species influences locally the thermodynamics of the reactions by determining the values of the partial pressures of gases at the electrodes.

Inside the SOC system, electrochemical reactions generate mass and energy sinks/sources and originate the motion of charge flows. Additional heat sources arise due to the charge transfer from ionic to electronic conductors and due the motion of electrical charges into the conductive media. The extent of the reduction/oxidation reactions is measured by total current of the cell, which is related to the gas flows consumed/produced in the electrochemical reactions according to Faraday's law:

$$\Delta\dot{n}_{redox} = \frac{I}{nF} \tag{2.1}$$

where $\Delta\dot{n}_{redox}$ is the molar flow rate (mol s^{-1}) of the produced/consumed chemical species, I (A) is the cell current (positive in SOFC mode and negative in SOEC mode), F is the Faraday's constant (96485 C mol^{-1}) and n is the number of moles of electrons transferred in the reaction per mole of reactant. The electrochemical reactions considered in this analysis are the reduction/oxidation of H_2O/H_2 and CO_2/CO (see (1.15) - (1.20) in *Chapter 1*), which involves the production/consumption of molar flows as follows:

$$\Delta\dot{n}_{H_2/COec} = -\left({}^{I}/_{2F}\right) \tag{2.2}$$

$$\Delta\dot{n}_{H_2O/CO_2ec} = \left({}^{I}/_{2F}\right) \tag{2.3}$$

$$\Delta\dot{n}_{O_2ec} = -\left({}^{I}/_{4F}\right) \tag{2.4}$$

The electrical power produced/consumed by the electrochemical reactions is the product between the operating voltage of the cell and the current:

$$W_{el} = V_{cell} \cdot I \tag{2.5}$$

Cell voltage is always positive, while the current follows the aforementioned convention, which implies that W_{el} is negative in SOEC operation and positive in SOFC. The operating voltage can be calculated as a positive or negative deviation (depending on the operating mode) from a reversible cell voltage (E_{rev}) by a current-dependent overpotential (η):

$$V_{cell} = E_{rev} + \gamma\eta \tag{2.6}$$

in which γ is the reaction coefficient (γ = +1 in SOEC mode and γ = −1 in SOFC mode). Reversible cell voltage and overpotential are functions of temperature and partial pressures of the chemical species, while η is also function of cell current. Equation (2.6) describes what is called current-voltage characteristic or polarization curve of the SOC. A representative current-voltage curve experimentally measured on a cell tested in reversible operation is given in *Figure 2.2*.

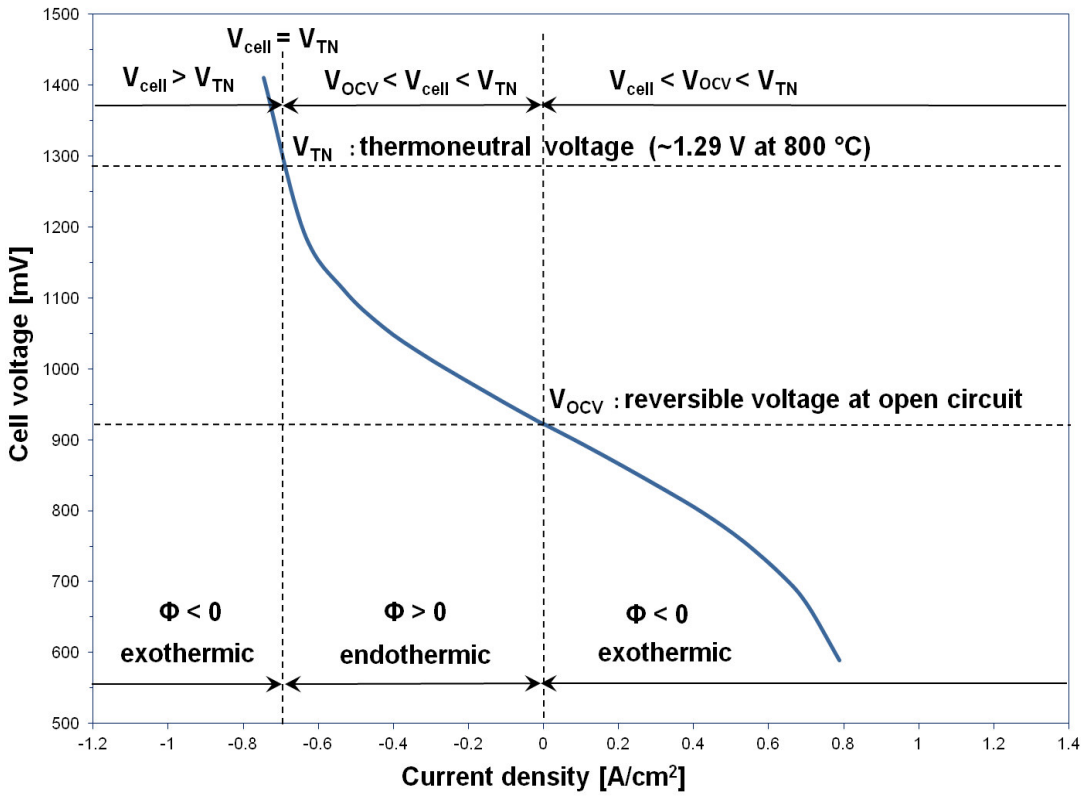

Figure 2.2 – Experimental rSOC polarization. Test with 50%$_{vol}$ H_2 / 50%$_{vol}$ H_2O at 800°C.

The heat sink/source related to an electrochemical reaction is function of temperature and entropy variation of the redox process:

$$\phi_{react} = T_{cell}\Delta S_{react} = -\gamma \cdot T_{cell} \cdot \frac{I}{nF}\Delta \bar{s}_{react} \tag{2.7}$$

where $\Delta \bar{s}_{react}$ (J/mol/K) is the molar entropy variation of the reaction. The entropy variation of oxidation processes is negative, thus the operation in fuel cell mode (i.e., oxidation of H_2 and/or CO), which is associated to a positive current production, generates a negative heat flux of the reaction. For the convention adopted, a negative flux means an exothermic operation (i.e., flux exiting from the control volume). Indeed, in SOFC operation the heat produced by the reaction must be removed by the system to maintain it in isothermal conditions. Reduction processes have an opposite thermal behavior, with positive entropy changes and positive heat flows. In fact, SOEC operation requires that heat is supplied to the cell to balance the endothermic reactions and maintain isothermal conditions. If we look at the isothermal system of *Figure 2.1*, heat can be supplied from an external source or it can be provided by internal irreversible processes. In SOC operation, these processes are associated the charge transfer and charge motion processes, that originate the overpotential η described in equation (2.6). More details on the irreversible processes and on the modeling approaches followed to describe them are given in *Section 2.2* of this Chapter.

As explained in *Chapter 1*, chemical reactions take place contemporary to the electrochemical ones. These reactions also originate sinks/sources of heat and chemical species, while are not involved in charge transfer processes. The molar flows of the species produced/consumed by chemical reactions are determined by the rate of the reactions and stoichiometry. For a generic chemical species α involved in k reactions, the net source/sink term can be expressed as:

$$\Delta \dot{n}_{\alpha,chem} = \sum_{i=1,k} \nu_{\alpha i} r_i \tag{2.8}$$

where r_i (mol s^{-1}) is the rate of the i-th reaction and $\nu_{\alpha i}$ is the stoichiometric coefficient of the α species in the i-th reaction. The chemical reactions considered within the SOC in this analysis are the water-gas shift (direct and reverse) and the methanation/reforming reaction (see (1.21) and (1.22) in *Chapter 1*), which involves the production/consumption of molar flows as follows:

$$\Delta \dot{n}_{H_2ch} = r_{WGS} + 3r_{MSR} \tag{2.9}$$

$$\Delta \dot{n}_{COch} = -r_{WGS} + r_{MSR} \tag{2.10}$$

$$\Delta\dot{n}_{H_2Och} = -r_{WGS} - r_{MSR} \tag{2.11}$$

$$\Delta\dot{n}_{CO_2ch} = r_{WGS} \tag{2.12}$$

$$\Delta\dot{n}_{CH_4ch} = -r_{MSR} \tag{2.13}$$

where r_{WGS} and r_{MSR} are the molar rates (mol s^{-1}) of the water gas shift and methane steam reforming reactions. These rates can be positive or negative depending on the equilibrium of the reactions. More details on the modeling approaches followed to describe the reaction rates are given in *Section 2.2*. The net heat sink/source related to chemical reactions is derived straightforward:

$$\Phi_{chem} = \sum_{i=1,k} r_i \Delta\bar{h}_{i,ch} \tag{2.14}$$

where $\Delta\bar{h}_{i,ch}$ (J mol^{-1}) is the molar enthalpy variation of the *i*-th reaction, which is negative for exothermic reactions and positive for the endothermic ones. The net chemical heat flux Φ_{chem} (W) follows the aforementioned sign convection of the system, thus is negative if the exothermic reactions prevails on the endothermic ones.

Once the effect of chemical and electrochemical reactions on mass and energy balances is established, first and second law of thermodynamics are applied to the system of *Figure 2.1*:

$$\Phi - W_{el} = \left(\dot{n}_{fuel,out}\bar{h}_{fuel,out} + \dot{n}_{ox,out}\bar{h}_{ox,out}\right) - \left(\dot{n}_{fuel,in}\bar{h}_{fuel,out} + \dot{n}_{ox,in}\bar{h}_{ox,in}\right) \tag{2.15}$$

$$\frac{\Phi}{T_{cell}} + \dot{\sigma}_{irr} = \left(\dot{n}_{fuel,out}\bar{s}_{fuel,out} + \dot{n}_{ox,out}\bar{s}_{ox,out}\right) - \left(\dot{n}_{fuel,in}\bar{s}_{fuel,out} + \dot{n}_{ox,in}\bar{s}_{ox,in}\right) \tag{2.16}$$

in which $\bar{h}_k$ and $\bar{s}_k$ are the molar enthalpy (J/mol) and molar entropy (J/mol/K) of the *k* flow, $\dot{\sigma}_{irr}$ (W/K) is the entropy generation rate in the system, Φ (W) is the net thermal power exchanged by the SOC and W_{el} (W) is the electric power generated/consumed. The molar enthalpy and entropy changes of chemical and electrochemical reactions considered in this study can be expressed as:

$$\Delta\bar{h}_{ec,H_2H_2O} = \gamma\left(\bar{h}_{H_2} + \tfrac{1}{2}\bar{h}_{O_2} - \bar{h}_{H_2O}\right) \tag{2.17}$$

$$\Delta\bar{h}_{ec,COCO_2} = \gamma\left(\bar{h}_{CO} + \tfrac{1}{2}\bar{h}_{O_2} - \bar{h}_{CO_2}\right) \tag{2.18}$$

$$\Delta\bar{s}_{ec,H_2H_2O} = \gamma\left(\bar{h}_{H_2} + \frac{1}{2}\bar{s}_{O_2} - \bar{s}_{H_2O}\right) \tag{2.19}$$

$$\Delta\bar{s}_{ec,COCO_2} = \gamma\left(\bar{s}_{CO} + \frac{1}{2}\bar{s}_{O_2} - \bar{s}_{CO_2}\right) \tag{2.20}$$

$$\Delta\bar{h}_{ch,WGS} = \left(\bar{h}_{H_2} + \bar{h}_{CO_2} - \bar{h}_{CO} - \bar{h}_{H_2O}\right) \tag{2.21}$$

$$\Delta\bar{h}_{ch,MSR} = \left(\bar{h}_{CH_4} + \bar{h}_{H_2O} - 3\bar{h}_{H_2} - \bar{h}_{CO}\right) \tag{2.22}$$

$$\Delta\bar{s}_{ch,WGS} = \left(\bar{s}_{H_2} + \bar{s}_{CO_2} - \bar{s}_{CO} - \bar{s}_{H_2O}\right) \tag{2.23}$$

$$\Delta\bar{s}_{ch,MSR} = \left(\bar{s}_{CH_4} + \bar{s}_{H_2O} - 3\bar{s}_{H_2} - \bar{s}_{CO}\right) \tag{2.24}$$

Equations (2.15) and (2.16) can be rearranged by using the above relations to show enthalpy and entropy changes associated to the considered reactions:

$$\Phi - W_{el} = -\gamma\left({}^{I}/_{2F}\right)\left(\Delta\bar{h}_{ec,H_2H_2O} + \Delta\bar{h}_{ec,COCO_2}\right) + r_{WGS}\Delta\bar{h}_{ch,WGS} + r_{MSR}\Delta\bar{h}_{ch,MSR} \tag{2.25}$$

$$\frac{\Phi}{T_{cell}} + \dot{\sigma}_{irr} = -\gamma\left({}^{I}/_{2F}\right)\left(\Delta\bar{s}_{ec,H_2H_2O} + \Delta\bar{s}_{ec,COCO_2}\right) + r_{WGS}\Delta\bar{s}_{ch,WGS} + r_{MSR}\Delta\bar{s}_{ch,MSR} \tag{2.26}$$

Deriving the electric power term from equation (2.25) by substituting Φ from equation (2.26), the final expression obtained is:

$$\begin{gathered} W_{el} = -\gamma\left({}^{I}/_{2F}\right)T_{cell}\left(\Delta\bar{s}_{ec,H_2H_2O} + \Delta\bar{s}_{ec,COCO_2}\right) + r_{WGS}T_{cell}\Delta\bar{s}_{ch,WGS} + \\ + r_{MSR}T_{cell}\Delta\bar{s}_{ch,MSR} + -T_{cell}\dot{\sigma}_{irr} + \gamma\left({}^{I}/_{2F}\right)\left(\Delta\bar{h}_{ec,H_2H_2O} + \Delta\bar{h}_{ec,COCO_2}\right) - \\ + r_{WGS}\Delta\bar{h}_{ch,WGS} - r_{MSR}\Delta\bar{h}_{ch,MSR} \end{gathered} \tag{2.27}$$

The expression can be further rearranged by highlighting the Gibbs free energy of the reactions:

$$\begin{gathered} W_{el} = \gamma\left({}^{I}/_{2F}\right)\left(\Delta\bar{g}_{ec,H_2H_2O} + \Delta\bar{g}_{ec,COCO_2}\right) - r_{WGS}\Delta\bar{g}_{ch,WGS} - r_{MSR}\Delta\bar{g}_{ch,MSR} - \\ T_{cell}\dot{\sigma}_{irr} \end{gathered} \tag{2.28}$$

in which the Gibbs free energy is defined as:

$$\Delta\bar{g} = \Delta\bar{h} - T\Delta\bar{s} \tag{2.29}$$

Equation (2.28) can be easily extended by adding other electrochemical (i.e., $\left({}^{I}/_{nF}\right)\Delta\bar{g}_{ec}$) and chemical terms (i.e., $r_{ch}\Delta\bar{g}_{ch}$) to take into account other reactions. It is worth noting that for chemical reactions $\Delta\bar{g}$ is zero at equilibrium. As shown later in the discussion, WGS and MSR can be considered at equilibrium within the fuel electrode of SOCs with a good approximation, especially in the case of fuel-electrode supported cells; hence, the terms related to chemical reactions in equation (2.28) become zero:

$$W_{el} = \gamma\left({}^{I}/_{2F}\right)\left(\Delta\bar{g}_{ec,H_2H_2O} + \Delta\bar{g}_{ec,COCO_2}\right) - T_{cell}\dot{\sigma}_{irr} \tag{2.30}$$

Equation (2.30) shows that the power required by the cell working in electrolysis (i.e., negative power) is the sum of two terms: the first is the electricity required by the reactions (negative term, as the cell current is negative and the Gibbs free energy variation is positive is SOEC), the second accounts for the energy losses generated by irreversibility. The first term can be considered as the minimum energy required by the electrolysis process when the cell is operating in ideal conditions without irreversible losses. In SOFC operation, the power produced by the cell is given by the difference between the maximum power that can be generated and the power lost by irreversibility. In *Section 2.1.3*, equation (2.30) will be rearranged to highlight the cell voltage.

If we consider an ideal reversible cell (i.e., $\dot{\sigma}_{irr} = 0$) and the separate contribution of H_2/H_2O and CO/CO_2 oxido-reduction reactions, the reversible cell power can be expressed per unit of current as:

$$\frac{W_{el,rev}}{\gamma I} = \frac{\Delta\bar{g}_{H_2/H_2O-CO/CO_2}}{2F} = \frac{\Delta\bar{h}_{H_2/H_2O-CO/CO_2}}{2F} - T_{cell}\frac{\Delta\bar{s}_{H_2/H_2O-CO/CO_2}}{2F} \tag{2.31}$$

in which all terms have the dimension of potentials (V). The terms of equation (2.31) have important physical meanings: $\Delta\bar{g}$ represents the minimum electricity required by the electrolysis reaction (or the maximum power that can be generated by the reaction in SOFC mode), $\Delta\bar{h}$ is the total energy absorbed/released by the reaction and $T_{cell}\Delta\bar{s}$ represents the heat required/produced by the reaction. Gibbs free energy and entropy are functions of temperature and pressure, while enthalpy depends nearly only on temperature, consequently $\Delta\bar{g}$ and $\Delta\bar{s}$ depends on T_{cell} and p_{cell}, while $\Delta\bar{h}$ only on T_{cell}. The trends of the three quantities are reported in *Figure 2.3* and *2.4* as functions of the temperature of the cell at standard pressure (i.e., the apex "0" indicates the standard pressure); *Figure 2.3* displays the quantities for the steam electrolysis and *Figure 2.4*

for carbon dioxide electrolysis, $\Delta\bar{g}^0$, $\Delta\bar{h}^0$ and $\Delta\bar{s}^0$ were calculated using the JANAF Tables (Chase et al. 1998). In the figures also the theoretical roundtrip efficiency is reported, the explanation of this quantity is given in the *Section 2.1.4*.

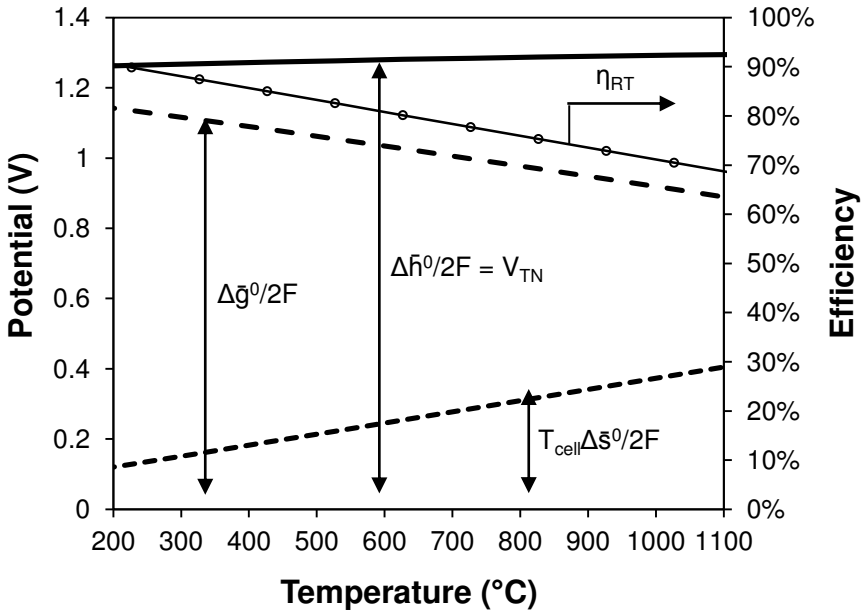

Figure 2.3 – Thermodynamics of H_2/H_2O redox reaction.

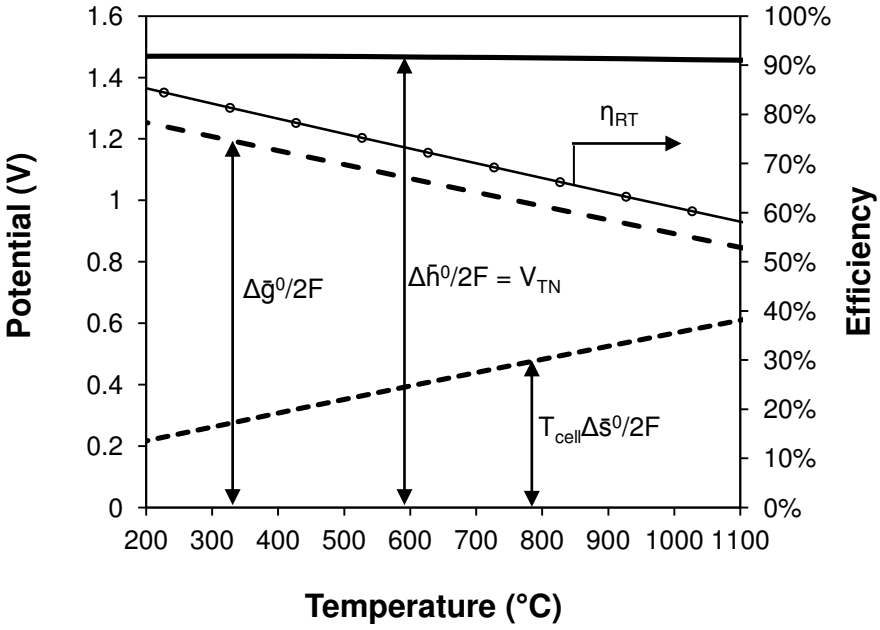

Figure 2.4 – Thermodynamics of CO/CO_2 redox reaction.

Figure 2.3 and *2.4* show that the Gibbs free energy change of the reaction decreases with the increasing temperature for both the redox chemistries, while the product of temperature and entropy change increases. Therefore, for reversible operation, the electrical work required/produced decreases with temperature, thus and a larger fraction of the total energy required for electrolysis can be supplied in the form of heat. From the exergetic point of view, it is a great advantage to replace a part of the electricity consumption with heat, since heat has lower exergetic content. The ratio of $\Delta\bar{g}^0$ over $\Delta\bar{h}^0$ is about 93% at 100 °C for steam electrolysis, decreasing to only about 70% at 1000 °C. Operation of the electrolytic cell at high temperature is also desirable from the standpoint of reaction kinetics and electrolyte conductivity, both of which considerably improve at higher operating temperatures. However, if thermodynamics and kinetics are advantageous for high-temperature electrolysis, potential drawbacks are the need of high-temperature process heat to preheat the reactants if the cell works below the thermo-neutral voltage (condition in which the cell cannot supply by itself the required reaction heat, as it will be explained later) and materials degradation. The SOFC operation is thermodynamically favored at low-temperature, as an higher fraction of the total energy of the redox reaction can be converted in electricity; however slow reactions kinetics and low electrolyte conductivity are the main drawbacks of the operation at low-temperature. Nevertheless, materials improvements are lowering the required temperature of fuel cells and intermediate temperature SOCs operating down to 650 °C or less have been developed (Brett et al. 2008).

2.1.2 Reversible Cell Voltage (Gibbs voltage)

The Gibbs free energy variation of redox reactions can be expressed as function of temperature and partial pressures of reactants, when ideal gas approximation is considered, as will be explained in *Section 2.2*. In the case of H_2/H_2O redox, the expression is the following:

$$\Delta\bar{g}_{H_2/H_2O}(T_{cell}, p_{cell}) = \Delta\bar{g}^o_{H_2/H_2O}(T_{cell}, p^0) + \gamma RT_{cell} ln\left[\frac{p_{H_2}}{p_{H_2O}}\left(\frac{p_{O_2}}{p^o}\right)^{1/2}\right] \quad (2.32)$$

in which p^0 is the standard pressure (i.e., p^0 = 1 atm). The reversible cell voltage can be expressed by substituting (2.32) in expression (2.31) and considering the absolute value of the cell power to obtain a general definition independent of the sign convention:

$$E_{rev,H_2/H_2O} = \frac{\gamma\Delta\bar{g}^o_{H_2/H_2O}(T_{cell}, p^0)}{2F} + \frac{RT_{cell}}{2F} ln\left[\frac{p_{H_2}}{p_{H_2O}}\left(\frac{p_{O_2}}{p^o}\right)^{1/2}\right] \quad (2.33)$$

The voltage $E_{rev,H_2/H_2O}$ corresponds to the potential difference that must be applied across the ideal reversible cell to accomplish the electrolysis reaction, or the potential that the cell can generate in case of fuel cell operation. The reversible voltage defined in (2.33) is composed by two terms; the first one is the ideal reversible potential with reactants and products at standard pressure. It is worth noting that this term is always positive, since the product of γ and Gibbs free energy variation of the reaction is always positive (i.e., both positive in SOEC and both negative in SOFC). The second term on the right side of equation (2.33) accounts for the effects of partial pressures of reactants and products. The effect of the total pressure of the cell can be highlighted by rewriting the Gibbs potential as follows:

$$E_{rev,H_2/H_2O} = \gamma \frac{\Delta \bar{g}^o_{H_2/H_2O}}{2F} + \frac{RT_{cell}}{2F} ln\left[\frac{y_{H_2}\left(y_{O_2}\right)^{1/2}}{y_{H_2O}}\right] + \frac{RT_{cell}}{2F} ln\left[\left(\frac{p_{cell}}{p^o}\right)^{1/2}\right] \qquad (2.34)$$

where y_{H_2}, y_{O_2} and y_{H_2O} are the molar fractions of the chemical species. The reversible voltage of the CO/CO_2 redox chemistry can be similarly obtained. When both CO/CO_2 and H_2/H_2O redox chemistries occur in the cell, it is possible to demonstrate that, under the assumption of having the fuel mixture in equilibrium conditions on the TPB surfaces of the electrode, the reversible voltages of the two reactions are equal because of the WGS reactions. The demonstration is given later when addressing the modeling of cell potentials (see *Section 2.2.4*).

The reversible cell voltage calculated in equation (2.33) is the well-known Nernst potential of the cell. In this dissertation we will refer to the potential calculated in (2.33) as the reversible voltage or Gibbs voltage of the cell. In the present thermodynamic analysis, the SOC is considered as a 0-D system with only one value of temperature and one partial pressure for each chemical species, thus the Nernst voltage assumes a unique value. However, it is worth noting that in real SOCs pressures of products and reactants and cell temperature vary along gas distribution channels and inside the porous electrodes when the cell is operating. Thus, the reversible potential defined in (2.33) cannot be uniquely defined. A detailed discussion about the interpretation of the reversible potential and on the modeling approaches for its modeling is given later in *Section 2.2* of this Chapter.

Equation (2.34) shows the dependence of the reversible voltage on temperature, pressure and molar fractions of reactants and products. Focusing on the effect of temperature and pressure, the reversible voltage decreases with the increasing temperature, while a pressure increase has the opposite effect to increase the voltage. Thus, from the thermodynamics point of view, high-

temperature, low-pressure operation is beneficial for the SOEC operation, as it lowers the operating voltage, while the low-temperature, high-pressure operation gives advantages to SOFC mode by increasing the produced voltage. However, diffusion and kinetics/charge conduction limitations are the drawbacks of low-pressure and low-temperature operation respectively. The standard-state potential is a completely ideal value that is never reached by real systems, even at open circuit, because in real cells reactants and products are always mixed and consequently none of them reach the total electrode pressure. In particular, in most practical SOEC systems, the incoming steam is mixed with some hydrogen to maintain reducing conditions on the steam-side electrode, typically a Nickel cermet, while in SOFC operation pure hydrogen is also allowed. On the oxygen side of the cells, air is usually feed in both SOEC and SOFC operation; hence the oxygen partial pressure at open circuit is only about 0.21 of the operating pressure. In fuel cell operation the use of pure oxygen instead of air is advantageous from the thermodynamics point of view as it allows a higher cell voltage. However, pure oxygen must be available to use it in the cell. This option is feasible in rSOC operation in P2P systems if the oxygen produced during electrolysis operation is stored and re-used during hydrogen oxidation. A discussion on the use of pure oxygen in P2P systems is given in *Chapter 5*. The main drawbacks of this practice are material issues associated with the handling of pure oxygen at elevated temperatures. In SOEC operation, the use of a sweep gas for the anode with the lowest possible concentration of oxygen is recommended from the thermodynamics point of view to maintain a low oxygen partial pressure at the electrode, thus reducing the reversible voltage of the cell. There are also other reasons to consider the use of a sweep gas on the oxygen side. Indeed, the use of a sweep gas will minimize the performance degradation associated with any leakage of hydrogen from the steam/hydrogen side to the oxygen side of the cell. Finally, lowering the oxygen concentration is beneficial for the materials, especially the metallic interconnects.

2.1.3 Thermoneutral voltage

Although the electrolysis reaction is endothermic, heat sources arise in SOEC operation due to the internal irreversibility related to charge transfer processes and charge motion into conductive media. It is possible to demonstrate that the heat produced by irreversibility exactly balances the heat absorbed by the electrolysis reaction at a particular value of the cell voltage, called themo-neutral voltage. The demonstration is given in the next paragraphs. Before addressing the mathematical definition of thermonetural, it is necessary to derive the heat

production by irreversibility. Equation (2.30) can be rearranged to show the effect of cell irreversibility on the energy balance of the cell by substituting equations (2.5), (2.6) and (2.7):

$$W_{el} = V_{cell} \cdot I = (E_{rev} + \gamma\eta) \cdot I = \gamma\left(I/_{2F}\right)\left(\Delta\bar{g}_{ec,H_2H_2O} + \Delta\bar{g}_{ec,COCO_2}\right) - T_{cell}\dot{\sigma}_{irr} \quad (2.35)$$

$$(E_{rev} + \gamma\eta) \cdot I = \gamma\left(I/_{2F}\right) \cdot \Delta\bar{g}_{ec}(T_{cell}, p_{cell}) - T_{cell}\dot{\sigma}_{irr} \quad (2.36)$$

The reversible voltage on the left side of equation (2.36) is equal to the first term on the left side of the equation, thus the overvoltage related to irreversibility can be expressed as:

$$\eta = -\frac{1}{\gamma \cdot I} T_{cell}\dot{\sigma}_{irr} = \frac{1}{\gamma \cdot I} \cdot \phi_{loss} \quad (2.37)$$

The term ϕ_{loss} in equation (2.37) represents the heat generated in the cell by irreversibility. The irreversibility generated (i.e., $\dot{\sigma}_{irr}$) is always positive and consequently heat losses are associated to a negative heat flux; thus, the heat generated by losses must be removed from the system to maintain the isothermal operation, consistently with the sign convention adopted. Another step needed before examining the energy balance of the cell to define the thermoneutral voltage, is the definition of the role of WGS in shifting the balance between H_2/H_2O and CO/CO_2 redox reactions. In equation (2.25) and followings, the total cell current has been considered. However, this current is composed by the contribution of both H_2/H_2O and CO/CO_2 redox reactions:

$$I = I_H + I_C \quad (2.38)$$

The WGS reaction (direct or reverse) converts a mole of reactant of one the two redox reactions considered into a mole of reactant of the other reaction. The same conversion takes place for the products. Thus, the WGS doesn't change the total ratio between reactants and products of the H_2/H_2O and CO/CO_2 redox chemistries. Moreover, the enthalpy variation of WGS reaction is the difference between the enthalpy variations of the redox reactions:

$$\Delta\bar{h}_{ch,WGS} = \Delta\bar{h}_{ec,H_2H_2O} - \Delta\bar{h}_{ec,COCO_2} \quad (2.39)$$

Consequently, if the WGS reaction is considered in the energy balance of the cell, it is irrelevant if a mole of electrons is produced/consumed by one of the redox reactions or by the other, since

the energy difference between the two is balanced by the WGS. Therefore, from the point of view of the global energy balance of the cell, it is correct to assume all the current produced/consumed by only one of the two redox chemistry if the WGS is considered in the balance. It is straightforward to demonstrate from (2.38) and (2.39) that if only the H_2/H_2O redox reaction is considered – together with WGS for taking into account the conversion of the CO to H_2 and the H_2O to CO_2 – the global balance is the same of considering the two separate redox paths:

$$\frac{I_H + I_C}{2F}\Delta\bar{h}_{ec,H_2H_2O} - \frac{I_C}{2F}\Delta\bar{h}_{ch,WGS} = \frac{I_H}{2F}\Delta\bar{h}_{ec,H_2H_2O} + \frac{I_C}{2F}\Delta\bar{h}_{ec,COCO_2} \tag{2.40}$$

Once the definition of heat losses is established, and given that only one electrochemical reaction can be considered in the energy balance of the cell, equation (2.25) can be rewritten as:

$$\phi - W_{el} = -\gamma\left({}^{I}/_{2F}\right)\left(\Delta\bar{h}_{ec,H_2H_2O}\right) + r_{WGS}\Delta\bar{h}_{ch,WGS} + r_{MSR}\Delta\bar{h}_{ch,MSR} \tag{2.41}$$

$$\begin{aligned}\phi - W_{el} = -\gamma\left({}^{I}/_{2F}\right)\left(\Delta\bar{g}_{ec,H_2H_2O} + T_{cell}\cdot\Delta\bar{s}_{ec,H_2H_2O}\right) + r_{WGS}\Delta\bar{h}_{ch,WGS} \\ + r_{MSR}\Delta\bar{h}_{ch,MSR}\end{aligned} \tag{2.42}$$

$$\phi - W_{el} = -E_{rev}\cdot I + \phi_{react} + r_{WGS}\Delta\bar{h}_{ch,WGS} + r_{MSR}\Delta\bar{h}_{ch,MSR} \tag{2.43}$$

$$\begin{aligned}\phi - V_{cell}\cdot I = \phi - (E_{rev} + \gamma\eta)\cdot I = \\ = -E_{rev}\cdot I + \phi_{react} + r_{WGS}\Delta\bar{h}_{ch,WGS} + r_{MSR}\Delta\bar{h}_{ch,MSR}\end{aligned} \tag{2.44}$$

$$\phi = \phi_{loss} + \phi_{react} + r_{WGS}\Delta\bar{h}_{ch,WGS} + r_{MSR}\Delta\bar{h}_{ch,MSR} = \phi_{loss} + \phi_{react} + \phi_{chem} \tag{2.45}$$

The net heat balance of the SOC is thus constituted by three terms: the exothermic heat losses by irreversibility, the heat generated (SOFC) or consumed (SOEC) by electrochemical reactions and the heat generated/consumed by the chemical reactions.

The thermoneutral voltage, V_{TN}, is a particular value of the cell voltage at which the net heat balance shown in equation (2.45) is zero, i.e. the produced heat balances the thermal energy required by the reactions. Thus, V_{TN} is the voltage that allows the system to be operated isothermal in adiabatic conditions. The thermoneutral voltage related with a redox reaction is

generally defined as the enthalpy change associated with an electrochemical reaction per mole of electrons transferred:

$$V_{TN,redox} = \frac{\Delta\bar{h}_{redox}(T_{cell})}{2F} \tag{2.46}$$

The mathematical definition of V_{TN} given in (2.46) can be extended including also the chemical reactions. The definition is derived directly from the heat balance of the cell (eq. (2.41)) by imposing the adiabatic operation (i.e., $\phi = 0$):

$$-V_{TN} \cdot I = -\gamma\left({}^{I}/_{2F}\right)\left(\Delta\bar{h}_{ec,H_2H_2O}\right) + r_{WGS}\Delta\bar{h}_{ch,WGS} + r_{MSR}\Delta\bar{h}_{ch,MSR} \tag{2.47}$$

$$V_{TN} = \gamma\frac{\Delta\bar{h}_{ec,H_2H_2O}}{2F} - \frac{r_{WGS}\Delta\bar{h}_{ch,WGS}}{I} - \frac{r_{MSR}\Delta\bar{h}_{ch,MSR}}{I} \tag{2.48}$$

$$V_{TN} = V_{TN,H_2H_2O} - \left(\frac{r_{WGS}\Delta\bar{h}_{ch,WGS}}{I} + \frac{r_{MSR}\Delta\bar{h}_{ch,MSR}}{I}\right) \tag{2.49}$$

The cell thermoneutral voltage is thus different from the thermoneutral voltage of the redox reaction due to the chemical side reactions occurring in the cell. In particular, exothermic reactions ($\Delta\bar{h}_{ch} < 0$) in SOEC operation (i.e., I<0) reduces the value of the thermonetural voltage.

Figure 2.2 graphically shows the thermoneutral voltage and the different thermal regimes of a cell starting from an experimental polarization with an H_2/H_2O mixture. From the thermodynamics point of view, the cell characteristic can be divided in three sections: an exothermic section in SOFC mode, in which all the heat sources (i.e., electrochemical and irreversibility, chemical reactions are not present with H_2/H_2O mixtures) are positive, an endothermic SOEC part for $V_{cell} < V_{TN}$ – in which the reaction heat is higher than the irreversibility heat generation – and an exothermic SOEC section for $V_{cell} > V_{TN}$. *Figure 2.5* shows the net heat balance obtained from the simulation of an electrolyte-supported cell (see *Section 5.3*).

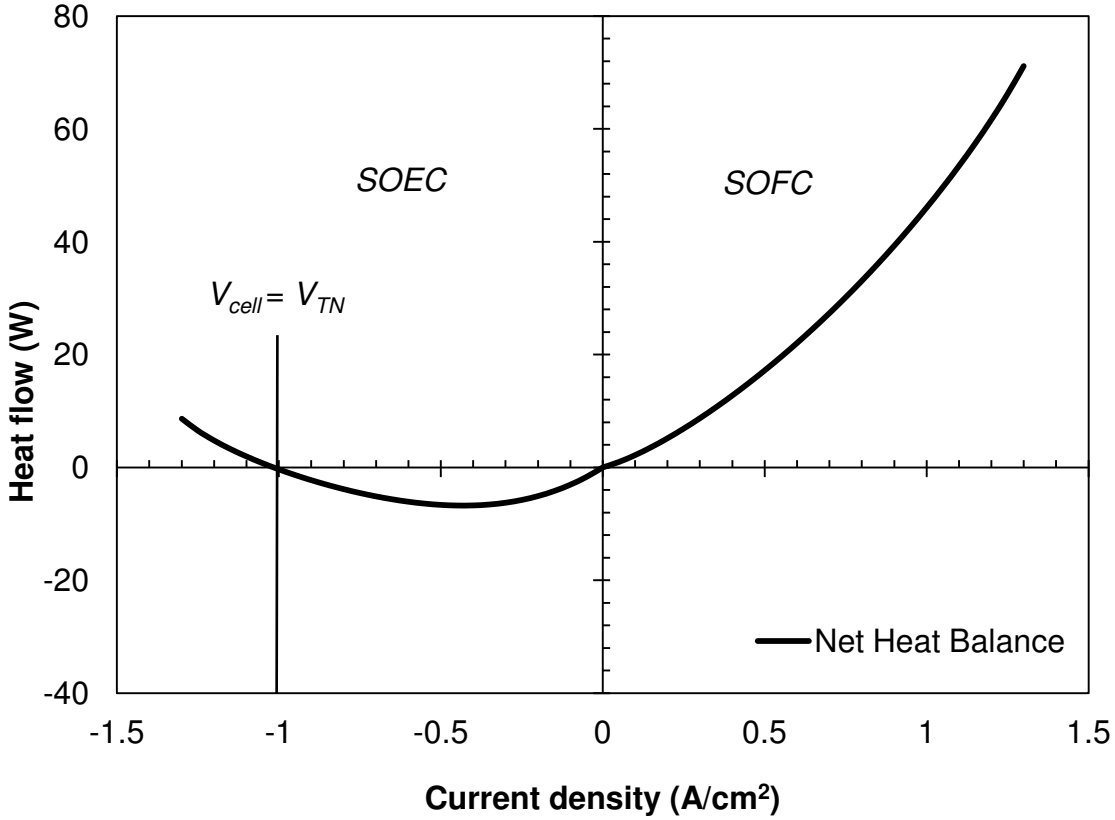

Figure 2.5 – Simulated net heat balance for an ESC cell operating at ambient pressure with pure oxygen as oxidant and gas mixtures composed by 90%H_2 / 10%H_2O (SOFC) and 10%H_2 / 90% H_2O (SOEC), with inlet gas temperatures 800 °C.

The net heat that must be provided/removed to/from an SOC to maintain the isothermal operation can be calculated as:

$$\phi = (V_{cell} - V_{TN}) \cdot I \tag{2.50}$$

In SOFC mode, heat is generated when the cell voltage is lower than the thermoneutral voltage of the cell (V_{TN}). It is worth noting that the SOFC cell voltage V_{cell} is always lower than the redox thermoneutral of the cell:

$$V_{cell} = E_{rev} - \eta I = \frac{\Delta \bar{g}_{ec,redox}}{2F} - \eta I = \frac{\Delta \bar{h}_{ec,redox} - T_{cell} \cdot \Delta \bar{s}_{ec,redox}}{2F} - \eta I$$
$$< V_{TN,redox} = \frac{\Delta \bar{h}_{ec,redox}}{2F} \tag{2.51}$$

However, the redox thermoneutral can be higher that the cell V_{TN}, for example when strongly endothermic reactions occur within the cell (i.e., methane steam reforming). In this case, the V_{TN} can be lower than the reversible voltage of the cell at open circuit, and SOFC can also operate in enodothermic regime at low currents. In SOEC operation, the cell is exothermic if $V_{cell} > V_{TN}$. In general, the higher is the difference between the cell voltage and the thermoneutral voltage, the larger is the magnitude of ϕ. It is straightforward that providing heat to an SOEC reduces the system efficiency, thus operating the cell at thermoneutral or over-thermoneutral voltage can be a solution to suppress the need for an external heat source. However, this option can be problematic if a high overpotential is required to reach V_{TN} because the high irreversibility limits the efficiency of the cell. When both the operating modes are considered, an SOC can operate exothermally if:

$$V_{cell,SOEC} > V_{TN} > V_{cell,SOFC} \tag{2.52}$$

If this condition is satisfied, the system efficiency is improved because an external heat sources are avoided. However, also the surplus heat produced in SOFC operation or in SOEC mode operating over thermoneutral can negatively affect the system efficiency by increasing the BoP energy required. For example, increasing the oxidant/sweep flow to the oxygen electrode to limit the temperature of the cell increases both venting/compression power required by BoP and also the heat required for preheating the inlet gas to the cell temperature. A detailed discussion about these aspects is given in *Chapter 5*. Therefore, in order to minimize both the heat requirements from external sources and the BoP energy requirements for cooling, an SOC must operate at voltage values slightly above (SOEC) or below (SOFC) the V_{TN}. Moreover, the cell voltage should be as close as possible to the reversible voltage (i.e. the overpotential must be minimum) to ensure a high electrical efficiency of the SOC. These conditions can be contemporary satisfied if the thermoneutral voltage V_{TN} is lowered to the value of the reversible voltageE_{rev}. Equation (2.49) suggests that is possible to act both on the redox thermoneutral and on the chemical reactions to reach this target. The enthalpy of redox reaction is a function of the cell temperature and consequently also the thermoneutral redox voltage. The dependency of $V_{TN,redox}$ on the temperature for H_2/H_2O and CO/CO_2 reactions is shown in *Figure 2.3* and *2.4*; the thermoneutral voltage is almost constant for the CO/CO_2 chemistry and increases only slightly in magnitude for H_2/H_2O redox over the typical operating temperature range for SOCs, from 1.287 V at 800°C to 1.292 V at 1000°C. Thus, the operating temperature is a parameter that cannot affect

significantly the thermoneutral redox. Pressure is even less important, as the enthalpy of reactions is independent from its value. Given that $V_{TN,redox}$ is almost constant in all the operating conditions of the cell, chemical reactions are the only parameter that can affect significantly the thermoneutral voltage of the cell and that can be used to reduce its value. This option has been widely investigated by Wendel et al. (2015a and 2015b) for the thermal management of an rSOC system. In their work, the thermoneutral voltage is lowered by methanation reactions at high pressure and intermediate temperature to operate an rSOC at high values of round-trip efficiency.

2.1.4 Efficiency considerations

The theoretical efficiency of an SOC system is usually defined in SOFC as the unit of electricity produced divided by the unit of energy available in the oxidation reaction and in SOEC as the unit of energy stored per unit of energy required by electrolysis. Given that in SOFC only a part of the total enthalpy variation of the oxidation reaction can be converted in electricity, the theoretical efficiency of the process is always less than 100%. In SOEC operation, both the heat and electricity provided in the electrolysis process are stored in the product; thus, an ideal electrolysis process without losses has always 100% efficiency. When considering an rSOC system, the theoretical roundtrip efficiency can be considered as the ratio between the maximum electricity that can be produced in SOFC (i.e., $\Delta\bar{g}^{o}_{redox}$) and the minimum energy consumed in SOEC (i.e., $\Delta\bar{h}^{o}_{redox}$):

$$\eta_{RT,th} = \frac{\Delta\bar{g}^{o}_{redox}}{\Delta\bar{h}^{o}_{redox}} \tag{2.53}$$

The theoretical roundtrip efficiency is shown in *Figure 2.3* and *2.4* for the H_2/H_2O and CO/CO_2 redox chemistries. At 800 °C, the $\eta_{RT,th}$ is around 67 % (CO/CO_2 redox) and 76% (H_2/H_2O redox). This theoretical definition does not take into account the irreversibility losses that can further reduce the efficiency of both operating modes; however, also the valorization of the heat produced by SOFC oxidation reaction is completely neglected. Moreover, in real systems the efficiency depends on both the cell and BoP. Thus, a general definition has to be established in order to take into account all the contributions. In this dissertation efficiencies have been calculated considering both heat and electricity provided/produced to/from the system, adopting the following definitions for SOEC and SOFC systems:

$$\eta_{SOEC} = \frac{{|I|}/{2F} \cdot \Delta\bar{h}_{ec,H_2H_2O}}{|W_{cell}| + \phi + \phi_{BoP} + |W_{BoP}|} \tag{2.54}$$

$$\eta_{SOFC} = \frac{W_{cell} - \phi - \phi_{BoP} - W_{BoP}}{{I}/{2F} \cdot \Delta\bar{h}_{ec,H_2H_2O}} \tag{2.55}$$

Electrical power and heat are different forms of energy that can be better compared by taking into account their exergetic value. In particular, the exergetic value of heat fluxes exchanged by the system with the external environment can be evaluated by associating a temperature to each flux:

$$Ex_{\phi} = \phi \cdot \left(1 - \frac{T_{amb}}{T_{flux}}\right) \tag{2.56}$$

Equation (2.56) states that a heat flux available at ambient temperature has a null exergetic value, as it cannot produce work. Electricity is considered as pure exergy, as it can be fully converted to work. By associating an exergetic value to the thermal fluxes it is possible to take into account the different temperatures at which the fluxes are available. In the system analysis performed in this Thesis, the exergetic values of the heat fluxes has been considered, and the exergetic efficiency of the SOC system has been calculated as:

$$\eta_{SOEC,ex} = \frac{{|I|}/{2F} \cdot \Delta\bar{h}_{ec,H_2H_2O}}{|W_{cell}| + Ex_{\phi} + Ex_{\phi_{BoP}} + |W_{BoP}|} \tag{2.57}$$

$$\eta_{SOFC,ex} = \frac{W_{cell} - Ex_{\phi} - Ex_{\phi_{BoP}} - W_{BoP}}{{I}/{2F} \cdot \Delta\bar{h}_{ec,H_2H_2O}} \tag{2.58}$$

In the case of P2P operation, the round-trip efficiency can be defined as the power produced by the SOFC system from the unit of chemical energy generated in SOEC mode, which is the product between the SOEC and SOFC efficiencies:

$$\eta_{RT} = \eta_{SOEC} \cdot \eta_{SOFC} = \frac{(W_{cell} - \phi - \phi_{BoP} - W_{BoP})_{SOFC}}{(|W_{cell}| + \phi + \phi_{BoP} + |W_{BoP}|)_{SOEC}} \tag{2.59}$$

It is straightforward to determine the roundtrip efficiency also in the exergetic form. In the above definitions of efficiencies, the ϕ term is the heat that must be provided or removed from the cell/stack to maintain the isothermal operation (i.e., ϕ is positive when provided and negative when removed). Given that an solid oxide cell/stack is insulated from the external environment, the heat is provided/removed through the gas fluxes that enter/exit the SOC. These streams are heated or cooled in the BoP of the SOC system. Thus, the thermal flux ϕ can be considered shifted from the SOC to the BoP and if the analysis is restricted to the cell/stack, only the W_{cell} is directly consumed/produced by the SOC. A cell roundtrip efficiency based only on electrical input/output can thus be derived:

$$\eta_{RT,cell} = \frac{V_{SOFC} \cdot I}{V_{SOEC} \cdot I} = \frac{V_{SOFC}}{V_{SOEC}} \tag{2.60}$$

System efficiency can be clearly higher or lower, depending on the BoP architecture; in general, the recovery of the surplus heat produced in both SOFC and SOEC operation increases the roundtrip efficiency of the system. Equation (2.60) can be rewritten as:

$$\eta_{RT,cell} = \frac{E_{rev} - \eta_{SOFC}}{E_{rev} + \eta_{SOEC}} \tag{2.61}$$

The cell roundtrip efficiency approaches the unity only in ideal operation when the overvoltage is zero; in this case the rSOC current-voltage characteristic is a flat curve that allows to move the operating point without affecting the cell efficiency. In real operation, irreversibility is always present; however, the lower is the ratio between V_{SOFC} and V_{SOEC}, the higher is the cell efficiency.

2.2 SOC mathematical modeling

A Solid Oxide Cell is a complex system consisting of three main components (electrolyte and porous electrodes, i.e. anode and cathode), each one composed of peculiar materials in which interconnected physical phenomena occur simultaneously involving gas and solid phases. In practical applications, the individual cells are stacked together to increase the available area for the electrochemical conversion of reactants and maximize the ratio between the active volume and the surface exposed to external ambient, which needs insulation in order to minimize the heat leakage towards the ambient and maintain the system at high temperature. If we consider the single unit of a stack of cells, which is called SRU (i.e. Stack Repeating Unit), other components as interconnects, seals and gas channels must be taken into account. Finally, if we look at the entire stack of cells, also gas manifolds, insulation and current collection plates have to be considered. Therefore, the modeling of SOC cells, SRUs and stacks is a challenging task due to the wide variety of the components involved.

SOC modeling can be carried on following different approaches, techniques and levels of details depending on the objective of the model (e.g. cell performance simulation, study of the degradation of materials, optimization of fluid distribution, etc.) and on the particular component or group of components on which the model is focused.

From a general point of view, SOC systems (whether they are single cells, SRUs or stacks) can be considered as non-linear dynamic systems with multiple inputs and outputs in which mass, momentum, energy and charge transfer take place together with chemical and catalytic reactions. The goal of modeling is to develop mathematical tools capable of simulating the response of the system, with the purpose to provide models that can be applied to the design, analysis, control or diagnostic of SOC systems.

SOC models can be generally classified into two main categories: experimentally based and physically based models (Wang K. et al., 2011).

Experimentally based models of SOC systems are developed using statistical-data driven approaches without applying equations derived from the knowledge of the involved physics. Regression based and artificial neutral network techniques are applied to experimental databases in order to identify the relationship between inputs and outputs of the system that are implemented into predictive models which are mostly applied in the design of SOC control strategies.

In the SOC literature, most of the models are physically based. These models range from microscale (atomic or molecular level) to macroscale due to the fact that physical processes of SOC systems have characteristic length and time scales from angstrom and femtoseconds to centimeters and seconds. Consequently, the modeling techniques adopted strictly depend on the length and time scale of the described phenomena.

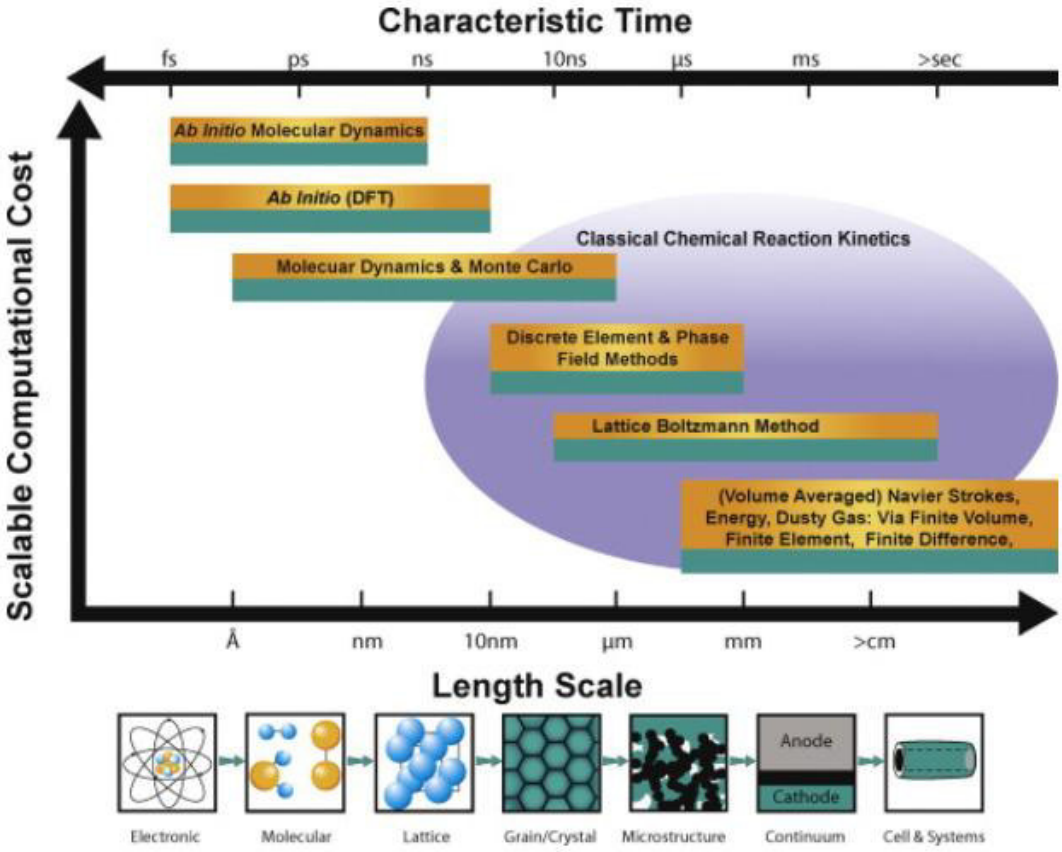

Figure 2.6 – Multidimensional SOC modeling. (Grew et al., 2012)

At the scale of the electronic structure of matter, *ab initio* methods are used for the study of atomic interactions, followed by Molecular Dynamics and Monte Carlo techniques at the level of molecular structures, while discrete elements and phase field methods are adopted at the characteristic length of grain and crystals. Lattice Boltzmann Methods can be applied for the study of the fluid transport within microstructures, and finally the modeling methods that follow the continuum approach and use volume averaged equations can be applied from the length scale of micrometers onwards to describe the physics of SOC systems from the macroscopic point of view (Grew et al., 2012).

In general, macroscopic models describe SOC systems by using conservation laws and governing equations of the involved physics and range from 0-D to 3-D depending on the model objectives. Multidimensional models take into account the spatial distribution of the physical variables (temperature, species concentration, etc.) and are typically aimed at simulate cell/stack for design or optimization purposes. The prediction of the steady-state and transient response at cell, stack and system level for diagnostic and control is frequently addressed by 0-D and 1-D models, due to their low computational cost.

When a macroscopic approach is adopted, many physical phenomena that are implicitly derived in the atomistic and molecular modeling are described by using empirical parameters. In particular, the representation of microscopic structures, chemical and electrochemical kinetics is assigned to macroscopic parameters (e.g. porosity, tortuosity, exchange current density, etc.) that can be estimated directly or indirectly (i.e. by fitting) from experimental measurements. Thus, in order to develop a physically based model, a representative set of experimental data is necessary.

Finally, physically based macroscopic models of SOCs can follow two main goals: they can be oriented to the simulation of the performance or they can study the degradation processes occurring in the materials. In the first case, the models calculate system responses mainly in terms of voltage, current, temperature, chemical species and pressure distributions; in the second, simulations focus on the calculation of thermal stresses, strain and stress fields.

The modeling approach followed in this Thesis is physically based and focuses on the macroscopic description of the phenomena with the purpose to develop a model which is able to predict the thermo-electrochemical performance of an SOC cell. A 2-D single cell model has been developed to calibrate and validate the electrode kinetics over experiments performed on SOC cells made by different materials (see *Chapter 4*), while the parameters related to cell microstructure and kinetics of chemical reactions have been assumed from the literature. The model has been later extend at SRU level and applied on 2-D and 3-D geometries to investigate the local effects cell control strategies.

In the following paragraphs, the modeling background for the phenomena of transport and conservation of mass, momentum, charge, energy is described and the basics of electrochemical and chemical reactions modeling is given. The description of the models developed is given in *Chapter 3*.

2.2.1 Mass transfer modeling

In SOC systems, mass transfer takes place both in the gas phase (i.e., stack manifolds, gas channels and porous electrodes) and in the solid phase (i.e., transport of ions in the electrolyte). The mass transfer of gases is studied in this section, while the transport of ions in the electrolyte is addressed in *Section 2.2.4* dedicated to the electrochemical modeling.

Mass transfer in the gas phase occurs by advection and diffusion. In general, mass transport and conservation can be expressed by using the continuity equation in the advection-diffusion form:

$$\frac{\partial \rho}{\partial t} + \nabla \cdot (\vec{J}_{adv} + \vec{J}_{diff}) = S \tag{2.62}$$

where ρ is the fluid density, t is the time, $\vec{J}_{adv}$ is the advective flux of mass due to the motion of the fluid, $\vec{J}_{diff}$ is the total diffusive flux of mass related to local gradients of temperature and partial pressures, and S accounts for the volumetric mass sources or sinks. At the high operating temperatures of SOC systems, fluids can be considered as ideal gases with a good approximation, thus the ideal gas law can be applied for the calculation of the fluid density:

$$\rho = \frac{pM_n}{RT} \tag{2.63}$$

where p is the total pressure of the gas mixture, M_n is the molecular weight of the mixture, T is the temperature and R is the ideal gas constant.

The composition of gas mixtures in SOC systems is not spatially homogeneous due to chemical and electrochemical reactions; moreover, a gas that moves in the electrodes can occupy only the void fraction of the porous domains. Hence, the mass transport equation (2.62) has to be re-elaborated to in order to formulate a species balance that takes into account the porosity of materials and the mass fractions of chemical species in the gas mixture. For each component, the mass balance can be written as:

$$\frac{\partial (\varepsilon \rho x_\alpha)}{\partial t} + \nabla \cdot (\vec{J}_{adv,\alpha} + \vec{J}_{diff,\alpha}) = S_\alpha \tag{2.64}$$

where ε is the porosity and x_α is the mass fraction of the α component. Equation (2.64) is also valid in non-porous domains, where the porosity assumes the value of 1. For non-porous domains, the advective term of equation (2.64) can be expressed as:

$$\vec{J}_{adv,\alpha} = \rho x_\alpha \mathbf{u} \tag{2.65}$$

where $\mathbf{u}$ is the fluid velocity field. In porous media, the advection term can be written as:

$$\vec{J}_{adv,\alpha} = \rho x_\alpha \bar{\mathbf{u}} \tag{2.66}$$

where $\bar{\mathbf{u}}$ is the superficial velocity of the fluid in the porous domain (also called velocity of permeation, filtration or Darcy velocity). The superficial velocity is given by the Dupuit-Forchheimer relationship: $\bar{\mathbf{u}} = \varepsilon \mathbf{U}$, being $\mathbf{U}$ the mean velocity of the fluid through the pore space of the electrode, obtained by averaging the fluid velocity over a macroscopic volume of the electrode (Nield and Bejan, 2006).

The source term of equation (2.64) accounts for the net volumetric production of the α species due to the electrochemical and chemical reactions. In general, S_α is given by:

$$S_\alpha = M_\alpha \sum_i \gamma_i \nu_{\alpha i} r_i \tag{2.67}$$

where r_i is the molar rate of the *i*-reaction, $\nu_{\alpha i}$ is the net stoichiometric coefficient of α species in the *i*-reaction and γ_i is a scaling factor that assumes either a unitary value if the *i*-reaction rate is given per unit volume or it has the unit of inverse length (i.e., surface area per unit volume) if the *i* reaction has a rate expressed per unit surface.

The molar rates of electrochemical reactions are given by the Farady's law:

$$r_i = \frac{|i_v|}{nF} \tag{2.68}$$

where F is Faraday's constant, n is the number of electrons released during the reaction of one fuel molecule and i_v is the volumetric current density. The calculation of the current density requires an electrochemical model that describes the charge-transfer chemistry in the SOC electrodes, this topic will be treated in *Section 2.2.4*.

The molar rates of chemical reactions can be calculated from the study of global or detailed reaction mechanisms, as described in *Section 2.2.5*.

The electrochemical reactions involve limited regions of electrodes where charge-transfer reactions occur on the electrochemically reactive sites characterized by the coexistence of electron and ion conductor phases in the presence of gas-phase reactants. These regions are called triple- or three-phase boundaries (TPBs) and spread from the electrode/electrolyte interface of SOCs into the electrode volume. In anode-supported cell models, the three-phase boundary is frequently assumed as a layer of negligible thickness at the anode/electrolyte interface (Costamagna et al. 2004, Ni 2009, Laurecin et al., 2011, and Ferrero 2015) and the mass sources due to the electrochemical reactions are imposed as boundary conditions at the border between electrode and electrolyte, instead of being included in the source term S_α. This is

the approach followed in this Thesis, in which the electrochemical reactions are always assumed at the electrolyte/electrolyte interface and implemented as boundary conditions.

Chemical reactions take place within the gas phase (i.e., homogeneous reactions) or on the surface of the solid medium of the electrode that acts as a catalyst for the reactions (i.e., heterogeneous reactions). In both cases, the volume in which chemical reactions occur covers the entire domain of SOCs electrodes and the reaction rates must be included in the volumetric source term of equation (2.64).

As stated before, the total diffusive flux of mass is due to the presence of temperature and partial pressures gradients. The thermal diffusion can be easily highlighted:

$$\vec{J}_{diff,\alpha} = \vec{J}_{d,\alpha} - D_{\alpha,T}\frac{\nabla T}{T} \tag{2.69}$$

where $D_{\alpha,T}$ is the thermal diffusion coefficient. The thermal diffusion of mass is also referred to as the Soret effect, which occurs in mixtures with high temperature gradients and large variations in molecular weight of the species. This type of diffusion is always neglected in SOC models. The diffusive flux $\vec{J}_{d,\alpha}$ related to partial pressure gradients of the species will be described in detail in the following sections, where different diffusion models are introduced.

The solution of the mass balances requires to combine equation (2.64) and (2.63) with a momentum balance (see *Section 2.2.2*) for the determination of the fluid velocity field, with a gas diffusion model (see later in this Section) for the calculation of the diffusive fluxes of the species, with an energy balance (see *Section 2.2.3*) for the determination of the temperature distribution, and also with electrochemical and chemical models (see *Section 2.2.4* and *Section 2.2.5*), which are required for the calculation of the species source term (see eq. (2.67)).

As will be shown later, some gas diffusion models for the porous media (i.e., Fick's model in the advection-diffusion form (2.83) and Dusty Gas Model (2.90)) already include the momentum balance. In these models, the mass flux determined by equation (2.66) – usually expressed as a function of the total pressure gradient by the application of Darcy's law (2.99) for the conservation of momentum – is included in the calculation of the total diffusive flux and referred to as a viscous flux.

The modeling of the gas diffusion depends on the medium where the diffusion occurs (i.e., porous or non-porous) and on the characteristics of the gas mixture (i.e, binary or multicomponent).

Before introducing the mathematical description of the diffusive flux $\vec{J}_{d,\alpha}$, a brief presentation of the diffusive models is given. In the SOC literature, three theoretical models are usually

applied to describe the diffusive mass transport: Fick model, Stefan-Maxwell model and Dusty Gas model.

Diffusion models based on Fick's law assume that the flux of a chemical species in a gas mixture is proportional to its concentration gradient. These models are often presented in the advective-diffusive form, in which molecular diffusion due to concentration gradients and viscous flow due to pressure gradients are linearly combined (Webb and Pruess, 2003). Fick's law is rigorously valid only for binary mixtures or in the case of diffusion of dilute species in a multicomponent mixture (Krishna and Wesselingh, 1997, He et al., 2014) and its application to the diffusion in porous media is consistent in a very narrow range of conditions (Bertei and Nicolella, 2015). Nevertheless, Fick-based models are widely employed not only in modeling the diffusion in binary mixtures, but also in the modeling of concentrated species diffusion in multicomponent mixtures in both porous and non-porous media, due to their simplicity (Ferguson et al., 1996, Ho et al., 2008, Goldin et al., 2009, Ho et al., 2009, Elizalde-Blancas et al., 2013).

The Stefan-Maxwell model is frequently used in the literature to overcome the limitations of Fick's law (Krishna and Wesselingh, 1997, Suwanwarangkul et al., 2003). This model is derived from the kinetic theory and correctly describes the multicomponent diffusion in non-porous domains, but it does not include the interaction between pore walls and gas molecules (Webb and Pruess, 2003, Suwanwarangkul et al., 2003). In some diffusion models, the Stefan-Maxwell equations have been modified to include also the gas-pore interactions, as in the binary-friction model of Kerkhof (1996) or in the work of Hussain et al. (2005).

The Dusty Gas model (Mason and Malinauskas, 1983), which takes into account both the interactions between the different components of a gas mixture and the gas-wall collisions, has proven to be the most suitable and rigorous model for the description of multicomponent diffusion in porous media (Suwanwarangkul et al., 2003, Hernández-Pacheco et al., 2004). Even if it has the higher predictive capability, the Dusty Gas model is not widely applied as the Fick's one due to its complexity. In particular, Fick and Stefan-Maxwell models can be solved analytically by deriving explicit expressions for the diffusion fluxes, while the Dusty Gas model requires a numerical solution (Suwanwarangkul et al., 2003). For this reason, the Dusty Gas model is frequently presented in simplified forms in the SOC modeling literature, usually by assuming uniform pressure in the electrodes (Jiang and Virkar, 2003, Hernández-Pacheco et al., 2004, Janardhanan and Deutschmann, 2006, Matsuzaki et al., 2011, Geisler et al., 2014, Ferrero

et al., 2015), and in the work of Kong et al. (2012) it has been reformulated in the form of a Fickian model in order to facilitate its implementation.

In this dissertation, different approaches have been followed for modeling the diffusion in porous and non-porous domains. In the model developed at single cell level for the calibration and validation of electrode kinetics, a simplified DGM has been applied for describing diffusion in porous domains, while non-porous domains were not included in the model. The 2-D/3-D cell and SRU models have addressed the diffusion modeling by using the Stefan Maxwell model in non-porous domains and Fick's in model in porous domains. The detailed description of the model is given in the next Chapter.

Modeling diffusion in non-porous domains: Fick and Stefan-Maxwell models

In the non-porous domains (i.e. gas channels and manifolds), $\vec{\boldsymbol{J}}_{\boldsymbol{d,\alpha}}$ is the mass flux originated by the molecular diffusion of the species α in the gas mixture, that can be binary (i.e., typically air in the cathode channels of SOFC) or multicomponent. The molecular diffusion (also called continuum or ordinary diffusion) is due to the relative motion of the different species of the gas mixture driven by partial pressure gradients. For the diffusion modeling in non-porous media, Fick and Stefan-Maxwell model are usually applied in the literature.

The simplest diffusion model is the Fick's one. The model is given by (Bird et al., 2006):

$$\vec{J}_{d,\alpha} = -\rho D_{\alpha m} \nabla x_{\alpha} \tag{2.70}$$

where $D_{\alpha m}$ is the diffusivity of the species α in the gas mixture. For a binary mixture, $D_{\alpha m}$ coincides with the ordinary diffusion coefficient of the gas phase, $D_{\alpha\beta}$, which is independent of the gas mixture composition and can be calculated using the theoretical correlation of Chapman-Enskog (Poling et al., 2001):

$$D_{\alpha\beta} = \frac{0.00266}{\sqrt{2}} \left(\frac{1}{M_{\alpha}} + \frac{1}{M_{\beta}} \right)^{1/2} \frac{T^{3/2}}{p \sigma_{\alpha\beta}^{2} \Omega_{\alpha\beta}} \tag{2.71}$$

where M_{α} and M_{β} are molecular weights, $\sigma_{\alpha\beta}$ is the average collision diameter, $\Omega_{\alpha\beta}$ denotes the collision integral and p is the total pressure of the gas mixture. In the literature, also the empirical correlations of Fuller, Schettler and Giddings (1966) are frequently used for the calculation of the binary diffusion coefficients:

$$D_{\alpha\beta} = \frac{0.00143 \cdot T^{1.75}}{p\left[\frac{2}{(1/M_\alpha + 1/M_\beta)}\right]^{1/2}\left[(\sum V_A)^{1/3} + (\sum V_B)^{1/3}\right]^2} \tag{2.72}$$

where $\sum V_i$ are the sums of the atomic diffusion volumes.

Many researchers have applied Fick's law also to multicomponent diffusion modeling; in this case, the ordinary diffusivity of the species α in the gas mixture is usually given by the Wilke's formula (Yakabe et al., 2000, Wilke, 1950):

$$D_{\alpha m} = \frac{1 - y_\alpha}{\sum_{\beta \neq \alpha} \frac{y_\beta}{D_{\alpha\beta}}} \tag{2.73}$$

Equation (2.73) is strictly valid for the diffusion of gases in a stagnant multicomponent mixture. When this assumption is not satisfied, as in the case of diffusion in SOC channels, manifolds and electrodes, the solution of the system of equations (2.70) leads to an intrinsic flux inconsistency, i.e. the sum of the diffusive fluxes is not zero (Désilets et al., 1997). In order to overcome this drawback of the model, it is necessary to replace one of the equations (2.70) with the consistency condition:

$$\sum_{\forall \alpha} \vec{J}_{d,\alpha} = 0 \tag{2.74}$$

In this way, one of the diffusion mass fluxes is "artificially" calculated so that their sum gives zero. A consistent method that combines Fick's law and flux consistency has been proposed by Ramshaw (1990):

$$\vec{J}_{d,\alpha} = -\rho D_{\alpha m} \nabla x_\alpha + \rho x_\alpha \sum_{\forall \beta} (D_{\beta m} \nabla x_\beta) \tag{2.75}$$

The Stefan-Maxwell model describes the multicomponent mass transport following a rigorous theoretical approach that allows to correctly describe the counterdiffusion effects of ternary mixtures of gases. Stefan-Maxwell equations are formulated as force balances on the chemical species of a gas mixture. The equations are written as a balance between the driving force of the motion of a species (i.e., the partial pressure gradient) and the friction between that species and each of the other species of the mixture (Krishna and Wesselingh, 1997). The equations are given by:

$$\sum_{\beta \neq \alpha} \frac{y_\beta \vec{J}_{d,\alpha} - y_\alpha \vec{J}_{d,\beta}}{D_{\alpha\beta}} = -\frac{p}{RT} \nabla y_\alpha \tag{2.76}$$

where $\vec{J}_{d,\alpha}$ is the molar diffusive flux relative to concentration gradients and the Stefan-Maxwell diffusion coefficient $D_{\alpha\beta}$ is equal to the binary diffusion coefficient used for Fick's law (2.72). Equation (2.76) can be rearranged to show the mass diffusive fluxes:

$$\sum_{\beta \neq \alpha} \frac{M_n}{M_\beta} \left(\frac{x_\beta \vec{J}_{d,\alpha} - x_\alpha \vec{J}_{d,\beta}}{D_{\alpha\beta}} \right) = -\rho \nabla x_\alpha \tag{2.77}$$

It is worth noting that Stefan-Maxwell expressed with equations (2.76)-(2.77) does not take into account the effect of total pressure gradients, as well as the Fick's model (2.70).

Some authors have proposed different diffusion models based on Stefan-Maxwell equations that also include the viscous effects due to the presence of a total pressure gradient.

In the works of Andersson et al. (2010), Stefan-Maxwell equations are formulated with a different approach (Curtiss and Bird, 1999) that includes the total pressure gradient in the forces balance on the gas species:

$$\vec{J}_{d,\alpha} = -\left(\rho x_\alpha \sum_i D_{\alpha i} \boldsymbol{d}_i \right) \tag{2.78}$$

where $\boldsymbol{d}_i$ is the diffusional driving force:

$$d_i = \nabla y_i + \frac{1}{p}[(y_i - x_i)\nabla p] \tag{2.79}$$

This formulation of Stefan-Maxwell model has been applied in the present work for modeling the diffusion in non-porous domains.

In the work of Novaresio et al. (2012), Stefan-Maxwell equations are derived by using a thermodynamic approach in which partial pressure gradients are expressed as the sum of the pressure gradients due to diffusive and viscous effects. The equation obtained is given by:

$$\frac{1}{RT} \nabla p_\alpha = \sum_{\beta \neq \alpha} \frac{y_\alpha \vec{J}_{d,\beta} - y_\beta \vec{J}_{d,\alpha}}{D_{\alpha\beta}} + \frac{1}{RT} x_\alpha \nabla p \tag{2.80}$$

For a multicomponent mixture composed by *n* gases, the Stefan-Maxwell model expressed by (2.76), (2.78) or (2.80) is a system of *n* equations in the *n* flux unknowns. However, only *n*-1 of the equations are linearly independent (Ramshaw, 1990). Thus, the flux consistency (2.74) has to be imposed to close the system of equations.

Finally, it is worth noting that both the Fick and Stefan-Maxwell models presented in this section do not comprise a momentum balance; thus, in the formulation of the complete mass transport model for the fluid, the momentum conservation equations have to be added. A complete comparison of the performance between Fick's and Stefan-Maxwell models is given in the works of Krishna and Wesselingh (1997) and Suwanwarangkul et al. (2003).

Modeling diffusion in porous domains: Fick and Dusty Gas Models

The prediction of partial pressure profiles within porous electrodes is of paramount importance to allow the correct estimation of current density, electrode potential and local reaction rates in a cell model. In order to correctly model the gas transport in SOC electrodes it is necessary to describe the motion of gas mixtures in porous media by taking into account the interactions of the gas species among themselfeves and with the walls of the pores.

The mass transport of gases in porous media is generally described by three mechanisms: viscous flow, molecular diffusion and Knudsen diffusion. The viscous flow is related to total pressure gradients, the molecular diffusion to partial pressure gradients, and the Knudsen diffusion is produced by both type of gradients combined with molecule-pore wall collisions. The transport of adsorbed gas molecules on the solid surfaces of pores is another transport mechanism that takes place in porous structures; however its contribution to the diffusivity is usually neglected (Froment et al., 1990, Kast and Hohenthanner, 2000).

In order to identify the type of transport mechanism that is dominant in the porous electrode, the Knudsen number is usually adopted (He et al. 2014):

$$Kn = \frac{\lambda}{L_p} \tag{2.81}$$

where λ is mean free path of gas molecules and L_p is the characteristic size of the pore, typically its diameter if pores are assumed as spherical. The mean free path of a gas molecule can be directly calculated from the kinetic theory:

$$\lambda = \frac{k_B T}{\sqrt{2} p \pi d_{mol}^2} \tag{2.82}$$

where d_{mol} is the molecule diameter and k_B is the Boltzmann constant.

Depending on the value assumed by the Knudsen number, three different flow regimes can be identified: a continuum regime for *Kn* smaller than 0.01, a transition regime for *Kn* in the range of 0.01-10, and a Knudsen regime when *Kn* is larger than 10.

Molecular diffusion and viscous flow are the dominant mechanisms in the continuum regime; in this case, the momentum transfer occurs by collisions between molecules, which are more frequent than the surface collisions between molecules and pore walls. In the continuum regime, concentration gradients lead to mass transfer due to molecular diffusion and a total pressure gradient produces a viscous flow.

In the Knudsen regime, the molecule-pore collisions are more frequent than the inter-molecular collisions, and the momentum transfer is determined by the interactions between molecules and pore walls. In this regime, a gradient of pressure or concentration leads to a mass transfer due to Knudsen flow, as there is no distinction between flow and diffusion in a non-continuum regime (Kast and Hohenthanner, 2000).

In an SOC electrode the gas flow takes place in a transitional regime, as the mean pore diameter usually ranges between 0.4 – 2.6 μm (Funahashi et al., 2007, Greene et al., 2006, Hao et al., 2008, Jung et al., 2006, Lanzini et al., 2009, Moon et al. 2008, Park et al., 2009, Yakabe et al., 2000, Zhu and Kee, 2003) and the mean free path for typical SOFC gases and operating conditions is about 0.2 – 0.5 μm (Hirschfelder et al., 1954); thus, in the presence of concentration and pressure gradients all the three mechanisms must be taken into account.

For the diffusion modeling in porous media, Fick and Dusty Gas Model are usually applied in the literature.

The Fick model given by equation (2.70) is also applied in the porous media. In order to consider the viscous diffusion, the model is frequently presented in the advective-diffusive form (Webb and Pruess, 2003):

$$\vec{J}_{d+a,\alpha} = -\rho\left(D_{\alpha mK}^{eff}\nabla x_\alpha + \frac{B_p x_\alpha}{\mu_g}\nabla p\right) \tag{2.83}$$

where B_g is the permeability of the porous medium, μ_g is the gas viscosity and $D_{\alpha mK}^{eff}$ is the effective diffusive coefficient which takes into account both the molecular and Knudsen diffusivity. The permeability can be expressed by thy Kozeny-Carman relationship (Bear 1972), which is based on the assumption that the porous electrode is formed by closely packed spherical particles:

$$B_p = \frac{\varepsilon^3 d_p^2}{72\tau_g(1-\varepsilon)^2} \tag{2.84}$$

where τ_g is the tortuosity parameter and d_p is the diameter of the particles.

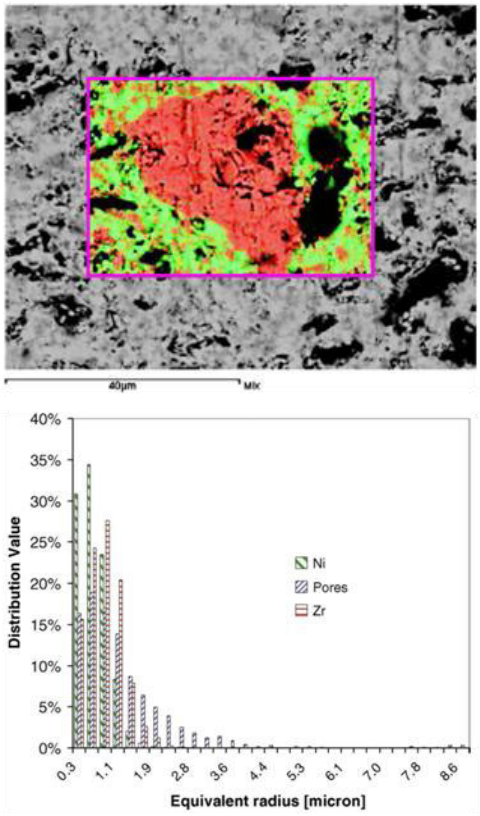

Figure 2.7 – Microstructural characterization of SOFC: in the upper panel, the EDS element mapping of Ni/YSZ anode regions (red: Ni, green: Zr, black: pore); in the lower panel, the average phase distribution of the anode. (Lanzini et al. 2009)

Firstly introduced by Carman (Carman 1956), the tortuosity takes into account the complexity of the diffusion path of a fluid inside the porous media and can be defined as the ratio between the lengths of real diffusion path and straight path. There is strong disagreement in the literature about the value of the tortuosity in fuel cell electrodes; the survey of Brus et al. (2014) shows values between 1 and 10 and indicates that the most precise estimations of tortuosity can be derived from the image analysis of real electrodes obtained by FIB-SEM methods (Lanzini et al. 2009, Wilson et al. 2011, Joos et al. 2011, Lee et al. 2013a, Iwai et al. 2010, Kishimoto et al. 2011). Using these techniques, the typical tortuosity of SOFC anodes is in the range of 1.5 – 4 (Brus et al. 2014).

The Knudsen diffusivity of the gas specie α in a porous media is given by (Lehnert et al. 2000):

$$D_{K,\alpha} = \frac{d_\varepsilon}{3}\sqrt{\frac{8RT}{\pi M_\alpha}} \tag{2.85}$$

where d_ε is the mean pore size of the porous media.

The molecular and Knudsen diffusion coefficients can be combined in a global diffusion coefficient (Welty et al. 2001):

$$\frac{1}{D_{\alpha mK}} = \frac{1}{D_{K,\alpha}} + \frac{1 - \Upsilon y_\alpha}{D_{\alpha m}} \tag{2.86}$$

The coefficient Y is usually assumed to be zero in the SOFC literature, leading to the Bosanquet formula (Suwanwarangkul et al., 2003, Pollard and Present, 1948, Veldsink et al. 1995):

$$D_{\alpha mK} = \left(\frac{1}{D_{K,\alpha}} + \frac{1}{D_{\alpha m}} \right)^{-1} \tag{2.87}$$

The Bosanquet relation is based on diffusion in aligned cylindrical pores and it doesn't take into account the real geometry of the electrode structure in which gases diffuse through convoluted paths. The effective diffusivity has been studied by Bruggeman (1935) who analyzed the properties of various heterogeneous substances. If the porous electrode is assumed as composed by a solid phase made of spheres and the bed phase surrounding the spheres is treated as the void fraction of the electrode, the Bruggeman's equation for the diffusivity can be used:

$$D_{\alpha mK}^{eff} = \varepsilon^{1.5} D_{\alpha mK} \tag{2.88}$$

In the SOC literature, the effective diffusivity is usually presented (Chan et al. 2001, Hajimolana et al. 2011) in a different form, which takes into account also the tortuosity of the porous structure:

$$D_{\alpha mK}^{eff} = \frac{\varepsilon}{\tau_g} D_{\alpha mK} \tag{2.89}$$

In the work of Webb and Preuss (2003), the Knudsen diffusion is included in the advective-diffusive form of the Fick model through the use of the Klinkenberg factor to obtain an effective permeability, while in the first term of equation (2.83) the effective diffusivity used does not include the Knudsen effect.

The Dusty Gas Model is derived from the kinetic theory and treats the porous medium as one component of the gas mixture. The medium is assumed as a gaseous phase of giant molecules (the 'dust') uniformly distributed in the porous domain, motionless and with infinite molar mass (Krishna and Wesselingh, 1997). By applying the Stefan-Maxwell equations to this mixture, the

transport of gases is described by an implicit expression that includes the effect of concentration and total pressure gradients (Mason and Malinauskas, 1983):

$$-\frac{1}{RT}\nabla p_\alpha = \sum_{\beta\neq\alpha}\frac{y_\beta\vec{J}_\alpha - y_\alpha\vec{J}_\beta}{D_{\alpha\beta}^{eff}} + \frac{\vec{J}_\alpha}{D_{K\alpha}^{eff}} + \frac{1}{D_{K\alpha}^{eff}}\frac{p_\alpha}{RT}\frac{B_p}{\mu_g}\nabla p \tag{2.90}$$

where $D_{\alpha\beta}^{eff}$ and $D_{K\alpha}^{eff}$ are the effective multicomponent and Knudsen diffusivities, directly calculated from $D_{\alpha\beta}$ and $D_{K,\alpha}$ by using (2.88) or (2.89). The Dusty Gas Model includes the momentum balance in the form of Darcy's Law, as can be seen from the last term of equation (2.90), which is the viscous flow, and intrinsically ensures the flux consistency. A large number of studies have shown the validity of the Dusty Gas Model (Krishna and Wesselingh, 1997, Veldsink et al., 1995, Tseronis et al., 2008, Wang et al., 2012) for multicomponent flows in porous media.

In the work of García-Camprubí et al. (2010) the total flux of a species in a multicomponent mixture obtained from the application of the Dusty Gas Model has been expressed as the contribution of three terms:

$$\vec{J}_\alpha = -\Gamma_\alpha\nabla p_\alpha + \vec{v}_\alpha^{\,p}p_\alpha + \vec{v}_\alpha^{\,N}p_\alpha \tag{2.91}$$

where:

$$\Gamma_\alpha = \frac{1}{RT\left[\sum_{\beta\neq\alpha}\left(\frac{p_\beta}{D_{\alpha\beta}^{eff}}\right) + \frac{1}{D_{K\alpha}^{eff}}\right]} \tag{2.92}$$

$$\vec{v}_\alpha^{\,p} = \frac{\Gamma_\alpha}{D_{K\alpha}^{eff}}\left[-\frac{B_p}{\mu_g}\nabla p\right] \tag{2.93}$$

$$\vec{v}_\alpha^{\,N} = \Gamma_\alpha RT\sum_{\beta\neq\alpha}\left[\frac{\vec{J}_\beta}{pD_{\alpha\beta}^{eff}}\right] \tag{2.94}$$

The first term represents the total diffusion of the species related to concentration gradients (i.e., a purely diffusive term), the second is the viscous flux due to pressure gradients and the third is the flow of the species α induced by the motion of the other species. The last term, peculiar of the Dusty Gas Model and totally neglected by Fick-based models, has a growing importance with the increasing of the current density. For this reason, the application of Dusty

Gas Model is recommended (Suwanwarangkul et al., 2003, Cayan at al., 2009) for predicting concentration overpotentials in SOFC models in the polarization regions where limiting currents occur due to the presence of high current densities and low concentration of electrochemical reactants.

The implicit formulation of fluxes and the presence of a term dependent on the pressure gradient make it difficult to implement the Dusty Gas Model. Therefore, many authors assume the viscous flow to be negligible and use the model in combination with the momentum equation given by Darcy's Law.

In this dissertation, both DGM and Fick models have been applied. In 2-D/3-D SRU models, the Fick formulation combined with a Darcy-Brinkmann flow model for the description of momentum conservation allowed to simplify the numerical solution of the equations. A simplified DGM has been applied in the combined 1-D/2-D model developed for the validation of electrode kinetics.

2.2.2 Momentum conservation

The momentum conservation equations derive directly from the application of the second Newton's law of motion. Mathematically, the momentum conservation in the non-porous domains (i.e., gas channel and manifolds) is described by the Navier-Stokes equations for compressible fluids:

$$\frac{\partial(\rho \boldsymbol{u})}{\partial t} + \nabla \cdot (\rho \boldsymbol{u}\boldsymbol{u}) = -\nabla p + \nabla \cdot \vec{\tau} + \rho F \tag{2.95}$$

where $\boldsymbol{F}$ are the body forces (e.g., gravity, electromagnetic forces, etc.) and $\vec{\boldsymbol{\tau}}$ is the stress tensor. Equation (2.95) represents a force balance on the fluid particles; it states that the total force applied to the particles is the sum of three contributions: pressure, stress and external forces. The external forces in SOFC channels are usually neglected. For a Newtonian compressible fluid, the stress tensor is given by:

$$\vec{\tau} = \left[\mu_g(\nabla \boldsymbol{u} + (\nabla \boldsymbol{u})^T) - \frac{2}{3}\mu_g(\nabla \cdot \boldsymbol{u})\right] \tag{2.96}$$

where μ_g is the dynamic viscosity of the fluid. This property can be estimated through the combination of the viscosities of single components by using the Wilke's formula (Wilke 1950):

$$\mu = \sum_{\forall i}\left[\frac{y_i \mu_i}{\sum_{\forall j}(y_j \theta_{ij})}\right] \tag{2.97}$$

where θ_{ij} is given by the equation:

$$\theta_{ij} = \frac{\left[1 + \left(\frac{\mu_i}{\mu_j}\right)^{1/2} \left(\frac{M_j}{M_i}\right)^{1/2}\right]^2}{\left(4/\sqrt{2}\right)\left[1 + \left(\frac{M_i}{M_j}\right)\right]^{1/2}} \tag{2.98}$$

The fluid flow through porous media is characterized by convoluted paths, and it's not possible to apply the classical laws of Mechanics separately to fluid and solid phases, due to the complex configuration of the contact boundaries between the phases. A continuum approximation has to be applied in order to formulate the momentum balance, and the macroscopic equations are derived by using averaging methods.

Several approaches have been proposed to formulate the momentum balance through a porous media; in the simplest form, the momentum conservation is expressed by Darcy's law, which assumes a linear proportionality between the flow velocity and the applied pressure difference:

$$\bar{\boldsymbol{u}} = -\frac{B_p}{\mu_g}\nabla p \tag{2.99}$$

This equation describes the balance on the fluid between the force applied by the pressure gradient and the frictional resistance due to the presence of a porous medium. In the Darcy's equation the inertia forces are neglected, and the validity of the model is limited to laminar flows in low porosity media dominated by viscous forces. Typically, the linear relation of Darcy's equation is valid for Reynolds number of the flow in the order of unity or smaller (Nield and Bejan 2006).

An extension of the Darcy model to high velocity flows in porous media, or to high porosity media, is given by the Forchheimer's equation:

$$\nabla p = -\frac{\mu_g}{B_p}\bar{u} - C_f \rho \frac{|\bar{\boldsymbol{u}}|\bar{\boldsymbol{u}}}{\sqrt{B_p}} \tag{2.100}$$

where C_f is a dimensionless drag constant. The last term of equation (2.100) is referred to as Forchheimer term and takes into account the inertia effects in the fluid flow. The C_f coefficient varies with the characteristics of the porous medium; a thorough discussion on the several different approaches adopted in the literature for the evaluation of this coefficient can be found in Nield and Bejan (2006).

The main limitation of the Darcy and Forchheimer equations is the impossibility to impose the no-slip boundary condition (Amhalhel and Furmański, 1997). Hence, when equation (2.99)

or (2.100) is imposed in the porous medium, it is difficult to define interfacial conditions with an adjacent domain in which there is a free flow and Navier-Stokes equations are applied, as typically happens at the electrode/channel interface of SOC cells (Andersson et al., 2010).

The Brinkmann-Darcy flow model can be adopted to overcome the limitations of Darcy-Forchheimer equations. The Brinkmann-Darcy equations are given by (Brinkman 1949a, 1949b):

$$\nabla p = -\frac{\mu_g}{B_p}\overline{\boldsymbol{u}} + \tilde{\mu}_g \nabla^2 \overline{\boldsymbol{u}} \tag{2.101}$$

where $\tilde{\mu}_g$ is an effective dynamic viscosity, that Brinkman set equal to the gas viscosity. More recent studies have shown that the effective viscosity is a function of the characteristic of the porous medium, in particular of the porosity (Amhalhel and Furmański, 1997, Nield and Bejan, 2006). The Brinkman-Darcy flow model allows to account for all boundary conditions at a solid or fluid interface.

A generalized flow model that includes the Forchheimer term into the Brinkman-Darcy equation has been derived by Hsu and Cheng (1990) starting from the Navier-Stokes equations and utilizing volume-averaging techniques:

$$\frac{1}{\varepsilon}\left[\frac{\partial(\rho\overline{\boldsymbol{u}})}{\partial t} + \nabla\cdot\left(\frac{\rho}{\varepsilon}\overline{\boldsymbol{u}}\overline{\boldsymbol{u}}\right)\right] = -\nabla p + \nabla\cdot\left(\frac{\vec{\tau}}{\varepsilon}\right) + \mu_g\nabla^2\overline{u} - \frac{\mu_g}{B_p}\overline{u} - C_f\rho\frac{|\overline{\boldsymbol{u}}|\overline{\boldsymbol{u}}}{\sqrt{B_p}} + \frac{F}{\varepsilon} \tag{2.102}$$

Equation (2.102) is known as Darcy-Brinkman-Forchheimer (DBF) flow model. In the work of Lage (1993), a complete study on the influence of each term of the DBF equation depending on the flow regime is presented.

The Darcy-Brinkman-Forchheimer equation is the most complete formulation of momentum conservation in the porous medium. When the free-flow approximation (i.e., infinite permeability and $\varepsilon = 1$) is applied in eq. (2.102), the equation reduces to the Navier-Stokes form (2.95). Therefore, when modeling a fuel cell, it is possible to apply equation (2.102) in both free-flow and porous-medium domains. With this approach, the velocity field is continuous in the entire domain and coupling conditions between porous electrodes and free channels are not need. The Darcy-Brinkman flow model (with or without the Forchheimer term) is the standard model used by many CFD softwares (Fluent, COMSOL Multiphysics, OpenFOAM, etc.) to deal with fluid transport problems in porous media.

2.2.3 Energy transport and conservation

Modeling the heat transfer in SOC systems allows the prediction of temperature distribution within cells and stacks, which is necessary for an accurate simulation of cell performance and for the prediction of thermo-mechanical degradation of cells and stack components.

Heat transport models must take into account the different heat transfer mechanisms, namely convective heat transfer between solid surfaces and gas mixtures, conductive heat transfer in gaseous and solid phases and radiative heat transfer. Moreover, energy conservation equations must include the presence of heat sources (or sinks) due to chemical and electrochemical reactions, and the heat production due to the motion of electronic and ionic charges.

The conservation of energy can be implemented in a model by applying the first law of thermodynamics, which assumes different forms depending on the heat transfer phenomena that dominate the domain under investigation.

In the following part of the section, the equations describing heat transfer and conservation are introduced by type of domain from the non-porous fluid and solid domains to the porous domains of the electrodes.

Heat transfer in non-porous media: fluid domains

The general form of the energy conservation equation for the heat transfer in a fluid domain is given by the enthalpy conservation equation, which can be expressed in terms of temperature, as follows:

$$\frac{\partial\left(\rho\, C_p T\right)}{\partial t} + \nabla \cdot \left(\rho\, C_p T\, \boldsymbol{u}\right) + \nabla \cdot \vec{q} = \frac{Dp}{Dt} + \phi_v + \rho \boldsymbol{f} \boldsymbol{u} + Q \tag{2.103}$$

where $\vec{q}$ is the heat flux by conduction, ϕ_v is the viscous dissipation, $\boldsymbol{f}$ are the specific body forces acting on the fluid (e.g., gravity) and Q represents the volumetric heat sources. The energy dissipation due to viscous forces is important for highly viscous fluids at high velocity, but is negligible for gas flows under the typical laminar regimes of SOCs. Also the pressure work may be neglected, since the pressure differences in fuel cells are very small. Moreover, it can be assumed with a good approximation that the body forces are irrelevant in the energy balance. Thus, equation (2.103) can be rewritten as:

$$\frac{\partial\left(\rho\, C_p T\right)}{\partial t} + \nabla \cdot \left(\rho\, C_p T\, \boldsymbol{u}\right) + \nabla \cdot \vec{q} = Q \tag{2.104}$$

The conductive heat transfer is given by the Fourier's law:

$$\vec{q} = -k_g \nabla T \tag{2.105}$$

where k_g is the thermal conductivity of the gas mixture. This property can be calculated by the Wilke's formula (see Eq. (2.97)), as in the case of the viscosity.

The volumetric heat sources in the fluid domains can be due to chemical reactions or radiative heating. The latter heating mechanism is related to the absorption, scattering and emission of radiation by the fluid that occur in the presence of participating gases.

The heat source term is negligible when considering the anodic fluids of SOCs, because they are composed by non polar molecules (i.e., oxygen and nitrogen) that do not react with each other and that can be considered as transparent gases non-interacting with thermal radiation at the conditions of SOC applications.

Chemical reactions between the typical fuel mixture components (i.e., H_2, H_2O, CO, CO_2 and CH_4) at SOC operating conditions occur when the gas flow come in contact with suitable catalysts, as typically happens within the porous structure of the anode. The studies of Gupta et al. (2006) and Walters et al. (2003) have shown that homogeneous reactions cannot be ignored in non-catalytic regions of SOFCs only with particular fuel mixtures, specifically air/methane and dry natural gas. However, if we consider the typical fuel mixtures in stack manifolds and cell channels, chemical reactions between components can be neglected. Moreover, the calculated gas transmittance for a typical SOC fuel stream composition at atmospheric pressure yields a value approaching unity (Damm and Fedorov 2005), thus also the fuel gas medium can be treated as transparent. Hence, the Q term is negligible for both anodic and cathodic gas mixtures in the non-porous domains of a SOC system.

Once the conservation equation has been imposed in the fluid domains of the model, proper boundary conditions have to be chosen. The conditions imposed at the boundaries of fluid domains strictly depend on the geometry and assumptions of the model. Most the models impose a fixed temperature at the fluid inlets and a convective flux at the outlets. Typical boundary conditions at the walls of fluid domains are thermal insulation, convective heat transfer, continuity of the temperature field across the boundary or periodic boundary conditions, depending on the model. Even if heat transfer by radiation is not included into the energy conservation equation, the radiative exchange between the surfaces of channel and manifolds can be considered when defining the boundary conditions at the walls of the fluid domains. The surface-to-surface radiation is usually modeled using view-factor methods (Sánchez et al., 2007,

Damm and Fedorov 2005). The radiative heat flux calculated at the surface can be then imposed as a boundary flux:

$$-\nabla \cdot (k\nabla T) = \nabla \cdot \vec{q}_{rad} \tag{2.106}$$

In this dissertation, the radiation heat transfer has been considered as a boundary condition for the cell in the 1-D/2-D cell model to reproduce the experimental conditions of the tested cells.

Heat transfer in non-porous media: solid domains

In the solid domains of SOC systems (i.e., electrolyte, interconnects and other impervious stack components), conduction is the dominant heat transfer mechanism and also radiation can play a role, while the convection is negligible since the material is not moving. In the absence of convective terms, the energy conservation equation is given by:

$$\frac{\partial(\rho\, C_p T)}{\partial t} + \nabla \cdot \vec{q} = Q_v \tag{2.107}$$

In order to determine whether or not to include radiation in the heat transfer model of solid domains, it is necessary to evaluate the magnitude of the heat transfer by radiation and compare it with that of the conductive heat flux. A simple evaluation method is suggested by Damm and Fedorov (2005), which is based on the comparison of the maximum possible heat flux exchanged by radiation between two black walls separated by a transparent medium with the conductive flux calculated by the Fourier's law. If the magnitude of the radiation is not negligible, the heat flux exchanged by radiation should be included in equation (2.107) into the source or heat flux terms.

The radiative heat flux can be calculated by solving the radiative transfer equation (RTE) (Modest, 2013). The RTE is an integro-differential equation, whose analytic solution exists only for few simple cases and its numerical solution has a high computational cost; thus the radiative flux is usually evaluated using approximate solutions of the RTE.

If the material is optically thin, radiation can be included in the energy conservation equation as a volumetric source that is accounted for in the Q_v term. In equation (2.107), the total volumetric heat source Q_v can be expressed as the sum of the Joule heating, which occurs in electrically conductive materials traversed by ionic or electronic current, and the radiative heating. Electrochemical and chemical reactions take place in the electrode domains and should not be accounted for in the source term. The resulting total source is given by:

$$Q_v = Q_{ohm} + Q_{rad} = \frac{\left|i_{e/i}\right|^2}{\sigma_{e/i}} - \nabla \cdot q_r \tag{2.108}$$

where $\sigma_{e/i}$ is the ionic/electronic conductivity of the material, $\left|\boldsymbol{i}_{e/i}\right|$ is the local current density (see *Section 2.2.4*) and q_r is the radiative heat flux, which derives from approximate solutions of the RTE, for example the Schuster-Schwartzchild two-flux approximation in the case of 1D models (Murthy and Fedorov, 2003). The traditional YSZ electrolyte of SOCs can be considered an optically thin material (Damm and Fedorov 2004), thus equation (2.108) is applicable in the YSZ domains. The work of Murthy and Fedorov (2003) has shown that the radiative heat flux strongly affects the temperature distribution in thick electrolytes (i.e., electrolyte supported cells), while the effect of radiation is negligible for thin electrolytes (i.e., anode supported cells).

If the material is optically thick, the radiative heat flux can be calculated by the Rosseland diffusion approximation and included into the $\vec{q}$ term of equation (2.107) (Murthy and Fedorov, 2003). The term $\vec{q}$ takes into account both the conductive and radiative heat fluxes, and is given by:

$$\vec{q} = -(k_s + k_{rad})\nabla T \tag{2.109}$$

where k_s is thermal conductivity of the solid and k_{rad} expressed by the Rosseland approximation is given by:

$$k_r = \frac{16n^2\sigma T^3}{3\beta} \tag{2.110}$$

where n is the refractive index of the medium, σ is Stefan-Boltzmann constant and β is the spectrally averaged mean extinction coefficient of the medium.

Heat transfer in porous media

The problem of modeling the heat transfer in the porous domains of SOCs, which are composed by mixed solid and gas phases, is usually addressed employing a local thermal equilibrium (LTE) approach that locally assumes the same temperature for gas species and solid structure. The LTE assumption is very common in thermal modeling of SOCs and allows to use only one energy conservation equation for both the phases in the computational domain of the porous medium (Andersson et al., 2013, Haberman and Young, 2004, Ferrero et al., 2015). The conservation equation is given by:

$$\left(\rho C_p\right)_{eff}\frac{\partial T}{\partial t} + \rho_g C_{pg}\boldsymbol{u}\cdot\nabla T = \nabla\cdot\left(k_{eff}\nabla T\right) + Q_v \tag{2.111}$$

where the terms $\left(\rho C_p\right)_{eff}$ and k_{eff} are effective transport parameters: namely, the energy stored per unit volume and the effective heat conduction flux, both obtained as volume averages of the quantities defined for the gas and solid phases. The effective properties are given by:

$$\left(\rho C_p\right)_{eff} = \varepsilon\rho_g C_{pg} + (1-\varepsilon)\rho_s C_{ps} \tag{2.112}$$

$$k_{eff} = \varepsilon k_g + (1-\varepsilon)k_s \tag{2.113}$$

where the subscripts “g” and “s” stand for gas and solid.

The validity of the LTE approach has been discussed by Damm and Fedorov for hydrogen fueled SOFCs (Damm and Fedorov, 2006) and subsequently by Zheng et al. (2013) who investigated the local thermal non-equilibrium (LTNE) effects in SOFCs electrodes in the presence of methane reforming and ammonia thermal cracking. Both studies indicates that LTNE effects within SOFC electrodes lead to insignificant local temperature differences between gas and solid phases of the order 10^{-2} – 10^{-3} K; thus, the LTE assumption can be safely adopted in the thermal modeling of SOCs.

The heat transfer by radiation is not included in equation (2.111), since SOC electrodes are opaque to radiation and have a negligible radiative conductivity (Damm and Fedorov, 2005). However, the radiative heat flux can be considered when defining the boundary conditions by using the same approach described for the heat transfer in fluid domains. In this case, surface-to-surface radiation is imposed on the boundary between electrode and gas channel.

The volumetric heat source term of equation (2.111) must include all the sources (or sinks) related to the phenomena that occur within the SOC electrode in both the solid and gas phases.

Heat generation is related to three different phenomena: 1) electrochemical reactions, 2) chemical reactions and 3) Ohmic losses due to the resistance of the materials to the charge flow (i.e., Joule effect).

The heat generation due to the electrochemical reactions can be divided in reversible and irreversible; the first one account for the thermodynamic heat released by the reactions and the second one takes into account the heat released for the activation of the charge-transfer reactions. These source terms are given by:

$$Q_{el,rev} = -\left(\frac{|i_v|}{nF}\right) T\Delta\bar{s} \tag{2.114}$$

$$Q_{el,irr} = \eta_{act}|i_v| \tag{2.115}$$

where $\Delta\bar{s}$ is the molar entropy change of the electrochemical reactions, the term $\left(\frac{|i_v|}{nF}\right)$ is the molar volumetric flow of reacted molecules stemming from the Faraday's Law and η_{act} is the activation overpotential (see *Section 2.2.4*). As previously stated, anode-supported cells models frequently assume the electrochemical reactions to be confined at the interface between the fuel electrode and the electrolyte. If this assumption is adopted, as in the present Thesis, the electrochemical heat generation should be imposed as a boundary condition at the electrode/electrolyte border instead of being included in the source term of equation (2.111).

In typical SOC systems, chemical reactions between the gas species occur in the fuel electrode, where gas streams typically containing H_2, H_2O, CO, CO_2 and CH_4 come in contact with the metal phase of the porous structure – usually nickel – which promotes the heterogeneous chemical reactions (see *Section 2.2.5*). The chemical reactions can be endo- or exothermic, thus the chemical source term of equation (2.111) can be positive or negative depending on the reaction. The chemical heat source is given by:

$$Q_{chem} = -\sum_i \gamma_i r_i \Delta\bar{h}_i \tag{2.116}$$

where $\Delta\bar{h}_i$ is the molar enthalpy of reaction.

The ohmic losses are due to electronic and ionic resistivities of the solid structure of the electrode. Under operating conditions, SOC electrodes are traversed by ionic and electronic currents – which depend on electrode morphology, temperature and reactant distributions – that can be determined by using an electrochemical model of the cell (see *Section 2.2.4*). The heat released in the electrode volume due to the ohmic losses is calculated as in equation (2.108) by

using the effective conductivity of the electronic/ionic phase in the porous media, whose expression is given in equation (2.142).

Finally, ohmic heating due to contact resistance between electrodes and interconnects should also be taken into account when defining the thermal boundary conditions.

$$-n \cdot (-k_{eff} \nabla T) = Q_{ohm,res} \tag{2.117}$$

This type of resistance is usually expressed in terms of an area specific resistance (i.e., Ωcm^2) that depends on the contact method, the interface area between the materials and their resistivities (Wu et al., 2013). The heating source is given by:

$$Q_{ohm,res} = R_{con} |\vec{\imath}_b|^2 \tag{2.118}$$

where $|\vec{\imath}_b|$ is the absolute value of the local current per unit surface that is crossing the boundary interface.

2.2.4 Electrochemical modeling

The goal of an electrochemical SOC model is to provide a mathematical formulation of the relation between the electrical variables of the cell (i.e., current and voltage) and the thermo-fluidic and chemical ones (i.e., temperature and species partial pressures). In order to do this, it is necessary to implement in the model equations that give a suitable description of the electrochemical phenomena occurring in an SOC.

Before going into the details of the physics-based modeling, a brief introduction is given to highlight the main phenomena that an electrochemical model must address.

A solid oxide cell is an electrochemical device that either performs the direct conversion of the chemical energy of a fuel into electricity or converts electricity to chemical energy through redox reactions. In both operating modes, the reactants are supplied in the gaseous form to the electrodes of the cell, where the electrochemical reactions take place, and an ion conductive layer – the electrolyte – ensures that the charged molecules produced in the redox processes can move between the electrodes. A potential difference arises between electrodes when reactants are supplied to them; if the electrodes are not electrically connected, this potential difference is exactly the electromotive force due to redox reactions, which represents the maximum potential difference that the cell could achieve with these reactants. Instead, if the electrodes are connected through an external electrical circuit, the electrons move from an electrode to the other driven by

the potential difference and irreversible phenomena connected to electrochemical reactions and charge transport occur and reduce the available potential difference.

A complete electrochemical model should encompass all these phenomena and give a mathematical description of: 1) generation of potential difference between electrodes, 2) electrochemical reactions and 3) charge transport.

In the following sections, the description of the three aforementioned phenomena is given by presenting an overview of the approaches usually followed in the physical-based SOC modeling.

Modeling the Equilibrium Potential

The generation of a potential difference between the anode and cathode of a solid oxide cell depends on the redox reactions occurring at the electrodes. In general, the overall half-cell reactions consist in the oxidation/reduction of fuel molecules at the fuel electrode and the reduction/oxidation of O_2 at the oxygen electrode.

In SOFC operation, typical fuels that are oxidized at the anode are hydrogen and carbon monoxide, but also solid carbon, hydrogen sulfide, methane and other higher hydrocarbons can participate directly to the electrochemical oxidation. In SOEC operation, water and carbon dioxide are typically reduced at the cathode. In this Chapter, the analysis will be limited to reactions involving H_2/H_2O and CO/CO_2 mixtures, as they are the electrochemical fuels in the vast majority of SOC applications. The methane is frequently provided directly to SOFCs, however it plays a role more as a reactant for internal reforming reactions in which H_2 and CO are produced (see *Section 2.2.5*) rather than being a reacting species of electrochemical oxidation processes.

The half-cell oxidation/reduction reactions for H_2 and H_2O and for CO and CO_2 in SOCs with oxygen conductive electrolytes are (1.15) - (1.18), as described in *Chapter 1*. The oxygen reduction/oxidation reaction is given by (1.19) and (1.20). The reversible potential of the cell generated by the redox reactions – which is also called equilibrium or Nernst potential/voltage – is the theoretical maximum potential difference that a fuel cell can produce between the electrodes for a given reactants composition or is the minimum potential difference required at the electrodes of an electrolysis cell to allow the redox reaction to evolve. The reversible potential can be expressed as the difference between the equilibrium potentials of the reactions occurring at the anode and the cathode (Bagotsky, 2005):

$$E_{rev} = E_{eq,c} - E_{eq,a} \tag{2.119}$$

The equilibrium potentials are functions of the Gibbs free energy of reaction, which depends on the temperature and activities of reactants and products. The equilibrium potential of a single electrode is given by:

$$E_{eq} = \frac{1}{n_e F}\left[\Delta\bar{g}_e^o + RTln\prod_k {a_k}^{\nu_k}\right] \tag{2.120}$$

where n_e is the number of electrons exchanged per molecule of fuel/oxidant in the electrode reaction, $\Delta\bar{g}_e^o$ is the molar standard-state free energy change of the reaction, a_k is the activity of species k and ν_k is the stoichiometric coefficient of the species (negative for reactants). In the case of gaseous reactants/products at low pressure – typical conditions of SOC electrodes – the activity can be expressed as the ratio of the partial pressure of the gas over the standard pressure. For the coupled reactions (1.15)/(1.19) – (1.16)/(1.19) and (1.17)/(1.20) – (1.18)/(1.20), equations (2.119) and (2.120) result in the Nernst's formulation of the reversible potential:

$$E_{rev,H_2/H_2O} = \frac{RT}{4F}ln\left(\frac{{p^{TPB}}_{O_2}}{p^o}\right) - \frac{1}{2F}\left[\Delta\bar{g}^o_{H_2/H_2O} + RTln\left(\frac{{p^{TPB}}_{H_2O}}{{p^{TPB}}_{H_2}}\right)\right] \tag{2.121}$$

$$E_{rev,CO/CO_2} = \frac{RT}{4F}ln\left(\frac{{p^{TPB}}_{O_2}}{p^o}\right) - \frac{1}{2F}\left[\Delta\bar{g}^o_{CO/CO_2} + RTln\left(\frac{{p^{TPB}}_{CO_2}}{{p^{TPB}}_{CO}}\right)\right] \tag{2.122}$$

where the partial pressures are those of the species on the reacting surfaces, i.e. the TPB, and the $\Delta\bar{g}^o_{H_2/H_2O}$ is that of the oxidation reaction in SOFC (i.e., it has a negative value).

In most of the SOCs models, the potentials given by equations (2.121) or (2.122) are rearranged to show the species concentration in the bulk of the feeding gases:

$$E_{rev,H_2/H_2O} = -\frac{\Delta\bar{g}^o_{H_2/H_2O}}{2F} + \frac{RT}{2F}ln\left[\frac{p^b_{H_2}}{p^b_{H_2O}}\left(\frac{p^b_{O_2}}{p^o}\right)^{1/2}\right] - \eta_{conc,a} - \eta_{conc,c} \tag{2.123}$$

where the first two terms on the right side grouped together are referred to as reversible voltage under open circuit conditions – usually named V_{oc} – and η_{conc} is the concentration overpotential due to the variation of the partial pressure of the species from the bulk of feeding streams to the reacting regions of the electrodes. The concentration overpotential is given by:

$$\eta_{conc} = \frac{RT}{n_e F}ln\left(\prod_k \frac{{p_k^b}^{\nu_k}}{{p_k^{TPB}}^{\nu_k}}\right) \tag{2.124}$$

The difference of species concentration between the feeding flow and the reacting zone is usually attributed to the depletion of fuel/oxidizer due to the electrochemical reactions and to the

mass transfer limitations in the electrodes that determine lower partial pressure of reactants in the TPB. Thus, the concentration overpotentials are frequently neglected at open-circuit, when electrochemical reactions do not occur. However, this is an oversimplification if gas streams contain components that can chemically react among themselves, in this case the species concentrations also vary because of the chemical reactions even if the cell is at open-circuit.

A large part of SOC models use equation (2.123) in combination with the activation and ohmic overpotentials to obtain the voltage of the cell:

$$V_{cell} = V_{oc} + \gamma\left(\eta_{conc,a} + \eta_{conc,c} + \eta_{act,a} + \eta_{act,a} + \eta_{ohm}\right) \tag{2.125}$$

where γ is the previously reaction coefficient (γ = +1 in SOEC mode and γ = −1 in SOFC mode). Equation (2.125) shows the compositions of the total overpotential introduced in equation (2.6) during the thermodynamic analysis.

This is the standard expression of the cell polarization, usually adopted in the models to impose a constraint to the sum of the overpotentials of the cell. Given certain temperature and species distributions calculated from the thermo-fluidic models, the dependent variable of the polarization equation is the current density, which is given by the solution of equation (2.125).

It is worth noting that the use of the Nernst's equation for the calculation of the reversible potential is not rigorously valid or applicable in all the models, unless proper assumptions are made. In particular, the Nernst's potential is a singular scalar value, whose calculation requires to evaluate the difference between the equilibrium potentials of anode and cathode; however, these two potentials are defined in different domains and the subtraction can be made if and only if each of them assumes a single scalar value. This is always true in 0D models, but for higher dimension models the equilibrium potentials in general are not constant within the electrodes. Common assumptions adopted in 1D and 2D models impose the electrochemical reactions at the electrode/electrolyte interface and assume the electrodes as ideal electron-conductors on which the electronic potential is constant (Ferrero et al., 2015, Ni 2009, Janardhanan and Deutschmann, 2007). In this way, the TPBs are treated as lines on which the equilibrium potential varies with the position along the length of the electrode and the Nernst potential can be calculated as the difference between the anodic and cathodic equilibrium potentials at each position of the electrode length. Another further assumption can be made by considering the equilibrium potential of the cathode as a constant, an acceptable approximation only for SOC applications with high excess air the oxygen electrode.

The use of Nernst's equation has no meaning in 3D models or 2D models where electrochemical reactions are imposed in the volume instead of being assumed at the electrolyte/electrode interface. In this case, a more general modeling approach based on the implementation of equations which contain the electronic and ionic potentials of the cell as dependent variables should be used. With this approach, it is not necessary to calculate a reversible potential to be introduced in a polarization equation, but it is sufficient to calculate the local electrode equilibrium potential with equation (2.123) or by using a potential expression dependent on oxygen partial pressure in the gas mixture at equilibrium, as shown later in the case of multi-fuel mixtures. The current density produced in the cell can be then calculated as a function of the difference between electronic, ionic and equilibrium potentials in the TPBs regions by implementing a Butler-Volmer equation for the charge transfer reactions, as will be shown in the next section, and the transport of charge is the result of the gradients of the potentials. In the general approach based on the potentials, the voltage of the cell is imposed on the surface of one of the electrodes as a boundary condition for the electrical potential, while on the surface of the other the ground potential (i.e., zero potential) can be assumed. This is the approach that has been adopted in the 2D/3D cell and SRU models developed in this dissertation.

Some considerations have to be spent in the case of multi-fuel mixtures. In principle, when two or more different electrochemical reactants (i.e., H_2/H_2O and CO/CO_2) are present at the anode at the same time, each oxidation-reduction reaction has a different value of equilibrium potential and thus it seems not possible to define a unique value of reversible potential. However, it is possible to demonstrate that, under the assumption of having the fuel mixture in equilibrium conditions on the TPB surfaces of the electrode, the equilibrium potential is the same for all the fuels, and consequently it is possible to define unambiguously the reversible potential of the cell. A demonstration for the H_2/H_2O and CO/CO_2 redox reactions is given in the following lines.

The difference between the equilibrium potential of H_2/H_2O and CO/CO_2 redox is given by:

$$E_{eq,H_2} - E_{eq,CO} = \frac{\Delta\bar{g}^o_{H_2/H_2O}}{2F} - \frac{\Delta\bar{g}^o_{CO/CO_2}}{2F} + \frac{RT}{2F} ln\left(\frac{p^{TPB}_{H_2O} p^{TPB}_{CO}}{p^{TPB}_{H_2} p^{TPB}_{CO_2}}\right) \tag{2.126}$$

$$E_{eq,H_2} - E_{eq,CO} = \frac{1}{2F}\left(\bar{g}^o_{H_2O} - \bar{g}^o_{H_2} - \bar{g}^o_{CO_2} + \bar{g}^o_{CO}\right) + \frac{RT}{2F} ln\left(\frac{p^{TPB}_{H_2O} p^{TPB}_{CO}}{p^{TPB}_{H_2} p^{TPB}_{CO_2}}\right) \tag{2.127}$$

The fuel gas is assumed to be in equilibrium; in these conditions, the Gibbs free energy change of the water gas-shift (WGS) reaction ($CO + H_2O \rightleftharpoons H_2 + CO_2$) is zero, because the

mixture has reached its equilibrium (see *Section 2.2.5*). The free energy change of WGS is given by:

$$\begin{aligned}\Delta\bar{g}_{WGS} &= \Delta\bar{g}^{o}_{WGS} + RTln\left(\frac{p^{TPB}_{H_2}p^{TPB}_{CO_2}}{p^{TPB}_{CO}p^{TPB}_{H_2O}}\right) \\ &= \bar{g}^{o}_{H_2} + \bar{g}^{o}_{CO_2} - \bar{g}^{o}_{CO} - \bar{g}^{o}_{H_2O} + RTln\left(\frac{p^{TPB}_{H_2}p^{TPB}_{CO_2}}{p^{TPB}_{CO}p^{TPB}_{H_2O}}\right)\end{aligned} \tag{2.128}$$

By substituting equation (2.126) in (2.128) we obtain the demonstration of the equality between the potentials:

$$E_{eq,H_2} - E_{eq,CO} = \frac{1}{2F}\left(\bar{g}^{o}_{H_2O} - \bar{g}^{o}_{H_2} - \bar{g}^{o}_{CO_2} + \bar{g}^{o}_{CO}\right) - \frac{\Delta\bar{g}^{o}_{WGS}}{2F} = 0 \tag{2.129}$$

When the chemical equilibrium of the gaseous species within the electrode is assumed, the Nernst's voltage can be also re-written in terms of the oxygen partial pressures in the anode and cathode TPBs:

$$E_{rev} = \frac{RT}{4F}ln\left(\frac{p^{TPB,cat}_{O_2}}{p^{TPB,an}_{O_2}}\right) \tag{2.130}$$

where the partial pressure of oxygen at the anode is directly evaluated by calculating the equilibrium composition of the gas mixture. Expression (2.130) is useful to evaluate the ideal reversible potential of multi-fuel mixtures inside the anode just from the equilibrium composition of the fuel mixture.

It is worth noting that the equality between the equilibrium potentials of different reactions in multi-fuel mixtures is not valid when the gas mixture within the anode is far from equilibrium. If we consider anode-supported SOCs with Ni/YSZ anodes, the equilibrium assumption can be considered applicable because the fuel gas has to cross a large volume of electrode before reaching the TPB and thus it has a sufficient contact time with the Nickel catalyst that allow gas-shift and other reactions to reach the equilibrium. However, the gas equilibrium assumption has to be carefully verified case by case before applying it into a model.

If the gas mixture is not in equilibrium, it is not possible to define a single value of equilibrium potential within the electrode and both the Nernst- and potentials-based approach are not applicable. In this case, an elementary mass-action formulation based on the modeling of the rates of the single charge transfer reactions is needed (Goodwin et al. 2009). As will be shown in the next section, with this approach it is possible to avoid the calculation of the equilibrium

potentials because the current generated by the electrochemical reactions is computed directly from the rates of the single charge transfer reactions and the use a Butler-Volmer formalism is not required.

Electrochemical Reactions Modeling

The electrochemical reactions can occur only where electron conductive, ion conductive and gas phase coexist. The simultaneous presence of the three phases allows the conduction of electrons, the migration of ions and the transport of gas molecules to/from the reaction sites. As stated before, these are the TPB regions of the electrodes.

The mere presence of the TPB is not sufficient to ensure the electrochemical reactions to happen, but the TPB must be connected to the rest of the structure. If either the electronic, ionic or pore network is interrupted or badly interconnected, the electrochemical reactions cannot take place properly because electrons, ions or gaseous reactants/products cannot reach or leave the TPB surfaces. Most of the electrode materials are predominantly electronic conductors (e.g., Ni metal and La-Sr-Mn oxides), and when these materials are used, the TPB is limited to the contact region between the electrode and the electrolyte. In particular, the commonly used anode Ni-YSZ cermets have a TPB extension that several studies have estimated in the order of 5-20 μm (Cai et al., 2011, Zhu and Kee, 2008). The TPB length of oxygen electrodes can be typically higher, when mixed ionic and electronic conductors are used.

The reaction mechanisms that occur on the TPB consist of complex chains of intertwined physiochemical phenomena, which include adsorption/desorption of gas molecules on/from the electrode surface, dissociation, surface transport and solid-state diffusion of adsorbed species, and charge transfer reactions. The study of electrochemical reaction mechanisms of SOC electrodes has been addressed by countless works and it is out of the scope of this chapter, a thorough review of the literature pertaining these mechanisms has been presented by Hanna et al. (2014) and Li et al. (2010).

The problem of modeling the electrochemical reaction mechanisms is usually addressed by following two different approaches: 1) by assuming a charge transfer step to be the rate-determining of the entire reaction mechanism and using Butler-Volmer expressions for the calculation of the current electrochemically generated in SOC (Noren and Hoffman, 2005) or 2) by using fundamental mass-action kinetics to describe each elementary reaction of the entire mechanism and calculating the electrochemical current from the rates of the elementary charge transfer reactions (Goodwin et al. 2009).

In the following paragraphs, these two different modeling approaches are described. In both approaches it is necessary to define what the elementary steps of the reactions are, but in the first one the total rate of the electrochemical reaction is assumed to be controlled only by the transfer of the electric charge at the TPB and not by the transport of the species. Most of the SOC models adopt this approach and use the Butler-Volmer equation either combined with a polarization equation that couples the reversible cell potential with the voltage losses (i.e. overpotentials) related to the irreversible phenomena, namely the activation, ohmic and concentration overpotentials or expressed as a function of the electric, ionic and equilibrium potentials. Some authors have also adopted a mixed approach where the description of elementary charge transfer reactions through mass-action kinetics is introduced into the Butler-Volmer formulation by adopting simplifying assumptions (Zhu et al., 2005, Menon et al., 2013).

When the global electrochemical reaction is assumed to be controlled by a charge-transfer step, the Butler-Volmer equation can be used to calculate the net current density generated in the electrode by the reaction (Bagostky, 2005):

$$i = i_0 \left[exp\left(\alpha_f \frac{n_{BV} F \eta_{act}}{RT}\right) - exp\left(-\alpha_b \frac{n_{BV} F \eta_{act}}{RT}\right)\right] \tag{2.131}$$

where i_0 is the exchange current density of the electrode reaction, α_f and α_b are symmetry parameters of forward and backward reactions, η_{act} is the activation overpotential of the reaction and n_{BV} is the number of electrons transferred in the charge-transfer step. It is worth noting that only if the electrochemistry is represented with a single, global charge-transfer process that corresponds with the half-cell reaction (Shi et al., 2011a), then n_{BV} is the number of electrons transferred in the half-cell reaction. If the Bulter-Volmer equation is describing a global charge-transfer reaction, the coefficients α_f and α_b have no constraints, while for elementary reactions – in which only one electron is transferred – these factors take on values between 0 and 1 and their sum is constrained to 1 (Goodwin et al., 2009).

The activation overpotential arises because the electric charge cannot move directly between the ionic and electronic conductive phases of a cell. Both the phases have free charge carriers and are globally neutral, however an excess charge is distributed on their surfaces. Therefore, at the interface between the phases – the TPB – an electric double layer is formed, with the charged surfaces behaving as the plates of a capacitor. During the charge-transfer reaction, the electrons are transferred across the double layer moving against the potential difference existing between the ionic and electronic phases. When the net current crossing the double layer is zero, the

potential difference between the phases is equal to the equilibrium potential of the electrode, while if a potential difference higher than the equilibrium is needed to allow a non-zero net current to exist. The activation overpotential measures the disequilibrium between the potential difference of the phases and the equilibrium potential:

$$\eta_{act} = \phi_e - \phi_i - E_{eq} \tag{2.132}$$

where ϕ_e is the electronic potential of the electrode, ϕ_i is the ionic potential and E_{eq} is the equilibrium potential of the electrode that can be expressed by using equation (2.120).

In most of models that use a Butler-Volmer approach, the activation overpotential is related to the current density by equation (2.132) that is coupled to the polarization equation (2.125) to solve the electrochemical problem and obtain the current density distribution without explicitly introduce the ionic and electronic potentials in the equations (Chan et al., 2001, Ni et al., 2007, Ferrero et al. 2015). However, for the distributed charge transfer modeling in 2D and 3D models, the electronic and ionic potentials are frequently used as dependent variables instead of the current density; in this case, the activation overpotential is expressed by using equation (2.132) and the Butler-Volmer equation is coupled with the charge transport equations to define the current density distribution within the electrodes (Zhu et al., 2005, Klein et al., 2007, Shi et al., 2007, Andersson et al., 2012).

The exchange current density provides a quantitative measure of the electrocatalytic activity of the electrode for a certain electrochemical reaction. Its value depends on the charge-transfer kinetics, temperature, partial pressures and electrode microstructure. The dependency of i_0 on so many parameters makes it difficult to define it without the use of semi-empirical relations. In most of the SOC literature, the exchange current density is expressed as the product of temperature dependent terms, written in Arrhenius form, and pressure dependent terms (Costamagna and Honegger, 1998, Hosoi et al., 2015):

$$i_0 = \gamma \cdot exp\left(-\frac{E_{act}}{RT}\right)\prod_k \left(\frac{p_k}{p_{k,ref}}\right)^{e_k} \tag{2.133}$$

where p_k is the partial pressure of the k species involved in the electrochemical reaction as reactant or product and $p_{k,ref}$ is a reference pressure for the k species. E_{act} is the activation energy of the electrode reaction, which depends on reaction and materials, e_k is a dimensionless exponent and γ is a pre-exponential parameter dependent on electrode materials and microstructure, and in some cases also on the temperature (Leonide 2010). The values of γ and e_k are widely scattered in the literature.

Equation (2.133) is a semi-empirical relation in which the parameter γ is usually determined by fitting experimental data. Theoretical expressions of the exchange current density have been derived for SOFC and SOEC operation by Hosoi et al. (2015), Menon et al. (2014 and 2015), Narasimhaiah and Janardhanan (2013), and Zhu et al. (2005) from the study of reaction mechanisms. In these works, the current density is expressed as a function of rates and equilibrium constants of the elementary reactions that are assumed to compose the entire reaction mechanism. The theoretical formulation of the exchange current density allows to describe its dependency on the partial pressures in a physically-based way; however, the high number of constant dependent on reactions and materials makes it necessary to use empirical data for a quantitative evaluation of i_0.

It is worth noting that the current density evaluated by equation (2.131) is expressed per unit of electrochemically active area of the electrode; thus, in order to obtain the volumetric current generated in the electrode – namely i_v – the current density has to be multiplied by the active electrode area per unit volume (Costamagna et al., 1998):

$$i_v = A_v i \tag{2.134}$$

In the work presented in this dissertation the Butler-Volmer approach has been adopted and the exchange current density has been derived from the fitting of the semi-empirical relations to experimental data.

The use of Butler-Volmer equation is consistent when the charge-transfer is the rate-determining step of the electrochemical reaction and its application requires the definition of an equilibrium potential within the electrode; however, if the gas mixture is not in equilibrium, it is not possible to define properly the equilibrium potential and the Butler-Volmer is not applicable. In this case, the current density generated by the electrochemical reaction can be calculated by using an elementary mass-action formulation of the rates of the elementary charge transfer reactions (Goodwin et al., 2009).

In general, a charge-transfer reaction can be written as:

$$A^a + B^b \leftrightharpoons C^c + D^d + \upsilon_e e^- \tag{2.135}$$

where A, B, C and D are the species having charge *a*, *b*, *c* and *d* that are involved in the transfer of υ_e electrons. For an elementary charge transfer reaction, the coefficient υ_e assumes the value of +1 for the forward (i.e., anodic) reaction – which "produces" electrons – and -1 for the

backward (i.e., cathodic) reaction. The net rate of the reaction is given by the difference of the forward and backward rates of the charge-transfer reaction, which can be written as:

$$q_{i,f} = k_f(T) \prod_{i,r} a_i \, exp\left(\frac{\beta_f F E_{el}}{RT}\right) \tag{2.136}$$

$$q_{i,b} = k_b(T) \prod_{i,p} a_i \, exp\left(-\frac{\beta_b F E_{el}}{RT}\right) \tag{2.137}$$

where the rate constants k can be expressed in the Arrhenius form, a_i are the activities either of the reactants in the case of the forward reaction or of the products for the backward one. The coefficient β_f and β_b are the symmetry coefficients, which range between 0 and 1 and are constrained to have sum equal to one. E_{el} is the electrode potential, which is given by:

$$E_{el} = \phi_e - \phi_i \tag{2.138}$$

The current generated for unit of TPB length is given by:

$$i_{TPB} = F \sum_i \left(q_{i,f} - q_{i,b}\right) \tag{2.139}$$

where the summation includes all the charge-transfer reactions. The volumetric current density is related to i_{TPB} by the volume specific TPB length (Janardhanan et al., 2008):

$$i_v = \lambda_{TPB} i_{TPB} \tag{2.140}$$

With this approach, it is possible to calculate the current generated by the electrochemical reactions by avoiding the Butler-Volmer formulation.

Charge transport and conservation

In an SOC stack, the charge transport takes place in the solid phases – ionic and electronic – of cells and components. Both the ionic and the electronic conductive materials exert a resistance to the charge flow and the movement of charges is driven by the potential difference existing between the electrodes of the cells. The charge flux is referred to as the current density, which is given by the Ohm's Law:

$$i_{i/e} = -\sigma_{i/e} \nabla \phi_{i/e} \tag{2.141}$$

where $\nabla \phi_{i/e}$ is the gradient of the ionic/electronic potential that drives the charge flow and $\sigma_{i/e}$ is the conductivity of the material. In the case of the impervious solids (i.e., electrolyte, interconnects and current collectors), the conductivity is that of the pure material, while in the

porous electrodes an effective conductivity must be calculated in order to take into account the presence of pores and electron-conductive phase. The effective conductivity can be calculated by using a statistical approach in which the porous electrode is assumed as system of packed spherical particles (Nam and Jeon 2006). The effective conductivity is given by:

$$\sigma_{i/e}^{eff} = \sigma_{i/e}\left[(1-\varepsilon)f_{i/e}P_{i/e}\right]^{k} \tag{2.142}$$

where $f_{i/e}$ is the volume fraction of the ionic/electronic phase in the electrode and $P_{i/e}$ is the percolation probability. The exponent k, generally larger than 1, depends on the distribution of the conductive phase in the electrode.

The conservation equation must be applied in the model to enforce the conservation of charge:

$$\frac{\delta \rho_{e/i}}{\delta t} + \nabla \cdot i_{e/i} = S_{i/e} \tag{2.143}$$

where $\rho_{e/i}$ is the volumetric charge density and $S_{i/e}$ is the volumetric charge source. The term $S_{i/e}$ is different from zero only when the charge transfer reactions are assumed to take place in the volume of the electrode. In this case, the charge is transferred from the ionic to the electronic phase of the electrodes in the TPB volume of the electrodes; the variation of ionic and electronic currents is given by:

$$S_{i/e} = \pm i_v \tag{2.144}$$

where i_v is the current that is transferred at the TPB, which is calculated from equation (2.134) or (2.140).

When the electrochemical reactions are imposed at the interface between electrode and electrolyte, the volumetric charge source is null and the continuity between the ionic and electronic current is imposed on the boundary.

In SOC models, the charge transport in the electronic conductive materials in usually neglected by assuming them as ideal conductors (i.e., infinite conductivity) and only the transport of ions in the electrolyte is taken into account. Also, the ions transport is frequently assumed to be one-dimensional and normal to the electrolyte/electrode interfaces. This assumption is valid for thin electrolytes, and allows to express the potential drop due to ion transport as the difference between the potentials at electrode/electrolyte interfaces:

$$\eta_{ohm} = \phi_{i,an} - \phi_{i,cat} \tag{2.145}$$

Equation (2.132) involve the electric/ionic potentials as dependent variables, which are put in relation by Butler-Volmer (2.131) or elementary rate equations (2.136) and (2.137) imposed on the TPB boundary or volume. On the external surface of the electrodes, or on the current collecting plates in the case of a stack, where only the electrical potential is defined because the ionic phase is not present, a boundary condition is needed in order to solve the charge-conservation equation. The cell (or stack) voltage is usually imposed on one of the electrode (or current collector) surfaces, while on the other the ground (i.e., zero) potential is fixed.

Another possible approach is to impose the ground potential on one of the electric boundaries and fix the total current value on the other by imposing a constraint to the integral of the current density:

$$\int_{\partial\Omega} i_e \cdot \vec{n} dS = I_{tot} \tag{2.146}$$

With this approach, the input of the electrical model is the current, while the voltage of the SOC cell/stack can be calculated from the difference between the potentials on the two electric boundaries.

2.2.5 Heterogeneous chemistry modeling

Chemical reactions can occur within the fuel stream at the typical operating conditions of SOCs. In particular, when fuels other than hydrogen are fed to the cells, the operating temperatures are sufficient to promote both homogeneous and heterogeneous reactions between the fuel components.

If we consider the typical SOC mixtures – which contain H_2, H_2O, CO, CO_2 and CH_4 – and operating conditions, the reactions that occur within the gas phase are very slow when compared to the heterogeneous ones, thus the homogeneous chemistry can be safely neglected in the fuel electrode domains (Zhu et al. 2005). In particular, when the fuel mixture come in contact with the porous structure of the electrode, typically made by a Ni/YSZ cermet, the heterogeneous reactions are promoted by the presence of the nickel that acts as a catalyst for the reactions, such as methane reforming/methanation and gas shifting. However, homogeneous reactions demonstrated to play a non-negligible role in non-catalytic SOFC regions when dry natural gas (Walters et al., 2003) or higher hydrocarbons are fed to the cells – especially at very high temperatures (T > 800 °C) – or when partial oxidation conditions are reached (Gupta et al. 2006) due to the presence of oxygen or air into the fuel stream. The homogeneous reaction modeling

has not been considered in this work, as the gas mixtures and operating conditions investigated are not favorable to this type of reactions.

This section will focus on the modeling of the heterogeneous reactions in the fuel electrode of SOCs. Modeling the reactions means to find a suitable mathematical description of the physics that allows to calculate the rates of the reactions. In particular, rates are necessary to interface the chemical model with the thermal and fluidic ones through the source terms of equation (2.67) and (2.116).

The problem of describing the heterogeneous reaction rates has been addressed in the SOC literature in two different ways: by using global expressions for the calculation of an overall reaction rate or through detailed kinetic models that include intermediate reaction steps. Both the approaches are based on the mean field approximation, which describes the surface state with average quantities and neglects the non-uniformity of the catalytic surfaces.

Global reaction mechanism

Two different approaches can be adopted when modeling the chemistry by using global rate expressions: one is based on the assumption that the reaction is controlled by kinetics and the other assumes that the reaction rate is limited by the equilibrium.

The first approach is based on modeling each reaction in a single step whose rate can be generally expressed by a kinetic power law expression:

$$r_{react} = \gamma \prod_i p_i^m \, exp\left(-\frac{E_a}{RT}\right) \tag{2.147}$$

where γ and reaction orders m of the i species participating to the reaction are derived from the fitting of experimental data. Alternatively to power law models, also Langmuir-Hinshelwood type models are used to describe the kinetics.

With the second approach, the reaction velocity is expressed through an equilibrium-limited rate expression defined by:

$$r_{react} = r_f \left(1 - \frac{\prod p_{products}^{\nu}}{\prod p_{reactants}^{\nu}} \frac{1}{K_r}\right) \tag{2.148}$$

where ν is the stoichiometric coefficient of the gaseous species, K_r is the equilibrium constant of the reaction and r_f is the rate of the forward reaction, usually given by a power law expression. It is worth noting that the rate expressed by equation (2.148) goes to zero when the equilibrium composition is reached.

The applicability of the equilibrium rather than the kinetic approach strictly depends on the reaction and on the complexity of the model. In general, if a lumped 0D model is used for the cell, the equilibrium of the reactions can be safely assumed, while if a multidimensional model is adopted, then it is more appropriate to apply a kinetic description of the reaction for the calculation of local rates.

The approaches described by equations (2.147) and (2.148) are valid for any reaction, however their application requires to fit the kinetic expressions to experimental data measured under reaction conditions that are relevant for the model. Experimental data are available in the literature for the most common reactions and cell materials; however if the model has to include particular reactions, conditions or materials, it is necessary to build specific experimental data sets in order to characterize the reactions and describe the catalytic activity of materials with respect to the investigated reactions.

The most common reactions included in SOC models are the heterogeneous methane steam reforming (MSR) and water-gas shift (WGS) reactions within Ni/YSZ anodes:

$$CH_4 + H_2O \leftrightharpoons CO + 3H_2 \tag{2.149}$$

$$CO + H_2O \leftrightharpoons CO_2 + H_2 \tag{2.150}$$

When these reactions are modeled using a global mechanism approximation, the kinetic approach is usually adopted for the steam reforming/methanation reaction (2.149), while the water gas shift (2.150) is frequently described under the equilibrium assumption. The kinetic expressions used for the steam reforming reactions are commonly derived from experimental studies either over commercial nickel-based catalysts (Xu and Froment, 1989, Hou and Hughes, 2001) or directly on Ni/YSZ anodes (Drescher et al. 1998, Achenbach and Riensche 1994, Ahmed and Foger 2000, Lee et al. 1990, Belyaev et al. 1995, Dicks et al., 2000). In the study of Nagel et al. (2008) different steam reforming models given by power law, Langmuir-Hinshelwood and equilibrium expressions have been compared showing the effect of the STR kinetics on the temperature distribution in the cell.

In the work of Sanchez et al. (2008), the equilibrium and kinetics approaches have been compared for both reactions (2.149) and (2.150). The work highlights that the rates of reactions are controlled either by kinetics or equilibrium depending on the local conditions of the cell, thus the choice between one approach and the other is strictly connected to the peculiarities of the modeled system and cannot be assumed a priori.

Besides the STR and WGS, other reactions are frequently included in SOC models by using global kinetics expressions: dry reforming ($CH_4 + CO_2 \leftrightharpoons 2CO + 2H_2$), CO_2 methanation ($CH_4 + 2H_2O \leftrightharpoons CO_2 + 4H_2$), Boudouard ($2CO \leftrightharpoons CO_2 + C$) and methane cracking ($CH_4 \leftrightharpoons C + 2H_2$) (Wang Y. et al. 2011, Ni 2013).

It is worth noting that the equations introduced in this section for the calculation of an overall reaction rate do not include neither the concentrations of intermediate surface species on the anodic structure nor explicit information on the microstructure of the electrode, even if they are describing heterogeneous kinetics.

In this Thesis, heterogeneous reactions have been described by adopting a global reaction mechanism approach.

Detailed surface reaction kinetics

Alternatively to the global rate expressions, the problem of modeling the heterogeneous chemistry can be addressed by using a mass-action formulation of the kinetics of the elementary reaction steps.

The principle is analogous to that showed when modeling the charge transfer with the mass-action formulation: instead of approximating the reaction with a global mechanism, a multi-step mechanism is developed and a rate is calculated for each step of the reaction.

The total molar rate of the *i-th* reaction step is given by the difference between forward and backward rates of reaction:

$$r_{react,i} = k_{fi} \prod_{k=1}^{K} [X_k]^{\nu'_{ki}} - k_{ri} \prod_{k=1}^{K} [X_k]^{\nu''_{ki}} \tag{2.151}$$

where k_{fi} and k_{ri} are the rate constants of the reaction, K is the total number of species – gaseous and adsorbed on the surface – involved in the reaction step, $[X_k]$ is the concentration of the k species and the exponents ν'_{ki} and ν''_{ki} are the stoichiometric coefficients of reactants and products. The concentration of the k species is expressed either as molar volumetric (mol/m^3) for the gas-phase species or as molar superficial (mol/m^2) for the surface species.

If equation (2.151) is applied to all the reaction steps involving the k species, the resulting net molar rate is given by:

$$\dot{s}_k = \sum_{i=1}^{K_r} \left[(\nu''_{ki} - \nu'_{ki}) k_i \prod_{k=1}^{K_g+K_s} [X]_k^{\nu'_{ki}} \right] \tag{2.152}$$

In equation (2.152), K_r is the total number of reaction steps, K_g is the number of gas-phase species in the *i-th* step and K_s is that of the surface species. The surface molar concentration can be expressed as a function of the surface coverage of the species:

$$[X_k] = \frac{\theta_k \Gamma}{\sigma_k} \tag{2.153}$$

where $\theta_k$is the surface coverage of the *k* species, σ_k is the coordination number (i.e., the number of surface sites that are occupied by species *k*) and Γ is the total surface site density.

The rate constants are expressed in Arrhenius form and can be also dependent on the surface coverage of adsorbed species:

$$k_i = A_i T^{\beta_i} exp\left(-\frac{E_{ai}}{RT}\right) \prod_{k=1}^{K_s} \theta_k^{\mu_{ki}} exp\left(-\frac{\epsilon_{ki}\theta_k}{RT}\right) \tag{2.154}$$

where μ_{ki} and $\epsilon_{ki}$are parameters for modeling the coverage dependence. When the elementary step is an adsorption reaction of a gas-phase species on the catalyst surface, the rate constant is given by:

$$k_i = \frac{\gamma_i}{(\Gamma)^m} \sqrt{\frac{RT}{2\pi M_g}} \tag{2.155}$$

where γ_i is the sticking coefficient of the reaction (i.e. a measure of the probability that the adsorption reaction takes place when the molecule collide with the surface, its value lies between 0 and 1), *m* is the sum of the stoichiometric coefficients of the reactants and M_g is the molecular weight of the gas-phase species adsorbed.

When equation (2.152) is solved for all the *k* species in combination with the fluidic, thermal and electrochemical equations, the surface coverages are included in the dependent variables and must be determined as a part of the solutions.

The surface coverage of a species depends on the position, because the local temperature and gas species concentrations vary within the electrode. However, the mean field approximation ensures that the surface species do not interact laterally, thus the surface coverage in a point of the surface is not influenced by the coverages in the neighboring positions of the computational domains and the time-dependent variation of θ_k can be written as:

$$\frac{\partial \theta_k}{\partial t} = \frac{\sigma_k \dot{s}_k}{\Gamma} \tag{2.156}$$

Equation (2.156) has to be imposed for all the surface coverages, and the solution of the resulting system of differential equations provides the values of θ_k. However, the times scales of

the surface reactions are several order magnitudes lower than those of the variation of temperature and gas-species concentrations. Therefore, the steady state approximation can be applied and the system of equations (2.156) reduces to a set of algebraic equations in which the net molar rates of the surface species are imposed to be equal to zero.

The approach based on elementary reaction mechanisms has a broader validity with respect global mechanism approaches since it can include all the possible chemical reactions occurring within the porous anode. Moreover, the mass-action formulation has a general validity can be applied also to homogeneous chemistry.

A multi-step reaction mechanism for the internal reforming of CH_4-CO-CO_2-H_2-H_2O-O_2 mixtures has been developed and validated over Ni/YSZ cermets by Hecht et al. (2005). The mechanism, which consists of 42 reaction steps that involve 6 gas-phase species and 12 surface species, has been recently applied in the modeling and validation of the heterogeneous chemistry in tubular SOFCs fed by biogas (Santarelli et al. 2013) and its comparison with a global kinetic approach is reported by Hoffman et al. (2009). The multi-step mechanism predicts slower methane conversion with respect to the global kinetic approximation (Hoffman et al. 2009) and shows that thermodynamic equilibrium conditions are not fully achieved inside the anode of a tubular fuel cell, consistently with the experimental observations (Santarelli et al. 2013).

2.2.6 Carbon deposition and sulfur poisoning models

Carbon deposition modeling

Carbon deposition identifies the phenomenon of formation of solid carbon within SOC electrodes. The carbon coking leads to two deleterious effects in SOCs: pore blocking and catalyst covering. The first consists in the progressive accumulation of solid carbon in the voids of the porous electrode structure that reduces the porosity of electrodes, thus increasing the transport resistance for gas species diffusing toward the TPB. The second effect is related to the reduction of the TPB area due to the physical coverage of the catalytic surface of electrodes due to the deposition of a carbon layer on it. Both the effects contribute to decrease the SOC performance. Moreover, the accumulation of carbon deposits generates mechanical stresses in the cell, which can eventually lead to the formation of fractures in the cell structure.

This section gives a brief introduction to the carbon coking mechanisms before addressing the modeling approach for its description.

Carbon depositions issues have long been investigated for Ni/YSZ anodes of SOFCs operating with CH_4 and other hydrocarbon fuels (He and Hill 2007, Koh et al. 2002, Lin et al. 2005, Sumi et al. 2011, Kim et al. 2006, Saunders et al. 2004). In fact, Ni has proven to exhibit a very high catalytic activity toward the carbon deposition reactions in the operating temperature range of SOCs. Several reaction mechanisms have been proposed for the solid carbon formation from carbonaceous gas mixtures in SOCs (Chen et al. 2011). Typical SOC mixtures contain C atoms in CO, CO_2 and CH_4 molecules that can be involved in carbon depositions reactions. In particular, CH_4 can directly lead to coke formation by methane cracking:

$$CH_{4(g)} \leftrightarrow 2H_{2(g)} + C_{(s)} \tag{2.157}$$

The Boudouard disproportionation reaction involves the conversion of CO into carbon and carbon dioxide:

$$CO_{2(g)} + C_{(s)} \leftrightarrow 2CO_{(g)} \tag{2.158}$$

Another reaction mechanism that can lead to the formation of solid carbon is the reduction of carbon monoxide by hydrogen (O'Brien and Giorgi 2012):

$$CO_{(g)} + H_{2(g)} \leftrightarrow C_{(s)} + H_2O_{(g)} \tag{2.159}$$

In the study of Li et al. (2015) it was also speculated that deposited carbon could be directly produced or consumed by the following electrochemical reaction at TPB:

$$C_{(s)} + O^{2-} \leftrightarrow CO_{(g)} + 2e^- \tag{2.160}$$

The solid carbon deposited can assume different morphologies depending on the formation pathway. A general distinction can be made between the carbon originating in the gas-phase by homogeneous reactions (pyrolytic carbon) and that generated in heterogeneous reactions because of the presence of catalytic surface (catalytic carbon) (Tanabe et al. 1981).

Pyrolytic carbon is an amorphous carbon that derives from the thermal cracking of hydrocarbons and deposits on the electrode surface. Once deposited, the amorphous carbon can change phase into a graphitic carbon that encapsulates the catalyst particles and leads to the electrode deactivation. Favorable conditions for the formation of this carbon are high

temperature (T > 600 °C) and low water/hydrocarbon ratio. Pyrolytic carbon formation in SOFCs is not significant for methane, but is relevant for other hydrocarbons and alcohols.

The catalytic carbon can assume two different forms: a film morphology or a fiber-like shape. The film structure is generated by polymerization of adsorbed hydrocarbons on the catalyst surface. This carbon typology is favored at low temperature (T < 500 °C) and low ratios of hydrogen/hydrocarbons and water/hydrocarbons. On metal catalysts such as Ni, Fe and Co, carbon deposits can grow in a fiber- or whisker-like shape (Alstrup 1988). Hydrocarbons are decomposed on the metal surface, and carbon atoms diffuse through the bulk of the metal until they precipitate on the rear side of the metal catalyst particle (Snoeck et al. 1997). The catalyst particle is thus lifted away from the support, but is not covered by carbon and remains active towards the hydrocarbons dissociation. Consequently, the growth of carbon whiskers is a continuous process not affected by saturation and considerable amounts of carbon can deposit leading the formation on long carbon fibers. The morphology of filamentous carbon has been studied deeply. Baker et al. (1972) describe carbon filaments as a duplex structure formed by an amorphous inner core surrounded by a layer of graphitic carbon; the study reports that a metal component is also present either as a particle at the head of the filament or as dispersion along the body. Dimensions and structure of filaments depends on the characteristics of the catalyst (particle size, surface area, etc.). Takeguchi et al. (2002) pointed out the structure of Ni/YSZ electrodes is favorable for carbon filament formation in SOCs. In case of whiskers formation in SOC electrodes, even if the catalyst surface is not deactivated toward the carbon deposition reaction, the TPB structure become inactive for the electrochemical reactions as the metal is separated from the ionic particles. The fibers can be also a serious issue for the integrity of the electrode, as they fill the pore space inducing mechanical stresses on the structure that can eventually lead to the cracking of the electrode. The formation of whiskers is favored at intermediate temperature (T > 450 °C) and low water-to-hydrocarbon ratios.

The carbon deposition is thus related to complex phenomena and its prediction and evaluation in SOC models is not straightforward. In the SOC literature, the most used approaches to predict the carbon formation are based either on the thermodynamic equilibrium analysis or on a kinetic analysis of the reactions. Methane cracking (2.157) and Boudouard reaction (2.158) are the two reactions identified in the literature as the major pathways for carbon deposition on Ni-based catalysts and SOFC anodes (Armor 1999, Lanzini et al. 2013).

Following the thermodynamic equilibrium approach, Klein et al. (2007) defined two ratios for measuring the distance from equilibrium of Boudouard and methane cracking reactions:

$$\alpha = \frac{p_{CO_2}}{p_{CO}^2} \cdot \frac{a_c}{K_B} \tag{2.161}$$

$$\beta = \frac{p_{H_2}^2}{p_{CH_4}} \cdot \frac{a_c}{K_C} \tag{2.162}$$

where K_B and K_C are the equilibrium constants of reactions (2.157) and (2.158) and a_c represents the carbon activity of the catalyst (i.e., a value between 0 and 1, 1 if the catalyst if fully active, 0 if the catalyst is inactive because of the carbon coverage), which is assumed equal to 1 in Klein's study. When the calculated α or β are < 1, the reaction is not yet at equilibrium and proceeds in the direction that brings the related coefficient to 1. The simultaneous effect of both reactions is investigated in the same study by a coefficient γ given by the product of α and β:

$$\gamma = \alpha \times \beta \tag{2.163}$$

In fact, if α is < 1 and β is > 1 (or vice-versa) the definition of α and β is not sufficient to give a prediction on the formation of carbon, as it is produced by one reaction and consumed by the other. Eveloy (2012) applied the γ coefficient to the study of carbon deposition in SOFCs operating with internal methane reforming. This modeling approach allows to define the areas where carbon depositions is thermodynamically favored within SOC electrodes starting from the distribution of partial pressures and temperature, which is needed for the calculation of equilibrium constants. Examples of this application are also given by the study of Vakouftsi et al. (2011) and Wang et al. (2009). In the second one, also the reaction of reduction of carbon monoxide by hydrogen (2.159) is considered and the carbon activities are derived from α, β and CO reduction ratios. Positive carbon activities indicate the thermodynamic possibility of carbon formation.

Other equilibrium-based analyses are performed on the basis of the Gibbs-free energy minimization (Sasaki et. al. 2003, Zhan and Barnett 2006, Gao et al. 2011). These studies consider an element balance of the species, thus including all the possible reactions between the assumed species.

Most of the analyses of carbon formation in SOFCs based on thermodynamic equilibrium assume that carbon deposits have the characteristics of graphite and thus calculate the equilibrium constants and the Gibbs free energy by considering all the solid carbon as graphite. Very few studies take into account different forms of carbon, for example the work of Cimenti

and Hill (2009) includes amorphous carbon in addition to graphite. In general, when carbon is deposited in different forms, also its thermodynamic properties differ from graphite. The study of Lee et al. (2013b) has shown the different energetic and entropic properties of catalytically grown carbon fibers and graphite. The study reports that little difference in carbon formation predictions are achieved between the two carbon types for methane mixtures, while higher hydrocarbons mixtures (e.g. methanol and propane) lead to higher differences in the predictions. The importance of particle size in the calculation of the Gibbs free energy of carbon fibers is also highlighted. Thus, in typical SOC mixtures where CH_4 is the higher hydrocarbon, the graphite assumption can be safely assumed when addressing the modeling of carbon deposition; however, a detailed model should also consider the different types of carbons and their correct thermodynamic properties to obtain more precise results.

All the modeling approaches based on thermodynamic equilibrium are focused at predicting the possibility of carbon deposition and can be applied for highlighting the areas of the electrodes where the risk of carbon deposition is higher. However, very few studies approached the problem of evaluating the amount of carbon deposited in SOC electrodes when the carbon formation occurs and the consequent effects on cell performance. For this type of analysis, the equilibrium approach is not sufficient, and the study of reaction kinetics is needed to evaluate the rates of deposition. Very few studies have addressed the evaluation of the carbon deposition through kinetics modeling. A global kinetic approach has been followed by Yan et al. (2012) that evaluated the rates of methane cracking and Boudouard reactions from kinetic studies on Ni-based catalysts and applied the rates in a dynamic model in which the global carbon deposition rate is defined as:

$$r_C = \frac{d\bar{c}_c}{dt} = a \sum_i r_{CD,i} \tag{2.164}$$

where $\bar{c}_c$ is the molar concentration of the deposited carbon, a is the catalyst activity, and $r_{CD,i}$ (mol m^{-3} s^{-1}) is the rate of carbon formation of the *i-th* reaction considered. In the model, the catalyst deactivation depends on the carbon deposition rate and concentration of deposited carbon following the relation of Zavarukhin and Kuvshinov (2004):

$$\frac{da}{dt} = -k_a \left(\frac{d\bar{c}_c}{dt}\right)^2 \cdot \bar{c}_c \cdot a \tag{2.165}$$

The reduction of the porosity due to carbon deposition can also be considered:

$$\frac{d\varepsilon}{dt} = -\frac{\varepsilon \frac{d\bar{c}_c}{dt} M_c}{\rho_c} \tag{2.166}$$

where M_C is the molar mass of carbon and ρ_C is the carbon density. The elementary kinetic approach described in the previous section allows to calculate the surface coverage of all the species (see equation (2.156)), including the solid carbon. This approach has been applied by Yurkiv (2014), who included solid carbon formation processes in the methane reforming mechanism described by Deutschmann and co-workers (Maier et al. 2011) and described the performance degradation of SOFC anodes fuelled with reformate. The model predicts the formation of pyrolytic and film carbon and also the dusting of Ni particles and uses experimental data for model validation.

It is worth noting that carbon deposition has been thoroughly investigated for SOFC operation, but very few researches have addressed the specific peculiarities related to carbon formation in co-electrolysis operation of SOCs. A recent experimental study investigated the carbon formation limits during co-electrolysis of H_2O and CO_2 in Ni/YSZ supported SOECs (Tao et al. 2014a) and reported carbon deposition also in conditions that were not thermodynamically favorable for its occurrence. The authors argued that diffusion limitations locally induced the formation of carbon deposits due to the electrochemical reduction of CO adsorbed on YSZ surface (Tao et al. 2014b). Another experimental study on patterned Ni/YSZ electrodes assessed the effect of SOEC and SOFC operation on carbon deposition with CO/CO_2 mixtures (Li et al. 2015).

The study showed that electricity significantly promoted the carbon deposition in SOEC and weakened it in SOFC. Authors speculated that deposited carbon could directly participate in the electrochemical reaction (2.160) and identified the deposited carbon mainly in the graphitic structure. Even if the electrochemical CO reduction (including the reverse C oxidation) has been identified as a possible path that can influence the carbon formation, there aren't modeling studies in the current literature that includes it in the carbon formation mechanisms.

In this Thesis, carbon deposition has been modeled following the global kinetic approach described above that includes Boudouard and methane cracking reactions.

Sulfur poisoning

One of the problems associated to the use of conventional Ni cermets for the fuel electrode of SOCs is their deactivation in the presence of H_2S, even at ppm levels. Hydrogen sulfide is a nano-contaminant for the SOCs, which can segregate at nickel active sites of the electrode, covering a fraction of the Ni surface available for chemical and electrochemical reactions. The effect on cell performance is the increase of charge transfer losses and the reduction of the chemical activity of the electrode, which lead to a decrease of the cell voltage in SOFC mode and to an increase of it in SOEC operation. The presence of H_2S in fuel mixtures of SOFCs is not unusual, as hydrogen sulfide is a quite common trace component of hydrocarbon fuels and biogas. If the option of separating CO_2 from biogas for using it as a co-electrolysis fuel is considered, the H_2S represents a possible contaminant also in SOEC operation. For this reason, the effect of H_2S on cell performance has been included in the model developed in this dissertation.

The interaction between H_2S and nickel is known to be related to two phenomena: chemisorptions and sulfidation (Papurello et al. 2016). The first mechanism consists in the adsorption of a sulfur molecule of the nickel surface (i.e., and the release of the H_2 molecule of H_2S), and the second in the electrochemical reaction of H_2S. The chemisorptions is the dominating mechanism at 700 – 800°C for H_2S concentrations below 50 ppm(v). This concentration is very high for practical applications, as a sulfur polishing step is always present in SOC plants in order to avoid the poisoning of cells and reactors. Thus, it is more interesting to investigate the adsorption of sulfur on Ni surface, rather than assessing its electrochemical interaction in the cell.

Studies have shown that the Ni surface cannot be fully covered by sulfur, but an equilibrium condition exists for the H_2S adsorption on Ni at which the sulfur coverage reaches the maximum value, which corresponds to the maximum saturation level of the Ni surface (Papurello et al. 2016, Alstrup et al. 1981). It is commonly reported in the literature that the saturation level depends on the partial pressures of H_2S and H_2 and on the temperature following a Temkin-like isotherm. Alstrup et al. (1981) obtained from the fitting of experimental data the following expression for the saturation sulfur coverage:

$$\theta_S = 1.45 - 9.53 \cdot 10^{-5} \cdot T + 4.17 \cdot 10^{-5} \cdot T \cdot \ln\left({p_{H_2S}}/{p_{H_2}}\right) \tag{2.167}$$

Alternatively, the sulfur coverage on Ni can be predicted by following a kinetic approach, as described by Appari et al. (2014). The process of H_2S adsorption is not instantaneous, but the coverage time to reach the saturation value is of the order of magnitude of hours for an SOFC, depending on the H_2S concentration in the fuel (Papurello et al. 2016). In this dissertation, the H_2S poisoning has been considered only in the stationary SRU model for co-electrolysis; thus, the time-to-coverage has not been the object of investigation.

Once that is established that the available Ni surface is affected by the presence of H_2S in the fuel following a Temkin-like isotherm expression, it is necessary to determine the effect of the reduction of the Ni surface on the chemical and electrochemical performance of SOC fuel electrode. Rostrup-Nielsen et al. demonstrated that the reforming activity of an SOFC anode decreases with sulfur coverage to the third power (Rostrup-Nielsen et al. 2006). In this dissertation it is assumed that all the chemical reactions occurring in the fuel electrode of the SOC are affected by the surface coverage with this trend; thus the reaction rate of the *i-th* chemical reaction in the presence of sulfur coverage can be expressed as:

$$r^*_{react,i} = r_{react,i} \cdot (1 - \theta_S)^3 \tag{2.168}$$

The effect of the sulfur coverage on the electrochemical performance has been predicted in the literature by assuming a linear relation between the available TPB length and the fractional coverage of sulfur. In particular, Janardhanan and Monder (2014) expressed the exchange current density of electrochemical reaction as a linear function of the surface coverage:

$$i_0^* = i_0 \cdot (1 - \theta_S) \tag{2.169}$$

In this Thesis, the effect of sulfur poisoning on the chemical and electrochemical activity of the SOEC SRU operating in co-electrolysis has been investigated. The presence of H_2S is clearly undesired in the SOC, and if CO_2 from biogas is recycled to a P2G plant, a cleaning system must be installed to prevent the cell poisoning. Thus, the H_2S content is assumed to be zero in nominal operating conditions. However, if a contaminant breakthrough through the gas cleaning system occurs, it would be interesting to study the effect on the SOC and system efficiency, in order to assess its effect in terms of increased energy costs. An increase of the energy expenditure in the P2G system corresponds to an increase of the cost for the produced SNG; thus also an economic cost can be associated to the contaminant breakthrough and consequently an economic target for

contaminant mitigation systems can be derived. However; this analysis is out of the scope of this dissertation and it is not included in the Thesis, which is only focused on the energetic aspect. Nevertheless, it should be taken in mind that a negative impact on the energetic balance of the P2G system has a consequence on the economics of the system.

2.3 System components modeling

The design and simulation of P2G systems requires the modeling of core-technologies – SOCs and methanation – and plant components. The physically based approach to SOC modeling adopted in this dissertation has been thoroughly described in previous sections. The modeling of methanation and plant components has been addressed at system level. In the following sub-sections, the approaches adopted for modeling the methanation section of the P2G systems analyzed and other plants components (i.e., gas compressors and heat exchangers) are described.

2.3.1 Methanation Unit for SNG production

A mature methanation technology has been chosen in this Thesis, which is aimed at the investigation of SOC-based P2G systems with state-of-the art technologies. The fixed-bed methanation by TREMP^{TM} process was selected, as it proved to be effective for SNG production from H_2 and syngas (Giglio et al. 2015a and 2015b). This process has been investigated for stationary operation and compressed gas buffers have been considered in the P2G system for decoupling the hydrogen/syngas production and methane synthesis.

In general, the simulation of a chemical reactor can be a quite complex task if the modeling of all the physical phenomena involved is addressed. Homogeneous and heterogeneous reactions, fluid distribution and heat transfer between different phases are the main aspects that must be considered (Jakobsen 2008, Froment et al. 1990). The complexity of the modeling approach followed strictly depends on the aim of the research: if the objective is the reactor's design, the thermo-fluidic modeling is needed as the local conditions inside the reactor are the targets of the investigation, while if the study is focused at the integration of the reactor in a system, the reactor can be modeled as a 0D component with a black-box approach focusing only on mass and energy flows crossing the boundary of the box. The latter is the approach followed in this dissertation.

The TREMP^{TM} process is a technological solution for the catalytic conversion of syngas in SNG. The technology has been developed by Haldor Topsøe from 1970s, initially for the conversion of the syngas obtained from solid fuels (i.e., biomass and coal) gasification to methane (Jensen et al. 2011, Haldor-Topsoe 2009). The process is based on the catalytic hydrogenation of CO (1.10) and CO_2 (1.12) with nickel-based catalysts in adiabatic fixed-bed reactors. Both the methanation reactions are strongly exothermic and are favored by low

temperature and high pressure. When methanation takes place in an adiabatic reactor with appreciable rates, the temperature increase can be potentially very high. Jensen et al. (2011) report that if methane-poor syngas is introduced to an adiabatic methanation reactor at 300 °C, the reaction may reach temperatures above 900 °C. This is the main challenge for the process, which requires a high-temperature stable catalyst that can also provide a high activity at low temperatures. The strong exothermic reactions are handled by having a high recycle and thus diluting the gas entering the reactor in order to keep the temperature below 450 °C. The disadvantage of recycling effluent is the necessity of compression of high volumetric flows. In order to minimize compression costs it is beneficial to minimize the recirculation flow by either reducing the inlet temperature or increasing the outlet temperature, or by applying both. This can be achieved by developing reactors that can efficiently convert the syngas at low temperature and can withstand a high temperature increase. In the TREMP™ process, the recycle of the methanation is controlled to limit the outlet temperature to 700 °C, the maximum acceptable for ensuring catalyst stability; however the conversion is not enough to reach a sufficient product quality in a single step.

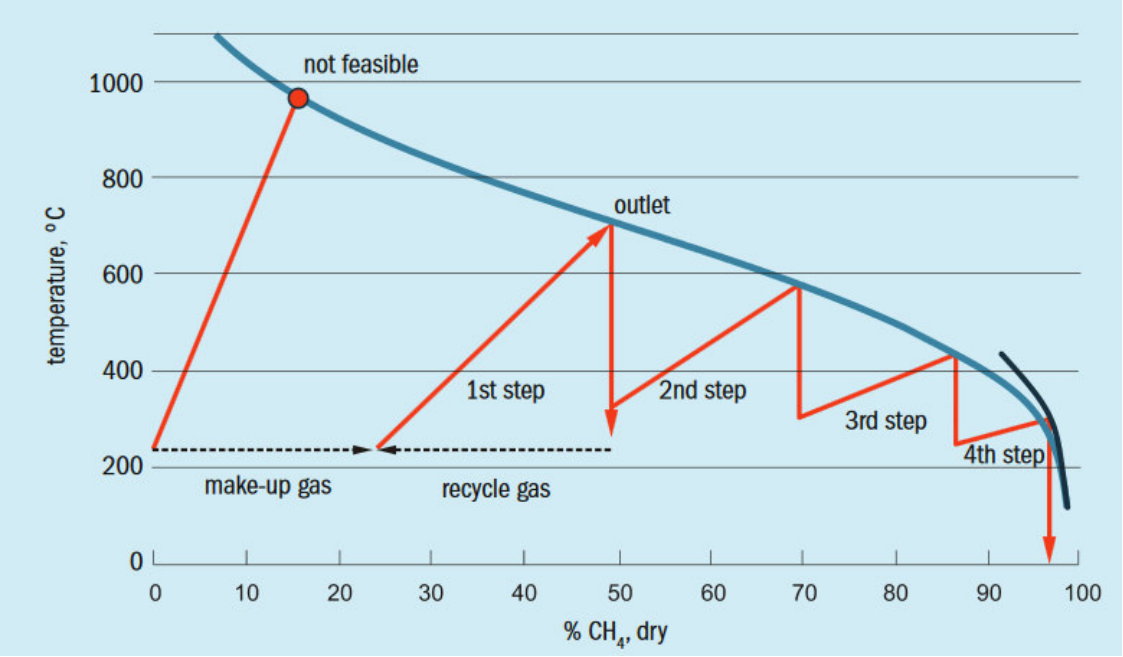

Figure 2.8 – Equilibrium curve for methanation. (Jensen et al. 2011)

As seen from the equilibrium curve depicted in *Figure 2.8*, in order to reach CH_4 levels of 95-98 %, it is necessary to use several methanation steps in adiabatic reactors operating at decreasing temperature levels and split by intermediate cooling.

Depending on required product quality, the final reactor of the TREMP™ process is operated at temperatures around 200-300 °C. The number of reactors is a result of an optimization based on requirements of product gas quality and heat recovery. Besides reducing the recycle, a high methanation temperature also offers the possibility to use the excess heat for high-pressure superheated steam production. This is the solution proposed by Haldor-Topsoe for an efficient heat recovery, as shown in *Figure 2.9*. The number of methanation reactors (usually three or more) depends on the operating conditions, such as pressure, as well as the SNG product specification. The process stream leaving the last methanation reactor is cooled, dried, compressed and eventually "corrected" to meet the final-user specifications, which are the pipeline ones if the SNG is injected in the NG grid.

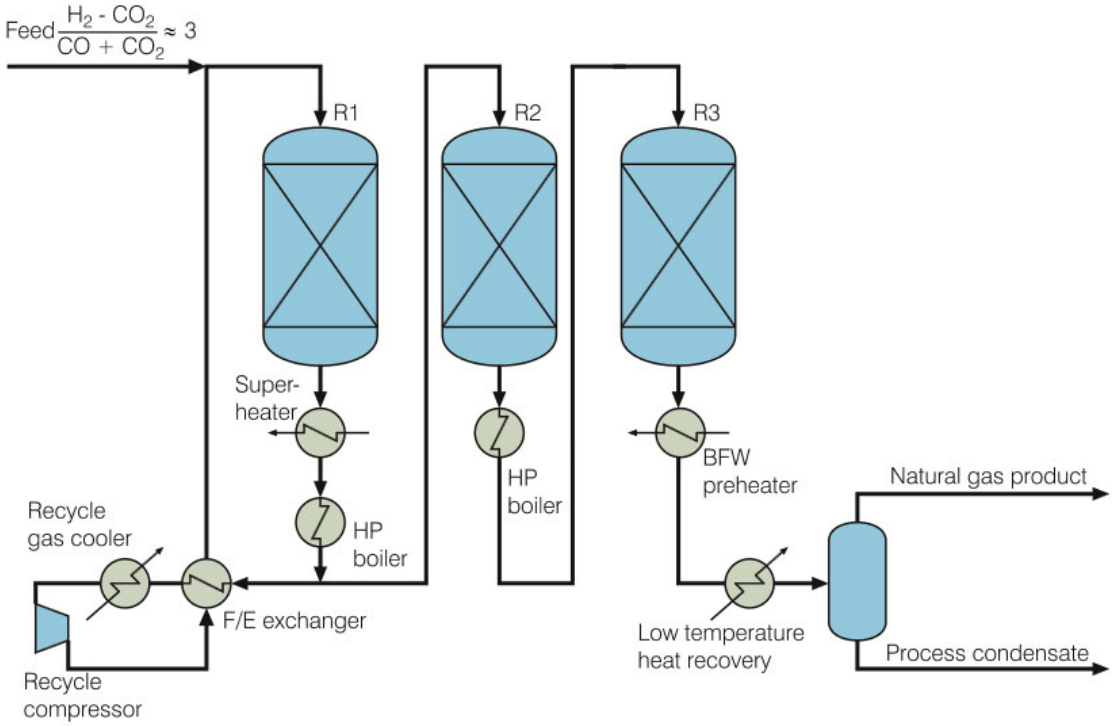

Figure 2.9 – Schematic of TREMP™ process. (Haldor-Topsoe 2009)

When addressing the modeling of the TREMP™ process from the system point of view, the main components to be included in the model are the reactors and the heat exchangers for the intermediate cooling. In the black-box approach, each component can be modeled by imposing the stationary equations of conservation of mass (or chemical species) and energy to its control volume:

$$\dot{n}_{\alpha,out} - \dot{n}_{\alpha,in} = \sum_{r} S_{\alpha.r} \tag{2.170}$$

$$\sum_{\alpha}\left(\dot{n}_{\alpha,out}\cdot\bar{h}_{\alpha}(T_{out})\right)-\sum_{\alpha}\left(\dot{n}_{\alpha,in}\cdot\bar{h}_{\alpha}(T_{in})\right)=\sum_{r}Q_{r}+\Phi+W \qquad (2.171)$$

where $\dot{n}_{\alpha}$ is the molar flow rate (mol s^{-1}) of the α species, $S_{\alpha.r}$ is the molar rate of production/consumption of the α species in the r-th reaction, Q_r is the heat flux generated in the r-th reaction (see equation (2.116)), Φ is the heat flux exchanged across the boundary of the component and W is the work power. It is straightforward that in the adiabatic reactors the Φ term is null and that in compressors and heat exchangers the source terms $S_{\alpha.r}$ and Q_r are not present.

When modeling chemical reactors, the determination of the reaction rates for the prediction of species concentrations in the outlet gas stream and heat sinks/sources can be approached in two different ways. One is based on the kinetics of the reactions involved and the other is based on thermodynamic equilibrium approach. Equilibrium models are widely employed, even if they cannot be used for reactor design because do not allow the prediction of temperature and partial pressure profiles, that can be predicted only by modeling the kinetics of reactions. The equilibrium approach is particularly suited for 0D models, which only require the calculation of the composition at the reactor's outlet. The thermodynamic equilibrium can be calculated either by minimization of Gibbs free energy of the system or by considering the reactions involved and their equilibrium constants. The advantage of the first method is that no chemical reaction needs to be known to find the solution. In this Thesis, the equilibrium approach based Gibbs free energy minimization has been applied to model the chemical reactions by using a commercial software for the calculation (Aspen Plus), which uses iterative methods for the solution of the minimization problem. More details on the model implemented for the methanation are given in *Chapter 6*.

Together with conservation equations and reactions modeling, constraints given by the technology must be imposed to the components. The constraints involve: 1) the inlet composition of the feed gas required at the inlet of the reactors' cascade to achieve high methane content in the produced SNG, 2) the inlet temperature of the reactors, which must be low to ensure favorable process thermodynamics, but enough high to allow appreciable kinetics and to avoid catalyst deactivation problems; 3) the outlet temperature of the reactors, which must be limited to avoid catalyst sintering, a process that lead to catalyst deactivation.

The first constraint is determined by methanation reactions stoichiometry. In order to achieve a product with as high methane content as possible it is important that the feed gas for the

methanation section has a composition with the correct ratio between the reactants, i.e. CO, H_2 and CO_2. The predominant methanation reaction is normally the hydrogenation of CO, and from the reaction equation it is seen that the stoichiometric ratio between H_2 and CO is 3. However, in order to take into account also the content of CO_2 in the feed gas for the methanation, the "feed gas module" has been developed (Jensen et al. 2011):

$$FEED = \frac{y_{H_2} - y_{CO_2}}{y_{CO} + y_{CO_2}} = 3 \tag{2.172}$$

When the FEED constraint is applied to SNG production from a mixture of CO_2 and H_2, the H_2/ CO_2 ratio derived from the constraint is 4. Thus, the FEED constraint imposes the ratio the produced hydrogen in SOEC and the CO_2 needed for methanation. In the case of methanation of a syngas mixtures obtained by co-electrolysis, the CO_2/H_2 ratio is not automatically fixed, but depends on the conditions of the co-electrolysis process which determine the composition of the gas mixture at the SOEC outlet.

The temperature constraints are strictly related to the materials employed in the process. For the TREMP™ process, the minimum inlet reactor temperature assumed in this Thesis is 220 °C and the maximum temperature allowed at the reactor's outlet is 700 °C.

2.3.2 Modeling BoP components

The Balance of Plant (BoP) of a P2G system includes components such as heat exchangers, compressors, pumps, gas storage systems and condensers. The modeling of these components can be performed at different levels of complexity. In this research work, the components have been modeled with thermodynamic equations including energy and entropy balances. This approach allows to calculate the energy fluxes required by BoP components as function of the thermodynamic conditions of streams at the inlet/outlet of the components, and thus to derive a global efficiency of the BoP as function of the operating conditions of the SOC in the various configurations investigated.

Gas compressors have been modeled as multistage intercooled machines. The ideal power required for the isoentropic compression of a gas stream was calculated as:

$$W_{comp,id} = \dot{m}_\alpha \cdot \frac{R}{M_\alpha} \cdot T_{in} \cdot \frac{\gamma}{\gamma - 1} \cdot \left[\left(\beta_{opt} \right)^{\frac{(\gamma-1)}{\gamma}} - 1 \right] \tag{2.173}$$

where $\dot{m}_\alpha$ is the mass flow rate (kg/s) of the gas, R is ideal gas constant, M_α is the molar mass of the gas, T_{in} (K) is the inlet temperature of the gas in the compressor, γ is the ratio of specific heat and β_{opt} is the optimal compression ratio of the single stage, which was calculated in equation as (Cornetti and Millo 2015):

$$\beta_{opt} = \left(\frac{p_{out}}{p_{in}}\right)^{1/N_S} \tag{2.174}$$

where p_{out} is the outlet pressure of compressed hydrogen and N_S is the number of compression stages. A two-staged compression was chosen in this Thesis for all the compressors. After each compression stage, it was assumed that gas was cooled down to the initial temperature and the intercooling heat was lost to the ambient. The compression power is thus calculated by assuming a fixed efficiency:

$$W_{comp} = \frac{W_{comp,id} \cdot N_S}{\eta_{comp}} \tag{2.175}$$

where η_{comp} is the efficiency of the compressor and includes both the isentropic and electric efficiency of the device. In this study, the value of η_{comp} was taken as 0.65, according to literature data (Cornetti and Millo 2015).

The compression of liquid water has been modeled as an isoentropic transformation of an incompressible fluid. Thus, the work required for the compression is:

$$W_{pump,H_2O} = \dot{m}_{H_2O} \cdot \frac{v_{H_2O,in}(p_{out} - p_{in})}{\eta_{pump}} \tag{2.176}$$

where $v_{H_2O,in}$is the specific volume of water (m^3/kg) at the inlet pump conditions. An efficiency value of 0.7 has been assumed, including both the isentropic and electric efficiency of the pump.

The storage systems considered in this Thesis were pressurized tanks at ambient temperature, while the option of cryogenic storage has not been explored. It was assumed that the storage can ideally maintain its nominal pressure without losses, thus the gas storage stage does not involve the consumption of energy. A storage pressure of 30 bars has been assumed in all the P2G configurations investigated, which is the pressure required for the operation of the methanation reactors. This storage pressure has been assumed also in the investigation of the P2P option, in order to maintain comparable conditions with the other P2G configurations.

The heat exchangers have been assumed as isobaric components perfectly insulated from the external ambient, as the methanation reactors. Particular attention has been paid to the modeling of the heat exchangers network that realizes the thermal integration of SOC streams to minimize the external thermal requirements. In order to minimize the external heat required, besides imposing the energy conservation to the heat exchangers, the *Pinch Analysis* methodology has been applied to model the heat exchangers network and calculate the heat fluxes that can be effectively recovered from internal streams. Pinch Analysis is a technique that allows to calculate the least amount of hot and cold heat fluxes that must be provided/removed from a process composed by a set of energy flows without knowing a priori the architecture of the heat exchanger network (Kemp 2011). An overview of the methodology is given in the next paragraph.

Modeling Heat Exchangers Networks: the Pinch Analysis

Pinch Analysis is used to model energy systems characterized by a heat exchangers network. In these systems there are constraints which have to be satisfied, given by the first and second principle of thermodynamics, which limit the temperature of involved fluids during the process to minimum/maximum values allowed by the coupling of the streams. In the pinch analysis, a "target function" must be chosen for network design, e.g. minimum of external heat requirement or minimum of heat exchange area. In this dissertation the target will be the minimization of heat requirement, as the analysis is focused on the energetic aspects of P2G systems, rather on the economics.

Solving a pinch analysis problem requires to know the properties of the streams involved (i.e., specific heat, latent heat of condensation/vaporization), the thermodynamic conditions at which they are available (i.e., temperature and pressure), their mass flow rates and the final temperatures that streams must reach. In addition to final fluids temperatures, another constraint that must be imposed in the analysis is the minimum temperature difference (ΔT_{min}) between hot fluids (i.e. those which have to be cooled down) and cold fluids (i.e. those which have to be heated up). The literature suggests that typical values of ΔT_{min} are included between 20 and 40 °C (Linnhoff 1998).

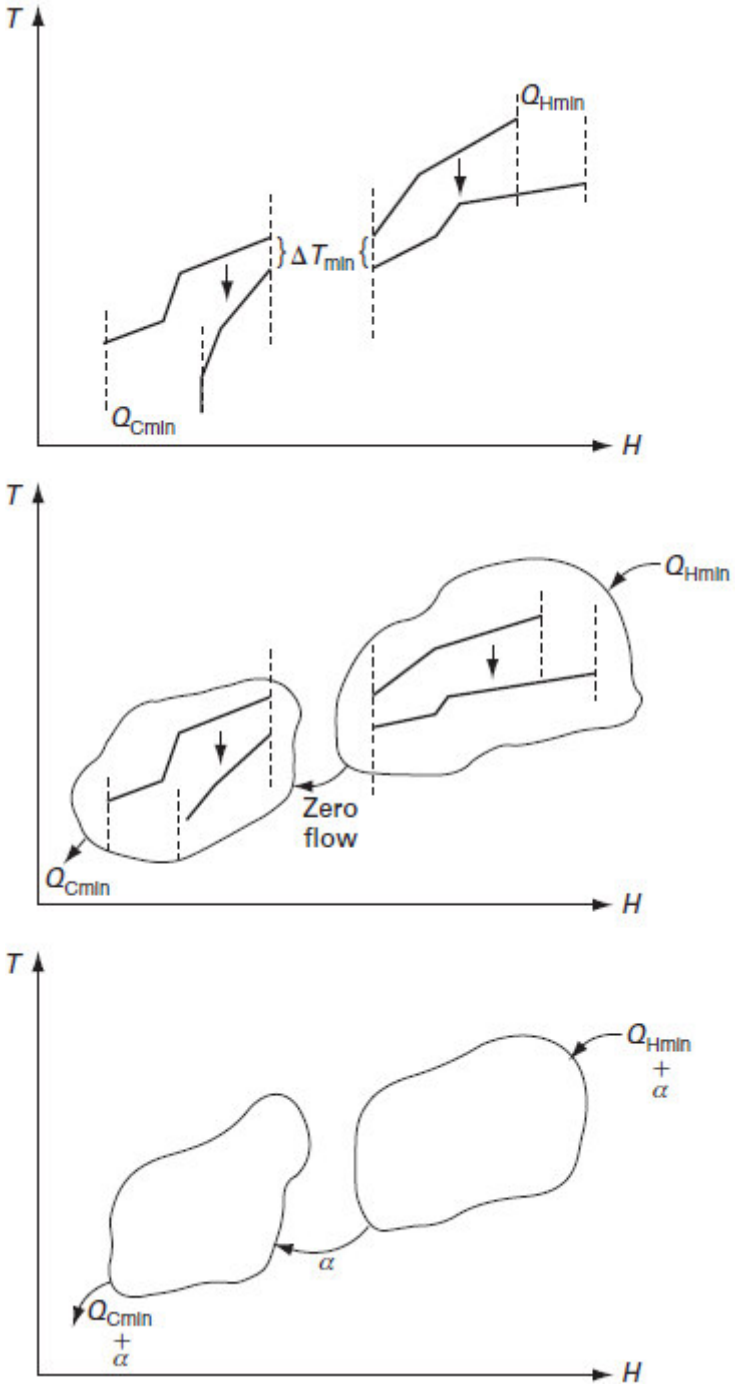

Figure 2.10 – Schematic explanation of the pinch point concept. (Kemp 2011)

The Pinch point of the analyzed system is the point of the entire system where the minimum value of temperature difference between a hot and a cold fluid is reached. The pinch point allows representing the system in two separated parts:

- Above pinch point: system requires a heat input and is therefore a net heat sink
- Below pinch point: system rejects heat and so is a net heat source

Figure 2.10 shows the temperature evolution of cumulated cold and hot flows highlighting the pinch point and the two parts of the system. In the "above pinch" region (i.e., on the right in the figure), the hot flows transfers all its heat to cold flows and only an external heat source is needed (Q_{Hmin}); conversely in the "below pinch" region, cooling only is required (Q_{Cmin}), as the cold flows are heated up only by the hot flows. For both the two parts, the thermal balance is obtained without heat exchange through the pinch point. When the heat exchanger network transfers an amount of heat α across the pinch, the heat balance of the regions requires that an additional α flow is provided to the above region and removed from the below region. Thus, if a heat flow α crosses the pinch, the hot utility must be increased by the same amount α to restore the heat balance and the cold utility requirement also increases by α. In conclusion, the consequence of a "cross-pinch heat transfer" is that both the hot and cold utility will increase by the cross-pinch duty. Similarly external heating below the pinch increases the overall hot and cold utility requirement by the amount of heat provided below the pinch. In the same way, external cooling above the pinch point increases both the hot and cold utility requirements.

To summarize, the understanding of the pinch gives three rules that must be followed in order to achieve the minimum energy targets for a process:

- Heat must not be transferred across the pinch
- External cooling above the pinch must be avoided
- External heating below the pinch must be avoided

If a heat exchanger network is requiring more energy from external sources/sinks than its thermodynamic minimum, it must be due to the violation of one or more of the three rules. The algebraic procedure for the calculation of the minimum energy requirements, which correspond to a perfectly designed heat exchanger network, is given in the next paragraphs.

The procedure starts with definition of temperature intervals. The bounds of these intervals are "fictitious temperatures" (T^*) defined as follows: inlet and outlet temperature of each cold fluid are increased of $½\Delta T_{min}$; inlet and outlet temperature of each hot fluid are decreased of the same value. Once the T^* are defined, they are sorted defining a certain number of intervals. For each interval, the global heat flux required is calculated:

$$\phi_i = (T_i^* - T_{i+1}^*) \cdot \left(\sum_j \dot{m}_{cj} \cdot c_{cj} - \sum_j \dot{m}_{hj} \cdot c_{hj} \right) \tag{2.177}$$

where the subscript "c" and "h" indicate the cold and hot flows, $\dot{m}$ is the mass flow and c is the specific heat. A positive ϕ_i corresponds to a deficit of thermal flux in the corresponding interval (otherwise there's a surplus). The heat fluxes related to phase change are exchanged at constant temperature, thus they are assigned to a specific temperature and not to an interval. The next step after assigning the heat flows to the related temperatures, is the definition of a cumulate of ϕ_i. The cumulate at a certain temperature is the sum of the heat flux between that temperature and the previous temperature level, the latent heat at that temperature and the cumulate the previous temperature. The calculation of the cumulate starts from the assumption that external heat input at first interval (i.e., the higher temperature level) is 0. Negative values of the cumulate are not acceptable, then the external heat is increased until each value of the cumulate will be positive or zero. The lower bound (in terms of T^*) of the temperature interval with cumulate equal to 0 is the pinch point (T_{pp}^*). Consequently, the pinch point temperature for hot fluids is $T_{pp,h} = T_{pp}^* + \frac{1}{2}\Delta T_{min}$, and for cold fluids is $T_{pp,c} = T_{pp}^* - \frac{1}{2}\Delta T_{min}$.

From the cumulate of the heat flows it is possible to individuate the minimum heat fluxes that must be provided and removed to the system to fulfill the thermodynamic constraints. The pinch analysis can be further extended by designing the heat exchanger network closer the ideal one that allows the minimum energy requirements. This was not the goal of this Thesis, in which the Pinch Analysis has been adopted for the evaluation of the minimum thermal energy requirements of the BoP of the SOC with the purpose to evaluate the BoP efficiency.

Chapter 3

Numerical SOC models – cell and SRU models

The study of SOC-based P2G (and P2P) systems requires to develop reliable models for the prediction of the thermo-electrical performance of an SOC stack operating in relevant conditions for a P2G system. The aim of the models is to simulate the current-voltage characteristic of the SOC cell/stack – and thus the consumed/produced power – and evaluate the conditions of the outlet streams (temperature and compositions) with variable inlet conditions (i.e., flow rates, compositions, temperature) with the purpose to individuate the optimal operating conditions to maximize the system efficiency, which strictly depends on the conditions of the streams entering/exiting the SOC. Moreover, the numerical simulation of temperature profile in the SOC allows to calculate the thermal gradients within the cell, in order to verify if the thermal stresses are compatible with the constraints imposed by state-of-the-art materials. The thermal analysis thus allows to identify acceptable ranges for the operating conditions. The verification of thermal constraints will be used in this Thesis to assess the feasible operating points for the SOCs operating integrated in P2P and P2G systems.

The modeling work has been structured on different levels of detail by developing different models depending on the objective of the simulations. First, a combined 1D/2D thermo-electrochemical model of a circular SOC has been developed in Matlab®. The model describes the electrochemical processes and mass transport of gaseous species at the electrodes and simulates the heat transfer within electrodes and electrolyte. The electrochemical kinetics are evaluated by semi-empirical relations which are used to calibrate the model on experimental data collected from state-of-the-art SOCs tested with H_2/H_2O and CO/CO_2 fuel mixtures. Model and experiments focused separately on carbon-based and hydrogen-based mixtures in order to highlight the electrode kinetics without overlapping the effects of the chemical reactions that occur with mixed H/C mixtures. The model is finally validated on current-voltage curves of the commercial cells tested in reversible operation. The detailed description of the model is given in this Chapter, while the model validation is presented in *Chapter 4* together with the experimental investigation of rSOC cells. The developed model and its validation have been published in 2015 (Ferrero et al. 2015).

A second cell model has been developed in Comsol Multiphysics® (version 5.2, license n. 13074300) from the previous one by extending the cell description to a full 2D domain which also includes gas channels and stack interconnects. The model applies the electrochemical kinetics validated in the single-cell model and also includes chemical reactions described with global rate expressions assumed from the literature. A square-cell geometry has been simulated for a fuel electrode-supported SOC. This model was employed in the analysis of SOC-based P2P and P2G systems. When applied to the study of the co-electrolysis of H_2O/CO_2, the model also included equations for the carbon deposition and sulfur poisoning modeling. In particular, the co-electrolysis model was also applied to a case-study for assessing the effect of H_2S traces in CO_2 on SRU performance and system efficiency. The description of the model is given in this Chapter. Results of simulations for P2P and P2G application are discussed in *Chapter 5* and *6*. The 2D model was also used as intermediate step for the development of a 3D SRU model.

The final step has been the extension of the 2D model to 3D for the transient analysis of the SRU. The full 3D model has been applied to the dynamic study of an ESC operating in P2P applications with H_2/H_2O mixtures, focusing on the investigation of thermal transients when time-dependent loads are applied to the SOC. Some preliminary results of this study have been presented at the 11th EFCF Conference in 2014 (Ferrero et al. 2014).

3.1 Single cell rSOC model

An integrated thermo-electrochemical model for the simulation of i-V characteristics of a reversible SOC has been developed and calibrated on experimental data collected on commercial circular cells. The model of a circular cell is composed by a 1D electrochemical stationary module and a 2D transient thermal module, both implemented in Matlab®. The first module describes the electrochemical processes and mass transport of gaseous species at the electrodes, while the second simulates the heat transfer within electrodes and electrolyte in the presence of distributed heat sinks/sources produced by electrochemical reactions and polarization overpotentials.

In the following sections, the model geometry and the algorithm structure is presented. The calibration and validation of the model on current-voltage curves of commercial cells tested with H_2/H_2O and CO/CO_2 mixtures, and discussion the simulated evolutions of overpotentials and temperature within the cell are given in *Chapter 4*.

3.1.1 Model geometry

A schematic of the cell model is illustrated in *Figure 3.1*. The model is implemented in Matlab® and is divided in two connected modules: the electrochemical module and the thermal one.

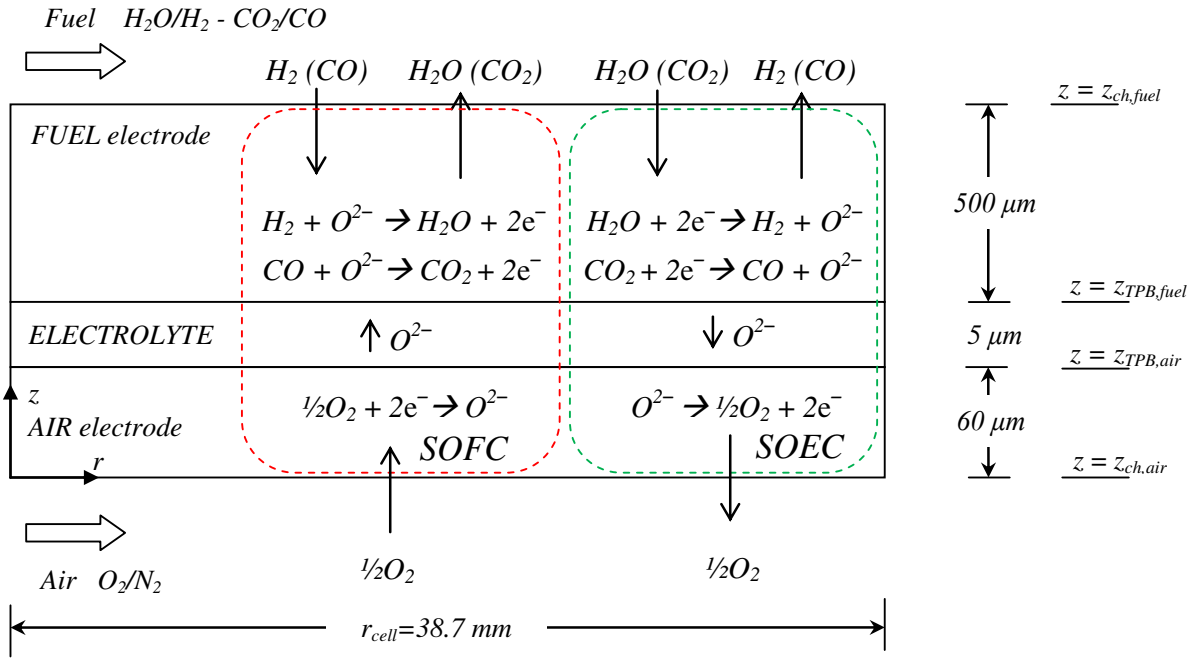

Figure 3.1 – Schematic of the simulated cell.

A one dimensional multi-layer approach has been adopted for the electrochemical module; while a two dimensional description has been chosen for thermal module. The domain of the cell shown in *Fig. 3.1* is contained in the (r,z) plane. The circular symmetry allows to have a description of the physics independent of the angular coordinate.

In the proposed model gases are distributed according to a parallel-flow arrangement, flowing in both the electrodes from the center of the cell to the rim (to accurately reproduce what actually takes place in the test-rig where experiments were performed). Reacting chemical species are allowed to diffuse in the electrodes in z direction from the electrode surface to the three phase boundary (TPB), or from the TPB to the electrode surface. The TPB is assumed to be located at the electrode/electrolyte interfaces on which the electrochemical reactions take place. Several studies have estimated that the TPB region has a limited extension of 5-20 μm from the electrolyte surface (Cai et al. 2011, Zhu and Kee 2008); thus, in electrode-supported cell models the TPB is frequently assumed as a layer of negligible thickness at the electrolyte/interface (Ni 2009, Laurencin et al.2011, Costamagna et al. 2004, Camprubì 2011).

The equations of the electrochemical module are solved in the r direction and integrated along the z axis (the diffusive equations, as explained in *Section 3.2.1*), so that the results of the electrochemical module are given on four layers: the surface of the electrodes (channel solutions, subscript 'ch') and at the electrode/electrolyte interfaces (subscript 'TPB').

In the thermal module, the temperature field is calculated in the (r,z) plane; a mean temperature distribution is derived by averaging the temperature field in the z direction, in order to have a temperature vector that depends only of the radial direction for the implementation in the electrochemical module. The results of the thermal simulations (see *Section 4.4*) show that the temperature difference between anode and cathode surfaces is negligible, thus the averaged temperature provides an acceptable approximation.

The electrochemical and thermal modules are coupled through: 1) the heat source/sinks terms calculated in the electrochemical module and given as input of the thermal; 2) the averaged temperature field calculated in the thermal module and used as input of the electrochemical. The solution of the whole model is iterative: a first solution of the electrochemical module is obtained using the initial distribution of the temperature in the cell; then, sources and sinks identified in the first step are used in the thermal module to calculate the temperature field. The process is repeated until convergence on the temperature distribution is reached.

The model does not include gas channels, which are taken into account only as part of the thermal boundary conditions (see *Section 3.1.3*).

3.1.2 Electrochemical module

The electrochemical module simulates the current-voltage characteristic of the cell in both SOFC and SOEC operation taking into account the electrochemical processes occurring at the electrodes together with the mass transport of gaseous species. The main assumptions of the module are listed below:

- Instantaneous electrochemical reactions, i.e. the time constants of the electrochemical reactions are considered negligible when compared to the thermal ones (Huang et al. 2011).
- Pressure drops within the volume of the electrodes are not taken into account in the mass transport equations, because the viscous gas flows driven by pressure gradients are negligible compared to the diffusive gas flows in porous electrodes (Laurencin et al. 2011, Yang and Virkar 2003).
- Ideal gas approximation is assumed, because gases are in a high temperature environment.
- Electrochemical reactions at the electrode/electrolyte interface (see *Section 3.1.1*).
- Electrical potential is considered constant on the surface of the electrodes, since they are good electrical conductors.
- Diffusive fluxes are assumed only in the z direction of the porous electrodes in the implementation of the Dusty Gas Model, as frequently reported in the modeling literature of solid oxide cells (Laurencin et al. 2011, Zhu et al. 2005). The concentration gradients in the r direction can be neglected because the thickness of the electrode is significantly smaller compared to its length.
- Electric current flow is considered only in the z direction, as the cell is electrically insulated on the border and the electrical potential is assumed constant on the electrode surface.

Production and consumption of chemical species within the electrodes is related to two different phenomena: 1) electrochemical reactions, the CO/CO_2 and H_2/H_2O oxido-reduction reactions were considered in the model; 2) the back-diffusion, i.e., the direct combustion of a fraction of H_2 (or CO) at the unsealed cell border produces steam (or CO_2) that diffuses from the rim to the internal of the cell. The model accounts for this phenomenon – present in both SOFC

and SOEC operation – in order to reproduce the conditions of the experimental setup in which the calibration and validation curves were obtained.

Local mass balances of the chemical species related to the electrochemical reactions are calculated as functions of the local current density, according to the Faraday's law:

$$\dot{N}_{\alpha}(r) = \nu \frac{i(r)}{n_{el}F} \tag{3.1}$$

$$\frac{d\dot{n}_{\alpha,el}(r)}{2\pi r\, dr} = \dot{N}_{\alpha}(r) \tag{3.2}$$

where the areic molar flow $\dot{N}_{\alpha}(r)$ of the species α is due to the electrochemical reaction, $\dot{n}_{\alpha,el}(r)$ is the molar flow rate of the chemical specie α on the surface of the electrode in the *r* direction, n_{el} is the number of electrons transferred per ion in the reaction and ν is the stoichiometric coefficient ($\nu = -1$ consumed species, $\nu = +1$ produced species). The molar flow rates related to back-diffusion are derived from the solution of the polarization equation of the model (see *Section 3.2.2*) at open circuit. The model estimates the equilibrium potential by using the Nernst equation and compares it with the experimental open circuit voltage (OCV); the difference is compensated by the generation of a H_2O (or CO_2) flow rate, i.e. $\dot{n}_{brn}$, due to the burning of H_2 (or CO), which is used to correct the molar balances on the surface of the fuel electrode. The corrected molar flow rates of the chemical species are:

$$\dot{n}_{H_2(CO)}(r) = \dot{n}_{H_2(CO)el}(r) - \dot{n}_{brn}(r) \tag{3.3}$$

$$\dot{n}_{H_2O(CO_2)}(r) = \dot{n}_{H_2O(CO_2)el}(r) + \dot{n}_{brn}(r) \tag{3.4}$$

The oxygen molar flow rate on the surface of the air electrode is only function of the electrochemical reactions, since there is no back-diffusion at the air electrode. The molar fractions of the species on the surface of the electrodes have been evaluated from the corrected molar flow rates:

$$y_{\alpha(fuel)}(r) = \frac{\dot{n}_{\alpha(fuel)}(r)}{\dot{n}_{H_2(CO)}(r) + \dot{n}_{H_2O(CO2)}(r)} \tag{3.5}$$

$$y_{\alpha(air)}(r) = \frac{\dot{n}_{\alpha(air)}(r)}{\dot{n}_{O_2}(r) + \dot{n}_{N_2}(r)} \tag{3.6}$$

The mass transport through the porous electrode (z direction) has been modeled using a simplified Dusty Gas Model in which pressure drops within electrode are neglected:

$$-\frac{p}{RT}\left(\frac{dy_\alpha}{dz}\right)=\frac{\dot{N}_\alpha}{D_{K,\alpha}^{eff}}+\sum_{\alpha\neq\beta}\frac{y_\beta\dot{N}_\alpha-y_\alpha\dot{N}_\beta}{D_{\alpha,\beta}^{eff}} \tag{3.7}$$

where $\dot{N}_\alpha$ is evaluated by the Faraday's law (see Eq. (3.1)), $D_{\alpha,\beta}^{eff}$ is the effective molecular diffusion coefficient for a binary mixture of gases (see equation 2.71 *Chapter 2*) and $D_{K,\alpha}^{eff}$ is the effective Knudsen diffusion coefficient (see equation 2.85 *Chapter 2*), calculated by assuming a mean pore radius of 0.5 μm, in agreement with typical values of the literature (Ni et al. 2006a, Chan et al. 2001).

The integration of Eq. (3.7) along the z direction has been performed following the methodology described by Laurencin et al. (2011), and the obtained molar fractions at the TPB layers are:

$$y_{O_2TPB}(r)=\frac{1}{\delta_{O_2}}+\left(y_{O_2}(r)-\frac{1}{\delta_{O_2}}\right)\cdot exp\left(-\frac{RT\dot{N}_{O_2}(r)l_{air}}{pD_{O_2N_2}^{eff}}\right) \tag{3.8}$$

$$y_{H_2(CO)TPB}(r)=y_{H_2(CO)}(r)+\frac{RT}{p}\dot{N}_{H_2}(r)\left(\frac{1}{D_{K,H_2(CO)}^{eff}}+\frac{1}{D_{H_2(CO),H_2O(CO_2)}^{eff}}\right)l_{fuel} \tag{3.9}$$

$$y_{H_2O(CO_2)TPB}(r)=y_{H_2O(CO_2)}(r)+\frac{RT}{p}\dot{N}_{H_2O}(r)\left(\frac{1}{D_{K,H_2O(CO_2)}^{eff}}+\frac{1}{D_{H_2O(CO_2),H_2(CO)}^{eff}}\right)l_{fuel} \tag{3.10}$$

where δ_{O_2} is expressed as:

$$\delta_{O_2}=\left(\frac{D_{K,O_2}^{eff}}{D_{K,O_2}^{eff}+D_{O_2,N_2}^{eff}}\right) \tag{3.11}$$

In the previous equations, the effective diffusivities are calculated using equation (2.89) (see *Chapter 2*) by assuming a porosity $\varepsilon = 0.3$ and a tortuosity $\tau = 3$ according to what reported in the literature (Lanzini et al. 2009, Menon et al. 2014) for fuel electrode supported cells similar to those tested in this work.

The electrochemical module calculates the evolution of molar flows along the radius of the cell by solving the equation of the polarization curve.

$$V_{cell} = V_{rev}(r) + \gamma\left(\eta_{act,an}(r) + \eta_{act,cat}(r) + \eta_{Ohm}(r) + \eta_{con,an}(r) + \eta_{con,cat}(r)\right) \quad (3.12)$$

In Eq. (3.12), $V_{rev}(r)$ is the reversible voltage, $\eta_{act,an}(r)$ and $\eta_{act,cat}(r)$ are the activation overpotentials of anode and cathode, $\eta_{Ohm}(r)$ is the Ohmic overpotential of the cell, $\eta_{con,an}(r)$ and $\eta_{con,cat}(r)$ are the conversion and diffusion overpotentials and γ is the reaction coefficient (γ = +1 in SOEC mode and γ = -1 in SOFC mode). The voltage of the cell, i.e. V_{cell}, is fixed according to the values measured during experiments (see *Chapter 4*). The reversible voltage is described by Nernst equation:

$$V_{rev}(r) = \frac{RT}{2F} ln\left[\left(y_{O_2}(r, i=0)\right)^{0.5}\right] - \left[\frac{\Delta\bar{g}(T,p_0)}{2F} + \frac{RT}{2F} ln\left[\left(\frac{y_{H_2O}(r,i=0)}{y_{H_2}(r,i=0)}\right)\right]\right] \quad (3.13)$$

with the first term representing the equilibrium voltage of the air electrode and the second that of the fuel electrode. The variation of the molar Gibbs free energy of the oxidation reaction, i.e. $\Delta\bar{g}(T,p_0)$ in the Nernst equation, that has a negative value, is evaluated using interpolated expressions obtained from the JANAF tables (Chase et al. 1998). It is worth noting that the chemical species in the Nernst equation (3.13) are included in terms of molar concentrations because of the constant ambient pressure assumption. This assumption allows to simplify the general form given in equations 2.121 and 2.122 (see *Chapter 2*) – where the chemical activity is expressed as the ratio of the partial pressures of the gases over the standard pressure – to the expression of equation (3.13).

The Ohmic overpotential is expressed as:

$$\eta_{Ohm}(r) = R_{Ohm} \cdot i(r) \quad (3.14)$$

The term R_{Ohm} includes all the Ohmic resistance terms within the cell: the ionic resistance of electrolyte, barrier layer and ion-conductive phases of the electrodes, the electronic resistance of electron-conductive phases of both electrodes and the contact resistances between electrodes and corresponding current collecting meshes. The R_{Ohm} has been estimated from measured impedance spectra (see *Table 4.1* in *Chapter 4*).

Butler-Volmer equation is applied to determine electrode activation overpotential.

$$i(r) = i_{0,electrode}\left[e^{\alpha_1(F/RT)\eta_{act}} - e^{-\alpha_2(F/RT)\eta_{act}}\right] \quad (3.15)$$

where $i_{0,electrode}$ is the exchange current density of the electrode, and α_1 and α_2 are the charge transfer coefficients, which are assumed equal as commonly simplified in many fuel cells models (Noren and Hoffman 2005). The Butler-Volmer equation can be expressed in explicit form for both the electrodes:

$$\eta_{act,air}(r) = \frac{RT}{\alpha_{air}F} sinh^{-1}\left(\frac{i(r)}{2i_{0,air}}\right) \tag{3.16}$$

$$\eta_{act,fuel}(r) = \frac{RT}{\alpha_{fuel}F} sinh^{-1}\left(\frac{i(r)}{2i_{0,fuel}}\right) \tag{3.17}$$

The values of the charge transfer coefficients of Ni/YSZ in SOFC and SOEC operation with H_2/H_2O mixtures were extrapolated from the study of Marina et al. (2007) (see *Table 3.1*).

Table 3.1 – Activation parameters of the electrodes and properties of cell materials

	Charge transfer coefficient			**Activation energy (kJ mol^{-1})**		
Fuel electrode	0.4[a] 1.15[b] (Marina et al. 2007)			120[c] (Suwanwarangkul et al. 2006)		
Air electrode	1[c] (Laurencin et al. 2011)			130[c] (Suwanwarangkul et al. 2006)		
	Layer thickness (µm)	**Thermal conductivity k (W m^{-1} K^{-1})**	**Density ρ (kg m^{-3})**	**Specific heat c_p (J kg^{-1} K^{-1})**	**Porosity ε**	**Tortuosity τ**
Ni/YSZ	500	11 (Barzi et al. 2011)	4760 (Barzi et al. 2011)	377 (Barzi et al. 2011)	30%	3
YSZ	5	2.7 (Wang H. et al. 2011)	5900 (Wang H. et al. 2011)	600 (Wang H. et al. 2011)	-	-
YSZ/LSM-LSCF	60	4 (Petruzzi et al. 2003)	4640 (Barzi et al. 2011)	377 (Barzi et al. 2011)	30%	3

[a] SOEC mode [b] SOFC mode [c] Both fuel cell and electrolysis operation

The charge transfer coefficients of the fuel electrode operating with CO/CO_2 mixtures were assumed to be the same of the H_2/H_2O mixtures. The value of the charge transfer coefficient for the air electrode was taken from Laurencin et al. (2011). The exchange current densities were estimated using semi-empirical equations that contain a power law dependency for the concentrations of reactants and products and an Arrhenius-type temperature dependency (Costamagna et al. 2004):

$$i_{o,air} = \gamma_{air}\left(y_{O_2,TPB}(r)\right)^{0.25} \cdot exp\left(\frac{-E_{act,air}}{RT}\right) \tag{3.18}$$

$$i_{o,fuel} = \gamma_{fuel}\left(y_{H_2(CO),TPB}(r)\right)\left(y_{H_2O(CO_2),TPB}(r)\right) \cdot exp\left(\frac{-E_{act,fuel}}{RT}\right) \tag{3.19}$$

where the pre-exponential kinetic parameters γ_{air} and γ_{fuel} are derived from the calibration of the model by fitting the simulated polarization curves to the experimental i-V characteristics (see *Chapter 4*). In general, the exchange current density depends on the ratio between the partial pressure of the species involved in the electrochemical reaction and the reference pressure, as previously shown in equation (2.133) (see *Chapter2*). However, when the electrode is operating at constant ambient pressure, as assumed in this model, the ratios between partial pressures of the chemical species and the reference pressure (i.e., the standard pressure) is equivalent to their molar concentration. Therefore, equations (3.18) and (3.19)directly include molar concentrations. The pre-exponential kinetic parameters are assumed to be independent of temperature, as typically found in the literature (Campanari and Iora 2004, Wang et al. 2007, Sanchez et al. 2006). The values of the activation energies $E_{act,air}$ and $E_{act,fuel}$ were chosen from the literature (see *Table 3.1*) and assumed equal for both SOEC and SOFC. It is worth noting that when evaluating activation overpotentials, activation energies and charge transfer coefficients were not varied among different mixture types; hence, only the kinetic parameter of the fuel electrode accounts for the different activation behavior of the cell operating with H_2/H_2O or CO/CO_2 mixtures.

The compositions of the gas mixtures on the reaction layers are different from those at the equilibrium conditions, due to gas conversion and diffusion phenomena. The reversible voltage calculated in Eq. (3.13) does not take into account such phenomena, so it is necessary to introduce the conversion and diffusion overpotentials:

$$\eta_{con,fuel}(r) = \frac{RT}{2F}\left\{\ln\left[\left(\frac{y_{H_2O(CO_2)}(r) \times y_{H_2(CO),TPB}(r)}{y_{H_2(CO)}(r) \times y_{H_2O(CO_2),TPB}(r)}\right)^{\gamma}\right] + \ln\left[\left(\frac{y_{H_2O(CO_2)}(r,i=0) \times y_{H_2(CO)}(r)}{y_{H_2(CO)}(r,i=0) \times y_{H_2O(CO_2)}(r)}\right)^{\gamma}\right]\right\} \tag{3.20}$$

$$\eta_{con,air}(r) = \frac{RT}{4F}\left\{\ln\left[\left(\frac{y_{O_2,TPB}(r, i \neq 0)}{y_{O_2}(r, i \neq 0)}\right)^{\gamma}\right] + \ln\left[\left(\frac{y_{O_2}(r, i \neq 0)}{y_{O_2}(r, i = 0)}\right)^{\gamma}\right]\right\} \quad (3.21)$$

In Eq. (3.20) and Eq. (3.21), the first term represents the diffusion overpotential and the second the voltage losses related to the conversion of the chemical species. As previously explained for the reversible voltage, the constant pressure assumption allows to calculate the concentration overpotentials as functions of the molar concentrations.

The electrochemical module calculates the heat source/sink terms as functions of the cell radius; these terms are required in the thermal module for the calculation of the temperature field. Heat sources and sinks are related to three different phenomena: 1) electrochemical reactions, 2) resistance of the materials to the charge flow (i.e., Joule effect), 3) non-Ohmic losses related to activation and concentration losses.

1) The heat generated/consumed in the reactions is calculated as the sum of the entropy balances of the chemical species multiplied by the temperature:

$$d\dot{Q}_{react}(r) = \sum_i \frac{\partial(\dot{n}_i \times T \times \bar{s}(p_i, T))}{\partial r} dr \quad (3.22)$$

where $\bar{s}(p_i, T)$ is the molar entropy of the chemical species i, which is dependent of the partial pressure and of the temperature.

2) The heat generated by Joule effect is given by:

$$d\dot{Q}_{Ohm}(r) = \eta_{Ohm}(r) \times i(r) \times 2\pi r \times dr \quad (3.23)$$

3) The heat generated by non-Ohmic sources is provided by the following expression:

$$d\dot{Q}_{irr}(r) = \left[\eta_{act,fuel}(r) + \eta_{act,air}(r) + \eta_{con,fuel}(r) + \eta_{con,air}(r)\right] \times i(r) \times 2\pi r \times dr \quad (3.24)$$

It is worth noting that the heat source related to concentration losses is a purely mathematical consequence of calculating the reversible voltage at open circuit using the concentration of chemical species in the channel boundary, but it is not related to a physical phenomenon. Assuming the reversible voltage as constant and equal to the open-circuit one overestimates its value and compels to adopt a concentration overvoltage to correct the overestimation. In the other models developed in this Thesis, this assumption will be overcome by calculating a

reversible voltage dependent of the concentrations of the species on TPB, thus eliminating the need for a concentration overvoltage term in the polarization equation.

3.1.3 Thermal module

The thermal behavior of the cell has been simulated using a 2D FEM model of the cross-section of the full cell. The local thermal equilibrium is assumed and the heat transport by convection and radiation within electrodes and electrolyte layers was not accounted for in this study. The temperature distribution inside the cell is obtained by imposing the energy equation:

$$\left(\rho c_p\right)_{eff} \times r \times \frac{\partial T(r,z,t)}{\partial t} - \nabla \cdot \left(k_{eff} \times r \times \nabla T(r,z,t)\right) = q_s(r, layer) \times r \qquad (3.25)$$

where the source term q_s includes all the heat generation/consumption terms (see Eq. (3.26)).

Porous electrodes are modeled as pure conductive homogenous media with distributed heat sinks/sources produced by electrochemical reactions and polarization overpotentials. The effective thermal proprieties $(\rho c_p)_{eff}$ and k_{eff} of the electrodes have been calculated as described in *Chapter 2* (see equation (2.112) and (2.113)). The thermal properties of gases have been taken from (Poling et al. 2001) and those of the solid materials are reported in *Table 3.1* with their respective references. The properties of the solids are assumed constant in the considered temperature range.

The heat sources/sinks are calculated according to Eqs (3.22),(3.23) and (3.24) and assigned to specific layers of the cell. The thermodynamic heat generation/consumption calculated by Eq. (3.22) has been distributed into a 10 μm thick region of the fuel electrode adjacent to the electrolyte, in order to take into account that reactions spread within the active layer of the electrode. The Ohmic heat source has been assigned to the electrolyte, assuming that almost the entire Joule heating takes place into this layer, while the other non-Ohmic heat sources have been assigned to their corresponding electrodes and located into the active layers. All the source terms have been divided by the volume of the layer to which they are assigned for the implementation in the thermal module; therefore, in each layer of the cell a specific volumetric source has been expressed as function of the cell radius:

$$q_s(r, layer) = \frac{d\dot{Q}_{react}(r) + d\dot{Q}_{Ohm}(r) + d\dot{Q}_{irr}(r)}{2\pi r \times h_{layer} \times dr} \qquad (3.26)$$

where h_{layer} is the thickness of the layer to which the source is assigned.

Convective heat transfer has been imposed as boundary condition on the electrodes surface, assuming a fully developed laminar flow of the gases in the channels, with a Nusselt number of 3.68 (Grew et al. 2007). Radiative heat transfer is the imposed boundary condition on the cell border, assuming pure radiation heat transfer with the furnace walls, which are found at the same temperature of the cell at the beginning of each i-V characterization. A cell emissivity of 0.8 has been assumed (Shi et al. 2011b).

3.2 Stack Repeating Unit models

The repeating unit of a planar SOC stack has been modeled on 2D and 3D geometries. The models were both implemented in Comsol Multiphysics® (version 5.2, license n. 13074300) and include cell, gas distribution channels and interconnects. The models have been used for the simulation of the thermo-electrochemical behavior of an rSOC operating in a stack contest. On both the geometries, the activation kinetics adopted for the electrochemical reaction are those obtained from the experimentally validated model presented in *Section 3.1.*

A 2D stationary model has been developed to simulate an SRU based on a fuel-electrode supported cell with square geometry. Parallel gas flows are assumed, and the repeating unit is assumed to reside in the center of a large stack to avoid the influence of end-effects on the results. The 2D model was applied to the study of both P2G and P2P configurations. Model geometry, assumptions and applied equations are described in the following sections. Results are shown in *Chapter 5* and *6.*

A 3D transient SRU model based on an electrolyte-supported cell has been developed for the simulation of thermal transients within a SRU in a cross-flow stack design. The model was applied to the study of the P2P operation. The model is presented in *Section 3.2.2* and results of the dynamic study are shown in *Chapter 5*.

3.2.1 Two-dimensional SRU model

A complete thermo-electrochemical and chemical model is provided. Mass, momentum, energy and charge conservation equations are applied on a 2D geometry and solved numerically by finite element methods.

The CFD model describes the fluid flow in the distributions channels by Navier-Stokes equations and Stokes-Brinkmann equations are applied in the porous electrode. Continuity equation is applied in fluid domains to impose the conservation of mass and chemical species. Electrochemical reactions are considered as boundary sources/sinks of chemical species located at the electrode/electrolyte interface, while chemical reaction sources/sinks are imposed in the fuel electrode volume. Gas diffusion is modeled with Stefan-Maxwell equations for multicomponent mixtures in non-porous domains and with Fick's model in the porous regions.

The conservation of electronic and/or ionic charge is imposed on electrode and electrolyte domains in combination with Ohm's law for the calculation of the charge flows. Electrochemical reactions are modeled by following a Butler-Volmer approach with activation overpotentials

calculated from the balance of ionic and electronic potentials on electrode/electrolyte boundaries. Exchange current densities are described by the experimentally validated kinetics presented in the 1D model (see *Section 3.1*). Total current is imposed as boundary condition on the surface of the fuel electrode surface and electrical potential is fixed to ground potential on the oxygen electrode. A contact resistance is imposed on the surface of the electrodes to take into account the effect of stack components on the SRU voltage.

Energy conservation equations include convective and conductive heat transfer. The heat released/consumed by the electrochemical reactions is accounted as a boundary source at the electrode/electrolyte interface, as the irreversible heating due to activation overpotential. Other heat source terms are the ohmic heating in the volume of electrode and electrolyte and the heat generation on the surface of electrodes due to the contact resistance. Heat sinks/sources related to chemical reactions are included as volume terms in the fuel electrode domain.

Chemical reactions are described with a global kinetics approach by using literature reaction rates for the WGS and MSR direct/reverse reactions. Carbon deposition and sulphur poisoning models are also included in the fuel electrode domain when applying the model to the simulation of co-electrolysis operation.

The input variables of the model are the inlet conditions of anodic and cathodic fluids – expressed in terms of temperature, gas composition, mass flow rate and total pressure – and the total cell current imposed on the fuel electrode boundary. The model calculates the distribution of: 1) fluid velocity, pressure and gas mixture composition within channels and electrodes, 2) electrical and ionic potentials in electrode and electrolyte domains, and 3) temperature in the entire model domain.

The equations are solved together by using a fully coupled solver provided by the CFD software Comsol Multiphysics® which uses a damped version of Newton-Raphson method for the solution of the equations. Details on the solution algorithm can be found in the reference manual of the software (COMSOL multiphysics user guide, 2015).

Model geometry, applied equations and imposed boundary conditions are described in the following paragraphs. Results of the simulations performed with the 2D model for the analysis of P2P and P2G systems are reported in *Chapter 5* and *6.*

Model geometry

The study considered a 2D model of an SRU based on a planar, square, fuel electrode-supported cell (CSC when operating in SOEC) with composite Ni/YSZ fuel electrode, YSZ electrolyte and

LSCF oxygen electrode. A fuel electrode-supported cell was selected because the electrode kinetics applied in the model have been validated on this type of cells. The cell is referred to as CSC in the following of the dissertation. The geometry of the model is depicted in *Figure 3.2*.

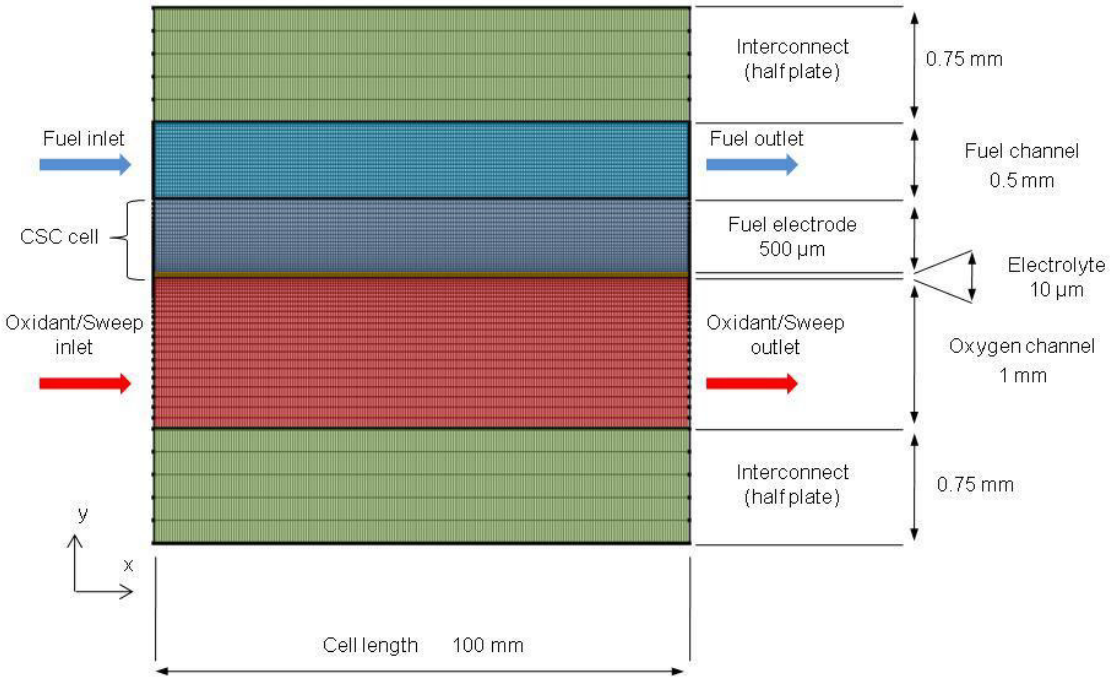

Figure 3.2 – 2D SRU model geometry.

The model domain is a rectangle on an (x,y) plane composed by six distinct layers: fuel electrode, electrolyte, fuel channel, oxidant/sweep channel and two interconnects. Each layer has a total length of 100 mm; the heights are reported in *Figure 3.2*.

Gases are distributed according to a parallel-flow arrangement in the channel regions, which are assumed as large flow passages (0.5 mm height the fuel channel and 1 mm the oxidant/sweep one). Flow patterns of interconnects are not considered in the model, as the 2D domain does not allow to include the ribs in the geometry. Consequently, the effects due to restriction of the current path in the elements connecting the interconnect plates to the electrodes are neglected in the model. Interconnects are modeled as solid layers made of Crofer22H® and are considered as half-layers on top and bottom of the SRU.

Cell geometry has been simplified by assuming the oxygen electrode as a boundary layer of negligible thickness. This assumption is justified by the relative thickness of the electrode with respect to the oxidant channel: in fact, an electrode thickness of 50 µm – a realistic value for oxygen electrodes in CSC – represents only 5% of the oxidant channel volume. Therefore, the

convective contribution of the channel is assumed predominant on electrode diffusion and the oxygen electrode is accounted only as a boundary layer where electrochemical reactions take place. The fuel-electrode domain is modeled as a porous homogeneous layer with constant porosity, and the electrochemical reactions are imposed at the electrode/electrolyte boundary. This assumption follows the previous consideration for the TPB thickness reported in *Section 3.1.1*.

The computational domain is constituted by rectangular elements. In the *y* direction, the domains' edges are divided as follows: 5 evenly spaced elements on interconnects and electrolyte, 20 evenly spaced elements on fuel channel, 25 elements on the fuel electrode distributed following an arithmetic sequence with an element ratio of 5 (higher elements concentration near the electrolyte), 25 elements on the oxygen channel distributed following an arithmetic sequence with an element ratio of 10 (higher elements concentration near the electrolyte). The cell length is divided in 200 evenly spaced elements along the x coordinate. The complete mesh is composed by 17000 domain elements and 1570 boundary elements. Details on the selection of number and size of mesh elements are given in the *Appendix A*.

Model assumptions

The main assumptions of the model are listed below:

- Ideal gas approximation is assumed.
- Electrochemical reactions are located at the electrode/electrolyte interface.
- Laminar flow in the gas channels.
- Oxygen electrode is assumed as a boundary layer of the electrolyte.
- Global kinetics approach for chemical reactions.
- Fick's model applied in porous media.
- Porous media are assumed as homogeneous, isotropic materials.
- The radiative heat transfer is neglected.

Governing equations and boundary conditions

In this section, the equations implemented in the model and the boundary conditions imposed are shown. Most of the equations have also been applied in the 3D SRU model that will be shown in the next section. Since the 3D model has been applied to dynamic simulations, the equations employed in both SRU models are presented in this section in the general transient form in order

to avoid repetitions in the text. It is straightforward that the transient terms of equations are zero when applied in stationary simulations. A thorough discussion on SOC modeling approaches is given in *Chapter 2*, which can be consulted for the detailed description of the equations employed.

Mass and momentum conservation

Continuity equation is applied in fluid domains to impose the conservation of mass and chemical species. A laminar, compressible flow is considered. In non-porous domains, the Stefan-Maxwell (SMM) model is applied to describe the diffusion in multicomponent mixtures, and the continuity equation is imposed in the following form:

$$\rho\frac{\partial x_\alpha}{\partial t}+\nabla\cdot\left(\rho x_\alpha\boldsymbol{u}-\left(\rho x_\alpha\sum_i D_{\alpha i}\left(\nabla y_i+\frac{1}{p}[(y_i-x_i)\nabla p]\right)\right)\right)=0 \tag{3.27}$$

Source terms are not considered in equation (3.27) as neither chemical nor electrochemical reactions are considered outside of the electrodes. Density has been evaluated from the ideal gas law. The binary diffusion coefficients have been calculated from the theoretical correlation of Chapman-Enskog shown in equation (2.71) (see *Chapter 2*) by using the coefficients reported in (Poling et al.2001). Momentum conservation in non-porous domains is imposed by Navier-Stokes equations:

$$\frac{\partial(\rho\boldsymbol{u})}{\partial t}+\nabla\cdot(\rho\boldsymbol{u}\boldsymbol{u})=\nabla\cdot\left[-p\boldsymbol{I}+\mu_g\left((\nabla\boldsymbol{u}+(\nabla\boldsymbol{u})^T)-\frac{2}{3}\mu_g(\nabla\cdot\boldsymbol{u})\boldsymbol{I}\right)\right] \tag{3.28}$$

where $\boldsymbol{I}$ is the unit matrix. The dynamic viscosity of the fluid – μ_g – has been estimated by the Wilke's formula, see equation (2.97) in *Chapter 2* and followings. The property databases of the COMSOL software have been used to evaluate pure gas properties (i.e., viscosity, thermal conductivity and specific heat at constant pressure). Volume forces (e.g., gravity, electromagnetic forces, etc.) are negligible and thus they are not considered in equation (3.28).

In the fuel electrode, continuity equation is applied in combination with Fick's model for the description of diffusive fluxes:

$$\frac{\partial(\varepsilon\rho x_\alpha)}{\partial t} + \nabla\cdot\left(\rho x_\alpha \mathbf{u} - \left(\rho D_{\alpha mK}^{eff}\nabla x_\alpha\right)\right) = S_\alpha \tag{3.29}$$

where the diffusion coefficient $D_{\alpha mK}^{eff}$ is calculated by applying the Bosanquet relation together with Wilke's formula and equation (2.85) in *Chapter 2* for the calculation of the Knudsen diffusivity. A mean pore radius of 0.5 μm is assumed in the calculation of the diffusivity. As previously explained in *Chapter 2,* Fick's formulation has several limitations that can lead to flux inconsistency; hence, the conservation of mass has been forced by imposing the calculation of the mass fraction of one of the *N* chemical species to close the mass balance:

$$x_N = 1 - \sum_{i=1}^{N-1} x_i \tag{3.30}$$

Momentum conservation in fuel electrode domain is imposed by Stokes-Brinkman equation:

$$\begin{aligned}\frac{1}{\varepsilon}\left[\frac{\partial(\rho\boldsymbol{u})}{\partial t} + \nabla\cdot\left(\frac{\rho}{\varepsilon}\boldsymbol{u}\boldsymbol{u}\right)\right] = \\ = -\nabla\cdot\left[-p\boldsymbol{I} + \frac{\mu_g}{\varepsilon}\left((\nabla\boldsymbol{u} + (\nabla\boldsymbol{u})^T) - \frac{2}{3}\frac{\mu_g}{\varepsilon}(\nabla\cdot\boldsymbol{u})\boldsymbol{I}\right)\right] \\ - \boldsymbol{u}\left(\frac{\mu_g}{B_p} + \sum_{\boldsymbol{\alpha}} S_\alpha\right)\end{aligned} \tag{3.31}$$

where the permeability B_p is calculated by thy Kozeny-Carman relationship (equation (2.84) in *Chapter 2*), in which the average particle diameter has been set to 2.5 μm (see *Table 3.2*). It is worth noting that the mass source term of equation (3.31) is different from zero only when carbon deposition reactions occurs, since the global mass balance of chemical reactions is zero and the electrochemical reactions are imposed as a boundary condition, but not in the volume. In other words, only carbon deposition reactions can add or subtract mass from gaseous streams in the volume of the fuel electrode.

The volumetric source terms S_α of equation (3.29) are related to chemical reactions, which occurs in the presence of carbon-hydrogen mixtures. Electrochemical reactions are considered as

boundary terms located on TPBs and thus they are not accounted for in the volumetric sources. The source term is given by:

$$S_\alpha = M_\alpha \sum_i \nu_{\alpha i} r_i \tag{3.32}$$

Chapter 2 has shown that only heterogeneous reactions play a significant role in the fuel electrode of SOCs. In particular, the most important reactions for typical SOC mixtures are the direct/reverse water-gas-shift (WGS) and the steam reforming/methanation reaction (MSR):

$$CO_{2(g)} + H_{2(g)} \leftrightarrow CO_{(g)} + H_2O_{(g)}$$

$$CO_{(g)} + 3H_{2(g)} \leftrightarrow CH_{4(g)} + H_2O_{(g)}$$

The rates of WGS and MSR reactions have been described by following a global kinetics approach. In order to accurately evaluate the rates, the most appropriate kinetics must be selected. Mogensen et al. (2011) provided a review of the kinetics reported in the literature for SOFCs anodes made by Ni/YSZ. A wide variety of kinetic equations are available, depending on the operating conditions of the experiments selected for the study. In the present model, the rate equations developed by Haberman and Young (2004) from the experiments of Lehnert et al. (2000) were utilized. The rates are expressed with an equilibrium-limited Langmuir-Hinshelwood type rate expression:

$$r_{MSR} = 2395 \ \exp\left(\frac{-231266}{RT}\right)\left(p_{CH_4}p_{H_2O} - \frac{p_{H_2}^3 p_{CO}}{K_{eq,MSR}}\right) \tag{3.33}$$

$$r_{WGS} = 0.017 \ \exp\left(\frac{-103191}{RT}\right)\left(p_{CO}p_{H_2O} - \frac{p_{H_2}p_{CO_2}}{K_{eq,WGS}}\right) \tag{3.34}$$

Reaction rates (mol m^{-3} s^{-1}) are expressed as functions of temperature, partial pressures (Pa) and equilibrium constants – $K_{eq,MSR}$ (Pa^2) and $K_{eq,WGS}$ (-) – which are implemented in the model as empirical equations (Haberman and Young 2004):

$$K_{eq,MSR} = 1.0267 \cdot 10^{10} exp\ (-0.2513Z^4 + 0.3665Z^3 + 0.5810Z^2 - 27.134Z + 3.2770) \tag{3.35}$$

$$K_{eq,WGS} = exp\ (-0.2935Z^3 + 0.6351Z^2 + 4.1788Z + 0.3169) \tag{3.36}$$

where is expressed as: Z = 1000/T(K) – 1.

Also carbon deposition reactions were included in the model. Methane cracking and Boudouard reactions were considered. The rate of carbon formation from methane cracking is calculated using the expression derived by Zavarkuhin and Kuvshinov (2004):

$$r_{C1} = \frac{\rho_{cat}}{3600} k_C \frac{p_{CH_4} - \frac{p_{H_2}^2}{K_P}}{\left(1 + k_H \sqrt{p_{H_2}}\right)^2} \tag{3.37}$$

$$k_C = exp\left(20.49 - \frac{1.04 \cdot 10^5}{R\,T}\right) \tag{3.38}$$

$$k_H = exp\left(-22.43 + \frac{1.63 \cdot 10^5}{R\,T}\right) \tag{3.39}$$

$$K_P = 5.09 \cdot 10^5 exp\left(-\frac{9.12 \cdot 10^4}{R\,T}\right) \tag{3.40}$$

The rate expression for the Boudouard reaction is derived from Snoeck et al. (2002):

$$r_{C2} = \frac{\rho_{cat}}{3600} \frac{k_{fB} K_{CO} \left(p_{CO} - \frac{p_{CO_2}}{k_{pB} p_{CO}}\right)}{\left(1 + K_{CO} p_{CO} + \frac{p_{CO_2}}{K_{CO_2} K_{CO} p_{CO}}\right)^2} \tag{3.41}$$

$$k_{fB} = 2.67 \cdot 10^7 exp\left(\frac{108379}{R\,T}\right) \tag{3.42}$$

$$K_{CO} = 1.02 \cdot 10^{-6} exp\left(-\frac{92543}{R\,T}\right) \tag{3.43}$$

$$K_{CO_2} = 3.02 \cdot 10^7 exp\left(\frac{89805}{R\,T}\right) \tag{3.44}$$

$$k_{pB} = exp\left(-\frac{170.4}{R}\right) exp\left(\frac{162481}{R\,T}\right) \tag{3.45}$$

In the previous equations for the calculation of carbon deposition rates r_{Ci} (mol m^{-3} s^{-1}), the partial pressures are expresses in *bar*, ρ_{CAT} is the catalyst density (g_{cat} m^{-3}). In the SOC fuel

electrode considered in this study (i.e., Ni/YSZ), the catalyst is the Nichel. The catalyst density has been estimated from surface site density Γ_{Ni} (mol m^{-2}), specific surface area S_{Ni} (m^2 m^{-3}) and molar weight of Nichel as follows:

$$\rho_{cat} = \Gamma_{Ni} \cdot S_{Ni} \cdot M_{Ni} \tag{3.46}$$

The values of the surface parameter adopted in the model are listed in *Table 3.2* with the related references, together with the other microstructure parameters of the cell.

The effect of sulfur poisoning on chemical and electrochemical reactions has been added to the model for the simulation of the impact of H_2S breakthrough on a co-electrolysis based P2G system in case of malfunctioning of CO_2 cleaning. The sulfur coverage – θ_s – of nickel surface reached at saturation has been calculated following the Temkin-like isotherm described in *Chapter 2* by equation 2.167. The effect of the coverage on the reaction rate of MSR, WGS and carbon deposition reactions has been calculated by reducing the rate of a factor depending on the θ_s:

$$r^*_{react,i} = r_{react,i} \cdot (1 - \theta_S)^3 \tag{3.47}$$

Energy conservation

The energy conservation equation is imposed for modeling heat transfer in non-porous domains:

$$\frac{\partial(\rho\, C_p T)}{\partial t} + \nabla \cdot \left(\rho\, C_p T\, \boldsymbol{u}\right) + \nabla \cdot (-k \nabla T\ ) = Q_v \tag{3.48}$$

where the thermal conductivity *k* and the specific heat capacity *Cp* are that of the gas mixture in the fluid domains – calculated by the Wilke's formula (see equation (2.97) in *Chapter 2*) – or that of the material in solid domains. Values of conductivity and specific heat capacity of solid materials are shown in *Table 3.1* with related references. The convective term is obliviously zero in solid domains. The local thermal equilibrium approach (LTE) described in *Chapter 2* is applied for the formulation of energy conservation in porous domains:

$$\left(\rho C_p\right)_{eff} \frac{\partial T}{\partial t} + \rho_g C_{pg} \boldsymbol{u} \cdot \nabla T = \nabla \cdot \left(k_{eff} \nabla T\right) + Q_v \tag{3.49}$$

where the terms $(\rho C_p)_{eff}$ and k_{eff} are effective transport parameters: namely, the energy stored per unit volume and the effective heat conduction flux, obtained as volume averages of the quantities defined for the gas and solid phases, as described by equations (2.112) and (2.113) of *Chapter 2*. The volumetric heat source Q_v is given by the sum of the heat generation due to ohmic heating in the solid electrically conductive domains (i.e., electrolyte and porous electrode) and the heat sources/sinks related to chemical reactions in the fuel electrode.

$$Q_v = Q_{ohm} + Q_{chem} = \frac{\left|\boldsymbol{i}_{e/i}\right|^2}{\sigma_{e/i}} - \sum_i r_i \Delta\bar{h}_i \tag{3.50}$$

where $i_{e/i}$ is the electronic/ionic current density, $\sigma_{e/i}$ is the electronic/ionic conductivity of the material – which becomes the effective one, calculated with equation (2.142) in the porous electrode – and the product between the reaction rate r_i (mol m^{-3}) and the reaction enthalpy $\Delta\bar{h}_i$ (J mol^{-1}) is the heat source/sink related to the *i-th* chemical reaction. In the evaluation of the effective conductivity of porous media, the statistical approach described by Nam and Jeon has been applied for the calculation of the percolation probability (Nam and Jeon 2006). Ohmic heating is not considered in the interconnects, as the effect of stack electrical resistances has been included in the contact resistance imposed at the electrode/interconnect boundary. The value of the contact resistance between electrodes and interconnects – R_{con} – has been chosen from recent experimental measurements on coated Crofer 22H interconnects (Spotorno et al. 2015). A value of 0.05 Ωcm^2 has been selected, which is acceptable for stack applications, as the acceptable area-specific resistance (ASR) level for interconnects is considered to be below 0.1 Ωcm^2 (Wu and Liu 2010). Also the heat generation related to activation losses of redox reactions is considered in the boundary conditions imposed at the electrolyte/electrode interface, as the reaction heat released/absorbed by electrochemical reactions.

Conservation of charge

The approach followed for modeling the electrochemistry in the SRU is based on the implementation of charge transfer and conservation equations in which ionic and electronic potentials of electrodes and electrolyte are the dependent variables. In this way, the punctual evaluation of the potentials has allowed the 2D and 3D evaluation of charge fluxes (i.e., electronic and ionic currents) and overpotentials, thus overcoming the assumptions followed in the 1D/2D cell model.

As described in *Chapter 2*, the mathematical description of electrochemistry must encompass three main phenomena: 1) generation of potential difference between electrodes due to electrochemical reactions, 2) activation of electrochemical reactions and 3) charge transport of electrons and ions in the SRU.

In the models developed, the equilibrium potentials of electrodes have been evaluated from the Gibbs free energy variation of the electrochemical reactions:

$$E_{rev}^{oxy} = \frac{RT}{4F} ln\left(\frac{p^{TPB}{}_{O_2}}{p^o}\right) \tag{3.51}$$

$$E_{rev,H_2/H_2O}^{fuel} = \frac{1}{2F}\left[\Delta\bar{g}_{H_2/H_2O}^{o} + RTln\left(\frac{p_{H_2O}}{p_{H_2}}\right)\right] \tag{3.52}$$

$$E_{rev,CO/CO_2}^{fuel} = \frac{1}{2F}\left[\Delta\bar{g}_{CO/CO_2}^{o} + RTln\left(\frac{p_{CO_2}}{p_{CO}}\right)\right] \tag{3.53}$$

where p^0 is the standard pressure (i.e., 1 atm) and the molar Gibbs free energy variations $\Delta\bar{g}^0$ were calculated using the JANAF Tables (Chase et al. 1998). Equation (3.51) is imposed on the oxygen electrode boundary and (3.52)-(3.53) are calculated in the entire volume of the fuel electrode.

The activation overpotential of the electrochemical reactions is due to charge transfer from the ionic to electronic form. In the model, it is has been calculated as the disequilibrium between the potential difference of the ionic and electronic phases and the equilibrium potential:

$$\eta_{act} = \phi_e - \phi_i - E_{eq} \tag{3.54}$$

where ϕ_e is the electronic potential of the electrode (V), ϕ_i is the ionic potential (V) and E_{eq} is the equilibrium potential of the electrode that is expressed by using equations (3.51)-(3.53). In the case of oxygen electrode, the electric potential ϕ_e is evaluated just on the electrolyte/electrode boundary, because the electrode is not included in the model. Even if the electrode produces negligible potential drops related to the movement of electrons, the electric potential at the electrolyte/electrode should take into account the presence of a contact resistance between the electrode and the interconnect. For this reason, an external electric potential is used

by the model in equation (3.54), which is given by the difference of the potential imposed at the boundary and the contact resistance between electrode and interconnect.

The activation overpotential is calculated on the electrolyte/electrode boundaries, where the Butler-Volmer equation is imposed for the calculation of the local current density generation due to electrochemical reactions:

$$i_{loc,j} = i_{0,j}\left[exp\left(\alpha_{f,j}\frac{F\eta_{act}}{RT}\right) - exp\left(-\alpha_{b,j}\frac{F\eta_{act}}{RT}\right)\right] \tag{3.55}$$

where the values of the charge transfer coefficients of the *j-th* reaction are those adopted in the cell model (see *Table 1* in *Section 3.1.2*) and the exchange current density $i_{0,j}$ (A cm^{-2}) of the *j-th* reaction is expressed as:

$$i_{o,oxy} = \gamma_{air}\left(\frac{p_{O_2}}{p^0}\right)^{0.25} \cdot exp\left(\frac{-E_{act,oxy}}{RT}\right) \tag{3.56}$$

$$i_{o,fuel} = \gamma_{fuel}\left(\frac{p_{H_2(CO)}}{p^0}\right)\left(\frac{p_{H_2O(CO_2)}}{p^0}\right) \cdot exp\left(\frac{-E_{act,fuel}}{RT}\right) \tag{3.57}$$

where the activation energies $E_{act,oxy}$ and $E_{act,fuel}$ were chosen from the literature (see *Table 1* in *Section 3.1.2*) and the values of the pre-exponential kinetic parameters γ_{air} and γ_{fuel} are those obtained from the cell model calibration (see *Table 4.4* and *Table 4.6*, *Chapter 4*).

The effect of the nickel coverage due to sulfur adsorption on the electrochemical reactions has been calculated by linearly reducing the exchange current density with θ_s:

$$i_0^* = i_0 \cdot (1 - \theta_S) \tag{3.58}$$

The charge conservation equation is applied in electrolyte and fuel electrode domains in combination with the Ohm's law:

$$\nabla \cdot \boldsymbol{i}_{e/i} = 0 \tag{3.59}$$

$$\boldsymbol{i}_{i/e} = -\sigma_{i/e}\nabla\phi_{i/e} \tag{3.60}$$

where $\nabla\phi_{i/e}$ is the gradient of the ionic/electronic potential that drives the charge flow and $\sigma_{i/e}$ is the conductivity of the material. In the case of the impervious solids (i.e., electrolyte and

interconnects), the conductivity is that of the pure material, while in the porous electrodes an effective conductivity is imposed. The conductivities of the materials and the distribution of the phases in the fuel electrode are listed in *Table 3.2* with the related references.

Table 3.2 – Materials parameters for the SRU structure

Parameters	Value	Units	Reference
Fuel electrode (Ni/YSZ)			
Thickness	500	µm	-
Porosity (ε)	0.3	-	(Lanzini et al. 2009)
Tortuosity (τ)	3	-	(Menon et al. 2014)
Average pore radius (d_ε/2)	0.5	µm	(Chan et al. 2001)
Average particle diameter (d_p)	2.5	µm	(Zhu et al. 2005)
Specific surface area of Ni (S_{Ni})	1.6	μm^{-1}	(Wilson et al. 2007)
Surface site density of Ni Γ_{Ni}	$2.60 \cdot 10^{-5}$	mol m^{-2}	(Zhu et al. 2005)
Electrical conductivity Ni (σ_e)	$3.27 \cdot 10^{6}$-1065.3·T	S m^{-1}	(Lanzini et al. 2009)
Ionic conductivity YSZ (σ_i)	$33.4 \cdot 10^{3} \cdot \exp(-10300/T)$	S m^{-1}	(Lanzini et al. 2009)
Volume fraction of Ni phase (f_e)	0.5	-	(Sumi et al. 2010)
Volume fraction of YSZ phase (f_i)	0.5	-	(Sumi et al. 2010)
Thermal conductivity (k)	11	W m^{-1} K^{-1}	(Barzi et al. 2011)
Density (ρ)	4760	kg m^{-3}	(Barzi et al. 2011)
Specific heat capacity (C_p)	377	J kg^{-1} K^{-1}	(Barzi et al. 2011)
Charge transfer coefficient (α_{fuel})	0.4[a] – 1.15[b]	-	(Marina et al. 2007)
Activation energy ($E_{act,fuel}$)	120	kJ mol^{-1}	(Suwanwarangkul et al. 2006)
Pre-exponential parameter (γ_{fuel})	*Table 4.4 Chapter 4*	A m^{-2}	from fitting
Oxygen electrode (LSCF)			
Charge transfer coefficient (α_{oxy})	1[c]	-	(Laurencin et al. 2011)
Activation energy ($E_{act,oxy}$)	130	kJ mol^{-1}	(Suwanwarangkul et al. 2006)
Pre-exponential parameter (γ_{air})	*Table 4.6 Chapter 4*	A m^{-2}	from fitting

Electrolyte (YSZ)			
Thickness	10	μm	-
Ionic conductivity YSZ (σ_i)	$33.4 \cdot 10^3 \cdot \exp(-10300/T)$	S m^{-1}	(Lanzini et al. 2009)
Thermal conductivity (k)	2.7	W m^{-1} K^{-1}	(Wang. H. et al. 2011)
Density (ρ)	5900	kg m^{-3}	(Wang. H. et al. 2011)
Specific heat capacity (C_p)	600	J kg^{-1} K^{-1}	(Wang. H. et al. 2011)
Interconnect (Crofer 22H)			
Thickness (half plate)	0.75	mm	-
Thermal conductivity (k)	from Table 3 of reference	W m^{-1} K^{-1}	(Crofer data sheet 2010)
Density (ρ)	7.8	g cm^{-3}	(Crofer data sheet 2010)
Specific heat capacity (C_p)	from Table 3 of reference	J kg^{-1} K^{-1}	(Crofer data sheet 2010)
Contact resistance with electrode (R_{con})	0.05	Ω cm^2	(Spotorno et al. 2015)

[a] SOEC mode [b] SOFC mode [c] Both fuel cell and electrolysis operation

Boundary conditions

The boundary conditions imposed in the model are listed in *Table 3.3*, in which the boundary numbers refer to *Figure 3.3*.

Table 3.3 – Boundary conditions

	Species transport and conservation	
Boundary 1 and 2	Inlet stream composition:	$\forall\alpha$: $\begin{cases} y_\alpha = \boldsymbol{y_{\alpha,in}} \\ x_\alpha = y_\alpha \cdot (M_\alpha / \sum_k y_k M_k) \end{cases}$
Boundary 3 and 4	Pure convective outflow (i.e., no diffusion): $\forall\alpha$: $\begin{cases} -\boldsymbol{n} \cdot \rho\omega_\alpha \sum_k D_{\alpha k}(\boldsymbol{d}_k) = 0 \\ \boldsymbol{d}_k = \left(\nabla y_k + \frac{\nabla p}{p}[(y_k - x_k)]\right) \end{cases}$	
Boundary 8 and 9	Species sinks/sources due to electrochemical reactions: $\forall\alpha$:	$-\boldsymbol{n} \cdot \boldsymbol{N}_\alpha = M_\alpha \sum_j \nu_{\alpha,j} \frac{i_{loc,j}}{n_j F}$
Boundary 10 and 7	Impervious boundary, no flux: $\forall\alpha$: $\begin{cases} -\boldsymbol{n} \cdot \boldsymbol{N}_\alpha = 0 \\ \boldsymbol{N}_\alpha = (\rho x_\alpha \boldsymbol{u}) + \left(\rho x_\alpha \sum_k D_{\alpha k}\left(\nabla y_k + \frac{\nabla p}{p}[(y_k - x_k)]\right)\right) \end{cases}$	
	Fluid transport: mass and momentum conservation	

Boundary 1 and 2	Mass flow inlet: $(\sum_k y_k M_k)$	$-l_{cell}\int_{\partial\Omega}\rho\,(\boldsymbol{u}\cdot\boldsymbol{n})dy=\dot{\boldsymbol{n}}_{in}\cdot$
Boundary 3 and 4	Outlet pressure:	$p=\boldsymbol{p}_{out}$
Boundary 8 and 9	Velocity at the electrode-electrolyte interface:	$\boldsymbol{u}=\frac{\boldsymbol{n}}{\rho}\sum_{j,\alpha}\left(M_\alpha\nu_{\alpha,j}\frac{i_{loc,j}}{n_jF}\right)$
Boundary 10 and 7	Wall boundaries:	$\boldsymbol{u}=0$
	Charge transport and conservation	
Boundary 11	Cell current:	$l_{cell}\int_{\partial\Omega}(\boldsymbol{i}_e\cdot\boldsymbol{n})\,dl=\boldsymbol{I}_{cell}$
Boundary 9	Electric Ground:	$\phi_e=0$
Boundary 8 and 9	Electrolyte-Electrode Interfaces:	$\begin{cases}\boldsymbol{i}_{i/e}\cdot\boldsymbol{n}=i_{cell}\\ i_{cell}=\sum_j i_{loc,j}\\ \eta_{act,j}=\phi_e-\phi_i-E_{eq,j}\end{cases}$
Boundary 5 and 7	Insulated boundaries:	$-\boldsymbol{i}_{i/e}\cdot\boldsymbol{n}=0$
	Heat transfer and energy conservation	
Boundary 1 and 2	Inlet fluid temperature:	$T=\boldsymbol{T_{in}}$
Boundary 3 and 4	Pure convection at the outlet :	$-\boldsymbol{n}\cdot(-k\,\nabla T)=0$
Boundary 8 and 9	Reaction heat source/sink: Δs_j	$-\boldsymbol{n}\cdot(-k\,\nabla T)=\sum_j\left(\frac{i_{loc,j}}{n_jF}\cdot T\cdot\right.$
Boundary 8 and 9	Reaction activation heat source:	$-\boldsymbol{n}\cdot(-k\,\nabla T)=\sum_j\left(\eta_{act,j}\cdot i_{loc,j}\right)$
Boundary 8 and 11	Contact resistance:	$-\boldsymbol{n}\cdot(-k\,\nabla T)=R_{con}\cdot i_{cell}$
Boundary 6	Symmetry (no heat flux across the boundary):	$-\boldsymbol{n}\cdot(-k\,\nabla T)=0$
Boundary 5	Thermal insulation:	$-\boldsymbol{n}\cdot(-k\,\nabla T)=0$

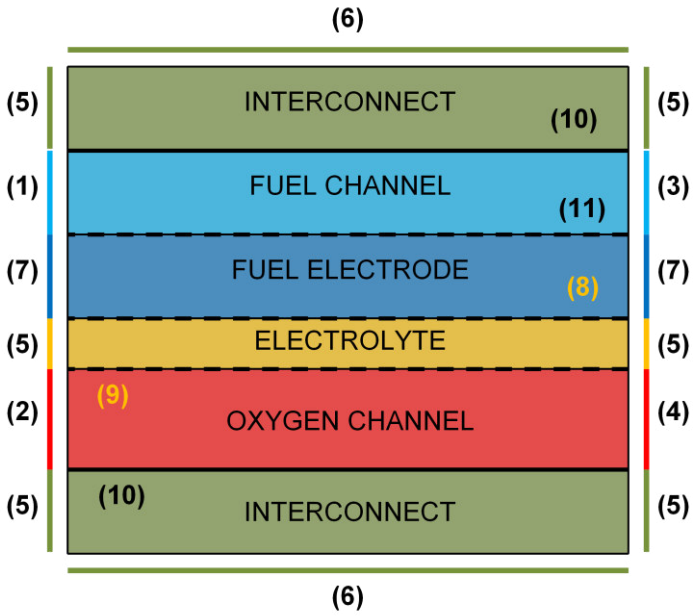

Figure 3.3 – 2D model boundaries

The boundary conditions listed in *Table 3.3* include the input variables of the model, which are the followings:

- mole fraction of each α species: $\boldsymbol{y}_{\alpha,in}$
- total inlet molar flow of fuel and oxidant/sweep flow: $\dot{\boldsymbol{n}}_{in}$
- inlet temperature of each fluid stream: $\boldsymbol{T}_{in}$
- total cell current: $\boldsymbol{I}_{\boldsymbol{cell}}$
- outlet pressure of the channels: $\boldsymbol{p}_{out}$

Input variables are written in bold in the text to better highlight them, even if they are all scalar values and not vectors. This convention will be followed in all the text.

In the modeling approach chosen, the pressure is imposed at outlet of the channels. When modeling the system, this pressure is considered as the outlet pressure of the stack. Thus, when imposing the pressurized operation of the SOC, it is intended that gases are exiting from the stack the operating pressure imposed. The inlet molar flows and the cell current were chosen not fully independently one from the other, but technological constraints were imposed. The assumptions and constraints of the input variables are explained in *Chapter 5*, together with the discussion of the model results.

3.2.2 Three-dimensional SRU model

The three-dimensional model is the application on a 3D domain of a simplified version of the 2D thermo-electrochemical model described in *Section 3.2.1*. The model is used for the simulation of an SRU based on an electrolyte-supported cell (ESC) operating only with H_2/H_2O mixtures, as the focus is on the study of SOC dynamics in P2P applications.

The ESC cell has been selected for this model mainly because its configuration allows to safely assume both the electrodes as flat layers on the surface of the electrolyte, which is the thickest layer of the cell. With this assumption it is possible to model the cell as a single layer without taking into account gas diffusion in porous electrodes. In this way, the numerical model does not need to catch the fine gradients of potentials and concentrations in the electrodes, and consequently the mesh employed for the solving the problem is significantly simplified and the computational effort is greatly reduced.

Therefore, the 3D model does not includes porous domains and also the equations describing chemical reactions, carbon deposition and sulfur poisoning are not implemented, because they are related to the presence of a H/C mixture, while the 3D model has been applied only with H_2/H_2O mixtures. In the case of the fuel electrode, the electric potential is evaluated only on the electrode/electrolyte interface, exactly as assumed for the oxygen electrode in the 2D model. Except these differences, the same equations and boundary conditions of the 2D model were applied, thus they are not reported again in this section.

The input variables of the model are again the inlet conditions of anodic and cathodic fluids – expressed in terms of temperature, gas composition, mass flow rate and total pressure – and the total cell current imposed on the fuel electrode boundary. The model calculates the distribution of: 1) fluid velocity, pressure and gas mixture composition within channels and 2) the ionic potential in the electrolyte domain and the electronic potentials on electrode/electrolyte interfaces and 3) the temperature in the entire model domain.

The equations are solved together by using a fully coupled solver provided by the CFD software Comsol Multiphysics® which uses a damped version of Newton-Raphson method for the solution of the equations. Details on the solution algorithm can be found in the reference manual of the software (COMSOL multiphysics user guide, 2015).

The geometry of the model is depicted in *Figure 3.4*. The model describes an SRU based on a planar, square, ESC with YSZ electrolyte. The model domain is a block defined in an (x,y,z) cartesian space. The block is composed by five distinct layers: electrolyte, fuel channel,

oxidant/sweep channel and two interconnects. Each layer has a total length of 100 mm; the heights are reported in *Figure 3.4*.

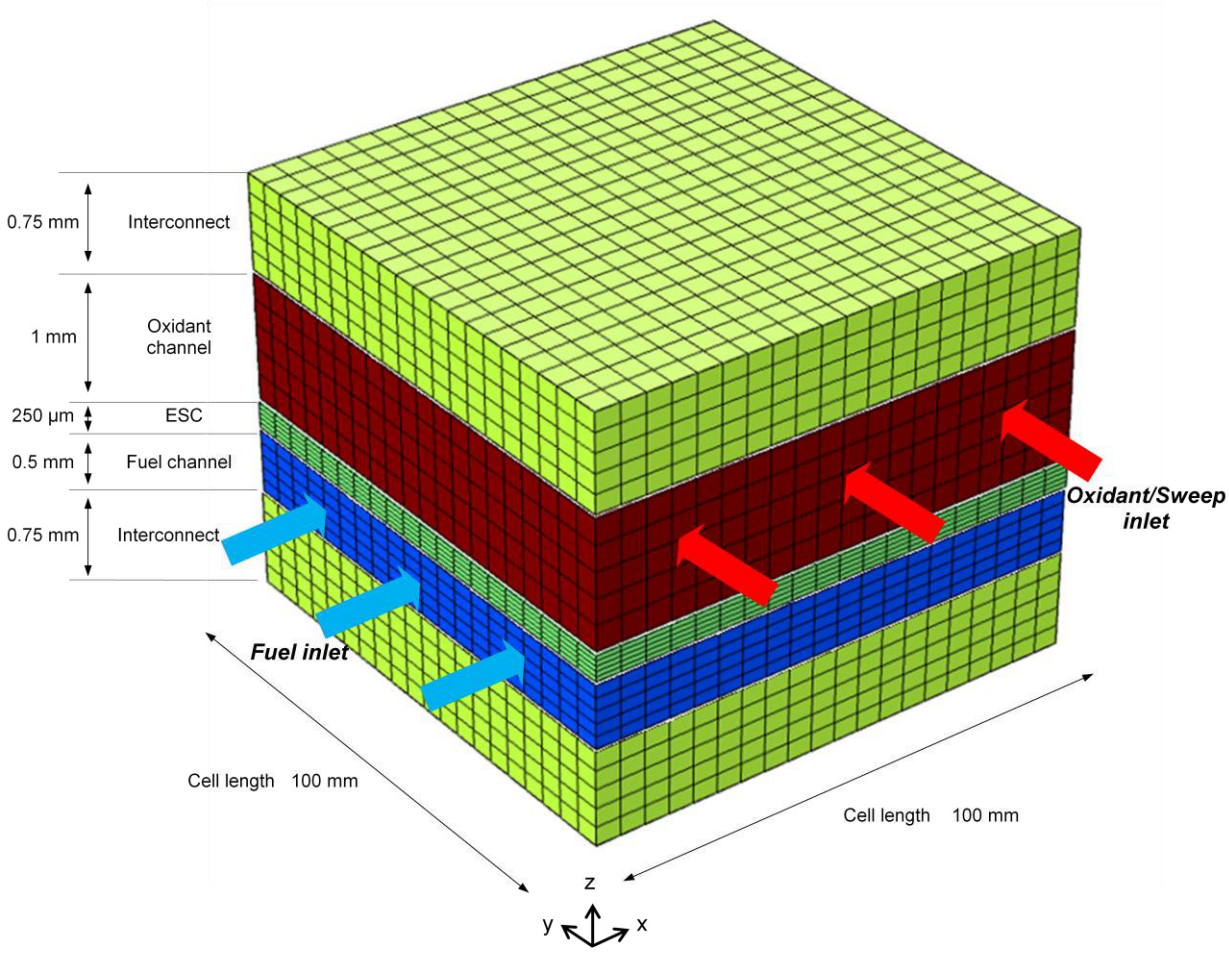

Figure 3.4 *– 3D model geometry.*

Gases are distributed according to a cross-flow arrangement in the channel regions, which are assumed as large flow passages (0.5 mm height the fuel channel and 1 mm the oxidant/sweep one). Flow patterns of interconnects are not considered in the model. Interconnects are modeled as solid layers made of Crofer22H® and are considered as half-layers on top and bottom of the SRU. The properties of materials and the SRU parameters adopted are listed in *Table 3.2*.

The computational domain is constituted by rectangular elements. In the x and y directions, the domains' edges are divided in 20 evenly distributed elements. In the z direction, each layer of the SRU is divided in 5 evenly spaced elements. The complete mesh is composed by 10000 domain elements, 4800 boundary elements, and 820 edge elements.

Chapter 4

Experimental and single-cell model validation

In this Chapter, the experimental characterization of reversible SOCs is presented. Two commercial Ni/YSZ supported planar SOCs with the air electrode made by either LSM/YSZ or LSCF were characterized. The operation with H_2/H_2O and CO/CO_2 gas mixtures was investigated by measuring current-voltage (i-V) curves and impedance spectra. The experimental setup and procedures are presented in *Section 4.1* and *Section 4.2*.

The experimental results are discussed in *Section 4.3*. The results were used for the calibration and validation of the single-cell rSOC model presented in *Chapter 3*. In *Section 4.4,* the activation parameters of the electrodes evaluated from the model calibration are discussed and their physical consistency is verified with the support of the published literature. Activation parameters show a significantly higher activity for the LSCF electrode compared to the LSM/YSZ electrode in both fuel cell and electrolysis mode and higher activation resistances for the fuel electrode are observed in the operation with CO/CO_2 mixtures, due to the faster kinetics of H_2/H_2O reactions. The rSOC model is finally validated on current-voltage curves of the commercial cells tested with H_2/H_2O mixtures, and the simulated evolutions of overpotentials and temperature within the cell are also briefly discussed.

4.1 Instrumentation

The experimental activity was performed at LAQ INTESE laboratory (High Quality Laboratory – Technological Innovation for Energetic Sustainability) of the Department of Energy of Politecnico di Torino, where a test facility for planar SOCs is available.

The test bench is designed for testing unsealed circular planar SOCs at ambient pressure. The schematic diagram of the test-rig is shown in *Figure 4.1*. The test-rig is composed by several subsystems: 1) the test chamber equipped with a fixture for circular planar cells, placed inside an oven to maintain cells at the imposed test temperature, 2) gas distribution system, 3) humidification system, in which water is added to dry gaseous streams, 4) electric auxiliaries, which supply electricity to oven resistances, 5) electronic load for cell characterization and 6) data acquisition and control system.

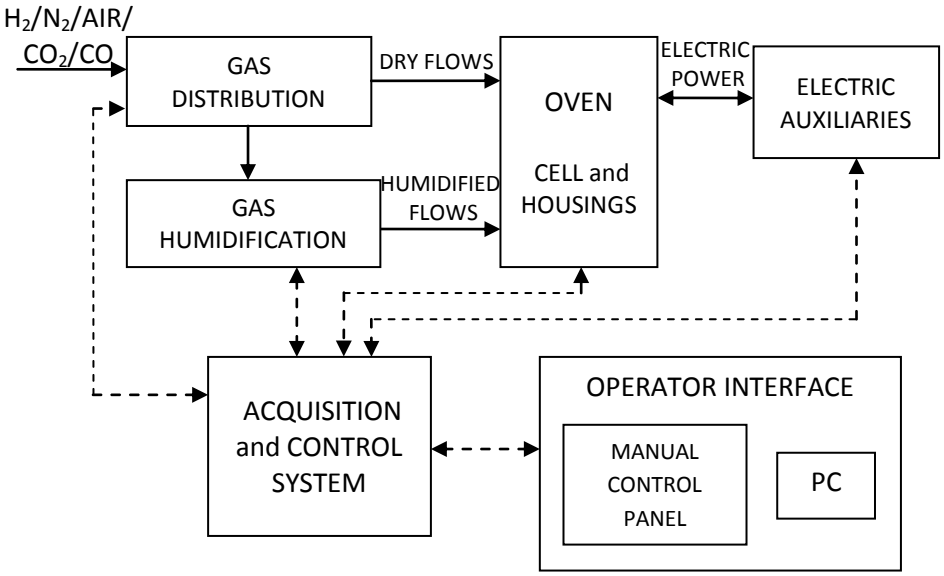

Figure 4.1 – Schematic diagram of the test-rig. Solid lines indicate mass and energy fluxes, dashed lines indicates data exchange between acquisition and control system and the other subsystems.

The test chamber (dimensions 35×35×15 cm) is heated by electrical resistances and insulated from the external environment by walls of removable refractory bricks. The oven heating system provides heat to the cell during the start-up phase and maintains the cell at a constant specified temperature during the experimental session, balancing heat dispersion to the environment. The oven is designed for a maximum temperature of 900 °C. Four electric resistances are located inside the oven, on the walls; each resistance is placed inside a provided ceramic structure. A

control thermocouple is located inside each resistance and electric DC current is supplied to the resistances by a dedicated electronic load. The current level is automatically regulated in order to keep the chamber at the desired test temperature.

SOCs are placed in a dedicated test-fixture during experiments. The test-fixture is composed by two alumina housings providing gas distribution and electrical connection to both electrodes. During the tests, the lower housing is in contact with the fuel electrode of the cell; this housing is screwed on a provided ceramic base integrated in the oven base and radially distributes gases from the cell center – where the gas inlet is located – to the rim. The upper housing is placed on the top of the cell and distributes air (or other mixtures of technical gases) to the oxygen electrode. Also on this side of the cell the gas is supplied radially from the center to the cell border. Metallic grids are placed on the housing side that is in contact with the cell electrode, in order to collect the electrons produced by the electrochemical reactions that take place at the electrode. The grids directly contact the cell electrode and are made by two superposed layers of Nickel (or Platinum for the oxidizing environments in order to avoid grid oxidation). Platinum wires contact the grids to act as current take-off buses and connect the cell to an external load. The cell voltage is measured with two separate Platinum sensing wires contacting the cathode and anode meshes, respectively. An N-type thermocouple (designed for temperatures up to 1300 °C) is located in the fuel electrode inlet channel near the electrode surface, providing the temperature in the gas flow near the cell center. The vertical cross-section of the assembled test-fixture is shown in *Figure 4.2*.

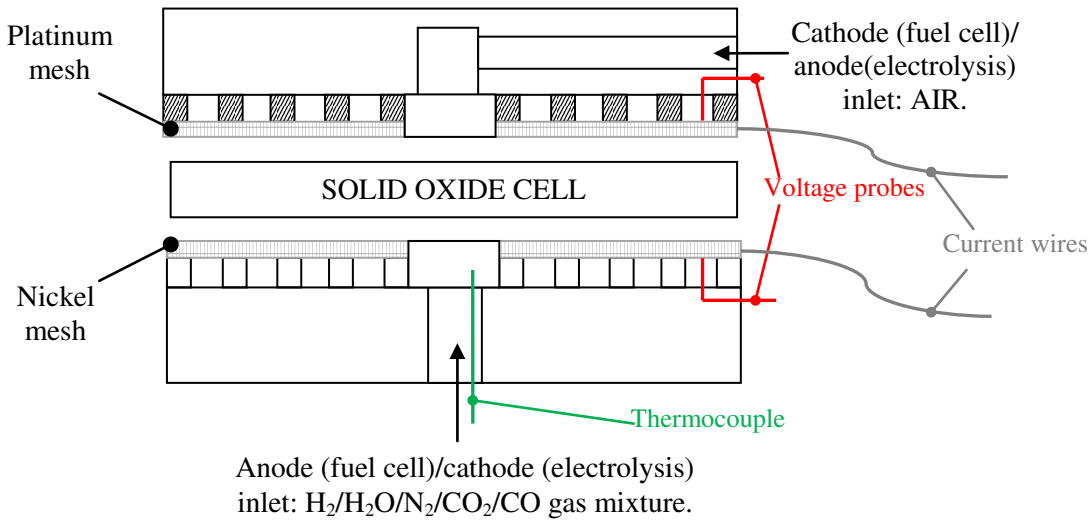

Figure 4.2 – Schematic of the vertical cross-section of the assembled test-fixture.

During experiments, the test-fixture is placed on the ceramic base of the oven. Piping for anodic/cathodic gases distribution, current wire braids and voltage wires cross the insulating walls through dedicated holes. Current wires are connected to a dedicated electronic load for cell characterization, while the voltage ones are connected to a terminal board from which the voltage signal is collected and carried to the data acquisition and control system. *Figure 4.3* shows a picture of the complete assembled test-fixture inside the oven.

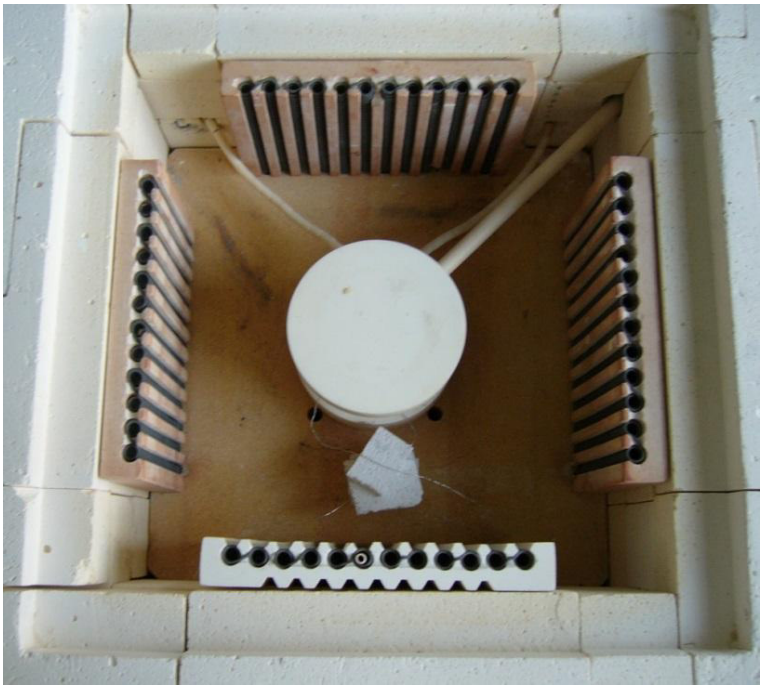

Figure 4.3 – Test-fixture assembled in the test chamber.

The gas distribution system connects the test-rig to the laboratory low-pressure gas lines and ensures that dry gas streams with specified flow rates and compositions are sent to the humidification system or directly to the SOC. This system is composed by pipes, valves (Swagelok) and mass flow controllers (Bronkhorst). Technical gases available in the laboratory are: H_2, CO, CO_2, CH_4, N_2 and dry air. The pressure of laboratory lines is controlled by pressure regulators. The connection of gas cylinders for feeding other gases to the SOC is also possible (e.g. for testing the effect of pollutants mixtures). A gas venting system with measuring sensors for explosive and toxic gases ensures the safety operation. The gas lines are connected to the test-rig through mass flow controllers operated through manual control panels or remotely by a PC interface. Manual valves are located before and after each mass flow controller, allowing the isolation of the single controller in case of malfunctions without interrupting of the experimental

activity. A filter is located after each controller in order to eliminate possible gas impurities that could damage the cell. The test bench has dedicated mass flow controllers, each of them is designed for a specified gas and flow rate range, however it is possible to feed the mass flow controllers also with gases different from the designed ones with appropriate flow rate corrections given by the manufacturer.

The humidification system for the fuel flow is constituted by a Controlled Evaporator Mixer (CEM). The CEM system is based on liquid water injection; the liquid water flow (controlled with a liquid flow controller) is mixed with the dry gas flow in a special valve, the dry gas flow acts as a carrier gas and transports the liquid to the evaporator-mixer where vaporization take place. The evaporator mixer is electrically heated to the vaporization temperature set by the operator in the control software; the vaporization temperature is a function of water and gas flow rates. Piping exiting CEM is maintained at 120 °C with electrical resistances to avoid water condensation and converge in the fuel feeding pipe. The demineralized water used for humidification is stored in a dedicated tank which is maintained at constant pressure (1.2 bar absolute) using nitrogen in order to ensure a sufficient pressure though the water level decreases to overcome the pressure drops of the CEM circuit.

The acquisition and control system is constituted by data acquisition boards (National Instruments) and a control software (LabVIEW-based). The data acquisition boards receive signals from thermocouples, mass flow controllers, CEM, electronic loads, voltage probes and transmit the elaborated signals to the control software installed in a dedicated computer. The software registers all the incoming signals and allows the control of set-point values of the instruments (i.e., oven temperature, gases and water flow rates, CEM temperature and cell current/voltage).

Two types of experiments can be performed in the SOC test-rig:

- Current-voltage measurements: experiments can be performed by imposing either the current (galvanostatic mode) or the voltage (potentiostatic mode) and measuring the current–voltage characteristics of SOCs. During experiments, the current/voltage is varied with desired steps by using an electronic load (PLZ 664, Kikusui, Japan). The current is generated with a DC power supply (SM 30-100, Delta Elektronica, The Netherlands).

- Electrochemical Impedance Spectroscopy (EIS) measurements: AC impedance measurements are performed on the cells by using a Gamry impedance analyzer (FC 350, Gamry Instruments, USA) in galvanostatic mode that modulates the current of the electronic load. Different current levels, amplitudes of variation of the current and frequency ranges can be applied during measurements. Data acquisition is performed by Gamry software.

4.2 Experimental procedures

Two types of commercial planar circular-shaped fuel electrode-supported solid oxide cells were characterized (H.C. Starck, Germany). The cells have a diameter of 80 mm with an active surface area of ~ 47 cm^2. The cells have identical fuel electrode and electrolyte with a different air electrode. Fuel electrodes consist of a porous 5-10 μm thick nickel/zirconia cermet (Ni/8YSZ) supported on a 450-550 μm thick Ni/8YSZ substrate, and the electrolytes of a 4-6 μm dense layer of 8YSZ. In one configuration, the air electrode consists of a porous double layer made by a 15-30 μm thick lanthanum strontium manganite/zirconia (LSM/8YSZ) composite with 15-30 μm of pure LSM current collector layer, in the other of a porous 30-60 μm thick lanthanum strontium cobalt ferrite (LSCF) layer with a 2-4 μm thick yttria doped ceria (YDC) blocking layer. For simplicity, the cell with LSCF air electrode is referred to as "cell A" while the one with the LSM/YSZ air electrode is "cell B" in the following of this dissertation. Cell characteristics, given by the producer, are summarized in *Table 4.1* and *Table 4.2*.

Table 4.1 – Cell A features

Active Area	47	cm^2
Anode support layer (NiO/YSZ)	465-555	Mm
Functional layer (NiO/YSZ)	5-10	μm
Electrolyte (YSZ)	6	μm
Barrier layer (YDC)	2-4	μm
Cathode functional layer (LSCF)	30-60	μm

Table 4.2 – Cell B features

Active Area	47	cm^2
Anode support layer (NiO/YSZ)	465-555	μm
Functional layer (NiO/YSZ)	5-10	μm
Electrolyte (YSZ)	6	μm
Cathode layer (Ni/LSM-LSM)	30-60	μm

The microstructural characteristics of the electrodes that will be used in the models are assumed from the literature, where characterizations are obtained by 3D reconstruction using FIB-SEM

techniques (Lanzini et al. 2009, Vivet et al. 2011). In particular, the estimated volume fractions of the solid phases reported in the literature for typical Ni/YSZ, LSM/YSZ and LSCF electrodes range between 40-50% (Ni), 45-50% (LSM), and 50-60% (LSCF) (Godula-Jopek 2015).

In all the experiments, the fuel electrode was fed with 500 NmL min^{-1} of gas composed by mixtures of either H_2/H_2O or CO/CO_2. The absolute humidity values of the H_2/H_2O mixture were 35-50-65-70 vol. % for the calibration tests and 20-35-50-65-80 vol. % for the validation ones (see *Section 4.3*), while the CO_2 fraction values in the CO/CO_2 mixture were 50-70 vol. %. The oxygen electrode was fed with 1500 NmL min^{-1} of dry air. Experiments were carried out at 800 °C and 850 °C, being the temperature values measured near the center of the cell on the fuel electrode side at the beginning of each i-V characterization and EIS measurement. The design of the experimental session of the calibration tests is presented in *Table 4.3*.

Table 4.3 – Experimental session with extrapolated ASR, R_{Ohm} and measured OCVs

H_2 %	H_2O %	CO %	CO_2 %	Temperature [°C]	ASR SOFC [Ωcm²]	ASR SOEC [Ωcm²]	R_{Ohm} SOFC [Ωcm²]	R_{Ohm} SOEC [Ωcm²]	OCV [mV]
Ni/YSZ – YSZ – YDC – LSCF (cell A)									
50	50	0	0	800	0.32	0.31	0.161	0.155	922
65	35	0	0	800	0.32	0.34	0.155	0.156	947
35	65	0	0	800	0.34	0.32	0.166	0.162	894
Ni/YSZ – YSZ – LSM/YSZ – LSM (cell B)									
50	50	0	0	800	0.51	0.48	0.162	0.151	919
50	50	0	0	850	0.35	0.35	0.115	0.107	902
30	70	0	0	850	0.40	0.37	-	0.118	866
0	0	50	50	800	0.75	0.76	0.167	0.163	928
0	0	30	70	800	0.93	0.78	-	0.183	896
0	0	50	50	850	0.49	0.47	0.139	0.139	902
0	0	30	70	850	0.62	0.53	-	0.149	870

Each experiment was performed in galvanostatic mode and current-voltage characteristics were obtained by varying the current with steps of 1 A (hold for 60 s each) using an electronic load. The AC impedance measurements were carried out using a Gamry impedance analyzer in galvanostatic mode that modulated the current of the electronic load. A current density of 0.25 A cm^{-2} (0.02 A cm^{-2} amplitude of variation) was applied during impedance measurements from 5 kHz to 10^{-1} Hz. EIS data acquisition was done with Gamry Framework software.

4.3 Experimental results

The polarization curves obtained from the experimental tests of *Table 4.3* are shown in *Figure 4.4* and *Figure 4.5*, together with the simulated curves (see *Section 4.4*) and the calculated power density.

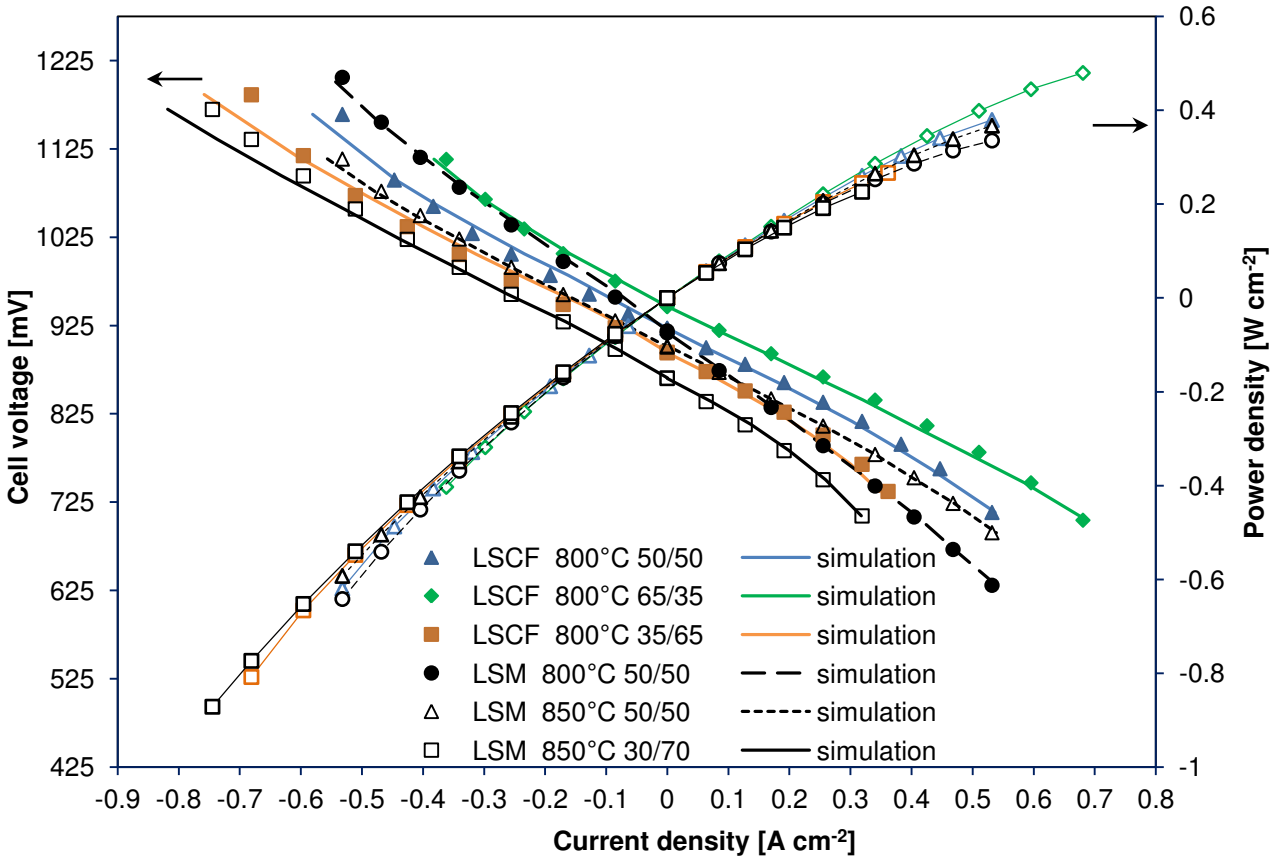

Figure 4.4 – Experimental and simulated polarization curves for SOEC/SOFC modes with H_2/H_2O mixtures.

In the figures, the cell current density shown on the axis of abscissae represents a mean value expressed as the ratio between the total current and the active area of the cell, and the power density shown on the axis of ordinates is calculated as the product between current density and measured voltage. Negative values of the power density indicate that the cell is consuming electricity, as it is working in SOEC mode. *Table 4.3* reports the measured OCVs, the area specific resistance (ASR) – evaluated from the linear region of experimental i-V curves at 25% of Reactant Utilization (RU) – and the Ohmic resistance – evaluated from impedance spectra – of each test in both SOFC and SOEC modes.

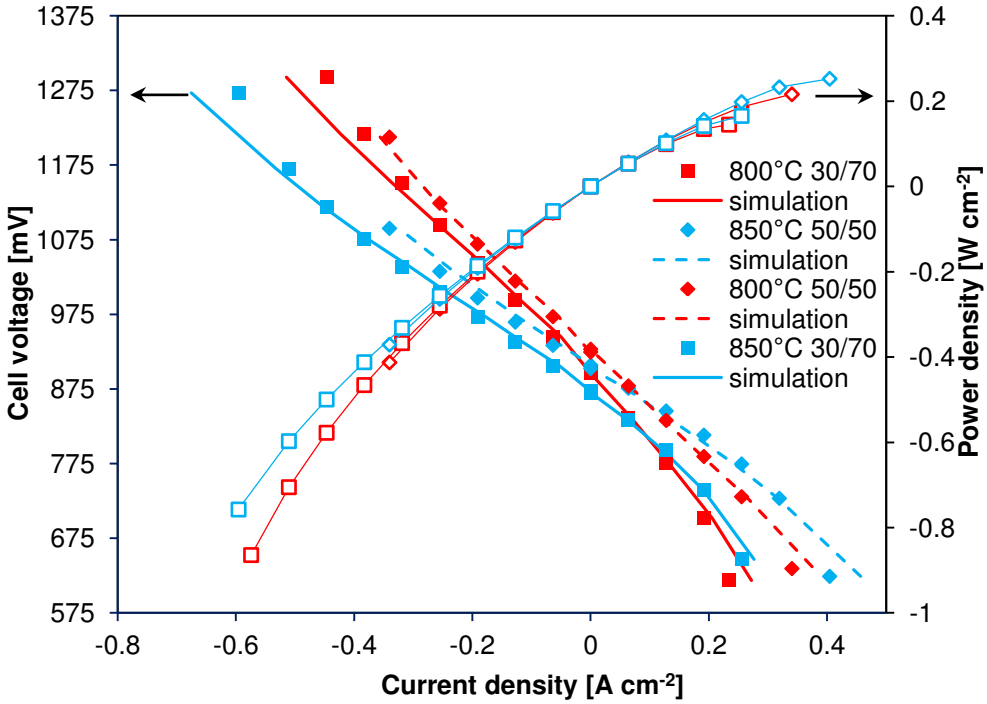

Figure 4.5 – Experimental and simulated cell B polarization curves for SOEC/SOFC modes with CO/CO_2 mixtures.

The impedance diagrams obtained from the AC characterization of the cells are shown in *Fig. 4.6*, *Fig. 4.7* and *Fig. 4.8*. The values of the Ohmic resistance of the cells (see *Table 4.3*) have been identified from the intersection of the high frequency impedance arc with the real axis of the plots, while the total resistance of the cell is given by the intersection with the low frequency arc. The differences between SOFC and SOEC Ohmic resistances evaluated for the same cell at the same temperature are negligible (7.5% maximum relative difference) and can be ascribed to experimental errors in the AC measurements.

The cell with the LSCF air electrode showed better performance than the LSM cell in both fuel cell and electrolysis operation modes and for all the gas compositions investigated (see *Figure 4.4* and *Table 4.3*). In particular, the ASR of cell A at 800 °C 50/50 H_2/H_2O was about 1.6 times lower than that of cell B in both SOFC/SOEC modes, and still lower than the ASR of cell B test at 850 °C. The SOFC and SOEC polarizations of the LSM cell were almost symmetric with both investigated fuel mixtures, while the LSCF cell showed higher losses in the electrolysis mode at high current density. This is in agreement with the literature that reports asymmetric polarizations for LSCF electrodes (Marina et al. 2007). This behavior can be attributed to the depletion of oxygen vacancies at the electrode/electrolyte interface that occurs

under SOEC mode. The air electrode shows a limiting current behavior under anodic polarization because the oxygen transport is slowed down by the depletion of vacancies; this effect is evident in highly oxygen deficient materials, as LSCF above 600 °C, while is less discernible for LSM that has an ionic conductivity of several orders of magnitude lower than LSCF (Marina et al. 2007, Svensson et al. 1998). At a current density of 0.5 A cm^{-2} (RU ~ 70%) the 50/50 H_2/H_2O test on cell A showed a difference of 34 mV between SOEC and SOFC total overpotential against only 2 mV of cell B in the same operating conditions. It must be emphasized that the effect of the back-flow diffusion can favor SOEC operation by generating new reactant at the cell border; therefore with a sealed-housing testing rig it could be expected an even worse behavior of the cells in SOEC at high RU. In *Fig. 4.6* is highlighted the asymmetrical behavior of the LSCF cell, which had lower total cell resistance in SOFC mode at all the tested RUs. The increase of the total cell resistance observed in *Figure 4.6* in both operational modes with increasing RU is due to enhanced conversion resistance (low frequency arcs are connected to fuel conversion phenomena (Hauch 2007)).

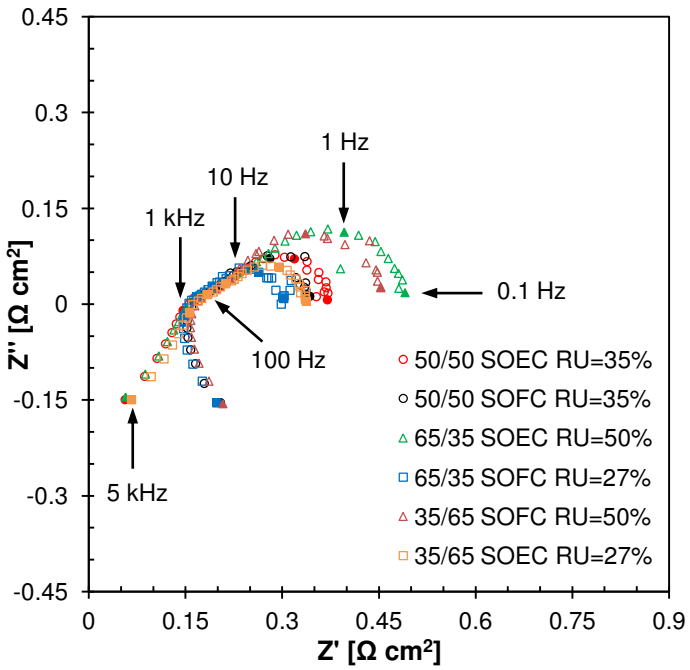

Figure 4.6 – Impedance diagrams of cell A (LSCF air electrode) for H_2/H_2O tests at 800 °C.

The LSM cell tested with CO/CO_2 mixtures showed worse performance than in the respective H_2/H_2O tests, as shown in *Figure 4.7*. The calculated ASR for CO/CO_2 tests are from 1.3 (50/50 SOEC test at 850 °C) to 1.6 (50/50 SOEC test at 800 °C) times higher with respect to the ASR of the corresponding H_2/H_2O experiments. The R_{Ohm} values (see *Table 4.3*) are higher in CO/CO_2

tests; the difference accounts from the 2% (50/50 SOFC test at 800 °C) to the 27% (50/50 SOEC test at 850 °C) of the total ASR increase from hydrogen to carbon tests. Therefore, most of the performance loss of cell B with CO/CO_2 mixtures can be attributed to the higher activation losses related to the slower kinetics of CO/CO_2 reactions (see *Section 4.4*) and to a lesser extent also to the different molecular diffusivities of the chemical species. The impedance diagrams for 50/50 tests of cell B (*Figure 4.7*) show a more pronounced difference in the shape of the impedance arcs from SOFC to SOEC spectra with CO/CO_2 mixtures, due to the different charge transfer kinetics and diffusivity between H_2/H_2O and CO/CO_2 mixtures.

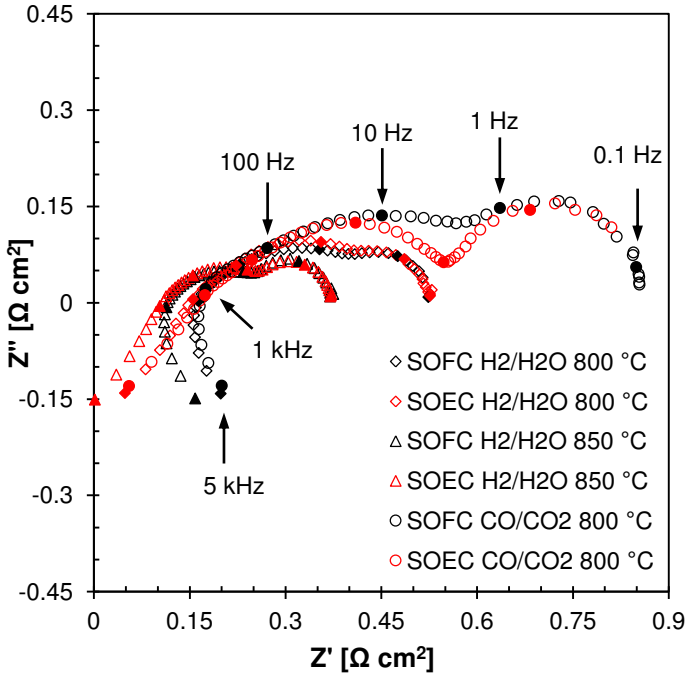

Figure 4.7 – Impedance diagrams for 50/50 cell B tests at RU=35%.

The increase of the temperature had a positive effect on the performance of the cells, reducing the voltage losses in all the tested conditions. The reduction of the ASR from 800 °C to 850 °C tests on cell B ranges from 27% to 38%. The effect of the temperature is shown in *Fig. 4.7* and *Fig. 4.8*, where the 850 °C spectra of 50/50 H_2/H_2O and CO/CO_2 tests show lower Ohmic and total resistances with respect to 800 °C tests carried out under the same gas feeding conditions and at same reactant utilization.

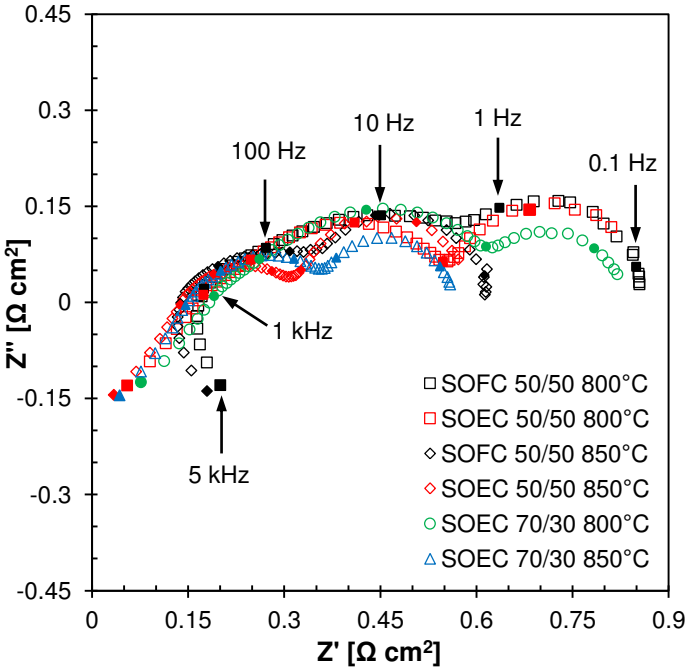

Figure 4.8 –Impedance diagrams of cell B for CO/CO_2 tests.

4.4 Single cell model validation

4.4.1 Model calibration

The model calibration has been performed through the identification of the values of the activation parameters γ_{air} and γ_{fuel} (see equation (3.56) and (3.57) in *Chapter 3*) which ensure the best fitting of the simulated polarizations to the experimental i-V curves. The best-fitting has been identified by minimizing the root-mean-square error (RMSE) between experimental and simulated i-V characteristics.

The simulated polarizations obtained using the best-fitting parameters are shown in *Figure 4.4* and *Figure 4.5*. In *Table 4.4* and *Table 4.6* the best-fitting parameters have been grouped for operation mode and type of mixture, and for each group a mean value of the parameters has been calculated. The mean values are reported in the tables, together with the relative standard deviation (RSD) of the mean value as a qualitative index of the dispersion of the fitting results. The parameters found through the calibration must be considered mainly as qualitative indicators of the activation behavior of the cells, while a detailed quantitative investigation of the activation phenomena is beyond the scope of this work. The results of the calibration are analyzed in detail in the following sections.

Fuel electrode parameters

The kinetic parameters of the Ni/YSZ electrode resulting from the model calibration are reported in *Table 4.4*.

The γ_{fuel} resulting from the fitting of H_2/H_2O polarizations are very similar (RSD $\leq$ 10%) for both SOFC and SOEC curves. The mean γ_{fuel} evaluated from the calibrations on SOFC H_2O/H_2 experiments is slightly higher for cell A (12.7×10^9 A m^{-2}) with respect to cell B (9.4×10^9 A m^{-2}); however this difference is lower than the maximum variation of γ_{fuel} in cell A calibrations (4×10^9 A m^{-2}) and can thus be considered included in the variability range of the fuel parameter. Also, in the SOEC calibrations on H_2O/H_2 experiments the difference between the mean γ_{fuel} of cell A and B is lower than the parameter variability. It is worth noting that even if cell A and B have the same fuel electrode materials and thickness, they are coming from different batches, therefore slight dissimilarity in the performance can be expected due to different microstructures. Therefore, the activation parameter of the Ni/YSZ electrode tested with H_2O/H_2 mixtures is exclusively describing fuel electrode reactions; otherwise it would be clearly affected by the

variations of the kinetics of the air electrode when the material changes from LSCF (cell A) to LSM/YSZ (cell B) with operating conditions of the fuel electrode being equal.

Table 4.4 – Best-fitting parameters of Fuel Electrode (Ni/YSZ)[a]

		H_2O/H_2		CO_2/CO	
SOFC	800 °C 50/50 (cell A)	800 °C 35/65 (cell A)	800 °C 65/35 (cell A)	800 °C 50/50 (cell B)	800 °C 70/30 (cell B)
	11.75	**11.25**	**15.25**	**3.25**	**2.75**
	800 °C 50/50 (cell B)	850 °C 50/50 (cell B)	850°C 70/30 (cell B)	850 °C 50/50 (cell B)	850 °C 70/30 (cell B)
	9	**10**	**9.25**	**4.75**	**4.25**
$\overline{\gamma}_{fuel}$	**10.25 (RSD[b] ≈ 10%)**			**3.75 (RSD[b] ≈ 24%)**	
SOEC	800 °C 50/50 (cell A)	800 °C 35/65 (cell A)	800 °C 65/35 (cell A)	800 °C 50/50 (cell B)	800 °C 70/30 (cell B)
	37.5	**30**	**35**	**9**	**10**
	800 °C 50/50 (cell B)	850 °C 50/50 (cell B)	850 °C 70/30 (cell B)	850 °C 50/50 (cell B)	850 °C 70/30 (cell B)
	33.5	**33.75**	**29**	**13**	**10**
$\overline{\gamma}_{fuel}$	**31.75 (RSD[b] ≈ 7.5%)**			**10.5 (RSD[b] ≈ 16%)**	

[a] values in 10^9 A m^{-2} [b] Relative Standard Deviation

Table 4.4 shows that γ_{fuel} is not affected by the fuel fraction in both H_2O/H_2 and CO/CO_2 calibrations. If we consider that the fuel fraction of the gas mixture covers a wide range of values (from 30% to 70%), it is demonstrated that the dependency of the exchange current density on the fuel composition is correctly described by the terms of Eq. (3.57) (see *Chapter 3*) that are dependent of the TPB molar fractions and that the γ_{fuel} does not take in account the effect of the concentrations. The temperature does not seem to affect the γ_{fuel} resulting from the fitting of H_2/H_2O polarizations, while the CO_2/CO calibrations in SOFC mode yielded slightly higher γ_{fuel} values at 850 °C. However, a broader range of temperatures should be considered to better investigate the effect on the fuel parameter.

The γ_{fuel} of SOEC tests is always higher than in SOFC tests (about 3 times for both H_2/H_2O and CO/CO_2 mixtures) and since it is a constant of the first order in Eq. (3.57) (see *Chapter 3*), also the exchange current density in SOEC operation at the Ni/YSZ electrode is higher with almost the same ratio between the dual operations. This result is confirmed by the study of Marina et al. (2007) on reversible operation of Ni/YSZ electrode with H_2/H_2O mixtures, which reports SOEC exchange current densities 2-3 times higher with respect to SOFC operation.

Further confirmation of the physical consistency of fuel electrode parameters comes from the mean values of the exchange current density for the H_2/H_2O SOFC tests calculated with the model (shown in *Table 4.5*), which are included between 3000 and 6000 A m^{-2}, that are values compatible with 5300 A m^{-2} usually assumed in the literature (Chan et al. 2001, Ni et al. 2006b). Moreover, also the fuel parameters obtained for SOFC operations with H_2/H_2O mixtures are included in the range of values usually found in the literature ($\gamma_{anode,SOFC}$ = 5.5×10^{8} A m^{-2} to 5.5×10^{10} A m^{-2} (Leonide 2010)).

Table 4.5 – Mean exchange current density of fuel electrode in SOFC operation

Ni/YSZ – SOFC – H_2/H_2O	$\bar{\imath}_{0fuel}$ **[A m^{-2}]**
800 °C 50/50 cell A	3957
800 °C 35/65 cell A	3933
800 °C 65/35 cell A	3148
800 °C 50/50 cell B	3083
850 °C 50/50 cell B	5952
850 °C 30/70 cell B	4471

The fuel electrode parameters of CO/CO_2 calibrations are slightly more dispersed than that of H_2/H_2O tests; however the higher values of RSD should not be misleading, since it is a relative indicator calculated on a lower number of γ_{fuel} values. The values of the kinetic parameters of the Ni/YSZ electrode obtained from CO/CO_2 curves are about 3 times lower than in H_2/H_2O tests, as expected from the slower kinetics of CO/CO_2 reactions reported in the literature. A study by Holtappels et al. (1999) has shown considerably slower kinetics for CO oxidation on Ni/YSZ electrodes with respect to the hydrogen oxidation reaction, and in the work of Matsusaki et al. (2000) an electrochemical oxidation rate of H_2 from 2 to 3 times higher than that of CO in the

1023-1273 K temperature range is reported. In the paper of Ebbesen et al. (2012), slower reduction and oxidation rates are reported for CO/CO_2 mixtures compared to H_2/H_2O mixtures tested on Ni/YSZ electrodes; the slower kinetics are explained by different reaction mechanisms, which involve proton diffusion on the nickel surface as one the major reaction paths for H_2/H_2O mixtures, whereas in the CO/CO_2 reactions is involved the migration of O^{2-} ions, which are less mobile than H^+ ions and can also interfere with impurities segregated on the YSZ surface.

Air electrode parameters

The values of γ_{air} are shown in *Table 4.6*. The activation parameters of the LSM electrode do not change significantly from H_2/H_2O to CO/CO_2 tests, consistent with the fact that the reaction at the air electrode is fully independent of the fuel electrode reaction. The maximum variation of γ_{air} in SOFC calibrations of cell B is 3.8×10^9 A m^{-2} for CO/CO_2 curves and 0.8×10^9 A m^{-2} for H_2/H_2O experiments, while the difference between the mean γ_{air} of H_2/H_2O and CO/CO_2 tests is 0.3×10^9 A m^{-2}, a value lower than the variability range of the air parameter. The activation parameters of the LSM/YSZ electrode are more dispersed in electrolysis calibrations, with a mean γ_{air} of 10.25×10^9 A m^{-2} for CO/CO_2 curves and 9.3×10^9 A m^{-2} for H_2/H_2O experiments. Also in this case, the difference between the mean γ_{air} of the two mixtures is compatible with the variability of the parameter.

The LSCF electrode shows kinetic parameters an order of magnitude higher than the LSM ones, in agreement with the literature that reports higher activity for air electrodes made by mixed conductors, such as LSCF, when compared to the LSM ones (Marina et al. 2007). Air electrode parameters of LSCF are lower in SOEC operations, in agreement with the slower kinetics of oxygen reactions in the electrolysis operation for this type of material, due to the depletion of oxygen vacancies which lead to higher activation losses in SOEC and to an asymmetrical dual operation, as reported in *Section 4.3*. Finally, the temperature does not seem to affect clearly the γ_{air}, as observed for the fuel electrode.

Table 4.6 – Best-fitting parameters of Air Electrode [a]

	LSM/YSZ (cell B)		**LSCF-YDC (cell A)**
	CO_2/CO	**H_2O/H_2**	**H_2O/H_2**
SOFC	800 °C 50/50	800 °C 50/50	800 °C 50/50
	8.4	**8.4**	**300**
	800 °C 70/30	850 °C 50/50	800 °C 35/65
	10	**8**	**300**
	850 °C 50/50	850 °C 70/30	800 °C 65/35
	6.2	**7.6**	**250**
	850 °C 70/30		
	6.2		
$\overline{\gamma}_{air}$	**7.8 (RSD[b] ≈ 13%)**		**283 (RSD[b] ≈ 10%)**
SOEC	800 °C 50/50	800 °C 50/50	800 °C 50/50
	14	**10**	**120**
	800 °C 70/30	850 °C 50/50	800 °C 35/65
	5.5	**9**	**120**
	850 °C 50/50	850 °C 70/30	800 °C 65/35
	12	**9**	**80**
	850 °C 70/30		
	9.5		
$\overline{\gamma}_{air}$	**9.8 (RSD[b] ≈ 13%)**		**105 (RSD[b] ≈ 20%)**

[a] Values in 10^9 A m^{-2} [b] Relative Standard Deviation

4.4.2 Model validation

Once the activation parameters are established through calibration, the model validation is performed by comparing simulated i-V curves with experimental polarizations obtained from two cells with the same characteristics of cell A and B tested in the experimental setup described in *Section 4.1*. The cells were tested in the reversible operation with fuel mixtures composed by H_2/H_2O with absolute humidity of 20-35-50-65-80 vol. % at 800 °C. The Ohmic resistances of the simulated curves have been derived from EIS data analysis, while the model has been applied by using the mean values of activation parameters shown in *Table 4.4* and *Table 4.6*. The validation results are shown in *Fig. 4.9* and *Fig. 4.10*.

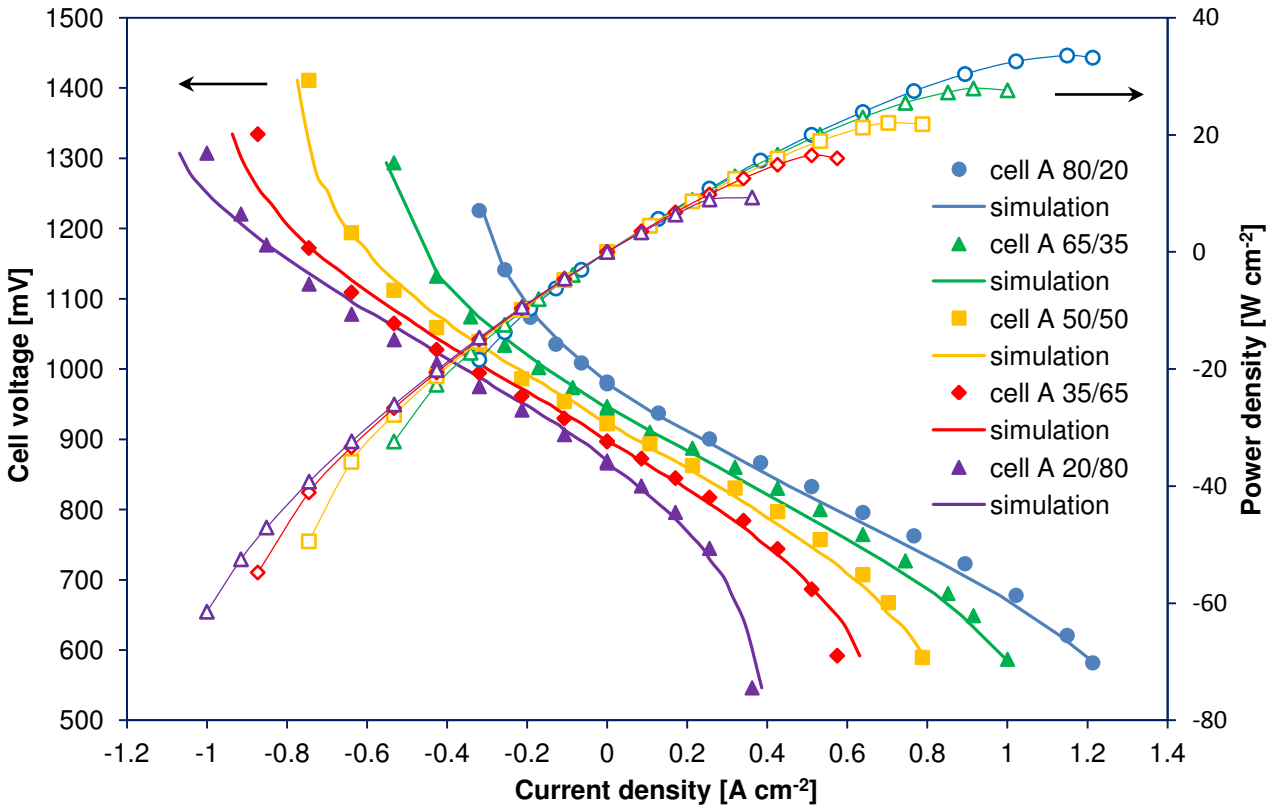

Figure 4.9 – Validation curves for cell A tested with H_2/H_2O mixtures

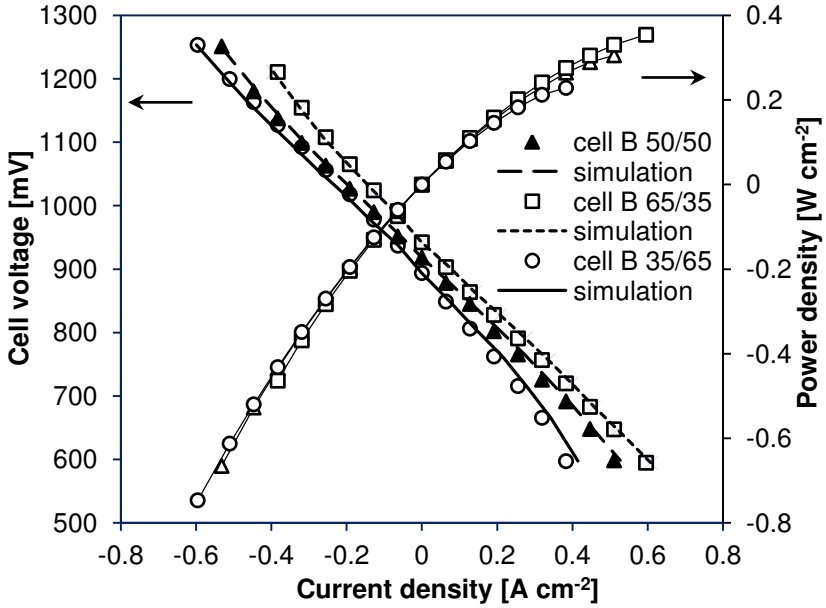

Figure 4.10 – Validation curves for cell B tested with H_2/H_2O mixtures.

The figures show a good agreement between experimental and simulated curves. The maximum error observed between the experimental and numerical data is 6.8% at 1.3 V for 80% H_2O, 20% H_2 gas mixture (cell A test).

4.4.3 Simulation results

The results of the simulations are presented for the dual operation with 50/50 H_2O/H_2 mixture.

The composition of the total losses for the two types of cell is shown in *Figure 4.11*. The diffusion losses at the air electrode are negligible in all the cases, since the air electrode is sensibly thinner than the fuel one. The conversion overpotential of the air electrode is also very small, because the oxygen utilization is sensibly lower than the fuel one in SOFC, while in SOEC the air acted as a sweep gas. The losses related to the reactant conversion at the fuel electrode show a rising predominant role with the increase of the cell radius; in particular, the SOFC fuel conversion losses increase along the radius from 0 to 45% for cell A and from 0 to 30% for cell B, while in SOEC mode the calculated increase is from 0 to 30% for cell A and from 0 to 23% for cell B. Air electrode activation losses of the LSCF cell are at most the 10% of the total losses in SOEC, while are negligible in SOFC, and the activation losses of the LSM electrode of cell B represent up to 35% of the total losses in SOFC mode.

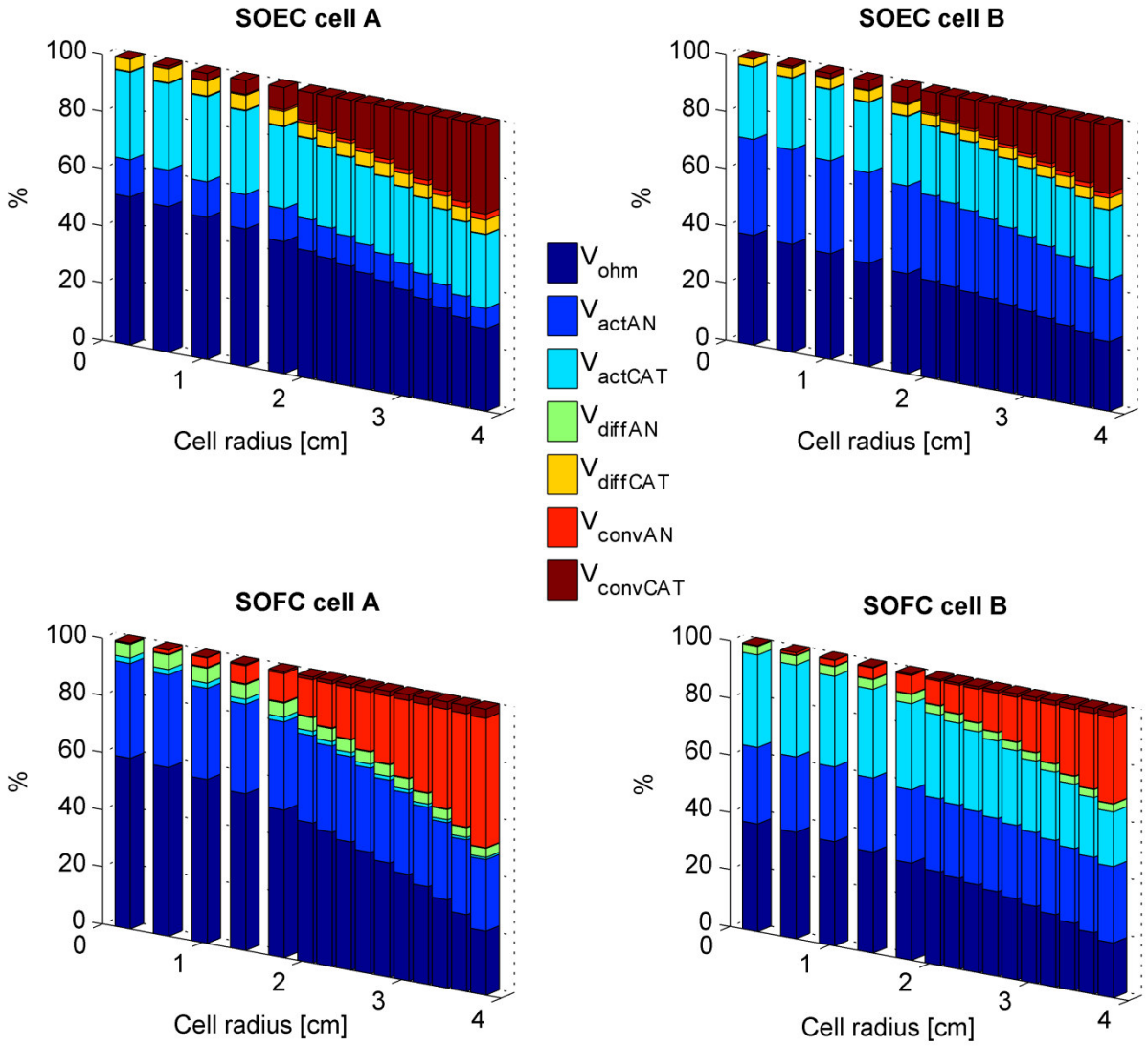

Figure 4.11 – Composition of the voltage losses in SOFC and SOEC operation for cells A and B.

The temperature distribution inside the cell is presented in *Fig. 4.12*. The model-calculated temperature gradients between cell center and border are modest (less than 3 °C), and the temperature difference between anode and cathode surface is almost negligible (less than 0.2 °C). Temperature distribution has a minimum in the cell center in SOEC mode, when the cell operates under the thermoneutral point (i.e., when the heat consumed by the reactions is higher than that produced by the losses inside the cell), while has a maximum in the center in SOFC mode.

The calculated temperature distribution is representative of theoretical thermal operating conditions of a solid oxide cell working in a controlled environment in which the imposed boundary conditions strongly constrain the temperature, as in the test-rig where the experiments were performed.

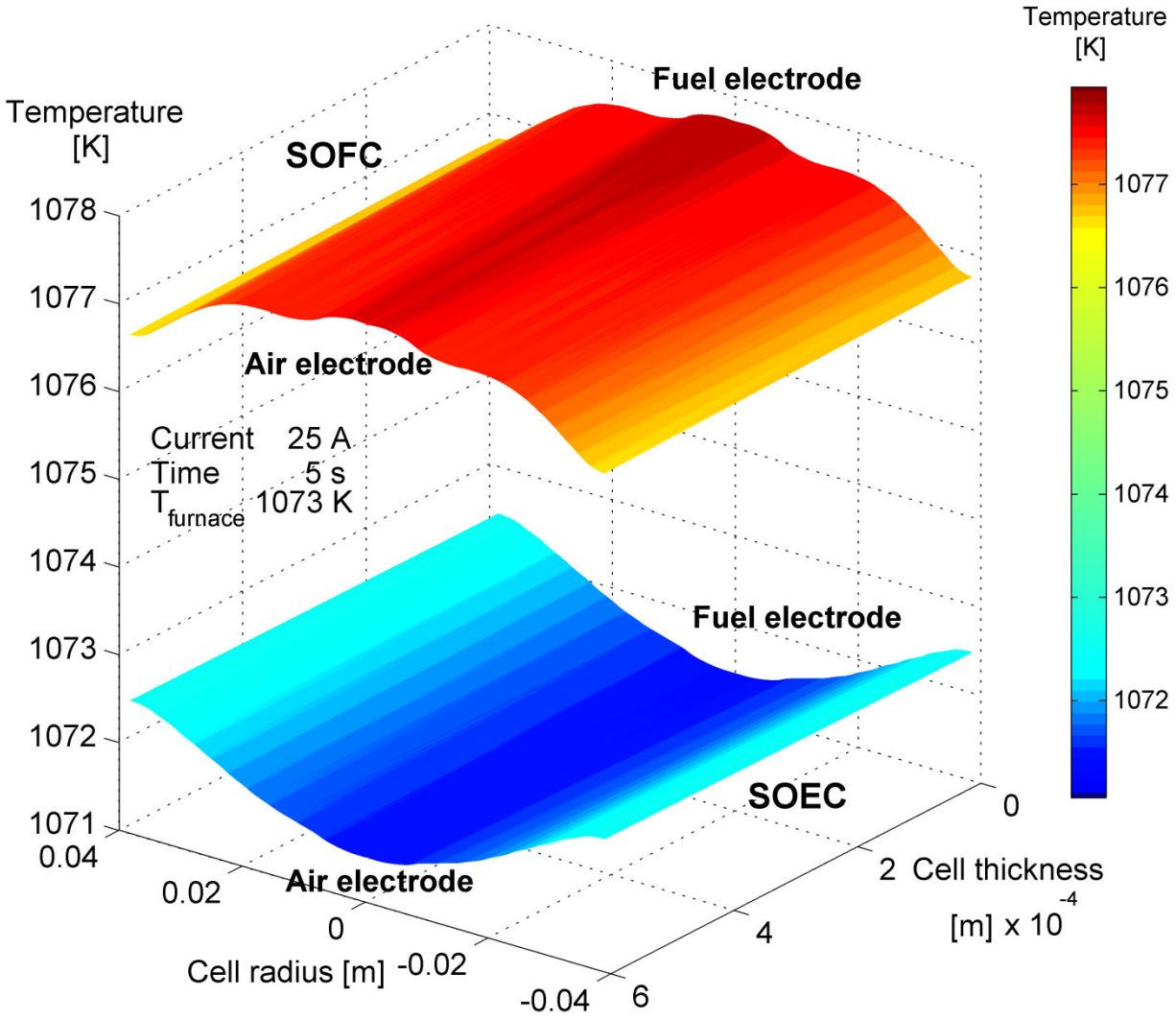

Figure 4.12 – Distribution of the temperature in the cross section of cell A in dual operation. Simulation performed at 0.5 A cm^{-2} for 50/50 H_2/H_2O fuel mixture at 800 °C initial temperature. Temperature profile drawn after 5 second simulation.

4.5 Conclusions

In this Chapter, the integrated single-cell thermo-electrochemical model for the simulation of current–voltage characteristics of planar rSOCs presented in *Chapter 3* has been calibrated and validated on experimental data.

Two types of commercial planar fuel-electrode supported SOC were experimentally characterized through polarization and impedance measurements. The observed asymmetry of the dual operation (i.e., higher losses in SOEC mode for high current densities) for the cell with LSCF air electrode has been highlighted. This type of electrode was found to be more active than LSM in both SOFC and SOEC operation modes.

The model can successfully reproduce *i–V* curves of single SOCs obtained from the experimental characterization of the two types of cells tested with H_2/H_2O fuel mixtures at different reactant fractions and temperatures. The kinetic parameters evaluated from the calibration of the electrochemical model were related to electrode materials and reactions and their physical consistency was verified with the support of literature studies on reversible electrodes and full cells.

Chapter 5

Analysis of SOC-based P2P applications

The scope of this Chapter is the investigation of SOC-based P2P systems. In the first two sections of the Chapter, the detailed investigation of a hydrogen-based P2P solution based on rSOCs is performed. The analysis includes: 1) the evaluation of the system roundtrip efficiency (both energetic and exergetic) and the investigation of its sensitivity toward rSOC operating parameters, and 2) the selection of the operating conditions that are acceptable within the limits of the thermal physical constraints of the SOC imposed by state-of-the art materials. The system analyzed is composed by an rSOC stack and the main auxiliaries: water pumps, gas compressors, compressed H_2 storage tank (and also O_2 in some configurations) and heat recovery exchangers. The rSOC response is simulated by the numerical 2D model implemented in COMSOL Multiphysics and described in *Chapter 3*, based on the validated electrochemistry described in *Chapter 4.* Electrical auxiliaries (i.e., pumps and compressors) are modeled following the thermodynamic approach described in *Chapter 2* directly implemented in the rSOC model. The heat recovery section is modeled through pinch analysis, following the approach described in *Chapter 2,* and calculates the maximum heat recoverable within the system and the minimum heat required from external sources. The heat recovery model is implemented in Matlab and solved as a function called in the rSOC model.

In the analysis, different system configurations are assessed and compared. In particular, ambient vs. pressurized SOC operation and the choice of the oxidant (i.e., pure oxygen vs. air) are discussed. The effects of inlet fluids temperatures, oxidant-to-fuel ratios and oxidant recirculation are also investigated. The final output of the analysis is the selection of optimal operating points that ensure the higher storage (SOEC), re-conversion (SOFC) and roundtrip (rSOC) efficiencies within the boundaries of the SOC thermal constraints. The analysis of the P2P system is performed by simulating the stationary operation in the investigated conditions.

After the assessment of the different P2P configurations, a dynamic analysis is performed on the rSOC to determine the characteristic times of the thermal response of an SRU coupled with variable loads. This analysis provides results that are complementary to the previous stationary analysis, as it allows to investigate the time of intervention required for regulation strategies. The

numerical 3D SRU dynamic model described in *Chapter 3* is applied for the simulation of transient thermo-electrochemical response of the SOC.

Finally, a case study is presented to show the EES application of a SOC-based P2P system for the mitigation of RES fluctuations in a grid-connected wind farm. The P2P system operates in the conditions selected by the analysis presented in the first two section of this Chapter, and the minimization of the imbalance between effective and forecasted wind production is achieved by optimizing the size of the rSOC stack.

5.1 Analysis of a hydrogen-based P2P system: methods

5.1.1 System description

The general schematic of the P2P system is depicted in *Figure 5.1*. In all the configurations analyzed, the system is composed by the rSOC stack, a heat recovery section, a hydrogen storage tank, a hydrogen compressor, and a water pump for feeding the SOEC. If the rSOC is feed with ambient air, an air compressor is also needed to feed the oxygen electrode of the cell, while if the rSOC is operating with pure oxygen, an oxygen compressor and an O_2 storage tank are needed.

Spent fuel recirculation has been imposed in all the conditions analyzed in order to maintain a fixed fuel-to-product ratio at the inlet of the rSOC, as explained in *Section 5.1.2*. The gas stream exiting the stack is a mixture of hydrogen and water steam in both SOEC and SOFC operation. This stream is fully recycled only at open circuit (i.e., when no hydrogen or water is consumed in the SOC), while during operation under current (i.e., H_2 or H_2O consumed by electrochemical reactions) it is only partially recirculated. The fraction of the exiting fuel stream which is not recycled is sent to the heat recovery section, where it is cooled by the inlet streams which are entering the SOC until it reaches the saturation temperature. The saturated stream enters the water condenser where H_2 is separated from H_2O; in SOEC operation the condensed H_2O is fully recycled to the fuel inlet, while in SOFC operation the separated H_2 is recovered. In this way, the unreacted fuel (i.e., H_2 in SOFC and H_2O in SOEC) is completely recycled and the fuel streams that must be provided to the SOC stack either from the ambient (i.e., H_2O for SOEC) or from the gas storage (i.e., H_2 for SOFC) are only those needed to replace the reacted flows.

On the oxygen side of the stack, the gas recirculation has not been considered in the baseline case, in order to maintain the inlet composition at fixed conditions when operating with air. In fact, the effect of an exhaust air recycle is the lowering of the inlet oxygen concentration in SOFC mode, because of the oxygen consumption in the stack, and the increase of its concentration in SOEC mode because of the oxygen release at the anode. Both effects are in principle not desired as a higher oxygen concentration on the anode of SOECs increases the reversible cell voltage, while a lower one on the cathode decreases the reversible voltage of SOFCs. In SOFC applications air recycle is usually performed for thermal purposes to preheat the inlet air by mixing fresh air with hot exhausts; however, in the modeled system the preheating is fully performed in the heat recovery section by maintaining the inlet and outlet flows separated.

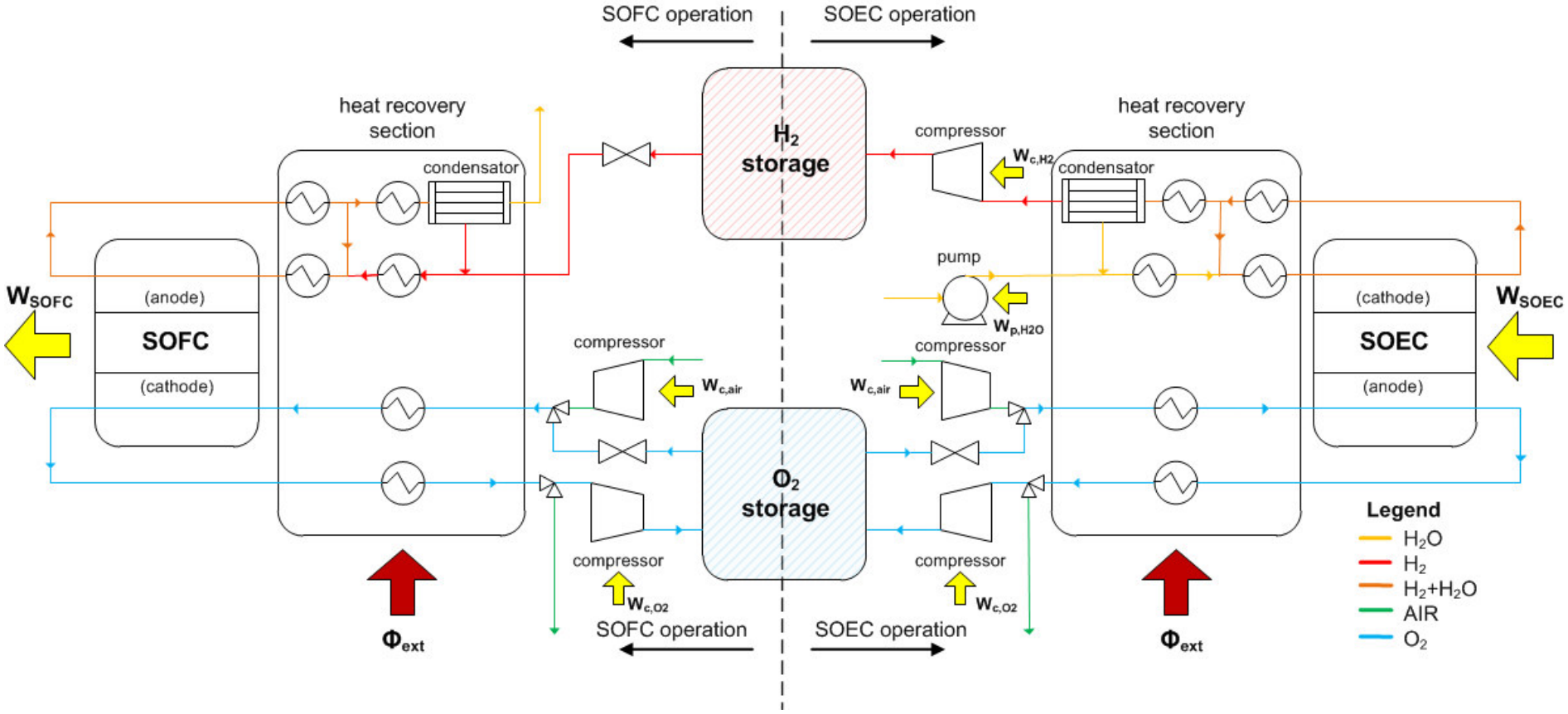

Figure 5.1 – Schematic of P2P system.

In the case of pure oxygen operation, the recycle of the O_2 stream immediately at the stack outlet is possible since it does not modify the composition of the oxygen electrode inlet stream. The recirculation option for both oxygen and air operation has been investigated during the sensitivity analyses on the operating parameters.

In the case of air operation, the fluid is compressed from ambient to stack pressure. When the rSOC is operating at ambient pressure, the air compressor is just a blower that balances the pressure drops of the system. After compression, air is sent to the heat recovery section for the preheating to inlet stack temperature. The exhaust air exiting the rSOC is returned to the ambient after the heat recovery section. In the analysis performed, pressure drops were neglected in the system and thus the compression power is assumed to be zero when the rSOC is operating at ambient pressure.

In the case of pure oxygen operation, in both SOFC and SOEC mode there is always an oxygen stream exiting the stack, as in SOEC mode O_2 is produced in the cell, while in SOFC operation the stack operation never reaches current levels that completely consume the available oxygen. If the O_2 flow exiting the stack is not fully recycled to the stack inlet, it is necessary to compress the stream from stack pressure to storage pressure in order to save all the produced oxygen into the storage and make it available for the SOFC operation. The oxygen stream exiting the stack is thus compressed to the storage pressure after cooling in the heat recovery section in both operation modes if a recycle is not performed. In this way, all the oxygen produced in SOEC operation is fully recoverable in the SOFC. Besides the positive impact on the energy balance of the system, the heat recovery from the oxygen flow exiting the stack also decreases the stream temperature from stack to ambient level allowing energy savings in the compression stage. In fact, the energy consumed in the compression depends on the initial temperature of the compression stage, and a lower stream temperature ensures a lower compression power (see *Chapter 2*). It is worth noting that the compression power also diminishes with the increasing of the SOEC stack pressure, as a lower pressure difference exists between stack and storage. When the system is in SOEC mode, the supply of an oxygen stream to the cell inlet is not strictly necessary from an electrochemical point of view. Moreover, the higher is the inlet oxygen flow, the higher is the outlet anodic flow – as electrochemical O_2 is added to the stream – and consequently the higher is the power required for the oxygen recompression to the storage pressure if a recycle is not performed, except for the case in which stack is operating at the same pressure level of the storage. However, the oxygen flow entering the SOEC anode can play an important role for the thermal control of the stack and thus is not

straightforward to set its value to zero for maximizing the system efficiency. A thorough discussion on this aspect is given later in this Chapter. Moreover, a gas stream entering the anode can assist the oxygen evacuation from the electrode, even if in the SOC model implemented the diffusion limitations in the anode are not considered, since the oxygen electrode is assumed as a boundary layer.

In all the cases analyzed, the stack operating pressure imposed is always lower with respect to that of the O_2 storage, and pressure drops are not considered in the system analysis; thus, the oxygen that is fed from the storage to cell has always a sufficient pressure level to reach the stack. The same consideration is valid for the stored H_2 used in the SOFC. When the gas storage pressure is higher than the operation pressure of the SOC, a pressure reducing valve is considered in the system. The option of power recovery from the gas flowing from the storage to the stack through an expansion turbine has not been considered in the analyzed configurations. This conservative choice has been adopted for both the O_2 flowing from storage to rSOC and the H_2 feeding the stack in SOFC mode. It is worth noting that the expansion of gases reduces their temperature, and thus the use of an expansion turbine upstream the rSOC stack increases the heat required for reactant preheating. Thus, its use is straightforward beneficial only in the case that the rSOC stack is operating enough exothermally to cover all the preheating requirements (i.e., condition reached only in SOFC operation at high currents, but which it is not feasible due to thermal constraints on the cell, as it will be shown in the results); in the other cases simulations have shown that the power recovery is almost completely balanced by the increase of the thermal requirements. For this reason, the gas expansion has not been considered as it increases the plant complexity without providing significant advantages to the system.

All the compressors considered in the system perform an intercooled two-stage compression, with the outlet temperature of the fluid corresponding to the inlet value. Conservatively, the heat removed from the fluid during the compression is assumed to be lost to the ambient.

The gas storage tanks are assumed at constant pressure and ambient temperature, thus all the cold fluids entering the heat recovery section either from environment (i.e., air and water in SOEC operation) or gas storages are at ambient temperature. The fluids are then heated to the imposed inlet temperatures of the rSOC by recovering heat from the gases exiting the stack and by providing heat from an external source, if required. The heat exchanger network has been modeled by pinch analysis to determine the minimum heat needed from an external source. The detailed design of the network has not been addressed in this Thesis, as it is out of the scope of the efficiency analysis for which the model has been built.

The assumptions adopted for the selection of the inlet rSOC conditions and the criteria followed for the choice of fuel and air/oxygen flows are discussed in the next section. Results of the efficiency analysis are presented in *Section 5.2.*

5.1.2 Definitions and assumptions

In this section, the definitions of SOC and system parameters used in the analysis are given and the assumptions adopted are discussed.

In order to evaluate the charging and discharging efficiency of a P2P system, it is first necessary to define a parameter that quantifies the fraction of reactant delivered to the SOC that is converted by electrochemical reactions. In the case of fuel cell operation, this parameter is called fuel utilization (*FU*) and it is defined as the ratio between the molar rate of hydrogen consumed in the oxidation reaction – calculated by Faraday's Law – and the molar flow of hydrogen entering the cell. In electrolysis operation, this parameter is defined as the ratio between the molar rate of H_2O consumed and the inlet molar flow of water entering the cell's cathode. Given a cell current I_{cell}, the molar rate of consumed H_2 (in SOFC) and H_2O (in SOEC) are both calculated by the Faraday's Law (considering the current always positive), and a general definition of the fuel utilization can be written:

$$FU = \frac{\frac{\boldsymbol{I}_{cell}}{2F}}{\boldsymbol{y}_{fuel,in} \cdot \dot{\boldsymbol{n}}_{in,fuel}} \tag{5.1}$$

where $\boldsymbol{y}_{fuel,in}$ is the inlet molar faction of water in SOEC and of hydrogen in SOFC. The definition given above can be also extended to the case of co-electrolysis operation; in this case, the molar flow considered at the denominator is the molar flow of water and carbon dioxide entering the cathode, while the numerator is unchanged because the total current is the sum of the currents "consumed" by H_2O and CO_2 reduction.

When the SOC is operating as fuel cell, a conversion parameter can be defined also for the oxygen delivered to the cell. The oxygen utilization (*OU*) is thus defined as follows:

$$OU = \frac{\frac{\boldsymbol{I}_{cell}}{4F}}{\boldsymbol{y}_{O_2,in} \cdot \dot{\boldsymbol{n}}_{in,oxi}} \tag{5.2}$$

where $\dot{\boldsymbol{n}}_{in,oxi}$ is the total molar flow entering the cathode of the cell. The subscript *oxi* indicates the oxidant flow, which corresponds to the oxygen flow only in the case of pure oxygen

operation, while in the operation with air it takes into account also the nitrogen that is entering the stack.

It is worth noting that all the definitions given above are valid also for the stack, as the cells are assumed to work with the same inlet conditions and to be electrically connected in series, such as the same current is flowing through all the cells. Fuel and oxygen utilization parameters express a theoretical electrochemical constraint of the cell, as a value higher than 100 % cannot be exceeded. If we take into account the realistic operation of fuel cells and electrolyzers, utilization values higher than 70 % are hardly reached in the nominal operation, as local gas diffusion limitations usually arise in the cell over this value leading to a steep increase of the overpotentials that produce a deterioration of cell performance. Moreover, the operation in near-starvation conditions can be detrimental for the durability of the cell especially is SOFC operation, where hot spots arise and the anode environment can become oxidizing for the Nickel in some points of the electrode due to the large amount of water produced in the cell. A high level of oxygen consumption can be even more detrimental for the SOFC, because the hydrogen oxidation reaction can directly consume oxygen atoms from the cell's materials if an insufficient oxygen partial pressure is established at the cathode. In the analysis presented in this Thesis, a nominal fuel utilization of 70 % and an oxygen utilization of 50 % have been fixed. These values are called FU_{nom} and OU_{nom} in the text.

Once the nominal values of the utilization parameters are fixed, it is necessary to establish a constraint either on the cell current or on the molar fuel flow entering the cell. In fact, as the definitions of FU and OU suggest, when the nominal values are imposed only the ratio between the cell current and the inlet molar flow of the fuel is fixed, and the current can theoretically assume any value if sufficient fuel is provided to the cell. An ideal condition for an SOC would be to have a flat polarization characteristic, in which the current value does not affect the overpotential losses and the operating point can be chosen arbitrarily by varying the current to reach a desired power value and adjust the fuel flow consistently to maintain the nominal FU and OU. However, in real SOCs the current value affects the total cell/SRU overpotential, which increases with the increasing current. A realistic value for the cell current can be considered 1 A/cm^2 for 70 % of reactant utilization, which also corresponds to the target value reported by Mogensen et al. (2012) that can promote the economic feasibility of SOECs. Once a nominal cell current is fixed, the total fuel and oxidant inlet molar flows can be calculated as:

$$\dot{\boldsymbol{n}}_{in,fuel} = \frac{\frac{\boldsymbol{i}_{cell,nom} \cdot A_{cell}}{2F}}{\boldsymbol{y}_{fuel,in} \cdot \boldsymbol{FU}_{nom}} \tag{5.3}$$

$$\dot{\boldsymbol{n}}_{in,oxi} = \frac{\frac{\boldsymbol{i}_{cell,nom} \cdot A_{cell}}{4F}}{\boldsymbol{y}_{oxy,in} \cdot \boldsymbol{OU}_{nom}} \tag{5.4}$$

A cell area (A_{cell}) of 100 cm^2 has been chosen in the analysis by considering square cells of 100 × 100 mm. In order to fix the inlet molar flows, the molar fraction of the inlet fuel/oxidant has still to be established. For SOEC operation, reducing conditions must be maintained on the fuel electrode during operation to avoid nickel oxidation. This is typically accomplished by including 10 % or a higher molar fraction of hydrogen in the inlet fuel flow. In the analysis presented, the H_2 molar fraction at the cathode inlet of the SOEC has been fixed at 10 %, and consequently the water molar fraction has been fixed at 90 %. In SOFC operation, an inlet H_2 fraction of 90 % has been assumed in order to maintain symmetrical conditions with respect to the SOEC operation. In this way, a fixed fuel-to-product molar ratio of 9 is imposed at the cell inlet. Air has been considered for the calculation of $\dot{\boldsymbol{n}}_{in,oxi}$, with an oxygen molar fraction of 21 %. In the case of pure oxygen operation, the molar flow imposed in the simulations has been the same of the air in order to compare the two options with the SRU operating with the same oxidant flow.

The fuel molar flow was maintained constant in all the cases considered in the analysis to enforce the *FU* constraint, as the symmetric assumptions made ensure that for a current of 1 A/cm^2 the *FU* is always 70 % in both SOEC and SOFC operation. The oxidant molar flow was varied in the analysis, as only in the case of SOFC operation it is necessary to enforce the *OU* constraint. The oxidant molar flow rate imposed has been related to the fuel molar flow through the $\boldsymbol{\lambda}$ index, defined as follows:

$$\boldsymbol{\lambda} = \frac{\dot{\boldsymbol{n}}_{in,oxi}}{\dot{\boldsymbol{n}}_{in,fuel}} \tag{5.5}$$

The variation of the oxidant flow has been imposed in the analysis by changing the $\boldsymbol{\lambda}$ index. A value of 3 has been imposed in the base case, and it can be easily demonstrated that $\boldsymbol{\lambda}$ = 3 corresponds to the OU_{nom} with air.

Once the constraints on *FU*, *OU* and cell current are imposed in the system, the extent of exhaust fuel recirculation at the fuel electrode is imposed in order to maintain the fixed fuel-to-product ratio of 9 at the inlet of the rSOC:

$$\dot{\boldsymbol{n}}_{rec,fuel} = \frac{\dot{\boldsymbol{n}}_{in,fuel} \cdot \left(1 - \boldsymbol{y}_{fuel,in}\right)}{\left(1 - y_{fuel,out}\right)} = \frac{\dot{\boldsymbol{n}}_{in,fuel} \cdot \left(1 - \boldsymbol{y}_{fuel,in}\right)}{\left(\frac{\dot{\boldsymbol{n}}_{in,fuel} \cdot \left(1 - \boldsymbol{y}_{fuel,in}\right) + \frac{\boldsymbol{I}_{cell}}{2F}}{\dot{\boldsymbol{n}}_{in,fuel}}\right)} \tag{5.6}$$

In both SOEC and SOFC operation, it is possible to fully recover the product fraction required at the cell inlet (i.e., H_2 in SOEC and H_2O in SOFC) from the exhaust fuel. In fact, it can be easily demonstrated form the above given expression that $\dot{\boldsymbol{n}}_{rec,fuel}$ is equal to $\dot{\boldsymbol{n}}_{in,fuel}$ when $\boldsymbol{I}_{cell}$ is zero (i.e., cell at open circuit), and that its value diminishes when the cell current is higher than zero. Thus, it is not necessary to provide externally the H_2 (SOEC) or H_2O (SOFC) needed to maintain the 10 % of product at the stack inlet. If we consider that all the remaining exhaust fuel is fully recovered in the heat recovery section, the fuel streams that must be provided to the SOC stack either from the ambient (i.e., H_2O for SOEC) or from the gas storage (i.e., H_2 for SOFC) are only those needed to replace the reacted flows.

The assumptions involving the components of the system are listed below:

- Adiabatic components. Gas storage tanks, rSOC stack, water pump and piping are assumed to be perfectly insulated from the external ambient. The gas compressors exchange heat flows with the ambient, as the heat removed by intercooling is assumed to be lost to environment. The heat recovery section also exchanges thermal flows with the ambient. An inward heat flow is provided to this section from an external source when the maximum heat recoverable from hot fluids is not sufficient for the preheating of the streams entering the stack. The heat exchanger network also releases heat to the ambient when the recovered heat exceed the preheating requirements or it is available at lower temperatures than required by the cold fluids. The pinch analysis (see *Chapter 2* for the details on the modeling approach) allows the calculation of the effectively recoverable heat flows and has been applied in the system model to evaluate the heating power required from external sources and the heat released toward the ambient.

- Ideal gas storage tanks. Gas storage tanks are assumed at constant pressure (30 bar) and ambient temperature (T_{amb} = 25 °C). Pressure fluctuations due to charge/discharge cycles are neglected in the analysis. The storage pressure assumed

(30 bars) is the operating pressure of methanation reactors considered in the P2G analysis. In order to perform a comparison of P2P and P2G operation, it is assumed that the storage pressure of H_2 in the P2P operation is the same of the hydrogen provided to the methanation section in the P2G system. The storage pressure of oxygen is assumed to have the same value of H_2 for reasons of symmetry in the analysis of system performance.

- Negligible pressure drops. Pressure drops are neglected in all the components and piping. In the case of the rSOC stack, the pressure field is evaluated in the SRU simulations and all the variables evaluated by the numerical model take into account the pressure distribution in the cell. In particular, the operating pressure of the cell is fixed at the outlet of the gas channels, thus the resulting inlet pressure is slightly higher. However, for the purpose of system analysis, the inlet pressure of the stack has been considered equal to the outlet one imposed. Results reported in *Section 5.2.1* show that this assumption is acceptable, as the simulated pressure drops are in the order of few millibars.

- Size independency. System analysis is performed by relating the values of all the calculated energy and exergy flows to the single SRU, and the assumed efficiencies of BoP components are thus considered independent of the size of the equipments. In this way, the results presented have a general validity being un-related to a specific size of the P2P system. The same assumption will be applied to the analysis of P2G systems.

- Minimum temperature difference of pinch analysis. Pinch analysis requires to know the properties of the streams involved, the thermodynamic conditions at which they are available, their mass flow rates and the final temperatures that streams must reach. All these parameters are imposed or derived from the SRU model, as described in the section dedicated to the architecture of the system model. The pinch analysis also requires to set the minimum temperature difference (ΔT_{min}) between hot and cold fluids. The literature suggests that typical values of ΔT_{min} are included between 20 and 40 °C (Linnhoff 1998). In this analysis, a conservative ΔT_{min} of 40 °C has been imposed.

In the analysis, system efficiency has been evaluated by considering all the heat and electricity flows provided/produced to/from the system components. The energy flows exchanged by BoP components have been evaluated by the thermodynamic approach described in *Chapter 2*. The rSOC stack produces electrical power during SOFC operation, while it absorbs power from external sources in SOEC. Globally, the system energy flows are:

- H_2 compression: W_{comp,H_2} calculated by equation (2.175) of *Chapter 2.*
- O_2 compression: W_{comp,O_2} calculated by equation (2.175) of *Chapter 2.*
- Air compression: $W_{comp,air}$ calculated by equation (2.175) of *Chapter 2.*
- Water pumping: W_{pump} calculated by equation (2.176) of *Chapter 2.*
- External heat supply: Φ_{ext} calculated by pinch analysis, see *Section 2.3.2* of *Chapter 2.*
- SRU power: $W_{cell} = V_{cell} \cdot I_{cell}$

Electricity and heat are different forms of energy that can be better compared by taking into account their exergetic value. In particular, the exergetic value of heat flows exchanged by the system with the external environment can be evaluated by associating a temperature to each flow, as shown in equation (2.56) of *Chapter 2*. In the pinch analysis, an external heat flow $\Phi_{ext,i}$ is calculated for each temperature interval in which the balance between hot and cold fluids is made. Each flow $\Phi_{ext,i}$ is associated by the model to its relative source temperature by assuming a minimum temperature difference of 40 °C between the higher temperature of the interval and the external source. In this way, an exergy flow is associated to each thermal flow:

$$Ex_{\phi_{ext,i}} = \phi_{ext,i} \cdot \left(1 - \frac{T_{amb}}{T_{source,i}}\right) \tag{5.7}$$

For the system evaluation, all the energy and exergy flows are summed into total flows:

$$\Phi_{ext} = \sum_i \phi_{ext,i} \tag{5.8}$$

$$Ex_{ext} = \sum_i Ex_{\phi_{ext,i}} \tag{5.9}$$

$$W_{BoP} = W_{pump} + \sum_{i} W_{compr,i} \tag{5.10}$$

The energy efficiency of the system can be expressed following the definitions given in *Chapter 2* (see equations 2.54-2.55). However, different efficiency parameters are used in the analysis presented in this Chapter. For SOEC operation, the efficiency is defined as the unit of charge absorbed by the cell per unit time (i.e. the cell current) per unit of power provided to the system. This efficiency will be called either charging efficiency or electricity storage efficiency in the dissertation. In SOFC mode, the efficiency is the power produced by the cell net of the power consumed by BoP components, calculated per unit of produced current. This efficiency will be called discharging efficiency in the text. Definitions are given below:

$$\eta_{SOEC} = \frac{|I_{cell,SOEC}|}{(|W_{cell}| + \phi_{ext} + W_{BoP})_{SOEC}} \tag{5.11}$$

$$\eta_{SOFC} = \frac{(|W_{cell}| - \phi_{ext} - W_{BoP})_{SOFC}}{|I_{cell,SOFC}|} \tag{5.12}$$

Dimensionally, the efficiencies such defined are equivalent to a voltage (SOFC) and the inverse of a voltage (SOEC). These efficiencies express the capabilities of absorbing power per unit of current in SOEC and releasing power per unit of current in SOFC. The choice of expressing the efficiencies per unit of currents eliminates the dependency of the efficiency on the definition of the energy content of the produced/consumed hydrogen, which can be expressed in LHV or HHV terms and depends on the gas conditions. Electrical charge is instead a quantity that is fully independent on the thermodynamic condition in which is stored and can be used without incurring in misleading definitions. Moreover, if we consider the P2P system analyzed, each unit of electrical charge stored in hydrogen by SOEC operation can be fully recovered in SOFC, as hydrogen is completely stored without mass losses and recycled only by electrochemistry without involving combustion reaction; therefore there is a complete equivalence between a hydrogen flow and the corresponding charge flow. Finally, the definition of efficiency based on electrical quantities can allow the comparison of the P2P system with competing technologies based on batteries without involving chemical quantities.

The exergetic efficiencies can be defined analogously:

$$\eta_{SOEC,ex} = \frac{\left|I_{cell,SOEC}\right|}{(|W_{cell}| + Ex_{ext} + W_{BoP})_{SOEC}} \tag{5.13}$$

$$\eta_{SOFC,ex} = \frac{\left(|W_{cell}| - Ex_{\phi} - W_{BoP}\right)_{SOFC}}{\left|I_{cell,SOFC}\right|} \tag{5.14}$$

The objective of the analysis is the evaluation of the roundtrip efficiency of the system with the changing operating conditions. The general definition of roundtrip efficiency – η_{RT} – is given by equation (2.59) of *Chapter 2*. This definition provide an evaluation of the ratio between the energy (or power) released over the energy (or power) absorbed by the system. The roundtrip efficiency alone is not sufficient for the complete description of a P2P system, as this parameter does not provide information about the charging and discharging rate. This information is fundamental when assessing a reversible P2P system; in fact, even if a system can store energy with high roundtrip efficiency (i.e., it absorbs a high fraction of incoming power and reconverts it in electricity with high efficiency), its applicability depends on the rate at which the energy is stored and released. For example, if a P2P system takes an infinite time to charge a unit of energy, it is completely useless even if it has high roundtrip efficiency, because the storage is still empty when energy is required. On the opposite, if the system takes an infinite time to discharge is also useless, as the energy stored cannot be retrieved also with a full storage. In the middle between these two extremes examples, if a storage system is faster to charge and slow to discharge, the consequence is that the nominal charging power is higher than the release one, and vice versa if it is faster to discharge. The rate of charge and discharge of a P2P system correspond to the current levels of the rSOC cell (i.e., $I_{cell,SOEC}$ and $I_{cell,SOFC}$). The higher is the SOEC current, the faster the H_2 is stored, and the higher is the SOFC current, the faster the H_2 is reconverted in electricity. Different currents correspond to different roundtrip efficiencies of the system, and the analysis performed on the P2P system will show that the maximum roundtrip efficiency is reached for a specific combination of $I_{cell,SOEC}$ and $I_{cell,SOFC}$. The analysis will also show that not all the operating points are feasible due to thermal constraints given by rSOC materials, thus only certain ranges of currents are applicable. If the P2P system is operating at certain current levels in SOEC and SOFC – which possibly ensure the maximum roundtrip efficiency – the charge and discharge rates are also fixed. It is possible to define a ratio between the operating currents in SOFC and SOEC to highlight the charge/discharge capability of the P2P system. This ratio will be called rate conversion factor in the dissertation, and it is defined as:

$$\boldsymbol{H} = \frac{\left|I_{cell,SOFC}\right|}{\left|I_{cell,SOEC}\right|} \tag{5.15}$$

The $\boldsymbol{H}$ factor measures the capability of the system to perform electricity storage/release with faster or lower rates. Low $\boldsymbol{H}$ values indicate that the system is operating in conditions suitable for fast-charging, while high $\boldsymbol{H}$ values indicate the P2P is operating in fast-discharging conditions. When the operating currents vary, the $\boldsymbol{H}$ factor varies consequently. For example, if more power is need in output from the P2P system, a higher current $I_{cell,SOFC}$ is required and the $\boldsymbol{H}$ factor increases; the opposite if an increasing power is provided to the SOEC. The energy constraint of the P2P system imposes that the released energy cannot be higher than the stored energy; that is:

$$\left|I_{cell,SOEC}\right| \cdot t_{SOEC} = \left|I_{cell,SOFC}\right| \cdot t_{SOFC} \tag{5.16}$$

where t_{SOEC} is the charging time of the H_2 storage and t_{SOFC} is the discharge time. The energy conservation constraint can be re-arranged to show the equivalence of the $\boldsymbol{H}$ to the ratio between the charge and discharge time of the P2P system:

$$\boldsymbol{H} = \frac{\left|I_{cell,SOFC}\right|}{\left|I_{cell,SOEC}\right|} = \frac{t_{SOEC}}{t_{SOFC}} \tag{5.17}$$

The roundtrip definition can be re-elaborated to obtain a formulation dependent on $\boldsymbol{H}$:

$$\begin{aligned} \eta_{RT} = \eta_{SOEC} \cdot \eta_{SOFC} = \\ = \frac{\left|I_{cell,SOEC}\right|}{(|W_{cell}| + \phi_{ext} + W_{BoP})_{SOEC}} \frac{t_{SOEC}}{t_{SOEC}} \cdot \\ \cdot \frac{(|W_{cell}| - \phi_{ext} - W_{BoP})_{SOFC}}{\left|I_{cell,SOFC}\right|} \frac{t_{SOFC}}{t_{SOFC}} \end{aligned} \tag{5.18}$$

$$\eta_{RT} = \frac{(|W_{cell}| - \phi_{ext} - W_{BoP})_{SOFC}}{(|W_{cell}| + \phi_{ext} + W_{BoP})_{SOEC}} \cdot \frac{t_{SOFC}}{t_{SOEC}} = \frac{(|W_{cell}| - \phi_{ext} - W_{BoP})_{SOFC}}{(|W_{cell}| + \phi_{ext} + W_{BoP})_{SOEC}} \cdot \frac{1}{\boldsymbol{H}} \tag{5.19}$$

The first ratio of the rearranged η_{RT} definition is a pure power ratio, which describes the power producible from a unit of power absorbed, and the second one takes into account the times in which the charge and release can take place.

In the analysis, at fixed operating conditions of the SOC (i.e., inlet fluid temperatures, operating pressure, air/oxygen selected, and $\boldsymbol{\lambda}$ value imposed) from the energetic and exergetic analysis it is possible to select the current values that maximize the efficiency during the electricity storage and during the release phase, and an $\boldsymbol{H}$ value can be associated to these currents. Therefore, once the operating conditions are fixed, it is possible identify the $\boldsymbol{H}$ value of the system operating at maximum efficiency. The analysis of the thermal constraints allows to clarify if the selected operating points are also compatible with the thermal stresses induced in the rSOC, and to identify acceptable current values. Sensibility analyses on the rSOC operating parameters will be performed to find the operating conditions that allow to shift the optimal current values toward ranges compatible with the thermal constraints.

Physical constraints

Four thermal constraints have been considered in the analysis: maximum cell temperature, minimum cell temperature, maximum total temperature gradient of the cell, maximum local temperature gradient in the cell. These constraints are listed as follows:

- Maximum cell temperature: T_{max} = 850 °C
- Minimum cell temperature: T_{min} = 700 °C
- Maximum total temperature gradient in the cell: ΔT_{cell} = 120 °C
- Maximum local in-plane temperature gradient: dT_{cell} = 10 °C/mm

The constraint on the maximum cell temperature has been selected by taking into account that the stack is composed not only by cells, but also by metal interconnects and sealing. In addition, the gases exiting the stack pass through the heat exchangers which are located immediately downstream the stack in the heat recovery section. It is possible to assume conservatively, but with a good approximation as shown later, that the exhaust gases are at the maximum temperature of the cell, and thus that at the heat exchangers inlet the temperature is the maximum reached in the cell. Therefore, the maximum temperature reached in the cell should be compatible with that acceptable for metal materials composing the SRU and heat exchangers. The value of the maximum cell temperature has been set to 850 °C, which is the acceptable limit

of conventional metal-based heat exchangers (Braun al. 2012). The minimum temperature value and the maximum total temperature gradient have been set respectively to 700 °C and 120 °C, following producers' indications for fuel-electrode supported SOCs and stacks. In particular, the total cell gradient is related to the macroscopic deformations induced on the cell that can damage the SRU structure leading to the loss of contact between cell and interconnects and gas leakage. The constraint on the local in-plane temperature gradient is related to the stresses that cell materials can withstand. This value has been set to 10 °C/mm from a study on the thermal stress of planar anode-supported SOFCs (Chiang et al. 2010).

5.1.3 Model architecture

System analysis is performed by coupling the numerical rSOC model presented in *Chapter 3* (see *Section 3.2.1*) with the thermodynamic equations for the BoP components presented in *Chapter 2* (see *Section 2.3.2*) and a pinch analysis tool developed for the simulation of the heat exchangers section (see *Section 2.3.2* of *Chapter 2*). All the equations are solved in the COMSOL architecture of the rSOC model.

The rSOC model receives as input the compositions and molar flows of fuel and oxidant mixtures, the inlet temperature of the fluids, the total cell current, the operating mode (i.e., SOEC or SOFC) and the pressure at the outlet of the channels:

- mole fraction of each α species: $\boldsymbol{y_{\alpha,in}}$
- total inlet molar flow of fuel: $\boldsymbol{\dot{n}_{in,fuel}}$
- total inlet molar flow of oxidant: $\boldsymbol{\lambda \cdot \dot{n}_{in,fuel}}$
- inlet temperature of each fluid stream: $\boldsymbol{T_{in}}$
- total cell current: $\boldsymbol{I_{cell}}$
- operating mode: **SOEC - SOFC**
- outlet pressure of the channels: $\boldsymbol{p_{out}}$

The inlet compositions of the fuel is fixed to 90 % fuel and 10 % product, and the inlet fuel molar flow is imposed to ensure the 70 % of *FU* at 1 A/cm^2, following the assumptions described in the previous section. Oxidant molar is fixed in relation to the fuel one by the $\boldsymbol{\lambda}$ coefficient. The inlet temperatures of fuel and oxidant, outlet pressure, and the total cell current are imposed independently of the other input parameters. The outlet pressure of anode and cathode is always imposed to be same, as the SOC cannot operate with differential pressure as the thin materials can withstand only very little pressure differences. The operating mode is a

trigger corresponding to -1 or +1 that changes the direction of the imposed current in the rSOC model.

The pinch analysis has been implemented as a function in Matlab and called by the COMSOL model. The function receives in input from the rSOC model the outlet conditions of the fuel and oxidant streams in terms of pressure (which is $\boldsymbol{p}_{out}$), temperatures (evaluated as average values on the outlet section of the channels), compositions, and thermodynamic properties of gases (i.e., density and specific heat evaluated from the COMSOL database). The properties of steam and water were calculated directly in Matlab by using the "X-steam" package by Holgrem (2007). In the pinch analysis tool, the molar flow of recirculated fuel is calculated as described in the previous section. A minimum temperature difference of 40 °C is imposed in the pinch analysis, as previously indicated. The inlet temperature of cold fluids is assumed to be the ambient temperature (T_{amb} = 25 °C) and the hot fluids are cooled down from their inlet temperature to 65 °C (that is the sum of T_{amb} and ΔT_{min}). The further cooling of hot fluids from 65 °C and 25 °C is considered, but the heat is released to the ambient. The pinch analysis routine calculates the minimum heat power required from an external source in each temperature interval and associates to the external heat source a temperature value, which is ΔT_{min} higher than the maximum temperature value of the interval. Finally, the Matlab function returns to the COMSOL model the values of the energy and exergy flows required from the external sources, and the efficiency parameters are calculated in COMSOL.

Electrical auxiliaries (i.e., pumps and compressors) are modeled following the thermodynamic approach by implementing the equations described in *Chapter 2* directly in the COMSOL architecture.

5.1.4 Cases analyzed

The analysis investigated first a baseline case with the operating conditions shown in *Table 5.1*, and then performed sensibility analyses on the input parameters to assess their effect on the system efficiency.

Baseline model

In the baseline model, the stack is operating at ambient pressure and the fluids are entering the cells at 800 °C. Air is considered as oxidant with a lambda ratio of 3. The conditions are reported in *Table 5.1*.

The analysis investigated the operation at different levels of cell current (from 0 A to ±130 A) in both SOFC and SOEC modes. The maximum current of ±130 A corresponds to a *FU* of 90 %. In the baseline model, the electrical consumption of water pump and air blower are negligible and thus are not shown in the analysis. The major contributions in terms of required energy flows from the BoP come from the heat recovery section and the H_2 compressor, the second operating only in SOEC mode. Results of the baseline case are reported in *Section 5.2.1*.

Table 5.1 – Baseline model input conditions

Input Parameter	Value
$T_{in,fuel}$	800 °C
$T_{in,oxi}$	800 °C
Oxidant	Air
λ	3
Pressure	1 bar
I_{cell}	0 – 130 A

Sensitivity analysis

The effect of the variation of operating parameters has been assessed by performing sensitivity analyses. The sensitivity parameters investigated are the followings:

- Cell Pressure
- Oxidant: air vs. oxygen
- Inlet temperature of Fuel and Air
- Oxidant-to-fuel ratio (λ)

The limits adopted for the sensitivity parameters are listed in *Table 5.2*. The maximum cell pressure investigated is 10 bar, assuming that as the limit pressure for the current state-of-the art technology.

When the system is operating with a pressurized rSOC stack, several BoP contributions arise. In fact, air compression from ambient to stack pressure and oxygen compression from stack pressure to storage pressure are needed. Also oxygen recompression from the stack pressure to the storage one is needed when operating with pure O_2 and the recirculation of the oxygen flow

is not imposed. Finally, water pumping from ambient to stack pressure represents another BoP contribution in pressurized operation.

Table 5.2 – Sensitivity analysis

Input Parameter	Value
$T_{in,fuel/oxi}$	700 – 850 °C
Oxidant	Air – Oxygen
λ	2.15 – 5
Pressure	1 – 10 bar
I_{cell}	0 – 130 A

The minimum oxidant-to-fuel ratio (λ) chosen – 2.15 – is the ratio that ensures an *OU* of 70 % when the system operates in SOFC at 1 A/cm^2, and the maximum ratio λ = 5 corresponds to 30 % of *OU* in nominal conditions.

Inlet temperatures of fuel and oxidant were imposed always equal and thus were varied together in the sensitivity analysis. This choice has been made because the parallel flow arrangement induces high temperature gradients at the cell inlet that easily exceed thermal constraints – especially on the local gradient – if the fluids enter at different temperatures. This happens because in the simulation the fluids are feed directly in the cell at an imposed temperature and thus recirculation does not affect their inlet temperature. This effect is further enhanced because the oxidant flow directly touches the electrolyte, while the presence of an oxygen electrode could dampen the thermal gradient in the inlet section of the cell. In real operation the temperature of fluids entering a cell is not imposed, but depends on their temperature at the inlet of the stack and on recirculation rates. Thus, the temperatures of fluids at the channels' inlets are different from their temperature at the stack inlet. In fact, fuel and oxidant are feed to a real stack usually at different temperatures, but the internal heat exchange in the stack before the cells allows to homogenize the temperature of the fluids so that the thermal gradient at cell inlet is lower than the temperature difference at the stack inlet. The distribution of fluids in stack manifolds and the internal heat exchange between fluids before the cell inlet have not been modeled in this dissertation, as they are strictly dependent on the geometry of a certain stack, while the results presented in this Thesis have the objective to provide general considerations independent of a specific configuration. In the model developed, the effect of

internal preheating due to recirculation has been considered in the heat recovery section, and only the contemporary variation of fuel and oxidant inlet temperatures has been investigated.

When investigating the effect of the oxidant type (i.e., air or oxygen) on the system performance, also the effect of oxidant recirculation has been assessed. In all the other sensitivity analyses the oxidant recirculation has not been considered. Results of the sensitivity analyses are reported in *Section 5.2.2*.

5.2 Analysis of a hydrogen-based P2P system: results

In the following sections, the results of baseline model and sensitivity analyses are presented.

5.2.1 Baseline model results

Current and potentials

The results shown in this section were obtained from the model run in the baseline conditions. In all the figures presented, the cell current is expressed per unit area of the cell; this value corresponds to an average current density of the SRU and should not be confused with the local current density within the cell, which is not uniform as will be shown in *Fig. 5.4* and *Fig. 5.5*. The simulated polarization characteristics of the SRU are reported in *Fig. 5.2*. The Figure shows the asymmetrical behavior of the SOC in the reversible operation. The contributions of the different overpotentials that produce the global current-voltage characteristic of the cell are depicted in *Fig. 5.3*.

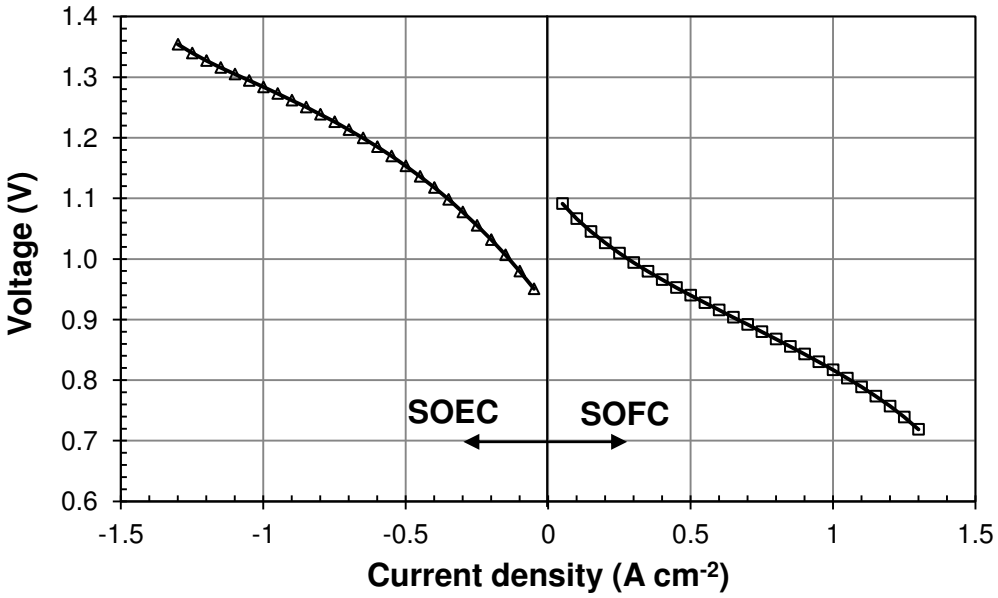

Fig. 5.2 – Simulated rSOC polarization of the SRU.

In the Figure, the green curves represent the reversible potential of the cell – V_{rev} – calculated as the difference of the reversible potentials of the electrodes (see equation (3.51) and (3.52) of *Chapter 3*) integrated over the electrolyte/electrode boundary surfaces. It is worth noting that V_{rev} is not constant with the varying current. Its value depends on the partial pressures of reactants and products and on the Gibbs free energy variation of the redox reaction (i.e., $\Delta\bar{g}^{o}_{H_2/H_2O}$) on the

cell's TPBs. Partial pressures vary with the current because the inlet fuel and oxidant flows are fixed, and consequently the electrochemically consumed/produced flows of H_2, H_2O and O_2 – which are linear functions of the current due to Faraday's law (equation (2.68) of *Chapter 2*) – increasingly affect the composition of the fuel and oxidant streams with the incresing current. The term $\Delta\bar{g}^o_{H_2/H_2O}$ depends on the temperature, which also varies with the current because all the heat source/sink terms are functions of it (see *Chapter 3*). In SOEC operation, the increase of hydrogen and oxygen concentrations with the current and the decrease of water partial pressure are the drivers of the progressive increase of V_{rev} with I_{cell}. The $\Delta\bar{g}^o_{H_2/H_2O}$ slightly increases at low currents because of the decreasing SOEC temperature. Only at high currents – when the cell is operating exothermally, over the thermoneutral voltage – it begins to diminish due to the rising temperature. The globlal effect is the increase of the V_{rev} in SOEC with the current. In SOFC operation, the opposite situation occurs: hydrogen and oxygen partial pressures decrease and the water concentration increses. In this case the temperature is always increasing with the current and thus the $\Delta\bar{g}^o_{H_2/H_2O}$ is always decreasing. The final effect is the more evident decrease of the reversible potential in SOFC than the increase in SOEC.

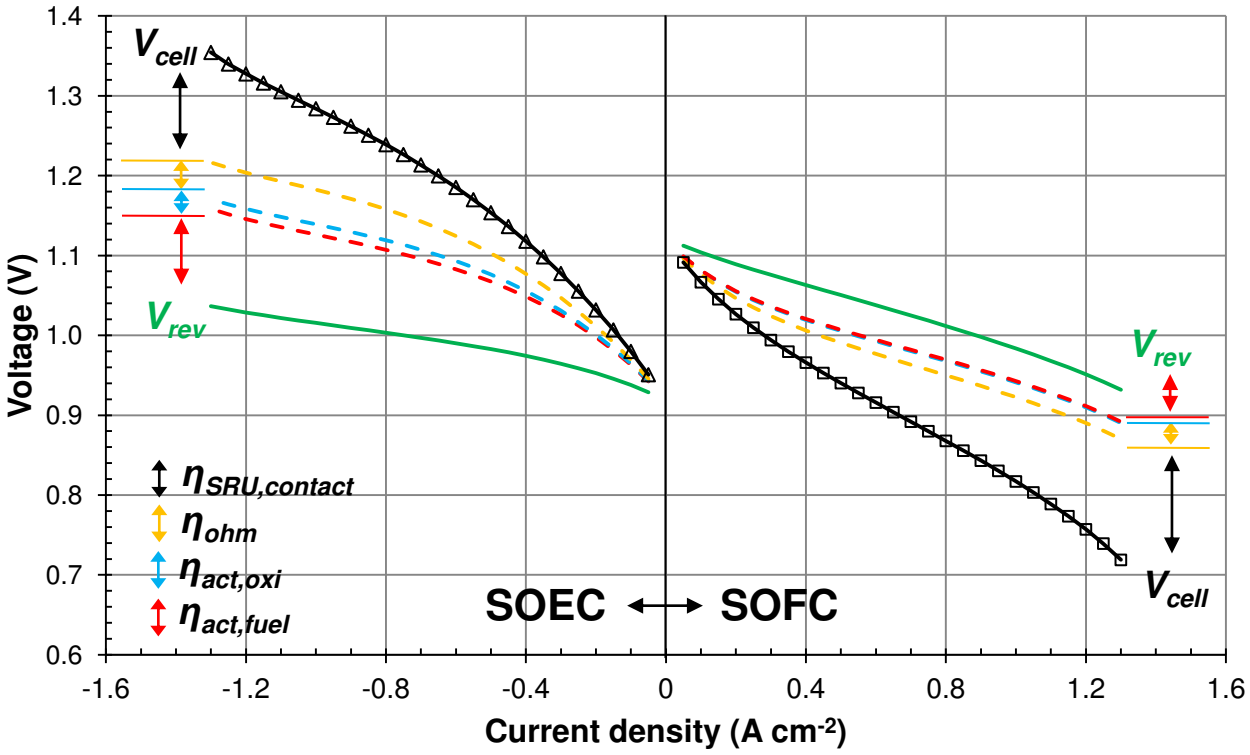

Figure 5.3 – SRU voltage composition in reversible operation.

In both cases, the variations of partial pressures contibute to shift the reversible potential towards the direction in which the redox reactions is less favored. The temperature plays a significant role in determining V_{rev} mostly in SOFC, due the higher temperature variations from the inlet fluid conditions.

All the overpotentials increase with the current. The activation contribution is mostly ascribable to the fuel electrode reaction, while the oxygen redox reaction on the LSCF electrode is the source of minor losses, as expected by the redox kinetics validated in *Chapter 4*. This behavior is particulaly evident is SOFC, where the cathode activation overpotentials is almost negligible. The ohmic overpotential of the cell depends on the conductivity of YSZ electrolyte. It is worth noting that this contribution is lower in SOFC operation due to the higher temperature that enhance the ionic conductivity of the electrolyte. The overpotential generated by the contact resistance plays an important role in the determination of the cell voltaghe. This overpotential has a linear increase with the current, and assumes the same value for both SOFC and SOEC operation at a certain current.

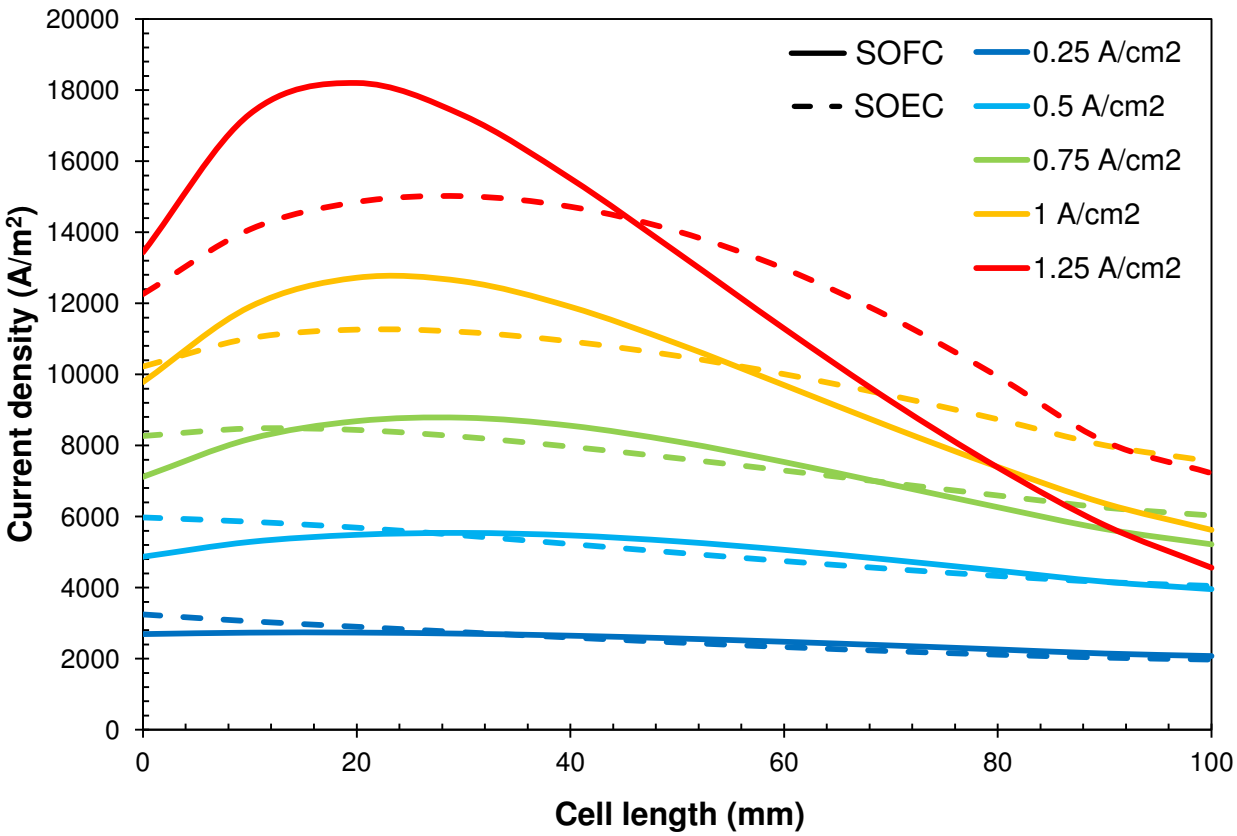

Figure 5.4 – Current density distribution on the TPB of the fuel electrode (legend values indicate the average current density of the cell).

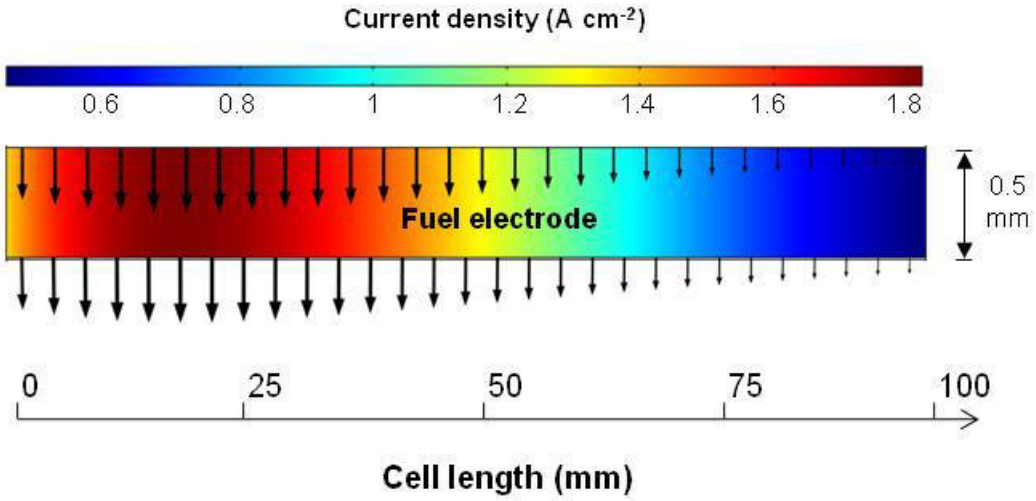

Figure 5.5 – Current density distribution within SOFC electrode at 1.25 A/cm^2. Color indicates the value of the module of the current density vector, arrows indicate the direction (i.e., from electrode surface to electrolyte).

The current density distribution on the fuel electrode's TPB and within the volume of the fuel electrode is depicted in *Figure 5.4* and *Figure 5.5*. In both SOEC and SOFC operation, current density is higher in the first half of the cell (i.e., from the gas inlet), where the higher partial pressures of reactants enhance the reaction kinetics. In SOFC operation a current density peak is evident at higher current values, while in SOEC the distribution is flatter. The SOFC peak progressively shifts towards the cell inlet with the increasing current. The presence of a peak is due to the combination of high temperatures and high concentration of reactants. In SOEC mode, the flatter temperature profile due to the balance between reaction endothermicity and heat generation due to irreversibility ensure a more homogeneous distribution of the current. *Figure 5.5* shows the 2D section of the anode in SOFC operation at 125 A. A peak of 1.8 A/cm^2 (50 % higher than the average current density of the cell, which is 1.25 A/cm^2) is noticeable in the first 25 mm of the cell's length.

Species distribution

The concentration of the chemical species within channels and fuel electrodes in both SOFC and SOEC operation are depicted in *Figure 5.6* and *Figure 5.7*.

Hydrogen distribution is quite symmetric between the two modes, as shown in *Figure 5.6*. Water concentration has not been shown as it is the complementary to 1 of that of the hydrogen.

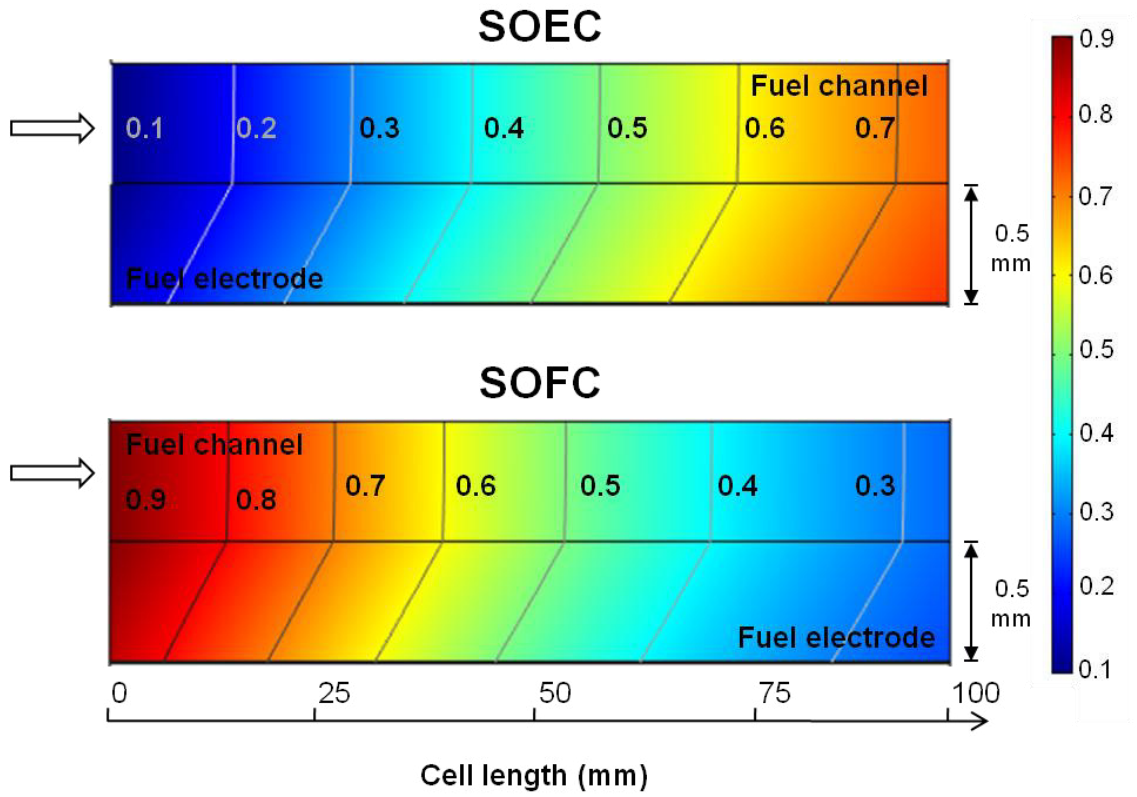

Figure 5.6 – H_2 molar faction within fuel channel and fuel electrode in both SOEC and SOFC operation at 1 A/cm^2.

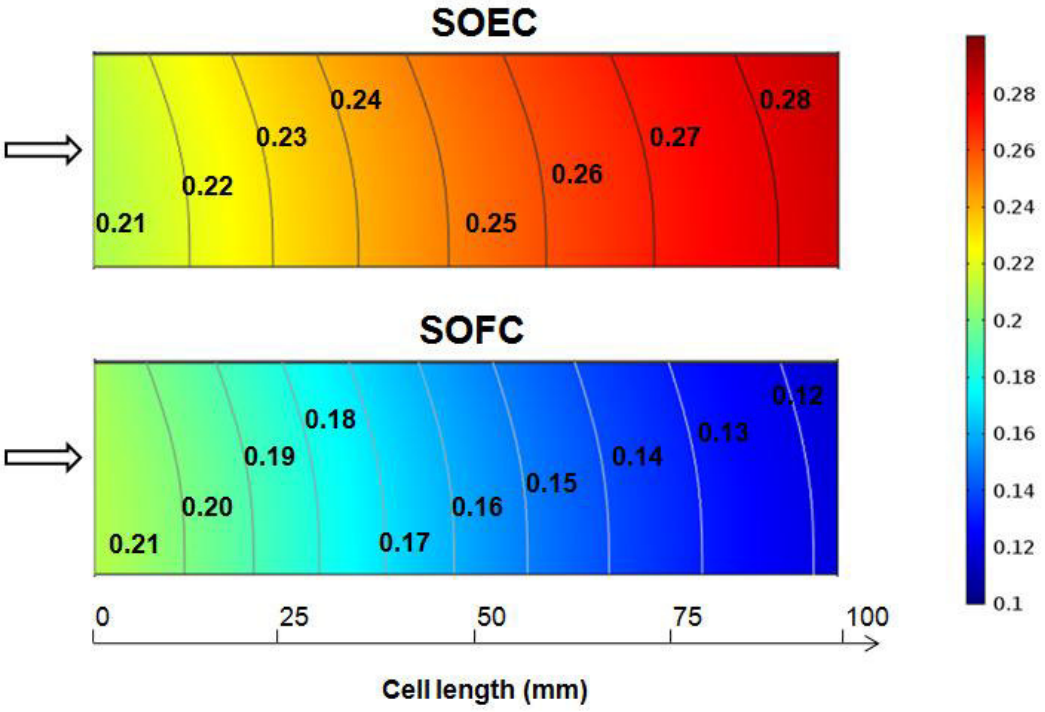

Figure 5.7 – O_2 molar faction within fuel channel and fuel electrode in both SOEC and SOFC operation at 1 A/cm^2.

The oxygen concentration depicted in *Figure 5.7* shows a sensibly lower variation in the oxidant channel domain with respect to H_2 and H_2O. Oxygen concentration is less affected by the electrochemical reaction because the molar flow of O_2 produced (or consumed) at a certain current is the half of the H_2O/H_2 consumed/ produced for the same current. Moreover, the inlet flow of air is 3 times higher than the fuel flow in the baseline case; thus, it is less senible to an oxygen inflow/outflow from TPB boundary.

The partial pressures almost follow the same distributions of the species concentrations, as the pressure variations in fluid are nearly negligible. An example of pressure distribution (given as difference with the outlet atmospheric pressure) is shown in *Figure 5.8* for the operation at 1 A/cm^2. The maxium pressure drop calculated is around 3 mbar in the fuel channel.

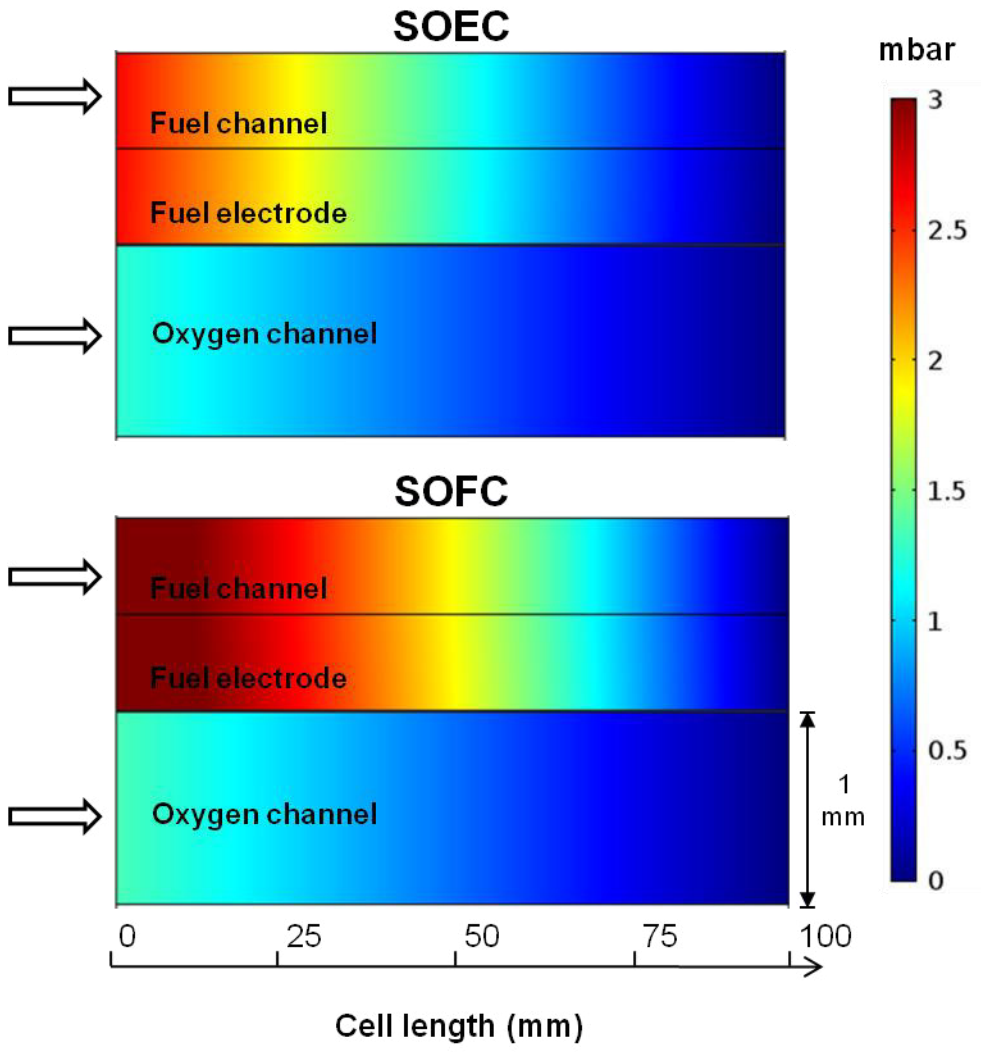

Figure 5.8 – Pressure drops in the cell at 1 A/cm^2.

Temperature distribution and heat sources

The temperature distribution in the SRU is shown in *Figure 5.9*, for the operation at ±0.4 A/cm^2.

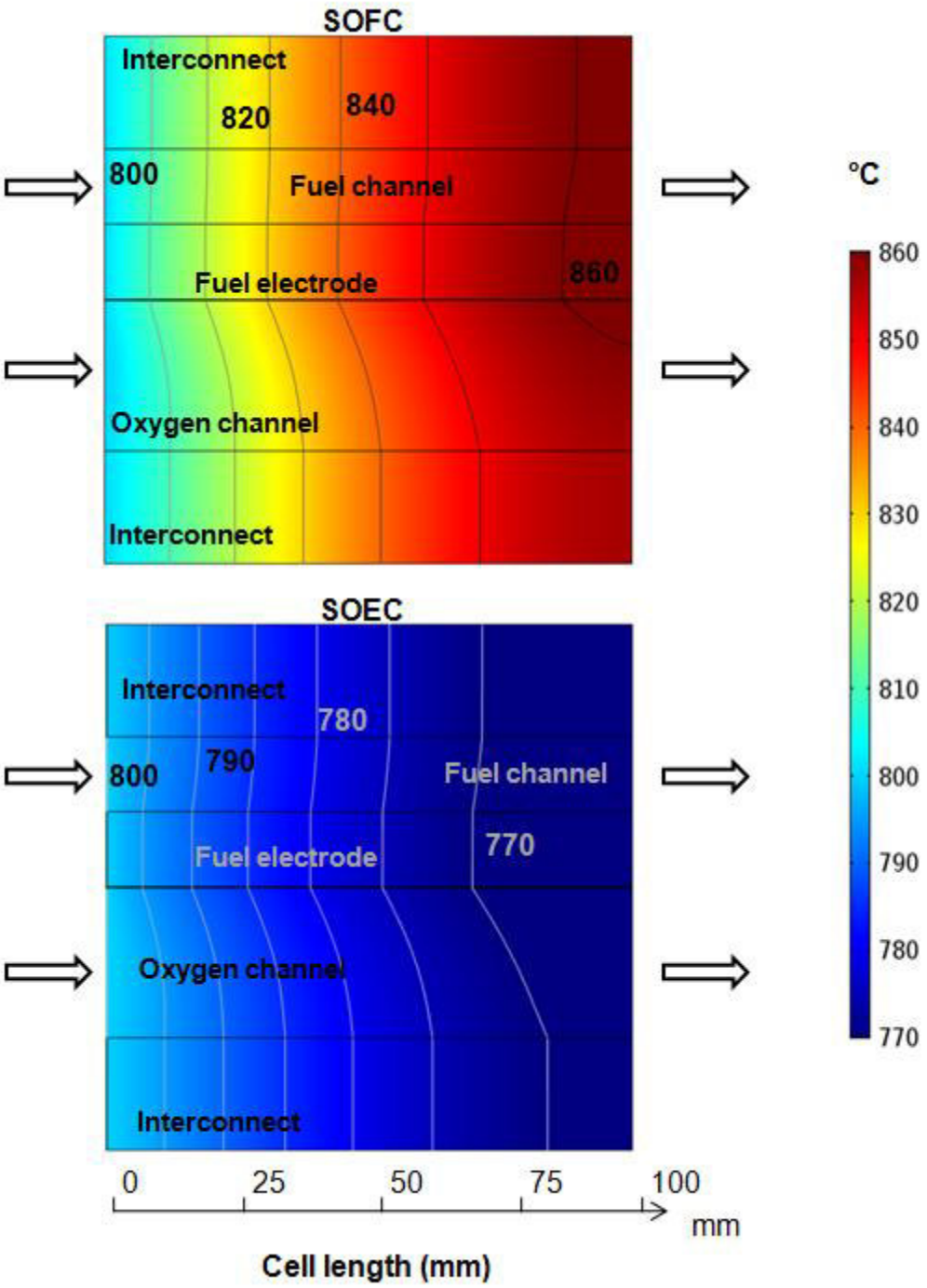

Figure 5.9 – Temperature distribution within the SRU at ±0.4 A/cm^2 (i.e., SOEC operation with negative current and SOFC operation with positive current).

From the figure it is evident the strong asymmetric thermal behavior between SOEC and SOFC operation. A peak of 860 °C is reached in the fuel cell, while the SOEC has a minimum temperature of 770 °C. In both cases, the temperature is quite uniform along the *y* direction in the cell (i.e., along the SRU thickness), interconnects and fuel channel. In the oxidant channel, a moderate effect of convection is visible in the curving isothermal lines. This is mainly due to the higher air flow with respect to fuel. In the *x* direction (i.e., along the channel/cell length), the isothermal lines are closer in the first half of the cell. In order to understand this distribution, it is necessary to discuss the positions of heat sinks and sources in the cell.

As previously shown, in the SRU model volumetric heat sources related to ohmic heating are placed in the electrode and electrolyte domains, while on the electrode/electrolyte boundary reaction heat sources/sinks are imposed together with the heat sources originated by activation overpotentials. The contact resistances with the related heat sources are placed on the electrodes' surfaces. The contributions of the different sources to the heat balance of the SRU are depicted in *Figure 5.10*.

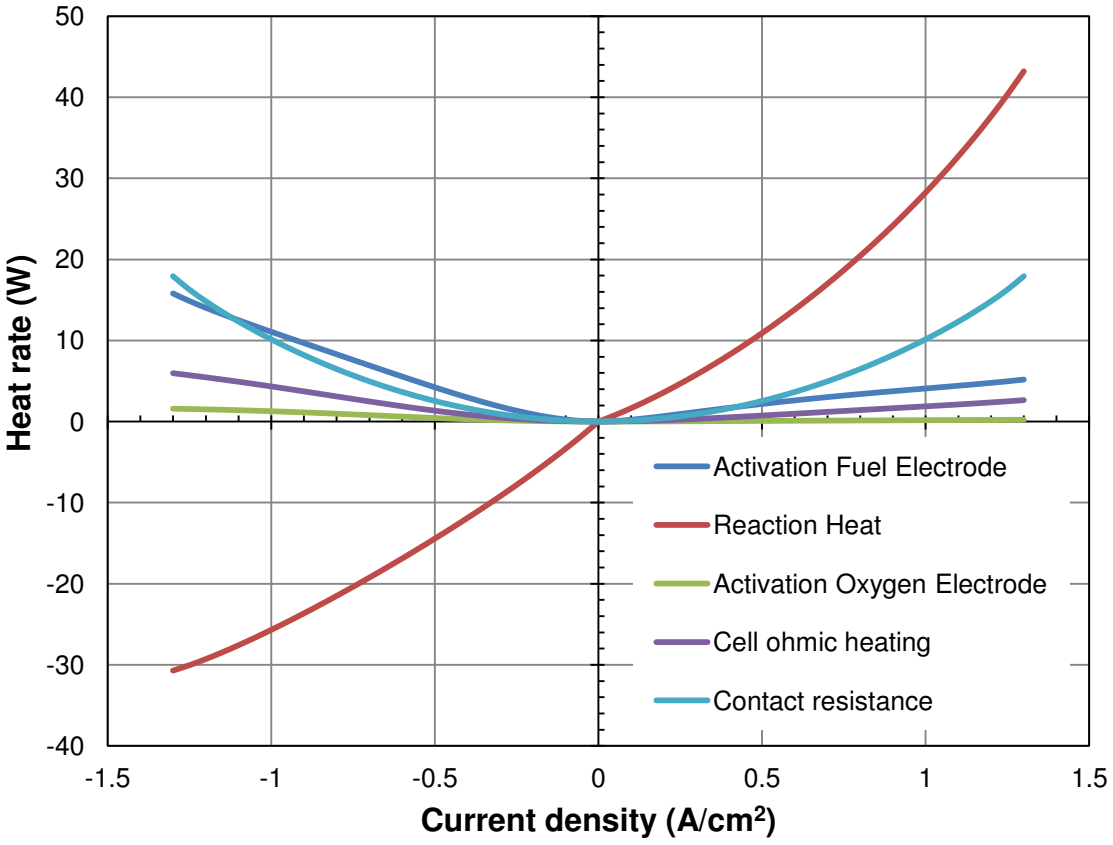

Figure 5.10 – Break down of heat sources of the rSOC SRU.

If we exclude the heat of reaction, all the other sources are always positive. The heat of reaction is positive in fuel cell operation, due to exothermicity of the hydrogen oxidation, while it is negative when the cell is operating in electrolysis. The reaction source is mostly concentrated at the fuel electrode's TPB, as the oxygen reduction/oxidation involves only small amounts of energy. It is worth noting that the heat source due to contact resistance is equal in two modes at the same current, as the resistance is considered as a constant parameter. The heat released by the activation of the redox reaction is higher in electrolysis mode, both for the slower kinetics of H_2O reduction with respect to H_2 oxidation and for the lower temperatures reached in electrolysis operation that increase the overpotential of reaction activation.

Heat sources related to overpotentials and contact resistances are functions of the cell current, as explained in *Chapter 2*. Also the heat released/absorbed by the H_2/H_2O redox reaction is a function of the number of moles locally reduced/oxidized (see equation (2.114) *Chapter 2*), which in turn depends on the local current density by the Faraday's law.

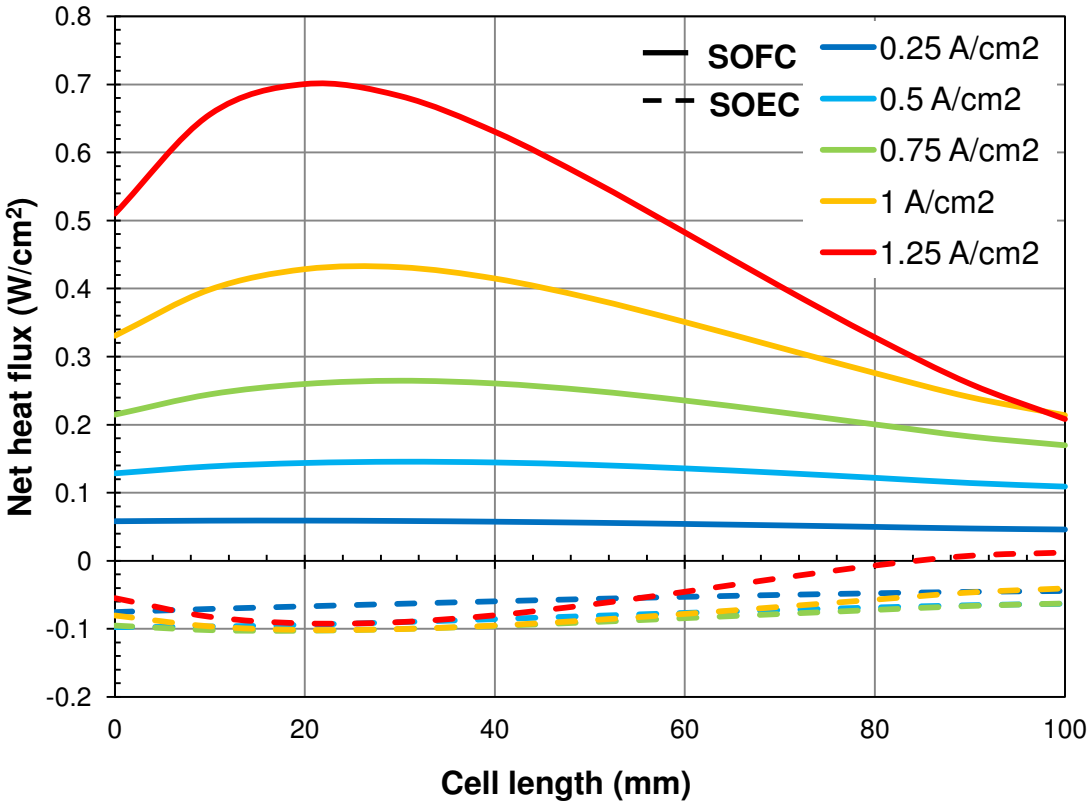

Figure 5.11 – Net heat flux distribution on the TPB of the rSOC cell.

Therefore, in both SOFC and SOEC operation, the sources are functions of the cell current. *Figure 5.4* shows the current distribution on the fuel electrode's TPB. The corresponding heat flux distribution on the TPB is depicted in *Figure 5.11*.

In SOFC operation the peak of current density and heat source distribution almost correspond, as the current density is the driver of the cell heating and most of the heat sources are located on the TPB of the anode. For this reason a temperature gradient of about 40 °C is generated in the first half of the SOFC at an average current density of 0.4 A/cm^2, as shown in *Figure 5.9*. In SOEC operation, the exothermic peak due overpotentials is less pronounced because: 1) the current density has a flatter profile, and 2) the endothermicity of reaction balances the heat generation determining a source profile with a mild negative peak in the first half of the cell, which induces a limited temperature gradient in the cell (i.e., around 20 °C at 0.4 A/cm^2, as shown in *Figure 5.9*).

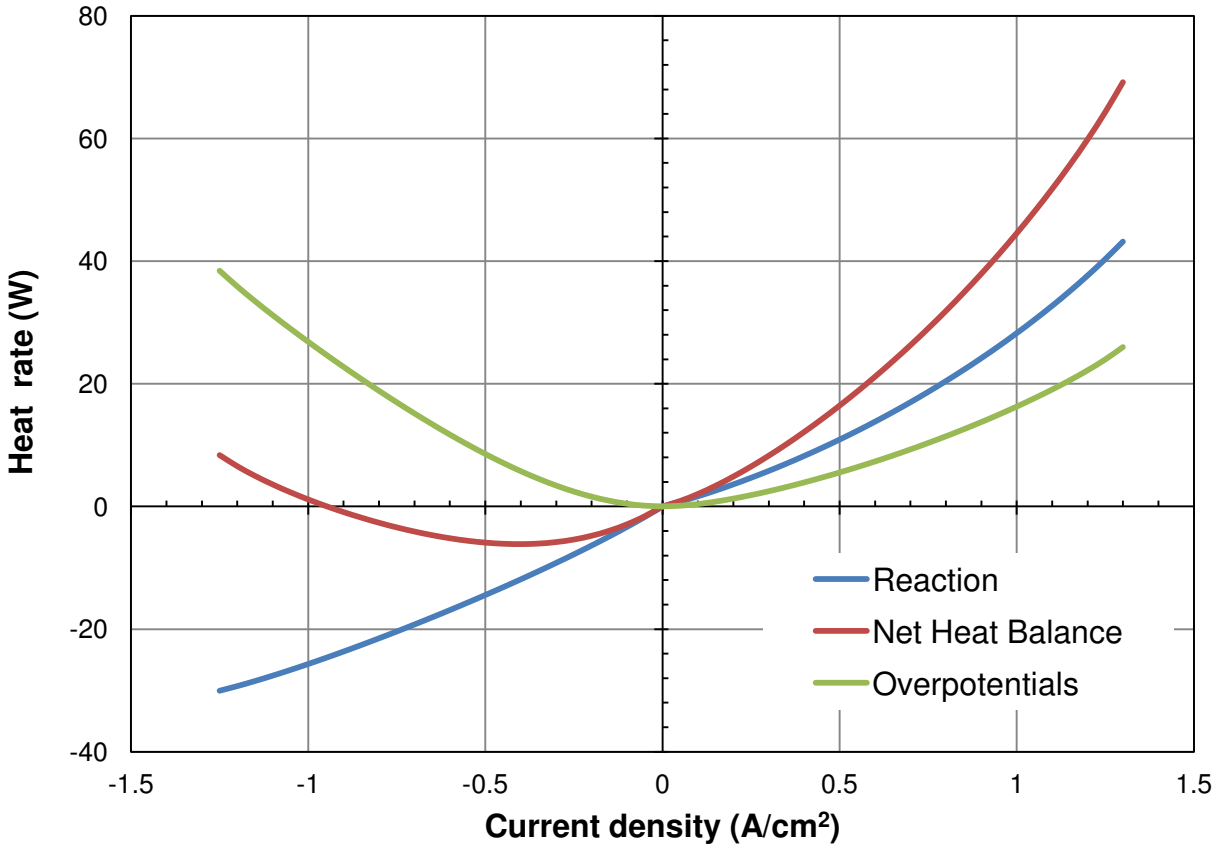

Figure 5.12 – Heat balance of the rSOC cell.

The temperature distribution of *Figure 5.9* also shows that the maximum cell temperature in SOFC operation is located at the end of the channels, due to the parallel flow arrangement. For this reason, the outlet temperatures of the fluids are very close to the maximum temperature of

the cell, and can be considered equal to this value with a good approximation. This assumption has been adopted for setting the limit on the maximum temperature allowable in the stack, as explained before in the discussion of the thermal constraints.

Finally, the heat balance of the rSOC cell is presented in *Figure 5.12*. It is worth noting that the net heat balance of the SOEC (i.e., negative currents) is zero for a current density of around 1 A/cm^2, that is the current value at which the thermoneutral voltage of the cell (that is ~ 1.29 V at 800 °C) is reached, as shown from the polarization plot (see *Figure 5.2*).

The rSOC simulations allowed to calculate the thermal profile in the imposed current range between 0 A and ±130 A. The maximum and minimum cell temperatures obtained from the thermal profiles of the cell and the total temperature gradient in the cell (i.e., given by the difference between the maximum and the minimum cell temperature) are depicted in *Figure5.13*. The Figure also reports the thermal constraints assumed on these three quantities.

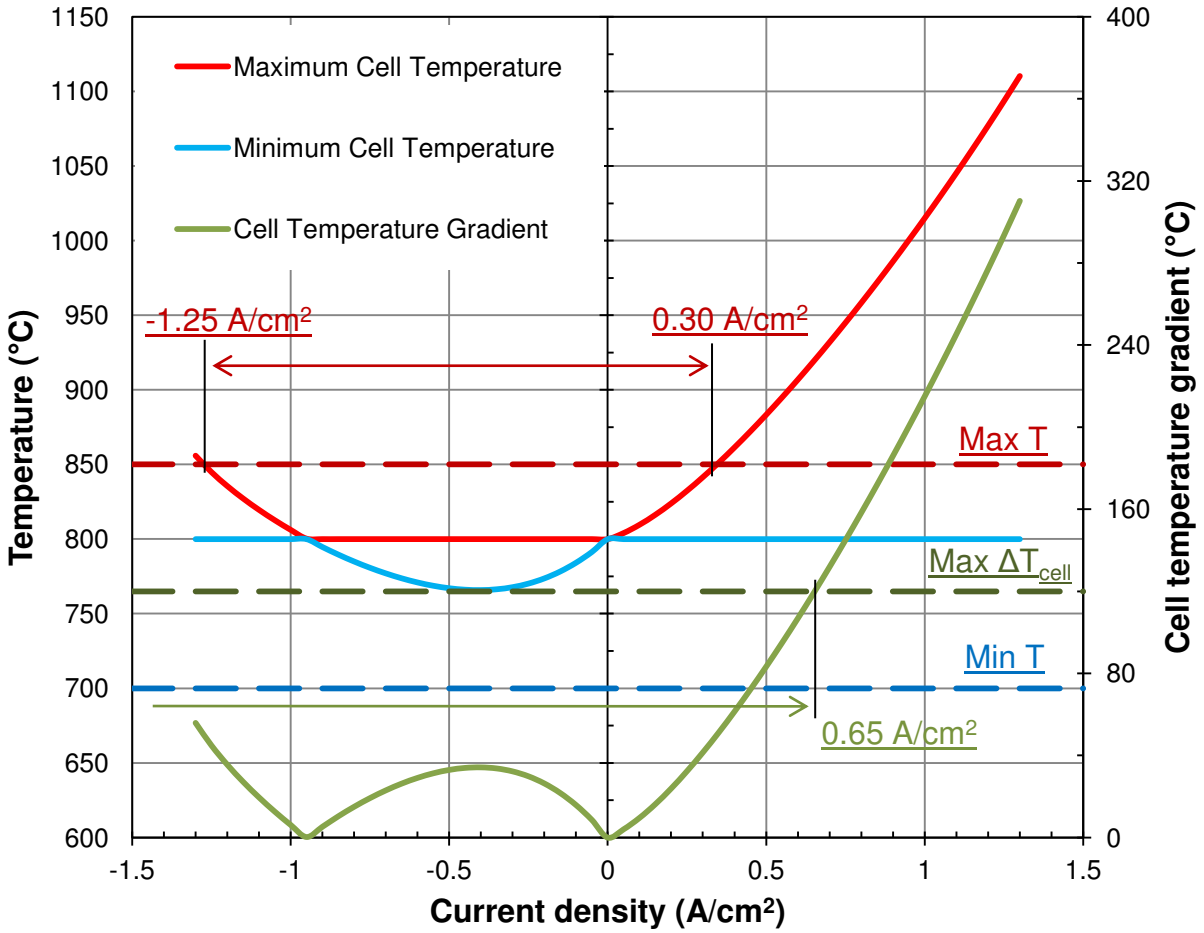

Figure 5.13 – Maximum and minimum cell temperature, and total temperature gradient in the cell with thermal constraints highlighted.

As expected, the maximum cell temperature (red line) corresponds to the inlet cell temperature of fluids (800 °C) in the current range in which the cell is operating in SOEC under the thermoneutral voltage (i.e., from 0 to -1 A/cm^2). Outside this range, the maximum temperature is obviously higher than 800 °C because of the exothermal operation. The current range in which the maximum temperature constraint is respected is between -1.25 and 0.30 A/cm^2. The minimum temperature has a complementary behavior, as it is lower than 800 °C only in under-thermoneutral operation. The minimum cell temperature never reaches the minimum constraint. The total temperature gradient in the cell is given by the difference between maximum and minimum cell temperature. This gradient exceeds the limit for a current density higher than 0.65 A/cm^2. In order to complete the verification of the thermal limits, also the maximum local temperature gradient in the cell must be checked. This gradient is depicted in *Figure 5.14*, together with the related constraint (red line on the plot). The local temperature gradient line crosses the limit at 0.85 A/cm^2, thus the local gradient is a less severe constraint with respect to the total cell gradient.

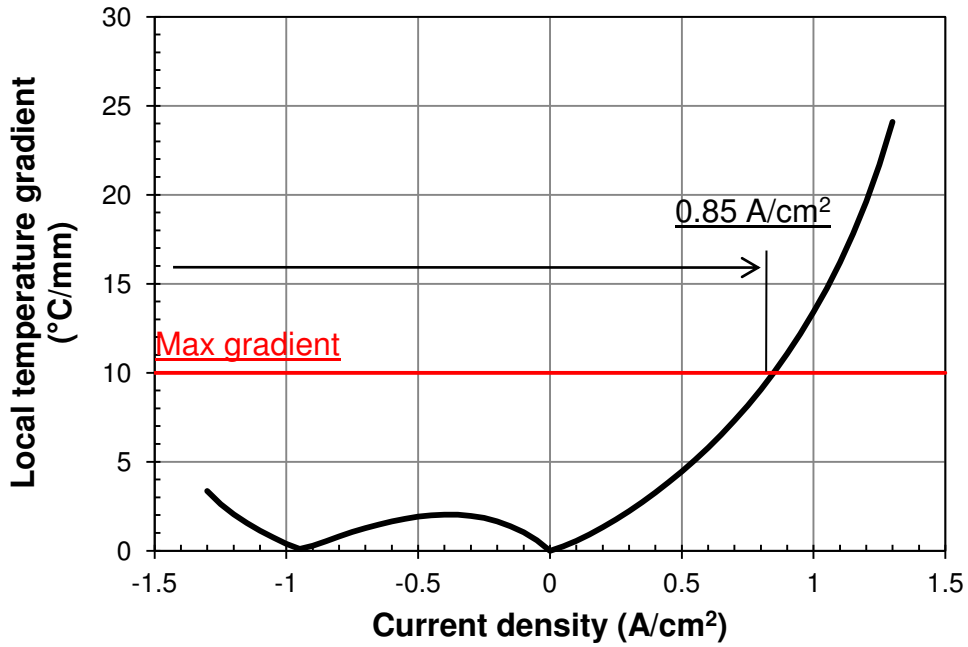

Figure 5.14 – Maximum local temperature gradient in the cell with thermal constraint highlighted.

From the analysis of the temperature parameters, it is found that the window in which the cell can operate safely from the thermal point of view is included between -1.25 A/cm^2 and 0.30 A/cm^2. The SOEC operation demonstrated to be safe in almost all the range of current, up to -1.25 A/cm^2 that correspond to a *FU* of ~ 87 %. The minimum cell temperature reached in SOEC

is around 760 °C, quite higher than the minimum constraint of 700 °C. Lowering the cell operation temperature increases the activation and ohmic losses, but not the endothermicity of the reaction, which is less endothermic at lower temperature, because the specific reaction heat ($T\Delta\bar{s}$) diminishes with the temperature, as shown in *Figure 2.3* of *Chapter 2*. For this is reason, it is expected that SOEC operation will not reach the minimum temperature constraint if a lower inlet temperature is imposed. This will be discussed in detail in *Section 5.2.2*. It is worth noting that a lower operation temperature can also potentially increase the maximum allowed SOEC current by reducing the maximum temperature reached by the cell; however, with the assumptions of the baseline model, at -1.3 A/cm^2 a *FU* of 91% is reached, thus there is only little room for enlarging the SOEC operating range.

SOFC operation is far the more critical mode of operation from the thermal point of view. The maximum temperature constraint strongly limits the operating range of the SRU, which reaches the limit at 0.30 A/cm^2. It is evident that lower inlet temperatures of the fluids or a higher air flow rate can positively affect the fuel cell mode by widening the safe operating range. This will be discussed in detail in the next section. Finally, if a T_{max} = 900 °C is considered (i.e., 100 °C above the inlet temperature, the same difference that divides the inlet temperature and T_{min}), the limiting current shifts to 0.575 A/cm^2, which is still far from the maximum current allowed in SOEC operation, but exposes the materials to critical conditions that cannot allow long-term operation.

Energy and exergy balance of the P2P system

The energy and exergy balance of BoP is shown in *Figure 5.16* and the electrical power exchanged by the SRU is depicted in *Figure 5.15*.

The electrical power produced (fuel cell) and absorbed (electrolysis) by the SRU is the product between cell voltage and current. The strong asymmetrical behavior is immediately visible from *Figure 5.15*. As the polarization curve suggests, the absorbed SRU power is higher than that produced by the fuel cell for most of the currents. The energetic and exergetic content of the electricity flow absorbed/produced by the cell is the same, as electricity can be theoretically fully converted in work.

The energetic and exergetic balances of the BoP are depicted in *Figure 5.16*. The contributions of the BoP are concentrated in two components: the heat recovery section of the BoP – which absorbs the thermal flow Φ_{ext} – and the hydrogen compressor. The compression power is a pure exergetic flow, while an exegetic flow is associated to the thermal one. The

water pumping power and that required by the air blower are neglected due to the cell operation at ambient pressure.

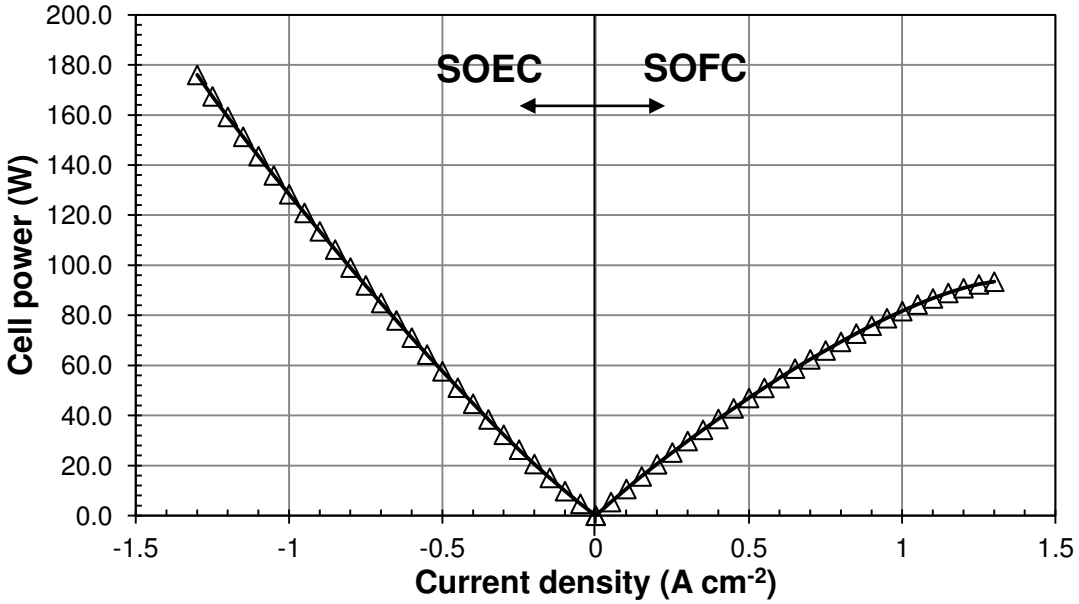

Figure 5.15 – Electrical power of the SRU (absolute value).

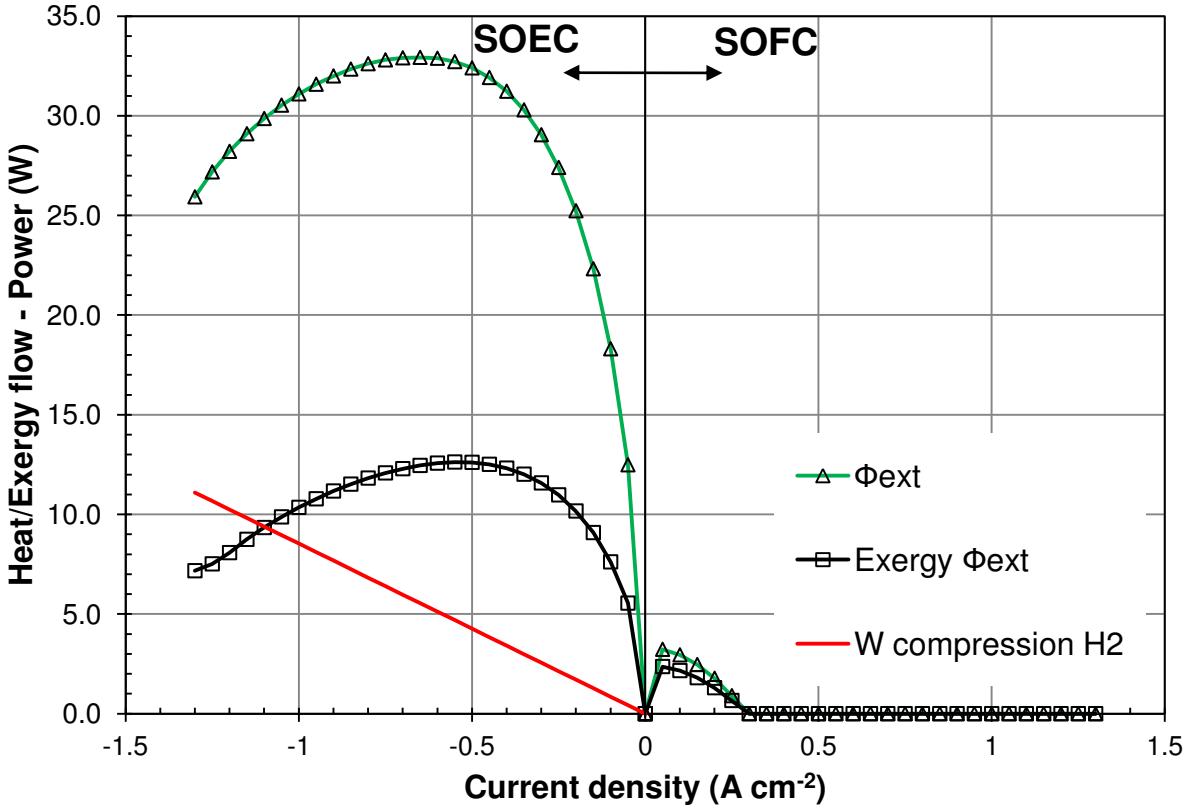

Figure 5.16 – Energy and exergy balance of the BoP.

The heat recovery section always requires an external thermal source when the system is operating in SOEC mode because of the low gas temperatures at the SRU outlet. In SOEC, the external heat flow required increases with the current until it reaches a maximum and then starts decreasing. This trend is clearly connected with the thermal behavior of the SRU: the lower is the outlet temperature of the cell, the lower is heat available from hot fluids in the heat recovery section, and consequently the higher is the external heat flow required for the preheating of cold fluids. In SOFC mode only a little contribution is needed from external sources until the SRU reaches 0.3 A/cm^2. Above this value, the exhaust fluids exiting the cell have a sufficient temperature level to allow the preheating of the incoming reactants without using external sources. It is worth noting that the exergy flow required in SOEC is sensibly lower with respect to the energetic one, while in SOFC the two values are very close. This is due to the temperature levels of the external heat sources, which are lower for electrolysis operation because a large amount of heat is needed for the steam production. In fact, water vaporization occurs at 100 °C at 1 bar and thus requires a heat source at 140 °C, given the assumption of using external sources with a ΔT_{min} of 40 °C with respect to the temperature of the cold fluid. In SOFC operation, heat is needed at high temperatures and thus its exergetic content is far higher than in SOEC; however, a lower amount of heat is required. The power required for the compression of the hydrogen produced in the SOEC from atmospheric pressure to30 bar has a linear trend with the current. This is due to the linear dependence of the produced hydrogen on the current for the Faraday's law, and on the linear relation between compression power and compressed flow. In SOFC operation, the option of recovery energy from the expansion of the hydrogen flowing in the SRU from the storage has been neglected.

The P2P efficiencies are reported in *Figure 5.17*. The Figure depicts the exergetic (dashed lines) and energetic (solid lines) charging and discharging efficiencies defined in *Section 5.1.2* (see equations (5.11) – (5.14)). The red symbols represent the operating points which satisfy the thermal constraints. In SOEC operation, the electricity storage efficiency (energetic) increases with the current until it reaches the value of η_{SOEC} = 0.61 A/W at -1.25 A/cm^2, which is the maximum current allowed by thermal constraints. This trend is due to combination of SRU and BoP energy flows; the decrease of Φ_{ext} is the driver that allows an efficiency increase also with increasing polarization losses. The exergetic storage efficiency in SOEC is higher, as the exergetic value of external heat is sensibly lower than the energetic one. The $\eta_{SOEC,ex}$ has a flatter profile, slightly decreasing at high currents. Maximum $\eta_{SOEC,ex}$ (0.67 W/A) is reached at -0.9 A/cm^2. In SOFC operation, the maximum efficiency η_{SOFC} = $\eta_{SOFC,ex}$ = 1 W/A is reached at 0.3

A/cm^2, condition in which the thermal flow required from external sources is zero. This point also satisfies the thermal constraints imposed.

The roundtrip efficiency of the P2P system operating at maximum efficiency points is thus 61 % energetic and 67 % exergetic (see equations (5.18) and (5.19) for the definition). The calculated ***H***-factor of the P2P system is 0.24 energetic and 0.33 exergetic at the maximum efficiency points. This means that for the P2P system of the baseline case, only a charging power 4 times higher with respect to the discharging one can ensure the operation in the maximum energy efficiency points.

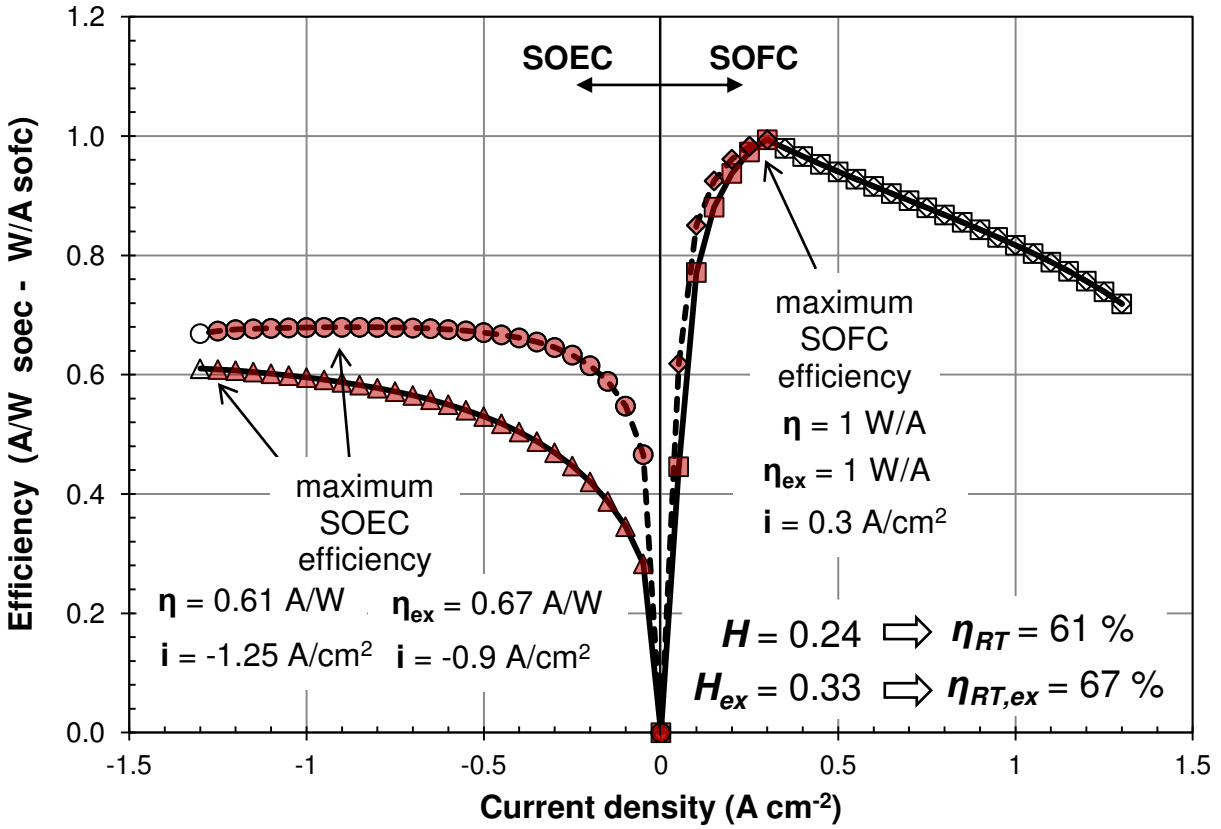

Figure 5.17 – Storage efficiency of P2P system, baseline case (1 bar, inlet gas 800 °C, air as oxidant with $\lambda = 3$, no recirculation on the oxidant side of the cell). Dashed lines are exergetic values, solid lines refer to energetic efficiencies. Red symbols represent the operating points which satisfy the thermal constraints.

The importance of ***H***-factor on the dimensioning of the P2P system can be shown with an example. Given a constant RES source of 100 kW, and conservatively considering that the RES is the only source available and thus provides energy to both rSOC and BoP, the dimensioning of the P2P system which works at the maximum roundtrip efficiency lead to a stack size of around 500 cells (i.e., 100 kW × 0.61 A/W / (1.25 A/cm^2 × 100 cm^2/cell) = 500 cells). With 500 cells, it

is possible to release around 15 kW (net power also considering BoP losses) from the SOFC operating at maximum efficiency current (i.e., 500 cell × 0.3 A/cm^2 × 100 cm^2/cell × 1 V/A), which is also the maximum allowable current. It is easily shown that the roundtrip efficiency of this system is 61 %, even if the power ratio between SOFC and SOEC is only 0.15:

$$\eta_{RT} = \frac{(|W_{cell}| - \phi_{ext} - W_{BoP})_{SOFC}}{(|W_{cell}| + \phi_{ext} + W_{BoP})_{SOEC}} \cdot \frac{1}{\boldsymbol{H}} = \frac{15\ kW}{100\ kW} \cdot \frac{1}{0.24} = 0.15 \cdot \frac{1}{0.24} = 0.61$$

Therefore, from 100 kW of RES power available, the discharging rate at maximum efficiency is only 15 kW, which cannot be exceeded for the thermal limits of the rSOC. Therefore, storing 100 kW with 61% of roundtrip efficiency, it doesn't mean that 61 kW can be retrieved at any time due to the asymmetric operation of the system. If we want to retrieve a higher power, the ***H*** value must be increased, but this will be paid with a loss of efficiency. For example, if ***H*** = 1 is imposed, all the points in which $I_{cell,SOFC} = I_{cell,SOEC}$ satisfy this condition, thus it is possible to chose a value of current equal for both SOEC and SOFC for which the maximum roundtrip efficiency at ***H*** = 1 is realized. The efficiency curves for ***H*** = 1 are plotted in *Figure 5.18*.

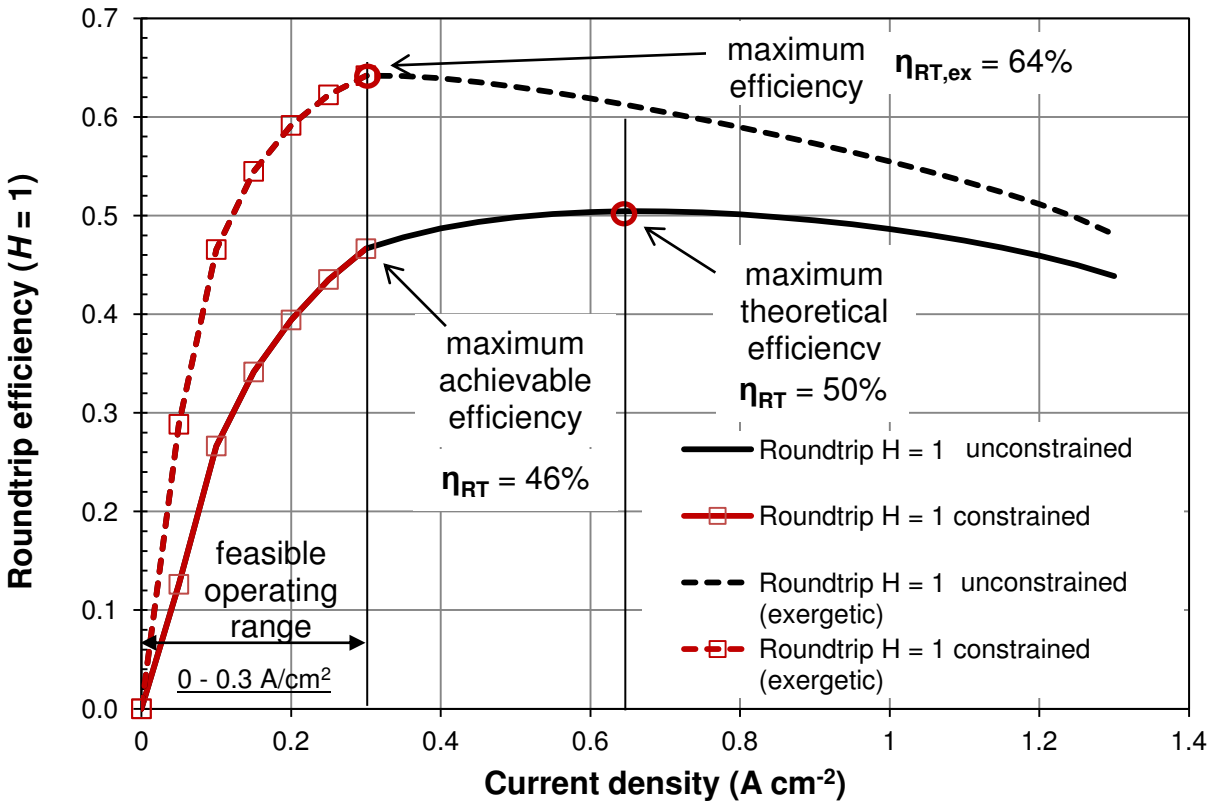

Figure 5.18 – Roundtrip efficiency of P2P with ***H*** = 1, baseline case. Red lines represent the feasible operating range.

The maximum theoretical roundtrip energetic efficiency (η_{RT} = 50%) is reached at 0.65 A/cm^2; however, this is not a feasible operating point because of SOFC thermal constraints. The maximum allowed current is 0.3 A/cm^2, for which η_{RT} = 46 % and $\eta_{RT,ex}$ = 64 %. Therefore, the operation of P2P system with $\boldsymbol{H}$ = 1 produces a loss of energetic roundtrip efficiency of 15 % with respect to the operation at $\boldsymbol{H}$ = 0.24. With reference to the example given before, if 100 kW of RES are available, the net power that can be obtained from the SOFC with $\boldsymbol{H}$ = 1 is 46 kW. In this case the charging and discharging time are the same, and 0.46 kW can be retrieved from 1 kW stored, which is exactly the roundtrip efficiency.

In general, the power ratio between SOFC and SOEC is the product between $\boldsymbol{H}$ and the roundtrip efficiency. A high value of $\boldsymbol{H}$ (i.e., fast discharging P2P) is the necessary condition to reach the highest SOFC/SOEC power ratio in the P2P system. The combination of a near zero SOEC operating current and the highest possible SOFC current (i.e., 0.3 A/cm^2) ensures the highest $\boldsymbol{H}$; however, the roundtrip efficiency is strongly penalized by the very low charging efficiency. For example, if the SOEC operating current is 0.05 A/cm^2 and the SOFC one is 0.3 A/cm^2, the $\boldsymbol{H}$ value is 6, the roundtrip efficiency is 28%, and the SOFC/SOEC power ratio is 1.68, which means that from 1 kW stored it is possible to obtain 1.68 kW, but with a very low efficiency (η_{RT} = 28 %).

Figure 5.19 shows the performance map of the P2P system, where the roundtrip efficiency of the P2P system operating in baseline case conditions is depicted as function of the SOFC and SOEC current densities. The efficiency curve for the operation at a certain value of $\boldsymbol{H}$ is given by the intersection of the efficiency surface of *Figure 5.19* with a vertical plane passing through the origin and with an inclination given by the ratio between the SOFC and SOEC current densities. In the baseline case analyzed, the maximum efficiency point is unique; thus, there is only one vertical plane that can crosses the efficiency surface in the maximum efficiency point. This plane has an inclination $\boldsymbol{H}$ = 0.24.

For each combination of the operating parameters of the rSOC (i.e., inlet temperatures, oxidant-to-fuel ratio, cell pressure, etc.) an efficiency map can be built, and from the map it is possible to predict the roundtrip efficiency of the P2P system operating with a certain $\boldsymbol{H}$ factor. The efficiency map allows to identify the operating currents at which the maximum roundtrip efficiency is reached in certain conditions, and consequently the charging and discharging powers of the P2P system that ensure the maximum efficiency when a certain size (i.e., number of cells) of the rSOC stack is fixed. However, the value of the power applied to the SOEC or required to the SOFC depends on the characteristics of the electricity source available for

hydrogen production and of the load that can retrieve the produced electricity. For a P2P system operating in baseline case conditions, the best would be to have a source and a load with a constant power ratio of 0.15 to work with the highest possible roundtrip efficiency (i.e., η_{RT} = 61 %) at $\boldsymbol{H}$ = 0.24 for all the operation time.

It is worth noting that when considering the use of P2P systems coupled with RES, the goal of the application could not be the maximization of roundtrip efficiency – as RES can be considered "free" sources – but for example the provision of the power required by users. In this case, since the target is to produce a certain power, the P2P is dimensioned for providing the required power profile given a certain RES availability, and not necessarily the operating currents that allow to satisfy the demand coincide with those that ensure the maximum efficiency. The case study presented in *Section 5.4* better explains this aspect by showing a realistic application of an rSOC-based P2P system coupled with a wind farm.

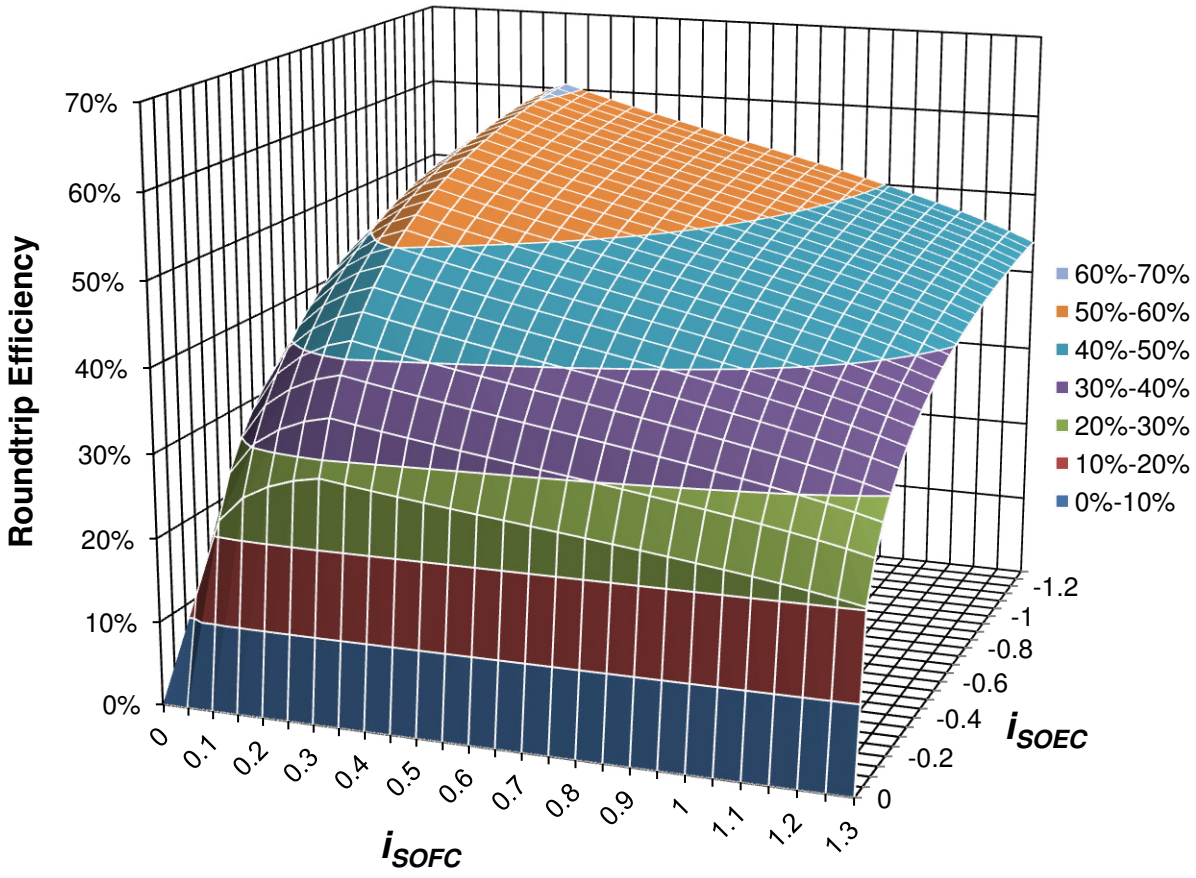

Figure 5.19 – Efficiency map of the P2P system (baseline case).

5.2.2 Sensitivity analysis results

Sensitivity analyses have been performed on the parameters listed in *Table 5.2*. The parameters were varied one by one maintaining fixed the others to the baseline model values, excluding the current that was always varied between 0 A and 130 A in each analysis. In this way, the effect of each parameter on the system behavior has been investigated. Inlet temperatures were varied in the range 700 – 850 °C, the pressure in the range 1 – 10 bar, and the air was changed to oxygen.

Pressurized operation

The effect of pressurized operation has been simulated by varying the operating pressure from 1 to 10 bar at the outlet of the channels. Simulations were run a 1, 5 and 10 bar.

The polarization curves are shown in *Figure 5.20*. The operating voltage of the cell constantly increases with the pressure for SOFC operation, while in SOEC decreases with pressure varying from 1 to 5 bar for a current density higher than -0.15 A/cm^2 and increases again from 5 to 10 bar at all the current levels. These trends can be understood by looking at the reversible voltage of the cell plotted in *Figure 5.21* and at the overpotential losses evolutions depicted in *Figure 5.22*.

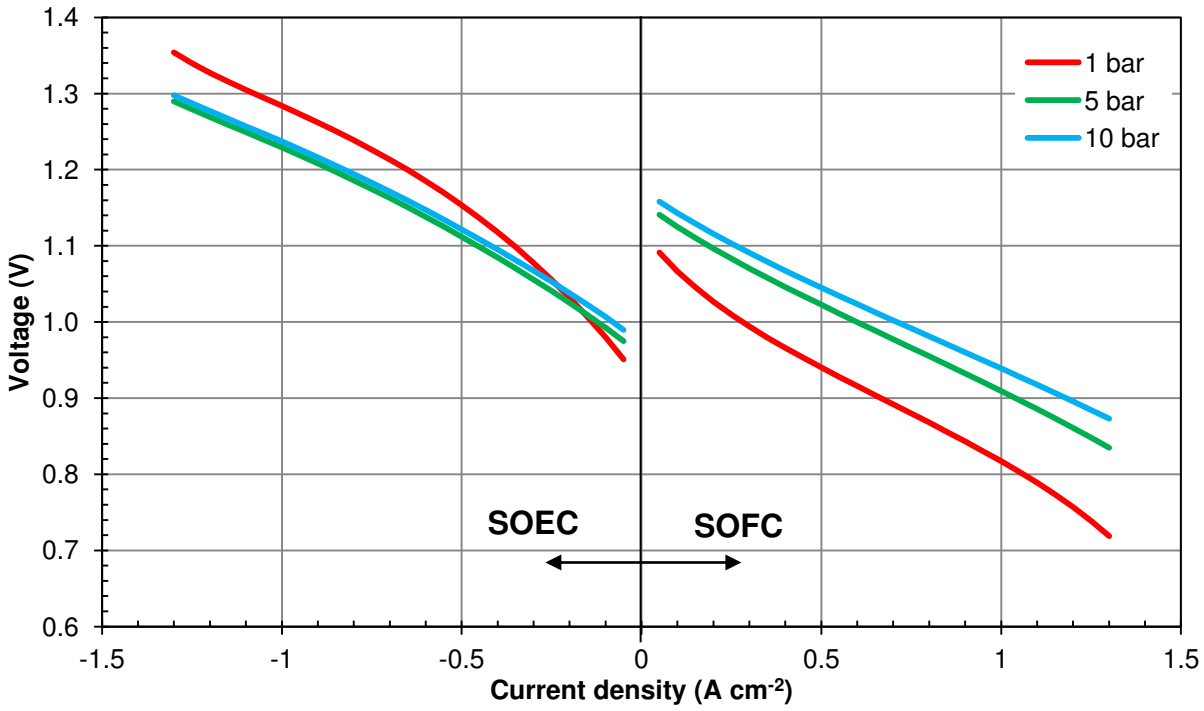

Figure 5.20 – Simulated rSOC polarization of SRU operating at 1, 5 and 10 bar.

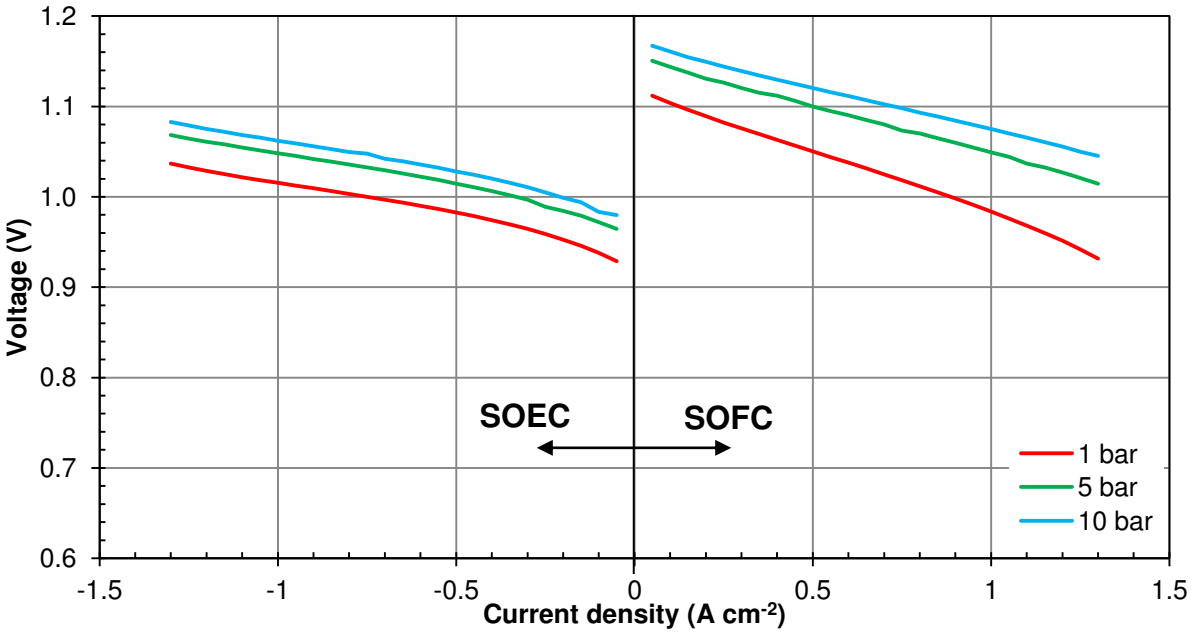

Figure 5.21 – Reversible voltage of rSOC operating at 1, 5 and 10 bar.

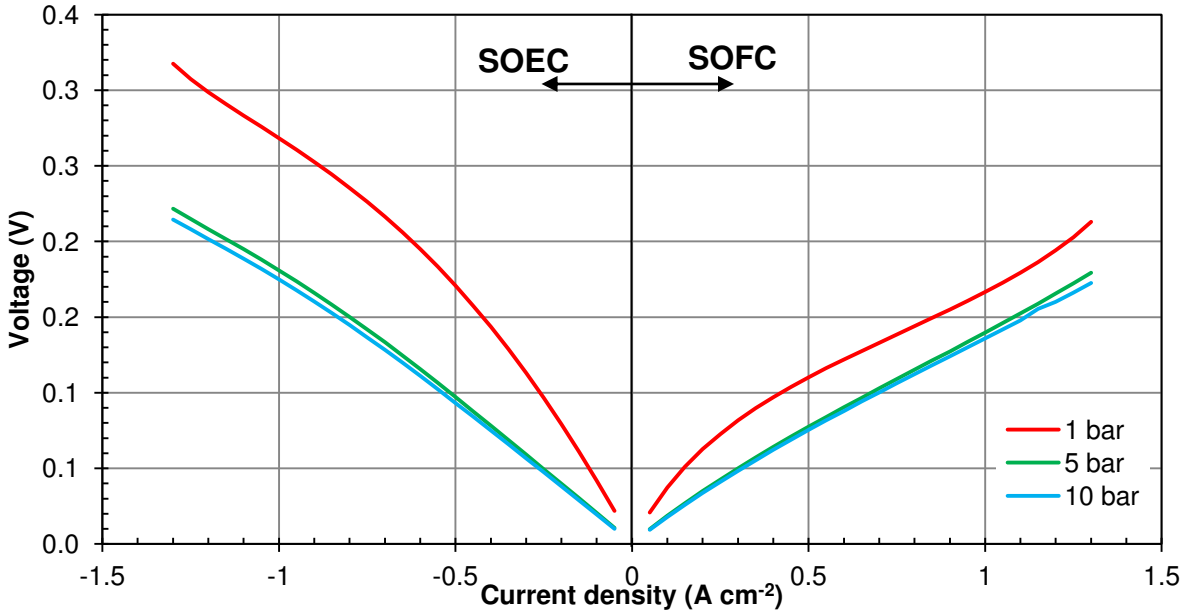

Figure 5.22 – Sum of overpotentials for the SRU operating at 1, 5 and 10 bar.

The reversible voltage always increases with pressure, as expected from its formulation given in *Chapter 2* (see equation (2.34)). This effect is beneficial in SOFC, while it has a negative impact on the SOEC operation. The overpotential losses decrease with pressure in all the conditions investigated, because the higher partial pressures reduce the activation losses of electrochemical reactions. The losses decrease is concentrated between 1 and 5 bar, while a further increase of the pressure is not very effective. It is worth noting that the activation kinetics used in the model

were validated at ambient pressure, thus their application to higher pressures is an extrapolation. Specific experiments in pressurized environment are need for a more precise evaluation of the kinetics in these conditions. The combination of decreasing losses and increasing reversible voltages produces the polarization of *Figure 5.20*. In the SOEC case, the increase of the pressure generates contrasting effects that lead the SRU voltage to be lower at 5 bar with respect to 10 bar.

The maximum and minimum cell temperatures calculated from the model and the total temperature gradient in the cell are depicted in *Figure 5.23*. The heat sources at 5 and 10 bars assume very similar values due to the fact that overpotentials are similar at these two pressures, as shown in *Figure 5.22*, and also the reaction heat slightly varies with pressure between 5 and 10 bars. For this reason, temperature profiles under pressurized operation are very close and only the maximum and minimum temperatures obtained from 5 bar operation are depicted in *Figure 5.23* for the sake of clarity.

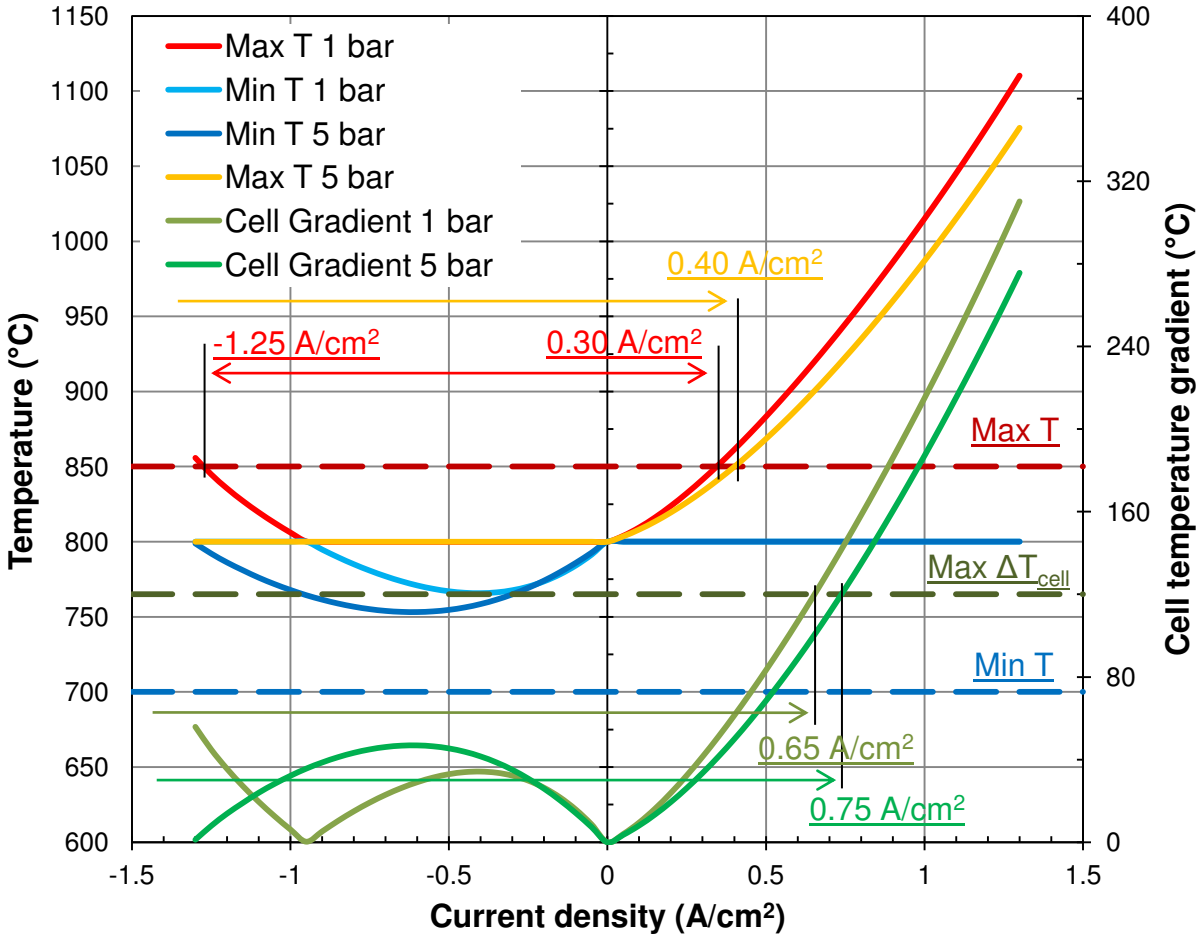

Figure 5.23 – Maximum and minimum cell temperature, and total temperature gradient in the cell with thermal constraints highlighted at different operating pressures.

The Figure shows that in SOEC operation the minimum cell temperature assumes lower values in pressurized operation due to the reduction of the overpotential losses that contribute to the heating of the cell. The current density interval in which the SOEC is endothermic is also wider under pressure because the thermoneutral voltage (~ 1.29 V at 800 °C) is reached at higher currents. In particular, in all the current range investigated the pressurized SOEC is operating under the thermoneutral voltage. Even if the minimum temperature is lower than in the baseline case, the thermal constraints is still widely satisfied. Also the maximum cell temperature decreases with respect to the baseline case, due to the diminishing of overpotentials heating. For this reason, the feasible operating current range is wider, and includes all the SOEC currents up to 0.4 A/cm^2 in SOFC. The total temperature gradient in the cell exceeds the constraint for a current density higher than 0.75 A/cm^2. In order to complete the verification of the thermal limits, also the maximum local temperature gradient in the cell must be checked. *Figure 5.24* shows that the pressurized operation enhances the local gradients, up to coincide with the total cell gradient at 5 bar, and reduces the feasible operating range. However, the limiting current due to the local gradient is still far higher than the maximum current related to maximum temperature constraint.

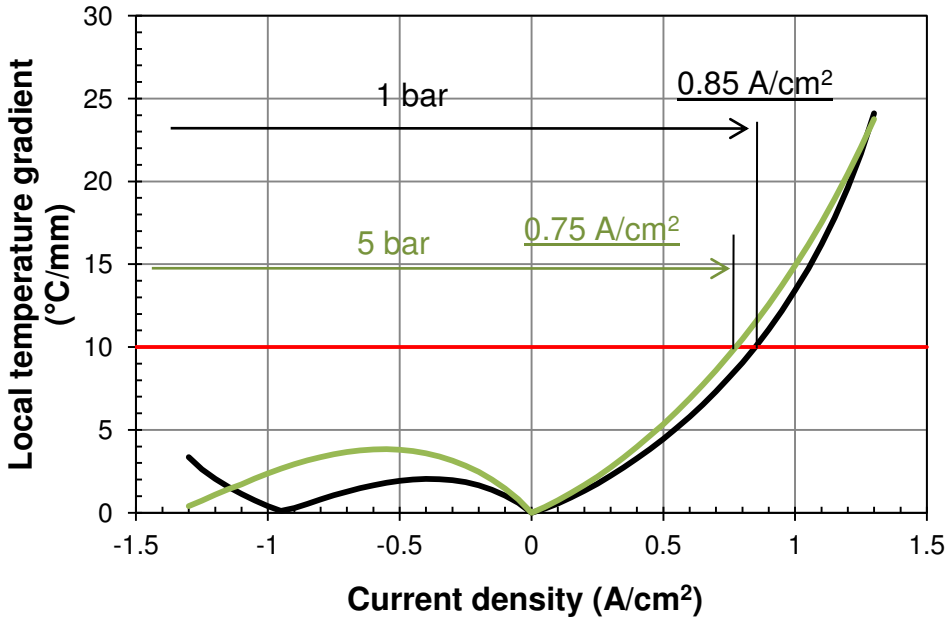

Figure 5.24 – Maximum local temperature gradient in the cell with thermal constraint highlighted at different operating pressures.

The electrical power exchanged by the SRU is depicted in *Figure 5.25*. The strong asymmetrical behavior between SOEC and SOFC is still present also in pressurized operation. Even if the SOFC power curve is more linear at higher pressures.

The energetic balance of the BoP is depicted in *Figure 5.26*. The contributions of the BoP are: the external heat flow Φ_{ext}, the air compression power (both present in both SOEC and SOFC operation), the hydrogen compression power and the water pumping power (the last two only in SOEC operation).

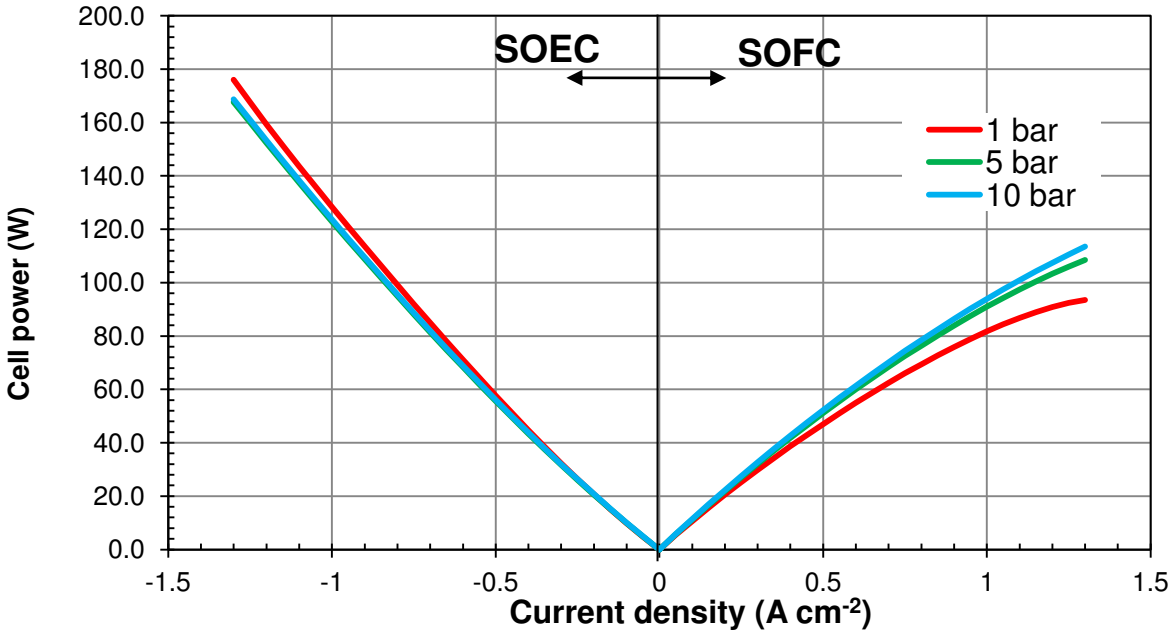

Figure 5.25 – Electrical power of the SRU (absolute value).

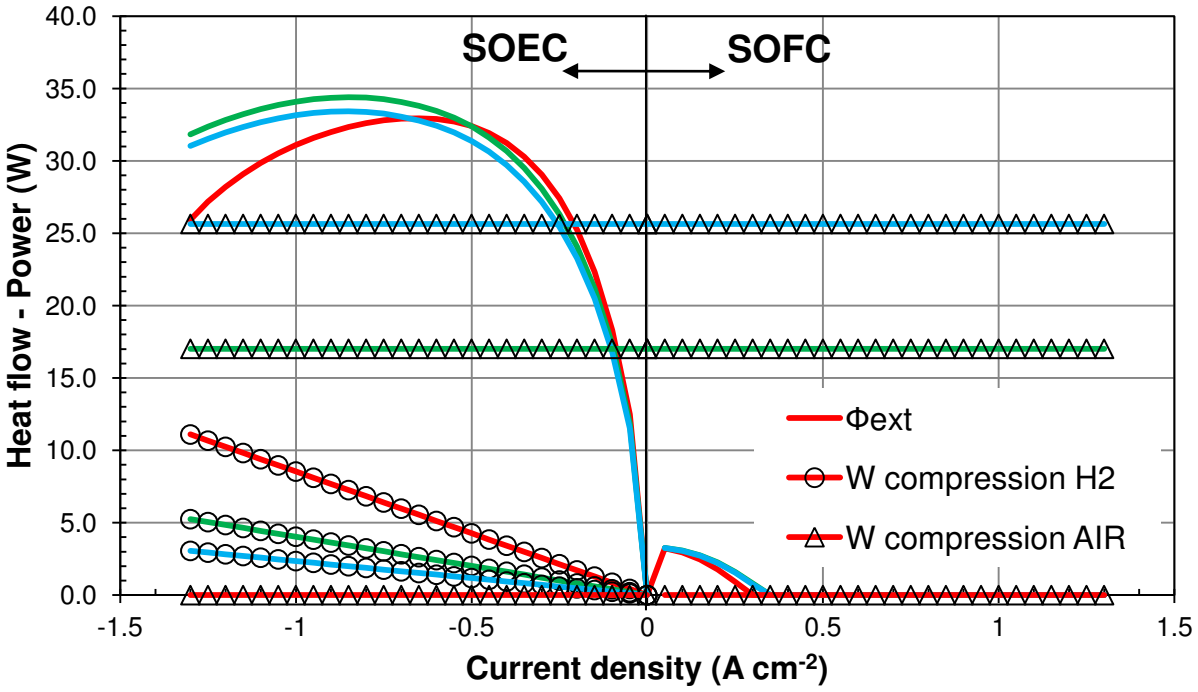

Figure 5.26 – Energy balance of the BoP. (Solid lines red: 1 bar, green: 5 bar, blue: 10 bar).

The power consumed by water pumping is negligible and thus is not reported in *Figure 5.26*. The trend of the absorbed heat flow in the heat recovery section of the BoP is similar at different operating pressures. In SOEC, at high current densities, a slightly higher heat flow is absorbed at 5 and 10 bar, mainly because of the lower temperature of the fluids exiting the SRU. The same for SOFC operation, in which the heat demand from external sources increases with pressure due to the lower temperatures reached at the outlet of the SRU in pressurized operation. The hydrogen compression power is linear with the current and decreases with the operating pressure, as the pressure gradient between SRU and storage (30 bar fixed) diminishes with the increasing pressure of the SRU. The air compression power is constant with the current because the air flow rate is fixed ($\lambda = 3$) and increases with the SRU pressure, as air is always available only at ambient pressure.

The charging and discharging efficiencies are reported in *Figure 5.27*. The Figure depicts the energetic efficiencies (solid lines; red: 1 bar, green: 5 bar, blue: 10 bar). Red symbols represent the operating points which satisfy the thermal constraints.

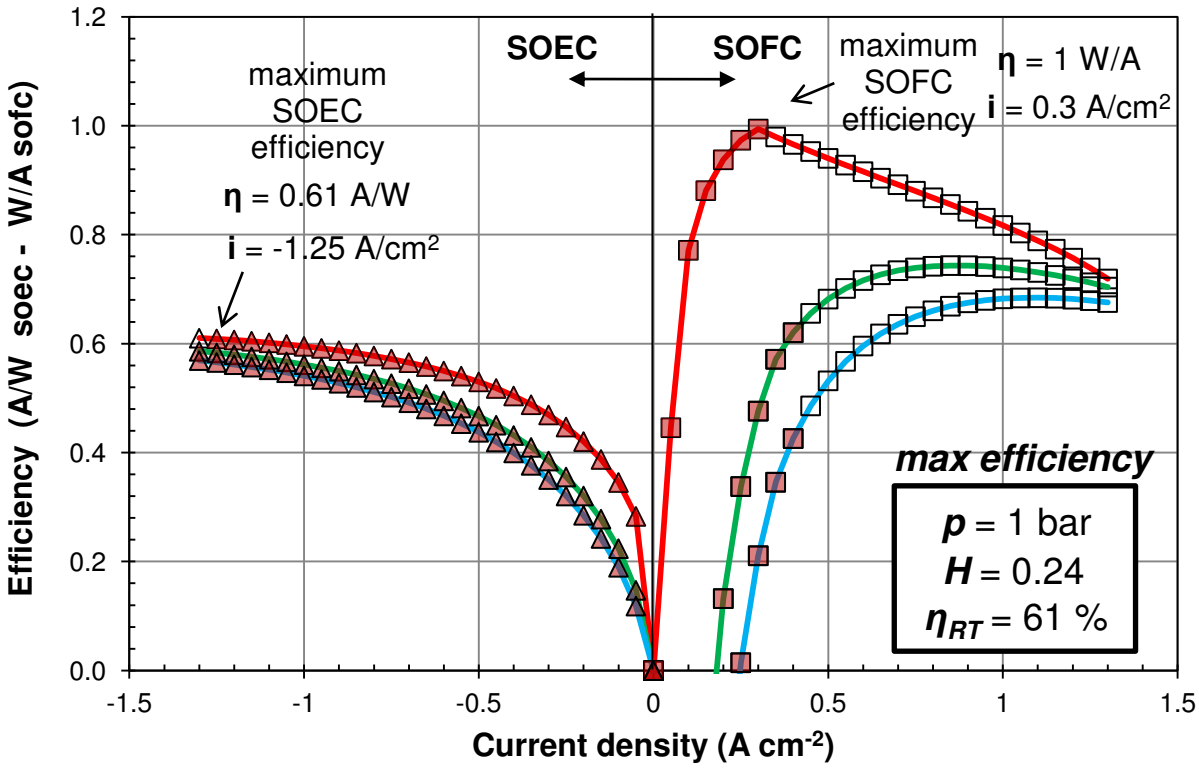

Figure 5.27 – Storage efficiency of P2P system. Solid lines refer to energetic efficiencies (red: 1 bar, green: 5 bar, blue: 10 bar). Red symbols represent the operating points which satisfy the thermal constraints.

In all the operating current range the pressurized operation shows lower efficiencies in both energy charging and the discharging. This is mainly due to the air compression power that strongly affects the BoP requirements. The only advantage of pressurized operation is the higher maximum allowable current in SOFC operation (i.e., 0.4 A/cm^2 instead of 0.3 A/cm^2); however, this positive effect is far less important than the drawbacks on the BoP.

The sensitivity analysis on the pressure parameter of the P2P system suggest that the optimal operation should be at ambient pressure if no recirculation of the oxidant is performed, because the improvement of stack performance related to the higher partial pressures of gases is largely balanced by the increase of BoP energy requirements. In particular, the increase of air compression power with the pressure is the main driver of the efficiency lowering. From *Figure 5.26* it is possible to see that the increase of the power required by air compression is always higher than the decrease of H_2 compression power with pressure, mainly due to higher flow of the oxidant stream. Therefore, a further increase of the operating pressure is expected to worsen the global efficiency even in the case the stack is operating at 30 bar and no compression is needed to store the produced hydrogen. Moreover, the pressurized operation increases the cost of the equipments, thus also the economics are expected to be negatively affected.

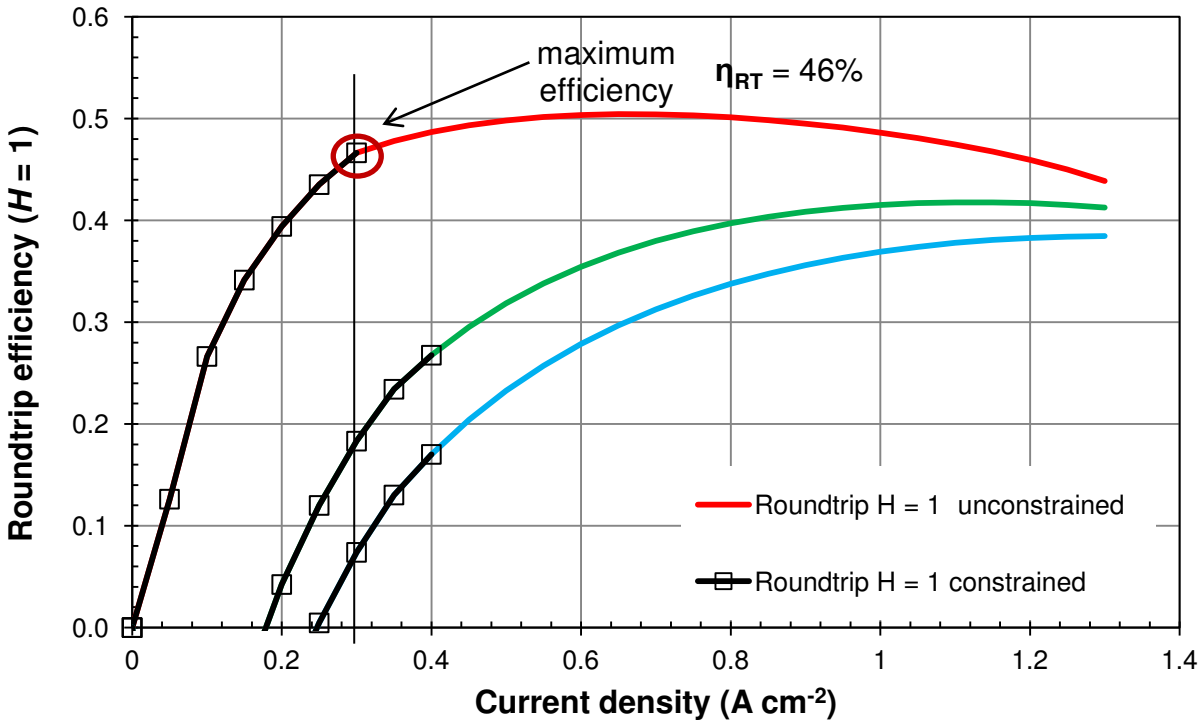

Figure 5.28 – Roundtrip efficiency of P2P with ***H*** = 1 (Solid lines red: 1 bar, green: 5 bar, blue: 10 bar). Black lines represent the feasible operating range.

It is worth noting that the SOFC system efficiency is the most affected by the pressurized operation because of the air compression power added to BoP energy requirements, while in the SOEC operation the system efficiency only slightly diminishes. Therefore, the pressurized option without oxidant recirculation can possibly be considered only for SOEC operation. In the case of operation at $\boldsymbol{H} = 1$, *Figure 5.28* shows that the maximum feasible roundtrip efficiency is 26 % for the 5 bar rSOC and 17 % for 10 bar, thus the P2P system experiences a considerable performance drop with respect to atmospheric operation that allows 46 % of efficiency, if oxidant recirculation is not considered.

Oxidant flow: Air vs. Oxygen operation

In this section, the comparison of rSOC operation using either air or pure oxygen as oxidant flow is assessed. The comparative analysis has been carried on at different operating pressures (1, 5, 10 bar) and also considering the effect of oxidant recirculation.

With respect to the use of air, in the case of pure oxygen operation the compression of the O_2 exiting the stack from stack pressure to storage pressure (i.e., 30 bar) is needed in SOEC operation. Moreover, if the oxygen is not fully recirculated, it is necessary to re-compress the non recirculated flow from the stack to the storage pressure. Oxidant recirculation is not a source of issues for the cell in case of pure oxygen operation, as at the cell inlet there is only pure oxygen independently on the recirculation rate, while in air operation the oxygen fraction at the cell inlet depends on the operating current and recirculation rate. The best solution for the pure oxygen operation would be the full recirculation of the oxidant at the cell outlet to avoid the recompression stage to the storage pressure.

When the rSOC is operated with air, recirculation has drawbacks on the inlet oxygen fraction. In fact, in SOEC operation recirculation increases the oxygen partial pressure at cell inlet and consequently the operating voltage of the cell. In SOFC mode, the effect is the opposite: when lean air exhaust is mixed with fresh air at the cell inlet, the O_2 partial pressure decreases and operating voltage decrease. Even if air recirculation is not optimal for the cell, it allows to perform energy savings in the BoP by reducing the air compression power when the rSOC is operating under pressure. However, the fraction of air recirculation cannot be set arbitrarily, as the oxidant molar flow entering the cell must contain enough oxygen to provide the reactant required by SOFC operation. Thus, a limit recirculation rate exists in SOFC operation. In SOEC operation, the recirculation is limited only by the desired fraction of O_2 at the cell inlet. In the analysis performed, a limit recirculation rate of 0.4 was chosen. This rate ensures an oxygen

fraction of 15 % at the inlet of the SOFC operating at 1 A/cm^2, corresponding to a molar fraction of 5 % of oxygen at the outlet. With this rate, it is also possible to operate the SOFC up to 1.3 A/cm^2 without occurring in oxygen starvation at the anode. This limit fraction has been adopted for both SOFC and SOEC operation in order to perform a symmetric analysis.

The results of simulations without recirculation are shown firts. The polarization curves obtained are depicted in *Figure 5.29* (SOFC) and *Figure 5.30* (SOEC).

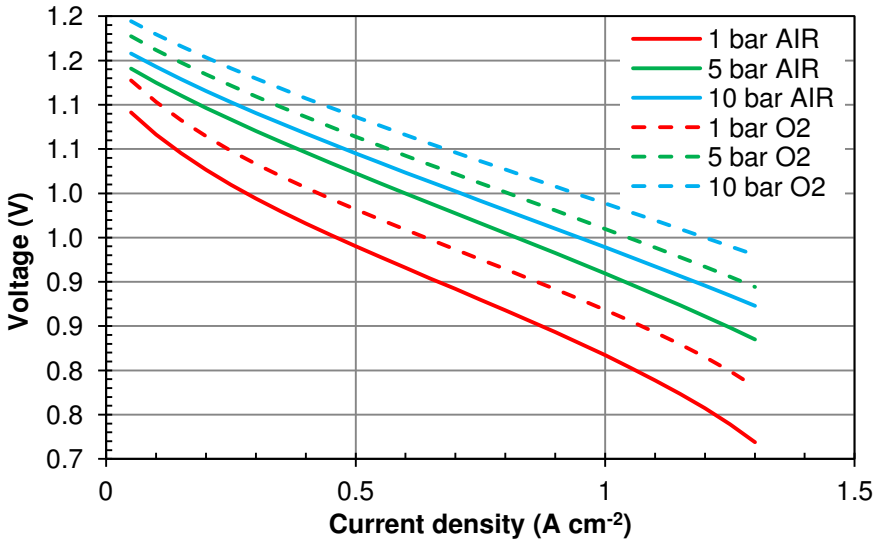

Figure 5.29 – Simulated SOFC polarization of SRU operating at 1, 5 and 10 bar using either air or pure oxygen as oxidant flow.

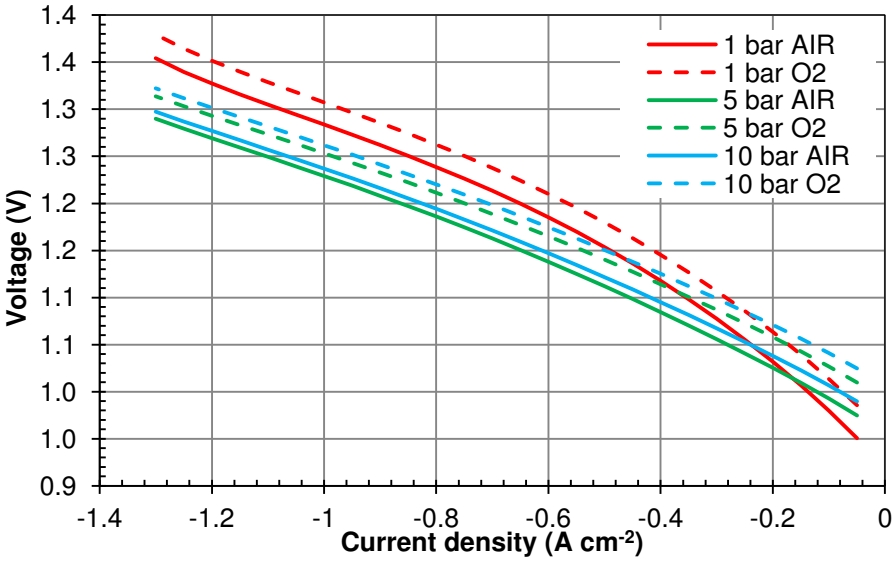

Figure 5.30 – Simulated SOEC polarization of SRU operating at 1, 5 and 10 bar using either air or pure oxygen as oxidant flow.

The Figures shows that the operation with pure oxygen is beneficial for SOFCs, as it increases significantly the cell voltage, while it has the opposite effect in SOEC mode. This effect is

mainly due to the increase of reversible voltage with pure oxygen, while overpotential losses remain essentially unchanged, as the activation overpotential of oxygen electrode is the only one to be directly affected by oxygen partial pressure, but it plays a minor role in determining the overall losses. In principle, this would suggest to use oxygen only in SOFC operation; however, if air is used in SOEC it is not possible to separate the oxygen produced from the nitrogen without using costly processes (i.e., costly both in terms of energy and money). Another option for SOEC operation is the use of a sweep gas without oxygen; this would decrease the cell voltage, but if the sweep gas is not separable from the produced oxygen the option is again not feasible in a P2P configuration that is designed to reuse the O_2.

Another possibility could be the use of water as sweep gas, because is the only fluid that can be easily separated from oxygen. However, the cycle of steam production (to reach the cell temperature) and condensation (to separate the oxygen) adds a considerable thermal burden to the heat recovery section and increases the complexity of the system. For this reason, this option has not been considered in the present study.

The effects of oxygen operation with respect to air operation on the temperature profiles are not highly significant, mainly because air and oxygen properties are very similar. The maximum cell temperature increases of few degrees (5-7 °C) at maximum cell currents (in both SOFC and SOEC) with pure O_2 operation for all the pressure levels. Lower increases are calculated for lower current values. The minimum cell temperature is also affected in the same way. Results are not reported due to the exiguity of the differences. Thus, pure oxygen operation does not change significantly the temperature reached within the cell and consequently also the limiting currents due to thermal constraints remain almost unchanged.

The charging efficiency of the SOEC system is depicted in *Figure 5.31*. The air operation at ambient pressure is still the option with the highest efficiency. The pure oxygen operation at 1 bar is the worst option, mainly due to oxygen re-compression at the cell outlet. In fact, the O_2 stored at 30 bar in a tank is feed at 1 bar to the cell without recovering energy from the pressure difference, and then the oxygen at inlet plus the oxygen produced are compressed again to the storage pressure. Thus, the use of oxygen as sweep gas is clearly an option that requires the maximum possible recirculation at the SOEC anode to avoid a costly recompression. The effect of recirculation has been investigated later in the discussion. When the system is operating at 5 bar, the efficiency of air operation is still higher than that with pure oxygen, always because of the oxygen re-compression. However, the difference between these two options is sensibly lower with respect to atmospheric operation. In fact, the increasing pressure reduces the energy

consumption of the oxygen recompression as less pressure difference is established between rSOC and storage, while the air compression power increases with the pressure. Thus, the efficiency trend with the varying pressure is opposite for air and oxygen operation.

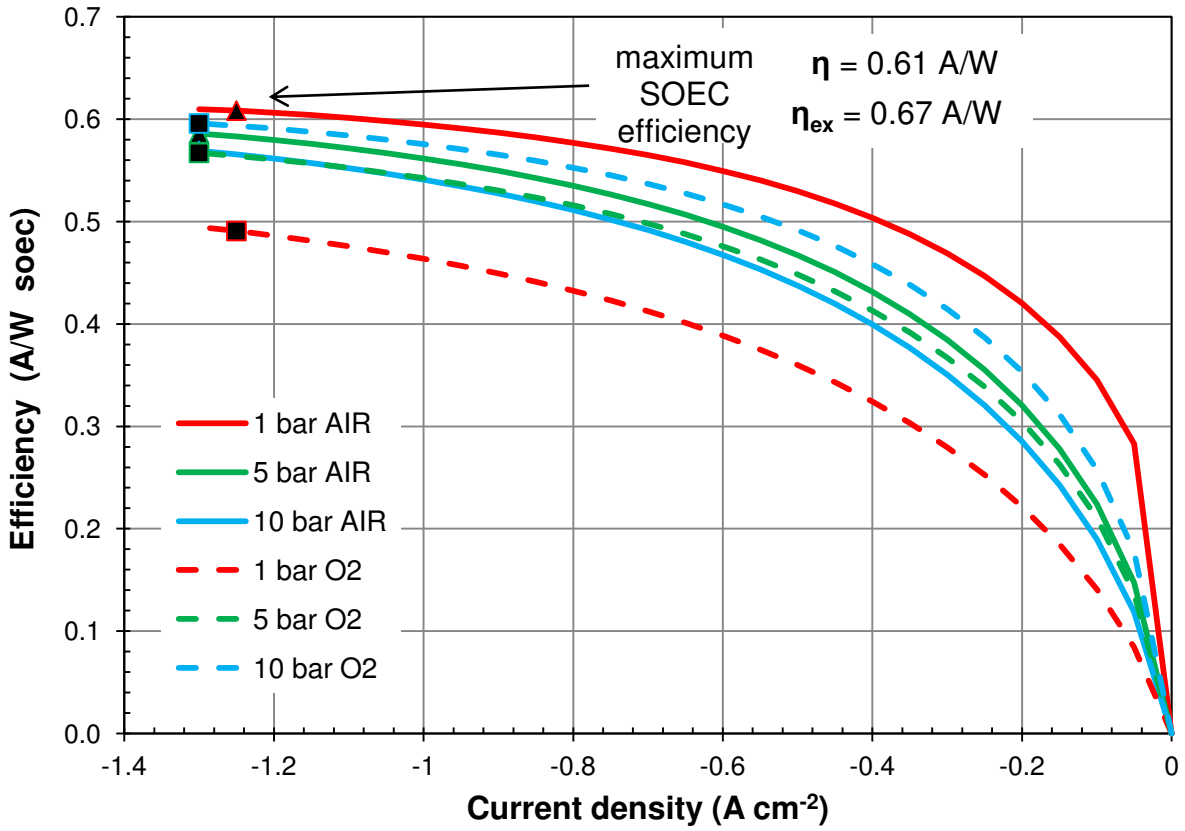

Figure 5.31 – Storage efficiency of SOEC system without oxidant recirculation. Solid lines refer to air operation and dashed lines to pure oxygen (red: 1 bar, green: 5 bar, blue: 10 bar). Black dots represent the limit operating points.

Due to these opposite trends, at 10 bar the SOEC efficiency is higher in the operation with pure oxygen, reaching a value of η_{SOEC} = 0.59 A/W at -1.3 A/cm^2. A higher level of operating pressure is expected to further increase the efficiency, eventually exceeding that of the ambient air operation.

Therefore, the analysis has shown that even without oxidant recirculation, the option of pressurized SOEC operation with the use of oxygen as sweep gas has a storage efficiency (0.59 A/W) close to that of the baseline case (0.61 A/W). The advantage of using oxygen as sweep gas lies in the possibility to store it without needing gas separation. The re-compression to storage pressure is the main drawback of its use; however, if it is stored at a pressure level very close to that of the cell, the energy consumption of re-compression can be sensibly lowered. Also oxidant

recirculation can sensibly reduce the volume of re-compressed oxygen and consequently the energy expenses of this BoP element.

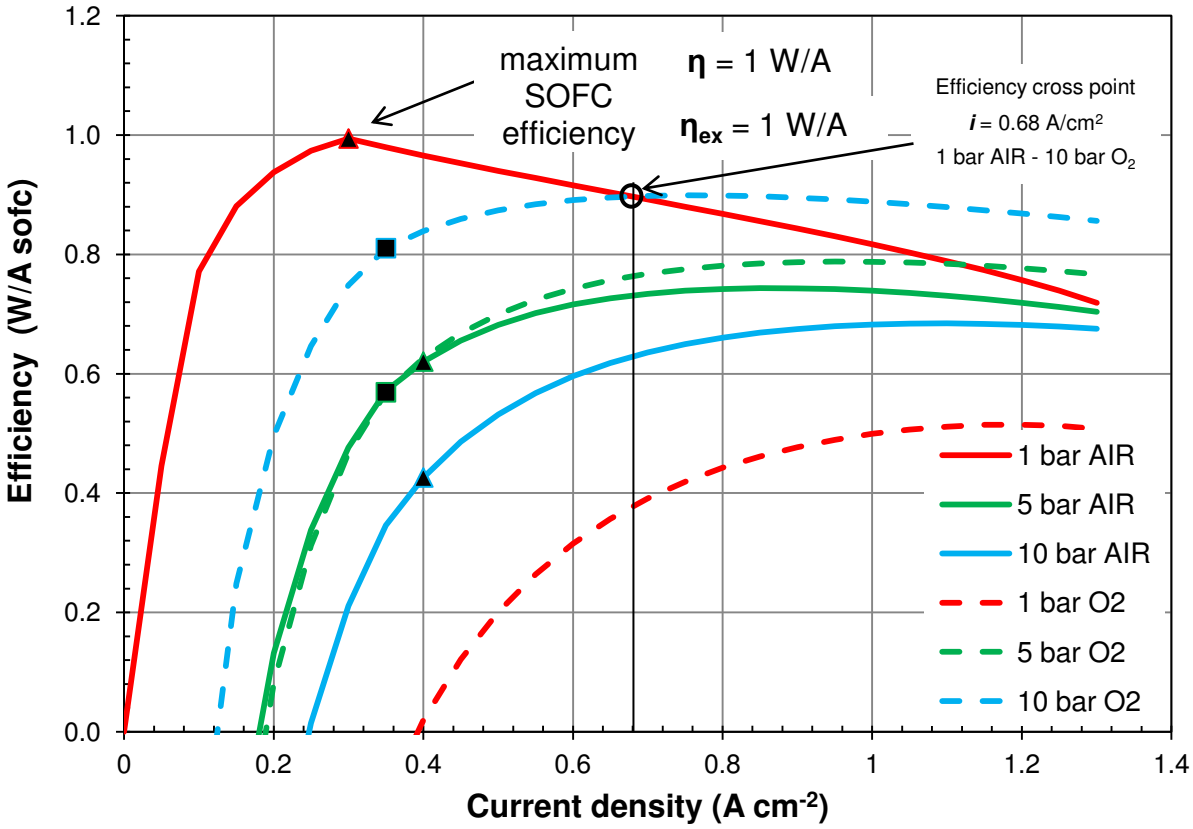

Figure 5.32 – Storage efficiency of SOFC system. Solid lines refer to air operation and dashed lines to pure oxygen (red: 1 bar, green: 5 bar, blue: 10 bar). Black dots represent the limit operating points.

The storage efficiency of the SOFC system is depicted in *Figure 5.32*. The trend of efficiency with pressure and pure oxygen as oxidant is similar to that described for the SOEC. In this case, the use of pure oxygen has a positive effect also on cell voltage that increases with the oxygen partial pressure. The effect on the system is visible at high current density, where pressurized SOFC operation with pure oxygen at the anode reaches higher efficiencies. At 0.68 A/cm^2, the 10 bar operation with O_2 has the same efficiency of ambient operation with air, which further increases at higher currents exceeding that of the baseline case.

Analysis of oxidant recirculation

The effect of recirculation has been investigated with both types of oxidant. An air recirculation rate of 40% has been simulated, while in the case of oxygen operation the full

recirculation has been assessed. In the air case, the rate of recirculation – 40% – is connected to the limitations in SOFC operation explained before in this section. The full recirculation in SOEC operation does not mean that all the outlet oxygen is introduced at the cell inlet; in fact the mass flow exiting the anode is higher than that at the inlet due to the oxygen production in the cell. Thus, only a fraction of the outlet flow equal to the inlet flow is recirculated, the remaining part of the exiting flow – which corresponds to the electrochemically produced oxygen – is compressed and sent to the oxygen storage. In SOFC operation the outlet flow can be fully recirculated as the oxygen is consumed in cell's cathode. In this case, the oxygen consumed is replaced with an incoming flow from the O_2 storage.

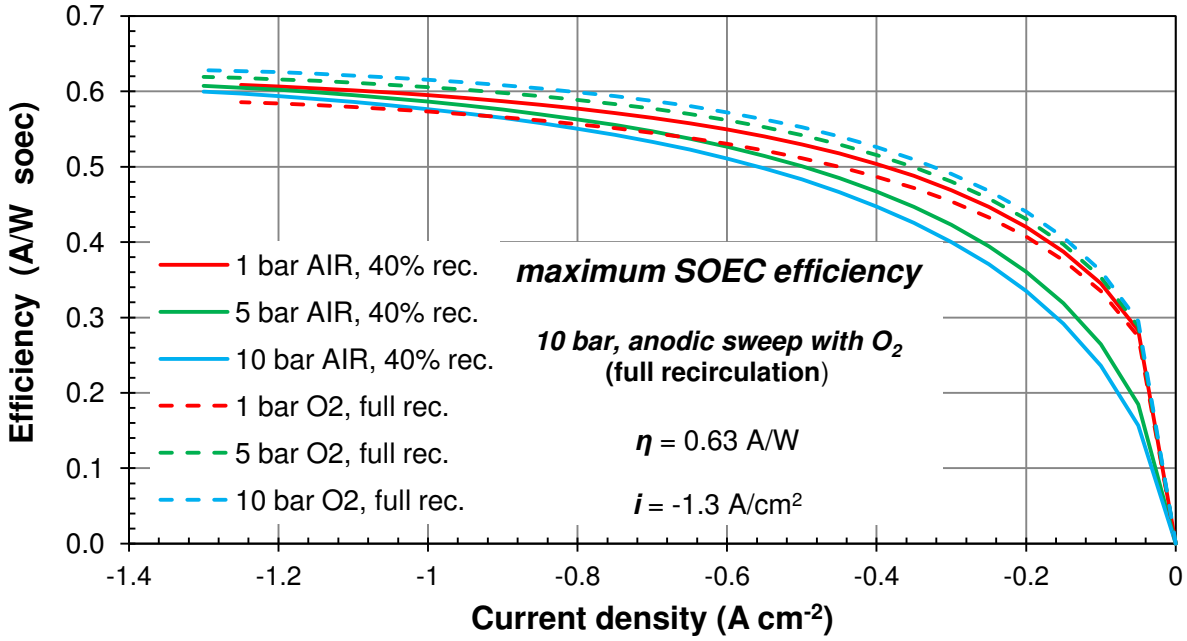

Figure 5.33 – Storage efficiency of SOEC system in feasible current ranges with oxidant recirculation imposed. Solid lines refer to air operation and dashed lines to pure oxygen (red: 1 bar, green: 5 bar, blue: 10 bar).

The charging efficiency (SOEC mode) is shown in *Figure 5.33*. The operation with air at ambient pressure is not affected by the recirculation, because the lower flow of incoming air does not produce energy savings, as air is not compressed. In the operation with oxygen at 1 bar, the recirculation greatly increases the efficiency (see *Figure 5.31* and *Figure 5.33* for comparison) because of the strong reduction of the re-compression work, which is limited to the produced O_2 flow with the full recirculation. In the SOEC operation under pressure, the efficiency of pure oxygen operation always exceeds that of the air operation, firstly because the

compression at the cell inlet is not needed as the pressure of the storage is exploited, and secondly because the full recirculation allows to maintain the re-compression power under the values absorbed by air compression, thanks to sensibly lower flow rates compressed due to the higher recirculation rates with respect to the air operation. The final result is that the 10 bar operation with O_2 and full recirculation has the highest efficiency (0.63 A/W at -1.3 A/cm^2), even higher than in the baseline case.

The storage discharge efficiency in SOFC mode is shown in *Figure 5.34* In this case, the ambient operation with pure O_2 oxidant flow is more efficient than the air operation, because the recirculation allows to eliminate the re-compression stage, and the performance of the cell is higher with pure oxygen. The pressurized operation further benefits of the pure O_2 option with full recirculation, as both the inlet compression and outlet re-compression are avoided: the first, because the pressure of storage is exploited, and the second because the oxidant is fully recirculated. As final result of the study, the maximum discharge efficiency is reached for the 10 bar operation with pure O_2 (fully recirculated), with a discharging efficiency of 1.12 A/W at 0.35 A/cm^2. This value is higher than in the baseline case and also allows to increase the operating current in SOFC with respect to the baseline case.

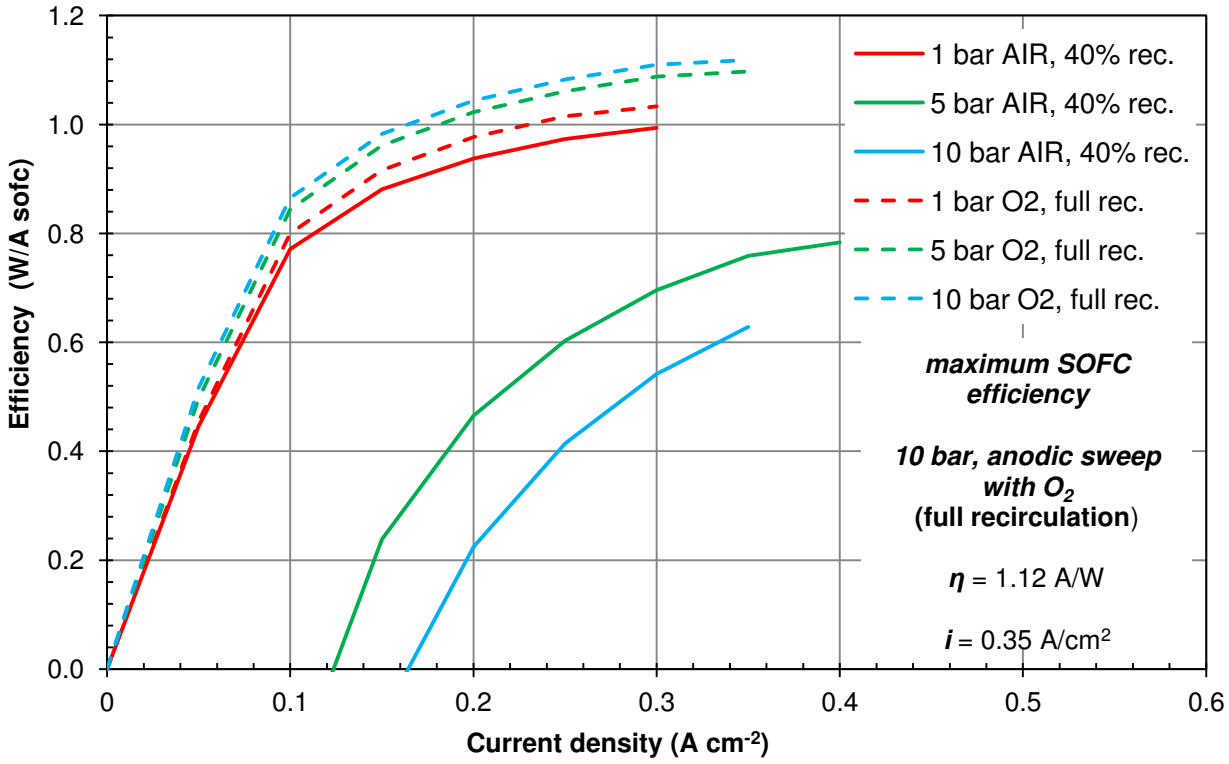

Figure 5.34 – Storage efficiency of SOFC system in feasible current ranges with oxidant recirculation imposed. Solid lines refer to air operation and dashed lines to pure oxygen (red: 1 bar, green: 5 bar, blue: 10 bar).

The assessment of oxidant type and recirculation allowed to identify the pressurized option with oxygen and full recirculation as the best operative option. A roundtrip efficiency of 70 % is estimated for the system operating at 0.35 A/cm^2 in SOFC and -1.3 A/cm^2 in SOEC, with an ***H*** factor of 0.27 for the P2P operating at 800 °C inlet flows temperature and $\lambda = 3$.

Inlet temperature

The sensitivity analysis on the inlet temperature of the flows has been performed for the following temperatures: 700 °C, 750 °C, 800 °C and 850 °C.

The effect of the temperature on polarization curves is shown in *Figure 5.35*. In SOEC mode, the cell voltage diminishes with the increasing inlet temperature, due to the lower reversible voltage and lower losses associated to the higher cell temperature. Both these effects contributes to decrease the cell voltage and thus the operation at higher temperature is straightforward beneficial for the cell operating in SOEC mode. In fuel cell operation, these two effects partially balance and produce less evident variations of the polarization curve with the temperature. The decrease of SOFC reversible voltage with the temperature is balanced by the lower overpotential losses under high temperature operation that increase the cell voltage. The final result is a higher SOFC voltage in a wide range of currents (excluding near OCV points, not reported in the figure) at higher temperatures.

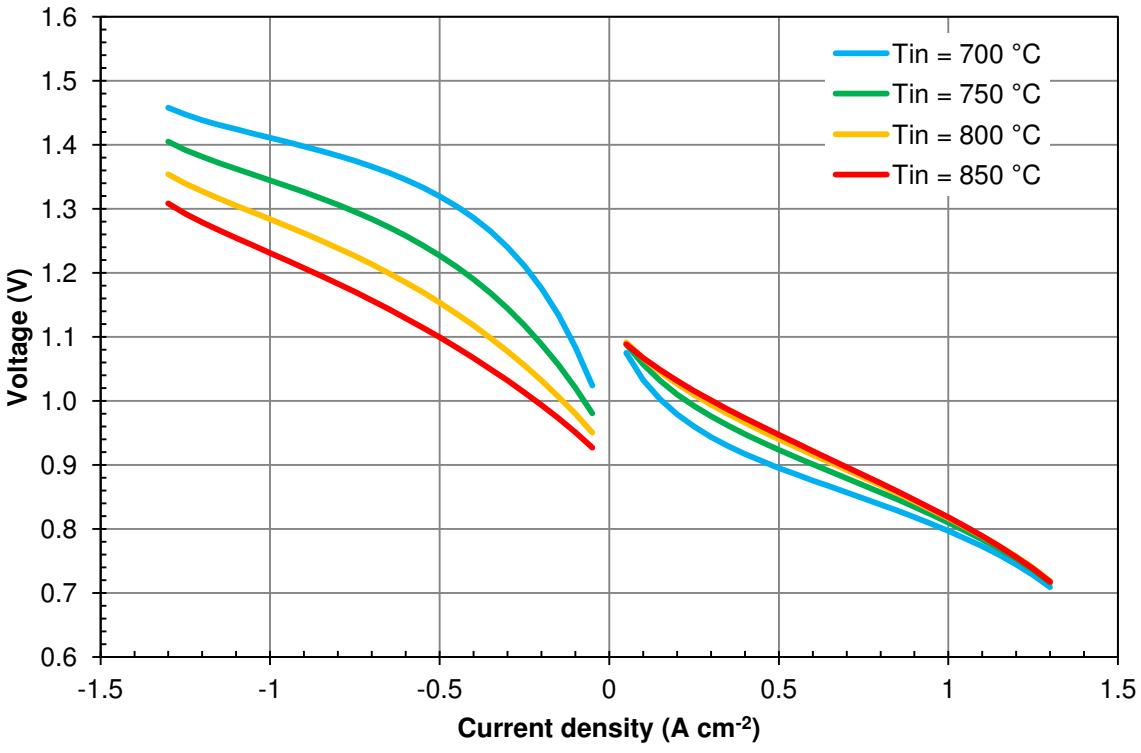

Figure 5.35 – Simulated rSOC polarization for different inlet temperatures.

The sensitivity of temperature profiles within the cell to the inlet temperature of the fluids is shown in *Figure 5.36 – 5.38*, where minimum (*Fig. 5.36*) and maximum (*Fig. 5.37*) cell temperatures and overall cell gradients (*Fig. 5.38*) are depicted. The minimum cell temperature corresponds to the inlet temperature of fluids in SOFC operation, and given that the inlet temperature is always higher or equal to the minimum acceptable value of 700 °C, the SOFC always satisfy the minimum temperature constraint. In SOEC mode, the temperature decrease due to endothermic operation shows two peculiar trends: the magnitude of the maximum temperature reduction progressively decreases with the decreasing inlet temperature, and the current density at which T_{min} is located increases with the inlet temperature. These effects are connected to the decrease of SRU heating due to overpotential losses and the increase of the reaction heat absorbed by water reduction. In fact, a higher inlet temperature of fluids produces a higher average temperature in the cell that implies reduced losses and a higher entropy variation of the reaction, as explained in *Chapter 2* (*Fig. 2.3*).

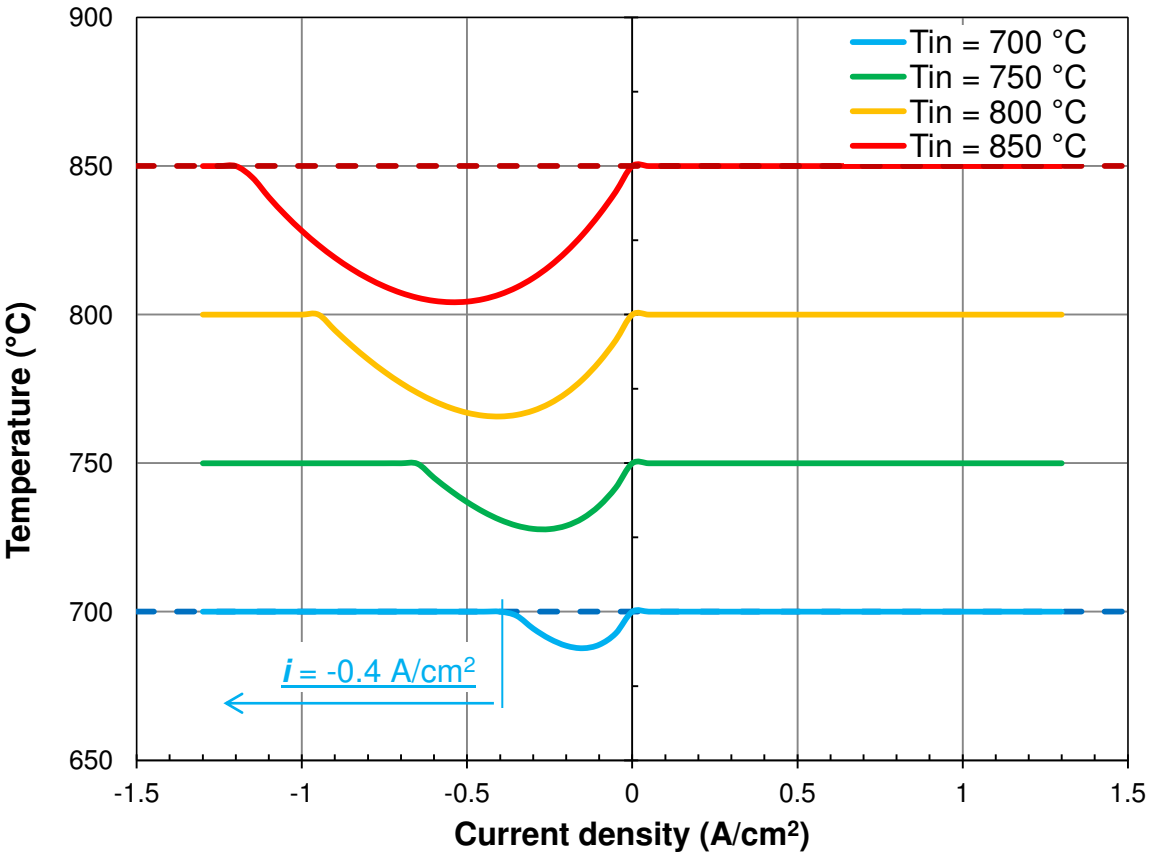

Figure 5.36 –Minimum cell temperature with thermal constraints highlighted.

Therefore, the magnitude of the temperature decrease from the inlet value is higher at higher temperatures due to the more endothermic balance of cell (i.e., higher reaction sink and lower overpotential source). In voltage terms, the reduction of the reversible voltage corresponds to the increase of reaction heat source (i.e., because $\Delta\bar{h}$ of reaction is almost constant with the temperature, and the increase of $\Delta\bar{s}$ is almost equal to the decrease of $\Delta\bar{g}$), and the remaining part of the voltage variation with the temperature is ascribable to overpotentials decrease. The total voltage decrease shifts the current density at which the thermoneutral voltage is reached toward higher values with the increasing temperature.

Among the analyzed cases, only that in which the inlet temperature is 700 °C does not satisfy the minimum temperature constraint at low current densities (i.e., less than 0.4 A/cm^2), as obviously expected from the endothermic SOEC operation.

The maximum cell temperature is depicted in *Figure 5.37*. The temperature trends are complementary to that of the minimum cell temperature.

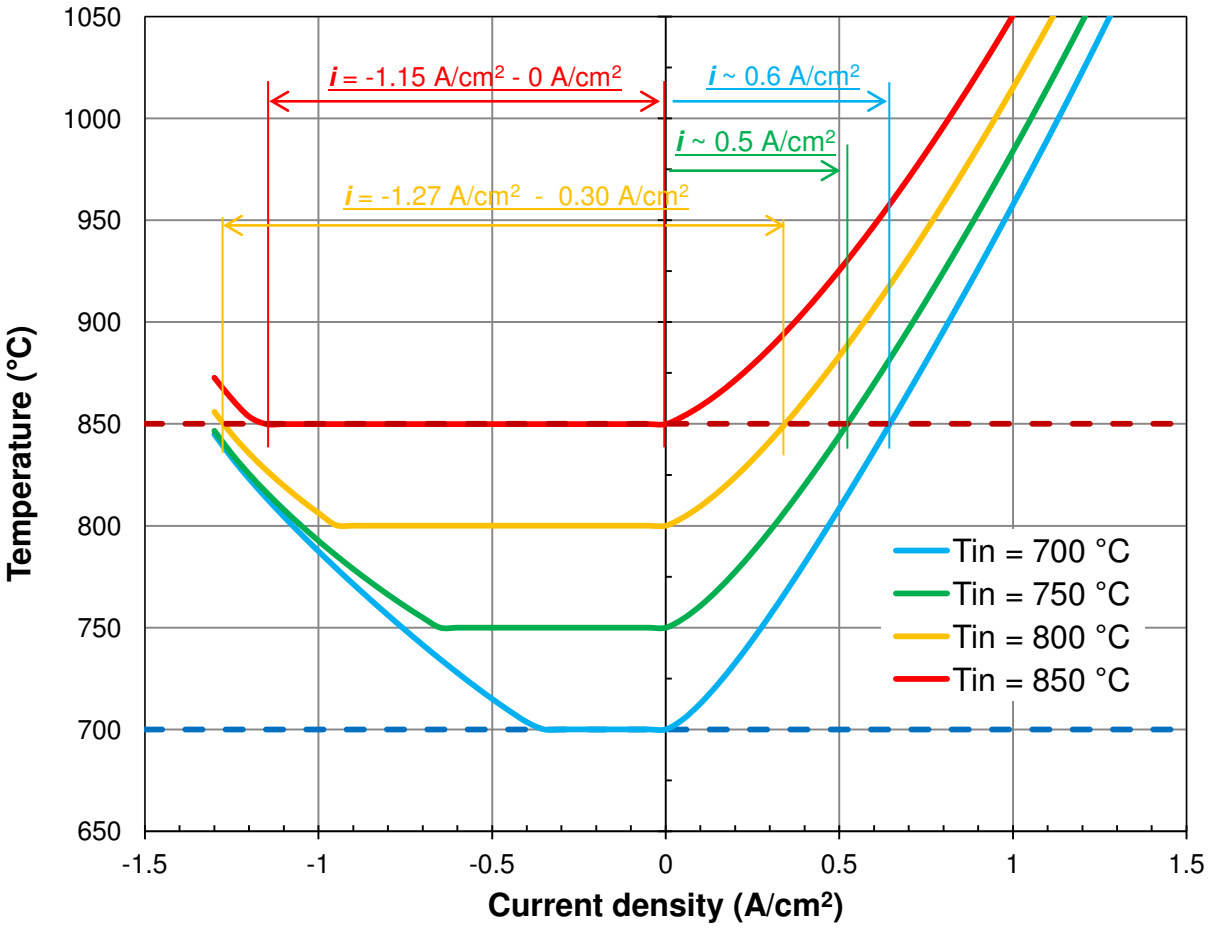

Figure 5.37 – Maximum cell temperature with thermal constraints highlighted.

The maximum temperature corresponds to the inlet temperature only when the cell is operating under the thermo-neutral operation, while is higher in all the other conditions due to the exothermal balance. When $T_{cell,in}$ is equal to 850 °C, only the SOEC operation is allowed. With the decreasing inlet temperature, the maximum allowable current density for SOFC progressively increases reaching up 0.6 A/cm^2 for the inlet fixed at 700 °C. Thus, the reduction of operating temperature can be an effective strategy in order to increase the allowable current of the SOFC. In SOEC operation, even if the inlet temperature is very high, there is a wide range of currents at which the cell can work in endothermic operation, with a maximum allowable current of -1.15 A/cm^2 at 850 °C. The maximum overall cell gradient is shown in *Figure 5.38*. At a certain current, the maximum ΔT_{cell} of the SOFC increases of magnitude with the decreasing inlet temperature. This is due to the higher overpotential heating at lower temperatures.

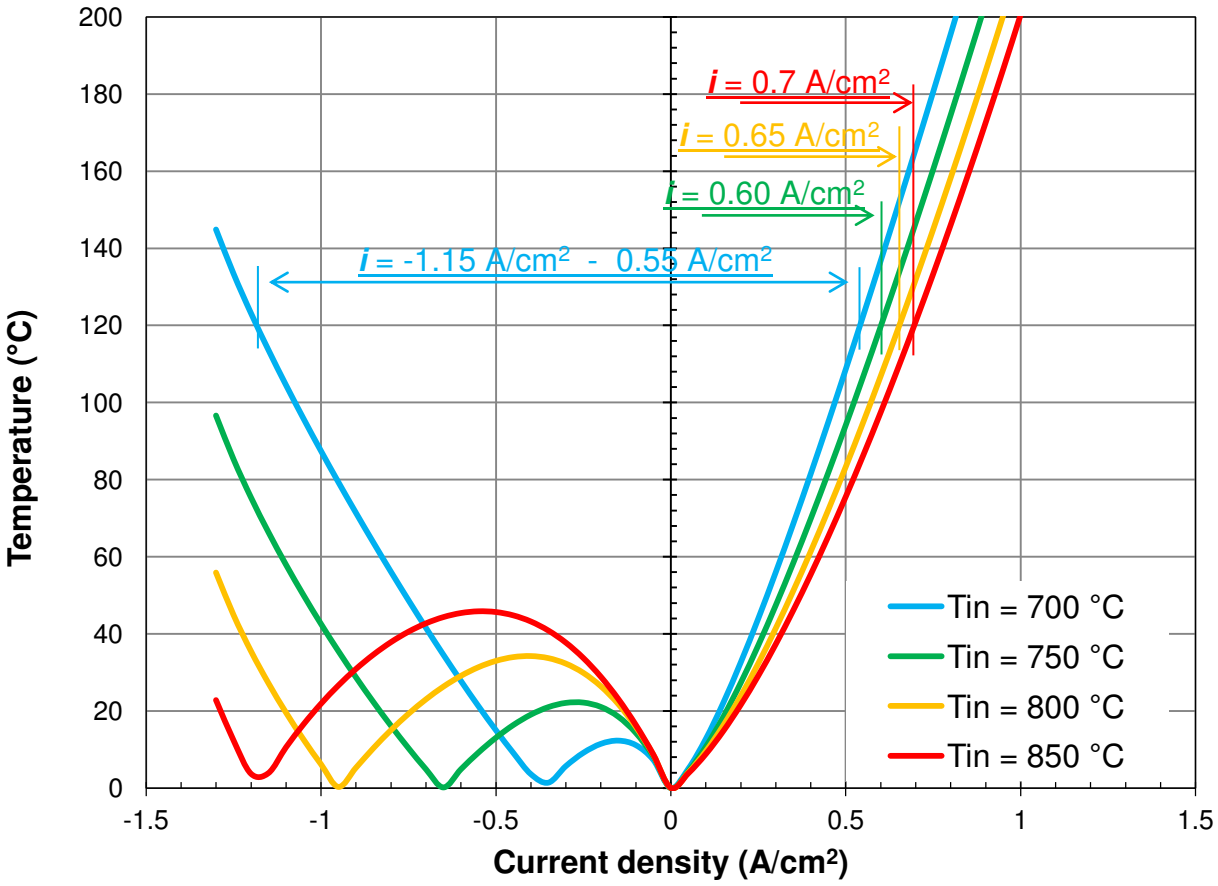

Figure 5.38 – Maximum temperature gradient in the cell.

Consequently, the limiting current density decreases with the inlet temperature (i.e., from 0.7 to 0.55 A/cm^2 varying $T_{in,fuel/oxi}$ from 850 °C to 700 °C). In SOEC operation two trends are visible: when the cell voltage is under the thermo-neutral, the maximum ΔT_{cell} is higher for higher values of $T_{in,fuel/oxi}$, due to the greater decrease of cell temperature at higher inlet temperatures, while it

becomes lower over the thermo-neutral voltage due to the higher cell heating for overpotential losses. A limiting cell current of -1.15 A/cm^2 is identified for SOEC operation at $T_{in,fuel/oxi}$ = 700 °C. The local temperature gradient is not reported, as its current density limits are always higher than those related to the global cell gradient.

The electrical power of the rSOC SRU is shown in *Figure 5.39*, and the thermal balance of BoP is depicted in *Figure 5.40*. The electrical power is sensibly affected by the temperature in SOEC mode, as the polarization curve suggests. The thermal energy required by the heat recovery section decreases with the inlet cell temperature in both SOEC and SOFC mode as expected. The storage charging and discharging efficiency is shown in *Figure 5.41* and *Figure 5.42*. The maximum charging efficiency is reached at 850 °C and -1.15 A/cm^2. This result proves that the increase of SOEC electrochemical performance due to the increase of inlet temperature is higher than the drawbacks related to the increased preheating requirements. In SOFC mode, the operating point with the highest efficiency is still that of the baseline case (i.e., 800 °C and 0.3 A/cm^2). However, lower temperatures ensure much higher limit currents in SOFC; thus, if higher power is required from the fuel cell, lowering the inlet temperature is the best strategy to safely increase the operating current.

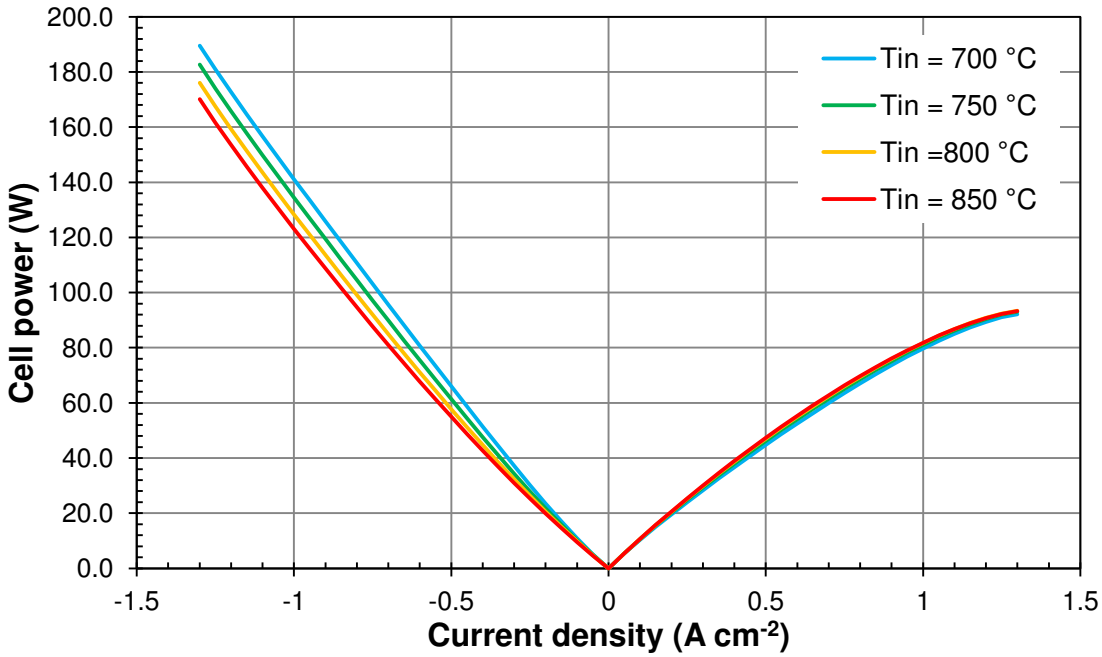

Figure 5.39 – Electrical power of the SRU (absolute value).

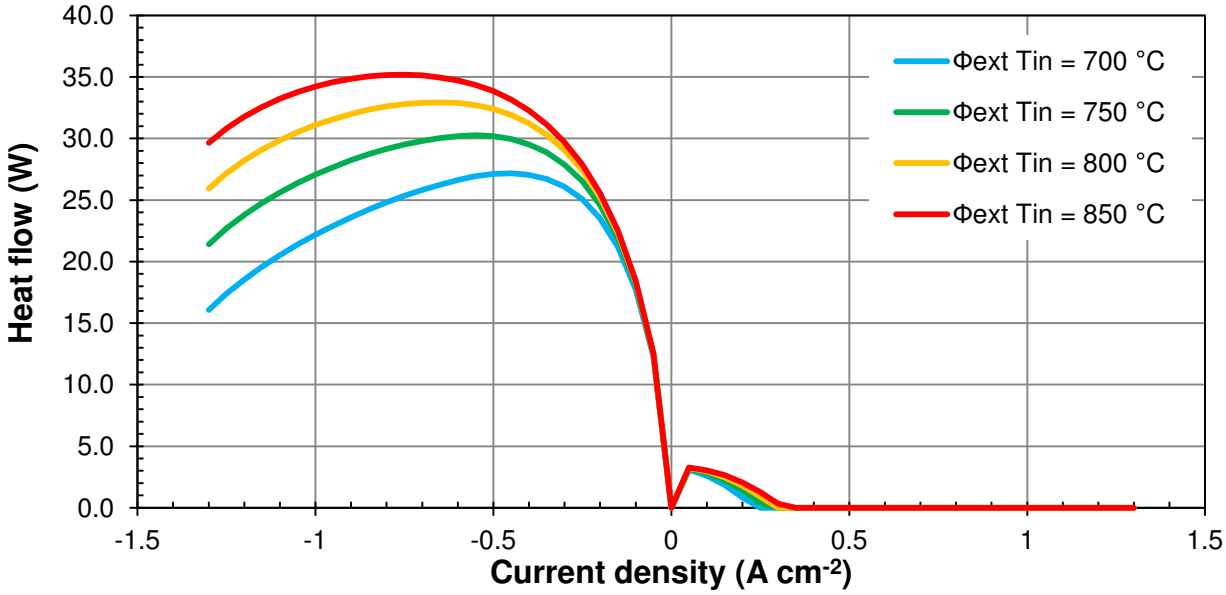

Figure 5.40 – Thermal balance of the BoP with different rSOC inlet temperatures.

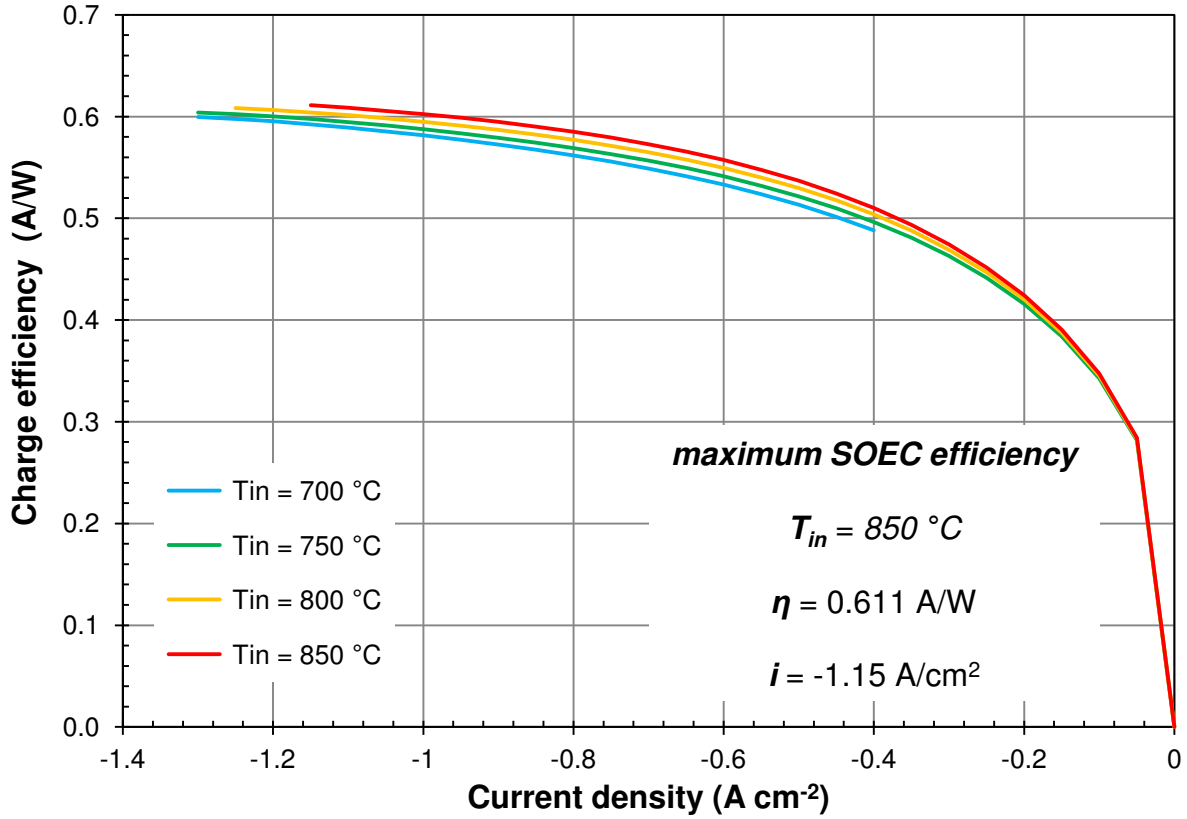

Figure 5.41 – Storage efficiency of SOEC system in feasible current ranges.

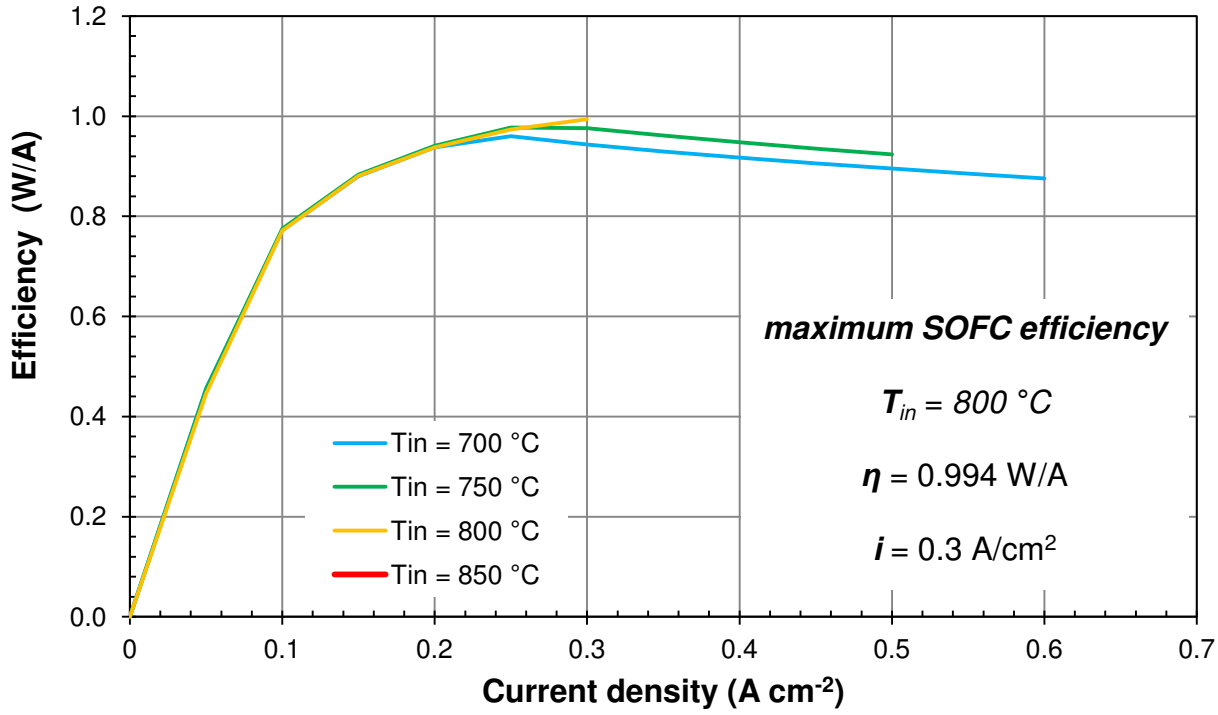

Figure 5.42 – Storage efficiency of SOFC system in feasible current ranges.

Oxidant-to-fuel ratio

The effect of oxidant-to-fuel ratio has been simulated by varying λ from 2.15 (corresponding to an *OU* of 70 % when the system operates in SOFC at 1 A/cm^2) to 5 (corresponding to 30 % of *OU* in SOFC at 1 A/cm^2). The polarization curves obtained are shown in *Figure 5.43*.

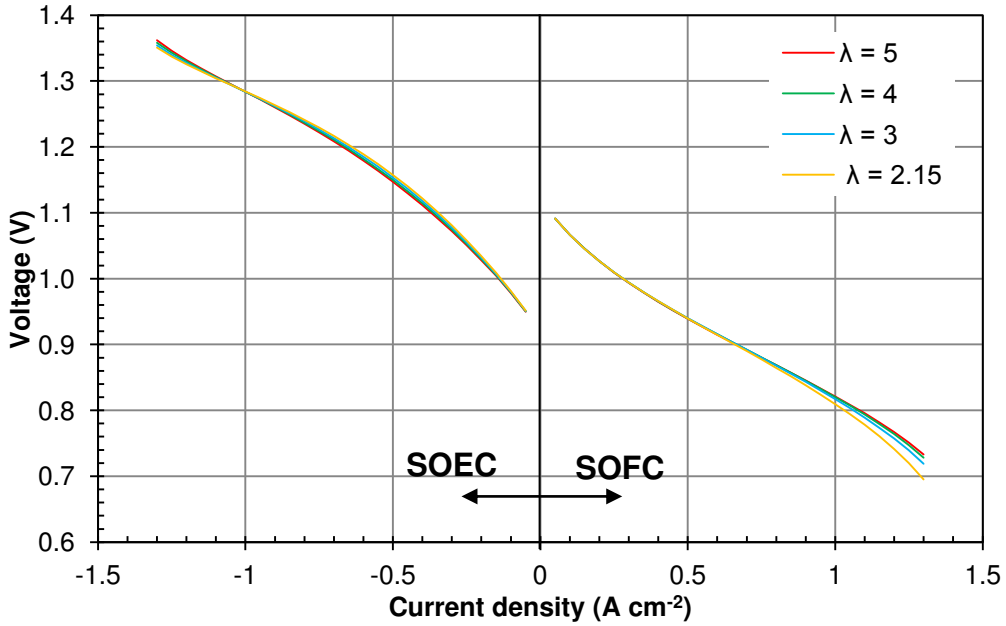

Figure 5.43 – Simulated rSOC polarization of SRU for different λ values.

The effect of lambda on the current-voltage characteristic is not very significant. The main effect is visible in SOFC operation at high current density, where low values of lambda produce the highest decrease of the cell voltage due to the sensible reduction of oxygen concentration at outlet of the cell.

The heat required for the preheating of the fluids entering the stack is shown in *Figure 5.44*. The heat flow provided from external sources to the heat recovery section increases with **λ** in both SOEC and SOFC operation, due to the increasing mass flow of air. The power required for the compression of H_2 is the same of the base case. The effect of lambda on the P2P system efficiency is shown in *Figure 5.45* (SOEC) and *Figure 5.46* (SOFC).

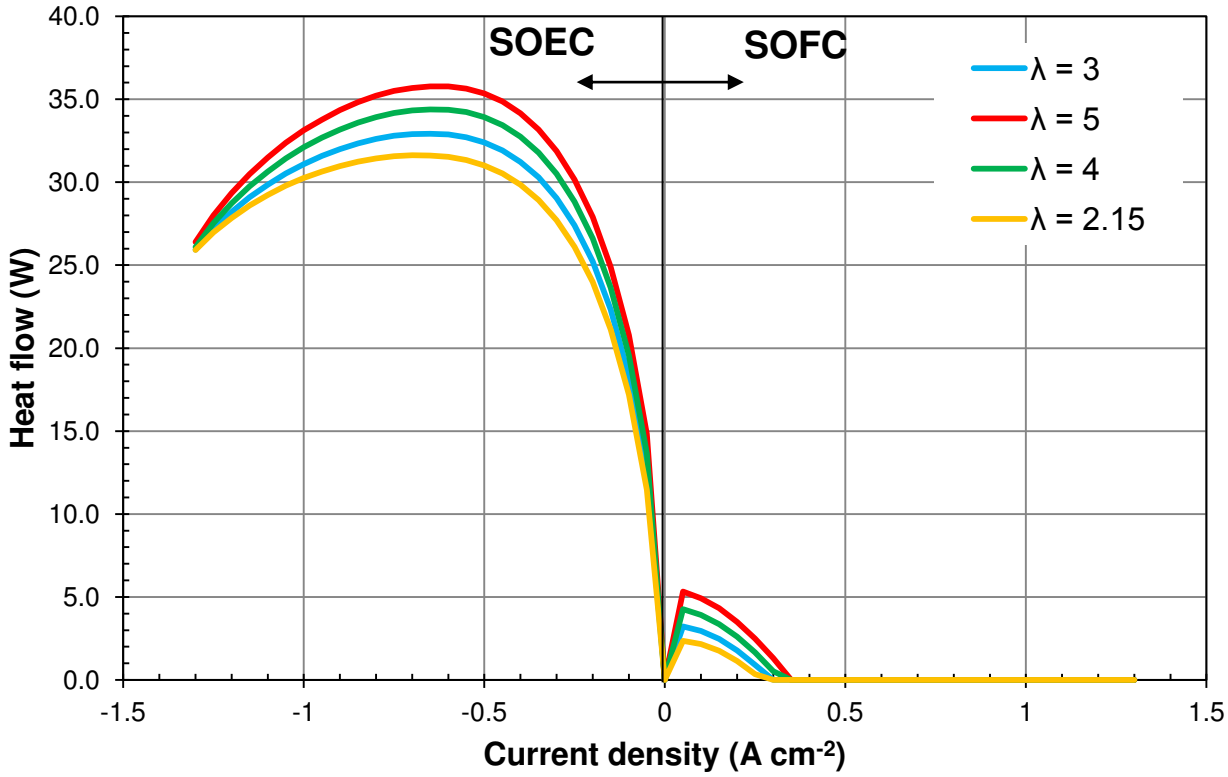

Figure 5.44 – Heat requirements of the BoP with variable **λ**.

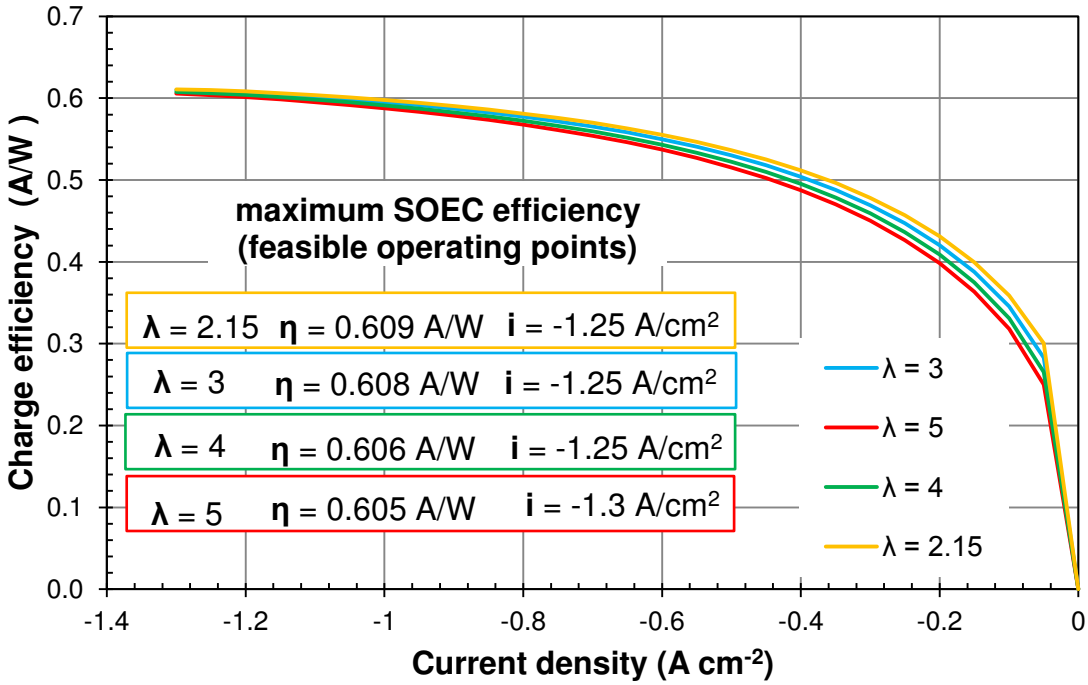

Figure 5.45 – Storage charging efficiency of P2P system for different λ values.

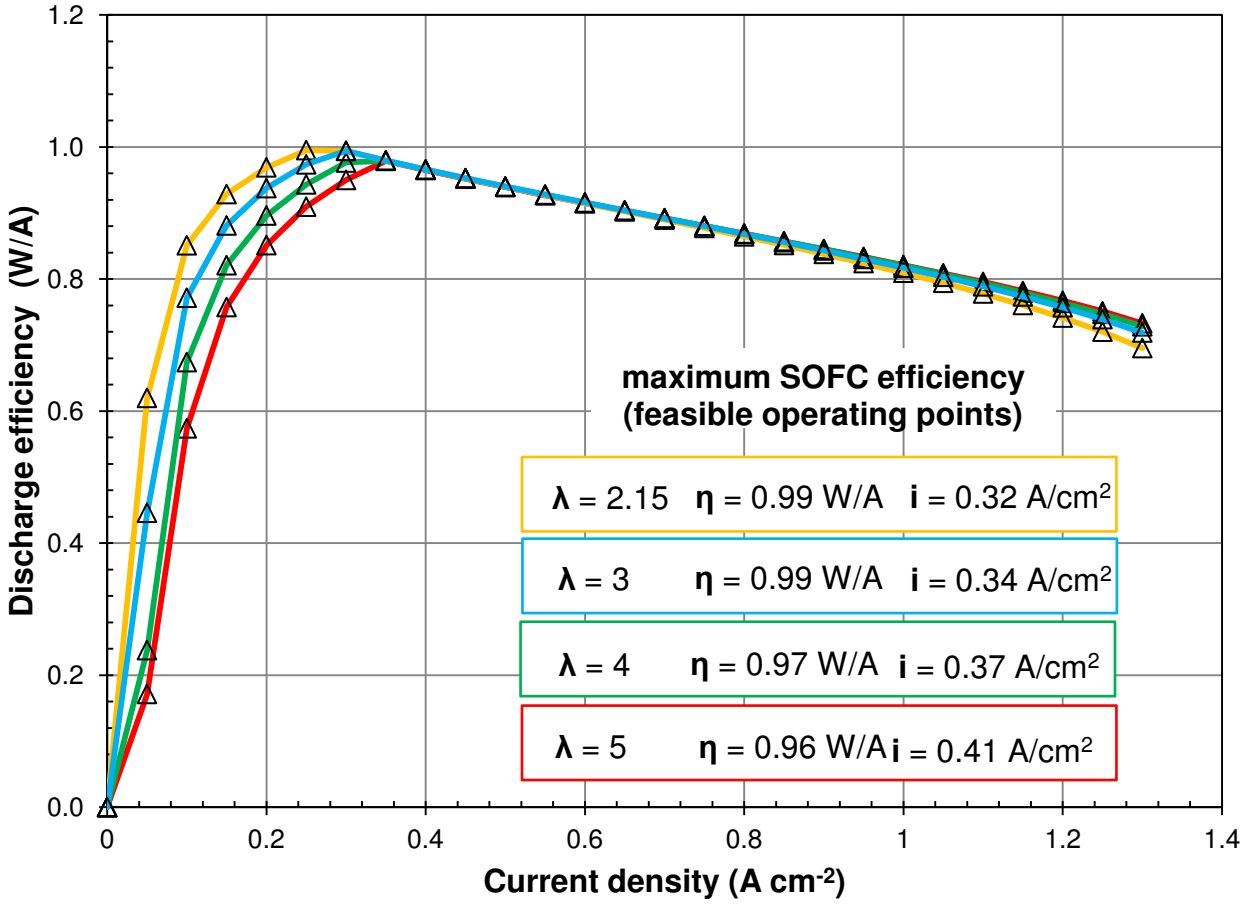

Figure 5.46 – Storage discharging efficiency of P2P system for different λ values.

The storage efficiency in SOEC mode is more affected by λ at low current densities, with a maximum efficiency variation of around 0.02 A/W from λ = 5 to λ = 2.15. The maximum efficiency points are still located at the highest currents, with a current of -1.3 A/cm^2 allowed for λ = 5, thanks to cooling effect of the higher air flow that reduces the temperature increase of the cell operating over the thermoneutral voltage. The maximum efficiency is reached for λ = 2.15, thanks to the lower heat requirement from the heat recovery section. The values reported in *Figure 5.45* indicate a negligible dependence of the maximum storage efficiency on the λ.

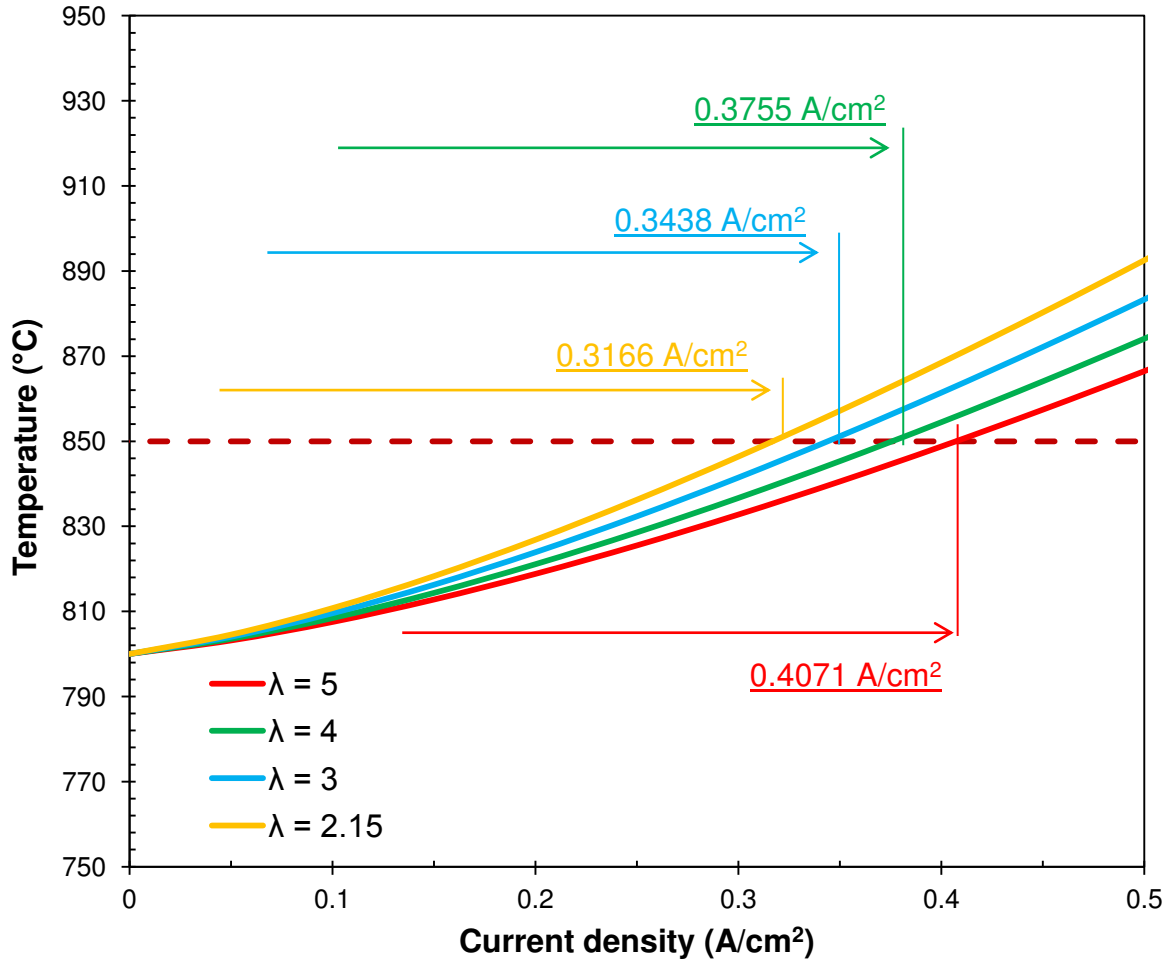

Figure 5.47 – Maximum cell temperature for different λ values.

Figure 5.46 shows that the discharge efficiency in SOFC is more affected by λ than in SOEC mode, especially at low current densities. Lower air flows ensure higher efficiencies thanks to the reduction of Φ_{ext}, and when the SOFC reaches the current value at which the external heat flow required is zero, the efficiency converges on the value of the cell voltage. The main effect connected to the variation of λ in SOFC is the progressive increase of the maximum current that satisfies the thermal constraints with the increasing λ. In fact, higher values of λ indicate higher air flow rates that entering the stack at 800 °C enhance the cooling of the cell shifting the current

limit at which the maximum temperature of 850 °C is reached toward higher values, as shown in *Figure 5.47*.

The sensitivity analysis on **λ** has shown two different effects of the parameter: lower values (i.e., lower air flows) reduce the preheating requirements and increase the storage charge/discharge efficiency, but also reduce the heat capacity of the air stream. The second effect leads to reduction of the minimum cell temperature for the SOEC operating under the thermoneutral and to an increase of the maximum temperature of the SOC operating exothermally (i.e., in SOFC and in SOEC over the thermo-neutral point). This is particularly important for the SOFC operation, for which the current level is limited by the maximum temperature constraint. In order to increase the allowed operation current of SOFC, it is thus necessary to increase **λ**. *Figure 5.47* shows that a variation of the oxidant-to-fuel ratio from 2.15 to 5 produces the increase of the maximum allowed current from 0.32 A/cm^2 to 0.41 A/cm^2 (i.e., 29 % of current increase).

5.2.3 Optimized P2P system simulation

The sensitivity analysis performed on the operating parameters of the rSOC allowed to individuate the conditions that allow to achieve the highest charge and discharge efficiency of the P2P system. The conditions are summarized in *Table 5.3*.

Table 5.3 – Optimized P2P system

Input Parameter	Value
$T_{in,SOFC}$	800 °C
$T_{in,SOEC}$	850 °C
Oxidant	Oxygen (full recirculation)
λ	2.15
Pressure	10 bar

The rSOC optimized for P2P must operate at high pressure (10 bar assumed) using an oxygen flow fully recirculated as oxidant, with the minimum oxidant-to-fuel ratio. The inlet temperature of the SOEC system should be the highest possible to reduce cell losses, while for the SOFC system the temperature must be near to the limit values imposed by materials to obtain the

highest efficiencies at low currents. However, if required, sensibly higher SOFC currents can be reached by reducing the inlet temperature with an acceptable loss of system performance.

The comparison between the current-voltage characteristics of the SRUs for the optimized operation and in the baseline conditions is depicted in *Figure 5.48*. The Figure shows that in the optimized P2P operation the performance of the SOFC SRU is sensibly increased. This is due to the fact that in SOFC operation with oxygen and full recirculation, the system performance is mostly determined by the cell, as the only contribution coming from BoP is the preheating thermal power at low currents. For this reason, the conditions that lead to higher P2P system efficiency in the hydrogen re-conversion to electricity are also those that determine the highest SOFC performance (i.e., the highest V_{cell} at a certain current). In SOEC mode, the SRU polarization in optimal P2P conditions is closer to that of the baseline case, and even shows a higher voltage at low currents. This is related to the fact that in SOEC operation the energy flows absorbed by system auxiliaries (i.e., stream preheating, hydrogen and oxygen compression) plays a more significant role with respect to the SOFC operation, and thus the system efficiency is not only determined by the SRU performance.

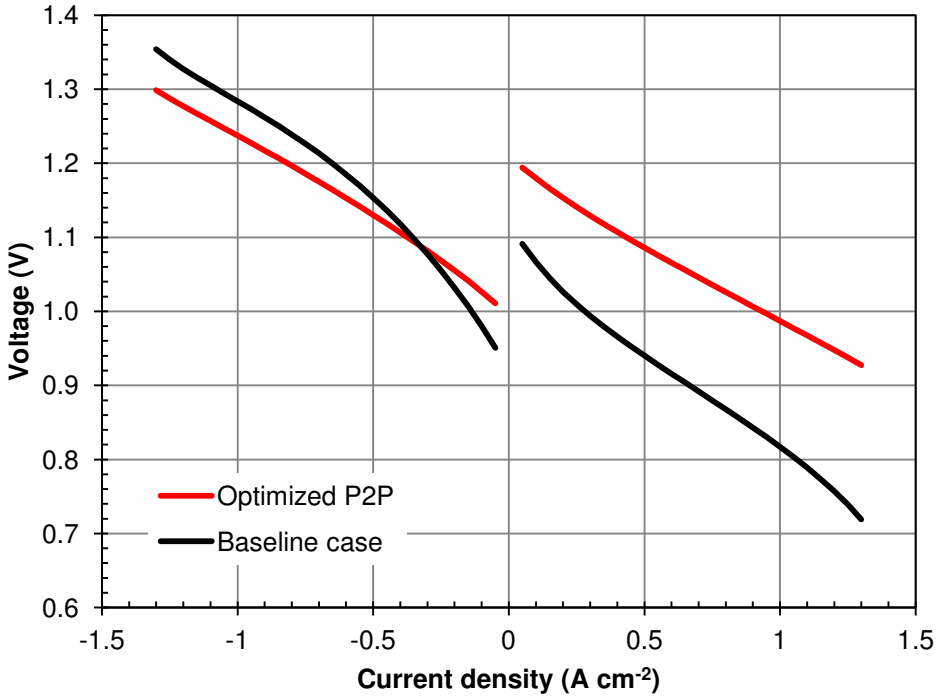

Figure 5.48 – Simulated rSOC polarization for baseline case and optimized P2P.

The BoP and SRU contributions to the energy balance of the P2P system are shown in *Figure 5.49* for the SOEC operation and in *Figure 5.50* for the SOFC one. In both cases, the SRU is the source of the higher contribution to the energy balance of the system. The major contribution of

the BoP comes from the external heating in SOEC mode. This heating is mostly related to water vaporization in the heat recovery section.

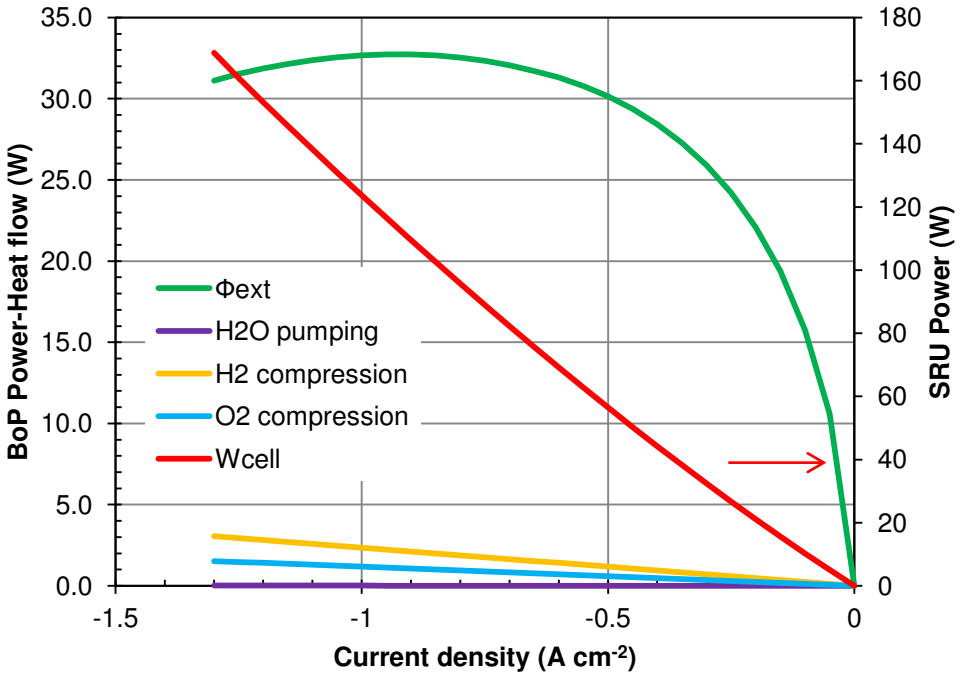

Figure 5.49 – SRU and BoP balance of optimized P2P system in SOEC operation.

It is worth noting that in SOEC operation the pumping power is totally negligible, and that the power absorbed in the compression of hydrogen and oxygen is a minor contribution. This is due to the use of recirculation on both electrodes, that allows to compress the minimum flows of H_2 and O_2.

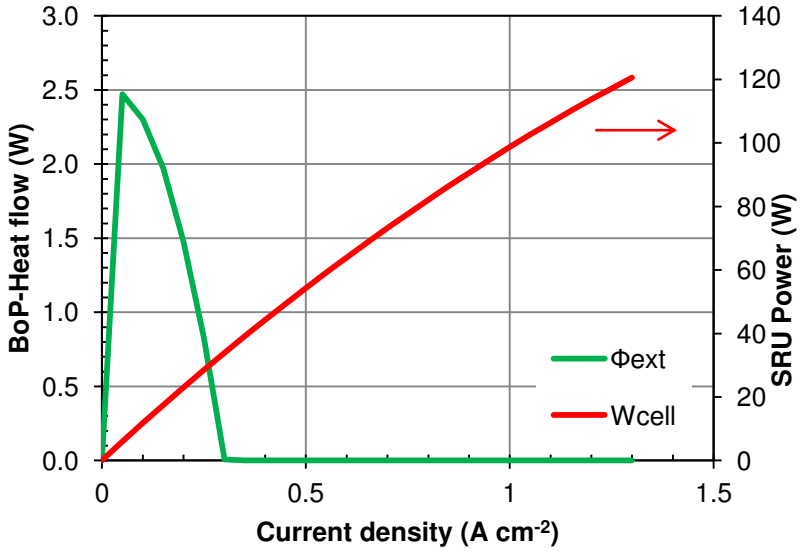

Figure 5.50 – SRU and BoP balance of optimized P2P system in SOFC operation.

In SOFC operation, hydrogen compression to the operating pressure of the cell is not required thanks to the pressure level of the H_2 tank and to the full recirculation of the unreacted H_2. The use of stored O_2 as oxidant in combination with full anodic recirculation also allows to eliminate the compression of the oxidant flow to cell pressure. This a clear advantage with respect to the operation with air, which has a limited recirculation rate allowed and requires the compression of both oxygen and nitrogen, the last one being not useful for the electrochemical reaction.

The energetic and exergetic charging and discharging efficiencies of the P2P system in both optimized configuration and baseline case are depicted in *Figure 5.51* and *Figure 5.52*.

The maximum charging efficiency (SOEC mode) η_{SOEC} = 0.635 A/W is reached at -1.3 A/cm^2, with a maximum exergy efficiency η_{ex} = 0.7 A/W for an average current density of -0.9 A/cm^2. *Figure 5.51* shows that the electricity storage efficiency of the optimized P2P system is always higher than in the baseline case. Thus, the operating parameters selected through the sensitivity analysis enable a higher efficiency at all the current levels investigated.

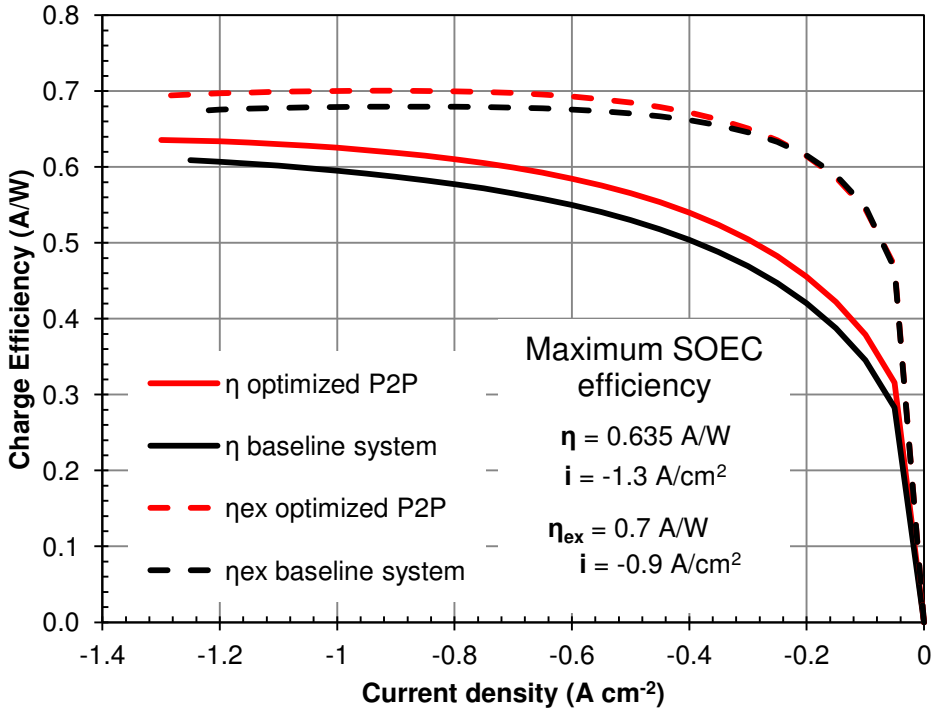

Figure 5.51 – Energetic (solid lines) and exergetic (dashed line) storage charging efficiency of P2P system.

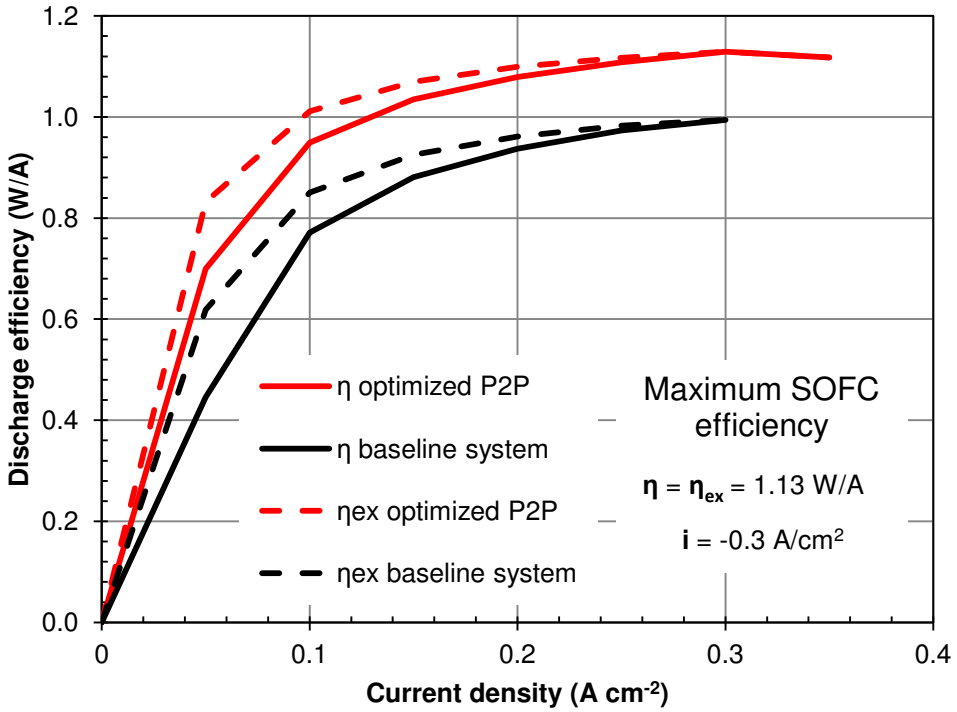

Figure 5.52 – Energetic (solid lines) and exergetic (dashed line) storage discharge efficiency of P2P system.

The maximum discharging efficiency (SOFC mode) $\eta_{SOFC} = \eta_{SOFC,ex}$ = 1.13 W/A is reached at 0.3 A/cm^2. *Figure 5.52* shows that the efficiency of the optimized P2P system is always higher than in the baseline case also in SOFC operation.

The roundtrip efficiency of the optimized P2P system is η_{RT} = 72 % ($\eta_{RT,ex}$ = 79 %) with an ***H***-factor of 0.23 (0.33 if the exergetic roundtrip efficiency is considered).

The results of the simulations for a P2P system based on a 1000 cells rSOC stack operating in optimized conditions in the maximum efficiency point (***H*** = 0.23) and with symmetric SOEC and SOFC currents (i.e., $i = \pm 0.35$ A/cm^2, corresponding to ***H*** = 1) are reported in *Table 5.4*. The Table shows that the contribution of the SOEC stack power to the total energy flow absorbed by the system is more than 80 % for the P2P system operating in the maximum efficiency point, while for the system with a unitary ***H*** factor it accounts for less than 60 %. The heat absorbed for the preheating of reactants is around the 15 % of the total energy absorbed by the P2P operating at maximum efficiency and 40 % for the operation at ***H*** = 1. This result suggests that the impact of thermal integration of P2P system with heat sources available from other processes on the system efficiency would be lower for the system operating at maximum efficiency.

The efficiency map of the optimized P2P system is depicted in *Figure 5.53*. The shape of the efficiency surface is similar to that of the baseline case, but shifted toward higher values. A large

area of the efficiency surface is above the 60 % iso-efficiency line, and most of the operating points are above 50 % of efficiency. Moving along the line of the maximum discharging efficiency, which corresponds to the SOFC current density of 0.3 A/cm^2, it is possible to see from *Figure 5.53* that for a SOEC current higher that -0.2 A/cm^2 the roundtrip efficiency is always higher than 50%, reaching up to 71.7 % for i_{SOEC} = -1.3 A/cm^2.

Table 5.4 – Plant Efficiency of H_2-based P2P system*

Component	Heat/Power flow (kW) (maximum efficiency) i_{SOEC} = -1.3 A/cm^2 i_{SOFC} = 0.3 A/cm^2	Heat/Power flow (kW) (H = 1) i_{SOEC} = -0.35 A/cm^2 i_{SOFC} = 0.35 A/cm^2
W_{SOEC}	169	38.3
$\phi_{ext,SOEC}$	31	27.3
$W_{compr,H2}$	3	0.82
$W_{compr,O2}$	1.5	0.41
$W_{pump,H2O}$	0.01	~ 0
W_{SOFC}	33.9	39.1
$\phi_{ext,SOFC}$	0.01	0
$\boldsymbol{H = i_{SOFC}/i_{SOEC}}$	0.23	1
Roundtrip Efficiency η_{RT}	**71.7 %**	**58.6 %**

*values calculated for a 1000 cells rSOC stack

In conclusion, the sensitivity analyses allowed to select the optimal configuration of the P2P system and to optimize the operating parameters within the thermal constraint imposed by the state-of-the art materials of the rSOC. The analysis demonstrated the advantages of pressurized operation with the use of pure oxygen as oxidant in both SOFC and SOEC operation. The final result is a considerably increased roundtrip efficiency of the P2P system with respect to the base case analyzed, which was 61 %. The most of efficiency improvement is concentrated in the re-conversion of hydrogen to electricity in the SOFC, whose performance strongly affects the roundtrip efficiency of the P2P system.

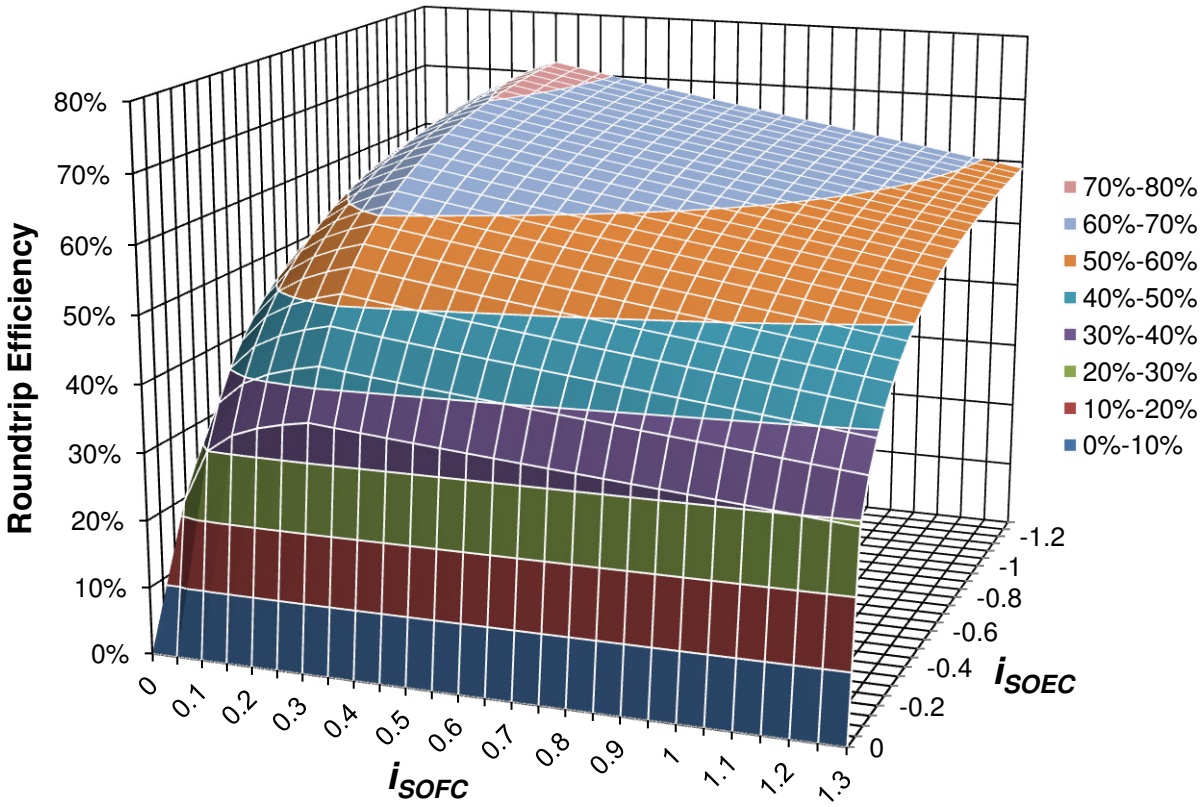

Figure 5.53 – Efficiency map of the optimized P2P system.

5.3 Dynamic analysis of an rSOC SRU operating in P2P conditions

The stationary analysis of a P2P system presented in *Section 5.1* and *Section 5.2* allowed to select the optimal SOC operating conditions for electricity storage into H_2 and its reconversion to electrical energy that satisfy the physical constraints imposed by state-of-the art materials. However, the analysis does not provide information on the dynamics of the system. In other words, the simulations performed do not allow to estimate the time in which the system reaches the stationary conditions.

This information is of paramount importance for a P2P system, which must be capable to cope with variable input/output loads and to adapt in time the operating parameters (i.e., inlet gas temperature, oxidant-to-fuel ratio, etc.) in order to maintain the system in safe and efficient conditions with variable loads available (SOEC) or required (SOFC). In fact, it is necessary to know the thermal response time of the SOC to a certain load variation in order to understand if the load variation leaves enough time to the control system to modify the operating parameters in the direction of reaching a safe/efficient operating point. A dynamic analysis is needed to identify the load variation rates that are acceptable for the SOC, i.e. the variation rates that allow a control system to timely adapt the operating parameters.

A dynamic analysis of the thermal response of an rSOC SRU operating in typical P2P conditions with variable load ramps has been performed. The 3D model of an rSOC SRU described in *Chapter 3* has been applied in the analysis. The model simulates the response of an ESC-based SRU operating in a cross-flow stack design. Simulations were run for the ESC operating at ambient pressure, fuel and oxidant entering the stack at 800 °C with an oxidant-to-fuel ratio of 2.15. The inlet fuel considered is composed by 90% of reactant (H_2O in SOEC mode and H_2 in SOFC mode) and 10% of product, while the oxidant is pure oxygen. The analysis investigated the response to current ramps from 0 to ±1 A/cm^2 with variable slope, listed in *Table 5.5*.

The thermal response of the SRU has been analyzed, as the model is focused on the identification of the characteristic times in which the thermal constraints are reached. Obviously, the steady state response of the SOC reached at the end of the transients is always the same for all the load ramps, as the final value of the current is the same for all the ramps. It worth noting that the analysis presented is investigating the response to a load increase from OCV; however, also the behaviors related to load variations under current will be discussed.

Table 5.5 – Load ramps applied*		
Ramp #1	0.01	(A min^{-1} cm^{-2})
Ramp #2	0.1	(A min^{-1} cm^{-2})
Ramp #3	0.25	(A min^{-1} cm^{-2})
Ramp #4	1	(A min^{-1} cm^{-2})
Ramp #5	60	(A min^{-1} cm^{-2})

*from 0 A to 100 A

The results of the steady-state SRU response are listed in *Table 5.6*. As expected, the SRU presents a strongly asymmetric behavior between SOFC and SOEC mode. For a current of -1 A/cm^2 the SOEC is operating near the thermoneutral point and the minimum temperature reached in the cell is very close to the inlet temperature of gases (800 °C); also the total and local cell gradients are very mild. Bearing in mind the physical constraints assumed in *Section 5.2.1*, the SOEC operation falls within the acceptable limits. The SOFC is instead operating in a point far from satisfying the thermal constraints.

Table 5.6 – Steady-state SRU response			
Operation mode	$T_{max(SOFC)-min(SOEC)}$ (°C)	ΔT_{cell} (°C)	dT_{cell} (°C)
SOEC	797	3	0.2
SOFC	1062	262	10

The temperature profiles at steady state on the fuel side of the ESC are depicted in *Figure 5.54* and *Figure 5.55*. The SOEC profile is mostly determined by gas convection, with the coldest point located in the top right corner of the cell looking to the (x,y) plane, which is the point farer from the streams inlets. The temperature profile of the SOFC presents a hot spot near the fuel inlet, on the opposite side of the oxidant inlet. This hot point arises because of the higher hydrogen concentration at the fuel inlet that enhances the electrochemical reactions and consequently increases the heat generation related to reaction and losses, as the current is concentrated where the H_2 oxidation takes place. The point is shifted toward the oxidant outlet because of the cooling effect of the oxidant flow.

The evolutions of the maximum cell temperature, maximum cell gradient and maximum local gradient for the SOFC are depicted in *Figure 5.56 – Figure 5.58*. The evolutions of the same quantities in SOEC mode are depicted in *Figure 5.59 – Figure 5.61*; in this case, the minimum cell temperature is plotted instead of the maximum one. In both SOEC and SOFC operation the transients have similar durations: around 30 minutes for load ramps ≥ ±0.1 A/cm^2/min and 100 minutes for ±0.01 A/cm^2/min.

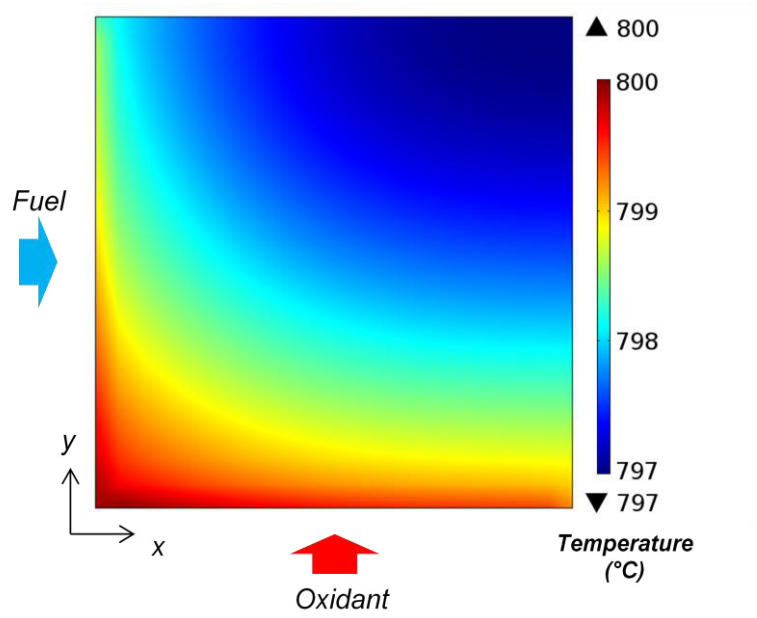

Figure 5.54 – Stationary temperature profile on fuel side of the ESC in SOEC operation at -1 A/cm^2.

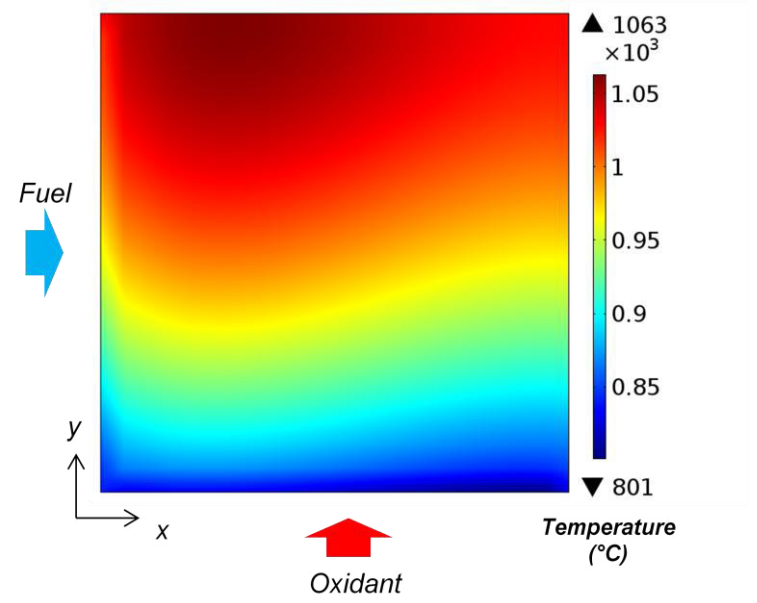

Figure 5.55 – Stationary temperature profile on fuel side of the ESC in SOFC operation at 1 A/cm^2.

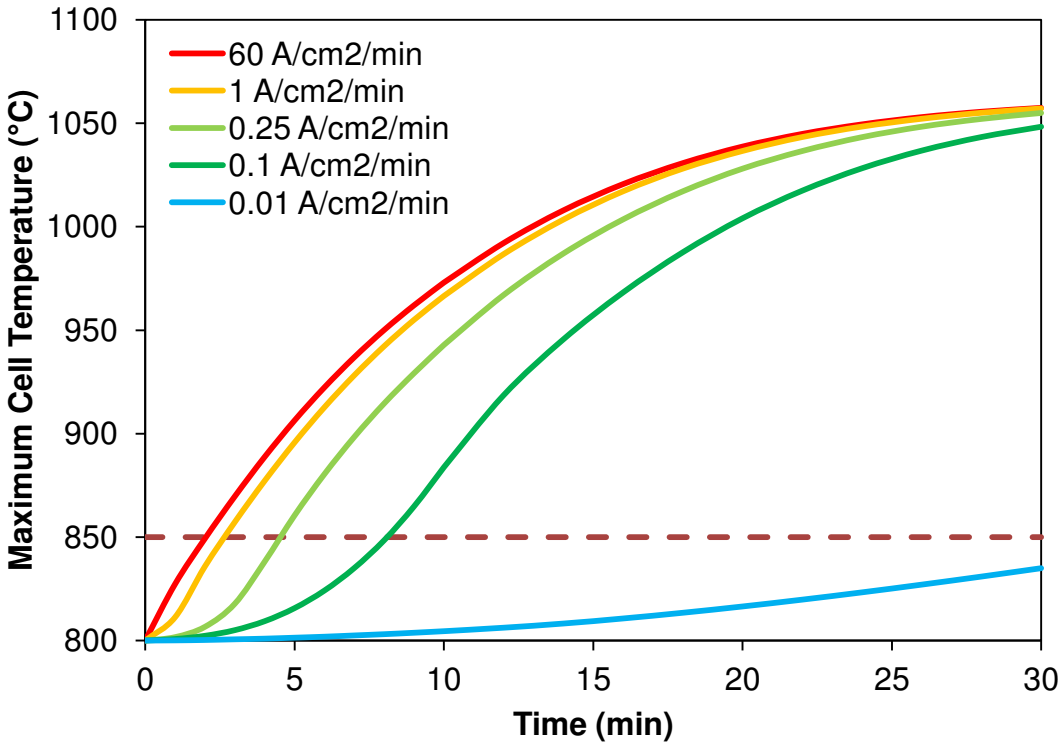

Figure 5.56 – Maximum cell temperature evolution in SOFC operation for different load ramps applied (from 0 to 1 A/cm^2). Dashed line indicates the thermal constraint.

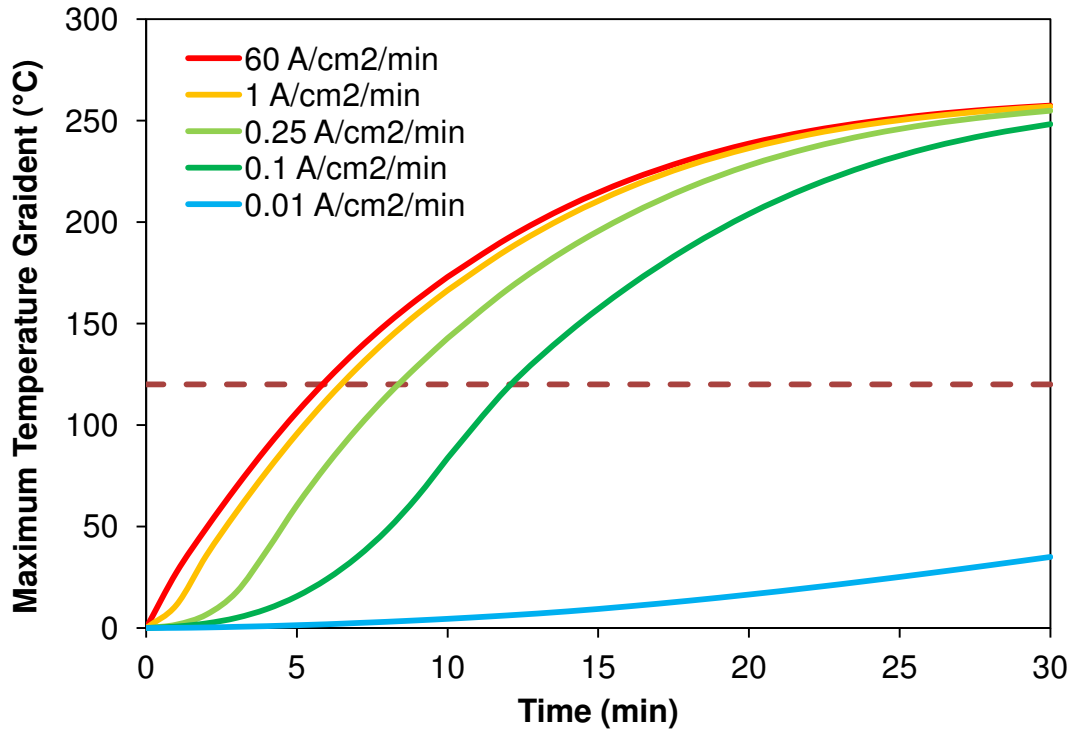

Figure 5.57 – Maximum temperature gradient evolution within SOFC for different load ramps applied (from 0 to 1 A/cm^2). Dashed line indicates the thermal constraint.

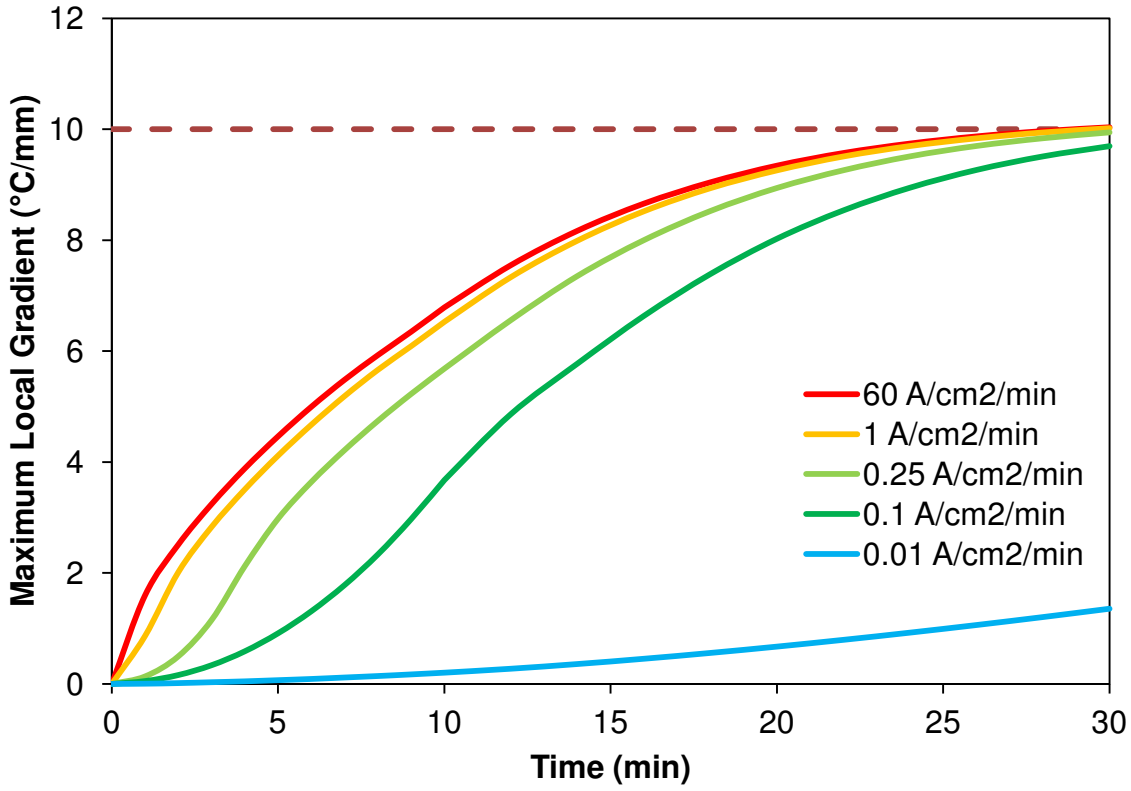

Figure 5.58 – Maximum local temperature gradient evolution within SOFC for different load ramps applied (from 0 to 1 A/cm^2). Dashed line indicates the thermal constraint.

The characteristic times employed by the SOFC to reach the thermal constraints are listed in *Table 5.7*. The results show that the maximum temperature constraint is the faster to be reached with all the simulated ramps. This constraint is reached with a characteristic time that go from 2 to 36 minutes with the decreasing slope of ramp rates. The selection of the acceptable ramps depends on the intervention time of the control system and on the time employed by the countermeasure applied to be effective on the system. The response analysis shows that a load ramp of 0.25 A/min/cm^2 or steeper applied to an SOFC operating with fluids at 800 °C and an oxidant-to-fuel ratio of 2.15 produces an unacceptable temperature increase in less than 5 minutes, a characteristic time which impose severe requirements to the control system. If we set 10 minutes as a realistic time for the effective intervention of the control strategies, the limiting load ramp is less than 0.1 A/min/cm^2.

The SOEC behavior is completely different. *Figures 5.59 – 5.61* show that the slower is the load ramp applied to the system, the higher are the maximum gradients reached in the cell and the lower is the minimum temperature achieved. This is due to the fact that at -1 A/cm^2 the SOEC is operating near the thermoneutral point, condition in which temperature gradients are

close to zero and the minimum cell temperature is near to the inlet temperature of gases, while at lower currents the cell is operating in endothermic conditions that enhance the thermal gradients and reduce the minimum cell temperature. For this reason, a faster ramp rate applied to the SOEC allows to reach the steady-state conditions in a shorter time without reaching the thermal equilibrium points at the intermediate currents. If the ramp rate is slower, the current values that determine the endothermic operation are hold for a longer time and the cell has the time to cool down and to get closer to thermal equilibrium for each value of current.

Table 5.7 – Characteristic times of SOFC response

Applied ramp rate		T_{max}		ΔT_{cell}		dT_{cell}	
		Time to constraint (min)	Increase rate (°C/min)	Time to constraint (min)	Increase rate (°C/min)	Time to constraint (min)	Increase rate (°C/min)
Ramp #1	0.01 (A min $^{-1}$ cm^{-2})	36	1.39	64	1.87	110	0.09
Ramp #2	0.1 (A min $^{-1}$ cm^{-2})	8	6.25	12	10	30	0.33
Ramp #3	0.25 (A min $^{-1}$ cm^{-2})	4	12.5	8	15	30	0.33
Ramp #4	1 (A min $^{-1}$ cm^{-2})	2	25	6	20	28	0.36
Ramp #5	60 (A min $^{-1}$ cm^{-2})	2	25	5	24	28	0.36

Hence, if we consider a SOC starting from OCV, slow ramp rates are the most dangerous for an SOEC, as they force the cell to operate for a longer time in endothermic conditions, where the cell is closer to thermal constraints and the conversion efficiency is also lower, as explained in *Section 5.2. Figure 5.62* shows the minimum temperature evolution for an SOEC subjected to a ramp rate of 0.01 A/cm^2/min with different inlet temperatures of the gases (from 725°C to 800°C). The thermoneutral current progressively reduces with the temperature, as higher losses occur at lower temperature and for an inlet temperature of 725 °C, the minimum SOEC temperature falls below the thermal constraint after 35 minutes. Therefore, even if the current set-point of the SOEC (i.e., -1 A/cm^2 in the analysis) is a safe point for the operation, the cell could work in undesired point if too slow rates are applied from OCV. However, slow rates allow to timely modify the operating parameters of the SOEC, for example by increasing the oxidant-to-fuel ratio to maintain an higher cell temperature during the phase in which the cell is operating at currents under the thermoneutral point.

It is worth noting that these considerations are valid for an SOEC operating at OCV and subjected to a load variation towards a thermoneutral point, thus moving in the endothermic operation range of the cell.

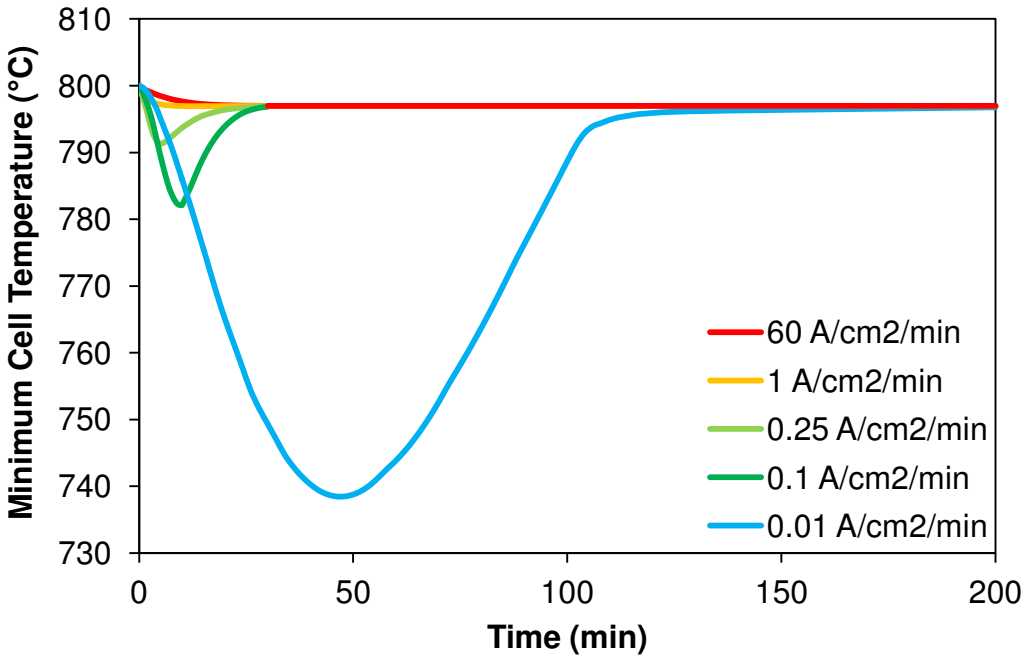

Figure 5.59 – Minimum cell temperature evolution in SOEC operation for different load ramps applied (from 0 to -1 A/cm^2).

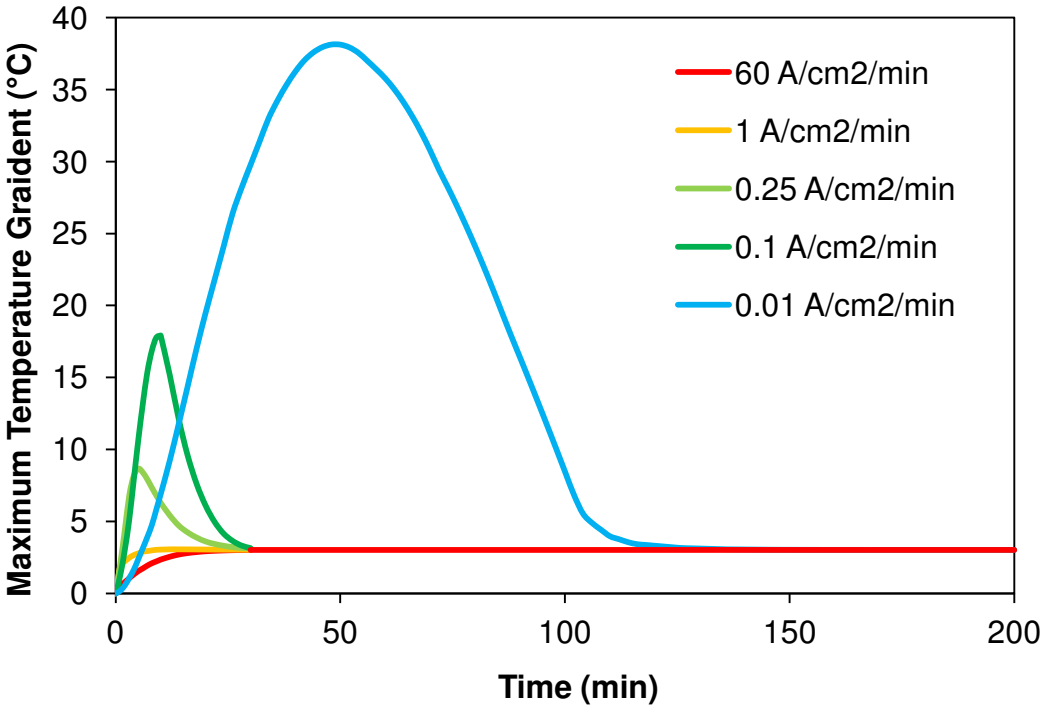

Figure 5.60 – Maximum temperature gradient evolution within SOEC for different load ramps applied (from 0 to -1 A/cm^2).

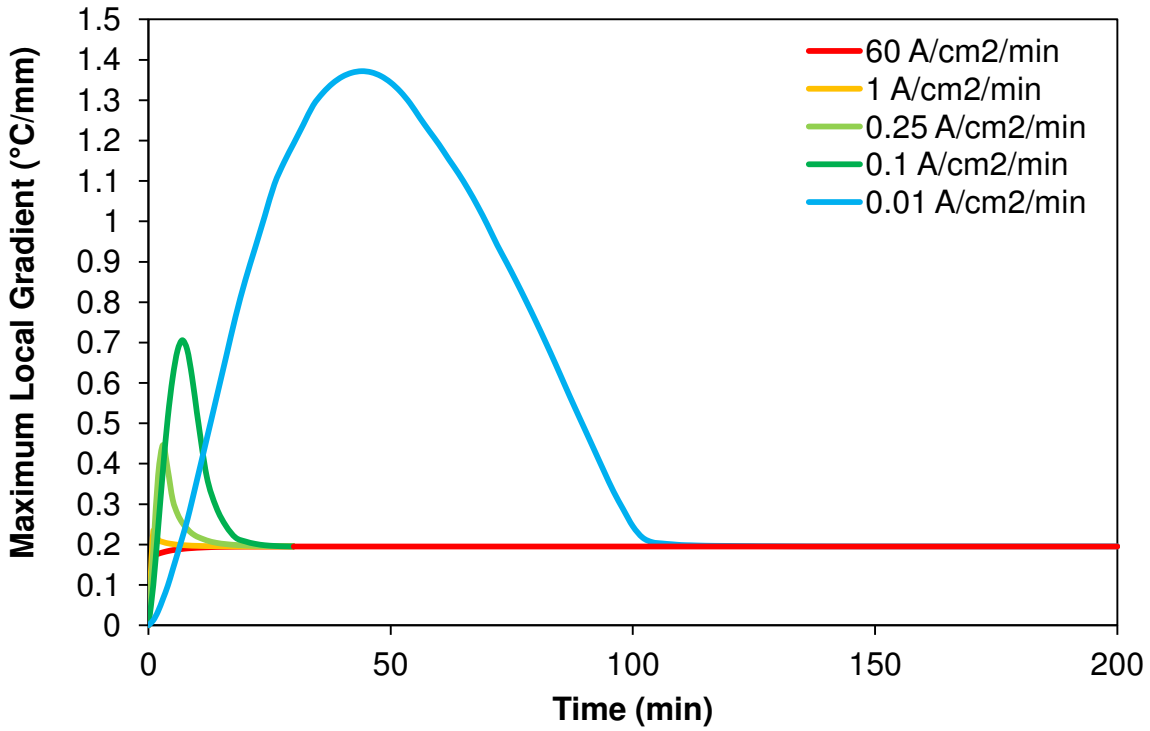

Figure 5.61 – Maximum local temperature gradient evolution within SOEC for different load ramps applied (from 0 to -1 A/cm^2).

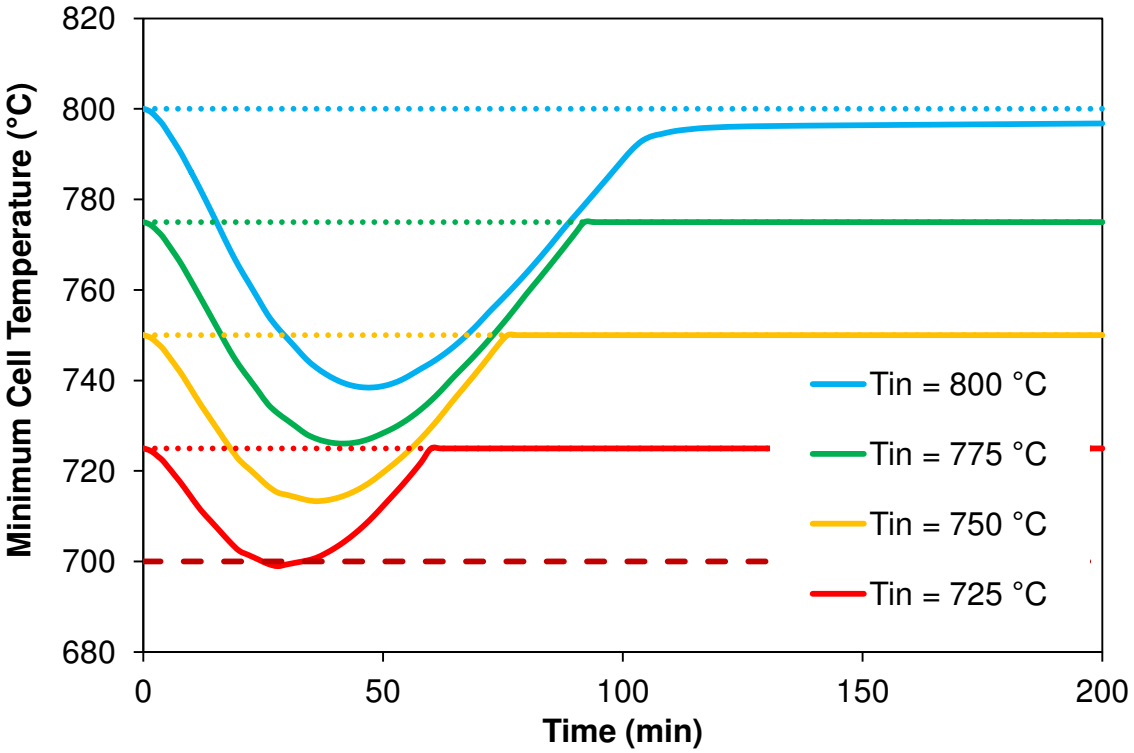

Figure 5.62 – Minimum temperature evolution within SOEC for a load ramp of 0.01 A/cm^2/min (from 0 to -1 A/cm^2) at different gas inlet temperatures. Dashed line indicates the thermal constraint, dotted lines the inlet temperatures.

However, as explained in *Chapter 2* the thermal behavior an SOEC varies from endothermic to exothermic above the thermoneutral current, and the cell assume a thermal behavior similar to SOFC over this current. In order to generalize the considerations, it is possible identify different transient situations in SOFC and SOEC operation. Depending on the net heat balance of the cell and on the current levels, different operating regions can be identified, as shown in *Figure 5.63*.

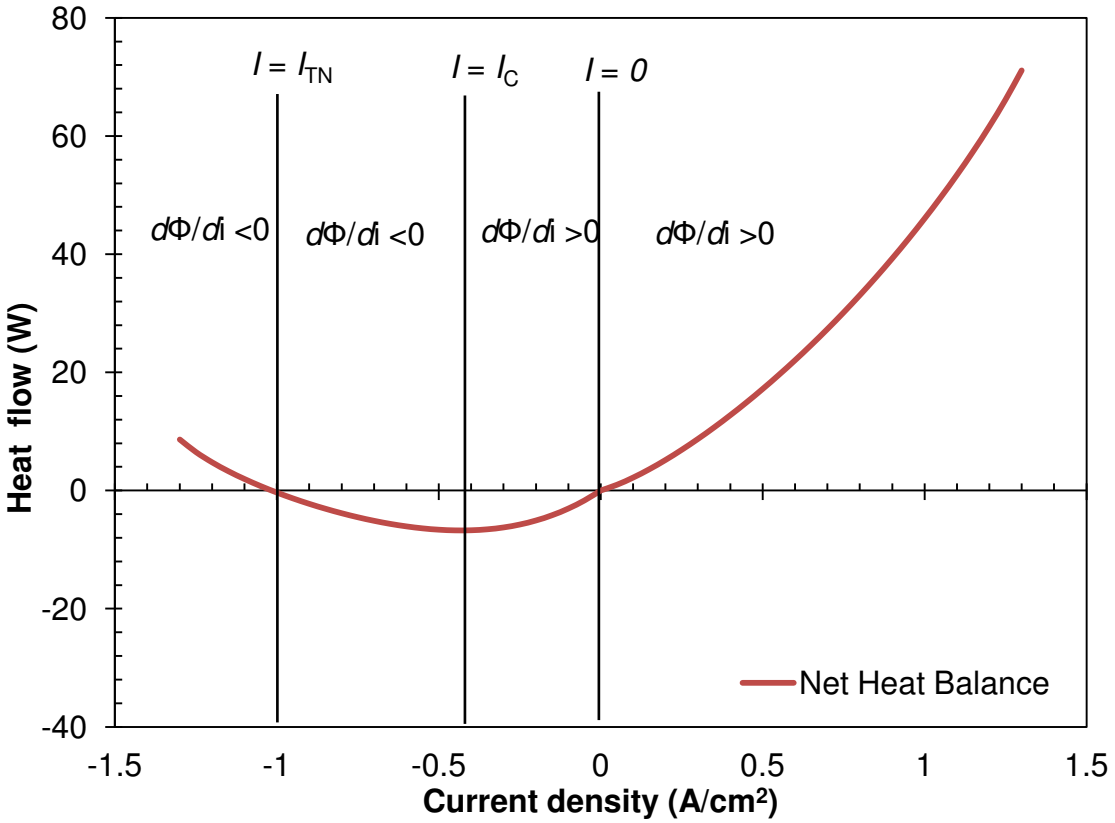

Figure 5.63 – Net heat balance in steady-state operation for the ESC cell in the simulated conditions (i.e., ambient pressure operation, inlet temperatures 800 °C, $\lambda = 2.15$).

In SOFC mode the cell is always exothermic with a positive net heat balance gradient with the current, which means the heat flow produced by the cell always increases with the current. In this situation, increasing the current – stating from OCV or from higher currents – always move the system towards higher temperature levels and nearer to the thermal constraints. If the thermal constraints are satisfied for the final current value imposed with the selected operating parameters, the applied ramp can be as fast as we want, also a step current can be applied, as it is not necessary to change the operating parameters to shift the operation in a safe region. However, if the cell is moving toward current levels that are not acceptable for the selected operating parameters, only very slow ramps can be applied to allow the control system to modify the parameters in time for including the final current imposed in the safe operating region. An

estimation of the acceptable ramps has been given in the dynamic analysis presented, in which a limiting ramp of less than 0.1 A/min/cm^2 is determined if the intervention time of the control system is of 10 minutes. The decreasing of the current is instead not problematic in SOFC and can be instantaneous, as it always moves the system toward safer regions.

In SOEC mode, three different operating regions can be identified (see *Figure 5.63*): one for the currents included between OCV and the operation point at which the net heat balance reaches the minimum value (i.e., $I = I_C$), one from this point to thermoneutral current (i.e., $I = I_{TN}$), and the last one for currents higher (in absolute value) than the thermoneutral one (i.e., $I > I_{TN}$). The first region presents a positive heat balance gradient, thus an increase of the current (in absolute value) produces an increase of the net heat absorbed by the cell, while the second and the last regions present a negative heat balance gradient; thus in these regions an increase of the current (in absolute value) moves the cell from endothermic to thermoneutral and then exothermic operation.

In the first region (i.e., $I_C < I < 0$), if the thermal constraints are satisfied for the final current value imposed with the selected operating parameters, any applied ramp is tolerable as the cell moves toward a safe operating point and the intervention of the control system is not required. If instead the cell is moving toward a current level that is not acceptable for the selected operating parameters, slow ramps must be applied to allow the control system to modify the parameters in time to avoid an excessive cooling of the cell. However, the heat balance gradients of the SOEC are milder with respect to SOFC operation (apart for very low currents) thanks to the balance between reaction endothermicity and heat generation due to losses; thus, the time employed by the cell to reach the thermal constraint is higher with respect to SOFC and consequently faster load ramps can be acceptable.

In the second region (i.e., $I_{TN} < I < I_C$), any current increase (in absolute value) moves the system away from the coldest operation point, thus fast ramp are beneficial for the SOEC; the opposite when decreasing the current (in absolute value) toward I_C, in this case slow ramps are required if I_C is a non-acceptable operating point with the selected operating parameters, as the control system must intervene to modify them.

In last region (i.e., $I < I_{TN}$), any current increase (in absolute value) moves the system nearer to the thermal constraints as the temperature increases until its maximum value or the gradients induced exceed the thermal limits. Thus, the same consideration made for the SOFC are valid: if the cell is moving toward current levels that are not acceptable for the selected operating parameters, slow ramps must be applied to allow the control system to modify the parameters,

while the decreasing of the current toward the thermoneutral value is not problematic and can be instantaneous. The only difference is that faster ramps can be acceptable with respect to SOFC due to lower net heat balance gradients.

In conclusion, the analysis has shown that the major issues arise from the dynamic operation in SOFC mode, condition in which the load ramps applied to the cell must be carefully limited to allow the timely intervention of control system to adapt the operating parameters (i.e., inlet gas temperature, oxidant-to-fuel ratio). In SOEC operation, the cell can potentially operate in unsafe regions both at intermediate currents (excessive cooling) and high currents (excessive heating). Thus, both the rates of current increase and decrease must be controlled to ensure that the control system can intervene to avoid the operation at unsafe points. However, the lower net heat balance gradients with respect to SOFC allow to accept steeper load ramps, as longer times become available for the control system to modify the operating parameters of the cell. The SOEC is thus intrinsically more suitable to work with variable loads thanks to the balance between reaction endothermicity and losses exothermicity that reduce the magnitude and the rate of temperature variation with the current.

5.4 Application of SOC-based P2P for RES imbalance mitigation: a case study

In this section, the sizing of a SOC-based P2P system employed for balancing the fluctuations of RES power production is presented through a case study on a wind farm.

In general, the storage (and re-use) of RES with P2P can be divided in two main fields of application: stand-alone systems and grid-connected systems.

In stand-alone installations based on RES, a productive capacity higher than the local demand is installed on-site and the excess electricity produced is stored by the P2P system and released to the users when RES production is lower than demand. In this type of application, the size of a SOEC-based P2P system must fit with both RES power production profile and demand profile. In particular, in SOFC operation the P2P system must be able to follow the load variations, which is quite challenging for the thermal management of the SOC, especially when demand peaks are present. In order to smooth the demand peaks, a stand-alone SOC-based P2P system can also include battery packs for providing the peak electricity.

In grid-connected RES installations, P2P systems can be installed to perform a different task: the mitigation of RES fluctuations to minimize the difference between forecasted production and effective production. In fact, electricity producers cannot feed into the grid all the power generated without any control, but they must trade the produced electricity on the power market. On the market, the producer bids the availability of an amount of power at a certain time, and the market accommodates power demand and supply on the basis of the electricity price. The power generated from fluctuating RES (i.e., wind and solar) cannot be scheduled exactly by the producers, which bid on the market a forecasted production. If the produced power is higher than the forecast, the excess production cannot be sold to the grid, and if it is lower, the producer must pay penalties for the electricity not produced. In both cases the difference between real and forecasted production represents a cost for the producer, in the first case for the unsold electricity and in the second for the penalties. The difference between effective and forecasted production is called imbalance. For a producer it is fundamental to minimize the imbalance in order to reduce costs. This can be achieved by storing the power production in excess with respect to forecast and feeding it into the grid when the RES power is lower than forecasted. Therefore, the P2P system is not designed to store all the electricity produced by the RES, but to minimize the imbalance. The sizing of the P2P must be performed on the basis of the imbalance profile, instead of looking at the production and demand profiles.

5.4.1 Case study: methodology and assumptions

In the case study, the sizing of a SOC-based P2P system designed for the minimization of the imbalance of a grid-connected wind farm is presented.

The wind farm analyzed is a 1 MW plant, whose imbalance profile has been generated by extrapolation from measured hourly data of real wind plants. The imbalance profile has been generated for a period of 6 months of operation, producing the hourly energy imbalance curve depicted in *Figure 5.64*. During each hour it is assumed that the wind farm is operating at constant power, thus from the energy values (kWh) shown in *Figure 5.64* the corresponding power values (kW) can be obtained dividing by 1 h.

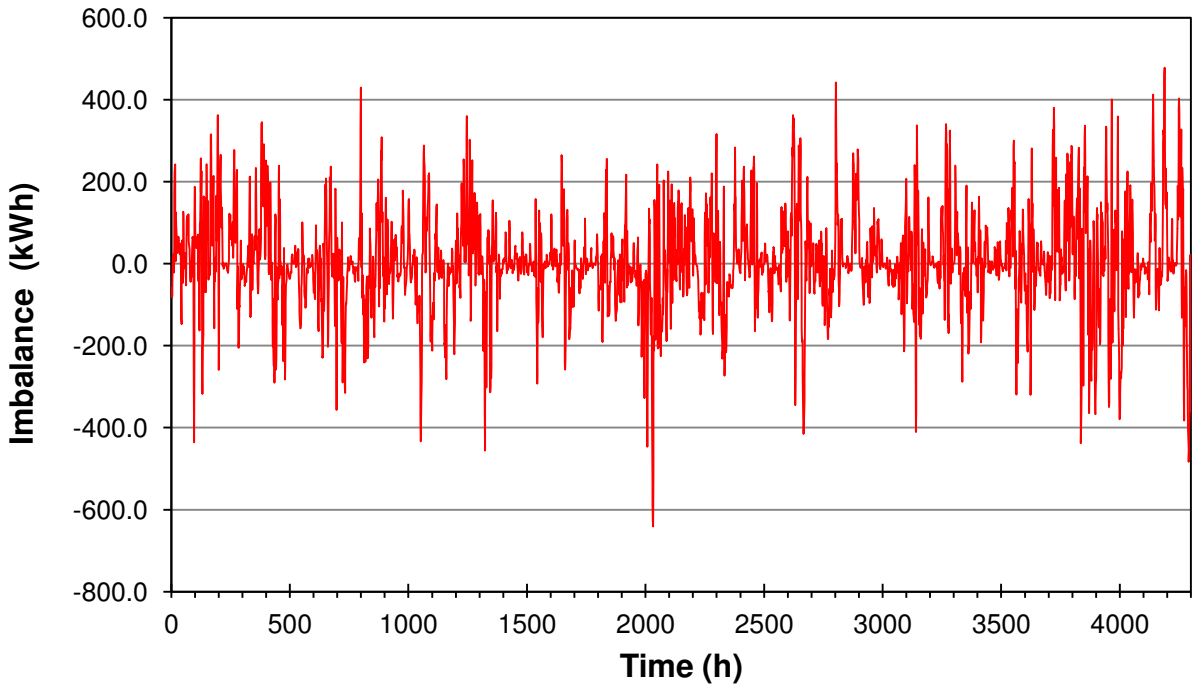

Figure 5.64 – Evolution of wind farm imbalance during 6 months of operation.

A negative imbalance occurs when the wind farm is generating less power than the forecast, while a positive one indicates an excess of production. Globally, the wind farm accumulates an imbalance of 360 MWh – evaluated as the summation of the absolute values of the hourly imbalances – during 6 months of operation. The positive imbalance is 185 MWh, and the negative one is 174 MWh; thus the excess electricity available is higher than the required one. If the time sequence of imbalances is such that the cumulated imbalance is always positive (i.e., at each hour the difference between the excess electricity and the deficit electricity of the previous hours is always positive), and consequently the storage is not empty when electricity is required to P2P, an ideal P2P system with 100% roundtrip efficiency can produce all the required power

from the stored electricity, even producing an extra amount of hydrogen (11 MWh) that can be used for other purposes (i.e., mobility, ect.). In the ideal case, the imbalance is thus reduced to the minimum value of 11 MWh. It is worth noting that is not possible to reduce the imbalance to zero even with this ideal P2P system because the energy exceeding the forecast is higher than the deficit electricity, or in other words the imbalance profile is not symmetric. The ratio between the negative and positive imbalance is 0.94, thus only a P2P system with roundtrip efficiency equal or higher than 94% can reduce the imbalance to the minimum value (11 MWh). In the case of an ideal P2P with 94% roundtrip efficiency, the imbalance is at the minimum and the end of 6 months of operation and the storage is empty.

The P2P system selected for this application is the one described in *Section 5.2.3* of this Chapter, which is based on a 10 bar pressurized rSOC stack with H_2 and O_2 storage at 30 bar that uses oxygen both as oxidant (SOFC) and sweep gas (SOEC) with a full recirculation loop on the oxygen side of the stack. The SOC stack of the P2P system is assumed to operate in the conditions selected by the sensitivity analysis presented in *Section 5.2*; these conditions are summarized in *Table 5.3* of *Section 5.2.3*. The charging and discharging curves of the rSOC in the selected conditions are shown in *Figure 5.51* and *5.52*. These curves express the charging efficiency of the SOEC in terms of electric current stored in hydrogen per unit of power provided to the P2P plant (i.e., A/W) and the discharging efficiency in terms of net power produced by the system per unit of current generated in the SOFC from the hydrogen stored (i.e., W/A).

It assumed that only the RES are available on the P2P site for supplying all the energy flows required by the BoP, thus the electricity generated by the wind farm is not only used for the electrolysis, but also for preheating the reactants (if necessary), pumping the water and compress the gases. Thus, the power absorbed by the P2P plant operating in SOEC mode is the total power required by the system, and the power produced by the P2P in SOFC operation is the net power that also accounts for the power consumed by BoP requirements.

The hydrogen-based P2P system presented in *Section 5.2.3* has a maximum roundtrip efficiency of 72%. Thus, even if operated for all the 6 months in the maximum efficiency points in SOFC and SOEC, the P2P system is able to store and release at maximum only 133 MWh of the available 185 MWh. Consequently, the imbalance can be reduced to 42 MWh, but only if the P2P can operate in the best conditions for all the hours. It is evident from the strong fluctuations of the available/required energy shown in *Figure 5.64* that the P2P system will hardly work in the maximum efficiency points during all the operation time.

The sizing of the P2P system has been performed using an optimization algorithm implemented in Excel™ that calculates the number of cells of the rSOC stack for which the wind farm imbalance is minimized. The optimization algorithm imposes constraints on maximum cell currents – which are limited to the acceptable values identified by rSOC simulations on the basis of the thermal constraints assumed – and on the stored hydrogen – if storage is empty, the SOFC cannot work –, and varies the number of cells of the stack until the minimum imbalance is reached.

The optimization procedure follows the sequence described in *Figure 5.65*.

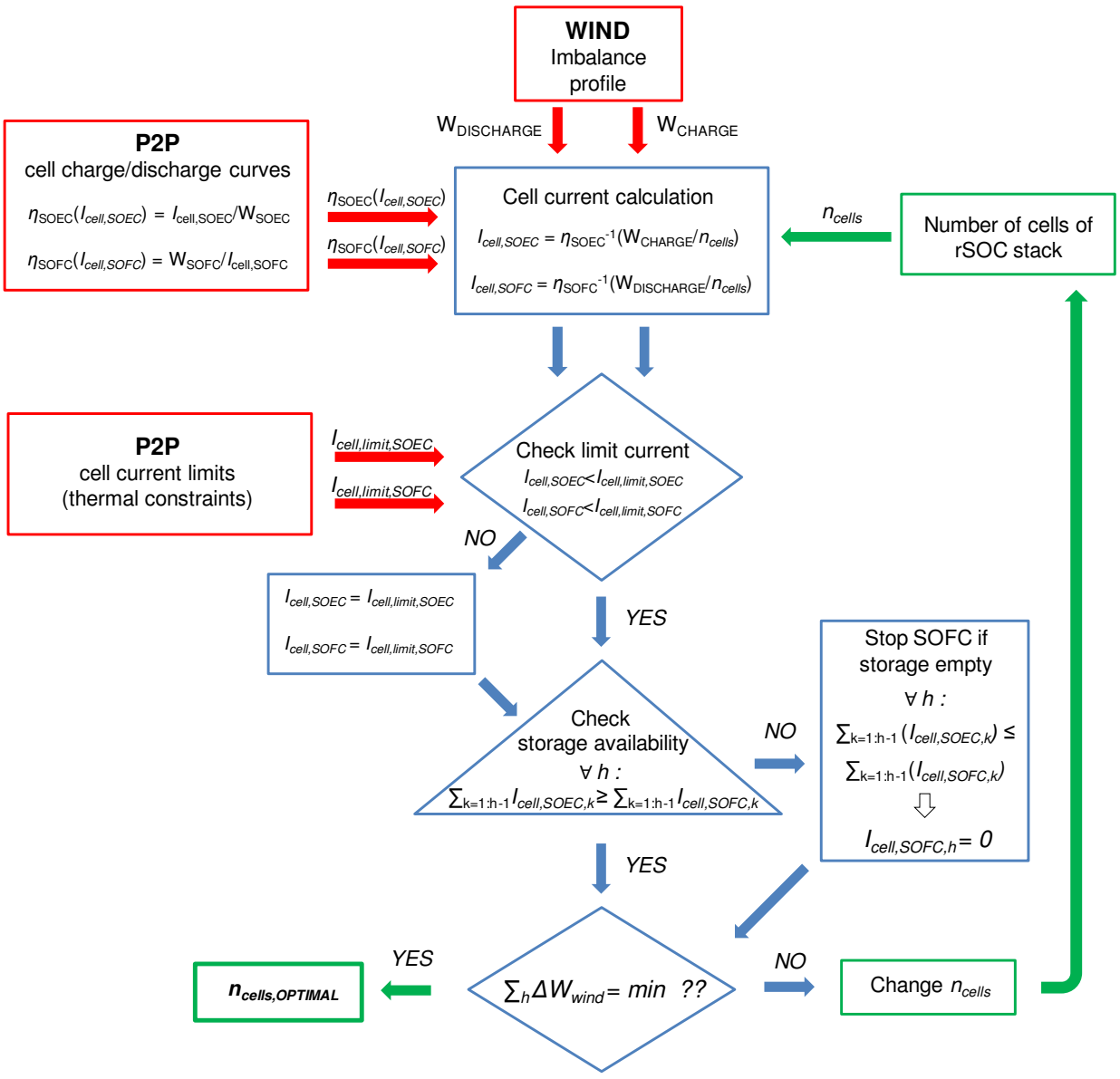

Figure 5.65 – Schematic of the optimization sequence for P2P sizing.

The sequence can be summarized as follows:

1) From the imbalance profile, the electric power available hour per hour for the storage (W_{CHARGE}) or required to the P2P system ($W_{DISCHARGE}$) is derived.

2) A number of cells is guessed to initialize the calculation, and the charging/discharging power per cell is calculated by dividing W_{CHARGE} and $W_{DISCHARGE}$ for the number of cells.

3) The cell operating current of the SOEC ($I_{cell,SOEC}$) and of the SOFC ($I_{cell,SOFC}$) is then derived from the charge and discharge curves of the P2P system (see *Figure 5.51* and *5.52*), given the power produced/supplied by/to the P2P for a single cell, which is calculated in the previous step. A cell current is obtained for each hour.

4) The cell current is compared with the limit value of the current obtained from rSOC simulations (i.e., $I_{cell,limit,SOEC}$ = -1.3 A/cm^2 , $I_{cell,limit,SOFC}$ = 0.35 A/cm^2, see *Section 5.2.3*), and if the cell current exceeds the limit, its value is fixed to the limiting one.

5) The constraint on the stored hydrogen is imposed by checking hour per hour that the current absorbed in the previous hours of SOEC operation (i.e., Ampere-hour stored in hydrogen; the corresponding amount of H_2 produced can be calculated by Faraday's Law) is equal or higher to the current produced by the SOC during the previous hours of operation as fuel cell. If the constraint is not fulfilled, there isn't enough hydrogen in the storage to supply the SOFC demand and the SOFC is stopped in the hours in which the constraint is not satisfied.

6) The total imbalance is calculated. If the value assumed is not the minimum one, the initial number of cells is changed.

5.4.2 Case study: results and discussion

Figure 5.66 shows the results of the size optimization. The number of cells which ensures the minimum imbalance is 2376, which corresponds to a P2P power of 486 kW for the system operating in SOEC mode at -1.3 A/cm^2 (including the power absorbed by the BoP of SOEC stack) and to a P2P power of 93 kW in SOFC operation at 0.35 A/cm^2 (value net of BoP losses). The imbalance of the wind farm operating with a P2P system of optimal size is 82.9 MWh,

which is 77% lower than the initial imbalance value (360 MWh). The roundtrip efficiency of the P2P system over the six months of operation is 54 %, with an ***H***-factor of 0.91 and at the end of the considered period, the amount of hydrogen in the storage is 930 litres (STP) corresponding to 2.78 MWh (LHW). This hydrogen can be either saved for the next period of operation, or used for other applications (e.g., mobility), or eventually sold to a user. Another byproduct is the oxygen, and 466 litres (STP) are available in the storage after six months of operation.

Figure 5.66 shows a fast decreasing of the imbalance with the increasing number of cells until a size of 1600 cells; then there is a slight decreasing until the minimum imbalance is reached at 2376 cells and then the imbalance starts to increase.

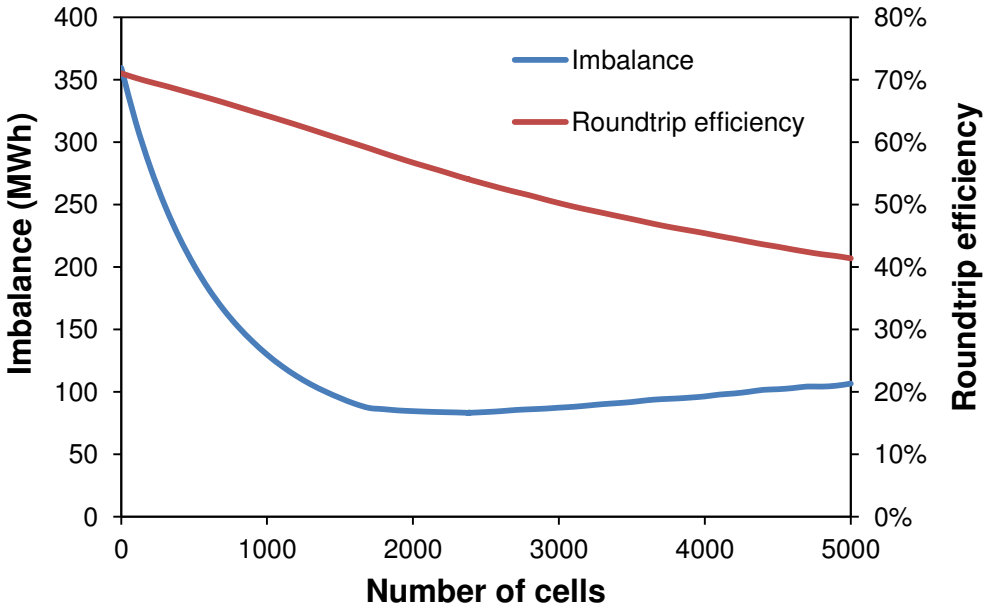

Figure 5.66 – Imbalance and roundtrip efficiency of P2P system.

This trend is related to the combination of different effects of the stack size on SOEC and SOFC operation.

When the rSOC stack is composed by few cells, the current required to the single cell exceed the limit due to thermal constraints in both SOEC and SOFC operation in most of the operating hours. Therefore, in the hours in which the limit is exceeded, the current level of cells is set to the limit values (i.e., $I_{cell,limit,SOEC}$ = -1.3 A/cm^2 , $I_{cell,limit,SOFC}$ = 0.35 A/cm^2) to avoid cell damaging, and the stack can store/produce only a fraction of the available/required electricity. The P2P system operating at limit currents in SOEC mode is at the maximum efficiency point (see *Figure 5.51*), while in SOFC mode is very near the maximum discharging efficiency (see *Figure 5.52*), which is reached at 0.3 A/cm^2. For this reason, the lower is number of cells, the

higher is the number of hours in which they operate at the limiting currents, and thus very near to the maximum efficiency conditions. In fact, *Figure 5.66* shows that the maximum roundtrip efficiency is reached for the minimum number of cells. If the stack is composed by only one cell, the roundtrip efficiency is 71.02%, as the P2P works for all the six months in conditions very close to the most efficient ones. When the number of cells is increases, the current required to the single cell diminishes, and the number of hours in which the cells are forced to work at limited currents decreases. This is shown in *Figure 5.67*, where the hours of operation at limited current in both SOFC and SOEC operation are depicted. The increase of the stack size allows to store and produce a progressively increasing amount of electricity, and consequently the imbalance diminishes, as shown in *Figure 5.66*. The drawback is that the cells works at lower currents and thus their charging and discharging efficiency progressively reduce with the increasing size of the stack, and consequently the round-trip efficiency reduces, as *Figure 5.66* shows.

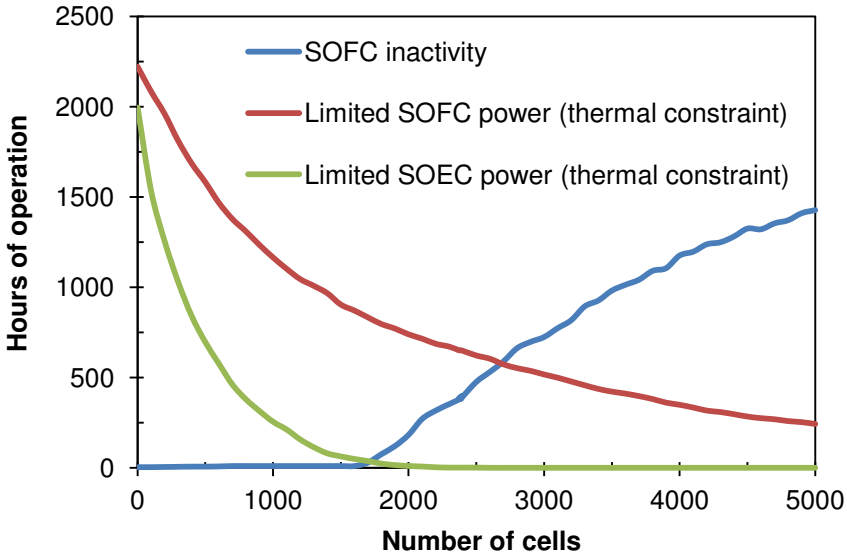

Figure 5.67 – Hours of SOFC inactivity due to hydrogen shortage in the storage (blue line) and hours of SOFC/SOEC operation at limited power because of thermal constraints (red/green lines).

Figure 5.67 shows that when a size of around 2000 cells is reached, the number of hours in which the stack operation in SOEC mode is constrained at limiting currents is almost zero. This means that a P2P system with a 2000 cells stack can absorb also the highest power peaks of RES imbalance in the analyzed case. In SOFC operation, even a 5000 cells stack is not able to provide the all the peak power required, and for around 250 h it must operate at limited currents.

With the increasing size of the stack, the number of hours of SOEC operation at low current – and consequently at low efficiency – increases, and as a consequence the stored electricity per

unit of power absorbed progressively decreases. The reduction of the storage rate due to SOEC operation at low efficiency has an impact also on SOFC operation, as the reduction of the rate of electricity conversion into hydrogen reduces the amount of H_2 stored per unit of electricity absorbed. Consequently, the P2P has to stop the fuel cell operation when there isn't enough hydrogen available in the storage for supplying the SOFC operation. The visible effect of this limitation is appreciable from a size of around 1600 cells, from which the hours of SOFC inactivity due to hydrogen shortage begin to increase (see *Figure 5.67*), reaching a value of 1427 h for a size of 5000 cells.

Therefore, the increase of the stack size has the positive effect to reduce the hours of activity at limited currents (and consequently at limited charging/discharging power), but contemporary decreases the efficiency of electricity storage and reconversion leading to longer periods of SOFC inactivity due to hydrogen shortage. The combined effects lead to the imbalance trend of *Figure 5.66*. For a size of around 2400 cells, the maximum reduction of the imbalance is achieved. This stack size implies a stop period of 380 h over 4320 h of operation due to hydrogen shortage, which means that around the 9 % of the operation hours the stack must be maintained in hot stand-by, or that the SOFC power must be further reduced below the thermal limits to ensure to have hydrogen availability for all the operating time. During the operation in SOFC mode, the optimal size P2P system is forced to operate at the current limit for 650 hours, this means that 15 % of the operating hours are affected to power limitation due to thermal constraints.

In conclusion, the sizing of an rSOC-based P2P system for RES imbalance mitigation has shown that it is possible to find an optimal number of cells that minimizes the imbalance – which is decreased by 77% in the analyzed case – but that does not correspond to the size which ensures the maximum roundtrip efficiency of the P2P system. The asymmetric operating characteristic of rSOCs suggests that an rSOC-based P2P system will perfectly fit an asymmetric imbalance profile, with high RES power to be stored for short periods followed by longer periods of electricity production at lower power, which will allow the exploitation of the P2P system near its limits and at the maximum efficiency for all the operation time.

5.5 Conclusions

In this Chapter, the investigation of an rSOC-based P2P system was performed. The system analyzed is composed by an rSOC stack and the main BoP components: water pumps, gas compressors, compressed H_2 storage tank (and also O_2 storage tank in some configurations) and heat recovery exchangers.

The performance of the P2P system was thoroughly assessed by analyzing the effects of operating parameters (inlet gas temperature, oxidant-to-fuel ratio, oxidant recirculation rate, and cell current) and system configurations (pressurized/ambient rSOC operation, air/oxygen as oxidant/sweep fluid) on stack and system efficiency. System operation was simulated by using for the SOEC the rSOC model developed at SRU level presented in *Chapter 3*, which uses the electrode kinetics experimentally validated in *Chapter 4*, and for the BoP components the thermodynamic modeling approach described in *Chapter 2*.

The analysis allowed to identify the most efficient configuration of the system, and to select the feasible operating currents within the limits given by the physical thermal constraints of SOC materials for which the highest roundtrip efficiency is achieved. Pressurized rSOC operation (10 bar) with pure oxygen as oxidant/sweep gas and full recirculation of the oxidant flow ensured the highest charging and discharging effectiveness, with a system roundtrip efficiency of 72% when the stack is operating at the maximum efficiency currents (-1.3 A/cm^2 in SOEC and 0.3 A/cm^2 in SOFC).

After the assessment of the different P2P configurations, a dynamic analysis was performed on the rSOC to determine the characteristic times of the thermal response of an SRU coupled with variable loads. The analysis showed that the major issues arise from the dynamic SOFC mode, in which fast load ramps can lead the system to operate in unsafe points in very short times. Thus, the load ramp applied to the SOFC must be carefully limited to allow the timely intervention of control system to shift the operating point in a safe condition by adapting the operating parameters (i.e., inlet gas temperature, oxidant-to-fuel ratio, etc.). In SOEC operation, the cell can potentially operate in unsafe regions both at intermediate currents (excessive cooling) and high currents (excessive heating). Thus, both the rates of current increase and decrease must be controlled to ensure that the control system can intervene to avoid the operation at unsafe points. However, the lower SOEC net heat balance gradients with respect to SOFC allow to accept steeper load ramps. The SOEC is thus intrinsically more suitable to work with

variable loads thanks to the balance between reaction endothermicity and losses exothermicity that reduce the magnitude and the rate of temperature variations with the current.

A case study was presented to show the application of a SOC-based P2P system with fluctuating RES. In the case study, the sizing of a P2P system employed for the minimization of the imbalance of a 1 MW grid-connected wind farm was performed. The P2P system operates in the most efficient configuration identified by the sensitivity analysis presented in the first part of the Chapter, and the minimization of the imbalance between effective and forecasted wind production was achieved by optimizing the size of the rSOC stack. The optimization procedure proposed takes into account the current limits due to thermal constraints and the constraint of stored hydrogen availability during the hourly operation. An optimal number of cells which minimizes the imbalance was found (i.e., ~ 2400 cells), for which the imbalance is reduced by 77 %. The roundtrip efficiency of the optimal-size P2P system coupled with the wind farm is 54 % ($\boldsymbol{H}$ = 0.91). The asymmetric operating characteristic of rSOCs suggests that an rSOC-based P2P system would perfectly fit an asymmetric imbalance profile, with high RES power availability for short periods followed by longer periods of required electricity production at lower power, which would allow the exploitation of the P2P system near its limits and at the maximum efficiency for all the operation time.

The results presented show that hydrogen-based P2P with rSOCs is an efficient solution for local RES storage, achieving a roundtrip efficiency from 54 % with realistic RES loads up to 72% in optimal operating points, values that demonstrate its competitiveness with other large scale EES options (i.e., PHS, CAES).

Chapter 6

Analysis of SOEC-based P2G applications

The scope of this Chapter is the investigation of SOEC-based P2G solutions. Two different configurations were analyzed. The first is a hydrogen-based P2G system, which produces SNG from the methanation of H_2 – produced by water electrolysis in an SOEC stack – and CO_2. The second P2G system is based on the direct co-electrolysis of H_2O and CO_2 in an SOEC stack and on the upgrading of the produced syngas to SNG by a methanation process. The produced SNG is injected in the natural gas network after upgrading it to the quality level required by the NG grid.

In both configurations the P2G system is composed by three sections: a hydrogen/syngas production and storage section based on an SOEC stack; a methanation section based on chemical reactors; and an SNG conditioning section for the upgrading to grid quality.

The design of the SOEC section and the operating conditions of the stack were selected following the results of the analysis performed on the rSOC system presented in *Section 5.2* of the previous Chapter. The electrolysis section of the P2G plant is composed by the SOEC stack, a water pump, intercooled gas compressors for CO_2 (only in the second P2G configuration analyzed), H_2 or syngas, a storage tank for the compressed H_2/syngas, and heat recovery exchangers.

The methanation section is based on the state-of-the art technology of the TREMP™ process described in *Chapter 2*, and it is composed by four catalytic reactors, heat exchangers, gas compressors for CO_2 (only in the first P2G configuration analyzed), SNG and N_2 (used for SNG conditioning). The methanation and SNG conditioning sections were modeled in Aspen Plus™. The simulation of P2G systems allowed to evaluate the efficiency of the two SNG production routes and to identify the components and operating conditions that mostly influence the effectiveness of electricity to SNG storage.

Finally, also the effect of biogas contaminants (i.e., H_2S) in the CO_2 feedstock on the P2G system efficiency has been assessed, the results are presented in *Appendix B*.

6.1 Analysis of a hydrogen-based P2G system for SNG production

This section investigates an SOEC-based P2G system for SNG production. The analysis is performed by simulating the stationary operation of the system, which is composed by three main sections: the hydrogen production and storage section based on SOEC, the methanation section based on chemical reactors, and the SNG conditioning section. The design of the SOEC section has been performed following the results of the analysis on the rSOC system presented in *Section 5.1*, while the methanation and SNG conditioning section has been designed following the state-of-the art technology of the TREMP™ process described in *Chapter 2*. The SOEC system was simulated by the numerical 2D model implemented in COMSOL Multiphysics and described in *Chapter 3*, and the methanation and SNG conditioning processes by a system model implemented in Aspen Plus™.

6.1.1 System description

The SOEC section has been described and analyzed in detail in *Section 5.1* and *5.2* of this Chapter. The analysis performed allowed to identify the operating conditions that ensure the higher efficiency for the storage of electricity in compressed hydrogen. The choice of the configuration of the SOEC-based hydrogen production section is based on the results presented and discussed in *Section 5.2.3*. The pressurized operation of SOEC stack (10 bar) with pure oxygen as oxidant has been selected, as it is the most efficient solution. The oxidant is fully recycled to realize a loop of the sweep gas with pure oxygen at SOEC anode. In principle, also other gases could be used for the sweep loop, but a gas separation system would be needed to eliminate the oxygen produced in the SOEC to re-obtain the initial sweep flow. In the P2P system investigated before, a storage tank is needed to contain all the oxygen produced in SOEC operation in order to make it available for the SOFC. In the P2G system it is not necessary to store all the produced oxygen under pressure, as oxygen is not required for the operation of the plant. In the system analyzed it is assumed that the produced oxygen is eliminated by venting in the coldest point of the sweep gas loop a mass flow corresponding to the oxygen flow produced by the electrochemical reaction in the stack. In this way, a fraction of the stream equal to the sweep flow required at the anode inlet is re-sent to the SOEC, while the remaining part that corresponds to the O_2 flow produced in the cell is vented away. Therefore, a fully recirculation of the sweep gas is realized without the need of an oxygen storage system with re-compression. The full recirculation of anode's exhaust is based on the assumption of negligible pressure drops;

otherwise an oxygen re-compression system would be needed to maintain the required pressure in the sweep loop. The storage tank is maintained in the P2G plant for the produced hydrogen, in order to realize a gas buffer between H_2 production and methanation, as the second process is stationary and requires a constant gas flow, while the first can be discontinuous if RES are the sources of electricity for H_2 production. On the basis of a predicted RES availability during the year, the H_2 storage can be dimensioned in order to allow the continuous operation of methanation during the year. Therefore, the H_2 production sections is composed by the SOEC stack and several auxiliaries: a water pump for feeding the SOEC cathode, a hydrogen compressor, the storage tank for compressed hydrogen and heat recovery exchangers for the preheating of inlet stack flows. The schematic of the SOEC section is shown in *Figure 6.1*.

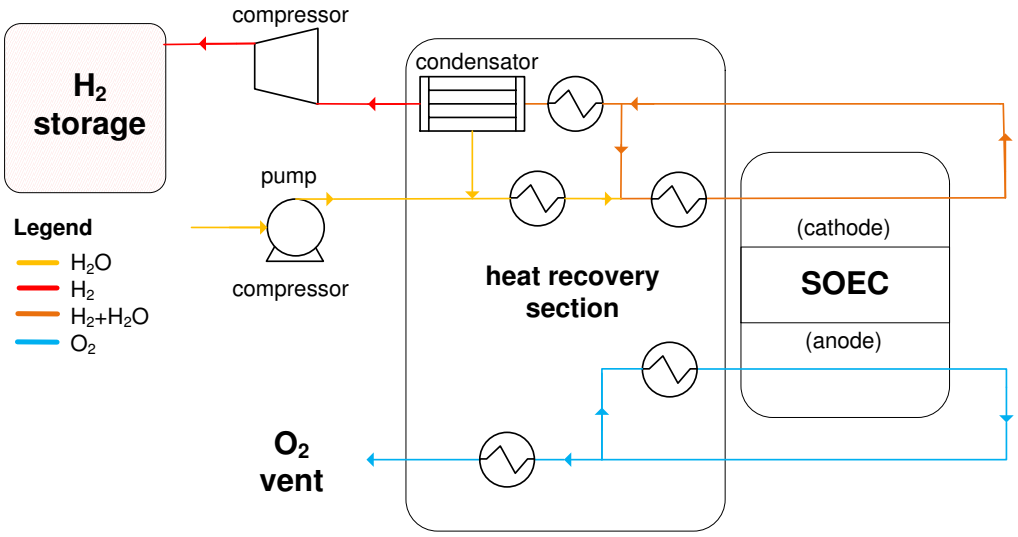

Figure 6.1 – Schematic of SOEC section of the P2G system.

A mature methanation technology has been selected for the SNG production, as this Thesis is aimed at the investigation of SOC-based P2G systems with state-of-the art technologies. The fixed-bed methanation by TREMP^{TM} process was selected, as described in *Chapter 2*. In this process, methanation takes place in a series of adiabatic reactors in which the Sabatier's reaction between H_2 and CO_2 occurs at 30 bar. The high pressure is needed to shift the equilibrium of the Sabatier reaction towards the production of methane; moreover, high pressure is needed if the SNG has to be injected in the NG grid. The schematic of the methanation section is depicted in

Figure 6.2, on the left side. This section is composed by four reactors, in order to obtain a syngas with a composition that is the closest possible to the equilibrium one. Reactors were simulated in the model with Gibbs reactors, which take the gas mixture to chemical equilibrium by minimizing the Gibbs free energy. The inlet temperature of the rectors has been fixed to 220 °C, thus hydrogen and CO_2 are heated up to this value before mixing and entering the first methanation reactor. Reactors are adiabatic components and the methanation is an exothermic reaction, thus the outlet gas flow has a higher temperature with respect to inlet one (fixed at 220 °C).

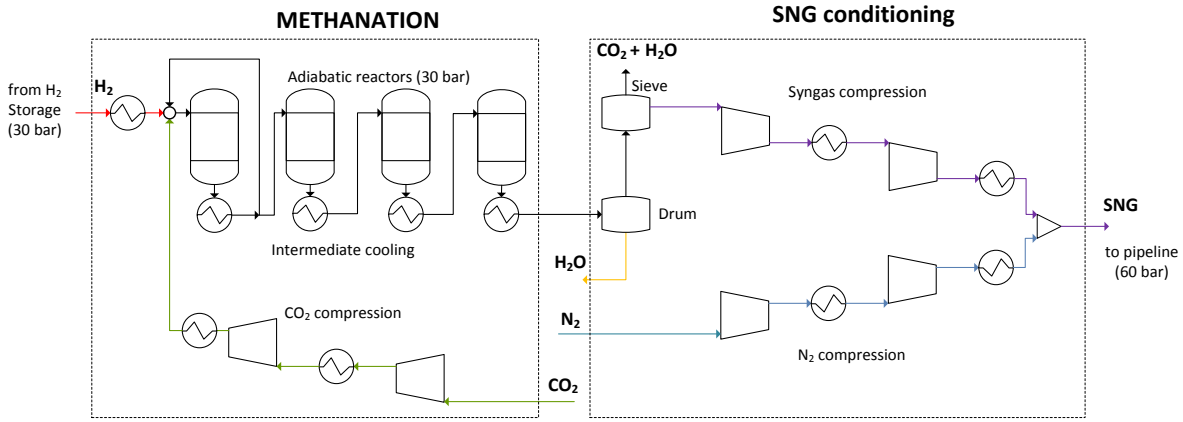

Figure 6.2 – Schematic of methanation and SNG conditioning section of P2G system.

The maximum temperature allowed for the reactors is 700 °C, thus the inlet gas flow must have a suitable composition that does not lead to an excessive heating in the reactor. The first reactor is the most problematic, as only reactants (H_2 and CO_2) are present in the inlet stream and thus very high conversion can be reached, and consequently high heating rates due to methanation are achieved. From simulations it is possible to find that if hydrogen and carbon dioxide are feed to the first reactor at 220 °C and with the stoichiometric FEED ratio (see equation (2.172), *Chapter 2*) of 3, a temperature higher than 700 °C is reached at the outlet of the first reactor. For this reason, it is necessary to adjust the H_2/CO_2 ratio at the inlet of the methanation section in order to decrease the gas conversion rate in the first reactor. The recirculation of a fraction of the flow exiting the first reactor is imposed in order to limit the outlet temperature of the reactor. The fraction that ensures an outlet temperature of 700 °C at the exit of the first reactor is iteratively calculated by the software. Results show that around 40 % of recirculation is needed in order to limit to 700 °C the outlet temperature of the first reactor feed with H_2 and CO_2 at 220 °C with a

ratio of 4:1. After each methanation reactor the temperature of the outlet gas is lowered to 220 °C through a heat exchanger. In the last stage, heat exchanger brings the outlet mixture in saturation conditions for the separation of water. The heat available from the four heat exchangers which realize the intermediate cooling of the syngas is considered as recoverable (e.g., for the preheating of reactants and/or cogeneration) and thus accounted as a positive flux in the thermal balance of the P2G system when calculating the efficiency.

The CO_2 feed to the P2G plant is assumed to be available at ambient pressure, and it is compressed up to 30 bar with an intercooled two-stage compression with an efficiency of 65%. The only difference with respect to the gas compression modeled in the P2P system is that the CO_2 is not assumed as ideal gas, but its thermodynamic properties derive from the Peng-Robinson model available in Aspen Plus. As in the P2P system, the heat derived from compression intercooling is considered lost to the ambient. After the second stage of compression, CO_2 is not further cooled, but it is directly sent to a heating stage that brings its temperature up to 220 °C. The H_2 is available at 30 bar from the storage, thus compression is not needed. Pressure drops in all the components are considered negligible, as their evaluation strictly depends on the size of the plant, while the simulations performed in this dissertation are valid for a general case, without specific reference to a certain size.

The SNG conditioning section is necessary to upgrade the produced syngas to the quality level required for the injection in the NG grid. The produced syngas is first sent to a water separator (i.e. named “drum” in the schematic), which has been modeled as a flash separator that allows thermodynamic equilibrium between liquid phase and gaseous phase. This component separates a large fraction of water from the syngas, which subsequently passes through a molecular sieve which is used for the capture of water and carbon dioxide. According to DOE/NETL (2011) it has been assumed that molecular sieve retains almost all the water and 98.5% of carbon dioxide. After the separation of water and almost all the CO_2, the SNG is further compressed to 60 bar, which is assumed to be pressure required for the injection in the natural gas pipeline. In the final stage of the conditioning section, SNG is mixed with a nitrogen stream, which is used to adapt the gas gravity of SNG to the standard of the NG grid. The prescriptions established in Italy for pumping natural gas into pipelines have been adopted (SNAM 2016). As explained in *Chapter 1*, three parameters must be verified in order to satisfy the quality requirements. These parameters are: gas gravity, Wobbe Index, and HHV of produced SNG. The major issue of the SNG is the low value of the gas gravity, due to the high fraction of methane and hydrogen in the mixture, thus it can be necessary to dilute the produced

SNG with a gas with a higher molecular weight (i.e., nitrogen). A gas gravity of 0.555 for the outlet SNG has been imposed as a target value from the lower limit indicated in (SNAM 2016). The nitrogen flow required to reach this target is iteratively calculated by the software.

6.1.2 Results and discussion

The results for a P2G plant based on the methanation of hydrogen produced from an SOEC stack composed by 1000 cells are reported in *Table 6.1*.

Table 6.1 – Plant Efficiency of H_2-based P2G system*

Component		**Energy flow (kW)**
W_{SOEC}		169
$\phi_{ext,SOEC}$		31.1
$W_{compr,H2}$		3.0
$W_{pump,H2O}$		0.01
$W_{compr,CO2}$		2.58
$\phi_{ext,METHANATION}$		-25.2
$W_{compr,SNG}$		0.44
$W_{compr,N2}$		0.09
Plant Streams		**Molar flows (kg/h)**
$H_2O_{(SOEC\ inlet)}$		43.6
H_2		4.85
CO_2		26.7
N_2		0.42
O_2		38.8
SNG		10.1
Plant Efficiency	η_{P2G}	**65.4 %**
Plant Efficiency (TI)	$\eta_{P2G,TI}$	**73.9 %**
Plant Efficiency (CHP)	$\eta_{P2G,CHP}$	**77.7 %**

*values calculated for a 1000 cells SOEC stack

The SOEC stack is operating at 10 bar, -1.3 A/cm^2, with an inlet temperature of 850 °C and uses pure oxygen as sweep gas with a full recirculation loop. In the operation, the stack absorbs 169 kW of electrical power and the BoP 3 kW for the H_2 compression and 31 kW of thermal energy for the preheating of reactants. The stack produces 4.85 kg/h of H_2, which are stored at 30 bar and ambient temperature, and an oxygen flow of 38.8 kg/h, which is vented away.

Hydrogen is supplied from the storage tank to the methanation section, where it is heated to 220 °C to reach the operating temperature of the first reactor. A carbon dioxide flux is provided to the methanation section with a ratio of 1:4 with the hydrogen, in order to satisfy the FEED ratio of 3, corresponding to 26.7 kg/h. CO_2 is assumed available at 25 °C and atmospheric pressure and compressed to 30 bar. The compression is performed with an intercooled compressor and after the second compression stage the CO_2 is heated to reach 220 °C. Hydrogen is not compressed because it is already available at 30 bar. On the first reactor, a recirculation loop is imposed to limit the outlet temperature at 700 °C. Diluting the inlet reactants with the partially reacted mixture – which contains the produced H_2O and CH_4 – is the easiest way to reduce the conversion rate and thus the heat generated in the adiabatic reactor. The recirculated flow is first cooled to 220 °C before mixing with the fresh H_2 and CO_2. The software iteratively calculates the recirculation ratio until the outlet temperature of the first reactor is below the limit imposed. The recirculation rate calculated is 38.46%.

The syngas at the outlet of the first methanation reactor (see *Table 6.2* for the syngas compositions in the plant) has 18.6 % of methane content (molar fraction) and 32% of hydrogen, thus other methanation stages are necessarily needed to increase the CH_4 content of the mixture. After cooling to 220 °C, the fraction of the syngas which is not recirculated (around 60%) is feed to the second methanation reactor. The heat recovered from the cooling between the first two methanation reactors is a valuable resource, as it is available from 700 °C to 220 °C, and it is used for covering the thermal preheating requirements of the methanation section. In particular, if we consider a minimum temperature difference of 40 °C between hot and cold fluids for the heat recovery in the methanation plant (as assumed for the SOEC section), an internal source at 260 °C is needed for heating the incoming CO_2 and H_2. The results of the simulation show that the heat available from the gas flow exiting the reactor in the temperature range between 700 °C and 260 °C is higher than the preheating requirements, thus the methanation section does not require external heat sources and even produces a thermal flux available outside the section.

It is not necessarily true that the extra-heat available from the methanation section can be used to cover the heat demand of the SOEC plant, because the two plants are not necessarily operative

at the same time. Moreover, the thermal levels of the available methanation heat and of the heat source required for the preheating of SOEC's reactant must coincide. A thermal integration between the SOEC and methanation parts of the P2G plant would require also a thermal storage to cope with the time mismatch between hydrogen generation and SNG production. Therefore, the design of the thermal integration requires information about plant size and operating profiles, as differently from the gas storage it cannot be supposed to store heat for an indefinite time without losses. Thus, the design of thermal storage strictly depends on the particular application. For this reason the thermal integration with heat storage has not been included in the model, as this dissertation is focused on a general analysis of P2P and P2G systems and not on a particular application. However, the effect of thermal integration has been considered in the analysis in the calculation of the efficiency. Three efficiencies have been calculated, one without thermal integration and considering lost the heat recoverable form the methanation section, another by considering an ideal thermal integration between SOEC and methanation, and the third without thermal integration, but assuming that a user is available for retrieving the heat produced in the methanation.

The syngas exiting the second methanation reactor has a higher methane concentration (28% molar), but still contains a considerable fraction of hydrogen (13% molar). The gas is thus cooled again to 220 °C and sent to a third methanation reactor. The heat recovered is from 525 to 220 °C, and thus considered as a valuable resource outside the plant. The third and fourth methanation stages bring the CH_4 concentration up to 33% and H_2 to less than 1%, the remaining part being water (66%) and 0.2 % of CO_2. The reactants are thus almost fully converted, and further methanation stages are not needed. In the energy balance of the P2G system, the heat recovered between the 3rd and the 4th reactor is considered as a useful output of the plant, while the heat available after the 4th stage is assumed as useless due to the lower temperature level. Thus, only the heat recovered from the cooling of the syngas between the methanation stages is considered as a valuable plant output.

The syngas exiting the methanation section is cooled until 25 °C (ambient temperature) and sent to a flash separator where the most of the water is separated from the syngas, which subsequently passes through a molecular sieve for the separation of the remaining water and CO_2. The syngas exiting the sieve is composed by 98% of CH_4 and 2% of H_2. This syngas has a gas gravity of 0.5447, lower than required by the NG grid. Thus a stream of nitrogen must be added to increase the gas gravity up to the lower limit. A stream of 0.42 kg/h of N_2 is needed for this purpose.

Syngas and nitrogen are compressed to 60 bar, mixed and injected in the NG grid. The heat removed from the fluids in the intercooled compressions is considered lost to the ambient. Finally, a stream of 10.1 kg/h of SNG can be produced by the P2G system from an H_2O stream of 43.6 kg/h entering the SOEC section of the plant and a CO_2 stream of 26.7 kg/h added in the methanation section. The power associated to the SNG can be calculated on the basis of the LHV, by considering both methane (LHV 50 MJ/kg) and hydrogen (LHV 120 MJ/kg) as fuels.

The energy and mass fluxes crossing the boundaries of the P2G system are shown in *Table 6.1*. In *Table 6.1*, the H_2 flux indicated is an internal stream, which is produced in the SOEC stack, stored and sent to the methanation section. For the sake of clarity, the numbers reported in *Table 6.1* are referred to a plant treating the full flux of hydrogen produced by an SOEC stack of 1000 cells working in the maximum efficiency point, without considering the time buffering of H_2 storage. The P2G is modeled as a stationary system working in fixed conditions independently of the volume of treated flows. Therefore, the energy flows reported in *Table 6.1* are linearly dependent on the treated hydrogen flow (i.e., if half of the hydrogen flow is processed, half the energy flows are produced/consumed) and consequently the efficiency of P2G system is not affected by the size of plant.

When methanation is performed on a higher/lower flux than that of the hydrogen produced in SOEC, just the duration of the H_2 storage is affected, but not the efficiency of the plant. Obviously, if SOEC and methanation are working with different hydrogen fluxes, different operating times must be considered (i.e., if the methanation section is treating half the hydrogen produced in SOEC, the SNG production will last the double of the electrolysis operation) and different energy flows are involved (i.e., the methanation section consumes half the energy flow, but for the double of time); however, the final P2G efficiency is always the same.

Three efficiencies have been estimated as follows:

$$\eta_{P2G} = \frac{\dot{m}_{SNG} LHV_{SNG}}{W_{SOEC} + \phi_{ext,SOEC} + \sum_k W_{compr,k} + W_{pump,H_2O}} \tag{5.1}$$

$$\eta_{P2G,TI} = \frac{\dot{m}_{SNG} LHV_{SNG}}{W_{SOEC} + \left(\phi_{ext,SOEC} - \left| \phi_{ext,METHANATION} \right| \right) + \sum_k W_{compr,k} + W_{pump,H_2O}} \tag{5.2}$$

$$\eta_{P2G,CHP} = \frac{\dot{m}_{SNG} LHV_{SNG} + \left| \phi_{ext,METHANATION} \right|}{W_{SOEC} + \phi_{ext,SOEC} + \sum_k W_{compr,k} + W_{pump,H_2O}} \tag{5.3}$$

The first one is the most conservative one, which does not account for the heat available from the methanation section. The second one assumes an ideal thermal integration between SOEC and methanation section, in which all the heat produced by methanation is effectively recoverable for the preheating of reactants of the SOEC stack. The third one takes into account cogeneration with the recovered heat from methanation section, but not the thermal integration between SOEC and methanation.

As *Table 6.1* shows, more than 80% of the energy consumption of the P2G plant is related to the electricity consumed by the SOEC and the remaining part is almost entirely consumed by the reactants preheating in the SOEC section (i.e., mostly for water vaporization). Gas compression is only a minor contribution. Therefore, the efficiency of SOEC cell has a determinant influence on the performance on the entire P2G plant.

The global efficiency of the plant is 65.4% without considering thermal integration or cogeneration. When the produced heat is used for thermal integration, the P2G efficiency can reach up to 73.9% if all the heat produced in the methanation is recovered. An efficiency of 77.7 % is reached when the heat produced is used for cogeneration.

Table 6.2 – Gas composition (molar fractions) in the P2G plant

Component	Inlet Met. #1	Outlet Met. #1	Outlet Met. #2	Outlet Met. #3	Outlet Met. #4	Syngas to N_2 conditioning	SNG to grid
H_2O	12.6%	40.2%	55.5%	64.3%	66.1%	0.0%	0.0%
H_2	65.1%	32.4%	13.4%	2.8%	0.7%	2.1%	2.0%
CO_2	15.6%	5.9%	3.2%	0.7%	0.2%	0.0%	0.0%
CO	0.9%	3.0%	0.2%	0.0%	0.0%	0.0%	0.0%
CH_4	5.8%	18.6%	27.7%	32.2%	33.0%	97.9%	95.6%
N_2	0.0%	0.0%	0.0%	0.0%	0.0%	0.0%	2.4%
Temperature (°C)	220	700	525	344	243	25	25

6.2 Analysis of a co-electrolysis-based P2G system for SNG production

This section investigates a P2G system based on co-electrolysis of H_2O and CO_2 in SOEC for SNG production. The analysis is performed by simulating the stationary operation of the system, which is composed by three main sections: the SOEC section where syngas is produced and stored, the methanation section based on chemical reactors, and the SNG conditioning section. The operating conditions of the SOEC were selected from the results of the analysis of the rSOC system presented in *Sections 5.1* and *5.2*, thus pressurized operation at 10 bar with pure O_2 as sweep gas was assumed. The methanation and SNG conditioning section has been designed as described for the hydrogen-based P2G option. The SOEC system was simulated by the numerical 2D model implemented in COMSOL Multiphysics and described in *Chapter 3*, and the methanation and SNG conditioning processes by a system model implemented in Aspen Plus™.

6.2.1 System description

The syngas production section of the plant is composed by the SOEC stack, water pump, CO_2 compressor, syngas compressor and heat recovery section. The schematic of this section is shown in *Figure 6.3*.

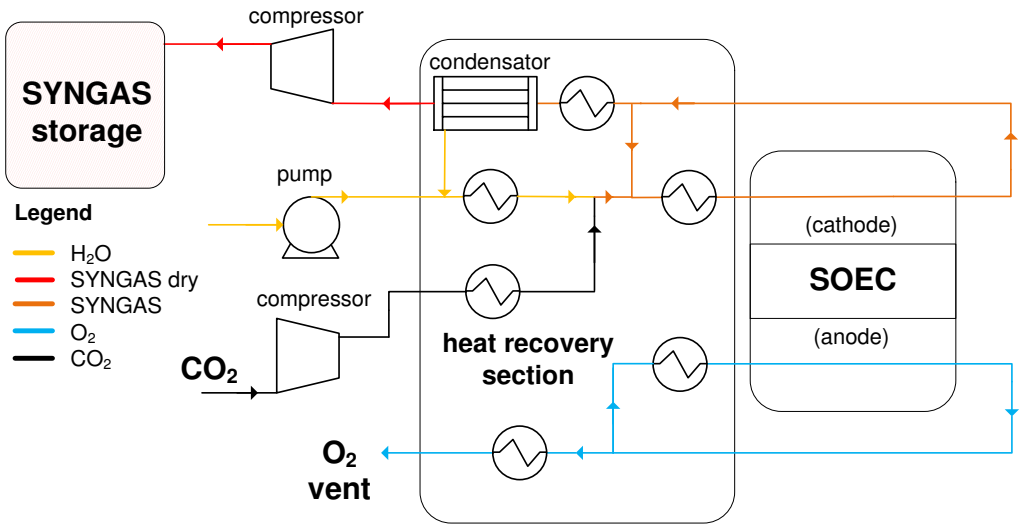

Figure 6.3 – Schematic of SOEC section of the P2G system.

The SOEC is operating at 10 bar with pure oxygen at the anode and a mixture of H_2O, CO_2, H_2, CO and CH_4 at the cathode. Oxidant and fuel flow rates are the same imposed in the SOEC

in the P2P configuration (see *Section 5.1.2*). Thus, the inlet fuel rate ensures a fuel utilization of 70% with a mixture composed at 90% of H_2O. If we assume that the electrochemical reduction of CO_2 provides only a minor contribution to the total cell current (results will show that more than 90% of the charge transfer occurs for the H_2O reduction) and if we consider that the inlet cathodic fraction of H_2O is about 70% when the system is operating in co-electrolysis (this fraction results from iterative calculations explained later in the text), it is necessary to rescale the operating current of the cell to ensure the same reactant utilization of the SOEC operating in the H_2-based P2G plant. By imposing the operation with the same *FU* in both plants, the ratio between the operating currents can be derived:

$$FU = \frac{I_{SOEC,H_2-P2G}/(2F)}{\dot{\boldsymbol{n}}_{in,fuel} \cdot 0.9} = \frac{I_{SOEC,coel-P2G}/(2F)}{\dot{\boldsymbol{n}}_{in,fuel} \cdot 0.7} \quad \rightarrow \quad \frac{I_{SOEC,coel-P2G}}{I_{SOEC,H_2-P2G}} = 0.77$$

A current density of -1.3 A/cm^2 has been selected for the SOEC in the hydrogen-based P2G configuration, thus in the co-electrolysis case an operating current of -1 A/cm^2 has been imposed. Cathodic recirculation is imposed to ensure 10% of hydrogen at the inlet of the cathode to maintain a reducing environment on the fuel electrode. In the co-electrolysis operation, the recirculated flow partially dilutes the inlet fuel, as also CO and CH_4 – which are produced in the cell – are mixed with the incoming H_2O and CO_2 streams. Thus, the inlet mixture is composed by 10% of hydrogen, and the remaining part is not only a mixture of H_2O and CO_2, but also contains CO and CH_4. The fuel dilution due to recirculation has an effect on the operating current, which is reduced to maintain the same fuel utilization of the H_2-based P2G. In the model, the recirculation rate has been calculated iteratively as the H_2 content of the outlet cathodic streams depends on the inlet composition of the fuel flow. A recirculation rate of 18.6 % has been found for the SOEC operating at -1 A/cm^2. The recirculated flow (volumetric composition 25.9 % H_2O, 54.5% H_2, 11.7% CO, 5.8% CO_2, 2.1 % CH_4) is mixed with water, which is feed to the cathode at 10 bar with a pump, and compressed CO_2. The remaining part of the syngas exiting the cathode is sent to heat recovery section, where water is condensed and recycled and the dry syngas is compressed at 30 bar and stored. The flow rate of CO_2 compressed is iteratively calculated by the model to ensure a FEED ratio of 3 in the dry syngas stored. The oxygen produced in the SOEC is vented after the heat recovery section.

The methanation and SNG conditioning section has been designed as described for the hydrogen-based P2G option. The schematic of this section is depicted in *Figure 6.4*.

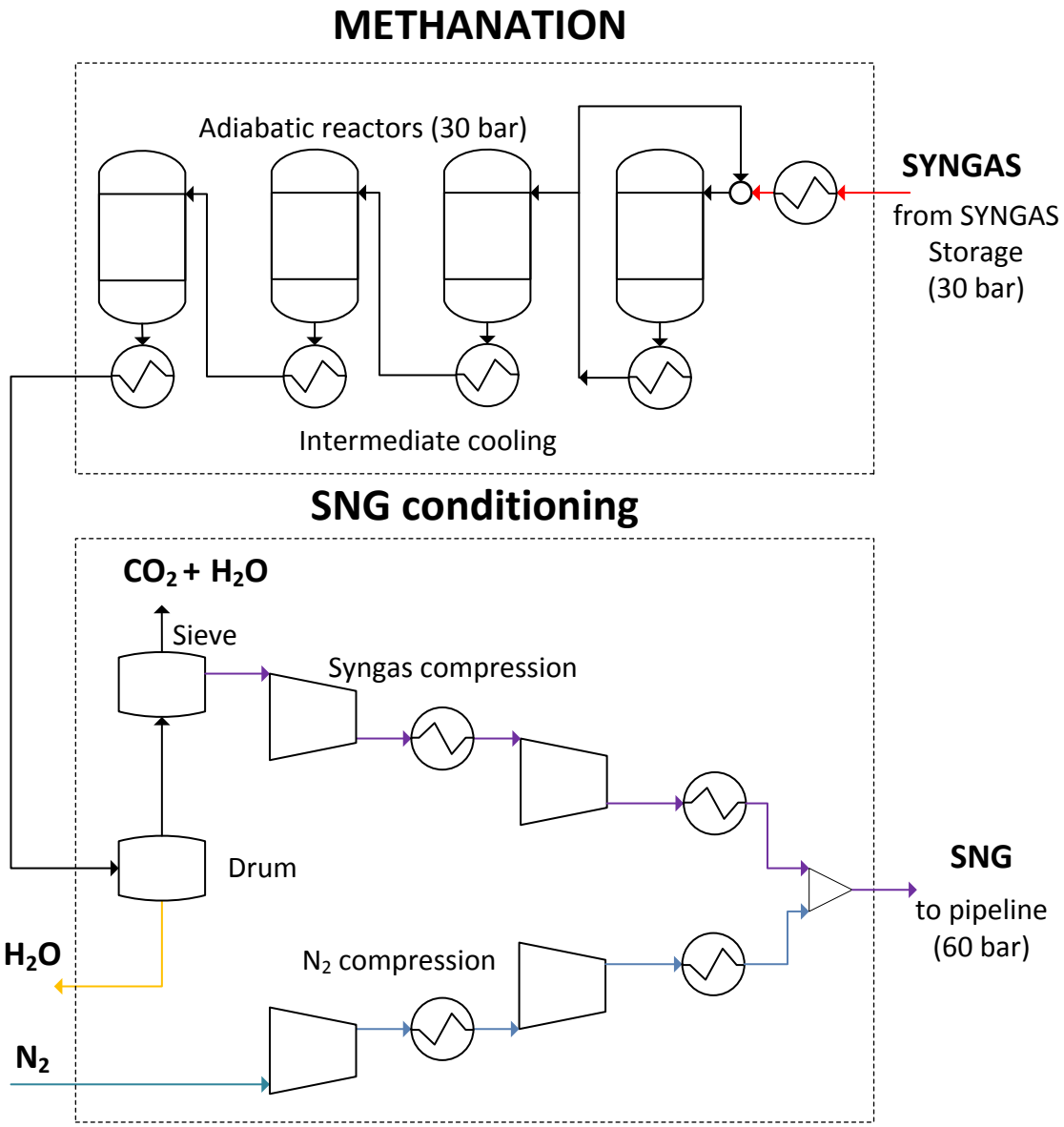

Figure 6.4 – Schematic of methanation and SNG conditioning section of P2G system.

Methanation reactors were simulated in the model with adiabatic Gibbs reactors operating at 30 bars, with an inlet temperature fixed to 220 °C, and a maximum outlet temperature allowed of 700 °C. On the first reactor, a recirculation rate of 60% is needed to limit the outlet temperature; this value has been calculated iteratively by the model. The syngas incoming from the storage is heated at 220 °C before entering the reactors cascade. After each methanation reactor the temperature of the outlet gas is lowered to 220 °C through a heat exchanger. In the last stage, heat exchanger brings the outlet mixture in saturation conditions for the separation of water. The

heat available from the four heat exchangers which realizes the intermediate cooling of the syngas is considered as recoverable (e.g., for the preheating of reactants and/or cogeneration) and thus accounted as a positive flux in the thermal balance of the P2G system when calculating the efficiency. Pressure drops in all the components are considered negligible, as assumed for the hydrogen-based P2G system.

The SNG conditioning section is the same described in *Section 5.4.1*. Water is removed from SNG in this section, and nitrogen is added to reach the required gas gravity of 0.555. As in the previous P2P and P2G system modeled, the heat derived from compression intercooling is considered lost to the ambient, and the final SNG obtained is compressed at 60 bar for the injection in the NG grid. The nitrogen flow required to reach the gas gravity target is iteratively calculated by the software.

6.2.2 Results and discussion

The results of the simulation of a P2G plant based on the methanation of syngas produced from co-electrolysis of CO_2 and H_2O in an SOEC stack are reported in this section. In *Appendix B* the effect of H_2S contamination on stack performance and system efficiency is further investigated.

In order to compare the results to those of the hydrogen-based P2G plant, a stack of the same size has been considered (1000 cells). Results are reported in *Table 6.3*.

The SOEC stack is operating at 10 bar and -1 A/cm^2, with an inlet temperature of 850 °C and pure oxygen as sweep gas with a full recirculation loop. Inlet stack composition is shown in *Table 6.4*. In the operation, the stack absorbs 123 kW of electrical power and the BoP 1.2 kW for the CO_2 compression, 2.2 kW for syngas compression, and 21 kW of thermal energy for the preheating of reactants. The SOEC section produces 16.2 kg/h of syngas (on dry basis), which are stored at 30 bar and ambient temperature, and an oxygen flow of 27.6 kg/h, which is vented away.

The performance of the stack in co-electrolysis is slightly worse (i.e., higher SRU voltage) than in the case of H_2O electrolysis for low currents, and slightly better for high currents (i.e., higher than -0.8 Acm^{-2}), as it is possible to see from the SRU polarizations depicted in *Figure 6.5*. This result is connected to both the thermal behavior of the cell and the electrochemistry. If we look at the electrochemistry, the stack operating in co-electrolysis is practically reducing only the water present in the fuel mixture, while carbon dioxide provides a very limited contribution to electrochemical reactions due to slower kinetics, as described in *Chapter 4*. *Figure 6.6* shows

the contributions of water and carbon dioxide reduction reactions to the total cell current. It is possible to the see that more than 90% of the electrical charge transferred in the cell is related to H_2O electrolysis. Therefore, even if activation losses are higher for carbon dioxide electrolysis, only a minor fraction of the total cell current is related to CO_2 electrolysis, and consequently the effect of higher activation losses on the total cell overpotential is moderately visible in the polarization, and only at low currents.

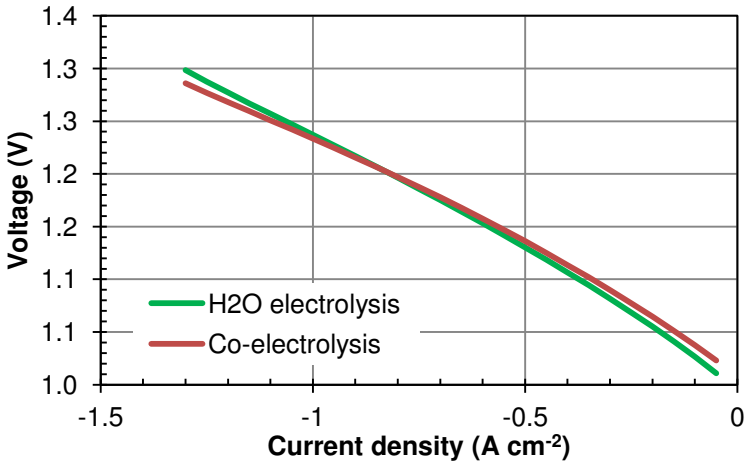

Figure 6.5 – SRU polarization for H_2O electrolysis and co-electrolysis. SOEC nominal conditions for P2G plants described in *Sections 5.4.1* and *5.5.1*.

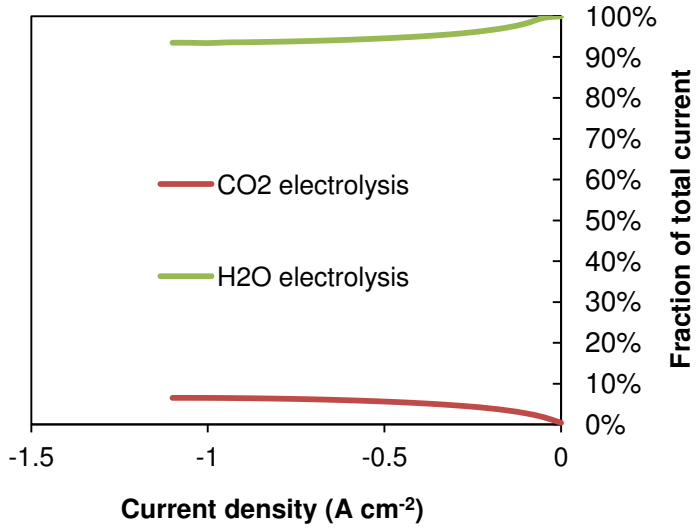

Figure 6.6 – Water and Carbon dioxide contributions to the total cell current.

The thermal profiles of the cell operating in electrolysis and co-electrolysis show instead appreciable differences. The temperatures at the outlet of the fuel channel of the SRU and along the channel length for electrolysis and co-electrolysis operation in the nominal conditions for the P2G plants (see *Section 5.4.1* and *Section 5.5.1*) are shown in *Figure 6.7* and *Figure 6.8*. It is

possible to see from the Figures that the outlet SRU temperature is slightly higher for H_2O electrolysis at low currents, while at -0.4 A/cm^2 the trend reverses and the temperature becomes higher for co-electrolysis, with a sensible difference with the electrolysis operation, up to 36 °C at -1.3 A/cm^2. The higher temperature is beneficial for the cell operation, as it enhances the kinetics of electrochemical reactions. The positive effect due to the temperature balances the higher activation losses due to CO_2 reduction and the SRU voltage of co-electrolysis operation becomes lower than that of the electrolysis operation at around -0.9 A/cm^2. It is worth noting that higher fractions of CO_2 in the inlet mixture would probability increase the contribution of carbon dioxide reduction to total cell current and consequently the losses related to co-electrolysis operation. Hence, the behavior described is typical for the mixture considered in this case, but it is not general for the co-electrolysis, which is expected to give worse performance than H_2O electrolysis with higher fractions of CO_2. Even if the higher temperature of co-electrolysis operation is beneficial for the cell, it must be noted that the outlet temperature exceeds 850 °C for currents higher than -1.15 A/cm^2, thus the operating points at high currents become unfeasible for the thermal constraints. Also for this reason the current has been limited to -1 A/cm^2 in co-electrolysis.

Given that the SOEC has lower overpotential losses in co-electrolysis at high currents, as shown by the polarization, the reason of the higher temperature must be sought in the chemical reactions occurring within the electrode. Water gas shift and steam-reforming/methanation are the reactions included in the model. The water gas shift is mildly exothermic (and the reverse one is moderately endothermic), while the MSR is strongly endothermic and the reverse MSR (i.e., CO methanation) produces large amounts of heat. The temperature profile along the fuel channel (*Figure 6.8*) during co-electrolysis suggests the presence of an exothermic source in the second half of the cell (from the gas inlet) that balances the endothermicity of the electrochemical reduction producing a flatter temperature profile with respect to H_2O electrolysis. The MSR rate depicted in *Figure 6.9* confirms that from around an eighth of the cell length, the rate is negative, thus CO methanation occurs. In the first millimeters of the electrode the MSR rate is positive, as the CH_4 coming from recirculation reacts with water in the steam reforming. When the rate becomes negative, methane starts to be produced in the electrode from CO and H_2. The methanation rate increases along the channel due to lowering of the water concentration (a product of methanation) that is electrochemically reduced, and due to the increase of H_2 and CO concentrations, that are the products of the electrochemical reactions. The

final balance is positive for CH_4 production, with the methane concentration increasing up to 2% at the cell outlet in the nominal electrolysis conditions.

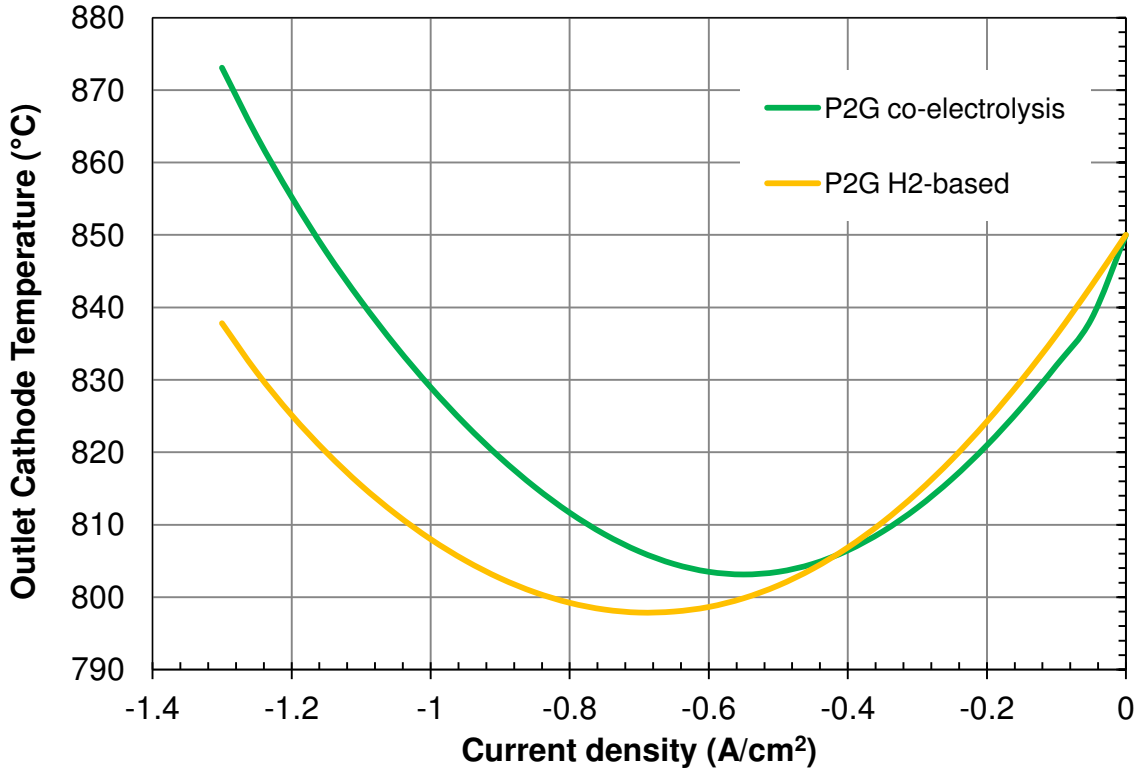

Figure 6.7 – Cell temperature measured at the outlet of the fuel channel of the SRU in electrolysis and co-electrolysis operation. SOEC nominal operating conditions of P2G plants described in *Sections 5.4.1* and *5.5.1*.

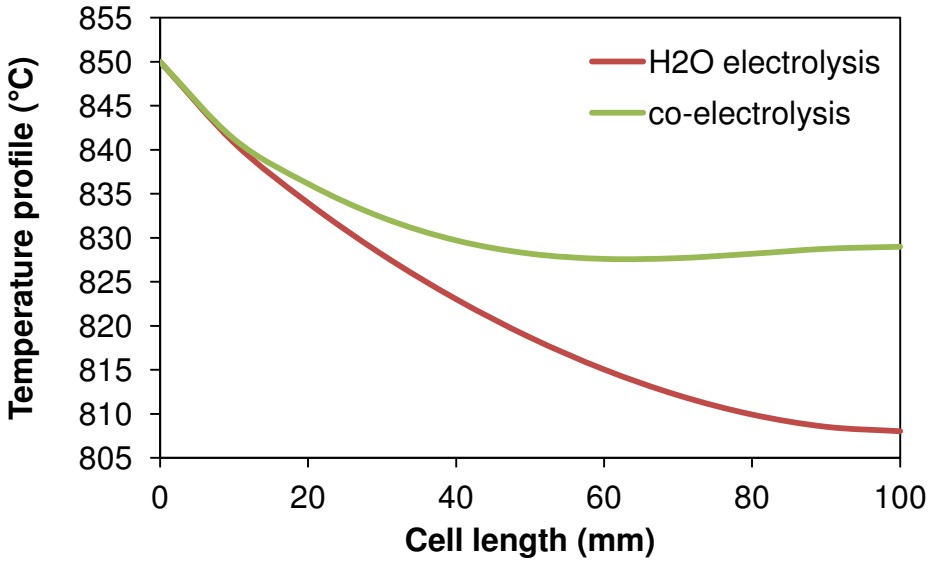

Figure 6.8 – Cell temperature measured along the fuel channel of the SRU in electrolysis and co-electrolysis operation at -1 A/cm^2 in the SOEC nominal operating conditions of P2G plants described in *Sections 5.4.1* and *5.5.1*.

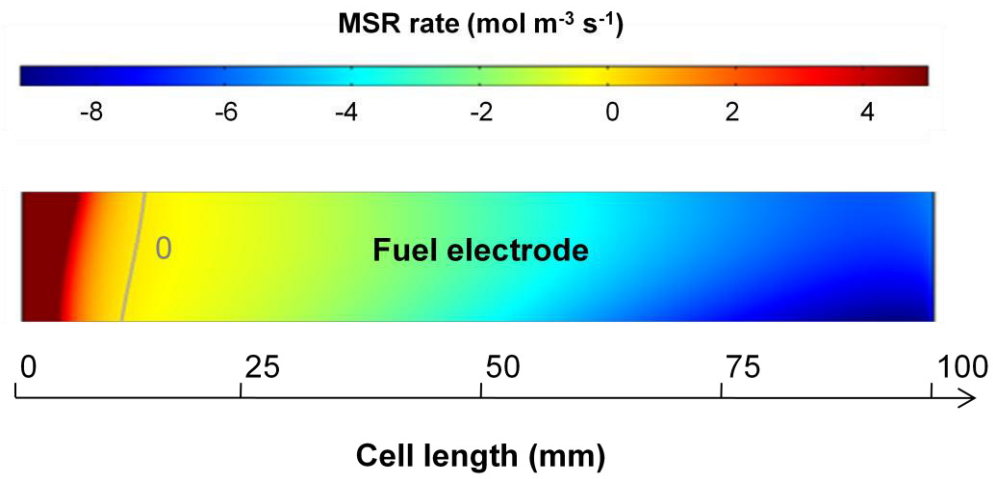

Figure 6.9 – Rate of methane steam reforming in the SOEC cathode (nominal co-electrolysis conditions). A negative rate indicates that CO methanation is occurring.

It is worth investigating if the co-electrolysis operation can lead to carbon formation in the cell. The rates of carbon formation due to methane cracking and Bouduard reaction are depicted in *Figure 6.10*. Both reactions have negative rates, thus the nominal co-electrolysis conditions investigated are safe from the point of view of carbon deposition.

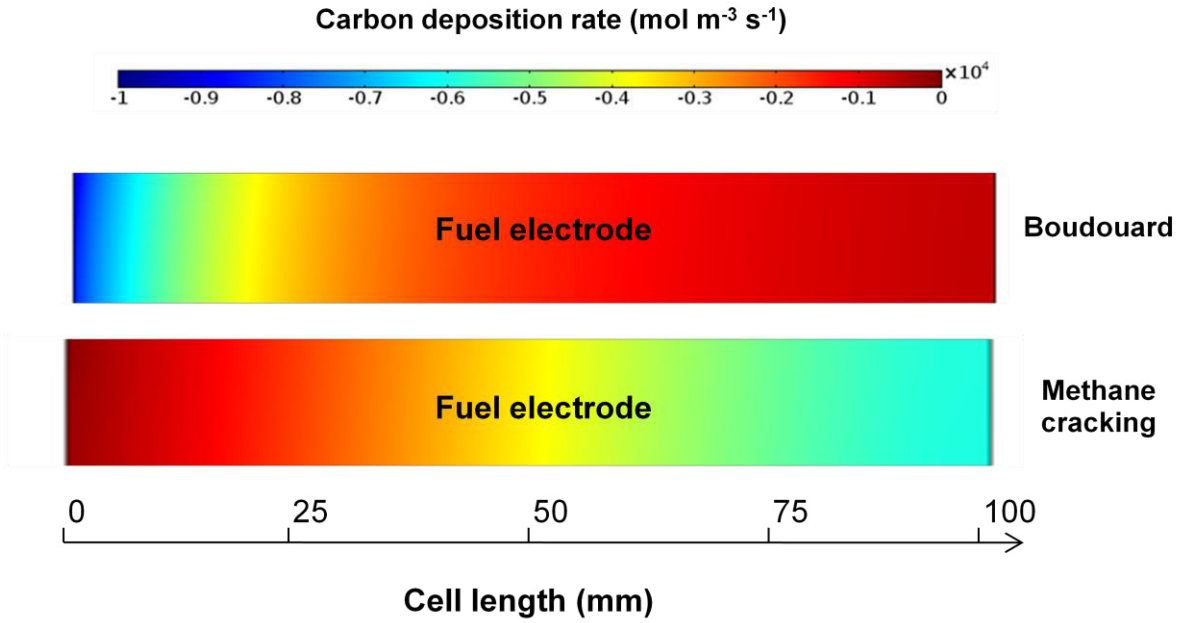

Figure 6.10 – Rates of carbon formation from Bouduard and methane cracking reaction (nominal co-electrolysis conditions). A negative rate indicates that carbon deposition is not occurring.

The syngas produced in the SOEC is stored in a tank at 30 bar after the heat recovery section, where water is condensed and recycled. The dry syngas stored (16.2 kg/h in nominal operating conditions) is composed by 75% of H_2, 7% of CO_2, 15.5% of CO and 2.5% of CH_4, corresponding to a FEED ratio of 3. This composition has been obtained by adjusting the CO_2 flow provided to the SOEC (19.1 kg/h in nominal operating conditions).

The syngas is supplied from the storage tank (ambient temperature) to the methanation section, where it is heated to 220 °C to reach the operating temperature of the first reactor. A recirculation loop is imposed on the first reactor to limit the outlet temperature at 700 °C. The recirculated flow is first cooled to 220 °C before mixing with the fresh syngas. The software iteratively calculates the recirculation ratio until the outlet temperature of the first reactor is below the limit imposed. The recirculation rate calculated is 59.79%. This is a very high rate with respect to the H_2-based P2G plant, which needs a recirculation of only 40% to limit the outlet temperature of the first reactor. This difference is due to the fact that the syngas contains a high fraction (15%) of CO, and the methanation of CO is more exothermic than the CO_2 methanation. Thus, the co-electrolysis based P2G system provides the first methanation reactor a mixture that intrinsically requires a higher dilution to limit the temperature increase.

The syngas at the outlet of the first methanation reactor (see *Table 6.4* for the syngas compositions in the plant) has 29 % of methane content (molar fraction) and 33% of hydrogen, thus other methanation stages are necessarily needed to increase the CH_4 content of the mixture. After cooling to 220 °C, the fraction of the syngas which is not recirculated is feed to the second methanation reactor. The heat recovered from the cooling between the first two methanation reactors is a valuable resource, as it is available from 700 °C to 220 °C, and it is used for covering the syngas preheating requirements of the methanation section. The results of the simulation show that the heat available from the gas flow exiting the first reactor in the temperature range between 700 °C and 260 °C is higher than the preheating requirements, thus the methanation section does not require external heat sources and even produces a thermal flow available outside the section. The syngas exiting the second methanation reactor has a higher methane concentration (40% molar), but still contains a considerable fraction of hydrogen (14% molar). The gas is thus cooled again to 220 °C and sent to a third methanation reactor. The heat recovered is from 522 to 220 °C, and thus considered as a valuable resource outside the plant. The third and fourth methanation stages bring the CH_4 concentration up to 44% and H_2 to 4%, the remaining part being water (52%). The reactants are thus fully converted, as no more CO and CO_2 are available and further methanation stages are not needed. In the energy balance of the

P2G system, the heat recovered between the 3rd and the 4th reactor is considered as a useful output of the plant, while the heat available after the 4th stage is assumed as useless due to the lower temperature level. Thus, only the heat recovered from the cooling of the syngas between the methanation stages is considered as a valuable plant output.

The syngas exiting the methanation section is cooled until 25 °C (ambient temperature), and after passing through the water separator and the molecular sieve its composition is brought to 93% of CH_4 and 7% of H_2. This syngas has a gas gravity of 0.5188, lower than required by the NG grid. Thus a stream of nitrogen must be added to increase the gas gravity up to the lower limit. A stream of 1.12 kg/h of N_2 is needed for this purpose.

It is worth noting that the SNG at the end of the methanation section has a higher content of hydrogen with respect to that obtained in the H_2-based P2G system. This is due to the fact that syngas processed in the methanation section contains both CO and CO_2, due to the co-electrolysis. The presence of CO has a double effect: a higher exothermicity in the first reactor, and consequently a higher recirculation needed, and a higher H_2 content in the SNG, balanced by a lower H_2O fraction. The second effect has a negative drawback on the P2G system, as it increases the need for nitrogen, and consequently the electricity absorbed by the BoP, as N_2 must be compressed up to 60 bar, and also decreases the LHV of the produced SNG.

Globally, the co-electrolysis based P2G system operating with a 1000 cells SOEC stack can produce a stream of 8.06 kg/h of SNG from an H_2O stream of 24.7 kg/h entering the SOEC section of the plant and a CO_2 stream of 19.1 kg/h. The power associated to the SNG can be calculated on the basis of the LHV, by considering both methane (LHV 50 MJ/kg) and hydrogen (LHV 120 MJ/kg) as fuels.

As discussed for the H_2-based P2G system, the thermal integration between the methanation and SOEC section is limited by the contemporaneity of the operation and by the thermal levels. Also in this case, the effect of thermal integration has been considered in the analysis when calculating the efficiency of P2G system. Three efficiencies have been calculated, one without thermal integration and considering as lost the heat recoverable form the methanation section, another by considering an ideal thermal integration between SOEC and methanation, and the third without thermal integration, but assuming that a user is available for retrieving the heat produced in the methanation.

The values of the energy and mass fluxes reported in *Table 6.3* are referred to a plant treating the full flux of syngas produced by an SOEC stack of 1000 cells without considering the time buffering of syngas storage. As already discussed for the H_2-based P2G system, also the co-

electrolysis P2G plant modeled is a stationary system working in operating conditions that are independent of the volume of treated flows. Therefore, the efficiency of P2G system is not affected by the size of plant.

The global efficiency of the plant is 65.5% without considering thermal integration or cogeneration. When the produced heat is used for thermal integration, the P2G efficiency can reach up to 74.8% if all the heat produced in the methanation is recovered. An efficiency of 77.9 % is reached when the heat produced is used for cogeneration. The efficiency values are very close to that of the H_2-based P2G system.

Table 6.3 – Plant Efficiency of co-electrolysis based P2G system*

Component		**Energy flow (kW)**
W_{SOEC}		123
$\phi_{ext,SOEC}$		21.7
$W_{compr,SYNGAS}$		2.17
$W_{pump,H2O}$		0.01
$W_{compr,CO2}$		1.18
$\phi_{ext,METHANATION}$		-18.4
$W_{compr,SNG}$		0.33
$W_{compr,N2}$		0.24
Plant Streams		**Molar flows (kg/h)**
$H_2O_{(SOEC\ inlet)}$		24.7
$CO_{2(SOEC\ inlet)}$		19.1
SYNGAS (dry)		16.2
N_2		1.12
O_2		27.6
SNG		8.06
Plant Efficiency	η_{P2G}	**65.5 %**
Plant Efficiency (TI)	$\eta_{P2G,TI}$	**74.8 %**
Plant Efficiency (CHP)	$\eta_{P2G,CHP}$	**77.9 %**

*values calculated for a 1000 cells SOEC stack

As *Table 6.3* shows, also in the co-electrolysis based P2G, more than 80% of the energy consumption of the P2G plant is related to the electricity consumed by the SOEC. The remaining part is almost entirely consumed by the reactants preheating of the SOEC section (i.e., mostly for water vaporization). In comparison with the H_2-based P2G system, the co-electrolysis operation presents a lower contribution of the reactant preheating on the total energy consumed by the SOEC section (15.3% for H_2-based P2G and 14.6% for the co-electrolysis P2G). The lower heat demand of the heat recovery section is mainly related to the higher outlet temperature of the SOEC due to the internal methanation. It is expected that a higher operating pressure and a lower inlet temperature of the SOEC could further enhance the internal methanation, leading to higher system efficiency. Moreover, a higher internal methanation would also reduce the CO content of the syngas mixture, thus enabling a higher methane content of the produced SNG.

Another interesting point is the productivity of the plant with a fixed stack size. The H_2-based P2G plant is able to work at higher current levels thanks to the higher reactant content in the fuel mixture entering the SRU cathode, while the co-electrolysis operation is limited at lower current levels due to fuel dilution and temperature limits related to internal methanation. In the operation at higher pressure it is expected that the thermal issue would be even more severe due to higher methane generation. Globally, a hydrogen-based P2G plant with a 1000 cells SOEC stack can produce up to 10 kg/h of SNG, that corresponds to 135 kW injected in the NG grid, while the co-electrolysis operation limits the productivity to 8 kg/h of SNG, corresponding to 97 kW injected in the NG grid. The results suggest that even if the co-electrolysis P2G system presents a higher efficiency, the optimization of cell operating conditions is needed to allow a better exploitation of the installed capacity.

Table 6.4 – Gas composition (molar fractions) in the co-electrolysis based P2G plant

Component	SOEC stack inlet (cathode)	SOEC stack outlet (cathode)	Storage (dry syngas)	Inlet Met. #1	Outlet Met. #1	Outlet Met. #2	Outlet Met. #3	Outlet Met. #4	Syngas to N_2 conditioning	SNG to grid
H_2O	72.0%	25.9%	0.00%	15.0%	30.0%	44.0%	51.5%	51.8%	0.0%	0.0%
H_2	9.93%	54.5%	74.7%	53.9%	32.7%	13.7%	3.91%	3.57%	7.41%	6.82%
CO_2	15.6%	5.78%	7.20%	5.96%	4.92%	2.46%	0.09%	0.0%	0.0%	0.0%
CO	2.06%	11.7%	15.5%	9.18%	3.35%	0.18%	0.0%	0.0%	0.0%	0.0%
CH_4	0.34%	2.09%	2.59%	16.0%	29.0%	39.6%	44.5%	44.6%	92.6%	85.2%
N_2	0.00%	0.00%	0.00%	0.00%	0.00%	0.00%	0.00%	0.00%	0.0%	7.96%
Temperature (°C)	850	830	25	220	700	522	332	223	25	25

6.3 Conclusions

In this Chapter, the investigation of SOEC-based P2G solutions was performed. Two different configurations were analyzed and simulated: SOEC-based electricity storage into hydrogen with subsequent SNG production, and electricity storage by co-electrolysis of water and carbon dioxide with SOEC for syngas production and subsequent upgrading to SNG. In both configurations the P2G system is composed by three sections: a hydrogen/syngas production and storage section based on an SOEC stack; a methanation section based on chemical reactors; and an SNG conditioning section for the upgrading of the produced SNG to grid-injection quality.

The design and operating conditions of the SOEC section were selected following the results of the analysis performed on the rSOC system presented in *Chapter 5*. Pressurized operation (10 bar) with pure oxygen as sweep gas (fully recirculated) were the conditions that ensured the highest SOEC efficiency. The methanation section was designed on the basis of the state-of-the art technology of the TREMP^{TM} process, in which methanation is performed in a cascade of catalytic adiabatic reactors, as described in *Chapter 2*.

The simulations indicated a plant efficiency of 65.4% for the H_2-based P2G and 65.5% for the co-electrolysis based P2G. When considering the thermal integration between SOEC section and methanation, the efficiency rises to 73.9% (H_2-based) and 74.8% (co-electrolysis based). Efficiencies of 77.7 % (H_2-based) and 77.9% (co-electrolysis based) are reached when the heat produced by the methanation is used for cogeneration. Even if the efficiencies are similar for the two P2G configurations, the storage capacity of the H_2-based P2G plant is higher, because the SOEC is able to operate at higher current levels thanks to the higher reactant content in the fuel mixture entering the SRU cathode, while the co-electrolysis operation is limited at lower current levels due to fuel dilution and temperature limits related to internal methanation.

Simulations showed that a H_2-based P2G plant based on a 1000 cells (100 cm^2 each) SOEC stack can produce up to 10 kg/h of SNG, that corresponds to 135 kW injected in the NG grid, while the co-electrolysis operation limits the productivity to 8 kg/h of SNG, corresponding to 97 kW injected in the NG grid. The results suggest that even if the co-electrolysis based P2G system presents a higher efficiency, the choice of a H_2-based P2G option can ensure a better exploitation of the installed capacity (thus reducing the storage costs), and also eliminates the risks connected to carbon-deposition in the stack related to the use of carbon containing mixtures and of stack

poisoning related to contaminants potentially present in CO_2 streams (e.g., hydrogen sulphide). A case study assessing the effect of H_2S poisoning of the SOEC stack on the P2G system performance was also presented in *Appendix B*.

In order to compare P2G and P2P electricity storage options, it is necessary to take into account that the P2G/P2P efficiencies calculated in *Chapter 5* and *6* refers to different forms of energy. In fact, the electricity storage efficiency calculated for the P2G solutions refers to a final product in the form of SNG injected in the gas grid, while the P2P roundtrip efficiency refers to the electricity produced from the stored hydrogen. Therefore, if we want to compare the solutions in terms of electricity obtained from the unit of electricity stored, it is necessary to take into account also the efficiency of SNG reconversion to electricity. If an efficiency of 60% is considered for the electricity production from SNG, and the electricity is assumed to be the only useful product of P2G solutions (i.e., cogeneration is not considered), the roundtrip efficiency achieved by the investigated P2G options is around 45 %. It is worth noting that this value of roundtrip efficiency is estimated assuming the P2G systems working constantly in the operating conditions that ensure the highest SOEC efficiency. If the SOEC stack is forced to work in unsteady conditions by a fluctuating RES load, the roundtrip efficiency will be inevitably lower.

The roundtrip efficiency of the P2P solution presented in the previous Chapter is 72 % with the system operating in the maximum efficiency conditions, and 54 % in a realistic P2P application for RES electricity storage. Therefore, the roundtrip efficiency of the P2P solution is sensibly higher with respect to electricity storage using P2G options. However, the electricity-to-SNG conversion by P2G can be advantageous for the spatial decoupling of electricity production and demand, by offering the possibility of transferring the stored electricity in SNG form through the existing natural gas infrastructure without congesting the electrical network, while the P2P is based on hydrogen and thus it is actually constrained to on-site applications because of the absence of an H_2 infrastructure that allows to move the stored electricity. Moreover, SNG is a multi-purpose energy carrier suitable for many applications with already existing technologies (i.e., mobility, heating, etc.), and P2G solutions could represent the technological bridge for transferring RES power to other markets different from the electrical one.

Appendices

Appendix A

Two-dimensional SRU model: mesh refinement study

A computational domain constituted by rectangular elements has been selected for the 2D model. The optimal number of elements has been chosen through a mesh refinement study, in which the spacing of the elements along the edges has been imposed as function of a mesh parameter *N*, which was varied parametrically. In particular, the cell length is divided in 200/*N* evenly spaced elements along the *x* coordinate. Domains' edges along *y* were divided in 5 evenly spaced elements on interconnects and electrolyte, 20/*N* evenly spaced elements on fuel channel, 25/*N* elements on the fuel electrode and 25/*N* elements on the oxygen channel. It is straightforward that the lower is the *N*, the finer is the mesh and that more accurate results are expected. However, a finer mesh implies a higher number of nodes on which the problem is solved. The product of number of nodes and number of dependent variables solved per node gives the total number of degrees of freedom in the model, which provides a direct measure of the computational cost of the numerical problem. More information on the relation between mesh size and degrees of freedom can be found in the software manual (COMSOL multiphysics user guide, 2015).

In order to verify the reliability of the numerical solution with the variable meshing, it is necessary to select a tracking parameter that assume a known value in the conditions simulated by the model and compare its theoretical value with the one evaluated by the numerical model. The total outlet mass flow of gases exiting the SOC operating either with H_2/H_2O or CO/CO_2 mixtures has been selected as the tracking parameter, as its value can be easily predicted from Faraday's law, as the inlet mass flows and total cell current are imposed in the model. The mass flow is a significant check parameter, since it includes information both about gas density, which is determined by temperature and fluid composition that are in turn affected by electrochemical and chemical reactions, and fluid velocity, which is determined by the solution of momentum and continuity equations. Therefore, if significant numerical errors due to meshing arise in the solution of fluidic, chemical and electrochemical equations, the total mass flow would be

affected, and thus the check of this value can give a global measure of the validity of the numerical solution.

Another possible check taken into account consists in the verification of the total energy conservation; however it resulted not as significant as the mass conservation check, since it was fairly affected by the meshing. Thus, only total mass conservation was selected. The difference between the theoretical value of the total outlet mass flow and that calculated with the model can be divided by the imposed total inlet mass flow to obtain the estimation of the relative error with respect to imposed conditions. *Figure A.1* shows the results of the mesh convergence test for a simulation performed in SOEC conditions with inlet anode gas 90% H_2O - 10% H_2 at 800 °C and inlet cathode flow consisting of air at 800 °C (air imposed with a molar ratio of 3 with respect to fuel), for a cell current density of 1 A/cm^2 and 70% of reactant utilization. The Figure reports the relative error calculated on the mass and the number of degrees of freedom of the numerical problem. The relative mass error decreases from 4.5% to almost 0% for *N* varying from 5 to 0.5. A mesh number of 1 has been selected, as it ensures a good compromise between accuracy and computational cost.

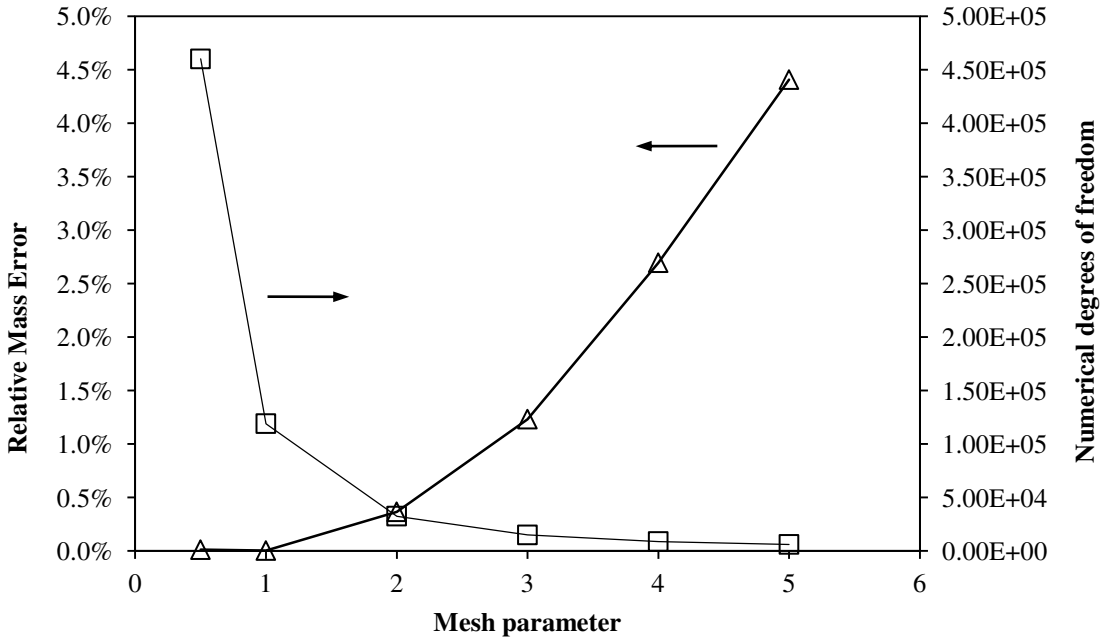

Figure A.1 – Mesh refinement study

Appendix B

Co-electrolysis based P2G systems: effect of contaminants

The effect of contaminants on the performance of SOFCs has been widely studied in the literature. Most of the studies investigate the effect of coal or biogas contaminants (i.e., sulfurous, siloxanes, halogenated and hydrocarbons) on the cell, as the use of syngas or biogas in the SOFC (direct use or reformate) is a promising application for an efficient valorization of gaseous fuels obtained from various substrates. Experimental investigations are the most used tool for the analysis of contaminants effects and very few works include modeling efforts for the simulation of contaminants effects.

When studies address SOEC applications, the interest toward contaminants is less evident, due to the fact that the majority of electrolysis systems operate with H_2/H_2O mixtures which are not recycled from processes that involve the presence of contaminants. Most of the contamination studies in SOEC are instead devoted to the effects of trace contaminants that can originate from stack components, for example from sealing or interconnects. However, when the SOEC operates in co-electrolysis mode, the CO_2 that is feed to the cell can be the carrier of several contaminants depending on the CO_2 source.

One interesting carbon dioxide source for P2G applications based on co-electrolysis is the biogas, which has a high CO_2 content (40%) that must be removed from to biogas during its upgrading to biomethane for grid injection. H_2S is one of the most abundant contaminants in the biogas, and its concentration depends on the substrate from which the biogas produced. In the case of biogas from municipal solid wastes, sulfur compounds are present in the range from tens to thousands of ppm(v) (Papurello et al. 2014). As explained in *Chapter 2*, H_2S is a well-known poison for nickel-based catalysts, because sulfur is adsorbed on the Ni surface and blocks the active sites; thus, the H_2S removal is a mandatory step for ensuring the safe operation of the SOEC. However, sulfur traces can reach the SOEC in case of malfunctioning or saturation of the cleaning system, and the investigation of the effect of sulfur breakthrough can provide useful information on the cost of the event in terms of energetic losses, and consequently also on the economic losses if monetary values are associated to energy.

For this reason, the analysis of the effect on the SOEC stack of different H_2S concentrations in the CO_2 stream feeding the co-electrolysis based P2G system presented in *Section 5.5* has been performed. The SOEC is feed with the mixture indicated in *Table 5.11*, but only a fraction of the CO_2 is coming directly from biogas separation, as around 20% of the cathodic stream is

recirculated (see *Section 5.5.1*). The SOEC model was run for three levels of H_2S concentration in the CO2 coming from biogas separation: 0.1, 1 and 10 ppm(v). The operating conditions of the SOEC were those of the P2G applications investigated in *Section 5.4* and *5.5* (gas inlet temperature 850 °C, λ = 2.15, pure oxygen at the anode). Both the operation at 1 bar and 10 bar was investigated.

The sulfur coverage calculated by the model (see *Chapter 2* for the explanation of the modeling approach followed) within the SOEC cathode for the different H_2S concentrations is depicted in *Figure 5.72*. The coverage increases with the sulfur concentration, and higher θ_s levels are reached at the inlet of the fuel electrode, where the hydrogen concentration is lower. The sulfur coverage progressively decreases in the cell with the increase of H_2 partial pressure due to H_2 production by electrolysis.

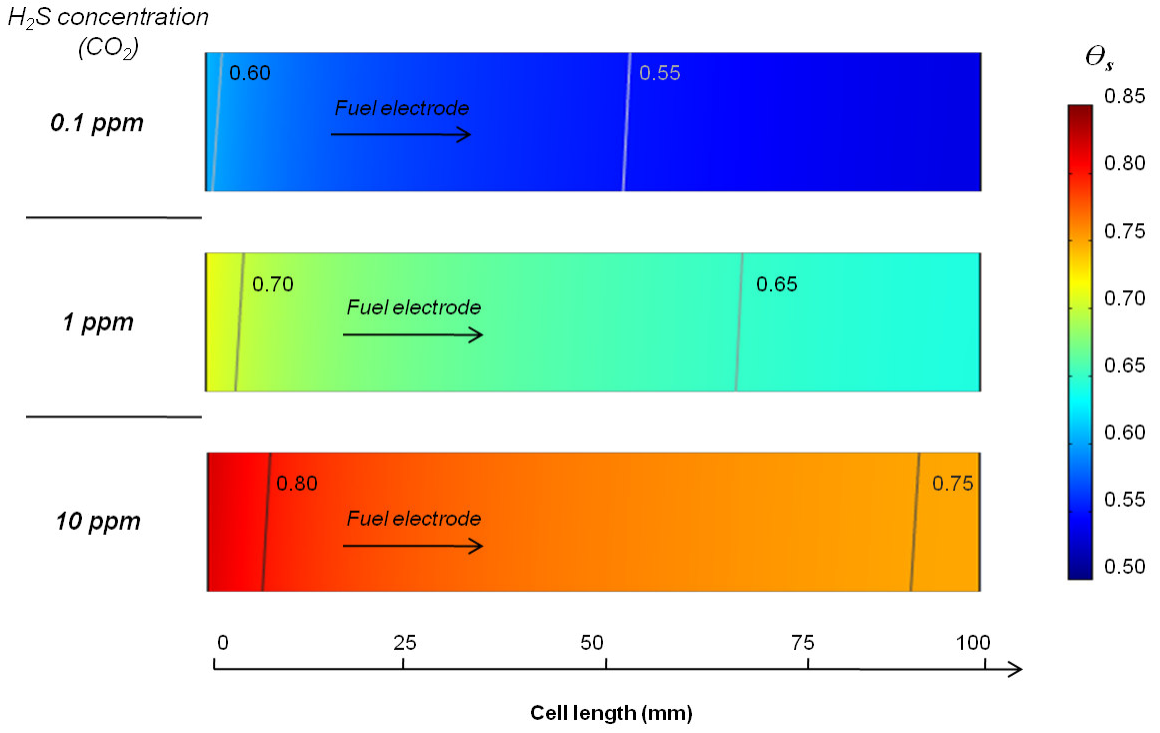

Figure B.1 – Sulfur coverage within SOEC cathode for different H_2S concentrations in the CO_2, 10 bar operation at -1 A/cm^2.

The effect on cell polarization is shown in *Figure 5.73*. The sulfur poisoning strongly affects the cell voltage in the operation at atmospheric pressure, reaching up to 12% of voltage increase for 10 ppm of H_2S at low current, as show in *Figure 5.74*. The voltage increase is higher at low

currents due to lower temperature of the cell; in fact, sulfur coverage reaches higher levels at lower temperatures. In the pressurized operation the sulfur poisoning slightly affects the SRU performance, with an increase of cell voltage limited to less than 1%. This happens mainly because the activation overvoltage is strongly reduced when the SOEC is operating under pressure and most of the losses are due to ohmic contributions; thus, a reduction of the active area due to sulfur coverage affects significantly only a minor source of voltage losses. It is worth noting that sulfur coverage expression used in the model (see equation (2.167), *Chapter 2*) has been obtained from the fitting of data obtained at atmospheric operation, and thus its application to the pressurized operation is not supported by experimental validation.

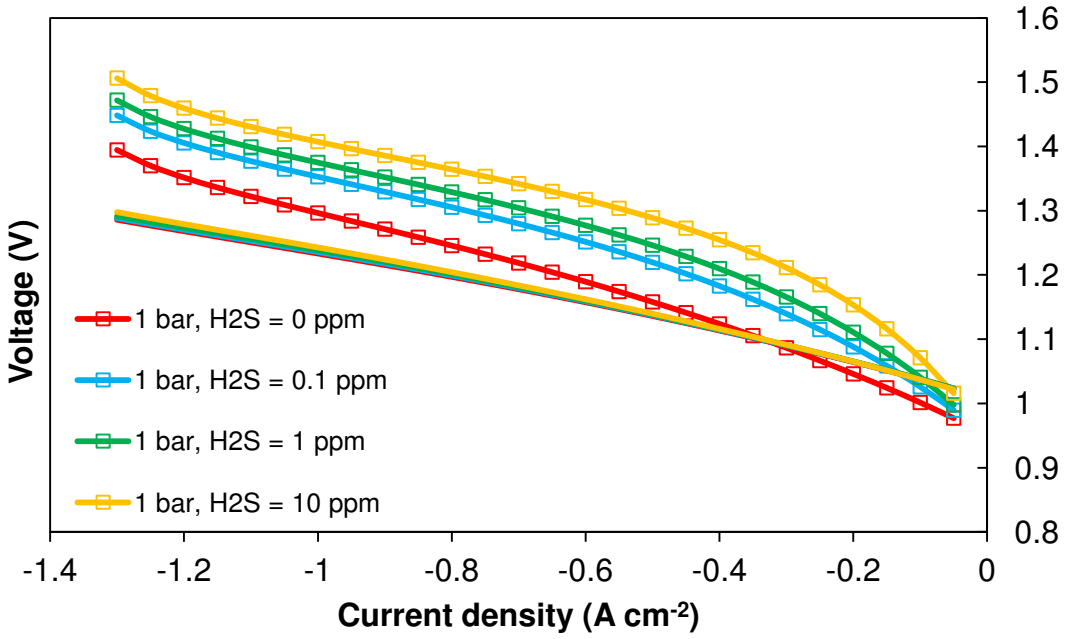

Figure B.2 – Effect of different levels of sulfur contamination on the SOEC performance at 1 and 10 bar.

The effect of sulfur contamination on the P2G plant efficiency has been estimated for both pressurized and ambient pressure co-electrolysis, and the results are shown in *Figure 5.75*. The P2G system has been simulated as described in *Section 5.5* in both cases; the main difference is the higher electricity consumption of the SOEC at ambient pressure, which reduces the efficiency of several points. It is possible to see from the Figure that the presence of H_2S is deleterious for P2G efficiency when the SOEC is operating at ambient pressure due to the strong increase of activation losses caused by sulfur poisoning, which severely affects the plant performance. For example, a P2G plant which is producing 100 kW of SNG suffers an increase of the energy demand of around 11 kW if a CO_2 contamination of 10 ppm(v) of H_2S occurs,

which corresponds to a loss of more than 10% of the energetic value of the product. A pressurized P2G plant suffers much lower losses, corresponding to 1% of the energetic value of the produced SNG.

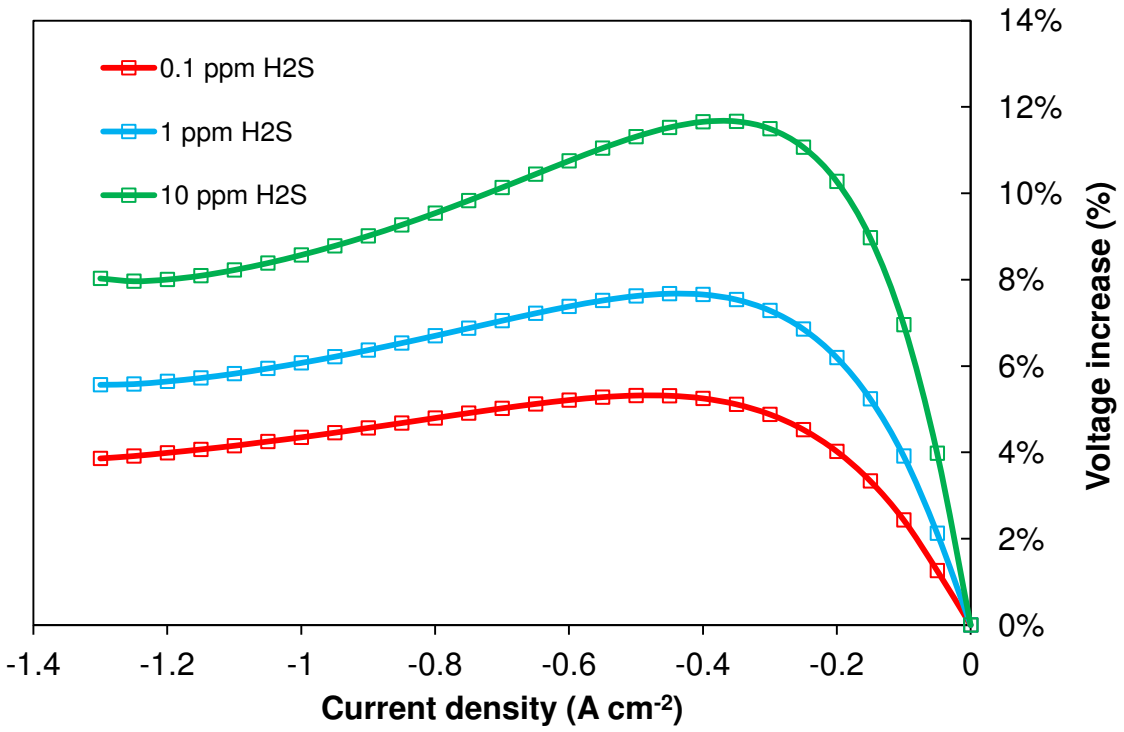

Figure B.3 – Voltage increase due to sulfur contamination at 1 bar.

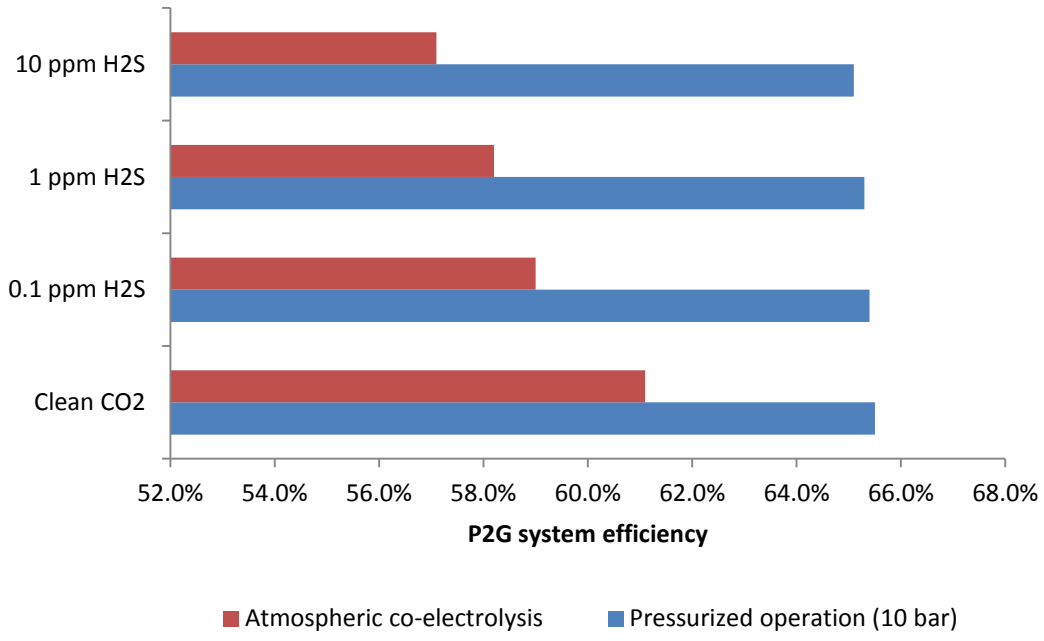

Figure B.4 – Effect on sulfur contamination on P2G system efficiency.

References

Achenbach, E., and Riensche, E. (1994). Methane/steam reforming kinetics for solid oxide fuel cells. *Journal of Power Sources*, 52(2), 283-288.

Ahmed, K., and Foger, K. (2000). Kinetics of internal steam reforming of methane on Ni/YSZ-based anodes for solid oxide fuel cells. *Catalysis Today*, 63(2), 479-487.

Ajitdoss, L. C., Smeacetto, F., Bindi, M., Beretta, D., Salvo, M., and Ferraris, M. (2013). Mn 1.5 Co 1.5 O 4 protective coating on Crofer22APU produced by thermal co-evaporation for SOFCs. *Materials Letters*, 95, 82-85.

Alstrup, I. (1988). A new model explaining carbon filament growth on nickel, iron, and Ni+Cu alloy catalysts. *Journal of Catalysis*, 109(2), 241-251.

Alstrup, I. B., Rostrup-Nielsen, J. R., and Røen, S. (1981). High temperature hydrogen sulfide chemisorption on nickel catalysts. *Applied Catalysis*, 1(5), 303-314.

Amhalhel, G., and Furmański, P. (1997). Problems of modeling flow and heat transfer in porous media. *Journal of Power Technologies*, 85, 55-88.

Andersson, M., Yuan, J., and Sundén, B. (2010). Review on modeling development for multiscale chemical reactions coupled transport phenomena in solid oxide fuel cells. *Applied Energy*, 87(5), 1461-1476.

Andersson, M., Yuan, J., and Sundén, B. (2012). SOFC modeling considering electrochemical reactions at the active three phase boundaries. *International Journal of Heat and Mass Yransfer*, 55(4), 773-788.

Andersson, M., Yuan, J., and Sundén, B. (2013). SOFC modeling considering hydrogen and carbon monoxide as electrochemical reactants. *Journal of Power Sources*, 232, 42-54.

Appari, S., Janardhanan, V. M., Bauri, R., Jayanti, S., and Deutschmann, O. (2014). A detailed kinetic model for biogas steam reforming on Ni and catalyst deactivation due to sulfur poisoning. *Applied Catalysis A: General*, 471, 118-125.

Armor, J. N. (1999). The multiple roles for catalysis in the production of H_2. *Applied Catalysis A: General*, 176(2), 159-176.

Bagotsky, V. S. (Ed.). (2005). *Fundamentals of electrochemistry* (Vol. 44). New York: John Wiley & Sons, 2nd edition.

Baker, R. T. K., Barber, M. A., Harris, P. S., Feates, F. S., and Waite, R. J. (1972). Nucleation and growth of carbon deposits from the nickel catalyzed decomposition of acetylene. *Journal of Catalysis*, 26(1), 51-62.

Barzi, Y. M., Raoufi, A., Rasi, N. M., Davari, S. (2011). Three Dimensional Simulation of a Counter-Flow Planar Solid Oxide Fuel Cell, *ECS Trans*. 35, 1021–1033.

BDEW (Bundesverband der Energie- und Wasserwirtschaf) 2014. Presseinformation. https://bdew.de/internet.nsf/id/96C1C1AF87BC5338C1257DBD00309E50/$file/141229_BDEW_veroeffentlicht_Erzeugungsmix_Anlagen_zur_PI.pdf (last visited 27/04/16).

Bear, J. (1972) *Dynamics of Fluids in Porous Media*. New York: American Elsevier.

Belyaev, V. D., Politova, T. I., Mar'ina, O. A., and Sobyanin, V. A. (1995). Internal steam reforming of methane over Ni-based electrode in solid oxide fuel cells. *Applied Catalysis A: General*, 133(1), 47-57.

Bertei, A., and Nicolella, C. (2015). Common inconsistencies in modeling gas transport in porous electrodes: The dusty-gas model and the Fick law. *Journal of Power Sources*, 279, 133-137.

Bi, L., Boulfrad, S., and Traversa, E. (2014). Steam electrolysis by solid oxide electrolysis cells (SOECs) with proton-conducting oxides. *Chemical Society Reviews*, 43(24), 8255-8270.

Bird, R., Steward, W., Lightfoot, E. (2006). *Transport Phenomena*. Amsterdam: John Wiley & Sons, revised 2nd Edition.

Braun, R. J., Vincent, T. L., Zhu, H., and Kee, R. J. (2012). Analysis, Optimization, and Control of Solid-Oxide Fuel Cell Systems. *Advances in Chemical Engineering*, 41, 383.

Brett, D. J., Atkinson, A., Brandon, N. P., and Skinner, S. J. (2008). Intermediate temperature solid oxide fuel cells. *Chemical Society Reviews*, 37(8), 1568-1578.

Brinkman, H. C. (1949a). A calculation of the viscous force exerted by a flowing fluid on a dense swarm of particles. *Applied Scientific Research,* 1(1), 27-34.

Brinkman, H. C. (1949b). On the permeability of media consisting of closely packed porous particles. *Applied Scientific Research*, 1(1), 81-86.

Bruggeman, D. A. G. (1935) Calculation of the various physical constants of heterogeneous substances. dielectric constants and conductivities of mixtures of isotropic substances. *Annual Physik*, (24), 636–664.

Brus, G., Miyawaki, K., Iwai, H., Saito, M., and Yoshida, H. (2014). Tortuosity of an SOFC anode estimated from saturation currents and a mass transport model in comparison with a real micro-structure. *Solid State Ionics*, 265, 13-21.

Budzianowski, W. M. (2012). Negative carbon intensity of renewable energy technologies involving biomass or carbon dioxide as inputs. *Renewable and Sustainable Energy Reviews*, 16(9), 6507-6521.

Bundesnetzagentur Monitorinbericht (2014). Monitoring report 2014. German Federal Network Agency.

Bünger, U., Michalski, J., Crotogino, F., Kruck, O. (2016). Large-scale underground storage of hydrogen for the grid integration of renewable energy and other applications. *Compendium of Hydrogen Energy: Hydrogen Use, Safety and the Hydrogen Economy*, Elsevier, pp. 133-16.

Cable, T. L., Setlock, J. A., Farmer, S. C., and Eckel, A. J. (2011). Regenerative performance of the NASA symmetrical solid oxide fuel cell design. *International Journal of Applied Ceramic Technology*, 8(1), 1-12.

Cai, Q., Adjiman, C. S., and Brandon, N. P. (2011). Investigation of the active thickness of solid oxide fuel cell electrodes using a 3D microstructure model. *Electrochimica Acta*, 56(28), 10809-10819.

Campanari, S., Iora, P. (2004). Definition and sensitivity analysis of a finite volume SOFC model for a tubular cell geometry. *J. Power Sources*, 132, 113–126.

Camprubì, M.G. (2011). *Multiphysics Models for the Simulation of Solid Oxide Fuel Cells* (Ph.D dissertation), University of Zaragoza.

Carman, P.C. (1956) *Flow of Gases Through Porous media*. Waltham: Academic Press.

Cayan, F. N., Pakalapati, S. R., Elizalde-Blancas, F., and Celik, I. (2009). On modeling multi-component diffusion inside the porous anode of solid oxide fuel cells using Fick's model. *Journal of Power Sources*, 192(2), 467-474.

Centi, G., and Perathoner, S. (2014). Perspectives and state of the art in producing solar fuels and chemicals from CO2. *Green Carbon Dioxide: Advances in CO2 Utilization*, 1-24. John Wiley & Sons.

Chan, S. H., Khor, K. A., and Xia, Z. T. (2001). A complete polarization model of a solid oxide fuel cell and its sensitivity to the change of cell component thickness. *Journal of Power Sources*, 93(1), 130-140.

Chase M.W. et al. (1998), NIST-JANAF Thermochemical Tables, 4th ed., American Chemical Society, American Institute of Physics for the National Institute of Standards and Technology.

Chen, T., Wang, W. G., Miao, H., Li, T., and Xu, C. (2011). Evaluation of carbon deposition behavior on the nickel/yttrium-stabilized zirconia anode-supported fuel cell fueled with simulated syngas. *Journal of Power Sources*, 196(5), 2461-2468.

Chiang, L. K., Liu, H. C., Shiu, Y. H., Lee, C. H., and Lee, R. Y. (2010). Thermal stress and thermo-electrochemical analysis of a planar anode-supported solid oxide fuel cell: Effects of anode porosity. *Journal of Power Sources*, 195(7), 1895-1904.

Choi, M. B., Singh, B., Wachsman, E. D., and Song, S. J. (2013). Performance of La 0.1 Sr 0.9 Co 0.8 Fe 0.2 O 3− δ and La 0.1 Sr 0.9 Co 0.8 Fe 0.2 O 3− δ–Ce 0.9 Gd 0.1 O 2 oxygen electrodes with Ce 0.9 Gd 0.1 O 2 barrier layer in reversible solid oxide fuel cells. *Journal of Power Sources*, 239, 361-373.

Cimenti, M., and Hill, J. M. (2009). Thermodynamic analysis of solid oxide fuel cells operated with methanol and ethanol under direct utilization, steam reforming, dry reforming or partial oxidation conditions. *Journal of Power Sources*, 186(2), 377-384.

COMSOL multiphysics user guide (Version 5.2). COMSOL, AB, 2015.

Cornetti, G., and Millo, F. (2015). *Macchine idrauliche*. Il capitello.

Costamagna, P., and Honegger, K. (1998). Modeling of solid oxide heat exchanger integrated stacks and simulation at high fuel utilization. *Journal of the Electrochemical Society*, 145(11), 3995-4007.

Costamagna, P., Costa, P., and Antonucci, V. (1998). Micro-modelling of solid oxide fuel cell electrodes. *Electrochimica Acta*, 43(3), 375-394.

Costamagna, P., Selimovic, A., Del Borghi, M., and Agnew, G. (2004). Electrochemical model of the integrated planar solid oxide fuel cell (IP-SOFC). *Chemical Engineering Journal*, 102(1), 61-69.

Crofer®22H Material Data Sheet No. 4050, June 2010 Edition, VDM Metals GmbH, http://www.vdm-metals.com/fileadmin/user_upload/Downloads/Data_Sheets/Data_Sheet_VDM_Crofer_22_H.pdf

Curtiss, C. F., and Bird, R. B. (1999). Multicomponent diffusion. *Industrial & Engineering Chemistry Research*, 38(7), 2515-2522.

Damm, D.L., and Fedorov, A.G. (2004). *Spectral Radiative Heat Transfer Analysis of the Planar SOFC*. In Proceedings of the ASME IMECE, Anaheim, CA, November 13-19, 2004. Paper No. IMECE2004-60142.

Damm, D. L., and Fedorov, A. G. (2005). Radiation heat transfer in SOFC materials and components. *Journal of Power Sources*, 143(1), 158-165.

Damm, D. L., and Fedorov, A. G. (2006). Local thermal non-equilibrium effects in porous electrodes of the hydrogen-fueled SOFC. *Journal of Power Sources*, 159(2), 1153-1157.

de Joode, J., Daniëls, B., Smekens, K., van Stralen, J., Dalla Longa, F., Schoots, K., and Holstein, J. (2014). *Exploring the role for power-to-gas in the future Dutch energy system*. ECN and DNV GL, Petten, The Netherlands.

de Vries, C., Claeys, M., and Schaub, G. (2015). Chemical energy storage in gaseous hydrocarbons via iron Fischer–Tropsch synthesis from H2/CO2—Kinetics, selectivity and process considerations. *Catalysis Today*, 242, 184-192.

Désilets, M., Proulx, P., and Soucy, G. (1997). Modeling of multicomponent diffusion in high temperature flows. *International Journal of Heat and Mass Transfer*, 40(18), 4273-4278.

Dicks, A. L., Pointon, K. D., and Siddle, A. (2000). Intrinsic reaction kinetics of methane steam reforming on a nickel/zirconia anode. *Journal of Power Sources*, 86(1), 523-530.

DOE/NETL (2001), *Cost and Performance Baseline for Fossil Energy Plants* Volume 2: Coal to Synthetic Natural Gas and Ammonia.

Dönitz, W. (1975). *Wasserstofferzeugung mittels Hochtemperatur-Dampfphase-Elektrolyse*, Patent DE 25 49 471.

Donitz, W. and Streicher, R. (1980) Hochtemperatur-Elektrolyse von Wasserdampf – Entwicklungsstand einer neuen Technologie zur Wasserstoff-Erzeugung. *Chem. Ing. Tech*., 52 (5), 436–438.

Dönitz, W., and Erdle, E. (1985). High-temperature electrolysis of water vapor—status of development and perspectives for application. *International Journal of Hydrogen Energy*, 10(5), 291-295.

Dönitz, W., Dietrich, G., Erdle, E., and Streicher, R. (1988). Electrochemical high temperature technology for hydrogen production or direct electricity generation. *International journal of hydrogen energy*, 13(5), 283-287.

Drescher, I., Lehnert, W., and Meusinger, J. (1998). Structural properties of SOFC anodes and reactivity. *Electrochimica Acta*, 43(19), 3059-3068.

Ebbesen, S. D., Graves, C., and Mogensen, M. (2009). Production of synthetic fuels by co-electrolysis of steam and carbon dioxide. *International Journal of Green Energy*, 6(6), 646-660.

Ebbesen, S. D., Graves, C., Hauch, A., Jensen, S. H. and Mogensen, M. (2010). Poisoning of solid oxide electrolysis cells by impurities. *J. Electrochem. Soc*. 157, B1419-B1429.

Ebbesen, S. D., Knibbe, R., and Mogensen, M. (2012). Co-electrolysis of steam and carbon dioxide in solid oxide cells. *Journal of The Electrochemical Society*, 159(8), F482-F489.

EE consultant, Hepsul and Solagro (2014). *Study on hydrogen and methanation as means to give value to electricity surpluses*. Study sponsors: ADEME, GRT-Gaz and GRdF. http://www.ademe.fr/sites/default/files/assets/documents/summary_study_powertogas_ademe-grdf-grtgaz.pdf (last visited 27/04/16)

Elizalde-Blancas, F., Celik, I. B., Rangel-Hernandez, V., Hernandez-Guerrero, A., and Riesco-Avila, J. M. (2013). Numerical modeling of SOFCs operating on biogas from biodigesters. *International Journal of Hydrogen Energy*, 38(1), 377-384.

Erdle, E., Dönitz, W., Schamm, R., and Koch, A. (1992). Reversibility and polarization behaviour of high temperature solid oxide electrochemical cells. *International journal of hydrogen energy*, 17(10), 817-819.

European Biofuels Technology Platform (EBTP). *Biogas/Biomethane for use as a transport fuel*. URL http://www.biofuelstp.eu/biogas.html#intro (last visited 27/04/16).

European Commission (2010). *Europe 2020: A Strategy for Smart, Sustainable and Inclusive Growth: Communication from the Commission.* Publications Office of the European Union.

Eveloy, V. (2012). Numerical analysis of an internal methane reforming solid oxide fuel cell with fuel recycling. *Applied Energy*, 93, 107-115.

Fan, H., Keane, M., Singh, P., and Han, M. (2014). Electrochemical performance and stability of lanthanum strontium cobalt ferrite oxygen electrode with gadolinia doped ceria barrier layer for reversible solid oxide fuel cell. *Journal of Power Sources*, 268, 634-639.

Ferguson, J. R., Fiard, J. M., and Herbin, R. (1996). Three-dimensional numerical simulation for various geometries of solid oxide fuel cells. *Journal of Power Sources*, 58(2), 109-122

Ferrero, D., Lanzini, A., Santarelli, M., and Leone, P. (2013). A comparative assessment on hydrogen production from low-and high-temperature electrolysis. *International journal of hydrogen energy*, 38(9), 3523-3536.

Ferrero D. et al. *Dynamic reversible SOC applications: Performance and Durability with simulated load/demand profiles*, Proceedings of the 11th European SOFC and SOE Forum 2014, 1-4 July 2014, Lucerne, Switzerland.

Ferrero, D., Lanzini, A., Leone, P., and Santarelli, M. (2015). Reversible operation of solid oxide cells under electrolysis and fuel cell modes: Experimental study and model validation. *Chemical Engineering Journal*, 274, 143-155.

Froment, G. F., Bischoff, K. B., and De Wilde, J. (1990). *Chemical reactor analysis and design* (Vol. 2). New York: Wiley.

Fu, Q., Mabilat, C., Zahid, M., Brisse, A., and Gautier, L. (2010). Syngas production via high-temperature steam/CO2 co-electrolysis: an economic assessment. *Energy & Environmental Science*, 3(10), 1382-1397.

Fu, Q., Schefold, J., Brisse, A., and Nielsen, J. U. (2014). Durability Testing of a High-Temperature Steam Electrolyzer Stack at 700 °C. *Fuel Cells*, 14(3).

Fuller, E. N., Schettler, P. D., and Giddings, J. C. (1966). New method for prediction of binary gas-phase diffusion coefficients. *Industrial & Engineering Chemistry*, 58(5), 18-27.

Funahashi, Y., Shimamori, T., Suzuki, T., Fujishiro, Y., and Awano, M. (2007). Fabrication and characterization of components for cube shaped micro tubular SOFC bundle. *Journal of Power Sources*, 163(2), 731-736.

Gahleitner, G. (2013). Hydrogen from renewable electricity: An international review of power-to-gas pilot plants for stationary applications. *International Journal of Hydrogen Energy*, 38(5), 2039-2061.

Gao, Z., Raza, R., Zhu, B., and Mao, Z. (2011). Development of methanol-fueled low-temperature solid oxide fuel cells. International *Journal of Energy Research*, 35(8), 690-696.

García-Camprubí, M. (2011). *Multiphysics Models for the Simulation of Solid Oxide Fuel Cells*. Ph.D. Dissertation, University of Zaragoza.

García-Camprubí, M., Sánchez-Insa, A., and Fueyo, N. (2010). Multimodal mass transfer in solid-oxide fuel-cells. *Chemical Engineering Science*, 65(5), 1668-1677.

Geisler, H., Kromp, A., Weber, A., and Ivers-Tiffée, E. (2014). Stationary FEM Model for Performance Evaluation of Planar Solid Oxide Fuel Cells Connected by Metal Interconnectors I. Model Framework and Validation. *Journal of The Electrochemical Society*, 161(6), F778-F788.

Giglio, E., Lanzini, A., Santarelli, M., and Leone, P. (2015a). Synthetic natural gas via integrated high-temperature electrolysis and methanation: Part I—Energy performance. *Journal of Energy Storage*, 1, 22-37.

Giglio, E., Lanzini, A., Santarelli, M., and Leone, P. (2015b). Synthetic natural gas via integrated high-temperature electrolysis and methanation: Part II—Economic analysis. *Journal of Energy Storage*, 2, 64-79.

Godula-Jopek A., *Hydrogen Production: by Electrolysis*, first ed., Wiley-VCH Verlag GmbH, Weinheim, 2015.

Goldin, G. M., Zhu, H., Kee, R. J., Bierschenk, D., and Barnett, S. A. (2009). Multidimensional flow, thermal, and chemical behavior in solid-oxide fuel cell button cells. *Journal of Power Sources*, 187(1), 123-135.

Goodwin, D. G., Zhu, H., Colclasure, A. M., and Kee, R. J. (2009). Modeling electrochemical oxidation of hydrogen on Ni–YSZ pattern anodes. *Journal of The Electrochemical Society*, 156(9), B1004-B1021.

Götz, M., Lefebvre, J., Mörs, F., Koch, A. M., Graf, F., Bajohr, S., Reimert R., and Kolb, T. (2016). Renewable Power-to-Gas: A technological and economic review. *Renewable Energy*, 85, 1371-1390.

Graves, C., Ebbesen, S. D., Mogensen, M., and Lackner, K. S. (2011a). Sustainable hydrocarbon fuels by recycling CO2 and H2O with renewable or nuclear energy. *Renewable and Sustainable Energy Reviews*, 15(1), 1-23.

Graves, C., Ebbesen, S. D. and Mogensen, M. (2011b). Co-electrolysis of CO2 and H2O in solid oxide cells: Performance and durability. *Solid State Ionics192*, 398-403.

Graves, C., Ebbesen, S. D., Jensen, S. H., Simonsen, S. B., and Mogensen, M. B. (2015). Eliminating degradation in solid oxide electrochemical cells by reversible operation. *Nature materials*, 14(2), 239-244.

Greene, E. S., Chiu, W. K., and Medeiros, M. G. (2006). Mass transfer in graded microstructure solid oxide fuel cell electrodes. *Journal of Power Sources*, 161(1), 225-231.

Grew, K. N., and Chiu, W. K. (2012). A review of modeling and simulation techniques across the length scales for the solid oxide fuel cell. *Journal of Power Sources*, 199, 1-13.

Grew, K.N., Joshi, A.S., Peracchio, A.A., Chiu, W.K.S. (2007). *Characterization and Quantification of Charge and Heat Transfer in a Solid Oxide Fuel Cell Anode*, in Proceedings of the ASME-JSME 2007 Thermal Engineering Heat Transfer Summer Conference, Vancouver, Canada, July 2007.

Grond, L., Schulze, P., and Holstein, J. (2013). *Systems Analyses Power to Gas: A Technology Review*. DNV KEMA Energy & Sustainability, Groningen.

Guan, J., Ramamurthi, B., Ruud, J., Hong, J., Riley, P., and Minh, N. (2006). *High performance flexible reversible solid oxide fuel cell*. GE Global Research Center Final Report for DOE Cooperative Agreement DE-FC36-04GO-14351.

Gupta, G. K., Hecht, E. S., Zhu, H., Dean, A. M., and Kee, R. J. (2006). Gas-phase reactions of methane and natural-gas with air and steam in non-catalytic regions of a solid-oxide fuel cell. *Journal of Power Sources*, 156(2), 434-447.

Haberman, B. A., and Young, J. B. (2004). Three-dimensional simulation of chemically reacting gas flows in the porous support structure of an integrated-planar solid oxide fuel cell. *International Journal of Heat and Mass Transfer*, 47(17), 3617-3629.

Hagen, A. (2014). *Overview of SOFC/SOEC development at DTU Energy Conversion*. Proceedings of the European Fuel Cell 2014-11th European Sofc and Soe Forum.

Hajimolana, S. A., Hussain, M. A., Daud, W. A. W., Soroush, M., and Shamiri, A. (2011). Mathematical modeling of solid oxide fuel cells: A review. *Renewable and Sustainable Energy Reviews*, 15(4), 1893.1917.

Haldor-Topsoe. *From solid fuels to substitute natural gas using TREMP*. Technical Report. 2009.

Hanna, J., Lee, W. Y., Shi, Y., and Ghoniem, A. F. (2014). Fundamentals of electro-and thermochemistry in the anode of solid-oxide fuel cells with hydrocarbon and syngas fuels. *Progress in Energy and Combustion Science*, 40, 74-111.

Hao, Y., and Goodwin, D. G. (2008). Numerical study of heterogeneous reactions in an SOFC anode with oxygen addition. *Journal of the Electrochemical Society*, 155(7), B666-B674.

Hauch, A., Jensen, S. H., Ramousse, S. and Mogensen, M. (2006). Performance and durability of solid oxide electrolysis cells. *J. Electrochem. Soc.* 153, A1741-A1747.

Hauch, A., (2007). *Solid Oxide Electrolysis Cells – Performance and Durability* (Ph.D dissertation), Technical University of Denmark.

Hauch, A., Ebbesen, S. D., Jensen, S. H., and Mogensen, M. (2008). Solid oxide electrolysis cells: microstructure and degradation of the Ni/yttria-stabilized zirconia electrode. *Journal of the Electrochemical Society*, 155(11), B1184-B1193.

He, H., and Hill, J. M. (2007). Carbon deposition on Ni/YSZ composites exposed to humidified methane. *Applied Catalysis A: General*, 317(2), 284-292.

He, W., Lu, W., and Dickerson, J. H. (2014a). Chapter 2: Gas Diffusion in Porous Media. *Gas Transport in Solid Oxide Fuel Cells*. New York: Springer, 1st edition.,pp. 9-17.

He, W., Lu, W., and Dickerson, J. H. (2014b). *Gas Transport in Solid Oxide Fuel Cells*. New York: Springer.

Hebling et al. (2016) *Perspectives on Power-to-Liquids & Power-to-Chemicals*, Workshop, Freiburg, 17-18 February 2016.

Hecht, E. S., Gupta, G. K., Zhu, H., Dean, A. M., Kee, R. J., Maier, L., and Deutschmann, O. (2005). Methane reforming kinetics within a Ni–YSZ SOFC anode support. *Applied Catalysis A: General*, 295(1), 40-51.

Heinisch, V. (2015, June). Effects of power-to-gas on power systems: A case study of Denmark. In *PowerTech*, 2015 IEEE Eindhoven (pp. 1-6). IEEE.

Hernández-Pacheco, E., Singh, D., Hutton, P. N., Patel, N., and Mann, M. D. (2004). A macro-level model for determining the performance characteristics of solid oxide fuel cells. *Journal of Power Sources*, 138(1), 174-186.

Hirschfelder, J. O., Curtiss, C. F., Bird, R. B., and Mayer, M. G. (1954). *Molecular theory of gases and liquids* (Vol. 26). New York: Wiley.

Ho, T. X., Kosinski, P., Hoffmann, A. C., and Vik, A. (2008). Numerical modeling of solid oxide fuel cells. *Chemical Engineering Science*, 63(21), 5356-5365.

Ho, T. X., Kosinski, P., Hoffmann, A. C., and Vik, A. (2009). Modeling of transport, chemical and electrochemical phenomena in a cathode-supported SOFC. *Chemical Engineering Science*, 64(12), 3000-3009.

Hofmann, P., Panopoulos, K. D., Fryda, L. E., and Kakaras, E. (2009). Comparison between two methane reforming models applied to a quasi-two-dimensional planar solid oxide fuel cell model. *Energy*, 34(12), 2151-2157.

Holgrem, M., (2007). X-Steam. Available at: http://www.mathworks.com/matlabcentral/fileexchange/9817-x-steam--thermodynamic-properties-of-water-and-steam.

Holtappels P., De Haart, L.G.J., Stimming, U., Vinke, I.C., Mogensen, M. (1999). Reaction of CO/CO2 gas mixtures on Ni±YSZ cermet electrodes, *J. Appl. Electrochem*., 29, 561–568.

Holtappels, P. (2013). *Power to Gas (& liquids)*. DTU International Energy Conference 2013, Lyngby, Denmark, 10/09/2013 http://www.natlab.dtu.dk/Energikonferencer/DTU_International_Energy_Conference_2013 (last visited 27/04/2016)

Hosoi, T., Yonekura, T., Sunada, K., and Sasaki, K. (2015). Exchange Current Density of SOFC Electrodes: Theoretical Relations and Partial Pressure Dependencies Rate-Determined by Electrochemical Reactions. *Journal of The Electrochemical Society*, 162(1), F136-F152.

Hou, K., and Hughes, R. (2001). The kinetics of methane steam reforming over a Ni/α-Al 2 O catalyst. *Chemical Engineering Journal*, 82(1), 311-328.

Hsu, C. T., and Cheng, P. (1990). Thermal dispersion in a porous medium. *International Journal of Heat and Mass Transfer*, 33(8), 1587-1597.

Huang B., Qi, Y. , Murshed, M. (2011). Solid oxide fuel cell: Perspective of dynamic modeling and control. *J. Process. Contr.,* 21, 1426–1437.

Hussain, M. M., Li, X., and Dincer, I. (2005). Multi-component mathematical model of solid oxide fuel cell anode. *International Journal of Energy Research*, 29(12), 1083-1101.

Hussain, M. M., Li, X., and Dincer, I. (2009). A general electrolyte–electrode-assembly model for the performance characteristics of planar anode-supported solid oxide fuel cells. *Journal of Power Sources*, 189(2), 916-928.

IEA (2014). *Technology Roadmap: Energy Storage*, OECD/IEA, Paris, France.

IEA (2015). *Technology Roadmap: Hydrogen and Fuel Cells*, OECD/IEA, Paris, France.

IEC (2011). *Electrical Energy Storage: White Paper*. http://www.iec.ch/whitepaper/pdf/iecWP-energystorage-LR-en.pdf (last visited 27/04/2016)

Inage, S. I. (2009). *Prospects for large-scale energy storage in decarbonised power grids*. International Energy Agency, IEA.

Isenberg, A. O. (1981). Energy conversion via solid oxide electrolyte electrochemical cells at high temperatures. *Solid State Ionics*, 3–4, 431–437.

Iwai, H., Shikazono, N., Matsui, T., Teshima, H., Kishimoto, M., Kishida, R., Hayashi, D., Matsuzaki, K., Kanno, D., Saito, M., Muroyama, H., Eguchi, K., Kasagi, N., and Yoshida, H. (2010). Quantification of SOFC anode microstructure based on dual beam FIB-SEM technique. *Journal of Power Sources*, 195(4), 955-961.

Jacobsen, T., and Mogensen, M. (2008). The course of oxygen partial pressure and electric potentials across an oxide electrolyte cell. *Ecs Transactions*, 13(26), 259-273.

Jakobsen, H. A. (2008). *Chemical Reactor Modeling. Multiphase Reactive Flows*, Berlin, Germany: Springer-Verlag.

Janardhanan, V. M., and Deutschmann, O. (2006). CFD analysis of a solid oxide fuel cell with internal reforming: Coupled interactions of transport, heterogeneous catalysis and electrochemical processes. *Journal of Power Sources*, 162(2), 1192-1202.

Janardhanan, V. M., and Deutschmann, O. (2007). Numerical study of mass and heat transport in solid-oxide fuel cells running on humidified methane. *Chemical Engineering Science*, 62(18), 5473-5486.

Janardhanan, V. M., Heuveline, V., and Deutschmann, O. (2008). Three-phase boundary length in solid-oxide fuel cells: A mathematical model. *Journal of Power Sources*, 178(1), 368-372.

Janardhanan, V. M., and Monder, D. S. (2014). Sulfur poisoning of SOFCs: a model based explanation of polarization dependent extent of poisoning. *Journal of The Electrochemical Society*, 161(14), F1427-F1436.

Jang, Y. and Virkar, A., (2003). Fuel Composition and Diluent Effect on Gas Transport and Performance of Anode-Supported SOFCs. *J. Electrochem. Soc*., 150, A942–A951.

Jensen, J. H., Poulsen, J. M., and Andersen, N. U. (2011). From coal to clean energy. *Nitrogen+ syngas*, 310, 34-38.

Jensen, S. H., Larsen, P. H., and Mogensen, M. (2007). Hydrogen and synthetic fuel production from renewable energy sources. *International Journal of Hydrogen Energy*, 32(15), 3253-3257.

Jensen, S. H., Graves, C., Mogensen, M., Wendel, C., Braun, R., Hughes, G., Gao, Z. and Barnett, S. A. (2015). Large-scale electricity storage utilizing reversible solid oxide cells combined with underground storage of CO2 and CH4. *Energy & Environmental Science*, 8(8), 2471-2479.

Jensen, S. H., Sun, X., Ebbesen, S. D., Knibbe, R., and Mogensen, M. (2010). Hydrogen and synthetic fuel production using pressurized solid oxide electrolysis cells. *International journal of hydrogen energy*, 35(18), 9544-9549.

Jentsch, M., Trost, T., and Sterner, M. (2014). Optimal use of power-to-gas energy storage systems in an 85% renewable energy scenario. *Energy Procedia*, 46, 254-261.

Jiang, Y., and Virkar, A. V. (2003). Fuel composition and diluent effect on gas transport and performance of anode-supported SOFCs. *Journal of The Electrochemical Society*, 150(7), A942-A951.

Joos, J., Carraro, T., Weber, A., and Ivers-Tiffée, E. (2011). Reconstruction of porous electrodes by FIB/SEM for detailed microstructure modeling. *Journal of Power Sources*, 196(17), 7302-7307.

Jung, H. Y., Kim, W. S., Choi, S. H., Kim, H. C., Kim, J., Lee, H. W., and Lee, J. H. (2006). Effect of cathode current-collecting layer on unit-cell performance of anode-supported solid oxide fuel cells. *Journal of Power Sources*, 155(2), 145-151.

Kast, W., and Hohenthanner, C. R. (2000). Mass transfer within the gas-phase of porous media. *International Journal of Heat and Mass Transfer*, 43(5), 807-823.

Kemp, I. C. (2011). *Pinch analysis and process integration: a user guide on process integration for the efficient use of energy*. Butterworth-Heinemann.

Kerkhof, P. J. (1996). A modified Maxwell-Stefan model for transport through inert membranes: the binary friction model. *The Chemical Engineering Journal and the Biochemical Engineering Journal*, 64(3), 319-343.

Kharton, V. V., Marques, F. M. B., and Atkinson, A. (2004). Transport properties of solid oxide electrolyte ceramics: a brief review. *Solid State Ionics*, 174(1), 135-149.

Khedim, H., Nonnet, H., and Méar, F. O. (2012). Development and characterization of glass-ceramic sealants in the (CaO–Al 2 O 3–SiO 2–B 2 O 3) system for Solid Oxide Electrolyzer Cells. *Journal of Power Sources*, 216, 227-236.

Kim, T., Liu, G., Boaro, M., Lee, S. I., Vohs, J. M., Gorte, R. J., and Dabbousi, B. O. (2006). A study of carbon formation and prevention in hydrocarbon-fueled SOFC. *Journal of Power Sources*, 155(2), 231-238.

Kim, J. H., Liu, W. K., and Lee, C. (2009). Multi-scale solid oxide fuel cell materials modeling. *Computational Mechanics*, 44(5), 683-703.

Kishimoto, M., Iwai, H., Saito, M., and Yoshida, H. (2011). Quantitative evaluation of solid oxide fuel cell porous anode microstructure based on focused ion beam and scanning electron microscope technique and prediction of anode overpotentials. *Journal of Power Sources*, 196(10), 4555-4563.

Klein, J. M., Bultel, Y., Georges, S., and Pons, M. (2007). Modeling of a SOFC fuelled by methane: from direct internal reforming to gradual internal reforming. *Chemical Engineering Science*, 62(6), 1636-1649.

Knibbe, R., Traulsen, M. L., Hauch, A., Ebbesen, S. D. and Mogensen, M. (2010). Solid oxide electrolysis cells: Degradation at high current densities.*J. Electrochem. Soc*.,157,B1209-B1217.

Koh, J. H., Yoo, Y. S., Park, J. W., and Lim, H. C. (2002). Carbon deposition and cell performance of Ni-YSZ anode support SOFC with methane fuel. *Solid State Ionics*, 149(3), 157-166.

Kong, W., Zhu, H., Fei, Z., and Lin, Z. (2012). A modified dusty gas model in the form of a Fick's model for the prediction of multicomponent mass transport in a solid oxide fuel cell anode. *Journal of Power Sources*, 206, 171-178.

Kötter, E., Schneider, L., Sehnke, F., Ohnmeiss, K., and Schröer, R. (2016). The future electric power system: Impact of Power-to-Gas by interacting with other renewable energy components. *Journal of Energy Storage*.

Krishna, R., and Wesselingh, J. A. (1997). The Maxwell-Stefan approach to mass transfer. *Chemical Engineering Science*, 52(6), 861-911.

Kuramochi, T. (2011). *CO2 capture in industries and distributed systems: possibilities and limitations*. Dissertation. Utrecht University.

Lackner, K. S. (2009). Capture of carbon dioxide from ambient air. *The European Physical Journal Special Topics*, 176(1), 93-106.

Lage, J. L. (1993). Natural convection within a porous medium cavity: predicting tools for flow regime and heat transfer. *International Communications in Heat and Mass Transfer*, 20(4), 501-513.

Laguna-Bercero, M. A., Campana, R., Larrea, A., Kilner, J. A., and Orera, V. M. (2010). Steam electrolysis using a microtubular solid oxide fuel cell. *Journal of The Electrochemical Society*, 157(6), B852-B855.

Laguna-Bercero, M. A., and Orera, V. M. (2011). Micro-spectroscopic study of the degradation of scandia and ceria stabilized zirconia electrolytes in solid oxide electrolysis cells. *International journal of hydrogen energy*, 36(20), 13051-13058.

Laguna-Bercero, M. A., Kilner, J. A., and Skinner, S. J. (2011). Development of oxygen electrodes for reversible solid oxide fuel cells with scandia stabilized zirconia electrolytes. *Solid State Ionics*, 192(1), 501-504.

Lan, R., Irvine, J. T., and Tao, S. (2012). Ammonia and related chemicals as potential indirect hydrogen storage materials. *International journal of hydrogen energy*, 37(2), 1482-1494.

Lanzini, A., Leone, P., and Asinari, P. (2009). Microstructural characterization of solid oxide fuel cell electrodes by image analysis technique. *Journal of Power Sources*, 194(1), 408-422.

Lanzini, A., Leone, P., Guerra, C., Smeacetto, F., Brandon, N. P., and Santarelli, M. (2013). Durability of anode supported Solid Oxides Fuel Cells (SOFC) under direct dry-reforming of methane. *Chemical engineering journal*, 220, 254-263.

Laurencin, J., Kane, D., Delette, G., Deseure, J., and Lefebvre-Joud, F. (2011). Modelling of solid oxide steam electrolyser: Impact of the operating conditions on hydrogen production. *Journal of Power Sources*, 196(4), 2080-2093.

Lee, A. L., Zabransky, R. F., and Huber, W. J. (1990). Internal reforming development for solid oxide fuel cells. *Industrial & Engineering Chemistry Research*, 29(5), 766-773.

Lee, K. T., Vito, N. J., and Wachsman, E. D. (2013a). Comprehensive quantification of Ni–Gd 0.1 Ce 0.9 O 1.95 anode functional layer microstructures by three-dimensional reconstruction using a FIB/SEM dual beam system. *Journal of Power Sources*, 228, 220-228.

Lee, W. Y., Hanna, J., and Ghoniem, A. F. (2013b). On the predictions of carbon deposition on the nickel anode of a SOFC and its impact on open-circuit conditions. *Journal of The Electrochemical Society*, 160(2), F94-F105.

Lefebvre-Joud, M. Petitjean, J.P. Ouweltjes, A. Brisse, J.R. Bowen, J.U. Nielsen (2010). *Analysis of the parameters controlling high temperature steam electrolysis efficiency and durability*, Proc. of 9th European SOFC Forum, Lucerne, 2010.

Lefebvre, J., Götz, M., Bajohr, S., Reimert, R., and Kolb, T. (2015). Improvement of three-phase methanation reactor performance for steady-state and transient operation. Fuel Processing Technology, 132, 83-90.

Lehner, M., Tichler, R., Steinmüller, H., and Koppe, M. (2014). *Power-to-gas: technology and business models* (Vol. 39). Springer.

Lehnert, W., Meusinger, J., and Thom, F. (2000). Modelling of gas transport phenomena in SOFC anodes. *Journal of Power Sources*, 87(1), 57-63.

Leonide, A. (2010). *SOFC Modelling and Parameter Identification by means of Impedance Spectroscopy*. Ph.D. Dissertation, Karlsruher Institut für Technologie.

Li, W., Shi, Y., Luo, Y., Wang, Y., and Cai, N. (2015). Carbon deposition on patterned nickel/yttria stabilized zirconia electrodes for solid oxide fuel cell/solid oxide electrolysis cell modes. *Journal of Power Sources*, 276, 26-31.

Li, Y., Gemmen, R., and Liu, X. (2010). Oxygen reduction and transportation mechanisms in solid oxide fuel cell cathodes. *Journal of Power Sources*, 195(11), 3345-3358.

Lin, Y., Zhan, Z., Liu, J., and Barnett, S. A. (2005). Direct operation of solid oxide fuel cells with methane fuel. *Solid State Ionics*, 176(23), 1827-1835.

Linnhoff, M. (1998). *Introduction to pinch technology*. available from Linnhoff March Ltd, UK.

Maier, L., Schädel, B., Delgado, K. H., Tischer, S., and Deutschmann, O. (2011). Steam reforming of methane over nickel: development of a multi-step surface reaction mechanism. Topics in Catalysis, 54(13-15), 845-858.

Marina, O.A., Pederson, L.R., Williams, M.C., Coffey, G.W., Meinhardt, K.D., Nguyen, C.D., and Thomsen, E.C. (2007). Electrode Performance in Reversible Solid Oxide Fuel Cells. *J. Electrochem. Soc*., 154, B452–B459.

Mason, E.A. and Malinauskas, A.P. (1983). *Gas Transport in Porous Media: The Dusty-Gas Model*. New York: Elsevier. 1-202.

Mathiesen, B. V., Ridjan, I., Connolly, D., Nielsen, M. P., Vang Hendriksen, P., Bjerg Mogensen, M., Jensen, S. H., and Ebbesen, S. D. (2013). *Technology data for high temperature solid oxide electrolyser cells, alkali and PEM electrolysers*. Department of Development and Planning, Aalborg University.

Matsui, T., Kishida, R., Kim, J. Y., Muroyama, H., and Eguchi, K. (2010). Performance deterioration of Ni–YSZ anode induced by electrochemically generated steam in solid oxide fuel cells. *Journal of The Electrochemical Society*, 157(5), B776-B781.

Matsuzaki Y., Yasuda, I. (2000). Electrochemical Oxidation of H2 and CO in a H2 - H2O - CO - CO2 System at the Interface of a Ni-YSZ Cermet Electrode and YSZ Electrolyte. *J. Electrochem. Soc.*, 147, 1630–1635.

Matsuzaki, K., Shikazono, N., and Kasagi, N. (2011). Three-dimensional numerical analysis of mixed ionic and electronic conducting cathode reconstructed by focused ion beam scanning electron microscope. *Journal of Power Sources*, 196(6), 3073-3082.

Menon, V., Janardhanan, V. M., Tischer, S., and Deutschmann, O. (2013). Internal Multi-Physics Phenomena of SOFC with Direct Internal Reforming. *ECS Transactions*, 57(1), 2475-2484.

Menon, V., Janardhanan, V. M., and Deutschmann, O. (2014). A mathematical model to analyze solid oxide electrolyzer cells (SOECs) for hydrogen production. *Chemical Engineering Science*, 110, 83-93.

Menon, V., Fu, Q., Janardhanan, V. M., and Deutschmann, O. (2015). A model-based understanding of solid-oxide electrolysis cells (SOECs) for syngas production by H2O/CO2 co-electrolysis. *Journal of Power Sources*, 274, 768-781.

Mergel, J., Carmo, M. and Fritz, D. (2013). Status on Technologies for Hydrogen Production by Water Electrolysis, in *Transition to Renewable Energy Systems* (eds D. Stolten and V. Scherer), Wiley-VCH Verlag GmbH & Co. KGaA, Weinheim, Germany.

Minh, N. Q., and Mogensen, M. B. (2013). Reversible solid oxide fuel cell technology for green fuel and power production. *Electrochem. Soc. Interface*, 22, 55-62.

Moçoteguy, P. and Brisse, A. (2013). A review and comprehensive analysis of degradation mechanisms of solid oxide electrolysis cells. *International journal of hydrogen energy*, 38(36), 15887-15902.

Modest, M. F. (2013). *Radiative heat transfer*. New York: Academic press, 3rd edition.

Mogensen, D., Grunwaldt, J. D., Hendriksen, P. V., Dam-Johansen, K., and Nielsen, J. U. (2011). Internal steam reforming in solid oxide fuel cells: Status and opportunities of kinetic studies and their impact on modelling. *Journal of power sources*, 196(1), 25-38.

Mogensen, M., Jensen, S. H., Ebbesen, S. D., Hauch, A., Graves, C., Høgh, J. V. T., and Pedersen, A. H. (2012). *Production of "green natural gas" using solid oxide electrolysis cells (SOEC): status of technology and costs.* In 25th World Gas Conference, WGC (pp. 2314-2320).

Moon, H., Kim, S. D., Park, E. W., Hyun, S. H., and Kim, H. S. (2008). Characteristics of SOFC single cells with anode active layer via tape casting and co-firing. *International Journal of Hydrogen Energy*, 33(11), 2826-2833.

Mougin, J. (2015). Hydrogen Production by High-temperature Steam Electrolysis. In: *Compendium of Hydrogen Energy: Hydrogen Production and Purification*, 1, 225. Elsevier.

Mougin, J., Chatroux, A., Couturier, K., Petitjean, M., Reytier, M., Gousseau, G., and Lefebvre-Joud, F. (2012). High temperature steam electrolysis stack with enhanced performance and durability. *Energy Procedia*, 29, 445-454.

Murthy, S., and Fedorov, A. G. (2003). Radiation heat transfer analysis of the monolith type solid oxide fuel cell. *Journal of Power Sources*, 124(2), 453-458.

Mutz, B., Carvalho, H. W., Mangold, S., Kleist, W., and Grunwaldt, J. D. (2015). Methanation of CO2: Structural response of a Ni-based catalyst under fluctuating reaction conditions unraveled by operando spectroscopy. *Journal of Catalysis*, 327, 48-53.

Nagel, F. P., Schildhauer, T. J., Biollaz, S. M., and Stucki, S. (2008). Charge, mass and heat transfer interactions in solid oxide fuel cells operated with different fuel gases—a sensitivity analysis. *Journal of Power Sources*, 184(1), 129-142.

Nam, J. H., and Jeon, D. H. (2006). A comprehensive micro-scale model for transport and reaction in intermediate temperature solid oxide fuel cells. *Electrochimica Acta*, 51(17), 3446-3460.

Narasimhaiah, G., and Janardhanan, V. M. (2013). Modeling CO2 electrolysis in solid oxide electrolysis cell. *Journal of Solid State Electrochemistry*, 17(8), 2361-2370.

Nguyen, V. N., Fang, Q., Packbier, U., and Blum, L. (2013). Long-term tests of a Jülich planar short stack with reversible solid oxide cells in both fuel cell and electrolysis modes. *International Journal of Hydrogen Energy*, 38(11), 4281-4290.

Ni, M., Leung, M.K.H., Leung, D.Y.C. (2006a) A modeling study on concentration overpotentials of a reversible solid oxide fuel cell. *J. Power Sources,* 163, 460–466.

Ni M., Leung, M.K.H., Leung, D.Y.C. (2006b). An Electrochemical Model of a Solid Oxide Steam Electrolyzer for Hydrogen Production. *Chem. Eng. Technol*., 29, 636–642.

Ni, M., Leung, M.K., and Leung, D.Y. (2007). Parametric study of solid oxide fuel cell performance. *Energy Conversion and Management*, 48(5), 1525-1535.

Ni, M. (2009). Computational fluid dynamics modeling of a solid oxide electrolyzer cell for hydrogen production. *International Journal of Hydrogen Energy*, 34(18), 7795-7806.

Ni, M. (2013). Modeling and parametric simulations of solid oxide fuel cells with methane carbon dioxide reforming. *Energy Conversion and Management*, 70, 116-129.

Nield, D. A., and Bejan, A. (2006). Chapter1: Mechanics of Fluid Flow through a Porous medium - *Convection in Porous Media*. New York: Springer, 3rd edition. 1-26.

Njodzefon et al. (2012). *Detailed Study of an Anode Supported Cell in Electrolyzer Mode under Thermo-Neutral Operation*, Proc. of 10th European Fuel Cell Forum, Lucerne, Switzerland, B0713.

Noren, D. A., and Hoffman, M. A. (2005). Clarifying the Butler–Volmer equation and related approximations for calculating activation losses in solid oxide fuel cell models. *Journal of Power Sources*, 152, 175-181.

Novaresio, V., García-Camprubí, M., Izquierdo, S., Asinari, P., and Fueyo, N. (2012). An open-source library for the numerical modeling of mass-transfer in solid oxide fuel cells. *Computer Physics Communications*, 183(1), 125-146.

O'Brien, J. S., and Giorgi, J. B. (2012). Solid oxide fuel cell with NiCo–YSZ cermet anode for oxidation of CO/H2 fuel mixtures. *Journal of Power Sources*, 200, 14-20.

O'Brien, J. E., Zhang, X., Housley, G. K., DeWall, K., Moore-McAteer, L., and Tao, G. (2012). *High temperature electrolysis pressurized experiment design, operation, and results*. Report for US Department of Energy Office of Nuclear Energy Under DOE Idaho Operations Office Contract DE-AC07-05ID14517.

Papurello, D., Lanzini, A., Leone, P., Santarelli, M., and Silvestri, S. (2014). Biogas from the organic fraction of municipal solid waste: Dealing with contaminants for a solid oxide fuel cell energy generator. *Waste Management*, 34(11), 2047-2056.

Papurello, D., Lanzini, A., Fiorilli, S., Smeacetto, F., Singh, R., and Santarelli, M. (2016). Sulfur poisoning in Ni-anode solid oxide fuel cells (SOFCs): Deactivation in single cells and a stack. *Chemical Engineering Journal*, 283, 1224-1233.

Park, E. W., Moon, H., Park, M. S., and Hyun, S. H. (2009). Fabrication and characterization of Cu–Ni–YSZ SOFC anodes for direct use of methane via Cu-electroplating. *International Journal of Hydrogen Energy*, 34(13), 5537-5545.

Petipas, F., Fu, Q., Brisse, A., and Bouallou, C., (2013). Transient operation of a solid oxide electrolysis cell. *International Journal of Hydrogen Energy*, 38, 2957-2964.

Petruzzi, L., Cocchi, S., Fineschi, F. (2003). A global thermo-electrochemical model for SOFC systems design and engineering. *J. Power Sources*, 118, 96–107.

Poling, B. E., Prausnitz, J. M., and O'connell, J. P. (2001). *The properties of gases and liquids* (Vol. 5). New York: McGraw-Hill.

Pollard, W. G., and Present, R. D. (1948). On gaseous self-diffusion in long capillary tubes. *Physical Review*, 73(7), 762.

Posdziech, O. *Development of High-Temperature Electrolysers for Renewable Electricity Storage*, Hydrogen Days Prague 2015. http://www.hydrogendays.cz/2015/presentations (last visited 27/04/16).

Pozzo, M., Lanzini, A., and Santarelli, M. (2015). Enhanced biomass-to-liquid (BTL) conversion process through high temperature co-electrolysis in a solid oxide electrolysis cell (SOEC). *Fuel*, 145, 39-49.

Qadrdan, M., Abeysekera, M., Chaudry, M., Wu, J., and Jenkins, N. (2015). Role of power-to-gas in an integrated gas and electricity system in Great Britain. *International Journal of Hydrogen Energy*, 40(17), 5763-5775.

Ramachandran, R., and Menon, R. K. (1998). An overview of industrial uses of hydrogen. *International Journal of Hydrogen Energy*, 23(7), 593-598.

Ramshaw, J. D. (1990). Self-consistent effective binary diffusion in multicomponent gas mixtures. *Journal of Non-Equilibrium Thermodynamics*, 15(3), 295-300.

Rostrup-Nielsen, J. R., Hansen, J. B., Helveg, S., Christiansen, N., and Jannasch, A. K. (2006). Sites for catalysis and electrochemistry in solid oxide fuel cell (SOFC) anode. *Applied Physics A*, 85(4), 427-430.

Sanchez, D., Chacartegui, R., Munoz, A., and Sanchez, T. (2006). Thermal and electrochemical model of internal reforming solid oxide fuel cells with tubular geometry, *J. Power Sources*, 160, 1074–1087.

Sánchez, D., Munoz, A., and Sánchez, T. (2007). An assessment on convective and radiative heat transfer modelling in tubular solid oxide fuel cells. *Journal of Power Sources*, 169(1), 25-34.

Sanchez, D., Chacartegui, R., Munoz, A., and Sanchez, T. (2008). On the effect of methane internal reforming modelling in solid oxide fuel cells. *International Journal of Hydrogen Energy*, 33(7), 1834-1844.

Santarelli, M., Quesito, F., Novaresio, V., Guerra, C., Lanzini, A., and Beretta, D. (2013). Direct reforming of biogas on Ni-based SOFC anodes: Modelling of heterogeneous reactions and validation with experiments. *Journal of Power Sources*, 242, 405-414.

Sasaki, K., and Teraoka, Y. (2003). Equilibria in fuel cell gases I. Equilibrium compositions and reforming conditions. *Journal of The Electrochemical Society*, 150(7), A878-A884.

Saunders, G. J., Preece, J., and Kendall, K. (2004). Formulating liquid hydrocarbon fuels for SOFCs. *Journal of Power Sources*, 131(1), 23-26.

Schaub, G., Eilers, H. and González, M. I. (2013). Chemical Storage of Renewable Electricity via Hydrogen – Principles and Hydrocarbon Fuels as an Example, in *Transition to Renewable Energy Systems* (eds D. Stolten and V. Scherer), Wiley-VCH Verlag GmbH & Co. KGaA, Weinheim, Germany.

Schefold, J., Brisse, A., Proc. of 11th European Fuel Cell Forum, Lucerne, Switzerland, B1302 (2014).

Schiebahn, S., Grube, T., Robinius, M., Zhao, L., Otto, A., Kumar, B., Weber, M. and Stolten, D. (2013). Power to Gas, in *Transition to Renewable Energy Systems* (eds D. Stolten and V. Scherer), Wiley-VCH Verlag GmbH & Co. KGaA, Weinheim, Germany.

Schiebahn, S., Grube, T., Robinius, M., Tietze, V., Kumar, B., and Stolten, D. (2015). Power to gas: Technological overview, systems analysis and economic assessment for a case study in Germany. *International Journal of Hydrogen Energy*, 40(12), 4285-4294.

Schill, W. P. (2014). Residual load, renewable surplus generation and storage requirements in Germany. *Energy Policy*, 73, 65-79.

Schiller, G., Ansar, A., Lang, M., and Patz, O. (2009). High temperature water electrolysis using metal supported solid oxide electrolyser cells (SOEC). *Journal of Applied Electrochemistry*, 39(2), 293-301.

Schimanke, D., Walter, C. (2014). Proc. of 11th European Fuel Cell Forum, Lucerne, Switzerland, A0804.

Shi, Y., Cai, N., and Li, C. (2007). Numerical modeling of an anode-supported SOFC button cell considering anodic surface diffusion. *Journal of Power Sources*, 164(2), 639-648.

Shi, Y., Li, C., and Cai, N. (2011a). Experimental characterization and mechanistic modeling of carbon monoxide fueled solid oxide fuel cell. *Journal of Power Sources*, 196(13), 5526-5537.

Shi, Y., Wang, H., Cai, N. (2011b). Simulation of Two-Dimensional Electrochemical Impedance Spectra of Solid Oxide Fuel Cells Using Transient Physical Models, *ECS Trans*. 35, 871–881.

Smeacetto, F., De Miranda, A., Polo, S. C., Molin, S., Boccaccini, D., Salvo, M., and Boccaccini, A. R. (2015). Electrophoretic deposition of Mn 1.5 Co 1.5 O 4 on metallic interconnect and interaction with glass-ceramic sealant for solid oxide fuel cells application. *Journal of Power Sources*, 280, 379-386.

SNAM Rete Gas (2016). *Codice di rete – Allegato 11/A*. http://www.snaretegas.it/it/servizi/Codice_di_rete/Aree/codice_rete.html (last visited 27/04/16).

Snoeck, J. W., Froment, G. F., and Fowles, M. (1997). Filamentous carbon formation and gasification: thermodynamics, driving force, nucleation, and steady-state growth. *Journal of Catalysis*, 169(1), 240-249.

Snoeck, J. W., Froment, G. F., and Fowles, M. (2002). Steam/CO2 reforming of methane. Carbon filament formation by the Boudouard reaction and gasification by CO2, by H2, and by steam: kinetic study. *Industrial & engineering chemistry research*, 41(17), 4252-4265.

Socolow, R., Desmond, M., Aines, R., Blackstock, J., Bolland, O., Kaarsberg, T., and Siirola, J. (2011). *Direct air capture of CO2 with chemicals: a technology assessment for the APS Panel on Public Affairs* (No. EPFL-BOOK-200555). American Physical Society.

Sørensen, B., Petersen, A. H., Juhl, C., Ravn, H., Søndergren, C., Simonsen, P., and Schleisner, L. (2004). Hydrogen as an energy carrier: scenarios for future use of hydrogen in the Danish energy system. *International Journal of Hydrogen Energy*, 29(1), 23-32.

Spotorno, R., Piccardo, P., Perrozzi, F., Valente, S., Viviani, M., and Ansar, A. (2015). Microstructural and Electrical Characterization of Plasma Sprayed Cu-Mn Oxide Spinels as Coating on Metallic Interconnects for Stacking Solid Oxide Fuel Cells. *Fuel Cells*, 15(5), 728-734.

Steinmüller, H., R. Tichler, and G. Reiter. "*Power-to-Gas–eine Systemanalyse*." Markt-und Technologiescouting und–analyse. Energieinstitut an der Johannes Kepler Universität Linz, TU Wien, MU Leoben, JKU Linz (2014)

Sterner, M., Jentsch, M., Holzhammer, U. (2011a) *Energiewirtschaftliche und ökologische Bewertung eines Windgas-Angebotes*. Fraunhofer IWES, Kassel.

Sterner M. et al. (2011b). *Renewable (power to) methane: Storing renewables by linking power and gas grids.* Fraunhofer ISE,ZSW, Solarfuel.

Stolten, D., Emonts, B., and Grube, T. (2013). Hydrogen as an Enabler for Renewable Energies, in *Transition to Renewable Energy Systems*, D. Stolten and V. Scherer, Eds. Weinheim, Germany: Wiley-WCH, pp. 195–215.

Stoots, C. M., O'Brien, J. E., Condie, K. G., and Hartvigsen, J. J. (2010). High-temperature electrolysis for large-scale hydrogen production from nuclear energy–experimental investigations. *International Journal of Hydrogen Energy*, 35(10), 4861-4870.

Sumi, H., Kishida, R., Kim, J. Y., Muroyama, H., Matsui, T., and Eguchi, K. (2010). Correlation between microstructural and electrochemical characteristics during redox cycles for Ni–YSZ anode of SOFCs. *Journal of The Electrochemical Society*, 157(12), B1747-B1752.

Sumi, H., Puengjinda, P., Muroyama, H., Matsui, T., and Eguchi, K. (2011). Effects of crystal Structure of yttria-and scandia-stabilized zirconia in nickel-based SOFC anodes on carbon deposition and oxidation behavior. *Journal of Power Sources*, 196(15), 6048-6054.

Suwanwarangkul, R., Croiset, E., Fowler, M. W., Douglas, P. L., Entchev, E., and Douglas, M. A. (2003). Performance comparison of Fick's, dusty-gas and Stefan–Maxwell models to predict the concentration overpotential of a SOFC anode. *Journal of Power Sources*, 122(1), 9-18.

Suwanwarangkul, R., Croiset, E., Entchev, E., Charojrochkul, S., Pritzkera, M.D., Fowler, M.W., Douglas, P.L., Chewathanakup, S., and Mahaudom, H., (2006) Experimental and modeling study of solid oxide fuel cell operating with syngas fuel. *J. Power Sources*, 161, 308–322.

Svensson, A. M., Sunde, S., Nişancioğlu, K. (1998).Mathematical Modeling of Oxygen Exchange and Transport in Air-Perovskite-Yttria-Stabilized Zirconia Interface Regions. *J. Electrochem. Soc.*, 145, 1390-1400.

Szymczewska, D., Molin, S., Venkatachalam, V., Chen, M., Jasinski, P., and Hendriksen, P. V. (2016). Assesment of (Mn, Co) 33O4 powders for possible coating material for SOFC/SOEC interconnects. In IOP Conference Series: *Materials Science and Engineering* (Vol. 104, No. 1, p. 012017). IOP Publishing.

Takeguchi, T., Kani, Y., Yano, T., Kikuchi, R., Eguchi, K., Tsujimoto, K., and Aizawa, M. (2002). Study on steam reforming of CH4 and C2 hydrocarbons and carbon deposition on Ni-YSZ cermets. *Journal of Power Sources*, 112(2), 588-595.

Tanabe, K., Anderson, J. R., and Boudart, M. (1981). *Catalysis Science and Technology*. Springer-Verlag, New York, 231(9).

Tang, E., Wood, T., Benhaddad, S., Brown, C., He, H., Nelson, J., and Petri, R. (2012). *Advanced Materials for RSOFC Dual Operation with Low Degradation*. No. DOE/EE0000464. Versa Power Systems, Inc., Littleton, CO, 2012.

Tao, Y., Ebbesen, S. D., and Mogensen, M. B. (2014a). Carbon deposition in solid oxide cells during co-electrolysis of H2O and CO2. *Journal of The Electrochemical Society*, 161(3), F337-F343.

Tao, Y., Ebbesen, S. D., Zhang, W., and Mogensen, M. B. (2014b). Carbon nanotube growth on nanozirconia under strong cathodic polarization in steam and carbon dioxide. *ChemCatChem*, 6(5), 1220-1224.

Trost, T., Horn, S., Jentsch, M., and Sterner, M. (2012). *Erneuerbares Methan: Analyse der CO2-Potenziale für Power-to-Gas Anlagen in Deutschland*. Zeitschrift für Energiewirtschaft, 36(3), 173-190.

Tseronis, K., Kookos, I. K., and Theodoropoulos, C. (2008). Modelling mass transport in solid oxide fuel cell anodes: a case for a multidimensional dusty gas-based model. *Chemical Engineering Science*, 63(23), 5626-5638.

Tsupari, E., Kärki, J., and Vakkilainen, E. (2016). Economic feasibility of power-to-gas integrated with biomass fired CHP plant. *Journal of Energy Storage*, 5, 62-69.

Vakouftsi, E., Marnellos, G. E., Athanasiou, C., and Coutelieris, F. (2011). CFD modeling of a biogas fuelled SOFC. *Solid State Ionics*, 192(1), 458-463.

Varone, A., and Ferrari, M. (2015). Power to liquid and power to gas: an option for the German Energiewende. *Renewable and Sustainable Energy Reviews*, 45, 207-218.

Veldsink, J. W., Van Damme, R. M. J., Versteeg, G. F., and Van Swaaij, W. P. M. (1995). The use of the dusty-gas model for the description of mass transport with chemical reaction in porous media. *The Chemical Engineering Journal and the Biochemical Engineering Journal*, 57(2), 115-125.

Virkar, A. V. (2010). Mechanism of oxygen electrode delamination in solid oxide electrolyzer cells. *International Journal of Hydrogen Energy*, 35(18), 9527-9543.

Vivet N., S. Chupin, E. Estrade, A. Richard, S. Bonnamy, D. Rochais and E. Bruneton (2011). Effect of Ni content in SOFC Ni-YSZ cermets: A three-dimensional study by FIB-SEM tomography. *J. Power Sources*, 196, 9989–9997.

Walker, S. B., Mukherjee, U., Fowler, M., and Elkamel, A. (2015). Benchmarking and selection of Power-to-Gas utilizing electrolytic hydrogen as an energy storage alternative. *International Journal of Hydrogen Energy*.

Walters, K. M., Dean, A. M., Zhu, H., and Kee, R. J. (2003). Homogeneous kinetics and equilibrium predictions of coking propensity in the anode channels of direct oxidation solid-oxide fuel cells using dry natural gas. *Journal of Power Sources*, 123(2), 182-189.

Wang, H., Shi, Y., and Cai, N. (2011). Numerical Simulation of Multi-Channel Planar Solid Oxide Fuel Cell Unit by Integrating Continuum Micro-Scale PEN Sub-Model. *ECS Trans.,* 35, 1065–1075.

Wang, K., Hissel, D., Péra, M. C., Steiner, N., Marra, D., Sorrentino, M., Pianese, C., Monteverde, M., Cardone, P., and Saarinen, J. (2011). A review on solid oxide fuel cell models. *International Journal of Hydrogen Energy*, 36(12), 7212-7228.

Wang, S., Worek, W. M., and Minkowycz, W. J. (2012). Performance comparison of the mass transfer models with internal reforming for solid oxide fuel cell anodes. *International Journal of Heat and Mass Transfer*, 55(15), 3933-3945.

Wang, Y., Yoshiba, F., Watanabe, T., and Weng, S. (2007). Numerical analysis of electrochemical characteristics and heat/species transport for planar porous-electrode-supported SOFC. *J. Power Sources*, 170, 101–110.

Wang, Y., Yoshiba, F., Kawase, M., and Watanabe, T. (2009). Performance and effective kinetic models of methane steam reforming over Ni/YSZ anode of planar SOFC. *International Journal of Hydrogen Energy*, 34(9), 3885-3893.

Wang, Y., Weng, S., and Weng, Y. (2011). Numerical investigation of the chemical and electrochemical characteristics of planar solid oxide fuel cell with direct internal reforming. *Frontiers in Energy*, 5(2), 195-206.

Webb, S. W., and Pruess, K. (2003). The use of Fick's law for modeling trace gas diffusion in porous media. *Transport in Porous Media*, 51(3), 327-341.

Weber E. (2013). *Energy Storage Technologies on the Way to the Global Market*, 8th Internat. Renewable Energy Storage Conference IRES 2013, Fraunhofer ISE.

Weissbart, J., and W. H. Smart (1967). *Study of electrolytic dissociation of CO2-H2O using a solid oxide electrolyte*. NASA CR-680." NASA contractor report. NASA CR. United States. National Aeronautics and Space Administration (1967): 1.

Welty, J. R., Wicks, C. E., Rorrer, G., and Wilson, R. E. (2001). *Fundamentals of momentum, heat, and mass transfer*. New York: John Wiley & Sons, 4th edition.

Wendel, C. H., Kazempoor, P., and Braun, R. J. (2015a). Novel electrical energy storage system based on reversible solid oxide cells: System design and operating conditions. *Journal of Power Sources*, 276, 133-144.

Wendel, C. H., Gao, Z., Barnett, S. A., and Braun, R. J. (2015b). Modeling and experimental performance of an intermediate temperature reversible solid oxide cell for high-efficiency, distributed-scale electrical energy storage. *Journal of power sources*, 283, 329-342.

Wilke, C. R. (1950a). A viscosity equation for gas mixtures. *The Journal of Chemical Physics*, 18(4), 517-519.

Wilke, C.R. (1950b). Diffusional Properties of Multicomponent Gases. *Chemical Engineering Progress*, 46, 95-104.

Wilson, J. R., Cronin, J. S., and Barnett, S. A. (2011). Linking the microstructure, performance and durability of Ni-yttria-stabilized zirconia solid oxide fuel cell anodes using three-dimensional focused ion beam–scanning electron microscopy imaging. *Scripta Materialia*, 65(2), 67-72.

Wilson, J., Kobsiriphat, W., Mendoza, R., Chen, H. Y., Hines, T., Hiller, J., and Mumm, D. R. (2007). Three dimensional reconstruction of solid oxide fuel cell electrodes using focused ion beam-scanning electron microscopy. *ECS Transactions*, 7(1), 1879-1887.

Winkler-Goldstein, R., and Rastetter, A. (2013). Power to gas: the final breakthrough for the hydrogen economy?. *Green*, 3(1), 69-78.

Wonsyld K., Bech, L., Nielsen, J. U., and Pedersen, C. F. (2014). *Operational Robustness Studies of Solid Oxide Electrolysis Stacks*, Proc. of 11th European Fuel Cell Forum, Lucerne, Switzerland, B1306.

Wu, J., and Liu, X. (2010). Recent development of SOFC metallic interconnect. *Journal of materials science & technology*, 26(4), 293-305.

Wu, W., Wang, G. L., Guan, W. B., Zhen, Y. F., and Wang, W. G. (2013). Effect of contact method between interconnects and electrodes on area specific resistance in planar solid oxide fuel cells. *Fuel Cells*, 13(5), 743-750.

WWEA (World Wind Energy Association) 2014. *WWEC2014: Key Statistics of World Wind Energy Report published*. http://www.wwindea.org/wwec2014-key-statistics-of-world-wind-energy-report-published/ (last visited 27/04/16).

Xu, J., and Froment, G. F. (1989). Methane steam reforming, methanation and water-gas shift: I. Intrinsic kinetics. *AIChE Journal*, 35(1), 88-96.

Yakabe, H., Hishinuma, M., Uratani, M., Matsuzaki, Y., and Yasuda, I. (2000). Evaluation and modeling of performance of anode-supported solid oxide fuel cell. *Journal of Power Sources*, 86(1), 423-431.

Yakabe, H., Ogiwara, T., Hishinuma, M., and Yasuda, I. (2001). 3-D model calculation for planar SOFC. *Journal of Power Sources*, 102(1), 144-154.

Yan, X. L., and Hino, R. (Eds.). (2011). *Nuclear hydrogen production handbook*. CRC Press.

Yan, M., Zeng, M., Chen, Q., and Wang, Q. (2012). Numerical study on carbon deposition of SOFC with unsteady state variation of porosity. *Applied Energy*, 97, 754-762.

Yue, X. (2013). *The development of alternative cathodes for high temperature solid oxide electrolysis cells.* Dissertation. University of St Andrews.

Yurkiv, V. (2014). Reformate-operated SOFC anode performance and degradation considering solid carbon formation: A modeling and simulation study. *Electrochimica Acta*, 143, 114-128.

Zavarukhin, S. G., and Kuvshinov, G. G. (2004). The kinetic model of formation of nanofibrous carbon from CH4–H2 mixture over a high-loaded nickel catalyst with consideration for the catalyst deactivation. *Applied Catalysis A: General*, 272(1), 219-227.

Zhan, Z., and Barnett, S. A. (2006). Operation of ceria-electrolyte solid oxide fuel cells on iso-octane–air fuel mixtures. *Journal of power sources*, 157(1), 422-429.

Zhan, Z., Kobsiriphat, W., Wilson, J. R., Pillai, M., Kim, I., and Barnett, S. A. (2009). Syngas production by coelectrolysis of CO2/H2O: the basis for a renewable energy cycle. *Energy & Fuels*, 23(6), 3089-3096.

Zheng, K., Sun, Q., Ni, M. (2013). Local Non-Equilibrium Thermal Effects in Solid Oxide Fuel Cells with Various Fuels. *Energy Technology*, 1(1), 35-41.

Zhu, H., and Kee, R. J. (2003). A general mathematical model for analyzing the performance of fuel-cell membrane-electrode assemblies. *Journal of Power Sources*, 117(1), 61-74.

Zhu, H., Kee, R. J., Janardhanan, V. M., Deutschmann, O., and Goodwin, D. G. (2005). Modeling elementary heterogeneous chemistry and electrochemistry in solid-oxide fuel cells. *Journal of the Electrochemical Society*, 152(12), A2427-A2440.

Zhu, H., and Kee, R. J. (2008). Modeling distributed charge-transfer processes in SOFC membrane electrode assemblies. *Journal of the Electrochemical Society*, 155(7), B715-B729.

Zoulias, E., Varkaraki, E., Lymberopoulos, N., Christodoulou, C. N., and Karagiorgis, G. N. (2004). A review on water electrolysis. *TCJST*, 4(2), 41-71.